Functional morphology of the hominin knee: locomotor signals in the trabecular structure of the distal femur and proximal tibia in extant and extinct hominoids

by

Andrea Lukova

School of Anthropology and Conservation

University of Kent

Contents

ACKNOWLEGEMENT

I would like to extend my sincere gratitude to my supervisors, Matt Skinner and Tracy Kivell. Your unwavering support, encouragement, patience, and flexibility were instrumental in helping me complete my PhD journey and have undoubtedly contributed to my growth as a scientist. Being part of your incredible and supportive team, with research that has continuously inspired me, has been an immense privilege. I am also deeply thankful to all the members of the Kivell/Skinner lab group. Your lively discussions, constructive criticism, and camaraderie have not only enriched my academic experience but also made it truly enjoyable. Special thanks to Chris Dunmore, Marine Cazenave and Zewdi Tsegai for their invaluable technical training and insightful discussions, and to Samar Seyda for her empathy and encouragement, which have been a source of strength during challenging times. Furthermore, I am indebted to my parents, Barbora Lukova and Martin Luka, as well as my sister Adela Krejcova and my grandmother Jarmila Cihlarova, for their unwavering support throughout my PhD journey, despite being miles away. Your constant presence and encouragement have meant the world to me. Lastly, I want to express my heartfelt appreciation to my partner, Maja Cvetkovska. Your patience, love, and positive attitude have been my rock throughout this journey, making the difficult moments more bearable and the joyful ones even sweeter. Together, all of you have played an indispensable role in shaping my academic and personal growth during my PhD, and for that, I am profoundly grateful.

For access to specimens in their collections I thank the following individuals/institutions: Max Planck Institute for Evolutionary Anthropology (C. Boesch, J-J. Hublin); Museum für Naturkunde - Leibniz Institute for Evolution and Biodiversity Science (F. Mayer, C. Funk, K. Mahlow); Powell-Cotton Museum (I. Livne); Johann-Friedrich-Blumenback-Institute for Zoology and Anthropology; Georg-August University, Goettingen (B. Grosskopf); Bavarian State Collection for Zoology (A. H. van Heteren); Mary Rose Trust (A. Miles); Royal Museum for Central Africa (E. Gilissen); University of Florence (J. Moggi-Cecchi, S. Bortoluzzi); Frankfurt Senckenberg Museum (V. Volpato); University of the Witswatersand (L. Berger, B. Zipfel).

This project has received funding from the European Research Council (ERC) under the European Union's Horizon 2020 research and innovation programme (grant agreement No. 819960).

LIST OF FIGURES

Main figures

Number of the OrthoSlize taken for the position of the cross-sections is 501 (distal view) and 745 (anterior view) and it was visualized in Avizo.

Figure 2.2: External and internal bone preservation of distal femur of *Australopithecus africanus* TM 1513 in anterior, distal, and posterior view. L, lateral; M, medial. Number of the OrthoSlize taken for the position of the cross-sections is 573 (distal view) and 677 (anterior view) and it was visualized in Avizo.

Figure 2.3: External and internal bone preservation of distal femur of *Australopithecus sediba* U.W. 88-63 in anterior, distal, and posterior view. L, lateral; M, medial. Number of the OrthoSlize taken for the position of the cross-sections is 317 and 219 (distal views) and 388 (anterior view) it was visualized in Avizo.

Figure 2.4: External and internal bone preservation of distal femur of *Homo floresiensis* LB1-8 in anterior, distal, and posterior view. L, lateral; M, medial. Vertical line shows where the cross-section in anterior view is positioned. Number of the OrthoSlize taken for the position of the cross-sections is 621 (distal view) and 744 (anterior view) and it was visualized in Avizo.

Figure 2.5: External and internal bone preservation of distal femur of *Homo floresiensis* LB1-9 in anterior, distal, and posterior view. L, lateral; M, medial. Vertical lines show where the cross-sections in the distal and posterior views are positioned. Number of the OrthoSlize taken for the position of the cross-sections 1629 (distal view) is (distal view) and 636 (posterior view) and it was visualized in Avizo.

Figure 2.6: External and internal bone preservation of proximal tibia of *Homo floresiensis* LB1-13 in anterior, posterior, lateral, and medial view. L, lateral; M, medial. Vertical lines show where the cross-section in the anterior view is positioned. Number of the OrthoSlize taken for the position of the cross-sections is 728 (anterior view), 892 (medial view), and 1580 (proximal view) and it was visualized in Avizo.

Figure 2.7: External and internal bone preservation of proximal tibia of *Homo floresiensis* LB8-1 in anterior, posterior, lateral, and medial view. L, lateral; M, medial. Vertical lines show where the cross-section in the anterior and medial views are positioned. Number of the OrthoSlize taken for the position of the cross-sections is 706 (medial view), 452 (posterior view), and 1582 (superior view) and it was visualized in Avizo.

Figure 2.8: External and internal bone preservation of distal femur of *Homo neanderthalensis* D322-15 in anterior, distal, and posterior view. L, lateral; M, medial. Number of the OrthoSlize

taken for the position of the cross-sections is 842 (distal view) and 1012 (anterior view) and it was visualized in Avizo.

Figure 2.9: Example of image orientation steps on a right *Pan* femur and tibia. (A) Anatomical orientation of the femur from various views. (B) The transformation matrix used to achieve the femur orientation. C) The size of the final volume image of the femur after it is cropped for faster processing. (D) Anatomical orientation of the tibia from various views. (E) The transformation matrix used to achieve the tibia orientation. F) The size of the final volume image of the tibia after it is cropped for faster processing.

Figure 2.10: Segmentation of the human distal femur by MIA.

Figure 2.11: Workflow of Medtool processing steps for distal human femur. A) Original mictro-CT scan; B) MIA segmentation; C) Close filter output; D) OuterMask; E) InnerMask; F) ThickMask; G) MaskSegIn; H) MaskSegOut; I) MaskSeg; J) finit element model of the cortical (yellow) and trabecular (pink) area; K) BV/TV representation.

Figure 2.12: Workflow of cHMA processing steps for distal human femur. A) Outer canonical atlas representing sample's mean size, position, and external right distal femur morphology; B) inner mesh representing rBV/TV distribution in whole human sample; C) an example of 2D PCA conducted on cHMA data; D) an example of 3D PCA conducted on cHMA data; E) an example of PCA loadings visualisation.

Figure 3.1: a) Surface of the studied distal tibia region (anterior view); b) unsegmented (raw) and overlapping segmented high-resolution scan (in distal view) with voxel size of 30 µm used as the baseline scan; c) serial unsegmented and overlapping segmented images of the same distal tibia (in distal view) scanned under the lower resolution with four different voxel sizes of 45, 60, 90 and 110 µm; d) the baseline scan downsampled to voxel size of 60, 90, 120, 150, 180 and 210 µm.

Figure 3.2: Workflow of Medtool processing steps (posterior view). A) Original micro-CT scan; B) Results of the MIA binary segmentation process; C) OuterMask; D) InnerMask; E) ThickMask; F) MaskSegIn; G) MaskSegOut; H) MaskSeg; I) finite element model of the cortical (pink) and trabecular (blue) area; J) BV/TV representation.

Figure 3.3: a) Boxplots of the grid BV/TV values for each voxel size for the baseline scan (red), the downsampled data (yellow) and for the specimen scanned at different resolution (blue); b) histogram of the grid BV/TV values for each voxel size for the baseline scan (red

line) and the downsampled data; c) histogram of the grid BV/TV values for each voxel size for the baseline scan (red line) and for the specimen scanned at different resolution.

Figure 3.4: Distal tibia model of BV/TV distribution of tested *Gorilla* individual for baseline scan (a), downsampled voxel sizes of 90, 150, and 210 µm (b), and scan voxel sizes of 45 – 110 µm (c). Vertical lines through the medial view show where the slices are positions for the cross-section mid-coronal view. Dark red represents the highest and dark blue the lowest BV/TV values. All colourmaps were scaled to baseline scan data range.

Figure 3.5: a) Boxplots of the grid DA values for each voxel size for the baseline scan (red), the downsampled data (yellow) and for the specimen scanned at the different resolution (blue); b) histogram of the grid DA01 values for each voxel size for the baseline scan (red line) and the downsampled data; c) histogram of the grid DA01 values for each voxel size for the baseline scan (red line) and for the specimen scanned at different resolution.

Figure 3.6: Distal tibia model of DA distribution of tested *Gorilla* individual for baseline scan (a), downsampled voxel sizes of 90, 150, and 210 µm (b), and scan voxel sizes of 45 – 110 µm (c). Vertical lines through the medial view show where the slices are positions for the cross-section mid-coronal view. Dark red represents the highest and dark blue the lowest DA values. All colourmaps were scaled to baseline scan data range.

Figure 3.7: Boxplots of the grid Tb.Th (a.), Tb.Sp (b.), and Tb.N (c.) values for each voxel size for the baseline scan (red), the downsampled data (yellow) and for the specimen scanned at the different resolution (blue).

Figure 4.1: (A) Ligament attachments of the knee showing in inferior view. Gold, anterior cruciate ligament; blue, posterior cruciate ligament; green, lateral collateral ligament; red, medial collateral ligament; brown, lateral meniscus; purple, medial meniscus. The medial collateral ligament inserts at the medial epicondyle of the femur and attaches along the medial border of the tibial plateau and on the medial surface of the tibial shaft. The lateral collateral ligament inserts on the lateral femoral epicondyle and attaches on the head of fibula. (B) Anterior cruciate ligament position during forward tibia and backward femur movements. (C) Posterior cruciate ligament position during backward tibia and forward femur movements. Cruciate ligaments position during (D) neutral knee position; (E) medial knee rotation; (F) lateral knee rotation. The anterior cruciate ligament arises from the anterior intercondylar space on the tibial plateau, runs upwards and posteriorly and attaches on the inside of the lateral condyle of the femur. The posterior cruciate ligament arises from well back on the posterior

intercondylar space, runs upwards and anteriorly and attaches on the inside of the medial condyle. (G) Surface models of right distal femur of *Homo*, *Gorilla*, *Pan* and *Pongo*. (G) Showing more elliptical shape of lateral condyle, square outline of distal surface and high lateral lip in humans compared to great apes.

Figure 4.2: Processing steps of distal femur of a *Homo* specimen showing in inferior view. A) Original high-res micro-CT image. B) Micro-CT image segmented by MIA (Dunmore et al., 2018). C) MaskSeg defined by Medtool (Pahr & Zysset, 2009) showing the distinction between inner trabecular area and outer cortex. D) Outer canonical atlas representing sample's mean size, position, and external right distal femur morphology computed by cHMA (Bachmann et al., 2022). E) Inner mesh representing rBV/TV distribution in human sample computed by cHMA (Bachmann, et al., 2022).

Figure 4.3: Species mean models of rBV/TV distribution in the patellar articular surface and femoral condyles of the distal femur of *Homo, Gorilla, Pan,* and *Pongo*. Vertical lines through the inferior view mean models show where the slices are positioned. Cross sections were positioned in the middle of lateral and medial condyle. (A) Showing approximate patellar and condyle position during flexed (90°) and extended knee position in humans in medial view; (B) showing approximate condyle position during flexed and extended knee position in great apes. L, lateral; M, medial.

Figure 4.4: Species mean models of rBV/TV distribution under the presumed insertion of cruciate ligaments of the distal femur of *Homo, Gorilla*, *Pan,* and *Pongo*. Vertical lines through the medial and lateral mean models show where the slices are positioned. Cross sections were positioned in the middle of presumed insertions of cruciate ligaments. Knee model shows anterior cruciate ligaments during neutral knee position in the anterior view.

Figure 4.5: Species mean models of rBV/TV distribution under the presumed insertions of collateral ligaments of the distal femur of *Homo, Gorilla*, *Pan*, and *Pongo*. Vertical lines through the medial and lateral mean models show where the slices are positioned. Cross sections were positioned in the middle of presumed insertions of collateral ligaments. Knee model shows lateral collateral ligaments attachments. L, lateral; M, medial.

Figure 4.6: Species mean models of rBV/TV distribution under the presumed gastrocnemius muscle attachments of the distal femur of *Homo, Gorilla*, *Pan*, and *Pongo*. Vertical lines through the posterior mean models show where the slices are positioned. Cross sections were

positioned in the middle of presumed gastrocnemius attachments. Lower limb model shows gastrocnemius attachments. L, lateral; M, medial.

Figure 4.7: Species mean models of DA distribution in the patellar articular surface (marked with square) and in the presumed insertions of gastrocnemius muscle attachments (marked with circle) of the distal femur of *Homo*, *Gorilla*, *Pan*, and *Pongo*. Vertical lines through the inferior view mean models show where the slices are positioned. Cross sections were positioned in the middle of lateral and medial condyle. L, lateral; M, medial.

Figure 4.8: HMA and segmented models showing high DA concentration in the lateral/medial condyle and under the presumed insertions of gastrocnemius muscle attachments (marked with circle) of the distal femur of (A) *Homo* and (B) *Gorilla* individual. Vertical lines/squares show where the slices are positioned. L, lateral; M, medial.

Figure 4.9: PCA of rBV/TV distribution in the distal femur of *Homo*, *Gorilla*, *Pan*, and *Pongo* showing separation among studied taxa. Thresholding models represent high 30% of the range of rBV/TV values for negative and positive PCAs. Models demonstrate the highest loading causing the separation between humans (negative PC1-3SD) and great apes (positive PC1+3SD); between *Pongo*, *Pan* (negative PC2-3SD) and *Gorilla* (positive PC2+3SD). L, lateral; M, medial.

Figure 4.10: PCA of DA distribution in the distal femur of *Homo*, *Gorilla*, *Pan*, and *Pongo* showing separation among studied taxa. Thresholding models represent high 30% of the range of DA values for negative and positive PCAs. Models demonstrate the highest loading causing the separation between humans (positive PC1+3SD) and great apes (negative PC1-3SD); between *Gorilla*, *Pan* (positive PC2+3SD) and *Pongo* (negative PC2-3SD). L, lateral; M, medial.

Figure 4.11: PCA of rBV/TV and DA distribution in the distal femur of *Gorilla* and *Pan*. (A) PCA of rBV/TV distribution of *Gorilla* and *Pan* showing separation between sexes in *Gorilla* and no separation in *Pan*. (B) PCA of DA distribution of *Gorilla* and *Pan* showing separation between sexes in *Gorilla* and no separation in *Pan*. Thresholding models represent high 30% of the range of rBV/TV and DA values for negative and positive PCs. Models demonstrate the highest loading causing the separation between female and male gorillas. L, lateral; M, medial; *F*, female; *M*, male.

Figure 5.1: Knee angles and postures in humans and non-human apes in anterior and lateral view. Lines in the anterior views represent the anatomical axis of the femur.

Figure 5.2: A) Model of outer canonical model showing orientation and external morphology of the right proximal tibia computed by cHMA. B) Inner mesh showing rBV/TV distribution in the whole proximal tibia of the human sample computed by cHMA. Note that the inner mesh of rBV/TV, as well as DA distribution, was generated for each taxon. C) The cropped tibial plateau used to test for differences in BV/TV between taxa. D) This tibial plateau sub-section was then cropped again in the sagittal plane to test for differences in BV/TV between the medial and lateral condyles.

Figure 5.3: Coronal cross-sections of the rBV/TV mean models of the tibial plateau and tibial condyles. Horizontal black lines through the superior view mean models show where the cross-sectional coronal planes are positioned. Hollow black circles indicate section plane position. Red colour shows the highest rBV/TV magnitude and blue colour shows the lowest rBV/TV magnitude. L, lateral; M, medial; A, anterior; P, posterior.

Figure 5.4: Sagittal (left middle) and coronal (right) cross-sections of the rBV/TV mean models under the insertion of patellar tendon and under the tibiofibular joint. Vertical black lines in the anterior and lateral views show where the cross-sectional coronal and sagittal planes are positioned. Hollow black circles in the anterior and medial views ad a black star I the lateral and posterior views indicate section plane position. Red colour shows the highest rBV/TV magnitude and blue colour shows the lowest rBV/TV magnitude. L, lateral; M, medial.

Figure 5.5: PCA of rBV/TV distribution in the proximal tibia. Thresholded models at each end of PC1 and PC2 identify the regions of high rBV/TV that are plus/minus 3 SD of variance along each axis. Humans are separated from non-huma apes along PC1 and *Pongo* is separated from *Gorilla* along PC2. L, lateral; M, medial.

Figure 5.6: Coronal cross-sections (left) of the DA mean models of the proximal tibia. Black lines in the superior view (middle) show where the cross-sectional coronal planes and segmented microCT images (right) are positioned. Hollow black circles in the anterior and superior views indicate section plane position. Red colour shows the highest DA magnitude and blue colour shows the lowest DA magnitude. Orientation axes represent the orientation for the superior view and of the segmented images. L, lateral; M, medial; A, anterior; P, posterior; PR, proximal; D, distal.

Figure 5.7: Sagittal cross-sections (middle) of the DA mean models under the insertion of patellar tendon. Black lines in the anterior view (left) show where the cross-sectional sagittal planes and segmented images are positioned. Hollow black circles in the anterior and medial views indicate section plane position. Red colour shows the highest DA magnitude and blue colour shows the lowest DA magnitude. L, lateral; M, medial.

Figure 5.8: PCA of variation in DA among the study taxa. There is no separation between taca on PC1, while *Gorilla* separates from *Homo/Pongo* on PC2. Thresholded models at the end of each PC axis represent the regions of high DA variance along PC1 and PC2. L, lateral; M, medial.

Figure 5.9: PCA of rBV/TV in the proximal tibia of *Gorilla* males and females. Thresholded models at each end of PC3 axis represent the regions of high rBV/TV that are plus/minus 3 SD along PC3, which broadly separates male and female *Gorilla*. L, lateral; M, medial; F, female; M, male.

Figure 5.10: PCA of DA showing sex differences within *Gorilla* on PC1. Thresholded models at the end of each axis represent the regions of high DA that are plus/minus 3 SD along PC1. L, lateral; M, medial; F, female; M, male.

Figure 5.11: (A) Mean tibial plateau BV/TV (measured as everything superior to the horizontal black line) by taxon, and (B) between lateral and medial sides of the tibial plateau (black line shows where the medial and lateral condyle were divided). Mean BV/TV is higher in lateral side of tibial plateau compared to medial side in humans and higher in medial side of tibial plateau compared to lateral side in all non-human apes. L, lateral; M, medial.

Figure 6.1: Positions of the individual landmark sets used for the cHMA registration of the fossil sample. L, lateral; M, medial.

Figure 6.2: BV/TV distribution in the lateral condyle of *A. africanus* StW 318 specimen. Vertical line in the distal view shows where the cross-section is positioned. L, lateral; M, medial.

Figure 6.3: PCA of the rBV/TV distribution in the lateral femoral condyle of *A. africanus* StW 318 specimen (red star), *Homo*, *Gorilla*, *Pan*, and *Pongo* showing in the different views.

Figure 6.4: Loading models of PC1 and PC2 of the rBV/TV distribution in the lateral femoral condyle of *A. africanus* StW 318 specimen (red star), *Homo*, *Gorilla*, *Pan*, and *Pongo*.

Figure 6.5: BV/TV distribution in both femoral condyles of *A. africanus* TM 1513 specimen. Vertical lines in the distal view show where the cross-sections are positioned. L, lateral; M, medial.

Figure 6.6: PCA of the rBV/TV distribution in both femoral condyles of *A. africanus* TM 1513 specimen (red star), *Homo*, *Gorilla*, *Pan*, and *Pongo* showing in the different views.

Figure 6.7: Loading models of PC1 and PC2 of the rBV/TV distribution in both femoral condyles of *A. africanus* TM 1513 specimen (red star), *Homo*, *Gorilla*, *Pan*, and *Pongo*.

Figure 6.8: PCA of the rBV/TV distribution in the lateral femoral condyle of *A. africanus* StW 318 (red star) and TM 1513 (green star) specimens, *Homo*, *Gorilla*, *Pan*, and *Pongo* showing in the different views. The sub-setting model shows which cells were used for the PCA. Note that the preserved elements of StW 318 were used for PCA, thus only the lateral condyle was analysed.

Figure 6.9: BV/TV distribution under the femoral patellar surface of *A. sediba* UW-88-63 specimen. L, lateral; M, medial.

Figure 6.10: PCA of the rBV/TV distribution under the femoral patellar surface of *A. sediba* U.W. 88-63 specimen (red star), *Homo*, *Gorilla*, *Pan*, and *Pongo* showing in the different views.

Figure 6.11: Loading models of PC1 and PC2 of the rBV/TV distribution under the femoral patellar surface of *A. sediba* U.W. 88-63 specimen (red star), *Homo*, *Gorilla*, *Pan*, and *Pongo*.

Figure 6.12: PCA of the rBV/TV distribution under the femoral patellar surface of *A. sediba* U.W. 88-63 (red star) and *A. africanus* TM 1513 (green star) specimens, *Homo*, *Gorilla*, *Pan*, and *Pongo* showing in the different views. The sub-setting model shows which cells were used for the PCA. Note that the preserved elements of U.W. 88-63 were used for PCA, thus only lateral condyle was analysed.

Figure 6.13: BV/TV distribution in both femoral condyles of *H. floresiensis* LB1-8 specimen. L, lateral; M, medial.

Figure 6.14: PCA of the rBV/TV distribution in both femoral condyles of *H. floresiensis* LB1-8 specimen (red star), *Homo*, *Gorilla*, *Pan*, and *Pongo* showing in the different views.

Figure 6.15: Loading models of PC1 and PC2 of the rBV/TV distribution in both femoral condyles of *H. floresiensis* LB1-8 specimen (red star), *Homo*, *Gorilla*, *Pan*, and *Pongo*.

Figure 6.16: BV/TV distribution in both tibial condyles of *H. floresiensis* LB1-13 specimen. Vertical lines in the anterior, lateral and medial views show where the cross-sections are positioned. L, lateral; M, medial.

Figure 6.17: PCA of the rBV/TV distribution in both tibial condyles of *H. floresiensis* LB1-13 specimen (red start), *Homo*, *Gorilla*, *Pan*, and *Pongo* showing in the different views.

Figure 6.18: Loading models of PC1 and PC2 of the rBV/TV distribution in both tibial condyles of *H. floresiensis* LB1-13 specimen (red star), *Homo*, *Gorilla*, *Pan*, and *Pongo*.

Figure 6.19: BV/TV distribution in both femoral condyles of *H. neanderthalensis* D322-15 specimen. Vertical lines in the distal view show where the cross-sections are positioned. L, lateral; M, medial.

Figure 6.20: PCA of the rBV/TV distribution in both femoral condyles of *H. neanderthalensis* D322-15 specimen (red star), *Homo*, *Gorilla*, *Pan*, and *Pongo* showing in the different views.

Figure 6.21: Loading models of PC1 and PC2 of the rBV/TV distribution in both femoral condyles of *H. neanderthalensis* D322-15 specimen (red star), *Homo*, *Gorilla*, *Pan*, and *Pongo*.

Figure 6.22: PCA of the rBV/TV distribution in the lateral femoral condyle of *A. africanus* StW 318 (dark green star), TM 1513 (light green star) and *H. neanderthalensis* D322-15 (red star) specimens, *Homo*, *Gorilla*, *Pan*, and *Pongo* showing in the different views. The sub-setting model shows which cells were used for the PCA. Note that the preserved elements of StW 318 were used for PCA, thus only lateral condyle was analysed.

Figure 6.23: PCA of the rBV/TV distribution under the femoral patellar surface of *A. sediba* U.W. 88-63 (brown star), *A. africanus* TM 1513 (green star), and *H. neanderthalensis* D322-15 (red star) specimens, *Homo*, *Gorilla*, *Pan*, and *Pongo* showing in the different views. The sub-setting model shows which cells were used for the PCA. Note that the preserved elements of U.W. 88-63 were used for PCA, thus only lateral condyle was analysed.

Supplementary figures

Figure S3.1: Distal tibia model of Tb.Th mm distribution of tested *Gorilla* individual for baseline scan (a), downsampled voxel sizes of 90, 150, and 210 µm (b), and scan voxel sizes of 45 – 110 µm (c). Vertical lines through the medial view show where the slices are positions for the cross-section mid-coronal view. Dark red represents the highest and dark blue the lowest Tb.Th values. All colourmaps were scaled to baseline scan data range.

Figure S3.2: Distal tibia model of Tb.Sp distribution of tested *Gorilla* individual for baseline scan (a), downsampled voxel sizes of 90, 150, and 210 µm (b), and scan voxel sizes of 45 – 110 µm (c). Vertical lines through the medial view show where the slices are positions for the cross-section mid-coronal view. Dark red represents the highest and dark blue the lowest Tb. Sp values. All colourmaps were scaled to baseline scan data range.

Figure S3.3: Distal tibia model of Tb.N distribution of tested *Gorilla* individual for baseline scan (a), downsampled voxel sizes of 90, 150, and 210 µm (b), and scan voxel sizes of 45 – 110 µm (c). Vertical lines through the medial view show where the slices are positions for the cross-section mid-coronal view. Dark red represents the highest and dark blue the lowest Tb.N values. All colourmaps were scaled to baseline scan data range.

Figure S3.4: Differences in mean levels of each tested parameter for all downsampled and scanned voxel sizes.

Figure S4.1: (A) Patella position during the range of flexed-extended knee showing in inferior view; red, maximum flexion; blue, maximum extension. (B) Patella position during 90° knee flexion showing in medial view. (C) Patella position during maximum knee extension in medial view. (D) Expected human knee posture during bipedal walking. (E) Expected *Gorilla* and *Pan* knee posture in maximum flexion during vertical climbing and maximum extension during terrestrial knuckle-walking. (F) Expected *Pongo* knee posture during arboreal locomotion.

Figure S4.2: PCA of rBV/TV distribution in the distal femur of *Homo, Gorilla, Pan,* and *Pongo* showing separation among studied taxa. Thresholding models represent high 30% of the range of rBV/TV values for negative and positive PC3. Models demonstrate the highest loading causing the separation between *Pongo* (positive PC3+3SD) and *Gorilla, Pan* (negative PC3-3SD). L, lateral; M, medial; D, distal; P, posterior; I, inferior; S, superior.

Figure S4.3: Species mean models of DA distribution under the presumed insertions of cruciate ligaments of the distal femur of *Homo, Gorilla, Pan,* and *Pongo.* Vertical lines through the mean medial and lateral models show where the slices are positioned. Cross sections were positioned in the middle of presumed insertions of cruciate ligaments. Knee model shows cruciate ligaments during neutral knee position. D, distal; P, posterior; I, inferior; S, superior.

Figure S4.4: Species mean models of DA distribution under the presumed insertions of collateral ligaments of the distal femur of *Homo, Gorilla, Pan,* and *Pongo.* Vertical lines through the mean medial and lateral models show where the slices are positioned. Cross

sections were positioned in the middle of presumed insertions of collateral ligaments. Knee model shows collateral ligaments attachments in the inferior view. L, lateral; M, medial; D, distal; P, posterior; I, inferior; S, superior.

Figure S4.5: (A) Species mean models of DA distribution in the anterior view of distal femur of *Homo*, *Gorilla*, *Pan*, and *Pongo*. (B) HMA and segmented models showing high DA concentration above the condyles of the right distal femur of *Homo* and *Gorilla* individual in the anterior view. Squares show where the slices are positioned. L, lateral condyle; M, medial condyle.

Figure S4.6: PCA of DA distribution in the distal femur of *Homo*, *Gorilla*, *Pan*, and *Pongo* showing separation among studied taxa. Thresholding models represent high 30% of the range of DA values for negative and positive PC3. Models demonstrate the highest loading causing the separation between *Gorilla* (positive PC3+3SD) and *Pan* (negative PC3-3SD). L, lateral; M, medial; D, distal; P, posterior; I, inferior; S, superior.

Figure S4.7: PCA of rBV/TV and DA distribution in the distal femur *Homo*. (A) PCA of rBV/TV distribution of *Homo* showing partial separation between Mary Rose (males) and rest of human sample (sex unknown). (B) PCA of DA distribution of *Homo* showing partial separation between Mary Rose (males) and rest of human sample (sex unknown).

Figure S4.8: Covariation between PC1 of rBV/TV and bone volume in the distal femur of *Homo*, *Gorilla*, *Pan*, and *Pongo* showing no significant positive relationship between the variables.

Figure S4.9: Covariation between PC1 of rBV/TV and bone volume in *Gorilla*, female *Gorilla* and male *Gorilla* showing no significant positive relationship in *Gorilla* and no significant negative relationship in female and male *Gorilla* between the variables.

Figure S4.10: Covariation between PC1 of rBV/TV and bone volume in *Pan*, female *Pan* and male *Pan* showing significant weak negative relationship in *Pan* and no significant weak negative relationship in female and male *Pan* between the variables.

Figure S4.11: Covariation between PC1 of rBV/TV and bone volume in humans and separately for the studied human populations showing no significant weak positive relationship in humans, no significant weak negative relationship in sedentary and in active populations between the variables.

Figure S4.12: Mean models of rBV/TV distribution in the distal femur of human sample separated by populations. Mary Rose represents an active population while other individuals were taken from the sedentary population. Oblique slices are in the centre of the lateral and medial condyles. Vertical lines through the distal view mean models show where the slices are positioned. L, lateral condyle; M, medial condyle.

Figure S4.13: PCA of rBV/TV distribution in the distal femur of human sample showing separation between an active population (Mary Rose) and sedentary population (1.0 kya-present). Thresholding models represent a high 40 % of the range of rBV/TV values for the mean model of each group. Models demonstrate locations of the highest loadings causing the separation. L, lateral condyle; M, medial condyle.

Figure S5.1: Taxa standard deviation models of rBV/TV values in the proximal tibia of *Homo, Gorilla, Pan,* and *Pongo.* Vertical and horizontal lines through the SD models show where the cross-sectional sagittal and coronal planes are positioned. Red colour shows the highest variability in the rBV/TV values and blue colour shows the lowest variability in the rBV/TV values. L, lateral; M, medial.

Figure S5.2: PC3 of rBV/TV distribution in proximal femur of *Homo, Gorilla, Pan,* and *Pongo* showing separation among studied taxa. Models at the end of each axis represent the regions of high rBV/TV driving variance along PC3. Models demonstrate the rBV/TV values separating between *Pongo* (positive PC3+3SD) and *Pan* (negative PC3-3SD). L, lateral; M, medial.

Figure S5.3: Taxa SD models of DA distribution of the proximal tibia of *Homo, Gorilla, Pan,* and *Pongo.* Red colour shows the highest variability in the DA values and blue colour shows the lowest variability in the DA values. L, lateral; M, medial.

Figure S5.4: PCA of DA distribution in the proximal tibia of *Homo, Gorilla, Pan,* and *Pongo* on PC3.

Figure S5.5: *Gorilla* mean models and PCA of rBV/TV distribution in the proximal tibia of *Gorilla* showing no separation on PC1 and partial separation on PC2 and PC3. Horizontal lines through the superior view mean models show where the cross-sectional coronal planes are positioned. Circles in the superior and anterior views represent the homologous locations. F, female; M, male.

Figure S5.6: PCA of rBV/TV distribution in the proximal tibia of (A) *Pan* and (B) *Homo* showing no separation between sexes. F, female; M, male.

Figure S5.7: PCA of DA distribution in proximal tibia of *Gorilla* showing no separation between sexes on PC2 and PC3. F, female; M, male.

Figure S5.8: PCA of DA distribution in proximal tibia of (A) *Pan,* and (B) *Homo* showing no separation between sexes. F, female; M, male.

Figure S5.9: PCA of rBV/TV distribution in the whole proximal tibia (A) of *Homo* showing no separation between populations; in the tibial plateau (above the line) (B); in the medial side of tibial plateau (C); in the lateral side of tibial plateau (D) showing the highest variability of rBV/TV values in the post-industrial population assumed to represent low levels of activity (Gottingen) and in the population from the Medieval period (11^{th} to 16^{th} centuries) assumed to represent higher levels of activity (NGA). Sample of young active male adults (Mary Rose/MR) is within the non-human ape sample.

Figure S5.10: PCA of DA distribution in the proximal tibia of *Homo* showing separation between populations on PC1 and no separation on PC2 and PC3. Models at the end of each axis represent the regions of high DA driving variance along PC1. Models demonstrate the regions loaded in the most stereotypical way causing the separation between Gottingen and MR populations (negative PC1-3SD) and NGA population (positive PC1+3SD). L, lateral; M, medial.

Figure S6.1: A bi-variate plot was generated based on the first two components from the CVA, which was conducted using the first three principal components of trabecular bone distribution in the lateral femoral condyle. The table includes the cross-validated typicality probabilities, indicating the likelihood of fossil specimens being assigned to each extant taxon, based on their canonical variate scores.

Figure S6.2: A bi-variate plot was generated based on the first two components from the CVA, which was conducted using the first three principal components of trabecular bone distribution under the patellar femoral surface. The table includes the cross-validated typicality probabilities, indicating the likelihood of fossil specimens being assigned to each extant taxon, based on their canonical variate scores.

Figure S6.3: A bi-variate plot was generated based on the first two components from the CVA, which was conducted using the first three principal components of trabecular bone distribution in the distal femur. The table includes the cross-validated typicality probabilities, indicating the

likelihood of fossil specimens being assigned to each extant taxon, based on their canonical variate scores.

Figure S6.3: A bi-variate plot was generated based on the first two components from the CVA, which was conducted using the first three principal components of trabecular bone distribution in the proximal tibia. The table includes the cross-validated typicality probabilities, indicating the likelihood of fossil specimens being assigned to each extant taxon, based on their canonical variate scores.

LIST OF TABLES

Main tables

Supplementary tables

LIST OF APPENDICES

Appendix A: Sample composition

ABBREVIATIONS

µCT	Micro-Computed Tomography (micro-CT)
A.	*Australopithecus*
Ar.	*Ardipithecus*
BV/TV	Bone volume to total volume
cHMA	Canonical holistic morphometric analysis
Conn.D	Connectivity
CVA	Canonical variates analysis
DA	Degree of anisotropy
G	Grid size
H.	*Homo*
HMA	Holistic morphometric analysis
Kc	Kernel size
Kya	Thousands of years ago
L	Probability filter
LB1	Liang Bua 1, *Homo floresiensis* holotype
LB8	Liang Bua 8, *Homo floresiensis*
LCA	Last common ancestor
MH1	Malapa hominin 1, *Australopithecus sediba*
MH2	Malapa hominin 2, *Australopithecus sediba*
MIL	Mean Intercept Length
Mya	Millions of years ago
Nc	Number of classes
PC	Principal component
PCA	Principal component analysis
rBV/TV	Relative bone volume to total volume
SDM	Statistical free-form deformation model
SpDM	Spatial Deformation Mapping
Tb.N	Trabecular number
Tb.Sp	Trabecular spacing
Tb.Th	Trabecular thickness
VOI	Volume of interest
µm	Micromicrons

GENERAL INTRODUCTION

Statement of the scientific problem

The study of fossil hominins' locomotor abilities, including their degree of arboreality and variations in bipedalism (such as facultative or obligate), continues to be a key area of focus in palaeoanthropology. Numerous studies have contributed to our understanding of this complex topic (e.g., Johanson & Taieb, 1976; Johanson & White, 1979; Stern & Susman, 1983; Susman et al., 1984; Susman, 1991; Crompton et al., 1998; Ryan & Ketcham, 2002; Carey & Crompton, 2005; Fajardo et al., 2007; Griffin et al., 2010; Raichlen et al., 2010; Saparin et al., 2011; Shaw & Ryan, 2012; Barak et al., 2013b; Skinner et al., 2015). The limb morphology of many Pliocene hominins has often been described as mosaic, suggesting that these species exhibited a variety of locomotor and postural behaviors. This implies that they possessed a mix of traits suited to both arboreal and terrestrial activities, reflecting an evolutionary transition in mobility and lifestyle during this period (e.g., Susman, 1991; Begun, 1992; Demes et al., 1994; Harcourt-Smith & Aiello, 2004). This mosaic pattern likely reflects a transitional form that gradually disappeared over time as arboreal behaviours diminished and habitual bipedalism became the dominant mode of movement (e.g., Bramble & Lieberman, 2004; Skinner et al., 2015).

Research examining different mosaic morphologies in hominins frequently focuses on the external structure of bones (e.g., Ward, 2002; Bloch & Boyer, 2003; Almecija et al., 2010). However, while it can be inferred that a hominin may have behaved in a particular way based on external bone morphology, it is unclear whether it actually practiced those behaviours during life. This is because the external form could represent ancestral morphology that had not yet been altered through natural selection. Additionally, the articular surfaces of joints facilitate a range of joint positions, and their external surface does not indicate which positions were predominantly used. Investigating internal bone structure, such as variation in the amount and organization of trabecular bone underlying joint articular surfaces, has proven crucial in revealing *in vivo* locomotor and postural behaviour among hominids (e.g., Georgiou et al., 2018; 2019; 2020; Tsegai et al., 2018b; Dunmore et al., 2020). This approach provides valuable insights into the behaviours of our early ancestors.

One of the most widely recognized defining traits of hominins, alongside the reduction of canines is bipedalism (e.g., Harcourt-Smith & Aiello, 2004; DeSilva, 2009). Historically, it was believed that the shift from arboreal locomotion to terrestrial bipedalism was rooted in adaptations from an arboreal lifestyle. This view suggested that early hominins evolved from

tree-dwelling ancestors, gradually transitioning to walking upright on the ground. Over time, this theory has evolved, with new evidence providing a more nuanced understanding of how bipedalism emerged, acknowledging a variety of locomotor behaviors and environmental factors that influenced the development of habitual bipedalism in early human ancestors (e.g., Morton, 1927; Schultz, 1936). One of the earliest proponents of this hypothesis was Charles Darwin himself, who suggested that bipedalism may have evolved from ancestors that lived in trees (Darwin, 1859). Darwin proposed that our ape-like ancestors, while moving through the branches, would have occasionally stood upright to reach for fruit or navigate between trees, eventually leading to habitual bipedalism. More recent studies, however, propose that knuckle-walking quadrupedalism may serve as a more accurate precursor to terrestrial bipedalism. Originally introduced by Washburn (1967) and later revisited by Tuttle et al. (1974), this model suggests that bipedalism evolved from an ancestor that was a terrestrial knuckle-walker, similar to modern *Pan*. Despite this, increasing skepticism has emerged regarding the strength of fossil evidence supporting a knuckle-walking origin (e.g., Stern & Susman, 1983; Ward et al., 1999). Dainton & Macho (1999) also questioned whether knuckle-walking was even a homologous trait in both *Pan* and *Gorilla*. However, some argue that the distal radial morphology of *Australopithecus afarensis* provides evidence for a knuckle-walking phase in evolutionary history (Richmond & Strait, 2000; Richmond et al., 2001). Others defend a knuckle-walking origin, citing similarities in curvature between hominins and *Pan* (Richmond & Jungers, 2008), although *Orrorin*, considered by its discoverers to be arboreally adapted, complicates this interpretation (Senut et al., 2001). Kivell & Schmitt (2009) argue that there are two functionally distinct modes of knuckle-walking in African apes. *Pan* is associated with wrist postures adapted to arboreal environments, while *Gorilla* exhibits a neutral wrist posture suited to terrestrial environments. They propose that the knuckle-walking traits observed in hominins are actually adaptations for life in the trees, suggesting that bipedalism originated from an arboreal ecological niche. Additionally, White et al. (2009) contend that the anatomical characteristics of the pelvis, foot, and lower limb bones in *Ardipithecus ramidus* indicate that knuckle-walking is unlikely to have been the ancestral form of locomotion. They suggest that *Ar. ramidus* may have engaged in complex locomotor behaviours indicating a form of bipedalism that differed from later hominins like *Australopithecus* and *Homo* genus. Their research highlights the evolutionary importance of *Ar. ramidus* as a transitional species, connecting the gap between the last common ancestor (LCA) of humans and chimpanzees and subsequent hominin species and it highlights the importance of understanding the early stages of hominin evolution and the adaptive pathways leading to bipedalism and other human-like traits.

An alternative to the terrestrial knuckle-walking model is the vertical climbing hypothesis, initially suggested by Fleagle et al. (1981). This theory is based on the similarities in lower limb muscle activity observed in African apes during vertical climbing and human bipedal walking. However, despite the parallels in movement patterns between vertical climbing and knuckle-walking, vertical climbing involves the hip and knee joints being in significantly flexed positions (e.g., Isler, 2002; Isler & Thorpe, 2003; Crompton et al., 2008). While hip and knee postures are extended during human walking, other human behaviours such as running, jumping, and squatting involve more flexed limb postures (e.g., Mann & Hagy, 1980; Nilsson & Thorstensson, 1989; Racic et al., 2009). The concept of "bent-hip/bent-knee" bipedalism refers to a particular style of bipedal locomotion where the hip and knee joints remain flexed throughout the stride cycle (e.g., Wang et al., 2003; Foster et al., 2013). This type of gait is often associated with some non-human primates, particularly *Pongo* (Watson et al., 2009), as well as with some interpretations of the locomotion of early hominins. In the context of early hominins, the debate surrounding "bent-hip/bent-knee" bipedalism centres on interpretations of fossil evidence, particularly the morphology of the pelvis and lower limb bones (e.g., Hogervorst et al., 2009; Lovejoy & McCollum, 2010; Mogg, 2018). Some researchers have suggested that certain early hominin species, such as *A. afarensis*, may have exhibited a form of bipedalism characterized by a "bent-hip/bent-knee" gait. This interpretation is based on features of the pelvis and hip joint that suggest a more ape-like posture during bipedal locomotion (e.g., Jungers, 1988; Sockol et al., 2007; Crompton et al., 2018). However, other researchers argue against the idea of "bent-hip/bent-knee" bipedalism in early hominins, instead proposing that these species walked with a more erect posture, like modern humans (Lovejoy & McCollum, 2010). This debate underscores the challenges of inferring locomotor behaviour from fossil evidence and the complex nature of human evolution. Moreover, numerous objections against the vertical climbing hypothesis have been raised by researchers. For example, DeSilva (2009) points out that the ankle joint morphology of early hominins is distinct from that of African apes. Similarly, Lovejoy (2005) argues that *Ar. ramidus* lacks the hand anatomical traits typically associated with vertical climbing.

Approaches to studying and interpreting locomotor repertoires in fossil hominins vary among researchers. However, all studies share the foundational concept that the origins of human bipedalism can be best understood by investigating the activities of living primates. A key question in palaeoanthropology remains: Why and how did bipedalism evolve from earlier forms observed in our ancestral lineaque to the obligate bipedalism exhibited by *Homo sapiens*?

The impact of knee postures on the internal structure of ape knees, particularly in non-human primates like *Pan*, *Gorilla*, and *Pongo*, can provide insights into their locomotor behaviours and evolutionary adaptations. Differences in knee postures and trabecular bone distribution can reflect adaptations to different modes of locomotion. Arboreal species like *Pongo* may exhibit greater variability in knee postures and trabecular bone distribution to accommodate the diverse demands of climbing and brachiation. In contrast, terrestrial knuckle-walkers like *Pan* and *Gorilla* may show more consistent patterns of knee flexion and trabecular bone density associated with quadrupedal locomotion. Comparisons of knee postures and trabecular bone structure among extant ape species can provide insights into the locomotor behaviours of their common ancestors and the evolutionary pathways that led to human bipedalism. By studying the internal structure of ape knees, researchers can infer the functional demands and selective pressures that shaped locomotor adaptations throughout primate evolution.

Thesis aims

The first aim of this thesis is to explore relationship between the trabecular bone structure of the **distal femur** in extant primates and their locomotor behaviors, both across species and within individual groups. The second aim is to investigate potential connections between the trabecular bone architecture of the **proximal tibia** in these primates. Furthermore, the third aim is to infer locomotor activities of certain extinct hominins based on their trabecular bone patterns. To achieve this, we analysed the trabecular structure of the **distal femur** in *Australopithecus sediba*, *Australopithecus africanus*, and *Homo neanderthalensis* as well as both the **distal femur** and **proximal tibia** in *Homo floresiensis*.

Overview

Chapter 1: General background

Chapter 1 provides an overview of hominin knee anatomy, locomotion, postures, and behaviours that may influence bone functional adaptation in the knee. It begins with detailed descriptions of trabecular bone and functional adaptation. Subsequently, the chapter reviews functional signals in the trabecular structure of extant apes and explores possible allometric effects when measuring trabecular bone parameters. Furthermore, the chapter investigates morphology, functional adaptation, and potential functional signals in the knee of fossil hominins. By examining these factors, the chapter sets the stage for deeper exploration into the evolutionary processes that shaped the knee morphology and function in hominins.

Chapter 2: Materials and methods

Chapter 2 provides a comprehensive overview of the materials and methods utilized in each research project. This includes a detailed examination of the experimental procedures, data collection techniques, and analytical methods employed to investigate trabecular bone architecture and functional adaptation in the knee. Furthermore, the chapter critically evaluates the limitations associated with the applied approaches. By addressing these limitations, the chapter provides insights into the challenges faced during the research process and acknowledges potential areas for improvement in future studies. Overall, **Chapter 2** serves as a foundational guide for understanding the methodologies employed in the subsequent analyses and contributes to the transparency and rigor of the research findings.

Chapter 3: Technical note: Does scan resolution or downsampling impact the analysis of trabecular bone architecture?

Chapter 3 consists of the technical note published in the *American Journal of Biological Anthropology* by Lukova et al. (2024). This research project is centred on the assessment of trabecular bone structure using micro-computed tomography (micro-CT). The primary aim of this study is to conduct a detailed investigation into the dependence of measures of trabecular bone structure on voxel size. Specifically, the chapter examines how varying voxel sizes impact the reliability and accuracy of results obtained from studies of trabecular bone architecture. Additionally, the research seeks to determine the reliability of results when using either lower voxel sizes due either to downsampling of a high-resolution scan or re-scanning a specimen at progressing lower resolution. By addressing these questions, **Chapter 3** contributes valuable insights into the methodological considerations and potential limitations associated with micro-CT imaging in studies of trabecular bone structure. Furthermore, it enhances our understanding of the factors influencing the interpretation of results in this field of research.

Chapter 4: Trabecular architecture of the distal femur in extant hominids

Chapter 4 presents the manuscript authored by Lukova et al. (2024), published in the *Journal of Anatomy*. This research focuses on analyzing the trabecular architecture of the distal femur in extant primates. The study tests two key hypotheses. The first hypothesis explores whether variations in locomotor behavior are reflected in differences in the trabecular architecture of the distal femur across *Homo*, *Pan*, *Gorilla*, and *Pongo*. The second hypothesis examines whether male and female *Gorilla* exhibit significant differences in trabecular architecture due to their varying levels of arboreality, while no substantial differences are anticipated between male and

female *Pan* or *Homo*, based on prior studies of their locomotor behaviors. By addressing these hypotheses, **Chapter 4** contributes to our understanding of the relationship between locomotor behaviours and trabecular bone architecture in living primates. Furthermore, it sheds light on potential variations in trabecular architecture within and between primate species, offering insights into the evolutionary adaptations of the musculoskeletal system.

Chapter 5: Trabecular architecture of the proximal tibia in extant hominids

Chapter 5 consists of the manuscript submitted to the *American Journal of Biological Anthropology* by Lukova et al. (currently under revisions). This study represents the first examination of trabecular structure in the proximal tibia among and within extant primates. The primary aim of this research is to investigate whether trabecular architecture of the proximal tibia reflects differing locomotor behaviours across *Homo*, *Pan*, *Gorilla*, and *Pongo*, as well as potential differences between males and females within the studied sample. By addressing these aims, **Chapter 5** contributes to our understanding of how trabecular bone architecture in the proximal tibia may be influenced by locomotor behaviours and sex differences across primate species. This research sheds light on the functional adaptation of the knee joint in relation to various locomotor strategies employed by different primate taxa.

Chapter 6: Trabecular architecture of the distal femur and proximal tibia in fossils hominins

Chapter 6 presents the results of the trabecular bone analyses in the distal femur of *Australopithecus sediba*, *Australopithecus africanus*, and *Homo neanderthalensis* and in the distal femur and proximal tibia of *Homo floresiensis*, comparing them to the extant primate sample. The chapter begins by discussing the knee functional morphology of each species, followed by a presentation of the results for each. Finally, based on these findings, **Chapter 6** infers the potential knee locomotor and postural behaviours of each fossil taxon.

Chapter 7: General discussion and conclusion

This chapter provides a summary of the four research projects and discusses how the findings contribute to addressing the scientific problem outlined earlier in the thesis. It evaluates the conclusions that can be drawn about the locomotor and postural behaviors of fossil hominins, with a specific importance on the evolution of the hominin knee. Additionally, the chapter acknowledges the limitations associated with both the sample size and the methodological approaches used in the research.

1 GENERAL BACKGROUND

1.1 Shape of the distal femur, proximal tibia and associated soft tissue structures of the ape knee

Extant primates exhibit a high degree of anatomical bone variation, including variability in knee joint proportions. This variation reflects the evolutionary trajectory related to motion capabilities (e.g., Tardieu, 1981; Frelat et al., 2017). Some of these anatomical variations are likely adaptations that help the knee endure increased stress during locomotion (e.g., Tardieu, 1981; Turnquist & Hong, 1995; Payne et al., 2006). Each bone within the knee joint serves as both a contact energy absorber, absorbing stress, and a power producer, generating stress, during each phase of locomotion. The morphology of the bone is adapted to provide the most efficient compromise between stability and mobility (Ruff et al., 2006). By examining the anatomical variation in knee joint proportions among extant primates, researchers gain insights into the adaptive strategies employed by different species to cope with locomotor demands. Understanding these adaptations contributes to our broader understanding of primate locomotion and postural behaviours and the evolutionary processes that have shaped musculoskeletal morphology.

The morphology of the knee is, to some degree, adapted to the locomotor repertoires of species (e.g., Sylvester & Pfisterer, 2012; Frelat et al., 2017). However, knee morphology also follows different evolutionary pathways (Sylvester & Pfisterer, 2012; Frelat et al., 2017), where certain morphological changes may indicate specific types of locomotor behaviour (e.g., Nakatsukasa, 1996; Gebo, 2010; Janis et al., 2012), while others may indicate taxon- or clade-specific synapomorphy patterns (Polk, 2002; Boyer et al., 2015). Altogether, the knee functions as an integrated complex, with the individual bones exhibiting a certain degree of functional and evolutionary independence (Kaplan, 1962). Movement in the knee is generally more limited due to the involvement of the distal femur and proximal tibia. The shape of the distal femoral epiphysis differs among apes, while the proximal tibial epiphysis tends to reflect the shape of the femoral epiphysis. As a result, there are slight shape differences between apes (Tardieu, 1981).

Soft tissue anatomy, alongside bony anatomy, plays a critical role in determining join range of motion and stress distribution on bones (Phillips & Coetsee, 2007). Muscle anatomy has significantly improved our understanding of primate behaviour in locomotion studies. While great apes generally show similar muscle architecture, subtle differences exist due to varying

demands for stability and mobility in different habitats (Myatt et al., 2011). Key factors influencing the contribution of a muscle to movement include muscle fascicle length and moment arm lenht. A longer muscle fascicle relative to the moment arm allows for a broader range of joint movement (e.g., Alexander & Ker, 1990; Payne et al., 2006). Variations in these muscle characteristics among primates suggest that non-human apes can achieve greater joint mobility compared to humans (Payne et al., 2006). Moreover, individuals adapted to specific modes of locomotion are expected to engage less muscle activity, thereby reducing stress on the skeleton compared to individuals whose bone and muscle morphology are less suited for that particular mode of locomotion (e.g., Basmajian, 1967; Hunt, 1991; Thorpe & Crompton, 2006).

1.1.1 Humans

Relative to body size, the knee is generally larger in humans, and the distal condyles of the femur are squarer compared to other primates (Tardieu, 1999). Additionally, in humans, the femoral and tibial condyles are approximately the same size, with the lateral femoral condyle being more elliptical compared to the medial condyle. This elliptical shape increases the articular surface of the lateral femoral condyle and its curvature in its inferior part, facilitating easier knee extension, which is crucial for bipedal walking (Lovejoy, 2007). Moreover, in its sagittal plane, the lateral condyle is flatter in modern humans (Figure 1.1a), maximizing tibiofemoral contact area and therefore stabilizing the joint during extended knee postures. This is crutial because the typical bipedal gait involves the knee being fully extended for most of its cycle (e.g., Tardieu, 1999; Landis & Karnick, 2006; Organ & Ward, 2006; Javois et al., 2009; Sylvester & Pfisterer, 2012). The femoral trochlea features a groove where the lateral lip is higher and more prominent anteriorly than the medial one (Figure 1.1b), adapting itself to stabilize the femoropatellar joint (Tardieu, 1999). Furthermore, medial and lateral femoral epicondyles are thicker in humans compared to other apes, with the proximal shaft curved to interact with them (Frelat et al., 2017). The tibial plateau is relatively flat and broad compared to non-bipedal primates. This shape helps to provide stability during weight-bearing activities such as walking and running. Additionally, the orientation of the tibial plateau is such that it facilitates efficient transmission of body weight through the knee joint during bipedal locomotion (Frelat et al., 2017). These anatomical features highlight the adaptations of the human knee joint to bipedal locomotion.

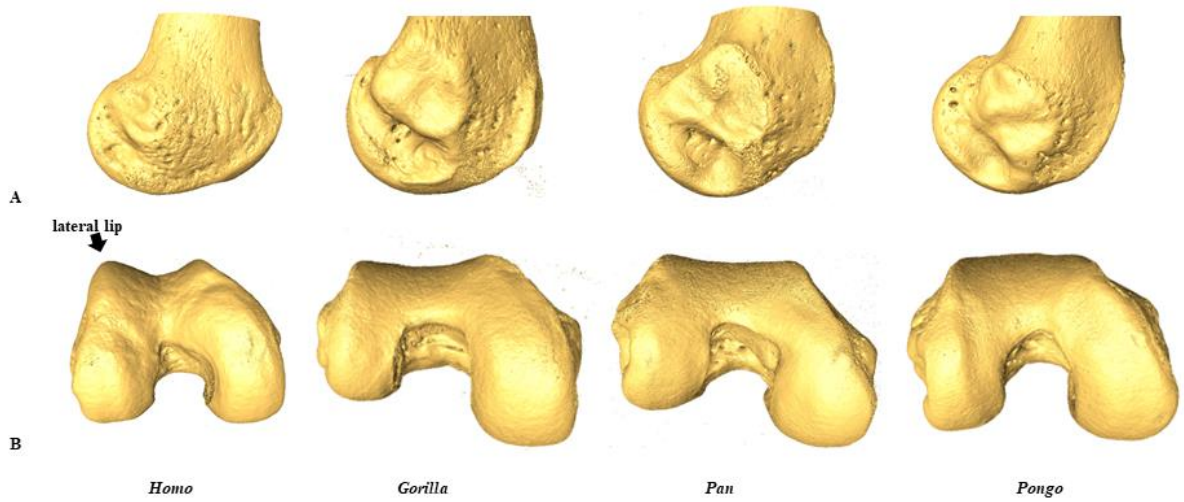

Figure 1.1: (A) Surface models of the lateral femoral condyle illustrate the more elliptical shape of the lateral condyle in humans compared to other great apes. (B) Surface models of the distal femur in a distal view demonstrate the squarer outline of the distal surface and the high lateral lip in humans compared to other great apes.

The human patella is roughly triangular, with a rounded proximal margin and a pointed distal margin. The quadriceps femoris muscle inserts on the proximal patellar surface and continues over the anterior surface, ultimately inserting via the patellar ligament on the tibial tuberosity. The vastus medialis and lateralis muscles insert on the medial and lateral margins of the patella (Figure 1.2), respectively, contributing to the knee stability against medial and lateral dislocation during knee extension by the quadriceps femoris. The broader lateral facet of the patella indicates a more extensive articulation with the lateral part of the femoral trochlea compared to the medial part. When the knee is fully extended, the ligament-femoral joint contact occurs at the distal end of the patella (Figure 1.4c). As flexion increases, the contact area between the patella and femur also increases (Figure 1.4a-b). The patella fits into the femoral trochlear groove, with the contact area apreading across the width of the patella and moving proximally (e.g., Aiello & Dean, 1990; Tardieu, 1999; Lovejoy, 2007). This mechanism enables higher stress absorption during knee flexion, as the contact area is maximized when the lateral facet articulates on the distal aspect of the lateral femoral condyle and the medial facet articulates with the medial femoral condyle at the edge of the intercondylar notch (Masouros et al., 2008).

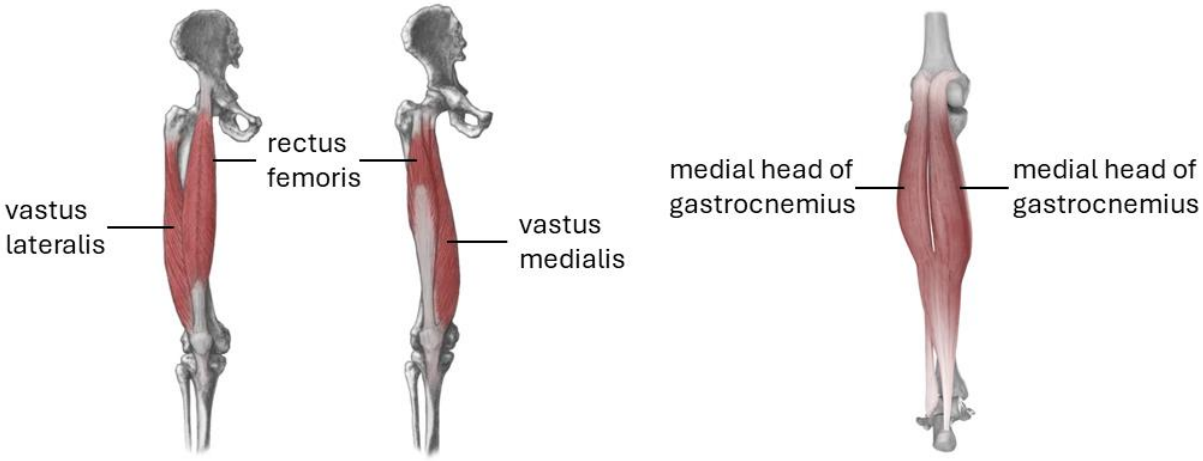

Figure 1.2: Muscle attachments of the knee showing from anterior and posterior view.

The medial meniscus is firmly attached to the joint capsule, the medial collateral ligament, and the tibia on its lateral side (Figure 1.3a). Similarly, the lateral meniscus is tightly attached to the tibia, posteriorly to the popliteus muscle, and via the anterior transverse ligament, to the medial meniscus. Together, these attachments create a mobile unit on the tibial plateau, enabling the menisci to accommodate the sliding and rotational movements of the femoral condyles. In addition to their role in accommodating femoral condyle movement, the menisci play a secondary role in stabilizing the knee joint alongside the cruciate ligaments (Figure 1.3b-f). During knee flexion, the popliteus tendon pulls the menisci posteriorly, while the contact point of the femoral condyle and tibial plateau also moves posteriorly. Conversely, during knee extension, the menisci move anteriorly along with the femoral condyle and tibial plateau (e.g., Aiello & Dean, 1990; Tardieu, 1999; Lovejoy, 2007). This coordinated movement of the menisci with the femoral condyles and tibial plateau helps maintain joint stability and ensures proper alignment during various knee movements (e.g., Geurts et al., 2016).

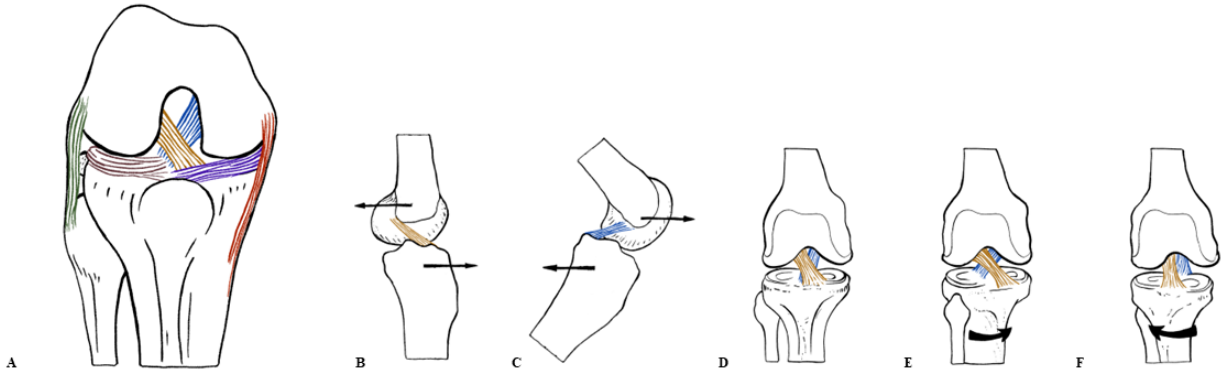

Figure 1.3: (A) Ligament attachments of the knee showing in inferior view. Gold, anterior cruciate ligament; blue, posterior cruciate ligament; green, lateral collateral ligament; red, medial collateral ligament; brown, lateral meniscus; purple, medial meniscus. The medial collateral ligament inserts at the medial epicondyle of the femur and attaches along the medial border of the tibial plateau and on the medial surface of the tibial shaft. The lateral collateral ligament inserts on the lateral femoral epicondyle and attaches on the head of fibula. (B) Anterior cruciate ligament position during forward tibia and backward femur movements. (C) Posterior cruciate ligament position during backward tibia and forward femur movements. Cruciate ligaments position during (D) Neutral knee position; (E) medial knee rotation; (F) lateral knee rotation. The anterior cruciate ligament arises from the anterior intercondylar space on the tibial plateau, runs upwards and posteriorly and attaches on the inside of the lateral condyle of the femur. The posterior cruciate ligament arises from well back on the posterior intercondylar space, runs upwards and anteriorly and attaches on the inside of the medial condyle.

1.1.2 Non-human great apes

Non-human great apes exhibit distinct femoral condyle morphology compared to humans. In African apes and *Pongo*, the femoral epiphyses are expanded more mediolaterally than anteroposteriorly (Figure 1.1b). This results in a larger medial condyle relative to the lateral condyle (Figure 1.1b), contributing to mediolateral knee rotation during terrestrial and arboreal locomotion (e.g., Tardieu, 1999; Sylvester & Pfisterer, 2012; Sylvester, 2013). Furthermore, the lateral femoral condyle in non-human great apes features a convex and circular sagittal plane without any junction or condylo-trochlear prominence (Figure 1.1a). This morphology maximizes points of contact in varied knee postures while reducing contact areas at each point, thus increases joint mobility during locomotion (e.g., Tardieu, 1999; Landis & Karnick, 2006; Organ & Ward, 2006; Javois et al., 2009; Sylvester & Pfisterer, 2012). However, this morphology also restricts full extension movements, resulting in limited knee extension movement (Tardieu, 1999). Additionally, the tibial plateau in non-human great apes is supero-inferiorly compressed, with distinct features such as a sharper edge on the medial side of the tibial tuberosity, a thin lateral epicondyle, and a convex proximal shaft surface (Frelat et al., 2017). These adaptations are indicative of the specific locomotor behaviours and habitat preferences of non-human great apes.

In non-human apes, the patella is both absolutely and relatively smaller compared to humans, primarily due to the smaller size of the quadriceps muscle. Across all primates, the quadriceps

muscles exert greater compression on the patella against the femur during flexion movements than during extension. The resulting joint stress depends on the size of the patellofemoral contact area. A larger contact area reduces joint stress by spreading the stress more evenly across the articular surface. Conversely, the quadriceps generate stronger tibiofemoral compression during extension movements compared to flexion (Lovejoy, 2007). Quadriceps function differs significantly between modern humans and quadrupedal species, leading to differences in external shape morphology. In humans, quadriceps muscles are considered ipsilateral muscles, meaning they affect the same side of the body where they are located. Consequently, they remain active during most activities, including standing, and stabilize the lower limb during fast walking or running. This results in higher tibiofemoral force compared to patellofemoral force during most locomotor activities (Lovejoy, 2007). In contrast, quadriceps act as extensors in quadrupedal primates during all knee movements. Their knee remains flexed (approximately 40 degrees) during locomotor activities, increasing both patellofemoral and tibiofemoral forces (Lovejoy, 2007). The flatter trochlea in quadrupedal primates allows the patellofemoral surface to bear higher stress when the quadriceps press the patella against it. Moreover, vastus medialis inserts more on the proximal rather than the medial margin of the patella. This, combined with the flatter trochlear surface, results in a flatter posterior articular surface of the patella compared to humans (Pina et al., 2014).

Differences in muscle position and function, particularly in the quadriceps, contribute to external knee morphology variations between primates, as pointed out by Lovejoy (2007):

1) Femoral condyles in humans are elongated in the sagittal plane compared to quadrupedal primates.

2) The femoral lateral condyle is elongated anteroposteriorly in humans, increasing joint stress during the last 20 degrees of extension while reducing stress from ground reaction force. This elongation creates multiple surfaces of the patella, bearing distinct angulated planes in different stages of flexion and extension. This mechanism is likely due to the anterior and posterior tibial attachments of the lateral meniscus in humans. In contrast, quadrupedal primates typically have a lateral condyle with a nearly perfect circular cross-section. This anatomical structure leads to consistent joint stress across various joint positions and reduces stress in the patellofemoral contact area during knee flexion.

3) In humans, the medial femoral condyle is elongated anterolaterally compared to quadrupedal primates.

Non-human great apes exhibit several distinctive differences in knee anatomy. For instance, the lateral meniscus is completely circular and attaches to the tibia at a single point. Additionally, the posterior surface is connected to the Wrisberg ligament (a ligament rarely found in humans), which attaches to the inner side of the medial femoral condyle (Girgis et al., 1975). Unlike humans, great apes lack an anterior transverse ligament, and their medial meniscus is not directly connected to the medial collateral ligament, as it is separated by a bursa. These anatomical differences allow for a greater range of knee movement in non-human great apes compared to humans. (e.g., Tardieu, 1999; Landis & Karnick, 2006; Organ & Ward, 2006; Javois et al., 2009; Sylvester & Pfisterer, 2012).

Due to differences in weight distribution through the lower limb and the size of femoral condyles, non-human apes exhibit a contrasting pattern of tibial condyle sizes compared to humans. Specifically, the medial tibial condyle is significantly larger and more convex than the lateral condyle. The tibial plateau in non-human apes is compressed in a supero-inferior direction, with a relatively thin lateral epicondyle (e.g., Berger & Tobias, 1996; Zipfel & Berger, 2009; Frelat et al., 2017). While the insertions and attachments of collateral and cruciate ligaments are similar in apes and humans (Figure 1.3), there are notable differences. In non-human apes, the posterior cruciate ligament attaches to the medial femoral condyle in a more anterior position and closer to the midline of the intercondylar notch than in humans (Aiello & Dean, 1990). This anatomical difference permits greater medial rotation of the tibia in non-human apes compared to humans (Tardieu, 1999).

These traits in non-human apes allow for greater rotation of the knee during locomotion compared to humans. In humans, the knee joint rotates only slightly during the last phase of the stance phase, and these traits assist more with knee extension (Tardieu, 1981).

1.2 Locomotor behaviour and biomechanics of knee posture during the gait cycle

1.2.1 Humans

In terms of locomotor and postural behaviors, humans primarily engage in bipedal walking but also perform activities like running, jumping, and squatting, which can significantly alter knee positioning (e.g., Mann & Hagy, 1980; Nilsson & Thorstensson, 1989; Racic et al., 2009). During walking, the knee joint is typically maintained in an extended posture (Figure 1.4d), leading to minimal variability in joint forces on the distal femur and proximal tibia (Preuschof & Tardieu, 1996). This results in both femoral condyles distributing load evenly across the tibial plateau during movement (e.g., Tardieu, 1999; Lovejoy, 2007; Sylvester & Pfisterer, 2012; Sylvester, 2013). When the lower limb is flexed, the knee allows about 45 degrees of external and 25 degrees of internal rotation, with the amount of axial rotation depending on external loading. When the lower limb is unloaded, the knee exhibits high rotational flexibility, which reduces with increased loading (Lovejoy, 2007). As the knee extends, the patellar tendon aligns with the center of knee rotation, enhancing the leverage of the quadriceps muscle due to the anterior projection and vertical extension of the tibial tuberosity. Whe the knee is at its full extension, slight mediolateral rotation stabilizes the knee joint (Tardieu, 1999). In both humans and African apes, the medial and lateral collateral ligaments tighten the knee during full extension, limiting rotation and hyperextension of the knee, while loosening in flexion to permit more rotational movement. The medial collateral ligament tightens during external rotation and loosens with internal rotation, whereas the lateral collateral ligament tightens during flexion-extension due to contraction of the biceps tendon (Hirschmann & Muller, 2015). The cruciate ligaments play a crucial role in preventing the femur from sliding off the tibia during the knee flexion or extension. Specifically, the posterior cruciate ligament prevents anterior sliding of the femur when the knee is flexed, while the anterior cruciate ligament prevents posterior sliding during knee extension (Figure 1.3b-f). These ligaments also limit medial rotation of the tibia relative to the femur, untwisting when the tibia rotates laterally (Aiello & Dean, 1990).

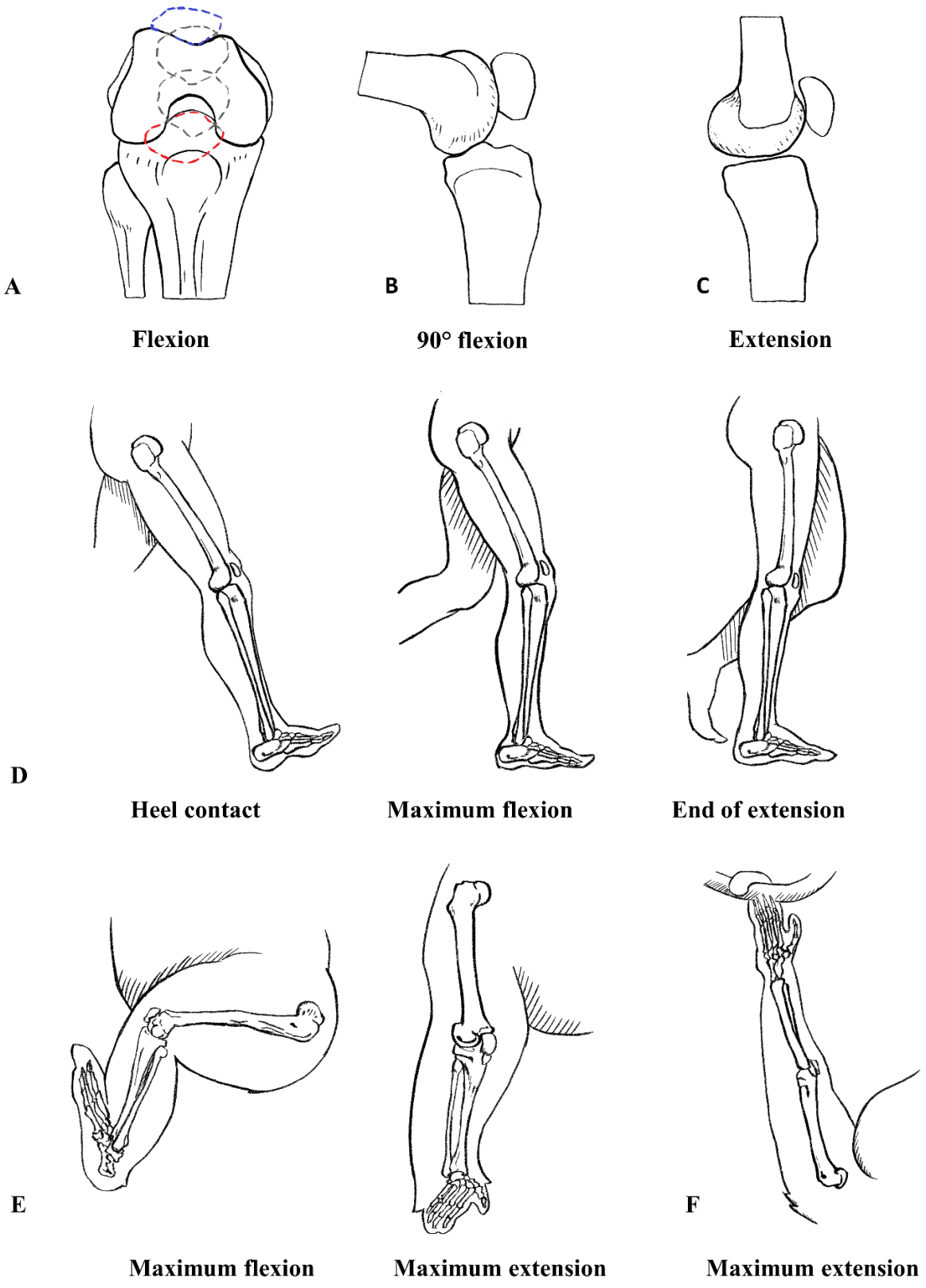

Figure 1.4: (A) Patella position during the range of flexed-extended human knee showing in inferior view; red, maximum flexion; blue, maximum extension. (B) Patella position during 90° human knee flexion showing in medial view. (C) Patella position during maximum human knee extension in medial view. (D) Expected human knee posture during bipedal walking. (E) *Gorilla* and *Pan* knee posture in maximum flexion during vertical climbing and maximum extension during terrestrial knuckle-walking. (F) Expected *Pongo* knee posture during arboreal locomotion.

The human foot is relatively short compared to the femur and tibia. This proportionality results in the knee being positioned further forward relative to the ground reaction force, while the hip joint is closer to the load, regardless of knee flexion (Preuschof & Tardieu, 1996). These anatomical features limit the extent to which the reaction force can shift forward toward the knee joint. Consequently, the lever arm of the ground reaction force tends to be long, leading to relatively high torques on the loads. Additionally, the force arm of the quadriceps muscle remains short, regardless of the knee position. To counterbalance these torques, a well-developed quadriceps muscle is essential (Preuschof & Tardieu, 1996).

1.2.2 Pan

Non-human great apes display a wide variety of locomotor behaviors, shaped by factors such as habitat, body size, and age (though this thesis focuses exclusively on adults in all projects), as well as sex (e.g., Harcourt-Smith & Aiello, 2004; Sylvester & Organ, 2010; Haile-Selassie et al., 2012; Sylvester, 2013; DeSilva et al., 2018). *Pan* species, for instance, predominantly engage in terrestrial knuckle-walking, yet a significant portion of their locomotor activities encompasses various terrestrial and arboreal behaviours. These behaviors include quadrupedal walking (22% of locomotor time), vertical climbing and descent (68%), bipedal walking (3%), brachiation and forelimb swinging (7%), and dropping and leaping (1%) (Thorpe & Crompton, 2006).

In all projects within this thesis, *Pan* is exclusively represented by *Pan troglodytes verus* from the Taï National Forest, Ivory Coast. Doran (1996; 1997) observed that Taï Forest *Pan* engaged in 84% terrestrial and 16% arboreal locomotion on average. While there are no significant sex differences in the overall frequency of terrestrial and arboreal locomotion, notable distinctions exist in arboreal locomotor behaviour between sexes. During arboreal locomotion, adult male *Pan* exhibit significantly less quadrupedalism (23.4% in males vs. 60.6% in females) and more vertical climbing (60.2% in males vs. 52.4% in females) (Doran, 1996). In both sexes, limbs often experience external forces (substrate reactions), resulting in varying degrees of knee flexion (Figure 1.4e) and hip abduction during both terrestrial and arboreal locomotion (e.g., D'Août et al., 2004; Isler, 2005; Pontzer et al., 2009; Ankel-Simons, 2000; Georgiou et al., 2018).

In non-human primates, including *Pan*, the ground reaction force typically passes in front of the knee due to the relatively long foot and short tibia. This biomechanical arrangement is compensated for by strong flexors rather than relying heavily on the knee joint itself, as

observed in humans (e.g., D'Août et al., 2004; Isler, 2005; Pontzer et al., 2009). During terrestrial knuckle-walking, knee flexion varies from about 161.4 to 117.4 degrees, with differences in vertical ground reaction force observed among individuals (Kozma et al., 2018). Although there is external rotation during knee extension in *Pan*, the knee primarily supports weight in flexed and varus postures during terrestrial locomotion (Lovejoy, 2007). Due to differences in the bicondylar angle compared to humans, the ground reaction force tends to pass more medially from the centre of the knee in *Pan* (Preuschof & Tardieu, 1996). The varying sizes of the femoral condyles result in mediolateral knee rotation during quadrupedal locomotion, with the medial condyle bearing more load than the lateral condyle (e.g., Tardieu, 1999; Landis & Karnick, 2006; Organ & Ward, 2006; Javois et al., 2009; Sylvester & Pfisterer, 2012; Sylvester, 2013). However, this condylar shape also limits tibial movement over the trochlear surface, preventing full extension (Tardieu, 1999). During climbing, *Pan* may utilize their full tange of knee flexion-extension (D'Août et al., 2002; Isler, 2005). The lateral meniscus's single attachment point enables both medial and lateral knee rotation in *Pan*, while the distinctive flattening of the femoral trochlea permits unrestricted movement of the patella during knee rotation, which is associated with foot grasping in arboreal activities (Tardieu, 1999).

1.2.3 Gorilla

Gorilla individuals primarily engage in terrestrial knuckle-walking, with varying levels of arboreality depending on their habitat and body size (Remis, 1994; Doran, 1996; 1997; Isler, 2005; Tocheri et al., 2011). They also engage in quadrupedal walking (53% of locomotor time), vertical climbing and descent (40%), bipedal walking (2%), and brachiation and forelimb swinging (5%) (Thorpe & Crompton, 2006). Different *Gorilla* species exhibit variations in locomotor behaviours based on their habitats, ranging from forests in high altitudes to lowland rainforests (Remis, 1994; Doran, 1996; 1997; Kuroda et al., 1996; Doran & McNeilage, 1998). In this thesis, the term *Gorilla* refers exclusively to *Gorilla gorilla gorilla* from Cameroon and the Democratic Republic of the Congo, which are more arboreal compared to mountain gorillas (*Gorilla beringei beringei*) (e.g., Isler, 2005, Remis, 1994). During terrestrial knuckle-walking, the knee is flexed, much like in *Pan*, and the hip is abducted to varying degrees. Knee angles range from approximately 163.2 to 126.6 degrees (Kozma et al., 2018). Hip abduction facilitates climbing, especially considering the large belly of *Gorillas*, which limits hip flexion in the sagittal plane during climbing and quadrupedal postures (Preuschof & Tardieu, 1996). This adducted lower limb establishes a varus knee angle and allows the foot to be placed underneath

the body mass centre (Preuschof & Tardieu, 1996). The flexion-extension range at the hip differs by more than 30 degrees in *Gorilla*, with females exhibiting a higher range compared to males (Hammond, 2014), impacting knee angles as well. Isler (2005) documented other sex differences in the proportion of arboreality in *Gorilla*, with females tending to be more arboreal. In adult female *Gorilla*, the maximal extension of the hip and knee during vertical climbing reaches approximately 135 degrees, which is notably greater than the 100 degrees observed in adult males (Isler, 2005). Furthermore, male *Gorilla* display a reduced range of motion in both the hip and knee joints during vertical climbing compared to females (Isler, 2005). When compared to *Pan*, *Gorilla* exhibit greater limb extension both during terrestrial locomotion and vertical climbing (Isler, 2005; Crompton et al., 2008; Kozma et al., 2018).

1.2.4 Pongo

Pongo, represented by *Pongo pygmaeus* and *P. abelii* in this thesis, exhibit diverse locomotor behaviours due to their highly arboreal lifestyle, characterized by extreme joint mobility to achieve balance (e.g., Payne et al., 2006; Thorpe & Crompton, 2006; Thorpe et al., 2009). Their locomotor repertoire includes quadrupedal walking (18% of locomotor time), vertical climbing (16%), vertical descent (9%), bipedal walking (7%), orthograde clamber and transferring (21-22%), brachiation and forelimb swinging (13-14%), dropping and leaping (1-2%), suspensory locomotion (3-4%), and swaying (6-7%) (Thorpe & Crompton, 2006). The use of these behaviours varies depending on habitat, support size, and purpose (e.g., Thorpe & Crompton, 2006; Manduell et al., 2012).

Pongo exhibits significant locomotor differences between species and individuals, influenced by environmental factors (Thorpe & Crompton, 2005; 2006; Manduell et al., 2012). For example, *P. abelii* engages in less suspensory locomotion and more pronograde locomotion compared to *P. pygmaeus*. Additionally, *P. abelii* descends to the ground less frequently, posibly due to the thread posed by predators such as the Sumatran tiger (Sugardjito & van Hooff, 1986). Overall, *Pongo* species differ from African apes in their use of torso-pronograde suspensory locomotion and exhibit a broader range of positional behaviors (Cant, 1987; Isler & Thorpe, 2003; Thorpe & Crompton, 2006; Thorpe et al., 2009).

During terrestrial locomotion, the knee of *Pongo* may not differ distinctly from that of African apes, with adult *Pongo* demonstrating knee extension comparable to adult female *Gorilla* but exhibiting greater hip joint mobility (Isler, 2005). In arboreal locomotion, *Pongo* shows a wide range of knee postures, from hyper-flexed to extended positions (Figure 1.4f), resulting in a

broader range of knee motion compared to *Pan* and *Gorilla* (Isler, 2005; Thorpe & Crompton, 2005; 2006; Payne et al., 2006; Thorpe et al., 2009). Additionally, *Pongo* elevates their feet much higher than both *Gorilla* and *Pan* and occasionally engages in bipedal locomotion on tree branches (Thorpe & Crompton, 2006). While some research suggests that female *Pongo abelii* are more arboreal, other studies have found no significant differences in arboreality between sexes (Cant, 1987; Galdikas, 1988; Thorpe & Crompton, 2005; 2006).

Locomotion and muscular activity impose stress on the skeleton, which in turn affects the trabecular bone structure. The positioning of joints during frequent and intensive locomotor activities is expected to be mirrored in the distribution of trabecular bone within major joints. Consequently, it is anticipated that apes will show unique organizational patterns in their knee joints. This thesis aims to identify these patterns in the distal femur and proximal tibia of living hominids and examine their relationship with locomotor behavior, with the ultimate goal of inferring locomotor patterns in extinct hominins.

1.3 The evolution of bipedalism in hominins

Primates are distinguished from most other mammals by their unique gait characteristics (e.g., Cartmill et al., 2002; Schmitt & Lemelin, 2002; Schmitt, 2003). The combination of locomotor characteristics, particularly in arboreal primates, results in a distinct functional differentiation between forelimbs and hindlimbs. The use of forelimbs during locomotion has been implicated in the evolution of obligate bipedalism (e.g., Reynolds, 1985; Schmitt, 1994; Larson et al., 2001; Schmitt & Lemelin, 2002). Obligate bipedalism has been widely accepted by paleoanthropologists as one of the defining traits of the hominin lineage (e.g., Harcourt-Smith & Aiello, 2004; DeSilva, 2009) and the ability to extend the hindlimb and adopt a habitual upright bipedal gait can be traced back to around 6 million years ago in the hominin lineage (e.g., Arnason et al., 1998; Pickford et al., 2002; Crompton et al., 2008). This period of human evolution is marked by a combination of traits that suggest the potential for bipedal movement alongside arboreal locomotion. However, differences between early hominin bipedalism and that of modern humans have been a topic of debate (e.g., Stern & Susman, 1983; Susman et al., 1984; Ward, 2002; Carey & Crompton, 2005; Lovejoy & McCollum, 2010; Raichlen et al., 2010). Early hominins exhibit ape-like features such as relatively short lower limbs, curved fingers and toes, and a varus knee angle, as well as derived features associated with bipedalism, including short, laterally facing iliac blades. Additionally, unique features like an exceptionally wide, platypelvic pelvis have been observed, sparking considerable debate among researchers (Stern, 2000; Ward, 2002). Some argue that the locomotor mode of early hominins was

kinematically distinct from modern human bipedalism (e.g., Oxnard, 1975; Tuttle, 1981; Stern & Susman, 1983; Berge, 1984; 1991; 1994; Susman et al., 1984; Berge & Kazmierczak, 1986; McHenry, 1986; Ruff, 1988; Berge, 1991; Duncan et al., 1994; Sanders, 1998; Stern, 2000). However, others suggest a similarity between the gait of early hominins and modern humans (e.g., Robinson, 1972; Latimer et al., 1987; Latimer & Lovejoy, 1989).

Sahelanthropus tchadensis, one of the earliest known hominins, offers significant insight into the origins of bipedalism. Despite uncertainties surrounding its exact locomotor behavior, the position of the foramen magnum, located more anteriorly than in non-bipedal apes, suggests that *Sahelanthropus* may have adopted an upright, bipedal posture. However, unlike later hominins, its femur and postcranial anatomy remain largely undiscovered, leaving open questions regarding the extent of its bipedalism (e.g., Cazenave et al., 2024; Daver et al., 2022; Harcourt-Smith & Aiello, 2004; Mayer et al., 2023; Neaux et al., 2017; Shapiro, 2009; Stamos & Alemseged, 2023). Moreover, *Orrorin tugenensis*, provides one of the earliest known evidence in femur for adaptations to upright bipedalism, such as relatively straight femoral shaft and enlarged femoral head which are consistent with weight-bearing and upright postures (Senut, 2002; Crompton et al., 2008; Richmond & Jungers, 2008). Further adaptations for bipedalism are evident in the pelvis and femur of *Ar. ramidus* (Lovejoy et al., 2009). These includes a broad iliac blade and an anteriorly oriented iliac crest, a relatively long and straight femoral neck, an enlarged femoral head, and a broad and robust femoral shaft, and a lumbar region with a slight curvature that helped to support the weight of the upper body during bipedal walking (Lovejoy et al., 2009). Although uncertainties persist regarding the function of morphological traits such as broadening of the sacrum and modification of the abductor apparatus (Lovejoy & McCollum, 2010). Despite being widely accepted as bipedal hominins, the degree of arboreality in the *Australopithecus* genus has been questioned (Berge, 1994), and the biomechanics of their bipedal locomotion remain debated (Stern & Susman, 1983; White & Suwa, 1987; Lovejoy et al., 2002; Ward, 2002; Carey & Crompton, 2005; Raichlen et al., 2010). Recent studies suggest that *A. afarensis* did not rely on a bent-hip, bent-knee gait (Sellers et al., 2004; Pontzer et al., 2009). *A. afarensis* exhibits a combination of primitive and derived traits, suggesting habitual bipedalism with varying degrees of arboreal locomotion. Evidence from the anatomy of the pelvis, femur, knee, foot, and spine suggests that *A. afarensis* was adapted for habitual bipedal locomotion. The pelvis is broad and bowl-shaped, with features such as a short iliac blade and anteriorly oriented iliac crest (Stern & Susman, 1983; Berger, 1994; Lovejoy, 2005; Harmon, 2009). The angle of the femur (valgus angle) is similar to that of

modern humans, contributing to stability during bipedal walking (Lovejoy & Heiple, 1970; Stern & Susman, 1983; Berger, 1994; Lovejoy, 2007; Harmon, 2009). The tibial plateau is large and weight-bearing with a relatively large lateral condyle (Stern & Susman, 1983; Berger, 1994; Lovejoy, 2007). The lumbar region of the spine exhibits a slight curvature (lumbar lordosis), contributing to stability during bipedal walking. The foot of *A. afarensis* shows a combination of ape-like and human-like features, with a divergent hallux (big toe) and a longitudinal arch, indicative of bipedalism (Stern & Susman, 1983; Clarke & Tobias, 1995; Ward et al., 2011). However, the foot also retains some adaptations for arboreal climbing, such as a mobile midfoot and robust, curved toe bones (Stern & Susman, 1983; Clarke & Tobias, 1995; Ward et al., 2011). Moreover, despite its bipedal capabilities, *A. afarensis* retained other arboreal adaptations, suggesting a partially arboreal lifestyle. The shoulder morphology suggests the retention of some climbing abilities, with features like a scapula positioned more dorsally and a mobile shoulder joint (Vrba, 1979; Green & Alemseged, 2012; Larson, 2013; Kivell et al., 2018). The curved phalanges and long arms also indicate adaptive modifications for climbing and arboreal locomotion, although they are less pronounced than those of earlier apes (Ricklan, 1987; Alba et al., 2003; Ward et al., 2014; Skinner at al., 2015).

The earliest members of the genus *Homo*, such as *Homo habilis*, also exhibit features indicative of bipedal locomotion alongside arboreal activities (e.g., curved phalanges, mobile shoulder joint, retention of a prehensile foot, longer arms relative to legs, enhanced joint stability, powerful hand grip and expanded rib cage). These features indicating the bipedal locomotion are forward position of the foramen magnum, S-shaped curvature of the spine, short and broad pelvis, broad iliac blades, valgus knee angle, long legs relative to arms, and shortened toes which all together provides stability and support for upright bipedal walking, although *H. habilis* may not have been as efficient or fully specialized bipedal walker as later hominin species (Susman & Stern, 1982; Susman, 1983; Susman et al., 1984; McHenry & Berger, 1998; Ward et al., 1999). The locomotor behavior of later hominins, such as *Homo erectus*, is less debated due to their more modern body form, characterized by long hindlimbs and robust joints (Jungers, 1988; McHenry, 1991). It is broadly accepted that *H. erectus* walked and ran in a manner similar to that of modern humans (Carrier et al., 1984; Stanley, 1992; Gruss & Schmitt, 2015).

In this thesis, we investigate trabecular bone distribution in *Australopithecus africanus*, *Australopithecus sediba*, *Homo floresiensis*, and *Homo neanderthalensis*. Although preserving trabecular structure in fossil knee bones presents challenges (refer to section 2.3 on the

Preservation of External and Internal Knee Morphology of Fossil Hominins), analyzing this tissue can still offer insights into past behaviors, as trabecular bone undergoes changes throughout an life of an individual. This thesis incorporates *Australopithecus* specimens to clarify locomotor indicators in the distal femur of Pliocene-Pleistocene South African hominins. Three distal femora (StW 318, StW 129, and TM 1513) from Sterkfontein caves, South Africa, are assigned to *A. africanus*. One distal femur (U.W. 88-63) from Mapala cave, South Africa, is assigned to *A. sediba*. Two distal femora (LB1-8 and LB1-9) and two proximal tibiae (LB1-13 and LB8-1) from Liang Bua cave, Indonesia, are assigned to *H. floresiensis*. *H. floresiensis* is included in the sample due to its unique lower limb morphology and its potential to reveal variability in bipedal walking within our ancestor lineage, which may be more diverse than previously thought. Additionally, one distal femur (D322-16) from Neandertal valley, Germany, is assigned to *H. neanderthalensis*, known for its obligate bipedalism, serving as a comparative model in the fossil record likely to show patterns of extended knee postures in trabecular structure.

These fossil specimens were selected for analysis based on their well-preserved or partially preserved trabecular structure, believed suitable for successful segmentation and analysis. Detailed preservation and segmentation information can be found in **Chapter 2**. Notably, the trabecular structure of some specimens in the sample has not been comprehensively analyzed previously, likely due to fragmentation, poor trabecular bone preservation, or limited accessibility of the distal femur or proximal tibia. Therefore, analyzing these specimens is particularly compelling as it may provide valuable insights into whether the preserved trabecular structure reflects any locomotor or postural patterns.

1.4 Australopithecus africanus

A. africanus, a South African hominin from around 3.3 to 2.1 million years ago (Alemseged, 2023), exhibits upper limb morphology suggestive of arboreal activities, while its lower limb features adaptations that align with habitual bipedalism. Research on limb proportions and joint sizes of *A. africanus* has highlited its relatively more ape-like skeletal morphology (Green et al., 2007). Additionally, investigations of the internal structure of the humerus in *A. africanus* have provided evidence consistent arboreal adaptations (Kivell et al., 2018). However, *A. africanus* also exhibits several features in the knee joint that suggest adaptations for bipedal locomotion. These include a relatively valgus (angled outward) knee joint similar to modern humans, which facilitates stability during bipedal walking (Jungers, 1988). Additionally, the distal femur and proximal tibia exhibit structural features indicative of weight-bearing

adaptations that align with habitual bipedalism (Barak et al., 2013b; Ryan et al., 2018). Moreover, studies on the attachment sites of ligaments around the knee joint in *A. africanus* suggest that they may have had a functional significance related to knee stability during locomotion (Moffett et al., 2015).

Comparisons with other australopith species, such as *A. afarensis*, reveal both similarities and differences in knee morphology, reflecting variations in locomotor behaviours and environmental adaptations among early hominins (Richmond et al., 2001). Additionally, analyses of the internal structure of the humerus in *A. africanus* reveal arboreal adaptations (Kivell et al., 2018). Studies of the femoral head and distal tibia suggest that *A. africanus* experienced hip loading during bipedal walking that resembles modern humans, with the lower limb predominantly in an extended position (Barak et al., 2013b; Ryan et al., 2018). The hand remains show a combination of morphological traits: the external structure of the wrist and metacarpals is intermediate between modern humans and great apes (McHenry, 1983; Green & Gordon, 2008), while the overall proportions of the hand bones indicate a shape more similar to modern humans than to apes (Richmond et al., 2016). However, the phalanges exhibit more ape-like characteristics, including robust shafts and a moderate degree of curvature (Kivell et al., 2020).

1.5 Australopithecus sediba

A. sediba is a late Pliocene australopith from South Africa, represented mainly by two individuals: Malapa Hominin 1 (MH1) and Malapa Hominin 2 (MH2), dated to approximately 1.98 million years ago (Dirks et al., 2010). The upper limb of *A. sediba* displays primarily primitive characteristics, while the lower limb shows a blend of both primitive and derived features (Berger et al., 2010; Zipfel et al., 2011; Churchill et al., 2013; 2018; DeSilva et al., 2018). Although the pelvis and lower limb indicate bipedality, the foot has ape-like morphology which suggests some climbing capability and/or a bipedal gait distinct from that of modern humans (Zipfel et al., 2011; DeSilva et al., 2018). Analysis of the knee joint external morphology in *A. sediba*, focusing on the distal femur and fragments of the proximal tibia, reveals a unique combination of ancestral traits associated with a flexed knee posture and derived features indicative of an extended knee posture. These traits suggest adaptations for both bipedal and arboreal locomotion (Churchill et al., 2013; DeSilva et al., 2018). The upper limb is noted for its relatively long forearms and a superiorly oriented glenoid fossa, which are advantageous for arboreal activities (Berger et al., 2010; Churchill et al., 2013; 2018). The hand, however, exhibits a blend of primitive and derived traits (Kivell et al., 2011; 2018). The nearly

complete right hand of MH2 displays a mix of ape-like and human-like features in the wrist, gracile metacarpals, and curved phalanges, with some proportions similar to those of modern humans (Kivell et al., 2011; 2018).

1.6 Homo floresiensis

H. floresiensis is a hominin species from the island of Flores in Indonesia, dating to approximately 100,000 to 60,000 years ago (Sutikna et al., 2016). The initial discovery of *H. floresiensis* was based on a nearly complete skeleton of specimen LB1, and subsequent excavations have revealed additional individuals of this species. The distinctive combination of upper and lower limb morphology in *H. floresiensis* is unique among fossil hominins. Currently, our understanding of the knee morphology of *H. floresiensis* is limited due to the scarcity of well-preserved tibial, femoral, and patellar elements. Studies have suggested that the knee joint of *H. floresiensis* shares some similarities with modern humans, indicating bipedal locomotion (Brown et al., 2004; Jungers et al., 2009). A study conducted by Jungers et al. (2009) examined the limb proportions and biomechanical implications of the LB1 skeleton. They found that while *H. floresiensis* had relatively long feet compared to their stature, the knee joint appeared to be more similar to that of humans than apes. This suggests that *H. floresiensis* likely engaged in bipedal locomotion, although there may have been some unique aspects to their gait due to their distinctive limb proportions (Brown et al., 2004; Jungers et al., 2009). Interestingly, the upper limb shows no clear evidence of adaptations for climbing. The bones of the upper limb are relatively robust for their length, featuring a scapula with a himan-like shape and a humerus showing minimal torsion (Morwood et al., 2005; Larson et al., 2007; 2009). These features suggest that *H. floresiensis* may have had limited dexterity and restricted range of motion in overhead arm movements. In terms of the hand, only wrist bones, phalanges, and a fragmentary metacarpal have been recovered (Larson et al., 2009). Both external and internal examinations of the wrist bones reveal a primitive, ape-like structure, lacking the specialized features typically associated with effective and forceful tool use (Tocheri et al., 2007; 2008; Orr et al., 2013; Bird et al., 2024). However, further research is necessary to fully understand the knee morphology and biomechanics of *H. floresiensis*.

1.7 Homo neanderthalensis

The locomotor and behavioral traits of *H. neanderthalensis* are often compared to those of modern humans due to similarities in the skeletal structure. However, notable morphological differences between *H. neanderthalensis* and *H. sapiens*, as well as variations in their respective

archaeological records, warrant distinct discussions about *H. neanderthalensis* behaviour. Generally, the *H. neanderthalensis* skeleton is characterized by a broader body, relatively shorter limbs, robust long bones with thick cortical bone, prominent muscle attachment sites, and a wider pelvis compared to modern humans (e.g., Wroe et al., 2018; Ocobock et al., 2021). The increased robustness of the *H. neanderthalensis* skeleton is thought to be an adaptation to diverse climatic conditions and a wide range of physical activities (e.g., Wroe et al., 2018; Ocobock et al., 2021). Additionally, the broad geographical range of *H. neanderthalensis* contributes to noticeable morphological variability across various populations of this species (Rosas et al., 2016). One notable feature of *H. neanderthalensis* knees is the presence of a relatively large and robust tibial tuberosity. This structure serves as an attachment site for the patellar ligament, indicating that *H. neanderthalensis* likely had a well-developed quadriceps muscle. The robusticity of the tibial tuberosity suggests that *H. neanderthalensis* exerted significant force through their knees, possibly due to activities such as climbing, squatting, or carrying heavy loads (e.g., Fennell & Trinkaus, 1997; Miller & Gross, 1998; Trinkaus et al., 1999; Pearson et al., 2006; Belcastro et al., 2020). Additionally, analyses of the shape and alignment of the knee joint in *H. neanderthalensis* suggest that they may have had a slightly different gait pattern compared to modern humans. While *H. neanderthalensis* were bipedal like us, their knees exhibited subtle differences in morphology that could have influenced the mechanics of their walking and running. For example, some studies suggest that *H. neanderthalensis* had a slightly more flexed knee posture during walking, which may have affected their overall stride length and energy efficiency (e.g., Hora & Sladek, 2014).

1.8 Trabecular bone functional adaptation

Trabecular bone is the spongy, porous tissue located in the epiphyses of long bones as well as within short and irregular bones (e.g., Keaveny et al., 2001). Comprising groups of lamellar bone, trabecular bone closely resembles cortical bone in composition, although cortical bone is generally denser and surrounds the marrow space (Choi & Goldstein, 1992). Bone modelling refers to the process by which bones change in size and shape throughout an individual lifetime in response to various mechanical, hormonal, and metabolic factors. It primarily occurs during growth and development, allowing bones to adjust their size and shape to accommodate changes in mechanical loading and functional demands. Bone modelling is responsible for the initial formation of bone during embryonic development and the growth of bones during childhood and adolescence. This process involves the coordinated actions of osteoblasts (bone-forming cells) and osteoclasts (bone-resorbing cells) to either deposit new bone tissue or remove existing

bone tissue in targeted areas of the skeleton. The rate of this (re-)modeling process is regulated by various calciotropic hormones, such as parathyroid hormone (PTH), thyroid hormones, and sex steroids, and depends on the activity of these resorptive and formative cell populations (Eriksen, 2010). Trabecular bone undergoes structural changes through osteoblastic deposition and osteoclastic resorption (e.g., Ehrlich & Lanyon, 2002; Ott, 2002; Dempster, 2003). This process requires precise regulation, as imbalances between bone resorption and formation can lead to excessive bone loss or abnormal bone mass, increasing the risk of fractures or compression syndromes (Eriksen, 2010). Trabecular bone modeling occurs on the surfaces of trabeculae and typically spans around 200 days (Eriksen, 2010). It begins with osteoclastic resorption, which creates a resorption gap over approximately 30-40 days, followed by new bone formation (Eriksen et al., 1986). By the end of this cycle, the resorption gap is fully renewed with new bone (Eriksen et al., 1990). Trabecular bone (re-)modeling sites are generally located near red bone marrow, whereas cortical bone remodeling sites are situated further from it (Parfitt, 2000). Consequently, the mechanisms of bone modeling are thought to differ between trabecular and cortical bone. For instance, cells involved in trabecular bone modeling migrate directly from red bone marrow to the bone surface, while those involved in cortical bone modeling access the bone through the vascular system (Eriksen, 2010). Compact bone adjusts its thickness to enhance resistance to bending forces, while trabecular bone maintains its structure to optimize the transfer of kinetic energy (e.g., Keaveny et al., 2001; Sugiyama et al., 2010; Reznikov et al., 2015).

Bone (re-)modelling is the continuous process by which mature bone tissue is resorbed and replaced throughout life to maintain bone strength, repair microdamage, and regulate calcium homeostasis. Unlike modelling, which primarily affects the overall shape and size of bones, remodelling occurs at the microscopic level, involving the turnover of individual bone tissue units called osteons or Haversian systems. (Re-)modelling involves the sequential actions of osteoclasts, which resorb old or damaged bone tissue, and osteoblasts, which deposit new bone tissue to replace the resorbed material. It occurs at discrete sites on bone surfaces known as remodelling units, where osteoclastic resorption and osteoblastic formation activities are tightly coupled. Bone (re-)modelling is influenced by a variety of factors, including mechanical loading, hormonal regulation, and systemic factors such as calcium and vitamin D levels. This process helps maintain bone strength and repair microdamage, ensuring that the skeleton remains structurally sound and capable of withstanding mechanical stressors (e.g., Parfitt, 2000; Keaveny et al., 2001; Eriksen, 2010; Sugiyama et al., 2010; Reznikov et al., 2015).

Several genetic and environmental factors, in addition to specific locomotor behaviors, can influence the (re-)modeling of bone internal structure (Ruff et al., 2006). Genetic factors, such as hormonal variations or differences in bone regulation among closely related species, may affect trabecular bone (re-)modeling (e.g., Turner et al., 2000; Loewen et al., 2001; Lovejoy et al., 2003; Paternoster et al., 2013). There may also be variations between sexes or across different life stages (Reginster & Burlet, 2006), which can result in phylogenetic differences in internal bone structure (Ryan & Shaw, 2013). Other factors, such as diet and the composition of the intestinal microbiome, can also play a significant role (McCabe et al., 2015). Additionally, the (re-)modeling processes are generally more effective during growth stages than in adulthood (e.g., Halloran et al., 2002; Seeman, 2003; Glatt et al., 2007; Wallace et al., 2013; Sarringhaus et al., 2014; Saers et al., 2020). The complexity of these factors makes it challenging to accurately determine the relationship between bone structure and an the behaviour of an individual, complicating the interpretation of research findings (e.g., Kivell, 2016; Wallace et al., 2017; Tsegai et al., 2018a).

Trabecular bone primarily function is to absorb and transfer joint loads to the cortical bone shafts (Currey, 2012). It adapts to local stress by responding to its mechanical environment (Ruff et al., 2006). Areas subjected to lower stress experience a gradual decrease in trabecular bone density, leading to a weaker bone structure, while regions under higher stress show an increase in trabecular bone density, resulting in a stronger bone structure (e.g., Pontzer et al., 2006; Barak et al., 2011; Sinclair et al., 2013). Research has shown that examining internal bone structure can offer insights into an individual's biomechanics throughout their life, providing additional information beyond what is evident from external bone morphology alone (e.g., Schilling et al., 2014).

Several experimental studies have shown the remarkable capacity of bones to adapt to extreme conditions, enduring loads without fracturing or causing permanent damage (e.g., Ehrlich & Lanyon 2002; Barak et al., 2011; Wallace et al., 2013; Tsegai et al., 2018a; 2018b). It is generally acknowledged that high impact loading is most effective during skeletal growth but decreases in efficacy with age. However, such loading also carries an increased risk of fracture, making it less common compared to loading with lower magnitudes. Interestingly, even loads from irregular directions may stimulate trabecular (re-)modelling, even at relatively low magnitudes (e.g., Nikander et al., 2005; 2006; 2009; Wallace et al., 2013). Rubin et al. (2001) revealed that bones adapt to a variety of loading conditions, which can range from low intensity and high frequency to high intensity and low frequency. This phenomenon is typically referred

to as bone functional adaptation (Ruff et al., 2006). A balance between bone mass and strength is often necessary due to energy constraints, leading to adaptations that enable species to support different locomotor activities, resist fractures, and conserve energy efficiently (Nicholson et al., 2006). Trabecular bone plasticity offers valuable insights into joint function and locomotor behaviour. Although the external morphology of joints appears relatively stable in terms of shape (Barak et al., 2011), trabecular bone distribution has been shown to vary across anatomical locations (e.g., Eriksen et al., 1984; Parfitt, 2000; Sinclair et al., 2013).

1.8.1 Trabecular bone quantification in anthropology

The study of trabecular bone structure holds significant importance in medical, orthopaedic, and evolutionary contexts (e.g., Klawitter & Hulbert, 1971; Hart et al., 1988; Pettermann et al., 1997; Uhthoff et al., 2006; Chen et al., 2007). Trabecular bone analysis aids in understanding human evolution (Kivell, 2016), biomechanical adaptations in modern human populations (Sievänen et al., 2007), and the (re-)modelling and biology of bones in general (e.g., Cowin, 1984; Bagge, 2000; Jacobs, 2000; Miller et al., 2002; Coelho et al., 2009). Differences in trabecular bone among extant species are often correlated with different behaviours. Establishing the relationship between structure and behaviour enables insights into the diverse lifestyles of human ancestors (e.g., Ryan & Ketcham, 2002; Griffin et al., 2010; Shaw & Ryan, 2012; Tsegai et al., 2013; 2018a; Skinner et al., 2015; Stephens et al., 2016).

Moreover, several studies have investigated the link between trabecular architecture and inferred joint position, shedding light on how skeletal structure reflects habitual loading and joint mechanics. Research has demonstrated that the trabecular architecture in the femoral head and neck correlates with hip joint orientation during different activities such as standing, walking, and running. Trabeculae in the femoral neck are oriented to resist compressive forces experienced during weight-bearing activities, aligning with the principal stress trajectories across the hip joint (e.g., Macchiarelli et al., 1999; Ryan & Ketcham, 2005; Shaw & Ryan, 2012; Kersh et al., 2018; Georgiou et al., 2019; Cazenave et al., 2021). Investigations into vertebral trabecular architecture have revealed correlations between trabecular architecture and spinal posture. Trabecular architecture in vertebral bodies reflects the curvature and loading patterns of the spine, with differences observed between regions associated with flexion, extension, and lateral bending (e.g., Jensen et al., 1990; Smit et al., 1997; Fields et al., 2009; Auger et al., 2020). Studies examining the humeral head have shown that trabecular architecture corresponds to habitual shoulder joint positions and loading patterns and reflects the direction of forces transmitted across the shoulder joint during activities like reaching, lifting, and

overhead movements (e.g., Shaw & Ryan, 2012; Scherf et al., 2016; Kivell et al., 2018; Doershuk et al., 2019). Overall, these studies provide compelling evidence that trabecular architecture is influenced by joint mechanics and loading patterns, allowing researchers to infer habitual joint positions and movements from skeletal morphology. However, approaches to studying trabecular bone may vary across studies.

1.8.1.1 History of trabecular bone studies in anthropology

In recent years, the analysis of trabecular bone structure has typically utilized a method involving the quantification of trabecular bone within a defined Volume of Interest (VOI), typically a sphere or cube placed within an epiphysis. This VOI approach is favored for its computational efficiency, enabling researchers to extract and analyze portions of complex trabecular structures from extensive micro-computed tomography (micro-CT) datasets. Techniques for determining the size and placement of VOIs vary (e.g., Ryan & Ketcham, 2002; Schilling et al., 2014), but debates exist regarding potential biases associated with VOI size and location (e.g., Fajardo & Müller, 2001; Maga et al., 2006; Kivell et al., 2011; Lazenby et al., 2011). The goal of using VOIs is to quantify representative sections of trabecular bone within a region or epiphysis. However, this method has limitations due to the constraints imposed by trabecular morphology. VOIs must be large enough to capture significant trabecular structure (e.g., at least four trabecular struts; Gross et al., 2014), but small enough to exclude cortical bone and anatomical features like foramina. This complicates the placement of VOIs near the subarticular surface, where initial joint loading occurs, because of potential differences in trabecular structure deeper within the epiphysis (Singh, 1978; Currey, 2002). Furthermore, identifying anatomically or biomechanically comparable VOIs across samples is challenging, especially with complex morphologies or significant variation (e.g., Maga et al., 2006; Kivell et al., 2011; Lazenby et al., 2011). Despite these challenges (e.g., Fajardo & Müller, 2001; Ryan & Ketcham, 2002a, b; Maga et al., 2006), the VOI method has remained a standard practice in non-human primate studies due to its computational advantages and the lack of alternative methods.

Recently, there has been progress in trabecular bone analysis with some studies using multiple VOIs within a single anatomical region to obtain more detailed information about joint loading, though with mixed success (DeSilva & Devlin, 2012; Su et al., 2013). Techniques such as principal components analysis (PCA) have been employed to examine multiple trabecular parameters simultaneously, revealing patterns that better distinguish primate locomotor behavior than single parameters alone (Ryan & Shaw, 2012; Scherf et al., 2013; Matarazzo,

2015). For example, Scherf et al. (2013) identified distinct differences in humeral trabecular structure among humans, *Pongo*, and *Pan* by considering bone volume fraction, trabecular thickness, number, and spacing collectively. Ryan & Shaw (2012) found that variations in trabecular parameters could differentiate primate locomotor groups in the femur and, to a lesser extent, in the humerus, although they noted significant overlap in trabecular morphology, emphasizing the challenges in defining joint loading patterns. Recent studies like those by Barak et al. (2013b) have integrated both comparative and experimental data to gain insights into the functional significance of trabecular structure variations across extant and fossil taxa. For instance, Barak et al. (2013b) investigated trabecular orientation differences between *Pan* and humans in the distal tibia, reflecting distinct joint loading patterns during bipedal walking and terrestrial knuckle-walking, which has been instrumental in interpreting trabecular structures of fossil hominin tibiae, suggesting a likely extended-hip-extended-knee bipedal gait for *A. africanus* (Barak et al., 2013a, b).

Additionally, methods initially developed for clinical applications (Pahr & Zysset, 2009) have been adapted for high-resolution trabecular bone analysis across primates (Gross et al., 2014). Holistic morphometric analysis (HMA) allows for the visualization and quantification of trabecular (and cortical) bone morphology throughout entire epiphyses or bones, offering a more comprehensive understanding of joint function and behavior. This approach has been successfully applied to hominoid metacarpals (Tsegai et al., 2013; Stephens et al., 2018), humeri (Kivell et al., 2018), and carpal bones (Bird et al., 2021), providing valuable insights into habitual locomotor and manipulative behaviors across hominoids. More recently, Bachmann et al. (2022), improved HMA with a canonical holistic approach (cHMA) which allows for statistical comparisons of trabecular patterns free of *a priori* subsampling and calculates mean species models that are homologous and thus can be statistically compared (Bachmann et al., 2022). More details about how the HMA and cHMA is implemented can be found in the section 2.5 Trabecular bone analysis.

In summary, recent advancements in trabecular bone analysis have improved our ability to reconstruct joint position and behaviour in both extant and fossil taxa. These methods offer enhanced insights into locomotor behaviour and functional morphology, contributing to our understanding of primate evolution.

1.8.1.2 Trabecular bone architectural variables

Mechanical properties of trabecular bone are typically quantified using variables such as bone volume fraction (BV/TV), degree of anisotropy (DA), trabecular thickness (Tb.Th), trabecular

spacing (Tb.Sp), connectivity (Conn.D), and trabecular number (Tb.N). BV/TV represents the proportion of trabecular bone within a given volume, with higher levels indicating greater bone density and strength, particularly in regions experiencing higher stress (Pontzer et al., 2006; Barak et al., 2011; Sinclair et al., 2013). DA describes the alignment of trabeculae in three-dimensional space, with high values indicating greater alignment and anisotropic structure. BV/TV and DA together can explain a significant portion of trabecular bone's elastic properties (Van Rietbergen et al., 1999; Homminga et al., 2003; Zysset, 2003). Tb.Th reflects trabecular thickness, while Tb.Sp measures the distance between trabeculae (Hildebrand & Rüegsegger, 1997; Dougherty & Kunzelmann, 2007). Tb.N denotes the number of trabeculae per unit length (Silva et al., 2012), but these parameters are not entirely independent of BV/TV and thus do not independently explain mechanical behaviour. Conn.D quantifies the number of connected structures within a region, providing insight into trabecular connectivity and redundancy. While there is a low correlation between Conn.D and trabecular bone strength, Conn.D is frequently reported in studies of bone loss (McCalden & McGeough, 1997; Bouxsein et al., 2010). Kinney & Ladd (1998) found no direct relationship between Conn.D and elastic modulus, as Conn.D is independent of contact area, which is crucial for mechanical loading transfer. However, changes in Conn.D may impact elastic fitness, with individuals who fail to recover connectivity exhibiting lower elastic modulus for equivalent trabecular bone volumes (Kinney & Ladd, 1998). Which trabecular parameters were studied and how they were computed in this thesis can be found in section 2.5.1 Trabecular parameters.

1.8.2 Functional signals in the knee trabecular structure of extant primates

While considerable research has focused on the functional anatomy of the knee (Haxton, 1945; Blackburn & Craig, 1980; Preuschof & Tardieu, 1996; Zheng et al., 1998; Tardieu, 1999; Lovejoy, 2007; Javois et al., 2009), investigations specifically focused on the trabecular structure of knee bones remains limited (Georgiou et al., 2018; Sukhdeo et al., 2020). This scarcity may stem from taphonomic challenges, such as the lack of fossil specimens, and the inherent difficulty in studying trabecular structure in relation to functional morphology. Interest in trabecular bone analysis, particularly regarding the evolutionary pathways and functional adaptations of knee bones in hominoids, has been growing. Two significant studies have contributed to this field by examining the trabecular structure of the hominoid knee joint. Sylvester & Terhune (2017) investigated the functional aspects of trabecular bone within the entire articular surfaces of the human knee using sliding semi-landmarks within spherical VOIs. This approach allowed them to analyze the full joint surface, rather than focusing on isolated

locations as seen in previous research (e.g., Whitehouse & Dysont, 1974; Kivell et al., 2011). Their findings revealed sex-based differences in subchondral trabecular bone spacing, with females showing less uniform trabecular structures compared to males. This study offered new insights into how the distribution of trabecular bone correlates with bone loading patterns. A more recent study by Georgiou et al. (2018) analysed the trabecular structure of distal femoral epiphyses across extant hominoids to explore locomotion-related differences using a whole-epiphysis analysis approach. They discovered that humans have a higher bone volume fraction, particularly in the posteroinferior region, and exhibit more anisotropic bone compared to other great apes. Conversely, both *Pan* and *Pongo* species showed higher bone volume fractions posteriorly compared to other hominoids.

Interspecific patterns in trabecular structure variation have been observed, with species exhibiting similar trabecular structure across various skeletal elements. For example, modern humans generally have lower volumes of trabecular bone in heavily loaded lower limb bones like the femur compared to other hominoids. In contrast, *Pan* species often display higher trabecular volumes across different skeletal regions (Griffin et al., 2010; Tsegai et al., 2013). However, interpreting these structures can be complex. Studies have shown that mean bone volume fractions vary within specific regions, such as the medial condyle. For instance, Sukhdeo et al. (2020) observed similar mean bone volume fractions in the medial and lateral condyles among baboons, *Pan*, and *Pongo*, but noted that humans had a higher mean bone volume fraction in the lateral condyle. Additionally, Mazurier et al. (2010) found that humans possess a thicker cortico-trabecular complex in the medial condyle of the proximal tibia compared to *Pan*, which corresponds with areas of maximum force during knee adduction in bipedal locomotion.

1.8.3 Functional signals in the lower limb trabecular structure of fossil hominins

Trabecular studies of the lower limb offer valuable insights into the behaviour of extinct hominins, particularly regarding locomotion patterns. The organization of pelvic trabecular bone has been extensively studied across various extinct hominin species. Rook et al. (2000) found shared traits between *Oreopithecus* and *Homo*, which they linked to bipedality, based on their analysis of iliac trabecular bone architecture. Similarly, Macchiarelli et al. (1999) identified a unique mosaic pattern in the iliac trabecular bone of *A. africanus* and *Paranthropus robustus*, associated with both arboreal and bipedal locomotion. Martinón-Torres (2003) found that the pelvic trabecular structure in *H. neanderthalensis* is similar to that of modern humans.

The trabecular architecture of the femur, particularly in the proximal femur, has also been used to presume locomotion patterns in fossil hominoids. Scherf (2008) identified variations in the trabecular structure of the proximal femur in *Paidopithex rhenanus* and *Pliopithecus vindobonensis* compared to Miocene apes. Ryan et al. (2018) highlighted similarities in trabecular patterns in the femoral heads of *A. africanus* and *P. robustus* with modern humans, suggesting comparable loading patterns, even though their bone volume fraction was higher. Extensive research has also been conducted on the trabecular structure of the ankle. Barak et al. (2013b) reported that *A. africanus* had a distal tibia with trabeculae orientation similar to modern humans, indicating prolonged ankle use. Likewise, DeSilva & Devlin (2012) found that the talus of *A. africanus* had *Homo*-like trabecular architecture, though some characteristics were similar to which found in African apes. Overall, the trabecular structures of the hip and ankle suggest that these species were likely capable of both arboreal and bipedal locomotion, without strong specialization.

Inconsistencies in results may arise from variations in analytical approaches used in trabecular structure studies of fossils. Fragmentation and taphonomic processes often limit analyses to isolated regions, potentially leading to a lack of functional signal. Therefore, studying trabecular architecture within whole epiphyses may be crucial for a comprehensive understanding and should always be considered.

1.8.4 Allometry

Allometry studies the relationship between the size of an organism and the size of various parts or features of its body. In biology, allometry often examines how the proportions of different body parts change as an organism grows or evolves. Allometric relationships can provide insights into evolutionary trends, functional adaptations, and ecological interactions within and between species. These relationships are commonly expressed as mathematical equations or graphs to quantify the scaling patterns observed across different organisms or within a single species across different developmental stages (e.g., Emerson & Bramble, 1993; Hernandez et al., 2009; Pelabon et al., 2014).

Understanding how body size or mass affects trabecular bone is essential for interpreting biomechanical and behavioral implications. Current research into allometry has produced varied results regarding the relationship between body size and trabecular bone structure (e.g., Hernandez et al., 2009; Barak et al., 2011; Doube et al., 2011; Ryan & Shaw, 2013). Nonetheless, body mass is a well-established factor influencing trabecular bone characteristics.

Comparative studies involving species with different body masses must account for allometric effects to accurately assess these implications (Ruff, 2018). As body size increases, gravitational forces also increase which leads to greater load forces applied on the knee joint. Consequently, bones generally adopt a more robust external shape to accommodate these increased loads (Doube et al., 2011). To counteract the greater stresses associated with larger body mass, trabecular bone properties such as volume, thickness, and connectivity are adjusted accordingly (Currey, 2003; Doube et al., 2011).

Research indicates that trabecular thickness, spacing, connectivity, and number are significantly correlated with body mass. Smaller mammals typically have thinner, more widely spaced, and more numerous trabeculae compared to larger species (e.g., Hernandez et al., 2009; Barak et al., 2013a; Doube et al., 2011; Ryan & Shaw, 2013; Saers et al., 2019). Conversely, bone volume fraction (BV/TV) and degree of anisotropy (DA) generally do not show significant correlations with body mass and are relatively consistent across different-sized species (Hernandez et al., 2009; Doube et al., 2011; Barak et al., 2013a; Ryan & Shaw, 2013). Barak et al. (2013a) observed that BV/TV can vary with body mass; for instance, in modern humans (around 70 kg), BV/TV increases through higher trabecular thickness (Tb.Th), while in much smaller rodents (approximately 40 g), BV/TV increases through a higher trabecular number (Tb.N). Furthermore, Kivell et al. (2018) found a negative allometric scaling relationship for Tb.Th and Tb.N, suggesting that smaller primates tend to have relatively thicker, more spaced, and more numerous trabeculae compared to larger primates. This finding aligns with Ryan & Shaw (2013), although Kivell et al. (2018) reported that BV/TV did not have a significant relationship with humeral epiphysis size, and DA exhibited only weak positive allometry.

In the context of this thesis, which examines species with body masses ranging from 36 kg (female *Pongo*) to 170 kg (male *Gorilla*; Smith & Jungers, 1997), previous studies on trabecular bone structure in extant hominids have not found significant allometric effects on BV/TV and DA (e.g., Hernandez et al., 2009; Barak et al., 2013a; Ryan & Shaw, 2013).

1.9 Summary

The evolution of bipedalism has been a central focus in evolutionary studies, yet debates persist regarding its origins and development into its modern form. Trabecular bone analysis holds significant promise in shedding light on this complex evolutionary pathway. The structure of trabecular bone enhances overall bone integrity while maintaining a lightweight framework, making it particularly responsive to the dynamic loads experienced by joints during movement.

Given that individuals with varying locomotor behaviors adopt different limb positions and encounter distinct mechanical stresses, it is expected that these variations will be reflected in unique trabecular patterns. Studying these patterns in extant apes can reveal how trabecular architecture correlates with specific behaviors, thereby providing crucial insights into the locomotion of extinct hominins. By understanding the relationship between trabecular structure and locomotor behavior in living species, we can make informed implications about the movement patterns of our ancient ancestors.

This study significantly expands upon previous research, which often focused on small, localized subvolumes of bone, by conducting a comprehensive analysis of the entire trabecular structure within the distal femur and proximal tibia of various hominid species. This holistic approach not only provides a more complete understanding of trabecular architecture but also allows for robust statistical comparisons between different groups. The trabecular structure of the proximal tibia, in particular, has not been thoroughly analyzed in previous studies, presenting a valuable opportunity to gain new insights into knee loading patterns across hominids.

The primary objective of this study is to elucidate the locomotor strategies employed by ancient human relatives through detailed trabecular bone analysis of the distal femur and proximal tibia. By examining these key skeletal regions, the research aims to uncover the diverse locomotor behaviors and mechanical stresses that influenced the evolution of bipedalism. This comprehensive analysis has the potential to refine our understanding of the biomechanics of bipedalism and its pivotal role in the evolutionary history of hominins. Moreover, this study seeks to bridge the gap between anatomical studies and functional interpretations of hominin locomotion. By integrating advanced imaging techniques and statistical analyses, it aims to provide a nuanced perspective on how trabecular bone adapts to different locomotor behaviors. This research not only contributes to the field of paleoanthropology but also enhances our broader understanding of human evolution, biomechanics, and the intricate relationship between form and function in the skeletal system.

2 MATERIALS AND METHODS

2.1 Study sample

This study analyzed 71 femora and 62 tibiae from four extant hominid species (modern humans, *Gorilla*, *Pan*, and *Pongo*) as well as four extinct species (*Australopithecus africanus*, *Australopithecus sediba*, *Homo floresiensis*, and *Homo neanderthalensis*). Research on living non-human great apes is crucial for both anthropological and medical investigations due to their close evolutionary relationship with humans, making them useful models for reconstructing locomotor and other behaviors in the hominin fossil record. The selected species offer a representative sample of primates whose locomotor behaviors may overlap with those of fossil hominins. The study of the entire distal femoral and proximal tibial epiphyses provides new insights into functional adaptations in the knee of hominids. A summary of the sample including taxon, number of individuals and sex is given below in Table 2.1. Further details of the study sample, including side, age, specimen provenance and voxel size range are provided in Appendix A Table A1.

Table 2.1: Sample composition.

		bone (n)		sex***		
Extant sample	**locomotor behaviour**	**femur**	**tibia**	**female**	**male**	**unknown**
*Homo sapiens (UT)**	Obligate biped	15	0	0	0	15
*Homo sapiens (Mary Rose)***	Obligate biped	11	10	0	11	0
Homo sapiens (GAUG-Inden)*	Obligate biped	0	9	3	6	0
Homo sapiens (NGA)**	Obligate biped	0	6	3	2	1
Gorilla gorilla gorilla	Terrestrial knuckle-walker	14	13	7	8	0
Pan troglodytes verus	Arboreal/knuckle-walker	15	15	8	7	0
Pongo sp.	Arboreal/Ratcheting	9	7	7	2	0
Extinct sample						
Australopithecus africanus StW-318	?	1	0	0	0	1
Australopithecus africanus StW-129	?	1	0	0	0	1
Australopithecus africanus TM-1513	?	1	0	0	0	1
Australopithecus sediba MH2_ U.W. 88-63	?	1	0	1	0	0
Homo floresiensis LB1-8	?	1	0	1	0	0
Homo floresiensis LB1-9	?	1	0	1	0	0
Homo floresiensis LB1-13	?	0	1			
Homo floresiensis LB8-1	?	0	1			
Homo neanderthalensis Neanderthal 1_D322-16	Obligate biped	1	0	0	0	1
Total		**71**	**62**			

*Sedentary population.

**Active population.

***Number of individuals associated with each sex.

2.1.1 Humans

Fifteen individuals (sex unknown) of the distal femur human sample are from the W.M. Bass collection curated by the Forensic Anthropology Centre at the University of Tennessee, USA. These femora represent diverse post-industrial populations. Additionally, eleven individuals (all males) of the distal femur human sample are crew members of the Mary Rose ship, dating back to the early 16th century (Barker, 1996) and curated at the Portsmouth Museum, Portsmouth, UK. The Mary Rose sample consists of young adult males known for their high activity levels (e.g., Stirland et al., 1997; Scorrer et al., 2021). The human sample of proximal tibia comprises individuals drawn from three populations. Nine individuals (3 females, 6 males) are from various post-industrial populations and are assumed to have engaged in comparatively lower levels of activity. Ten individuals (all males) were crew members of the Mary Rose ship, known for their high activity levels. Additionally, six individuals (3 females, 2 males, 1 unknown) from the Medieval period (11th to 16th centuries AD) excavated from St. Gregory's Priory in Canterbury, UK. These individuals are also presumed to have engaged in higher activity levels compared to our post-industrial human sample. All human samples, both from the proximal femur and distal tibia, exhibited no obvious signs of pathologies within their postcranial skeleton.

2.1.2 Non-human great apes

Fourteen individuals (7 females, 7 males) from the *Gorilla* distal femur sample are curated at the Powell-Cotton Museum in Birchington-on-Sea, UK, with thirteen individuals originating from Cameroon and one from the Democratic Republic of the Congo. Similarly, thirteen individuals (7 females, 6 males) from the *Gorilla* sample of proximal tibia are sourced from the same individuals as the distal femur sample from Cameroon. Fifteen individuals (9 females, 6 males) from the *Pan* sample of distal femur and proximal tibia (all same individuals as for the distal femur) are sourced from the Taï Forest National Park and are curated at the Max Planck Institute for Evolutionary Anthropology in Leipzig, Germany. The *Pongo* sample is sourced from the Bavarian State Collection for Zoology in Munich, Germany, and the Natural History Museum in Berlin, Germany. Six individuals (4 females, 2 males) from the distal femur sample are *Pongo pygmaeus*, two (females) are *P. abelii*, and the species of one individual (female) is unknown. The sample of *Pongo* proximal tibiae consists of five individuals (3 females, 2 males) of *P. pygmaeus*, one (female) *P. abelii*, and the taxon of one individual (female) is unknown. The individuals of the proximal tibia sample are the same as those of the distal femur sample.

All great apes were wild born adults with no obvious signs of pathologies within their postcranial skeleton.

For most of the femur (91%) and tibia (62%) sample, the right distal femur/proximal tibia was used. However, in cases where it was not possible due to preservation or methodological issues (such as low resolution of the CT scan), the mirrored left distal femur/proximal tibia was utilized.

2.2 Preservation of the external and internal knee morphology of fossil hominins

This section addresses the preservation of the external and internal structures of the distal femur and proximal tibia in the fossil hominin sample. Furthermore, it highlights the absence of information regarding the preservation of trabecular bone in all fossil samples included in this thesis in the existing literature.

2.2.1 Australopithecus africanus

2.2.1.1 Distal femur StW-318

2.2.1.1.1 Cortical bone preservation

StW-318, depicted in Figure 2.1, is a fragment of the lateral distal end of the right femur. It encompasses the lateral condyle, epicondyle, and over half of the lateral portion of the patellar surface. Overall, these sections are fairly well-preserved, with some wear evident on the lateral edge, exposing trabecular bone. The most proximal part is represented by a bone shaft, with the lateral side, including the epicondyle, exhibiting good preservation. Lateral features include deep pits for the popliteus and lateral head of the gastrocnemius muscle (DeSilva & Grabowski, 2020). For further details, including measurements and a detailed description of the external morphology of StW-318, along with accompanying images, refer to DeSilva & Grabowski (2020).

2.2.1.1.2 Trabecular bone preservation

The trabecular structure of StW-318 in the remaining lateral condyle is well preserved (Figure 2.2). The micro-computed tomography (micro-CT) scan is clean, showing no signs of invasive sedimentation and there is no sign of the growth plate (Figure 2.2).

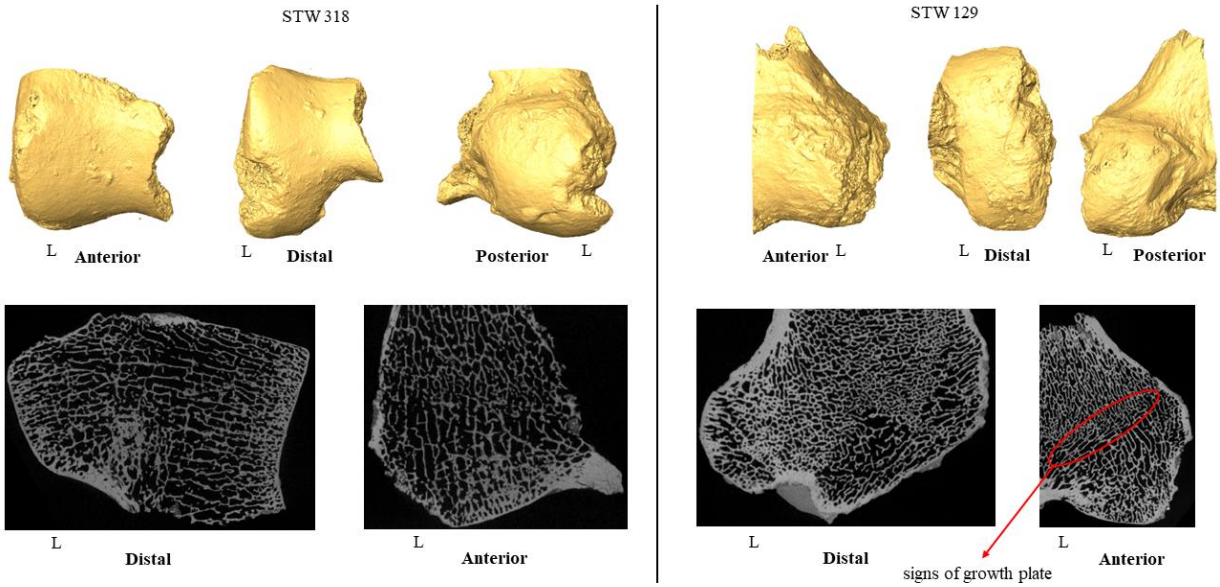

Figure 2.1: External and internal bone preservation of distal femur of *Australopithecus africanus* StW 318 and StW 129 in anterior, distal, and posterior view. L, lateral; M, medial. Number of the OrthoSlize taken for the position of the cross-sections is 501 (distal view) and 745 (anterior view) and it was visualized in Avizo.

2.2.1.2 Distal femur StW-129

2.2.1.2.1 Cortical bone preservation

StW 129 comprises a left lateral condyle and a portion of the distal femoral shaft (Figure 2.2.) It consists of two parts that have been neatly glued together: a fragment of the shaft and the remaining distal shaft with a partial lateral condyle (DeSilva & Grabowski, 2020). The latero-posterior portion of the distal condyle is missing, and the medial condyle is sheared away. There are three deep grooves running lengthwise on the popliteal surface, as well as at the break between the two portions. The anterior surface is well-preserved, including a portion of the patellar surface. Additionally, there is a distinct attachment for the lateral head of the gastrocnemius and a groove for the tendon of the popliteus. For additional information, including measurements and a comprehensive description of the external morphology of StW-129, as well as accompanying images, please consult DeSilva & Grabowski (2020).

2.2.1.2.2 Trabecular bone preservation

The trabecular structure of StW-129, like that of StW-318, is well-preserved, showing no signs of invasive sedimentation throughout the micro-CT scan (Figure 2.2). However, the trabecular structure resembling a growth plate observed in the anterior view of StW-129 suggests that this individual may have been an adolescent at the time of death. Due to the focus of the thesis on adult individuals, StW-129 was not included in further analyses.

2.2.1.3 Distal femur TM-1513

2.2.1.3.1 Cortical bone preservation

TM-1513 is a well-preserved distal end of the left femur (Figure 2.2). However, the lateral aspect of the bone has been sheared away (DeSilva & Grabowski, 2020), resulting in the loss of the lateral epicondyle and a small portion of the lateral patellar surface. Some abrasion is present on the top of the medial condyle, and the surface cortex displays noticeable abrasion and pitting, although sections of smooth cortical bone remain (DeSilva & Grabowski, 2020). The popliteal surface is generally well-preserved, with a small but sharp and pronounced adductor tubercle (DeSilva & Grabowski, 2020). Medially, just inferior to the medial epicondyle, there is a distinct groove running along the rim of the articular surface of the medial condyle (DeSilva & Grabowski, 2020). The condyles exhibit asymmetry, with the medial side being significantly larger than the lateral side, and both articular surfaces are well defined. Moreover, the medial wall of the intercondylar notch indents slightly onto the medial condyle, marking the insertion point for the posterior cruciate ligament (DeSilva & Grabowski, 2020). Along the posterior aspect of the lateral wall of the intercondylar notch, there is a distinct pit for the anterior cruciate ligament (DeSilva & Grabowski, 2020). Again, for detailed measurements of the external morphology please consult DeSilva & Grabowski (2020).

2.2.1.3.2 Trabecular bone preservation

The trabecular structure of TM-1513 exhibits good preservation, although it is affected by sedimentation and fossilization processes, as depicted in Figure 2.2. Both condyles are filled with invasive sediment, as is the intercondylar notch and the area under the patellar surface on both condyles (Figure 2.2). All trabeculae throughout the distal condyle are preserved. However, the grey values of the trabeculae in the distal parts of the condyles and under the patellar surface become more similar to those of the local matrix in the micro-CT scan (Figure 2.2). There are no signs of growth plates throughout the distal femur of TM-1513 (Figure 2.2).

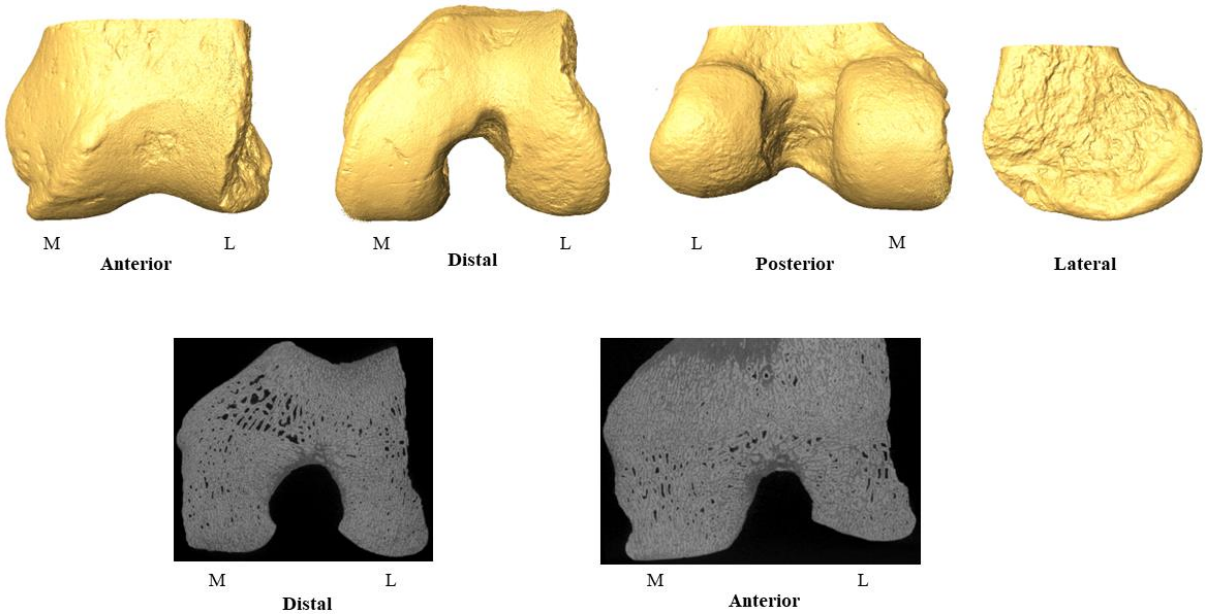

Figure 2.2: External and internal bone preservation of distal femur of *Australopithecus africanus* TM 1513 in anterior, distal, and posterior view. L, lateral; M, medial. Number of the OrthoSlize taken for the position of the cross-sections is 573 (distal view) and 677 (anterior view) and it was visualized in Avizo.

2.2.2 Australopithecus sediba

2.2.2.1 Distal femur U.W. 88-63

2.2.2.1.1 Cortical bone preservation

U.W. 88-63, depicted in Figure 2.3, represents the right distal femur of MH2, an adult individual, measuring 86.7 mm in length from the most proximal point of the oblique break through the shaft to the distal ends of the femoral condyles (DeSilva et al., 2018). Its width spans 54.5 mm from the lateral epicondyle to the most medial aspect of the broken medial epicondyle (DeSilva et al., 2018). Despite some damage, enough bone is preserved on U.W. 88-63 to delineate a medial border to the medial condyle (DeSilva et al., 2018). The posteromedial portion of the bone has been sheared away, and there is erosion along the medial aspect of the medial condyle. However, the lateral condyle, patellar articular surface, anterior shaft portion, and some of the medial condyles remain well-preserved (Figure 2.3). Anteriorly, a sub-trochlear hollow is evident just superior to the patellar surface. The patellar surface itself is concave medio-laterally and convex posterodistally. Impressions for both the anterior and posterior cruciate ligaments are observable, with the anterior cruciate ligament impression notably indenting into the lateral condyle (DeSilva et al., 2018). The lateral condyle is well-preserved, with its proximal portion dominated by a projecting lateral patellar lip, rising notably above the patellar articular surface (Figure 2.3). In an inferior view, the medial condyle extends anteriorly much more than the lateral condyle. Additionally, a well-developed tubercle for the lateral collateral ligament is present, posterior to which lies a small impression for the lateral

head of the gastrocnemius (DeSilva et al., 2018). For further details, including measurements and a detailed description of the external morphology of U.W. 88-63, along with accompanying images, refer to DeSilva et al. (2018).

2.2.2.1.2 Trabecular bone preservation

The trabecular structure of U.W. 88-63 exhibits poor preservation, as depicted in Figure 2.3. The distal part of the shaft and medial condyle are particularly affected by poor preservation, being filled with invasive sediment. Similarly, the intercondylar notch and the area under the patellar surface on its medial side are also filled with sediment (Figure 2.3). Trabeculae in the remaining shaft are preserved along the lateral edge. In the medial condyle, trabecular structure is preserved only at the top and under the patellar surface in the medial patellar lip, visible in the micro-CT scan when viewing inferiorly towards the shaft. Trabecular structure in the lateral condyle is better preserved, extending approximately to its middle when scrolling (i.e., visual inspection of the cross-sectional images generated by micro-CT scan) through the micro-CT scan in an inferior view. However, as one scrolls through the micro-CT scan in lateral view, towards to the intercondylar notch, there is a higher impact by sedimentation and fossilization, causing the trabeculae to become almost unidentifiable (i.e., the grey values of the trabecular structure become continuous with those of the local matrix in the micro-CT scan). Even in the lateral condyle, trabeculae are well-preserved under the patellar surface and in the lateral patellar lip. All remaining trabeculae show no signs of fossilization or growth plates. Refer to Figure 2.3 for visual representation of these observations.

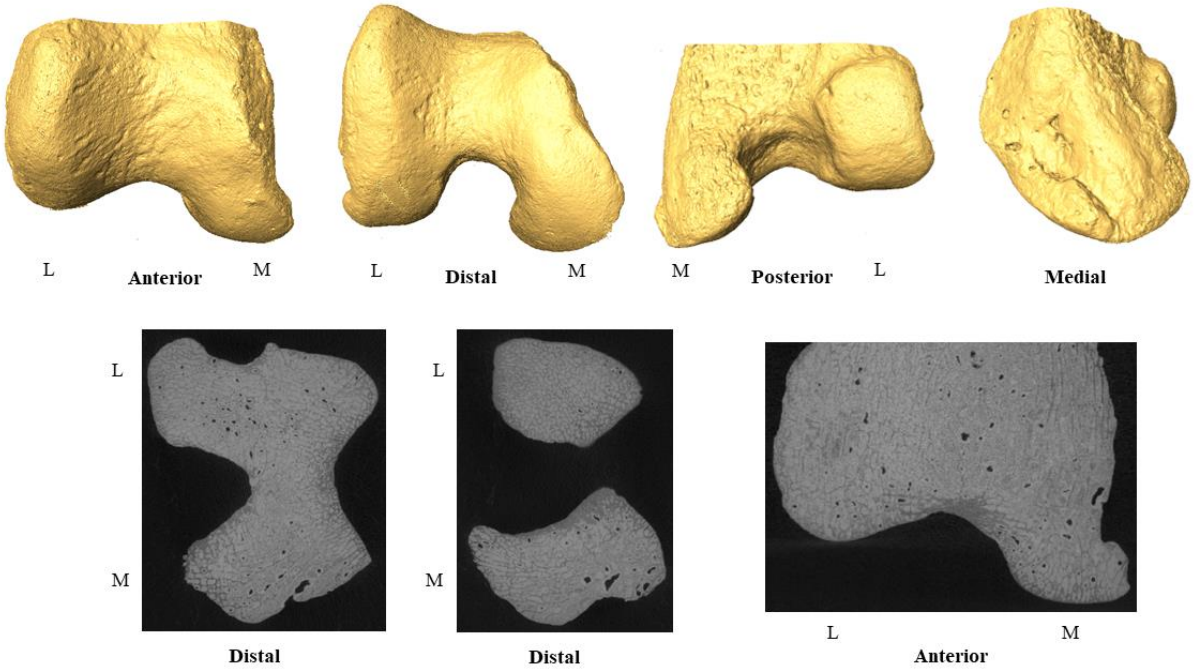

Figure 2.3: External and internal bone preservation of distal femur of *Australopithecus sediba* U.W. 88-63 in anterior, distal, and posterior view. L, lateral; M, medial. Number of the OrthoSlize taken for the position of the cross-sections is 317 and 219 (distal views) and 388 (anterior view) it was visualized in Avizo.

2.2.3 Homo floresiensis

2.2.3.1 Distal femur LB1-8

2.2.3.1.1 Cortical bone preservation

LB1-8, as depicted in Figure 2.4, represents the right femur of an adult LB1 individual (Jacob et al., 2006). While its distal part is more complete compared to the left femur of LB1, it appears to have sustained damage through crushing (Jungers et al., 2009b). The patellar articular surface is preserved proximally but is damaged by crushing in the anteroposterior plane (Figure 2.4). The lateral condyle shows compression in the anteroposterior plane and is broken off below the lateral epicondyle. However, the anterior portion of the articular surface of the lateral condyle, including the lateral patellar lip, remains preserved. On the medial side, the patellar articular surface is preserved proximally, but the medial condyle is also compressed in its anteroposterior plane, with the medial epicondyle missing (Figure 2.4). The remaining anteroposterior dimension of the medial condyle measures just over 34mm (Jungers et al., 2009b). However, the articular surface of the medial condyle remains preserved proximally (Figure 2.4). Previous studies have provided descriptions of the external bone morphology of LB1 femurs, as referenced in Brown et al. (2004), Jacob et al. (2006), and Jungers et al. (2009b).

2.2.3.1.2 Trabecular bone preservation

The trabecular structure of LB1-8 (Figure 2.4) has been significantly impacted (most likely) by crushing (Jungers et al., 2009b), with the distal part of the shaft being filled with invasive sediment. Trabeculae are preserved along the cortical bone laterally and medially, but they are impacted, particularly on the lateral side. The remaining trabeculae in the shaft appear thick without signs of fossilization (Figure 2.4). A visible crack is observed through the shaft just above the condyles, and most of the trabeculae are missing above the intercondylar notch, which is also filled with sediment (Figure 2.4). The trabecular structure in the medial condyle is the most affected (most likely by crushing), with the medial condyle being filled with sediment (Figure 2.4). Some parts of the cortical bone are interposed inside the medial condyle (Figure 2.4). There are very few unimpacted trabeculae in the medial condyle, mostly confined to its posterior part along the cortical bone. In contrast, the trabecular structure in the lateral condyle is relatively well-preserved (Figure 2.4). However, some parts below the lateral epicondyle are missing, and the posterior part of the lateral condyle is filled with sediment. Particularly well-preserved trabeculae can be found anteriorly in the lateral condyle and in the lateral patellar lip. There are no signs of growth plates in LB1-8 distal femur, and the cortical bone in all distal femurs appears porous, especially in both the lateral and medial femoral condyles (Figure 2.4).

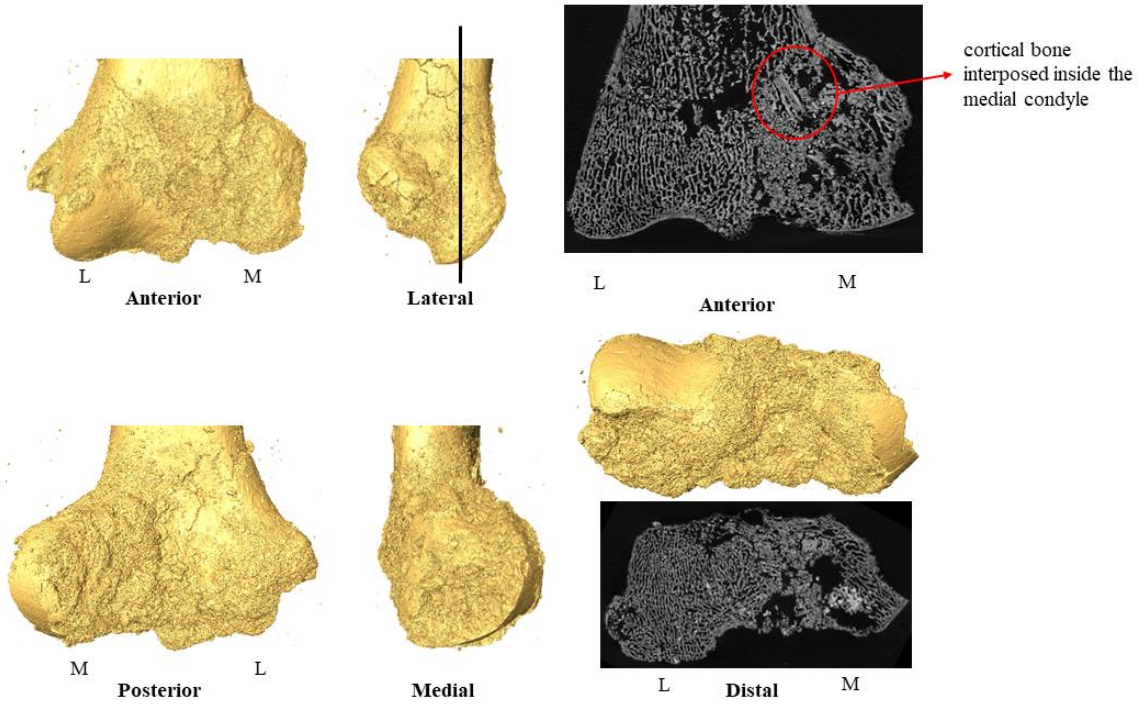

Figure 2.4: External and internal bone preservation of distal femur of *Homo floresiensis* LB1-8 in anterior, distal, and posterior view. L, lateral; M, medial. Vertical line shows where the cross-section in anterior view is positioned. Number of the OrthoSlize taken for the position of the cross-sections is 621 (distal view) and 744 (anterior view) and it was visualized in Avizo.

2.2.3.2 Distal femur LB1-9

2.2.3.2.1 Cortical bone preservation

LB1-9 (Figure 2.5), the left femur [incorrectly listed in Brown et al. (2004) as the right femur] of the LB1 individual, exhibits surface morphology and geometry similar to the right femur of LB1 (Jacob et al., 2006). However, LB1-9 is less complete distally compared to LB1-8. Both the patellar articular surface and the posterior parts [incorrectly listed as anterior parts in Jungers et al. (2009b)] of both femoral condyles are missing in LB1-9 (Figure 2.5). Only a thin shell of the articular surface of the lateral condyle remains, with approximately 27mm of its inferior aspect being intact (Figure 2.5).

2.2.3.2.2 Trabecular bone preservation

The trabecular structure of LB1-9 is mostly not preserved (Figure 2.5). The distal part of the shaft is broken with no remaining trabeculae. There is a visible deformation and crack just above the lateral condyle (Figure 2.5). The remaining medial condyle is full of sediment, retaining only a few somewhat preserved trabeculae anteriorly. However, even these trabeculae are not well-preserved but mostly crushed. The remaining trabeculae seem to be with no signs of fossilisation, although it is not possible to clearly define most of them (Figure 2.5). Trabeculae in the lateral condyle are missing, as there is just a thin shell of cortical bone preserved. There are no signs of growth plates in LB1-9 distal femur. The remaining cortical bone of the left distal femur is porous (Figure 2.5). As the trabecular structure of LB1-9 is mostly not preserved, LB1-8 only was used for further analyses.

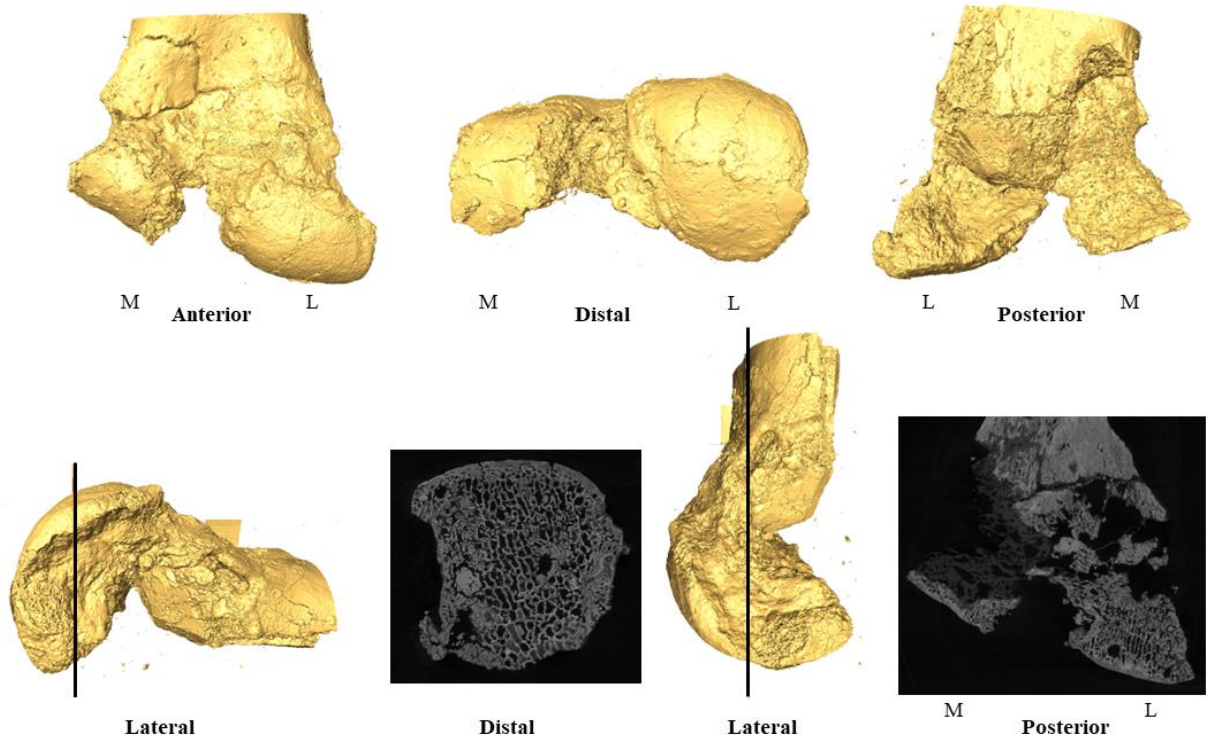

Figure 2.5: External and internal bone preservation of distal femur of *Homo floresiensis* LB1-9 in anterior, distal, and posterior view. L, lateral; M, medial. Vertical lines show where the cross-sections in the distal and posterior views are positioned. Number of the OrthoSlize taken for the position of the cross-sections 1629 (distal view) is (distal view) and 636 (posterior view) and it was visualized in Avizo.

2.2.3.3 Proximal tibia LB1-13

2.2.3.3.1 Cortical bone preservation

LB1-13 (Figure 2.6) is an almost complete right tibia of an adult LB1 individual (Jungers et al., 2009b). The proximal part of LB1-13 is complete, with both condyles and intercondylar tubercles of the intercondylar eminence preserved. The superior fibular articular facet is flat without clear margins, and the tibial tuberosity is prominent (Figure 2.6). Previous studies have reported detailed descriptions of the external bone morphology of LB1-13, including measurements of the proximal tibia (Brown et al., 2004; Jacob et al., 2006; Jungers et al., 2009b).

2.2.3.3.2 Trabecular bone preservation

The trabecular structure of LB1-13 (Figure 2.6) is largely impacted by invasive sediment. The tibial plateau is particularly affected by sedimentation, leading to crushed trabeculae, especially between the lateral and medial condyles (Figure 2.6). In the lateral condyle, the trabecular structure is mostly preserved, although it becomes more impacted by sedimentation anteriorly and internally. Conversely, the medial condyle shows greater impact from sediment compared to the lateral condyle, with few trabeculae preserved anteriorly and many missing posteriorly

due to visible cracks (Figure 2.6). The medullary cavity of LB1-13 is filled with sediment from the tibial plateau towards the distal part, observable when visually inspecting the cross-sectional images of the micro-CT scan in the anterior/posterior view. However, under the tibial tuberosity, there are well-preserved trabeculae, particularly evident when inspecting the cross-sectional images in the medial/lateral view. Moving more medially, trabeculae are missing due to visible cracks, and the remaining ones are impacted by sedimentation (Figure 2.6). Preservation of trabeculae is higher more laterally from the centre of the tibial tuberosity towards the lateral side of the shaft (Figure 2.6). No signs of growth plates are observed in LB1-13 proximal tibia. The remaining cortical bone of the right proximal tibia of LB1 has been previously discussed to be pathologically thin based on CT-scans measurements by Jacob et al. (2006). However, Jungers et al. (2009b) concluded that the posterior cortical bone thickness is within the normal human range.

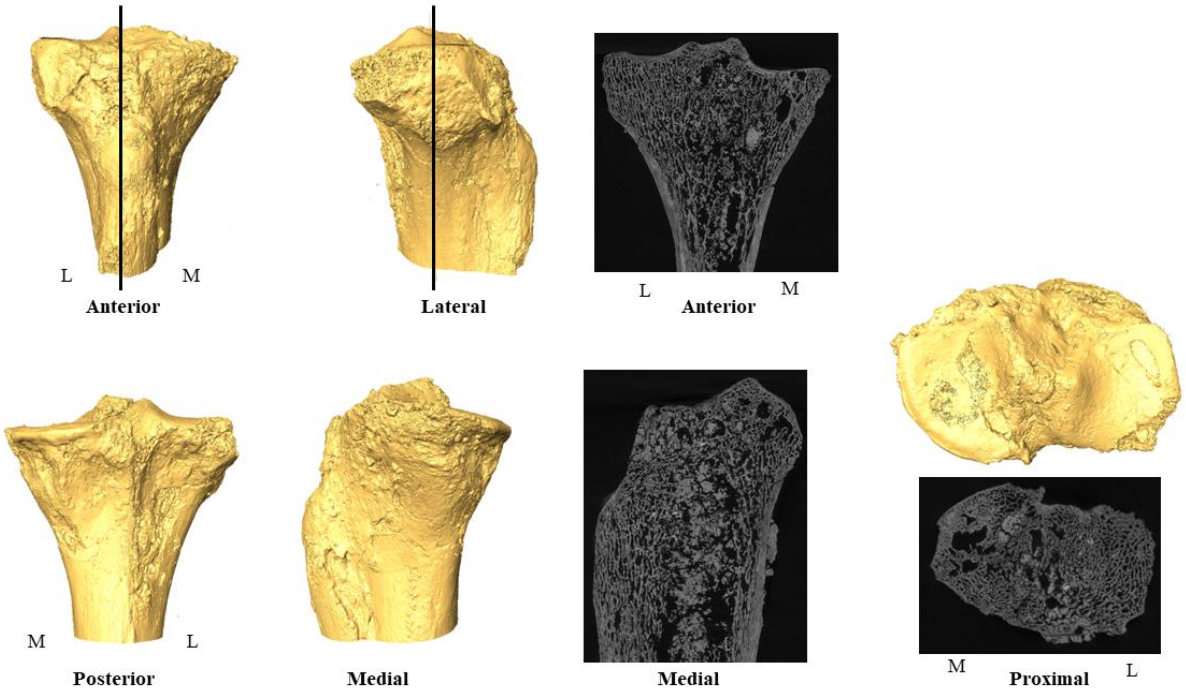

Figure 2.6: External and internal bone preservation of proximal tibia of *Homo floresiensis* LB1-13 in anterior, posterior, lateral, and medial view. L, lateral; M, medial. Vertical lines show where the cross-section in the anterior view is positioned. Number of the OrthoSlize taken for the position of the cross-sections is 728 (anterior view), 892 (medial view), and 1580 (proximal view) and it was visualized in Avizo.

2.2.3.4 Proximal tibia LB8-1

2.2.3.4.1 Cortical bone preservation

The proximal part of LB8-1 (Figure 2.7), the almost complete right tibia of an adult LB8 individual, exhibits several notable features. The proximal lateral condyle, which includes the tibial plateau and facet for the fibula, is missing. Additionally, part of the proximal medial

condyle is absent posteriorly. However, the intercondylar eminence is preserved medially. Despite these missing portions, the tibial tuberosity is intact and prominent (Jungers et al., 2009b). Previous studies have provided detailed descriptions of the external bone morphology of LB8-1 proximal tibia (see Jungers et al., 2009b; Morwood et al., 2005).

2.2.3.4.2 Trabecular bone preservation

The trabecular structure of LB8-1 (Figure 2.7) is largely not preserved. Only a few remaining trabeculae are observed under the tibial tuberosity. However, the trabeculae in the remaining portion of the medial condyle are mostly impacted by sedimentation, indicating poor preservation in this region (Figure 2.7). Due to the poor trabecular preservation, proximal tibia LB8-1 was not used for further analyses.

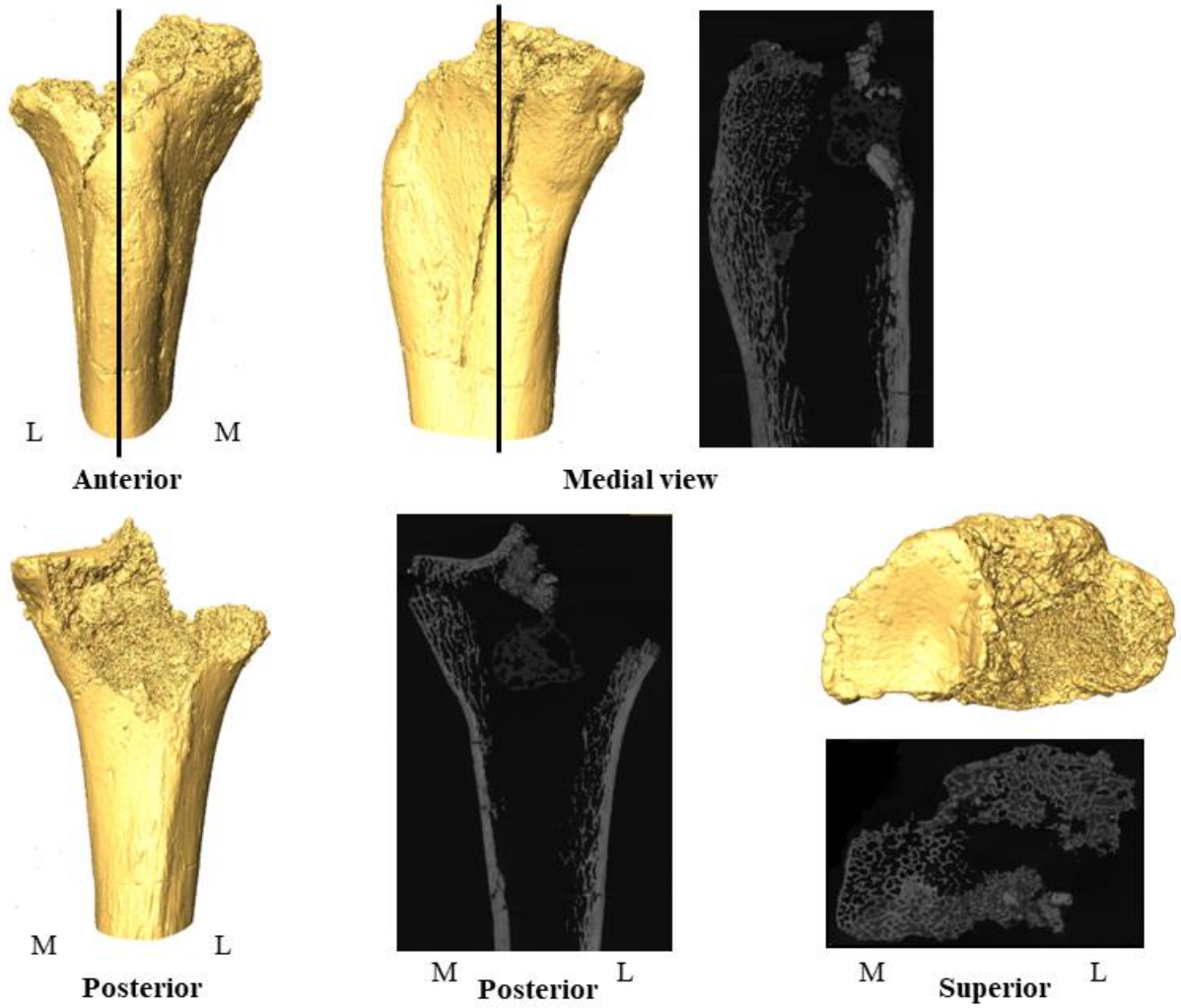

Figure 2.7: External and internal bone preservation of proximal tibia of *Homo floresiensis* LB8-1 in anterior, posterior, lateral, and medial view. L, lateral; M, medial. Vertical lines show where the cross-section in the anterior and medial views are positioned. Number of the OrthoSlize taken for the position of the cross-sections is 706 (medial view), 452 (posterior view), and 1582 (superior view) and it was visualized in Avizo.

2.2.4 Homo neanderthalensis

2.2.4.1 Distal femur Neanderthal 1 D322-15

2.2.4.1.1 Cortical bone preservation

The description of D322-15 (depicted in Figure 2.8) indicates it as an almost complete left distal femur of an adult Neanderthal 1 individual. The only missing parts are the small distal section of the medial condyle and medial epicondyle, as shown in Figure 2.8.

2.2.4.1.2 Trabecular bone preservation

The trabecular structure of D322-15 (depicted in Figure 2.8) is well preserved, with trabeculae appearing unaffected by sedimentation or fossilization processes. Trabeculae are clearly distinguished from the non-bone matrix, and there are no visible signs of growth plates, as shown in Figure 2.8.

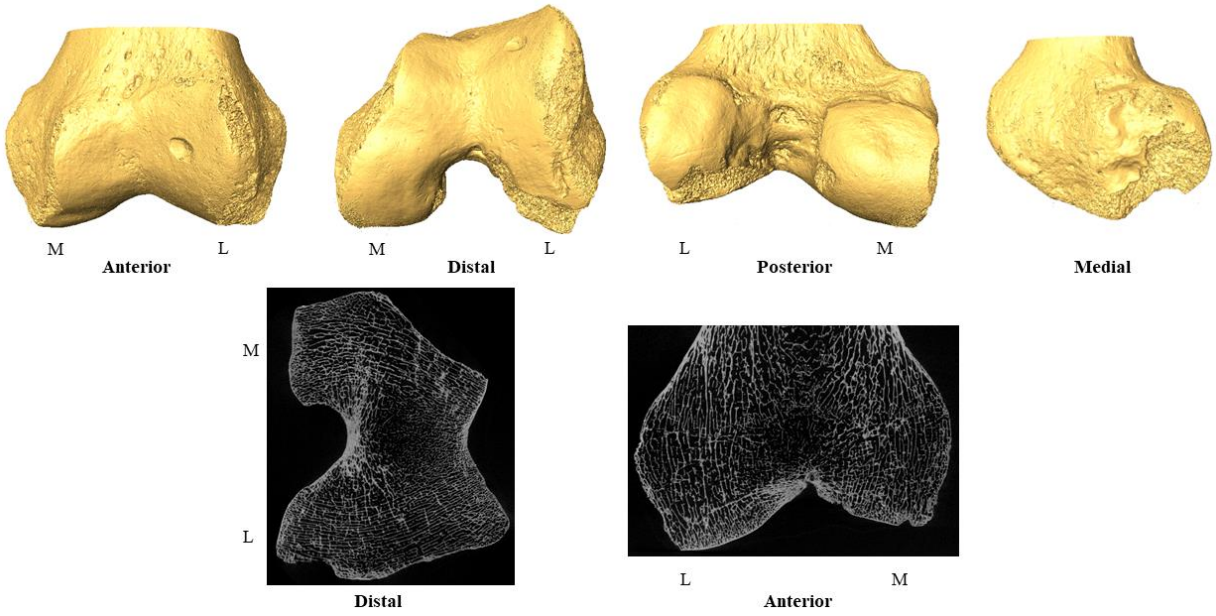

Figure 2.8: External and internal bone preservation of distal femur of *Homo neanderthalensis* D322-15 in anterior, distal, and posterior view. L, lateral; M, medial. Number of the OrthoSlize taken for the position of the cross-sections is 842 (distal view) and 1012 (anterior view) and it was visualized in Avizo.

2.3 Computed tomography

All specimens underwent scanning using micro-CT, which is the standard imaging technique used for quantifying trabecular architecture (Bouxsein et al., 2010). The development of micro-CT technology has recently allowed scan resolution to be below 100 µm (Buzug, 2011). Previous studies have demonstrated that trabecular architecture can be accurately quantified with a resolution of less than 60 µm (Müller et al., 1996; Müller et al., 1998; Isaksson et al., 2011). However, there are numerous computational processes associated with the analysis of

micro-CT scans that may potentially affect the accuracy of the trabecular structure in the scans. Several studies have previously indicated that the voxel size, if not appropriately low (low voxel size indicates high resolution and *vice versa*) compared to the dimensions of the structure being measured, may strongly affect trabecular or cortical bone results. When the resolution is low enough the voxel size is larger than the size of the structure in question, making it challenging to differentiate between small structures (Müller et al., 1996; Kim et al., 2007). The impact of voxel size on the estimation of bone morphology measures has remained relatively unexplored (Kothari et al., 1998; Tabor, 2004; Magland & Wehrli, 2008; Sode et al., 2008). **Chapter 3** of this thesis provides a study of how far voxel size impacts trabecular parameters.

The extant and extinct specimens underwent micro-CT scanning using various scanners housed at different institutions. These scanners included the BIR ACTIS 225/300, Diondo D3, and Skyscan 1172 at the Department of Human Evolution, Max Planck Institute for Evolutionary Anthropology in Leipzig, Germany; the Phoenix Nanotom S X-ray tomograph at the Department of Micro-CT Laboratory, Museum of Natural History in Berlin, Germany; the Nikon 225/XTH scanner at the Cambridge Biotomography Centre, University of Cambridge in Cambridge, UK; and the Diondo D1 scanner at the Imaging Centre for Life Sciences at the University of Kent in Canterbury, UK. The scan parameters varied, with acceleration voltages ranging from 100 to 160 kV and currents ranging from 100 to 140 μA. A 0.2 to 0.5 mm copper or brass filter was used in the scanning process. The isometric resolution of extant distal femur reconstructed scans ranged from 0.024 mm to 0.058 mm, while the scan resolution of extant proximal tibiae ranged from 0.025 mm to 0.063 mm. For fossil specimens, the isometric scan resolution of distal femora ranged from 0.030 mm to 0.060 mm, while the scan resolution of proximal tibiae ranged from 0.028 mm to 0.031 mm. The resolution depended on the size of the bone and the specific scanner used (refer to Table A1 in the Appendix). Subsequently, all images were reconstructed as 16-bit TIFF stacks and reoriented to approximately the same anatomical position using Avizo 6.0 or 9.0 software developed by Visualization Sciences Group, SAS. All femora and tibiae were reoriented so that their posterior side is aligned with the z-axis with their distal/proximal end approximating the xy-plane (Figure 2.9a, d). These images were then further cropped and saved. The exact transformation matrix used, and the number of pixels cropped, were recorded for each individual to ensure repeatability (Figure 2.9b, c, e, f). The bone image was then saved as .nii format file and segmented (see below).

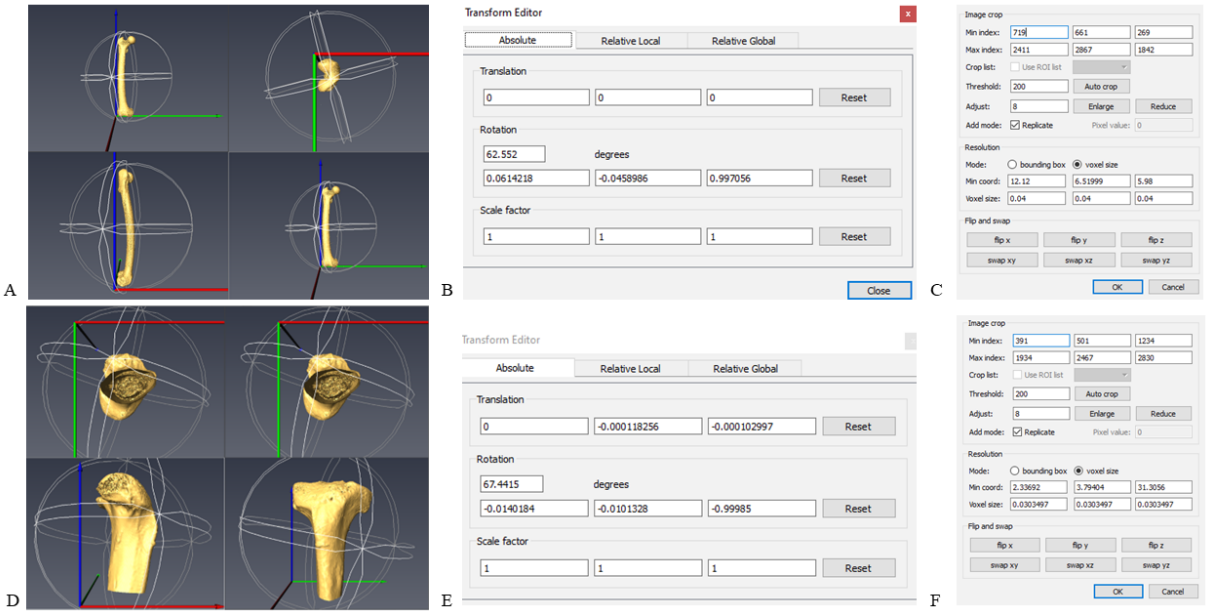

Figure 2.9: Example of image orientation steps on a right *Pan* femur and tibia. (A) Anatomical orientation of the femur from various views. (B) The transformation matrix used to achieve the femur orientation. C) The size of the final volume image of the femur after it is cropped for faster processing. (D) Anatomical orientation of the tibia from various views. (E) The transformation matrix used to achieve the tibia orientation. F) The size of the final volume image of the tibia after it is cropped for faster processing.

2.4 Segmentation

Bone segmentation refers to the process of identifying and delineating bone tissue within medical imaging data, such as CT scans. It involves separating the bone tissue from other tissues or structures present in the image, such as soft tissue, surrounding matrix or air. Bone segmentation is an essential step which enables quantitative analysis of bone structure, in our case trabecular bone structure. The medical image analysis (MIA) clustering method was employed for segmenting all micro-CT scans in this thesis (Figure 2.9). MIA-clustering is favored for its capability to achieve finer separation of trabeculae and its adaptability in managing surrounding non-bone elements compared to alternative bone segmentation techniques (Dunmore et al., 2018). By assigning voxels to distinct classes based on their highest membership probability, MIA-clustering globally segments structures across the entire image. However, this approach may not consistently capture all details due to challenges like intensity irregularities in input images, which can arise from scanning artifacts or variations in fossil mineralization levels. To address this limitation, a subsequent step employs local fuzzy c-means segmentation. This technique involves dividing the image into smaller, localized regions and applying a fuzzy clustering algorithm, known as the fuzzy c-means algorithm, within each region. By performing segmentation locally, it enables more precise delineation of structures and finer detail within the image, compensating for any shortcomings of the initial global

segmentation (Dunmore et al., 2018). This approach allows for more precise trabecular bone extraction and ensures that the resulting data is suitable for detailed analysis of trabecular architecture.

The MIA-clustering method requires the user to input the desired number of classes (e.g., two classes if only bone and air are included in the scan, three classes if the scan includes matrix as well etc.) to be detected in the image, as well as determine a grid size for the iterative k-means and fuzzy c-means clustering processes. This grid size dictates how the volume is partitioned into overlapping cubes. Each cube is then assigned a vector of class membership probabilities, which are initialized using probabilities derived from the initial global segmentation. During the process, if the total sum of membership probabilities for all voxels within a sub-volume falls below a predefined threshold, that particular class is excluded from further refinement in the local c-means clustering step (Dunmore et al., 2018). This threshold helps in avoiding unnecessary computation and focusing efforts on areas where clear distinctions between classes can be made (Dunmore et al., 2018). Here is a detailed description of how the process works:

The image is divided according to the specified grid size, and the MIA program initially utilizes the k-means clustering algorithm to group greyscale values at each voxel based on the predetermined number of classes which have been specified (Dunmore et al., 2018). The k-means algorithm works by minimizing the total squared distances between data points and their respective cluster centroids. It operates iteratively, first assigning each data point to the closest centroid and then recalculating the centroids as the average of the points within each cluster. This process repeats until the centroids stabilize or a set number of iterations is completed. Fuzzy c-means clustering then determines membership probabilities for each voxel in the image based on their greayscale values. The goal is to classify voxels into different classes such that each voxel belongs to a class with a certain degree of membership, indicating how likely it is to belong to that class compared to others. This process ensures that each voxel within a class is as similar as possible to other voxels in the same class in terms of greyscale intensity. Conversely, each voxel should be as dissimilar as possible to voxels assigned to other classes (Dunmore et al., 2018). In contrast to k-means, which assigns each data point to a single cluster, c-means clustering marks data points to belong to multiple clusters at once, with varying levels of membership. Each data point in c-means clustering is assigned a membership value for every cluster, representing the extent to which it is associated with that cluster. These membership values are iteratively adjusted throughout the clustering process to improve the accuracy of the cluster assignments. The algorithm aims to minimize the objective function, which measures

the total weighted squared deviations of data points from cluster centroids, considering their membership degrees. The class membership is determined by the probability that a specific voxel belongs to a certain class. For example, it might be 90% likely that a voxel is grey and 10% likely that it is white (Dunmore et al., 2018). Users can adjust this probability threshold, making class membership either very strict (with a high probability threshold) or more inclusive (with a lower probability threshold). If the highest membership coefficient of a particular voxel does not meet the threshold, the voxel is excluded from that class. In such cases, voxels that do not meet the threshold for their highest probable class are given a grayscale value of zero, while the grayscale values for all other classes are incremented by one (Dunmore et al., 2018). Based on the number of classes, MIA will result in binary (two classes), trinary (three classes), etc., segmented volume images. If more than two classes are defined, the arithmetic in Avizo can be then used for binarization (Figure 2.10) and saved as a .raw file for data collection.

For all extant sample, the grid size was determined by measuring the thickness of the thickest trabeculae in a 2D cross-section using Avizo to determine their width in pixels. The grid size was then set a few voxels larger than these measurements to ensure that the local segmentation focuses on features within the phase of interest. This enabled effective segmentation throughout the entire epiphyses (Dunmore et al., 2018). No probability filter was applied, and a maximum of three classes (if the soft tissues was present) were used across all extant individuals. For the details of fossil segmentation, see the Extinct sample segmentation section.

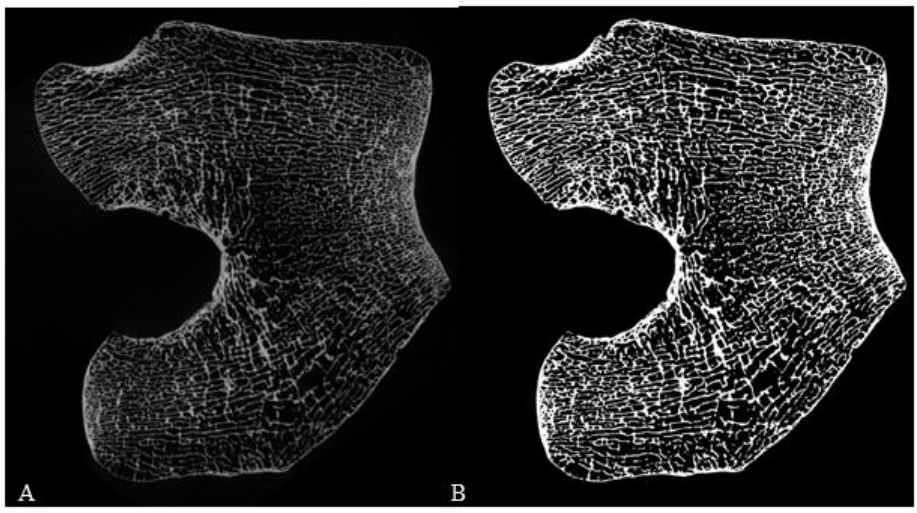

Figure 2.10: Segmentation of the human distal femur by MIA.

2.4.1 Extinct sample segmentation

Identifying different materials in MIA relies heavily on distinguishing grayscale values at each voxel and sorting them into groups based on predefined class numbers. However, segmenting scans of materials with similar densities or high homogeneity can pose a significant challenge. This is particularly challenging when segmenting fossil specimens due to fossilisation and taphonomic processes. During fossilization, organic materials in bones can be replaced by minerals such as calcium carbonate, calcium phosphate, and silica. This process can lead to the preservation of the bone shape and structure but often results in increased hardness and density. In some cases, the original organic components of bone are completely replaced by minerals. This can result in the formation of a fossil that retains the external shape of the bone but lacks its original organic structure. Moreover, over time, minerals within the bone can undergo recrystallization, leading to changes in crystal structure and orientation. This process can alter the mechanical properties of the fossilized bone. Taphonomic processes encompass a range of natural and environmental factors that can influence the preservation of bone structure in fossils, such as decomposition, disarticulation, sedimentation, mineralization etc. In such cases, the segmenting protocol needs to be adjusted to deal with these issues. For instance, if a bone was submerged in water, sediment such as silt could accumulate within the fossil, appearing in the scan data. To isolate only the fossilized bone for analysis, we employ a process called digital excavation, which involves segmenting out the fossil from the surrounding sediment.

In this thesis, each fossil was segmented using a customized protocol to achieve the best possible segmentation with minimal manual clesning to avoid subjective decision making of the cleaning which decreases the reproducibility of results. Although in some fossils manual cleaning was applied (Appendix A; Figure A1 – A5). Manual cleaning can be applied in Labels field in Avizo, and it requires the user to manually clean every structure out of interest throughout whole scan. Alongside MIA, the image filters available in Avizo 6.3 were used to help segment difficult fossils where typically the grey scale values of the trabeculae were similar to the grey scale values of surrounding matrix. These steps involve removing bright inclusions in the labels field in Avizo and/or applying the 'Smooth Labels' function, which identifies voxels connected to larger regions by fewer than a user-defined number of voxels, such as 15. This process eliminates small accretions on the edges of trabeculae or 'islands'. Additionally, by applying a median filter across the scan, small irregularities within the trabeculae, such as cracks or minor accretions, are averaged out and removed. After this is done, the fossil can be segmented by MIA. A probability filter often needs to be applied to get the

best segmentation possible. The MIA output then needs to be checked against the reconstructed scan. In some cases, the segmentation output can still include non-trabecular structure and/or some trabeculae might not be segmented. If that is the case, MIA output needs to be manually cleaned in Avizo or used to mask the original stack image and segmented again, to gets the best segmentation possible. Adjusted segmentation protocols of each fossil can be found in Appendix A; Figure A1 – A5.

2.5 Trabecular bone analysis

The external and internal volumes of all bones in the extant and extinct sample were defined using Medtool v 4.5 (www.dr-pahr.at/medtool) and substracted from each other to create the thick cortical bone shell, following established protocols (Gross et al., 2014; Pahr & Zysset, 2009; Tsegai et al., 2013). The binary images from MIA (Figure 2.11b), where bone voxels are classified as 1 and non-bone voxels as 0, serve as ubouts for Medtool. Initially, the ***"Clean"*** filter is initially applied to identify white bone voxels that are not connected to the main bone structure. The primary structure, consisting of the most contiguous white voxels, is identified, and any floating, non-contiguous voxels are set to zero (black voxels). Morphological filters in Medtool are then used to fill the bone, isolating the external and internal edges of the cortical bone in 3D. This results in a mask of both the internal bone volume and the outer cortical bone. During the filling process, small pores in the cortical bone are identified and filled as bone based on the kernel radius size. The kernes size, denoted as $kc, is a key parameter read from the parameter file and is initially set to three voxels. This value is evaluated and adjusted as necessary. This method ensures that while fine porosity in the cortical bone is not preserved, moderate gaps, representing genuine differences in shape or separation of trabeculae are maintained. The output of this process is the ***"Close"*** image stack (Figure 2.11c). For this, a ray-casting method is used. Each primary ray is traced through the scene to determine if it interacts with any objects. At this stage, rays are cast from the edge of the image. These rays are dimensionless mathematical vectors and are not rasterized. They originate from seven directions, including three along orthogonal axes and four along diagonals of a cube. When five of these rays intersect with a bone voxel, it is marked as a fill voxel. If two voxels are marked by the same cast ray, the space between them is treated as fill or bone. Subsequently, closing and opening operations are performed to fill in the gaps in the bone structure, resulting in the creation of the ***"OuterMask"*** (see below). Medtool makes this differentiation using the same kernel size defined for the ***"Close"*** filter (see above). When the filling process is completed, the rays can identify trabecular space. To identify trabecular spaces, the same ray casting

process is employed, but with a starting point at the edge of the ***"OuterMask"*** instead of the image edge. Rays terminate upon encountering air voxels rather than bone voxels. The ***"Close"*** image stack is utilized in this step to prevent cortical pores from prematurely terminating these rays. Closing and opening operations are then applied to fill in areas where rays have traversed directly through trabeculae, creating voids in the ***"InnerMask"*** (see below).

When the processes of ray-casting are completed, Medtool has created an ***"OuterMask"*** (Figure 2.11d) and ***"InnerMask"*** (Figure 2.11e) masks. As mentioned above, ***"Close"*** image stack is used to define ***"OuterMask"*** and, as the rays detect the outer contour of the whole bone, ***"OuterMask"*** defines the overall geometry of the bone. ***"InnerMask"*** is similar to ***"OuterMask"*** in that it defines the 3D geometric limitations of the trabecular bone region and the air within the whole bone. Once both masks are completed, Medtool subtracts the ***"InnerMask"*** from the ***"OuterMask"*** and creates a ***"ThickMask"*** (Figure 2.11f). This is a mask of the cortical bone thickness only. When ***"InnerMask"***, ***"OuterMask"***, and ***"ThickMask"*** are created, Medtool generates three final volumes, which are passed for analysis. ***"MaskSegIn"*** (Figure 2.11g) is the representation of the trabecular bone and internal space and has had the ***"ThickMask"*** removed leaving only the trabecular bone and internal space. ***"MaskSegIn"*** is created by adding the overlapping parts of the ***"Clean"*** to ***"InnerMask"***. ***"MaskSegOut"*** (Figure 2.11h) is the representation of the cortical bone (including pores) and has had the ***"InnerMask"*** removed leaving only the cortical bone. ***"MaskSegOut"*** is created by adding the overlapping parts of the ***"Clean"*** to ***"ThickMask"***. ***"MaskSeg"*** (Figure 2.11i) is the representation of all elements of cortical bone and pores, trabeculae, and internal space and is created by adding ***"MaskSegIn"*** and ***"MaskSegOut"*** together.

The CGAL 4.9 mesher is then employed on the ***"InnerMask"*** and ***"OuterMask"*** to generate a finite element model representing the cortical and trabecular volumes (Figure 2.11j). This mesh is crutial for canonical holistic morphometric analysis (cHMA) method (see bellow) and further data visualisation. Iterative optimization processes ensure a smooth boundary without overlaps or gaps between tetrahedra. Tetrahedra are chosen over hexahedra due to their geometry, which preserves trabecular architectural details better (Müller and Rüegsegger 1995; Ulrich et al. 1998; Alberich-Bayarri et al. 2007). To gather material property data, a 3D grid with 2.5mm cells is positioned as a bounding box over the ***"MaskSegIn"*** (or ***"MaskSegOut"*** if cortical bone is the subject of interest) volume image. Next, 5mm diameter sampling spheres were centred on each vertex in the grid. Sampling spheres then move between the grid nodes across the entire

grid, iteratively measuring trabecular parameters. The 5mm spheres were chosen to ensure overlap between spheres. Spheres were employed to mitigate cornering effects, which can result in inadequate sampling of features near orthogonal axes, a common issue observed in cubic volume of interest (VOI) configurations (Ryan & Ketcham, 2004). By aligning the finite element mesh with the sampling sphere nodes, each of the trabecular parameters can be interpolated onto the mesh. When all these steps are taken, holistic morphometric analysis (HMA) is completed, and trabecular parameters can be measured within the bone. Trabecular parameters were measured by the mia-multi module in Medtool (see below). Medtool outputs quantitative data as well as options for the quantitative visualisation of the data. These interpolated meshes are visualised in Paraview 4.8.2 (Ahrens et al., 2005) (Figure 2.11k). However, these maps do not represent the mean trabecular values of each species, but rather represent the unique features of each bone from every individual separately. Thus, for the further analysis, cHMA was used (see below). This method allows for the creation of a canonical model with mean scalar trabecular values mapped per group that are homologous within each other and therefore can be statistically compared across groups (Bachmann et al., 2022).

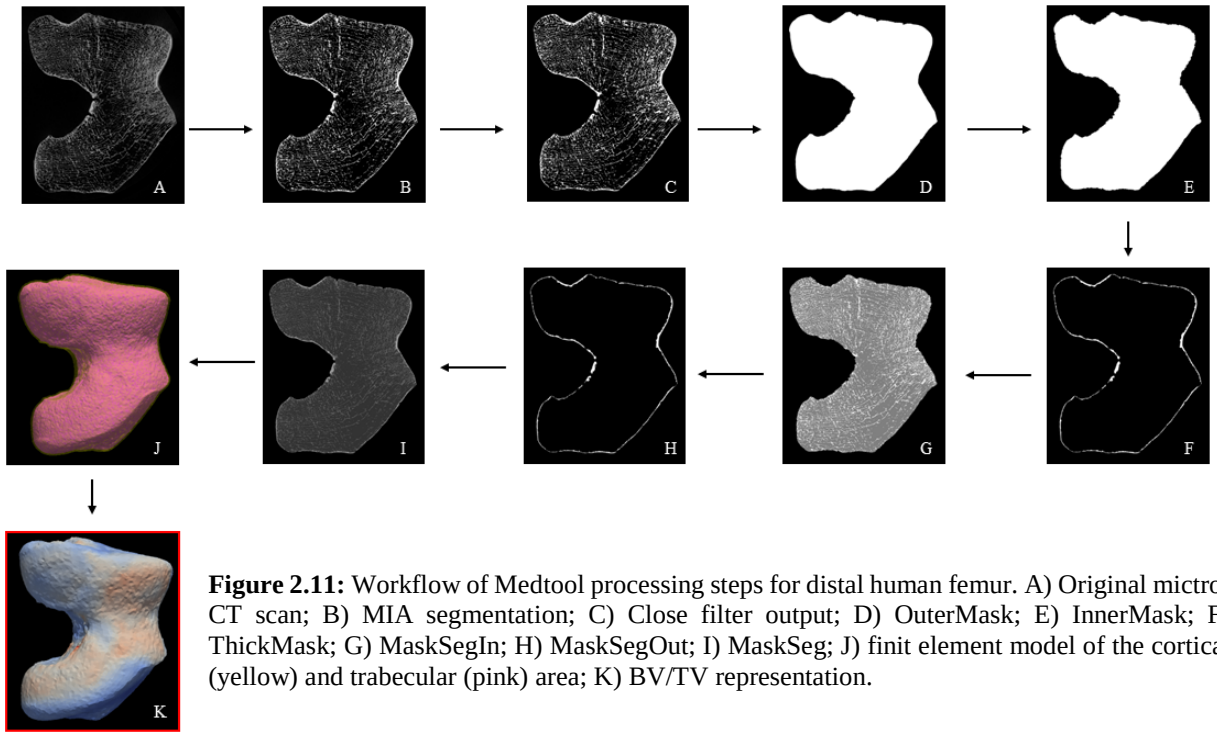

Figure 2.11: Workflow of Medtool processing steps for distal human femur. A) Original mictro-CT scan; B) MIA segmentation; C) Close filter output; D) OuterMask; E) InnerMask; F) ThickMask; G) MaskSegIn; H) MaskSegOut; I) MaskSeg; J) finit element model of the cortical (yellow) and trabecular (pink) area; K) BV/TV representation.

2.5.1 Trabecular parameters

Bone strength is closely associated with bone volume fraction (BV/TV) and degree of anisotropy (DA), which together account for up to 98% of the bone's Young's modulus, or stiffness (Cotter et al., 2009; Maquer et al., 2015; Hart et al., 2017). In this thesis, BV/TV for each individual was calculated based on the BV/TV values from each mesh element. Specifically, BV/TV was determined by dividing the number of segmented bone voxels by the total number of voxels within each Volume of Interest (VOI) sphere. To control for potential systematic differences among taxa and to analyze bone volume distribution while accounting for overall magnitude, each tetrahedron's BV/TV was normalized by the individual's average BV/TV, resulting in a measure of relative bone volume (rBV/TV). This normalization allows for meaningful comparisons between individuals and species with differing absolute BV/TV values (Dunmore et al., 2019; Sukhdeo et al., 2020). BV/TV is influenced by several factors, including trabecular thickness (Tb.Th), trabecular spacing (Tb.Sp), and trabecular number (Tb.N), which are interrelated. Trabecular spacing (Tb.Sp) is calculated by inverting scalar values from ***"MaskSegIn"***, converting internal air voxels into bone scalar values, and expanding spheres within these internal voxels. Consequently, Tb.Th and Tb.Sp together define the total bone volume, with Tb.Th and Tb.Sp inversely related. Trabecular number (Tb.N) is derived from Tb.Th and Tb.Sp using the formula 1/(Tb.Th + Tb.Sp).

DA is assessed using the Mean Intercept Length (MIL) method (Whitehouse, 1974). This technique involves casting vectors of equal length from random points within the image and measuring their traversal through the sample until they encounter a bone voxel. The mean intercept length is calculated by dividing the total length of these vectors by the number of intersections. A second-rank tensor is then fitted to the orthogonal directions and lengths of these vectors, and the three principal eigenvectors are decomposed. DA is computed using the formula 1 – (min. eigenvalue/max. eigenvalue), which subtracts the ratio of the smallest to the largest eigenvalue from 1, yielding a value between 0 (complete isotropy) and 1 (complete anisotropy). High DA values indicate well-aligned trabeculae that effectively resist forces along their alignment, while low DA values signify trabeculae that are oriented in multiple directions, providing resistance across various forces.

2.5.2 Canonical holistic morphometric analysis (cHMA)

To analyze trabecular bone distribution patterns across the entire epiphysis of the distal femur and proximal tibia in extant taxa, the cHMA approach was utilized, combining HMA with a statistical free-form deformation model (SDM), as outlined by Bachmann et al. (2022). The

SDM process begins with the preparation of masked volumetric images of the bones, referred to as ***"OuterMask"***. These images are first aligned to a randomly selected reference image using a similarity transformation, which adjusts for translation, rotation, and scaling in 3D space without changing the size or shape of the ***"OuterMask"***. Once all images are registered to the reference, their similarity transformations are averaged, with the center of rotation fixed to maintain consistency across the dataset. After this alignment phase, a free-form deformation is applied using cubic B-spline transformations. This deformation model allows for the flexible and precise mapping of trabecular bone distribution patterns, accommodating variations in bone morphology across different specimens. This integrated approach enables detailed and comparative analysis of trabecular bone structures within the studied epiphyses. The steps of registering and averaging are repeated twice. Firstly, the canonical image is created using a single randomly chosen individual, as above. Secondly, the canonical image is created using all individuals in the given sample. As a result, an average bone model is created, representing the mean size, shape, and position of the entire sample (Figure 2.12a). Research has shown that the final average shape is not significantly influenced by the initial reference image of an individual (Bachmann et al., 2022). At this point, the average bone model is a volumetric representation of the entire sample and does not include any internal structural details. Since this model is derived from all bones in the sample, it's important that each bone reflects the same side of the body. Therefore, before this process begins, all left distal femora and left proximal tibiae were mirrored in Avizo to represent the morphology of a right-side bone. The registration process concludes with an evaluation of surface distances, which measure the distance (in millimeters) between each transformed individual specimen and the average bone model, providing an indication of the registration error. The registration of the ***"InnerMask"*** does not necessitate rerunning the deformation process again. Note that fossil sample was not included in these canonical bone creations. Due to their preservation, all fossil specimens were registered to the canonical bone of the extant distal femur/proximal tibia using individual landmark sets. Detailed information about individual landmark sets for each fossil and about how the fossils were registered to the canonical bone and further analysed can be found in the **Chapter 6**.

The next step, known as meshing, is also performed in Medtool. Initially, Medtool generates a tetrahedral finite element mesh for the outer canonical model, creating a canonical finite element structure. Then, the ***"InnerMask"*** segmentation from each individual is aligned with the canonical ***"InnerMask"*** model using the same process of rigid and non-rigid transformations. During this stage, the transformation data is applied to adjust the tetrahedral

canonical mesh to match the data of each individual. Only the mesh nodes are adjusted to prevent any gaps from forming in the mesh. Afterward, morphometry (HMA) can be conducted on the original images and then mapped onto the adjusted canonical mesh. The original grid node data is interpolated onto the transformed canonical bone mesh, which is subsequently reverted to its canonical shape for visualization in Paraview. Since the data is interpolated onto the canonical mesh, and the data corresponding to each mesh element are gathered from each individual, it becomes geometrically comparable and can be analyzed statistically.

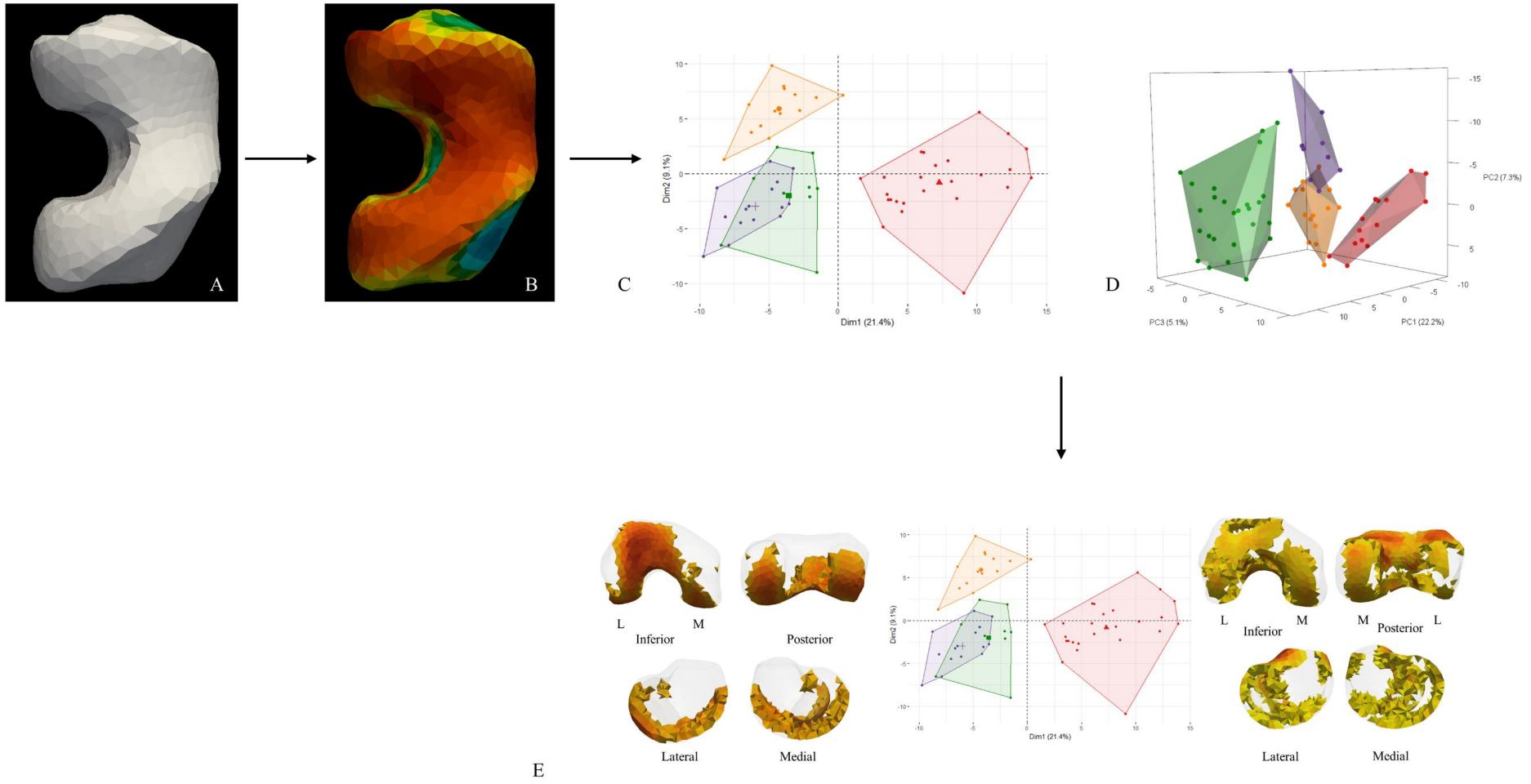

Figure 2.12: Workflow of cHMA processing steps for distal human femur. A) Outer canonical atlas representing sample's mean size, position, and external right distal femur morphology; B) inner mesh representing rBV/TV distribution in whole human sample; C) an example of 2D PCA conducted on cHMA data; D) an example of 3D PCA conducted on cHMA data; E) an example of PCA loadings visualisation.

2.6 Statistical analyses

As all specimens have the same number of tetrahedral elements and the same topology, the homology is accounted for and thus, all quantitative comparisons of measured variables and statistical analyses can be conducted on the scalar data at each mesh element generated from cHMA (Bachman et al., 2022).

To analyse the distribution of trabecular bone measures in each species, principal component analysis (PCA) was run in R software (Figure 2.12c-d), creating PCA models for any trabecular parameter separately using the individual scalars associated with tetrahedral elements of the canonical mesh as input variables for the PCA. This allows for visual comparison of the differences in genus-specific patterns. Alongside the standard PCA visualisation, it is possible to produce models of the principal component (PC) loadings for any given trabecular parameter (Figure 2.12e). This creates a model illustrating the trabecular distributions driving variation along the PCs within the sample. The loading models can be thresholded in Paraview by a given percentile to demonstrate cells with the highest/lowest values of the PCA extremes given in volumetric 3D (Figure 2.12e). In this thesis, all PCA plots were conducted using R v4.2.2 (R Core Team, 2017). Further elaboration on the methodologies employed for the PCAs conducted on the distal femora sample is provided in **Chapter 4**, while the PCAs performed on the proximal tibiae sample are discussed in **Chapter 5**. Additionally, **Chapter 6** offers insights into the PCAs conducted on the fossil sample.

Shapiro-Wilk tests were used to assess normality and Levene's tests were used to assess equality of variance of the datasets used in **Chapter 3**. Kruskal-Wallis and Dunn's post hoc tests were used to test if the means of a specific parameter (rBV/TV, DA, Tb.Th, Tb.Sp and Tb.N) differed significantly between whole datasets used in **Chapter 3**. To explore whether interspecific allometry contributes to species differentiation in **Chapter 4**, a regression of PC1 on "bone volume" across all studied individuals was performed (Supplementary Figure S4.8). To investigate potential intraspecific allometry in **Chapter 4**, I conducted a regression of PC1 on bone volume for each taxon separately (Supplementary Figure S4.9-S4.11). To evaluate inter- and intra-taxon distinctions within the datasets in **Chapter 5**, I employed Kruskal-Wallis tests followed by post-hoc Dunn's tests with a Bonferroni correction (Supplementary Table S5.2; Table 5.2). Significance was determined at $\alpha=0.05$ for all statistical analyses. Moreover, pairwise permutational MANOVAs were conducted on the first two principal components to test for quantitative inter- and intra-taxon differences in the datasets in **Chapter 5**.

3 TECHNICAL NOTE: DOES SCAN RESOLUTION OR DOWNSAMPLING IMPACT THE ANALYSIS OF TRABECULAR BONE ARCHITECTURE?

Published artical: Lukova, A., Dunmore, C.J., Tsegai, Z.J, Bachmann, S., Synek, A., & Skinner, M.M. (2024). Technical note: Does scan resolution or downsampling impact the analysis of trabecular bone architecture? *American Journal of Biological Anthropology*.

3.1 Abstract

The 'gold standard' for the assessment of trabecular bone structure is high-resolution micro-CT. In this technical note, we test the influence of initial scan resolution and *post hoc* downsampling on the quantitative and qualitative analysis of trabecular bone in a *Gorilla* tibia. We analysed trabecular morphology in the right distal tibia of one *Gorilla gorilla* individual to investigate the impact of variation in voxel size on measured trabecular variables. For each version of the micro-CT volume, trabecular bone was segmented using the Medical image analysis method. Holistic morphometric analysis was then used to analyse bone volume (BV/TV), anisotropy (DA), trabecular thickness (Tb.Th), spacing (Tb.Sp), and number (Tb.N). Increasing voxel size during initial scanning was found to have a strong impact on DA and Tb.Th measures, while BV/TV, Tb.Sp and Tb.N were found to be less sensitive to variations in initial scan resolution. All tested parameters were not substantially influenced by downsampling up to 90 µm resolution. Colour maps of BV/TV and DA also retained their distribution up to 90 µm. This study is the first to examine the effect of variation in micro-CT voxel size on the analysis of trabecular bone structure using whole epiphysis approaches. Our results indicate that microstructural variables may be measured for most trabecular parameters up to a voxel size of 90 µm for both scan and downsampled resolutions. Moreover, if only BV/TV, Tb.Sp or Tb.N is measured, even larger voxel sizes might be used without substantially affecting the results.

3.2 Introduction

Trabecular bone is a porous tissue found in the epiphyses of long, short, and irregular bones (Keaveny et al., 2001). Although the structure of trabecular bone is partially genetically determined (Loewen et al., 2016; Paternoster et al., 2013; Turner et al., 2000), (re)modelling is at its peak during growth and gradually declines into the adulthood (Glatt et al., 2007; Halloran et al., 2002; Saers et al., 2020; Seeman, 2003; Su et al., 2013). Trabecular bone tissue is thought to respond to biomechanical forces and functionally adapt to its mechanical environment (Ruff et al., 2006). In places where incurred load is lower, there is thought to be a reduction in the amount of trabecular bone, resulting in a weaker structure (Schulte et al., 2013). Conversely, in places where stress is higher, there should be an increase in trabecular tissue, resulting in a stronger bone structure (Barak et al., 2011; Pontzer et al., 2006; Schulte et al., 2013; Sinclair et al., 2013). These changes in trabecular bone architecture can include the thickness of trabecular struts, their spacing, and their orientation. Therefore, analysis of trabecular structure can provide insights into the biomechanical loads incurred by bones during life. It can be used to understand the skeletal morphology of living taxa and reconstruct behaviour in fossil taxa (Chirchir, 2019; Kivell, 2016; Komza & Skinner, 2019; Ryan & Shaw, 2012; Saers et al., 2020).

The traditional method of analysing trabecular structure in 3D is to quantify trabecular bone in a volume of interest (VOI). The main advantage of the VOI method is that it allows for the extraction and quantification of a portion of a complex structure from a much larger micro-CT data set. However, defining a homologous VOI, both its size and location, is far from straightforward, especially across taxa and/or an ontogenetic series where there can be substantial differences in both size and morphology (Gross et al., 2014; Kivell et al., 2011; Lazenby et al., 2011). Moreover, the region of trabecular structure that differs most amongst the study sample could be outside of the VOI region when determined *a priori*. More recently, several studies have placed multiple VOIs throughout an anatomical region, revealing the presence of regional differences in trabecular bone structure (DeSilva & Devlin, 2012; Griffin, 2018; Su et al., 2013). Some studies used geometric morphometrics (GM), where sliding semilandmarks are used to define homologous locations across surfaces in order to place multiple VOIs, to assess trabecular variation beneath the articular surfaces of the talus and distal femur (Sylvester & Terhune, 2017), in the metacarpals (Dunmore et al., 2019; Dunmore et al., 2019; Dunmore et al., 2020) and in the proximal femur (Georgiou et al., 2020). Furthermore, a method originally developed for finite-element material-mapping (Pahr & Zysset, 2009), has been adapted for analyses of high-resolution trabecular bone across primates (Tsegai et al.,

2013; Gross et al., 2014). Holistic morphometric analysis (HMA) quantifies trabecular morphology through the entire epiphysis rather than in one or a few sub-surface VOIs. Recently, Bachmann et al., (2022), developed HMA with a canonical holistic approach (cHMA), which allows for statistical comparisons of trabecular patterns between groups, free of *a priori* subsampling, by calculating mean models that contain homologous spatial units of analysis.

Studies of trabecular bone architecture often analyse scans with different resolutions across the studied species and/or individuals (Cazenave et al., 2019, Georgiou et al., 2018; Lukova et al., 2024; Sylvester & Terhune, 2017). This can be due to collection of micro-CT scans by different researchers with different protocols, due to specimen size limiting resolution on different CT systems, or scans may be downsampled (i.e., process of reducing the resolution or dimensions of a digital image by decreasing the number of pixels in the image) after collection due to the computational limitations of processing large datasets. Previous studies have shown that downsampling can impact the accuracy and precision of measurements of trabecular architecture. For example, trabecular thickness (Isaksson et al., 2011; Kothari et al., 1998; Majumdar et al., 1996; Muller et al., 1996; Sode et al., 2008) or measures of anisotropy can be highly sensitive to voxel size (Isaksson et al., 2011; Kothari et al., 1998; Sode et al., 2008). In general, it is expected that lower resolutions (the lower resolution the larger voxel size) create blur in the scan images making some features hard to segment and may lead to loss of thin trabeculae, i.e., if the feature is smaller than voxel size it may well be averaged out in favour of another phase such as background (partial volume averaging). Majumdar et al. (1996) showed that trabecular thickness tends to be increasingly overestimated at lower resolutions when analysing magnetic resonance (MR) and micro-CT images. Similarly, Müller et al. (1996) found that trabecular spacing and number can be precisely measured at resolutions up to 175 µm, however, trabecular thickness required a much higher resolution for accurate assessment. Moreover, Isaksson et al. (2011), using micro-CT scans, found that with decreasing resolution, the originally detected differences between normal and osteoporotic groups diminished. Kim et al. (2004) used three different scanning and voxel sizes (a high-resolution voxel size (21µm), a commonly used intermediate voxel size (50µm), and a voxel size applicable to scans of whole human vertebral bodies (110µm) to examine the effect of voxel size on stereological measures of human trabecular bone. They found that the error in stereological parameters ranged from 0.1% to 102% depending on the voxel size analysed. Peyrin et al. (1998) examined a series of vertebral samples with voxel sizes of 1.4, 6.7, and 14µm. They concluded that voxel sizes as large as 14µm provide a reasonably accurate measurement of trabecular architecture.

Christiansen (2016) investigated micro-CT scans of mouse trabecular bone measures with voxel sixes at 6-30 µm. They demonstrated that voxel size strongly affects connectivity density and trabecular thickness. All these studies suggest that high resolution scans should be used, when possible, to accurately measure trabecular bone microstructure.

In this study, we test the impact of 1) scanning the same specimen at different resolutions and 2) downsampling a high-resolution scan of this specimen to lower resolutions using a whole-epiphysis approach. The trabecular variables tested include bone volume fraction (BV/TV), degree of anisotropy (DA), trabecular thickness (Tb.Th), trabecular spacing (Tb.Sp) and trabecular number (Tb.N). We also assess the impact of scan resolution and downsampling on material maps of BV/TV and DA, which are some of the most biomechanically informative aspects of trabecular architecture and are widely reported in the literature (Goldstein et al., 1993; Odgaard et al., 1997; Van Rietbergen et al., 1998).

3.3 Materials and methods

The study sample of micro-CT scans of varying resolutions was created from scans of a complete right distal tibia of a *Gorilla gorilla* individual from Cameroon, curated at the Powell-Cotton Museum in Birchington-on-Sea, UK.

The specimen was scanned using a Diondo D1 scanner at the Imaging Centre for Life Sciences at the University of Kent (Canterbury, UK). The scan parameters included an acceleration voltage of 130 kV, a tube current of 130 µA and a 1.0 mm aluminium filter. Images were reconstructed as 16-bit TIFF stacks.

Two samples were created to test the impact of voxel resolution on the measurement and visualization of trabecular architecture. In the first, the tibia was rescanned four additional times to produce volumes with voxel sizes of 45, 60, 90 and 110 µm (Figure 3.1c). To create the second sample, a scan with a voxel size of 30 µm was downsampled to 60, 90, 120, 150, 180 and 210 µm (Figure 3.1d). Downsampling was conducted in medtool v4.5 (www.dr-pahr.at/medtool) using whole-integer factors only to avoid aliasing (for more details on aliasing, see e.g., He et al., 2021; Tward & Siewerdsen, 2009; Yen et al., 1999; Zbijewski & Beekman, 2003). For example, when downsampling 30 to 60µm eight (2^3) voxels are averaged and from 30 to 90µm 27 (3^3) voxels are averaged.

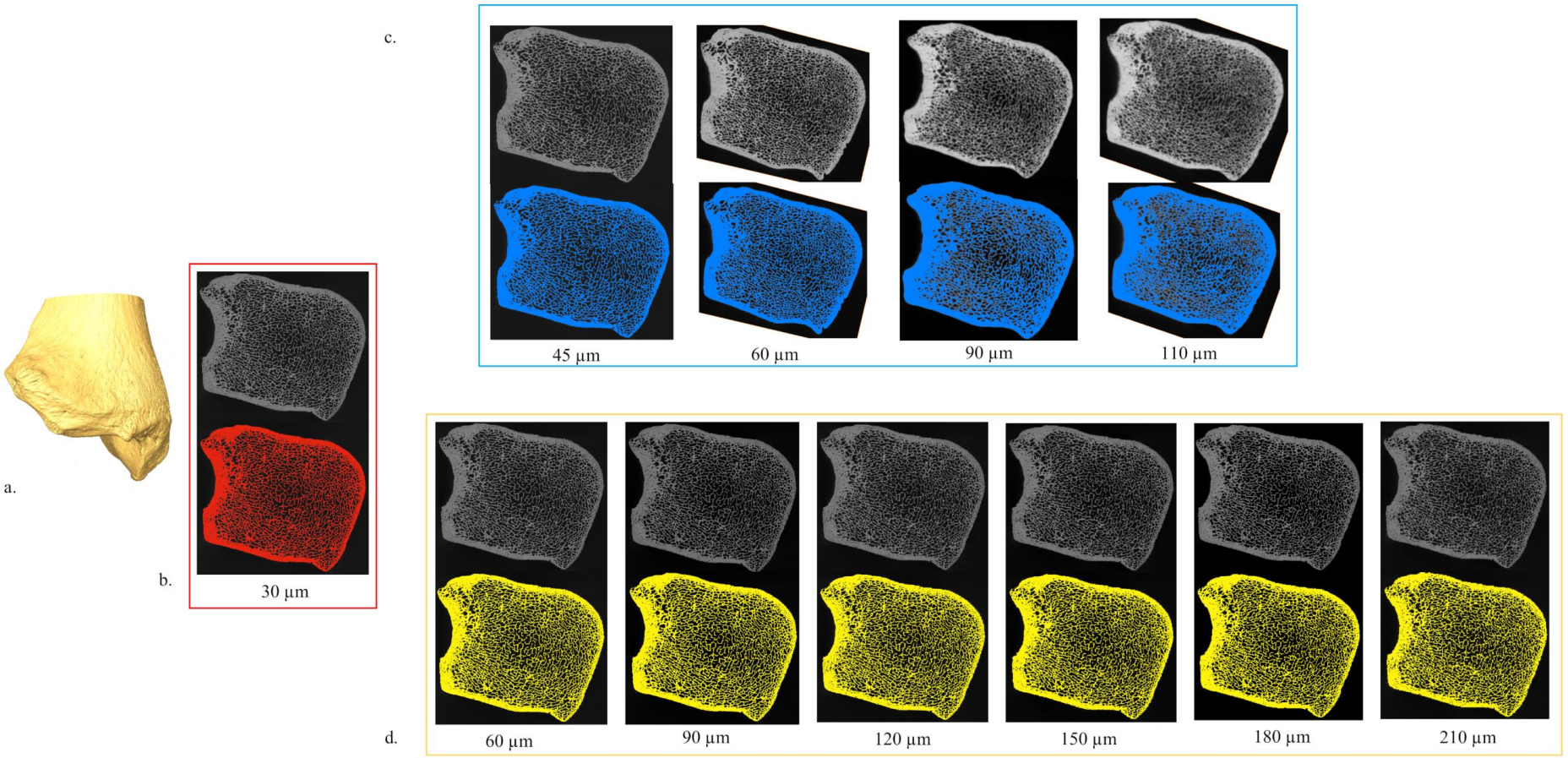

Figure 3.1: a) Surface of the studied distal tibia region (anterior view); b) unsegmented (raw) and overlapping segmented high-resolution scan (in distal view) with voxel size of 30 µm used as the baseline scan; c) serial unsegmented and overlapping segmented images of the same distal tibia (in distal view) scanned under the lower resolution with four different voxel sizes of 45, 60, 90 and 110 µm; d) the baseline scan downsampled to voxel size of 60, 90, 120, 150, 180 and 210 µm.

All images were segmented into a binary phase of background and bone using the MIA-clustering algorithm (Dunmore, Wollny, & Skinner, 2018). This method requires the definition of a grid size, which was selected by measuring the thickness of the thickest trabeculae in a 2D cross-section using Avizo to determine their width in pixels. The grid size was then set a few voxels larger then this measurement to ensure that the local segmentation focused on features within the phase of interest (Table 3.1) (Dunmore et al., 2018). Two classes were used for all scans (Table 3.1). To assess if the same volume of bone was segmented in each image stack, we measured segmented bone volume for each scan in Avizo 6.3 (Visualization Science Group, SAS). Each segmented image was then used for further analysis of trabecular parameters (Figure 3.2).

Table 3.1: Segmentation parameters.

Method	Resolution (µm)	Trabecular thickness (mm)*	Trabecular thickness/resolution (mm/µm)	Grid size (px)	Number of classes	Probability filter
baseline scan	30	0.27	9.0	10	2	none
downsampled	60	0.28	4.7	5	2	none
downsampled	90	0.31	3.4	5	2	none
downsampled	120	0.33	2.8	5	2	none
downsampled	150	0.35	1.9	5	2	none
downsampled	180	0.37	2.0	5	2	none
downsampled	210	0.37	1.8	5	2	none
rescanned	45	0.40	8.9	10	2	none
rescanned	60	0.32	5.3	10	2	none
rescanned	90	0.39	4.3	5	2	none
rescanned	110	0.45	4.1	5	2	none

*Measured in a 2D cross-section.

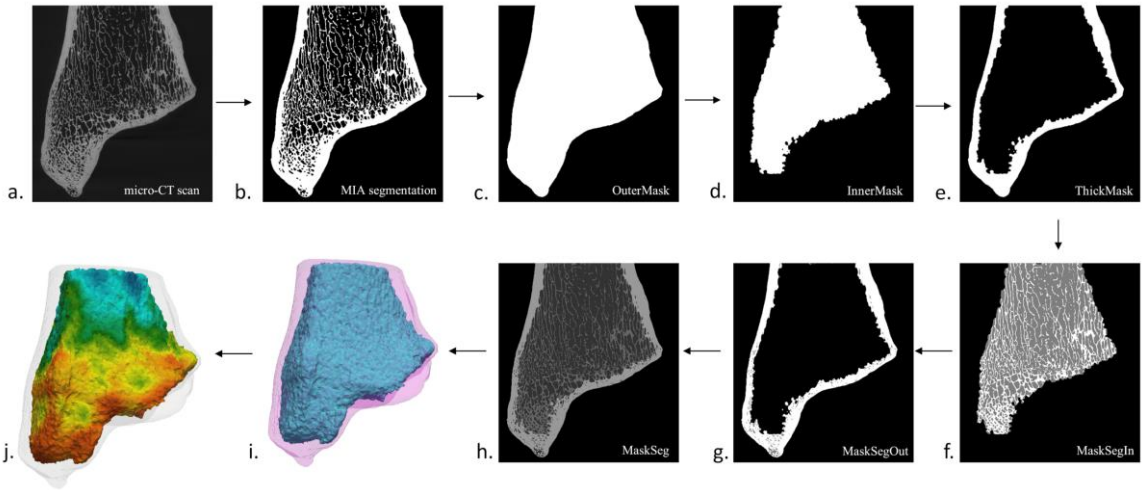

Figure 3.2: Workflow of Medtool processing steps (posterior view). A) Original micro-CT scan; B) Results of the MIA binary segmentation process; C) OuterMask; D) InnerMask; E) ThickMask; F) MaskSegIn; G) MaskSegOut; H) MaskSeg; I) finite element model of the cortical (pink) and trabecular (blue) area; J) BV/TV representation.

The external and inner volumes of all images were defined using medtool v 4.5 (www.dr-pahr.at/medtool) and taken from each other to produce the thick cortical bone shell, following published protocols (Pahr & Zysset, 2009; Tsegai et al., 2013; Gross et al., 2014). The binary images (in which bone voxels can be classified as 1 and non-bone voxels as 0) from MIA

(Figure 3.2b) were used as inputs for medtool. The primary structure in the image was identified as the one containing the most contiguous voxels with a greayscale values of one (white voxels). Subsequently, any isolated voxels not connected to the bone were assigned a value of zero or black. Morphological filters in medtool were then applied to fill the bone, thereby isolating the external and internal edges of the cortical bone in 3D. This process resulted in a mask delineating the internal bone volume and outer cortical bone. During the bone filling process, small pores within the cortical bone were identified and filled based on the size of the kernel radius. This method ensured that the fine porosity of the cortical bone was preserved, while moderate gaps indicative of genuine variations in trabecular shape or separation were maintained. For this, a ray-casting method was used. Subsequently, closing, and opening operations were performed to fill in the gaps in the bone structure, resulting in the creation of the *OuterMask* (Figure 3.2c). To identify trabecular spaces, the same ray casting process was employed, but with a starting point at the edge of the *OuterMask* instead of the image edge. Rays terminated upon encountering air voxels rather than bone voxels. Closing and opening operations were then applied to fill in areas where rays had had traversed directly through trabeculae, creating voids in the *InnerMask* (Figure 3.2d). The *OuterMask* delineated the overall geometry of the entire bone by detecting its outer contour using rays. Conversely, the *InnerMask* served a similar purpose to the *OuterMask*, but specifically defined the 3D geometric boundaries of the trabecular bone region within the entire bone structure. Once both masks were completed, medtool subtracted the *InnerMask* from the *OuterMask* and created a *"ThickMask"* (Figure 3.2e), which specifically represented the thickness of the cortical bone. Following the creation of *InnerMask*, *OuterMask*, and *ThickMask*, medtool generated three final volumes for subsequent analysis. *MaskSegIn* (Figure 3.2f) represented the trabecular bone and internal spaces. It was derived from *OuterMask* with *ThickMask* removed, focusing solely on the trabecular bone and internal spaces. *MaskSegOut* (Figure 3.2g) represented the cortical bone, including its pores. It was derived from *InnerMask* with *OuterMask* removed, isolating only the cortical bone. *MaskSeg* (Figure 3.2h) represented all elements including cortical bone, pores, trabeculae, and internal spaces. *MaskSeg* was created by combining *MaskSegIn* and *MaskSegOut*.

The CGAL (Computational Geometry Algorithms Library, https://www.cgal.org) 4.9 mesher was then applied to the *InnerMask* and *OuterMask* to create a finite element model of the cortical and trabecular volumes (Figure 3.2i). This mesh was created for each resolution separately and all meshes were later used for data visualisation. Each mesh underwent

optimization through a series of iterative processes to achieve a smooth boundary, ensuring there were no overlaps or holes between the tetrahedra. Tetrahedra were chosen over hexahedra because their geometry results in a smoother boundary, minimizing the loss of trabecular architectural information (Müller & Rüegsegger, 1995; Ulrich et al. 1998; Alberich-Bayarri et al., 2007). To gather material property data, a 3D grid with 2.5mm cells was placed as a bounding box over *MaskSegIn*. Subsequently, a 5mm sampling sphere moved between the grid nodes across the entire bounding box, iteratively measuring trabecular parameters. By aligning the finite element mesh with the nodes of the sampling sphere, each of the trabecular parameters was interpolated onto the mesh. When all these steps were taken, HMA was completed, and trabecular parameters were measured within the bone. Trabecular parameters were measured by the mia-multi module in medtool. Medtool outputted quantitative data as well as options for the quantitative visualisation of the data. These interpolated meshes are visualised in Paraview 4.8.2 (Ahrens et al., 2005) (Figure 3.2j).

The measure of BV/TV is the proportion of trabecular bone of the total volume in each region and was calculated as the ratio of bone voxels to non-bone voxels within the masked volume of each sampling sphere (VOI). DA in 3D was calculated using the mean-intercept-length method (Whitehouse, 1974; Odgaard et al., 1997). The value of DA is zero if the minor and major eigenvectors are of equal magnitude (i.e., isotropic), and is one if the minor and major eigenvectors are maximally different (i.e., anisotropic). A value between 0 and 1 is produced via the formula 1 – (min. eigenvalue/max. eigenvalue) (Kivell et al., 2011). To calculate Tb.Th, medtool computed the distance map of the bone voxels of the *MaskSegIn* (Figure 3.2f) and extracted the distance ridge from which the average distance was calculated. Tb.Sp was calculated in a similar way by inverting bone and background labels. Tb.N was calculated using Tb.Th and Tb.Sp via the formula 1/(Tb.Th+Tb.Sp).

Boxplots and histograms summarizing the data distribution of each variable were generated directly from all VOIs of each respective scan. Shapiro-Wilk tests were used to assess normality and Leven's tests were used to assess equality of variance of each trabecular variable (Table S3.1-S3.5). The Kruskal-Wallis and Dunn's post hoc tests were used to test if the means of a specific parameter differed significantly between datasets. The differences were tested between all combinations of groups within the downsampled images and then separately within the rescanned images. All statistical analyses were conducted in R v3.4.1 and plots were generated using the ggplot2 package (R Core Team, 2017; Wickham, 2016).

3.4 Results

3.4.1 Total bone volume

The total segmented bone volume for the 30 µm scan is 28082 mm^3 (Table 3.2). When downsampling, the segmented bone volume remains similar until 210 µm, at which point there is a reduction of 0.7% (27897 mm^3) (Table 3.2). Rescanning the specimen results in a stepped increase at 45 (1.5%) and 60 (2.1%) µm, with the segmented volume then remaining similar in scans at 90 and 110 µm (Table 3.2).

Table 3.2: Segmented bone volume for all tested CT scans.

Voxel size (µm)	Technique	Segmented bone volume (mm3)	Segmented bone volume change (%)
30	baseline micro-CT scan	28082	0.00
60	downsampled	28037	-0.16
90		28058	-0.09
120		27985	-0.35
150		28061	-0.08
180		28118	0.13
210		27897	-0.66
45	rescanned	28505	1.51
60		28674	2.11
90		28682	2.14
110		28700	2.20

3.4.2 Bone volume fraction

Distributions of BV/TV values for each VOI of the background grid in the baseline scan, downsampled volumes and rescanned volumes are presented in Figure 3.3. The variance of BV/TV values remains relatively similar for all scans and any outliers represent the elements with both lowest and highest BV/TV values. When downsampling, there appears to be a slight decrease in median BV/TV values compared to the baseline scan (Figure 3.3a), however, the distributions strongly overlap. When rescanned at 45 µm, the median BV/TV is similar, but then increases slightly at voxel sizes of 60, 90 and 110 µm. Similarly, histograms of BV/TV values from each VOI show that the general data distribution pattern remains stable and not normally distributed across all voxel sizes using both downsampled and rescanned images

(Figure 3.3b, c; Table S3.1). Table 3.3 shows that the mean BV/TV values (of the VOI's) gradually decrease with downsampling (reaching 12.1% at 210 µm). Rescanning at 45 µm results in a mean BV/TV decrease (0.64%), while there are increases in mean BV/TV at 60 µm (8.06%), 90 µm (3.87%) and 110 µm (5.81%) compared to the baseline scan (Table 3.3).

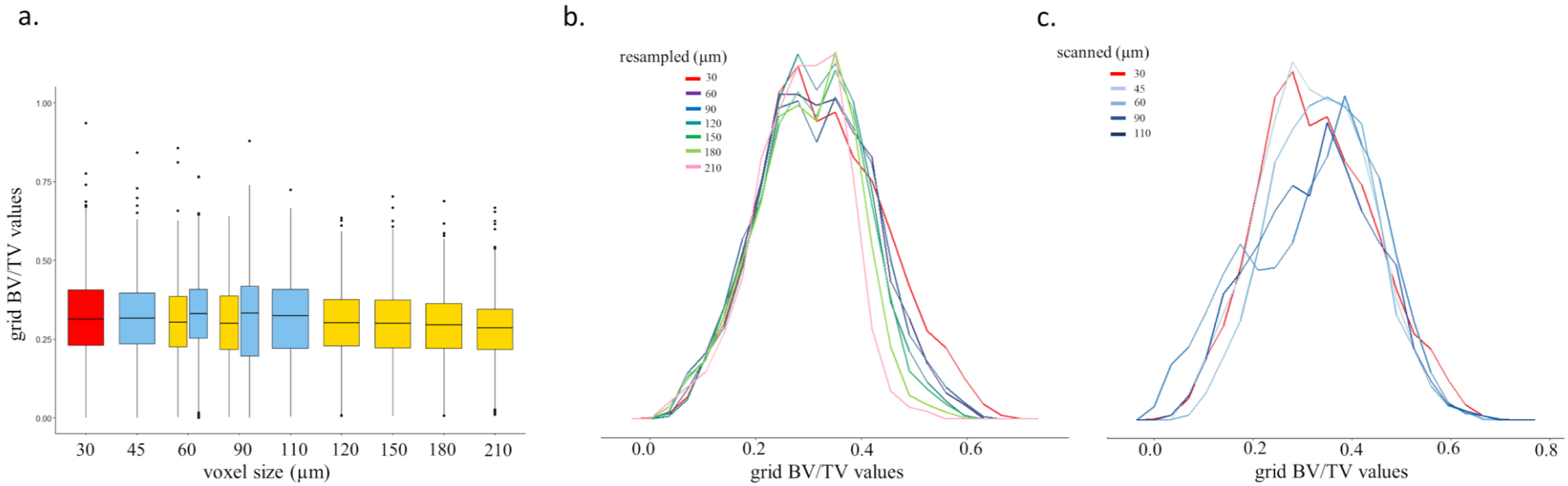

Figure 3.3: a) Boxplots of the grid BV/TV values for each voxel size for the baseline scan (red), the downsampled data (yellow) and for the specimen scanned at different resolution (blue); b) histogram of the grid BV/TV values for each voxel size for the baseline scan (red line) and the downsampled data; c) histogram of the grid BV/TV values for each voxel size for the baseline scan (red line) and for the specimen scanned at different resolution.

Table 3.3: The mean and SD values of all tested trabecular parameters.

Voxel size (μm)	Technique	mean BV/TV (SD)	mean DA (SD)	mean Tb.Th (SD)	mean Tb.Sp (SD)	mean Tb.N (SD)	N of grid nodes*
30	baseline micro-CT scan	0.313 (0.105)	0.470 (0.112)	0.272 (0.081)	0.267 (0.759)	1.001 (0.154)	734423
60	downsampled	0.301 (0.098)	0.498 (0.117)	0.291 (0.078)	0.786 (0.786)	0.954 (0.136)	648989
90		0.302 (0.099)	0.479 (0.116)	0.316 (0.080)	0.252 (0.802)	0.916 (0.124)	646690
120		0.299 (0.095)	0.421 (0.105)	0.338 (0.076)	0.247 (0.818)	0.885 (0.118)	683156
150		0.293 (0.091)	0.353 (0.092)	0.370 (0.072)	0.244 (0.846)	0.840 (0.108)	535414
180		0.284 (0.087)	0.296 (0.079)	0.404 (0.061)	0.242 (0.873)	0.799 (0.101)	527357
210		0.275 (0.086)	0.261 (0.074)	0.446 (0.048)	0.240 (0.905)	0.754 (0.093)	573089
45	rescanned	0.311 (0.101)	0.488 (0.114)	0.295 (0.085)	0.264 (0.783)	0.954 (0.140)	699828
60		0.335 (0.094)	0.481 (0.114)	0.336 (0.092)	0.254 (0.777)	0.918 (0.119)	668455
90		0.322 (0.128)	0.420 (0.102)	0.427 (0.112)	0.278 (0.921)	0.768 (0.121)	682908
110		0.328 (0.107)	0.391 (0.102)	0.442 (0.116)	0.249 (0.859)	0.781 (0.087)	583379

*Number of intreal grid nodes on which each VOI is centred.

The Kruskal-Wallis test shows a statistically significant difference in BV/TV within the downsampled and (separately) within the scanned images (Table 3.4). Additionally, a Tukey's HSD post hoc test was performed to further explore these differences. The post hoc tests indicate that there are significant differences in BV/TV within all combinations of downsampled and scanned images (Table S3.6).

Table 3.4: The Kruskal-Wallis test for BV/TV, DA, Tb.Th and Tb.Sp grid values within downsampled and scanned images.

BV/TV			
technique	df	Chi-squared	p-value
downsampling	6	11400	**<0.001**
scanning	4	6025	**<0.001**
DA			
downsampling	6	399906	**<0.001**
scanning	4	95682	**<0.001**
Tb.Th			
downsampling	6	16247	**<0.001**
scanning	4	7770	**<0.001**
Tb.Sp			
downsampling	6	1907	**<0.001**
scanning	4	864	**<0.001**
Tb.N			
downsampling	6	6100	**<0.001**
scanning	4	3352	**<0.001**

To understand if any of these outliers are spatially organised, and thus potentially affecting functional interpretation, we visualized the BV/TV distribution throughout the distal tibia for the baseline scan and all downsampled and rescanned volumes. Figure 3.4 shows the colourmaps, i.e. interpolations of the values from the VOI's discussed above, of BV/TV distribution. Compared to the baseline scan (Figure 3.4a), the general pattern of BV/TV distribution is maintained in all downsampled images, up to a voxel size of 210 µm (Figure 3.4b). In this volume the region of highest BV/TV (in red) extends further above the malleolus and is more concentrated in the malleolar groove and, in the mid-coronal view, the region of highest BV/TV is concentrated more laterally and BV/TV is lower in the malleolar region (Figure 3.4b). The BV/TV concentration on the posterior side of the malleolus, as well as anteriorly and posteriorly on the articular surface, is also higher at the downsampled voxel size

of 210 µm (see the distal view Figure 3.4b). Rescanning at 60 µm presents a broadly similar pattern of BV/TV on each surface and in the mid-coronal cross section (Figure 3.4c). However, after rescanning at 90 and 110 µm the distribution pattern is less consistent. The high BV/TV concentration along the malleolar region and under the articular surface is lost (see mid-coronal view in Figure 3.4c).

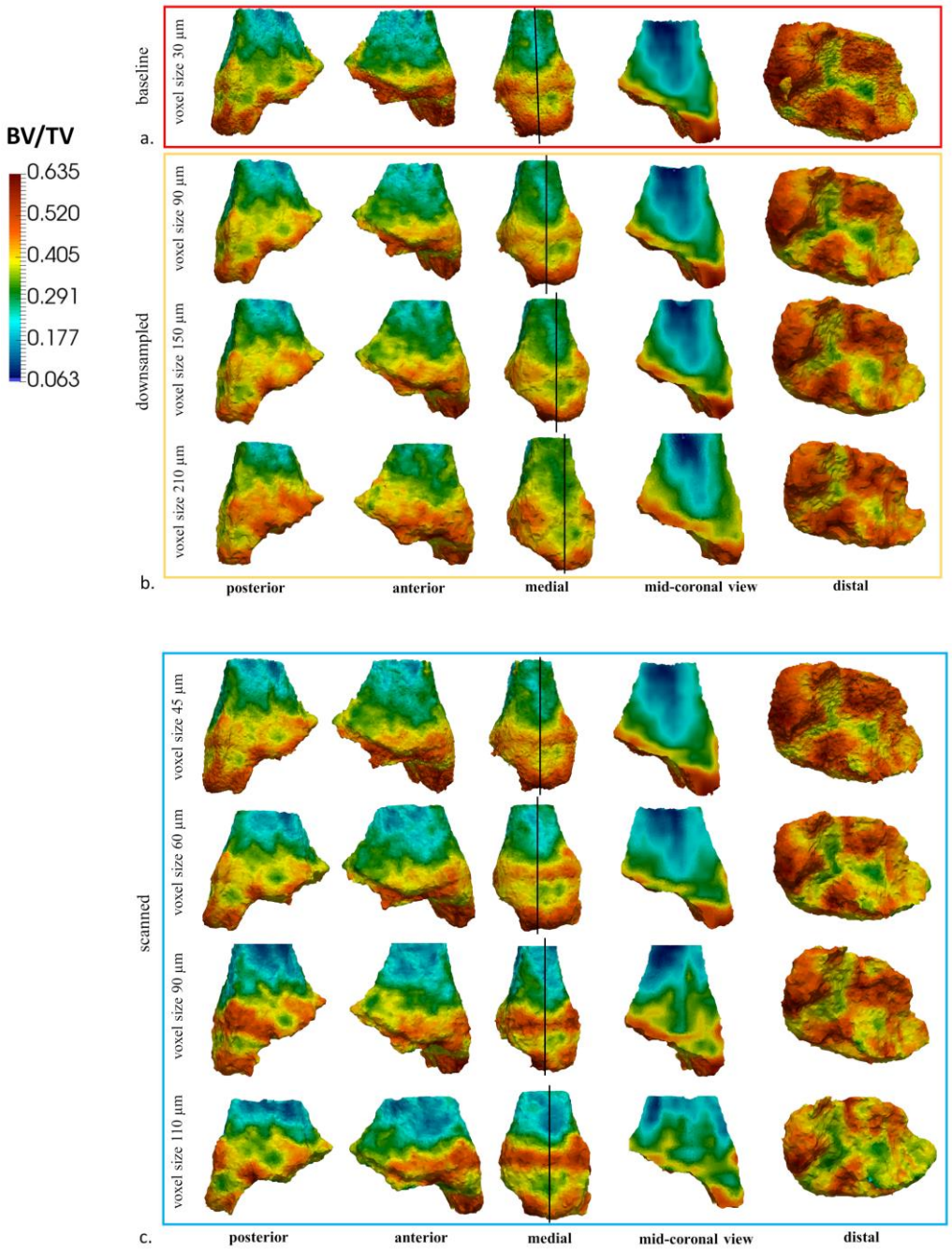

Figure 3.4: Distal tibia model of BV/TV distribution of tested *Gorilla* individual for baseline scan (a), downsampled voxel sizes of 90, 150, and 210 µm (b), and scan voxel sizes of 45 – 110 µm (c). Vertical lines through the medial view show where the slices are positions for the cross-section mid-coronal view. Dark red represents the highest and dark blue the lowest BV/TV values. All colourmaps were scaled to baseline scan data range.

3.4.3 Degree of anisotropy

Downsampling from the baseline to 60 and 90 µm does not result in a large change in DA values; however, there is a marked reduction in DA when downsampling between 120 and 210 µm (Figure 3.5). Similarly, rescanning at 45 and 60 µm does not result in a change in DA, but DA drops to a greater degree in scans at 90 and 110 µm. The general DA data distribution for the baseline scan is not normally distributed and overlaps across all scan voxel sizes (Figure 3.5b; Table S3.3), even in the downsampled voxel size of 90 µm (Figure 3.5b). However, the data moves towards an apparent positively skewed distribution pattern when downsampled to 120-210 µm (Figure 3.5b; Table S3.2). Table 3.3 shows that mean DA values are closest to the baseline scan at downsampled voxel sizes of 60 and 90 µm and the lowest mean DA values drop 44.5% from the baseline scan at 210 µm. The mean DA values are close to the baseline in rescans at 45 and 60 µm, while there is a 19.9% drop in DA when rescanned at 110 µm (Table 3.3).

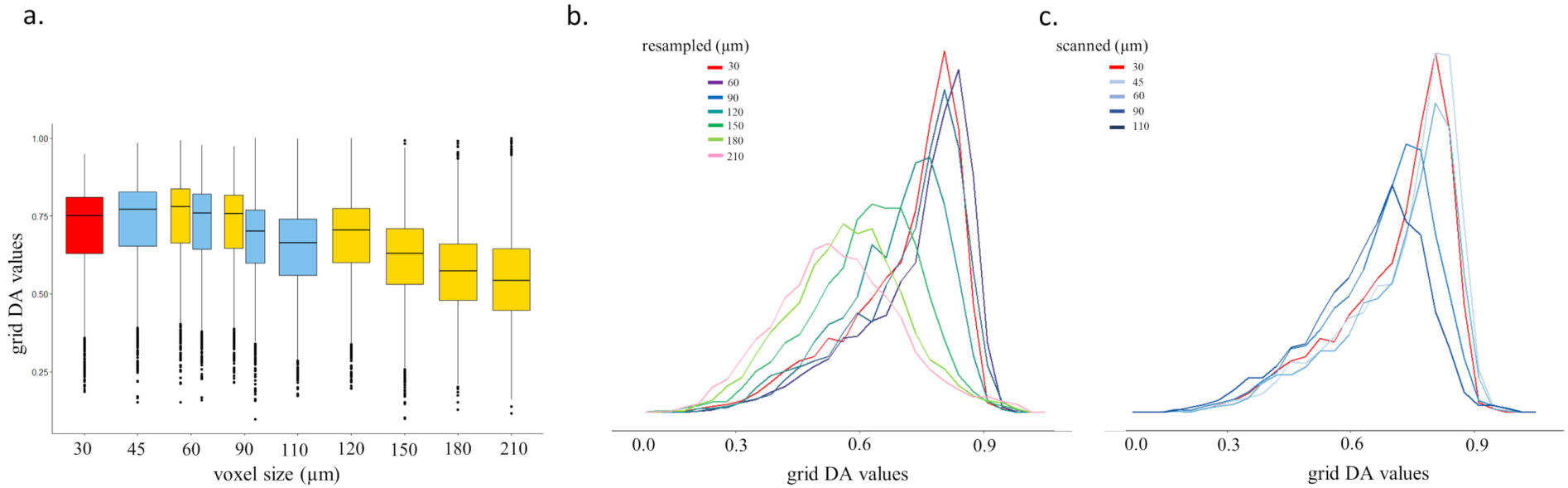

Figure 3.5: a) Boxplots of the grid DA values for each voxel size for the baseline scan (red), the downsampled data (yellow) and for the specimen scanned at the different resolution (blue); b) histogram of the grid DA01 values for each voxel size for the baseline scan (red line) and the downsampled data; c) histogram of the grid DA01 values for each voxel size for the baseline scan (red line) and for the specimen scanned at different resolution.

The Kruskal-Wallis test shows a statistically significant difference in DA within the downsampled and scanned images (Table 3.4). Additionally, the Tukey's HSD post hoc test indicates that there are significant differences in DA within all combinations of downsampled and scanned images (Table S3.6).

Figure 3.6 shows colourmaps of the DA distribution throughout the distal tibia for the baseline scan and all downsampled and rescanned volumes. The DA colourmaps are more impacted by voxel sizes compared to the BV/TV distribution maps. Compared to the baseline scan (Figure 3.6a), the general pattern of DA distribution is consistent in all downsampled images until the voxel size of 120 µm (Figure 3.6b). The general DA distribution pattern is visible even at the downsampled voxel size of 150 µm. However, in this volume the low DA (blue colour) starts to be concentrated randomly above the articular surface where high DA is found in higher resolution scans (see mid-coronal view in Figure 3.6c). This is even more apparent in the larger voxel sizes of 180 and 210 µm. The general DA distribution pattern of the baseline scan disappears completely at a voxel size of 210 µm and high DA is inconsistently concentrated throughout the distal tibia (Figure 3.6b). Rescanning at 60 µm presents a broadly similar pattern of DA on each surface and in the cross-section (Figure 3.6c). However, after rescanning at 90 and 110 µm the distribution pattern becomes less consistent. The high DA values are lost laterally above the articular surface at a rescanning voxel size of 90 µm and medially above the malleolus at a voxel size of 110 µm (see mid-coronal view in Figure 3.6c)

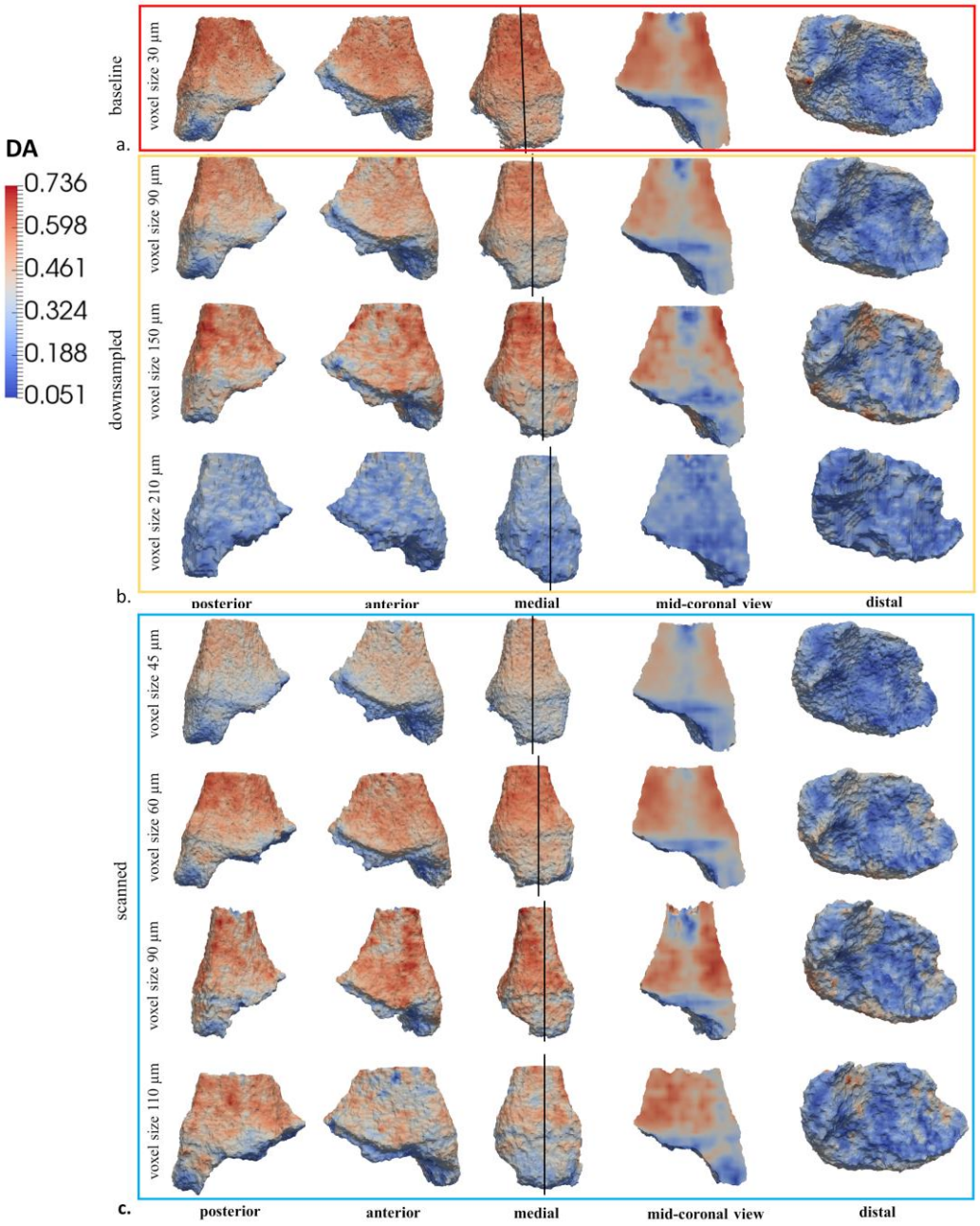

Figure 3.6: Distal tibia model of DA distribution of tested *Gorilla* individual for baseline scan (a), downsampled voxel sizes of 90, 150, and 210 µm (b), and scan voxel sizes of 45 – 110 µm (c). Vertical lines through the medial view show where the slices are positions for the cross-section mid-coronal view. Dark red represents the highest and dark blue the lowest DA values. All colourmaps were scaled to baseline scan data range.

3.4.4 Trabecular thickness, spacing and number

Distributions of Tb.Th, Tb.Sp and Tb.N values for each VOI of the background grid for the baseline scan, downsampled and rescanned volumes are presented in Figure 3.7. Voxel size changes in both rescanning and downsampling images has the strongest effect on the quantification of Tb.Th and a weaker effect on the quantification of Tb.Sp and Tb.N (Figure 3.7). The outliers represent the elements with the lowest/highest Tb.Th (Figure 3.7a), Tb.Sp

(Figure 3.7b) and Tb.N (Figure 3.7c). In both downsampled and rescanned images, median values of Tb.Th and Tb.Sp increase gradually, while median values of Tb.N decrease gradually across all voxel sizes compared to baseline scan (Figure 3.7). When scanning at different resolutions, the Tb.Sp range remains approximately the same up to a voxel size of 60 µm compared to the baseline scan (Figure 3.7b), however, the distributions overlap across all voxel sizes.

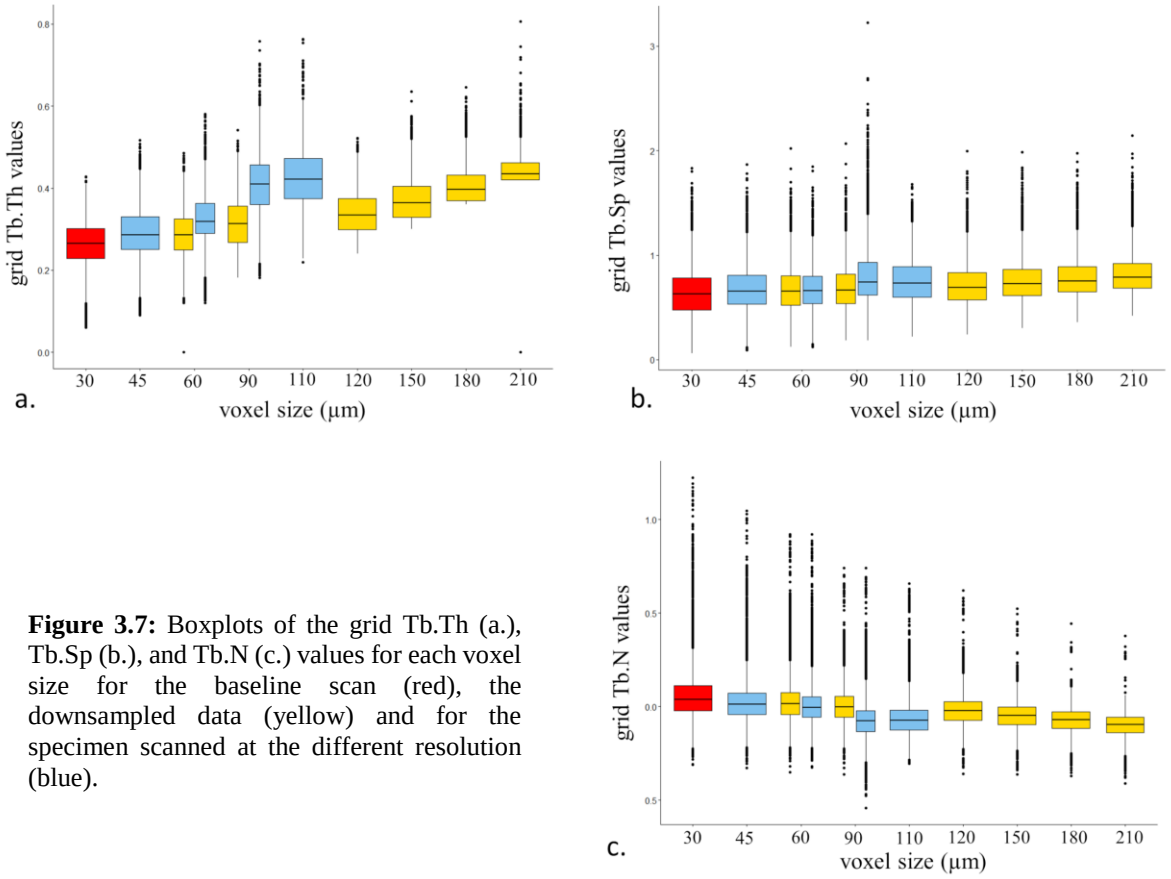

Figure 3.7: Boxplots of the grid Tb.Th (a.), Tb.Sp (b.), and Tb.N (c.) values for each voxel size for the baseline scan (red), the downsampled data (yellow) and for the specimen scanned at the different resolution (blue).

Table 3.3 shows that mean Tb.Th values gradually increase with increasing voxel size in both downsampled (reaching 64.0% at 210 µm) and rescanned (reaching 62.5% at 110 µm) images. The mean Tb.Sp values are unstable with increasing voxel size in both downsampled (reaching highest increase 194.4% at 60 µm and highest decrease 11.1% at 210 µm) and rescanned (reaching highest increase 4.1% at 90 µm and highest decrease 6.7% at 110 µm) images compared to the baseline scan (Table 33.). The mean Tb.N values gradually decrease with increasing voxel size in downsampled (reaching 24.7% at 210 µm) images compared to the baseline scan (Table 3.3). Mean Tb.N drops off 23.3% at a rescanned voxel size of 90 µm compared to the baseline scan and increases again at 110 µm (reaching 1.7%) compared to the 90 µm scan (Table 3.3).

The Kruskal-Wallis test shows a statistically significant difference in Tb.Th, Tb.Sp, and Tb.N within the downsampled and scanned images (Table 3.4). Additionally, the Tukey's HSD post hoc test indicates that there are significant differences in Tb.Th, Tb.Sp, and Tb.N within most combinations of downsampled and scanned images (Table S3.7). There are no significant differences in Tb.Sp between the downsampled 60 and 90 µm datasets or between scanned voxel sizes of 45 and 90 µm. Moreover, there is no significant difference in Tb.N between scanned voxel sizes of 60 and 110 µm (Table S3.7).

Colourmaps of the Tb.Th, Tb.Sp and Tb.N distribution are presented as supplementary material (Supplementary Figure S3.1-S3.3). Compared to the baseline scan, the general pattern of the Tb.Th distribution is consistent when downsampled to 150 µm and rescanned at 45 µm (Supplementary Figure S3.1). Tb.Th values are higher in the malleolus and under the articular surface and lower above the articular surface when downsampled to 210 µm (see the cross-section mid-coronal view in the Supplementary Figure S3.1b). Tb.Th values are lower across the entire distal tibia at rescanned voxel sizes of 90 and 110 µm (Supplementary Figure S3.1c). The general pattern of the Tb.Sp distribution is consistent for all images up to a voxel size of 60 µm (Supplementary Figure S3.2). The Tb.Sp values are lower in the malleolus and under the articular surface when rescanned at 90 µm compared to the baseline scan (Supplementary Figure S3.2c). The Tb.Sp values in the malleolus are higher at 110 µm compared to the baseline scan (see the mid-coronal view in Supplementary Figure S3.2c). The general pattern of Tb.N distribution is consistent when downsampled to 150 µm and rescanned at 110 µm (Supplementary Figure S3.3). However, in both cases, high Tb.N values above the articular surface are spread more broadly across all voxel sizes compared to the baseline scan (see the mid-coronal view in the Supplementary Figure S3.3).

3.5 Discussion

This study investigated the impact of voxel size (in downsampled and rescanned micro-CT volumes) on the quantification of trabecular bone morphology of the distal tibia of a *G. gorilla* individual. Rescanning was found to have a stronger effect on DA and Tb.Th, while BV/TV, Tb.Sp and Tb.N remained relatively constant across all tested voxel sizes. Downsampling was found to have less of an effect on trabecular parameters compared to rescanning. However, a strong impact on trabecular parameters when downsampling was found in DA and Tb.Th, while BV/TV, Tb.Sp and Tb.N were less sensitive to increasing voxel sizes.

Quantification of the total bone volume after segmentation demonstrated differences in the number of bone voxels segmented in each protocol. This bone volume changed more for rescanned voxel sizes compared to downsampled voxel sizes. However, the differences were below 5% compared to the baseline scan across all scans. When the baseline scan was downsampled to larger voxel sizes, the total segmented bone volume decreased gradually. However, the opposite pattern was found in rescanned images where the total segmented bone volume gradually increased with larger voxel sizes. Changes in total segmented bone volume within the rescanned images often represented fundamental differences that could also be observed on visual inspection of the voxel data. With the lowest scanned resolution, a more substantial difference in volume was found, and the trabecular structure captured is less comparable to that at higher scan resolutions. However, for the results of the downsampled images, where the data captured was based on the voxel set acquired at a higher resolution, there was less divergence in bone volume from the baseline scan.

Our results for Tb.Th and Tb.Sp imply that while the trabecular spacing remains relatively stable, Tb.Th increases at larger voxel sizes. Because Tb.Sp is higher than Tb.Th, it is less sensitive to scanning/downsampling at tested resolutions. This might suggest that the thickness of the trabeculae is overestimated, i.e. trabeculae are segmented as thicker, in very low-resolution scans. Another explanation could be that small trabeculae are lost during the downsampling/rescanning to larger voxels and thus the distribution of the thickness changes more rapidly than it is the case for Tb.Sp. Partial volume averaging occurs when the boundaries of small structures within an image intersect multiple pixels or voxels. This can lead to a blurring effect, where the intensity values of different tissues or structures are averaged within the pixels or voxels. This can compromise the spatial resolution of the image and make it difficult to accurately delineate the small structures or detect fine details (Chakeres, 1984; Plewes & Dean, 1981). Downsampling/rescanning to larger voxel sizes can exacerbate the effects of partial volume averaging, especially if the original image already contains small structures that are near the limit of resolution. Thus, when an image is downsampled/rescanned, the smaller structures may be spread across even fewer pixels or voxels, increasing the degree of averaging, and further blurring the image, i.e. downsampling/rescanning can amplify the problem of partial volume averaging by reducing the number of pixels or voxels available to represent small structures within an image (Chakeres, 1984; Conradi et al., 2010; Plewes & Dean, 1981). Thus, it is possible that in the end only the largest trabeculae persist, giving the impression that the average Tb.Th is as large as the maximum of the initial Tb.Th. Moreover,

this partial volume averaging could also explain how BV/TV remains constant despite trabeculae getting thicker (on average). It must be emphasized that the trabecular parameters are measured on the segmented images and thus, the changes in the segmented images are another source of potential error in the measurement of trabecular parameters. As mentioned above, MIA is a voxel-size dependent segmentation method (Dunmore et al., 2018). Although we used the same protocol for each bone segmentation, ultimately any segmentation algorithm is limited by the size of the voxels it is classifying.

Our result suggests that the BV/TV, Tb.Sp and Tb.N can be measured with reasonable precision up to 210 µm, as can DA and Tb.Th up to 90 µm, when downsampling. In contrast, the mean of BV/TV, DA, Tb.Sp and Tb.N increases from 90 µm when rescanning. We found Tb.Th to be the most sensitive to voxel size changes, where the mean increased for scans above 45 µm. This is visible especially when looking at the colourmaps of the distribution patterns of all studied parameters. The discrepancies might be due to the inconsistencies in thed definition of the *InnerMask* as medtool uses morphological filters this is influenced by resolution due to kernel size. However, the morphological filter kernel sizes (in voxels) of the fill algorithm were adjusted for each resolution, so definition of the *OuterMask* and *InnerMask* was kept as consistent as possible.

Previous studies of the impact of CT and micro-CT resolution on quantification of trabecular structure observed dependence of trabecular bone parameters on voxel size, consistent with our results. Isaksson et al. (2011) found BV/TV to be less dependent on the voxel sizes compared to DA, Tb.Sp and Tb.N which were more sensitive to changes in voxel sizes. Similarly, Kim et al. (2004) found mean Tb.Th. and Tb.Sp to increase and Tb.N to decrease with larger voxel sizes which is again consistent with our results. However, they also found mean BV/TV to increase significantly with larger voxel sizes (Kim et al., 2004), which is not consistent with our results. Nevertheless, as supported by our study, Christiansen (2016) found mean BV/TV to be rather consistent within the voxel sizes and Tb.Th to be strongly affected by changes in voxel size. Overall, other studies that tested all or some of other trabecular parameters such as Tb.Th, Tb.Sp and Tb.N have reported higher dependency on voxel size in all these parameters especially compared to BV/TV, and also compared to DA if included in the study (Isaksson et sl., 2011; Kim et al., 2004; Kothari et al., 1998; Majumdar et al., 1996; Maquer et al., 2015; Müller et al., 1996; Peyrin et al., 1998; Sode et al., 2008; Stauber et al., 2006; Tabor, 2004).

This study is the first to show the effect of micro-CT voxel size using a whole-bone mapping approach to analyse trabecular bone morphology. Although this study only included a single

specimen, and was not extended to other anatomical sites, we recommend using high-resolution if possible. To speed up trabecular analysis, downsampled images rather than low-resolution scans could be used for certain trabecular parameters. This is especially important if DA and Tb.Th are quantified. Our results suggest that trabecular structure may be more precisely measured by quantifying most trabecular parameters up to voxel size of 90 µm (excluding trabecular thickness). Moreover, BV/TV, Tb.Sp and Tb.N are more robust and can be quantified at even larger voxel sizes with a greater degree of certainty than the other parameters, which are more sensitive to voxel size changes.

Though it was beyond the scope of this study, there are additional factors, such as segmentation method and/or the use of multiple micro-CT scanners for sample acquisition, that have the potential to impact quantification of trabecular architecture and may warrant future investigation. It is also possible that the effect of voxel size on trabecular bone is different for regions with higher or lower trabecular bone volume fraction. Thus, including trabecular bone from taxa that differ in mean BV/TV, as well as BV/TV range, is an important future direction. For example, large primates, such as *Gorilla*, tend to have robust trabecular bone network to support their larger body mass. In contrast, small primates generally exhibit relatively less trabecular bone structures compared to larger primates as their smaller body size results in lower mechanical loads on their bones, reducing the need for extensive trabecular bone networks (Saparin et al., 2011; Ryan & Shaw, 2013). Based on our results, it might be expected that relatively less trabecular bone structure would be more sensitive to the resolution changes. This could potentially lead to less sensitivity to the resolution changes in BV/TV and potentially other parameters as micro-CT scanning is generally more effective at detecting more gracile structures compared to less gracile structures (e.g., Pyka et al., 2014; Vasarhelyi et al., 2020). Overall, this diversity in sample selection would help address potential sensitivity to resolution changes, particularly in smaller/less more gracile structures, which may lead to a reduction in trabecular network visibility and subsequently affect measured trabecular parameters.

3.6 Supplementary material

Table S3.1: Shapiro-Wilk's test of normality and Levene's test for equality of variances for BV/TV.

Method	Resolution (µm)	W	p-value	F	df	p-value
baseline scan	30	0.99	<0.01			
downsampled	60	0.99	<0.01			
downsampled	90	0.99	<0.01			
downsampled	120	0.99	<0.01	1512	6	**0.00**
downsampled	150	0.99	<0.01			
downsampled	180	0.99	<0.01			
downsampled	210	0.98	<0.01			
scanned	45	0.99	<0.01			
scanned	60	0.99	<0.01	3582	4	**0.00**
scanned	90	0.98	<0.01			
scanned	110	0.99	<0.01			

Table S3.2: Shapiro-Wilk's test of normality and Levene's test for equality of variances for DA.

Method	Resolution (µm)	W	p-value	F	df	p-value
baseline scan	30	0.9	<0.01			
downsampled	60	0.89	<0.01			
downsampled	90	0.92	<0.01			
downsampled	120	0.95	<0.01	7138	6	**0.00**
downsampled	150	0.98	<0.01			
downsampled	180	0.99	0.01			
downsampled	210	0.99	<0.01			
scanned	45	0.89	<0.01			
scanned	60	0.91	<0.01	907	4	**0.00**
scanned	90	0.95	<0.01			
scanned	110	0.97	<0.01			

Table S3.3: Shapiro-Wilk's test of normality and Levene's test for equality of variances for Tb.Th.

Method	Resolution (µm)	W	p-value	F	df	p-value
baseline scan	30	0.94	<0.01			
downsampled	60	0.98	<0.01			
downsampled	90	0.99	<0.01			
downsampled	120	0.98	<0.01	256	6	**0.00**
downsampled	150	0.94	<0.01			
downsampled	180	0.88	<0.01			
downsampled	210	0.77	<0.01			
scanned	45	0.95	<0.01			
scanned	60	0.97	<0.01	99	4	**0.00**
scanned	90	0.96	<0.01			
scanned	110	0.98	<0.01			

Table S3.4: Shapiro-Wilk's test of normality and Levene's test for equality of variances for Tb.Sp.

Method	Resolution (µm)	W	p-value	F	df	p-value
baseline scan	30	0.99	<0.01			
downsampled	60	0.98	<0.01			
downsampled	90	0.98	<0.01			
downsampled	120	0.97	<0.01	30	6	**0.00**
downsampled	150	0.96	<0.01			
downsampled	180	0.95	<0.01			
downsampled	210	0.95	<0.01			
scanned	45	0.98	<0.01			
scanned	60	0.92	<0.01	52	4	**0.00**
scanned	90	0.98	<0.01			
scanned	110	0.99	<0.01			

Table S3.5: Shapiro-Wilk's test of normality and Levene's test for equality of variances for Tb.N.

Method	Resolution (µm)	W	p-value	F	df	p-value
baseline scan	30	0.36	<0.01			
downsampled	60	0.41	<0.01			
downsampled	90	0.47	<0.01			
downsampled	120	0.49	<0.01	126	6	**0.00**
downsampled	150	0.54	<0.01			
downsampled	180	0.56	<0.01			
downsampled	210	0.57	<0.01			
scanned	45	0.38	<0.01			
scanned	60	0.45	<0.01	37	4	**0.00**
scanned	90	0.35	<0.01			
scanned	110	0.46	<0.01			

Table S3.6: Dunn's test for BV/TV, and DA grid values between all voxel sizes.

		BV/TV					DA				
resolution (µm)	technique	n1	n2	diff	p adj	*r**	n1	n2	diff	p adj	*r**
30 - 60	downsampled	155823	198255	-14.7853	**<0.001**	0.074	155823	198255	60.407	**0.000**	0.264
30 - 90		155823	150599	-10.203	**<0.001**	0.057	155823	150599	24.448	**0.000**	0.116
30 - 120		155823	144257	-28.7889	**<0.001**	0.138	155823	144257	-91.934	**0.000**	0.383
30 - 150		155823	138161	-41.8204	**<0.001**	0.196	155823	138161	-229.217	**0.000**	1.034
30 - 180		155823	130992	-59.3747	**<0.001**	0.271	155823	130992	-343.550	**0.000**	1.650
30 - 210		155823	121202	-87.3542	**<0.001**	0.395	155823	121202	-400.722	**0.000**	2.034
60 - 90		198255	150599	3.857741	**<0.001**	0.017	198255	150599	-35.656	**0.000**	0.151
60 - 120		198255	144257	-15.9308	**<0.001**	0.065	198255	144257	-150.432	**0.000**	0.661
60 - 150		198255	138161	-29.8139	**<0.001**	0.124	198255	138161	-285.975	**0.000**	1.324
60 - 180		198255	130992	-48.4502	**<0.001**	0.200	198255	130992	-398.650	**0.000**	1.951
60 - 210		198255	121202	-78.0276	**<0.001**	0.331	198255	121202	-454.298	**0.000**	2.229
90 - 120		150599	144257	-18.5441	**<0.001**	0.082	150599	144257	-115.157	**0.000**	0.509
90 - 150		150599	138161	-31.5868	**<0.001**	0.142	150599	138161	-251.085	**0.000**	1.173
90 - 180		150599	130992	-49.1514	**<0.001**	0.218	150599	130992	-364.243	**0.000**	1.804
90 - 210		150599	121202	-77.1444	**<0.001**	0.351	150599	121202	-420.609	**0.000**	2.196
120 - 150		144257	138161	-13.111	**<0.001**	0.061	144257	138161	-135.784	**0.000**	0.678
120 - 180		144257	130992	-30.7561	**<0.001**	0.136	144257	130992	-249.416	**0.000**	1.330
120 - 210		144257	121202	-58.8662	**<0.001**	0.271	144257	121202	-307.668	**0.000**	1.744
150 - 180		138161	130992	-17.6403	**<0.001**	0.077	138161	130992	-114.297	**0.000**	0.663
150 - 210		138161	121202	-45.7416	**<0.001**	0.212	138161	121202	-174.739	**0.000**	1.099
180 - 210		130992	121202	-28.0989	**<0.001**	0.140	130992	121202	-61.9528	**0.000**	0.453
30 - 45	scanned	155823	148428	-0.469	**<0.001**	0.018	155823	148428	51.557	**0.000**	0.125
30 - 60		155823	141014	57.520	**<0.001**	0.214	155823	141014	25.514	**0.000**	0.056
30 - 90		155823	144465	46.402	**<0.001**	0.075	155823	144465	-179.300	**0.000**	0.493
30 - 110		155823	123962	42.902	**<0.001**	0.138	155823	123962	-239.464	**0.000**	0.746
45 - 60		148428	141014	57.308	**<0.001**	0.238	148428	141014	-19.508	**0.000**	0.067
45 - 90		148428	144465	46.315	**<0.001**	0.093	148428	144465	-179.329	**0.000**	0.607

45 - 110	148428	123962	42.877	**<0.001**	0.159	148428	123962	-229.238	**0.000**	0.852
60 - 90	141014	144465	-11.203	**<0.001**	0.113	141014	144465	-157.669	**0.000**	0.535
60 - 110	141014	123962	-12.363	**<0.001**	0.067	141014	123962	-207.911	**0.000**	0.779
90 - 110	144465	123962	-1.601	**<0.001**	0.050	144465	123962	-56.630	**0.000**	0.258

*Effect size was calculated to quantify the magnitude of differences between the compared groups. Size effects were considered as small if r ≤ 0.1 / between 0.1 to 0.3, medium if r ≤ 0.3 / between 0.3 to 0.5, and large if r > 0.3 / between =0.5 to 1.0 (Cohen, 1988). A large effect size indicates practical significance while a small effect size indicates limited practical applications.

Table S3.7: Dunn's test for Tb.Th, Tb.Sp and Tb.N grid values between all voxel sizes.

		Tb.Th					Tb.Sp					Tb.N				
resolution (µm)	technique	n1	n2	diff	p adj	*r**	n1	n2	diff	p adj	*r**	n1	n2	diff	p adj	*r**
30 - 60		155823	198255	11.040	**0.000**	0.395	155823	198255	6.118	**0.000**	0.155	155823	198255	-8.827	**0.000**	0.161
30 - 90		155823	150599	25.514	**0.000**	0.814	155823	150599	8.542	**0.000**	0.213	155823	150599	-15.904	**0.000**	0.244
30 - 120		155823	144257	39.234	**0.000**	1.298	155823	144257	14.460	**0.000**	0.335	155823	144257	-25.354	**0.000**	0.328
30 - 150		155823	138161	58.407	**0.000**	1.854	155823	138161	21.438	**0.000**	0.487	155823	138161	-37.802	**0.000**	0.420
30 - 180		155823	130992	79.416	**0.000**	2.587	155823	130992	27.837	**0.000**	0.616	155823	130992	-49.691	**0.000**	0.482
30 - 210		155823	121202	101.528	**0.000**	3.497	155823	121202	35.327	**0.000**	0.763	155823	121202	-62.395	**0.000**	0.533
60 - 90		198255	150599	14.409	**0.000**	0.439	198255	150599	2.406	0.091	0.059	198255	150599	-7.043	**<0.001**	0.106
60 - 120		198255	144257	27.977	**0.000**	0.912	198255	144257	8.257	**0.000**	0.181	198255	144257	-16.392	**0.000**	0.228
60 - 150		198255	138161	47.167	**0.000**	1.488	198255	138161	15.284	**0.000**	0.335	198255	138161	-28.900	**0.000**	0.375
60 - 180	downsampled	198255	130992	67.991	**0.000**	2.300	198255	130992	21.616	**0.000**	0.466	198255	130992	-40.688	**0.000**	0.477
60 - 210		198255	121202	90.000	**0.000**	3.169	198255	121202	29.080	**0.000**	0.617	198255	121202	-53.347	**0.000**	0.561
90 - 120		150599	144257	13.452	**0.000**	0.428	150599	144257	5.843	**<0.001**	0.121	150599	144257	-9.307	**<0.001**	0.139
90 - 150		150599	138161	32.773	**0.000**	0.991	150599	138161	12.907	**0.000**	0.275	150599	138161	-21.910	**0.000**	0.320
90 - 180		150599	130992	53.484	**0.000**	1.678	150599	130992	19.232	**0.000**	0.406	150599	130992	-33.665	**0.000**	0.453
90 - 210		150599	121202	75.488	**0.000**	2.556	150599	121202	26.709	**0.000**	0.557	150599	121202	-46.339	**0.000**	0.563
120 - 150		144257	138161	19.597	**0.000**	0.617	144257	138161	7.186	**0.000**	0.156	144257	138161	-12.806	**<0.001**	0.199
120 - 180		144257	130992	40.373	**0.000**	1.356	144257	130992	13.518	**0.000**	0.288	144257	130992	-24.591	**0.000**	0.357
120 - 210		144257	121202	62.552	**0.000**	2.337	144257	121202	21.052	**0.000**	0.443	144257	121202	-37.364	**0.000**	0.492
150 - 180		138161	130992	20.432	**0.000**	0.686	138161	130992	6.205	**<0.001**	0.132	138161	130992	-11.562	**0.005**	0.181

150 - 210		138161	121202	42.404	**0.000**	1.620	138161	121202	13.651	**0.000**	0.288	138161	121202	-24.185	**0.000**	0.348
180 - 210		130992	121202	22.141	**0.000**	0.996	130992	121202	7.501	**0.000**	0.157	130992	121202	-12.710	**0.034**	0.181
30 - 45	scanned	155823	148428	31.759	**0.000**	0.917	155823	148428	7.018	**0.000**	0.167	155823	148428	-15.864	**0.000**	0.200
30 - 60		155823	141014	66.738	**0.000**	1.820	155823	141014	24.864	**0.000**	0.600	155823	141014	-46.112	**0.000**	0.367
30 - 90		155823	144465	13.377	**0.000**	0.412	155823	144465	6.441	**0.000**	0.159	155823	144465	-9.781	**0.000**	0.109
30 - 110		155823	123962	69.799	**0.000**	2.030	155823	123962	20.381	**0.000**	0.449	155823	123962	-43.010	**0.000**	0.358
45 - 60		148428	141014	33.936	**0.000**	0.981	148428	141014	17.466	**0.000**	0.440	148428	141014	-29.548	**0.000**	0.226
45 - 90		148428	144465	-18.255	**0.000**	0.502	148428	144465	-0.605	0.999	0.001	148428	144465	6.071	**0.001**	0.093
45 - 110		148428	123962	37.854	**0.000**	1.180	148428	123962	13.234	**<0.001**	0.303	148428	123962	-26.896	**0.000**	0.213
60 - 90		141014	144465	-52.641	**0.000**	1.440	141014	144465	-18.173	**0.000**	0.426	141014	144465	35.859	**0.000**	0.284
60 - 110		141014	123962	4.881	**0.000**	0.171	141014	123962	-3.875	**0.000**	0.187	141014	123962	1.992	0.972	0.023
90 - 110		144465	123962	56.071	**0.000**	1.640	144465	123962	13.900	**0.000**	0.289	144465	123962	-33.042	**0.000**	0.273

*Effect size was calculated to quantify the magnitude of differences between the compared groups. Size effects were considered as small if $r \leq 0.1$ / between 0.1 to 0.3, medium if $r \leq 0.3$ / between 0.3 to 0.5, and large if $r > 0.3$ / between =0.5 to 1.0 (Cohen, 1988). A large effect size indicates practical significance while a small effect size indicates limited practical applications.

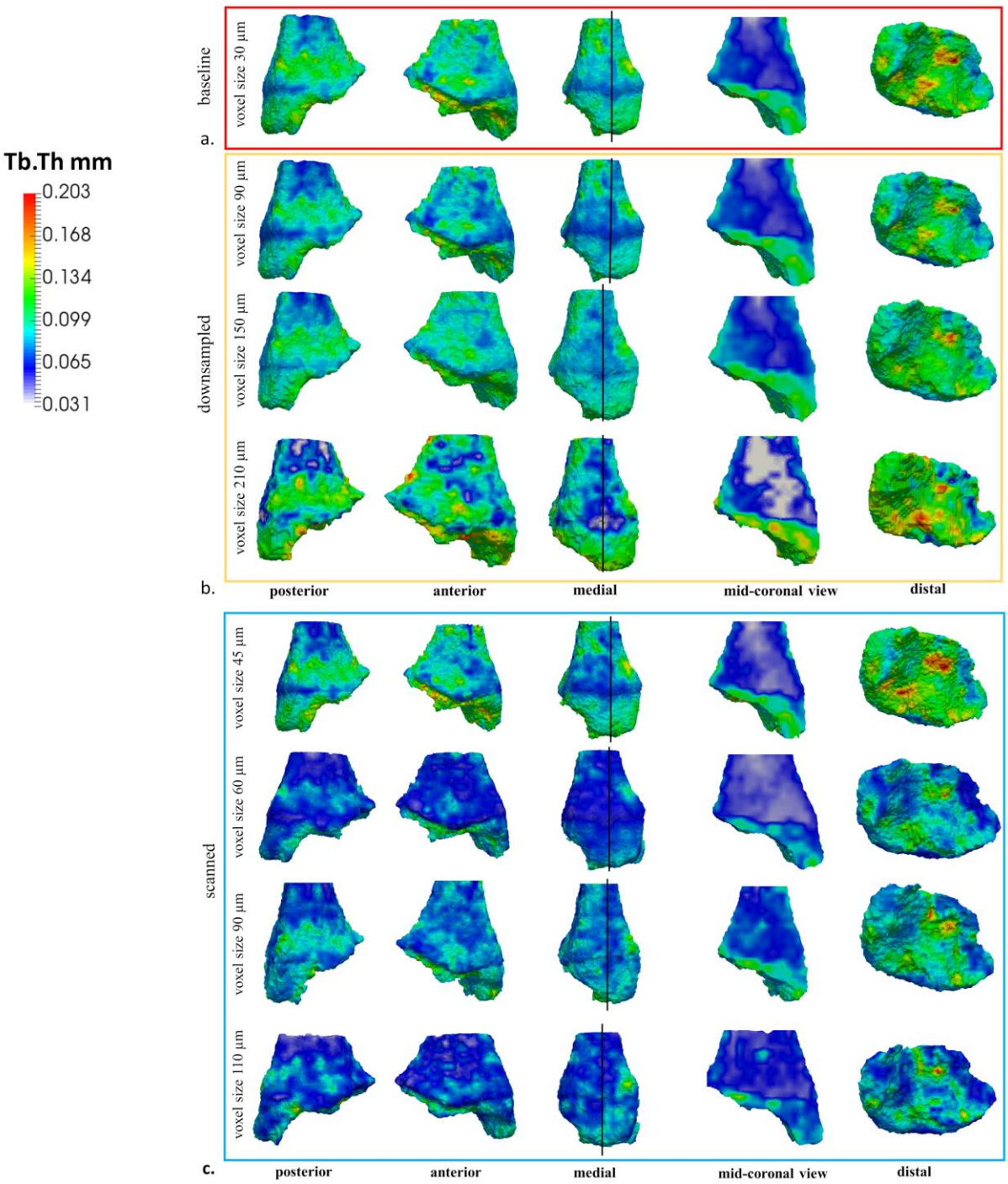

Figure S3.1: Distal tibia model of Tb.Th mm distribution of tested *Gorilla* individual for baseline scan (a), downsampled voxel sizes of 90, 150, and 210 µm (b), and scan voxel sizes of 45 – 110 µm (c). Vertical lines through the medial view show where the slices are positions for the cross-section mid-coronal view. Dark red represents the highest and dark blue the lowest Tb.Th values. All colourmaps were scaled to baseline scan data range.

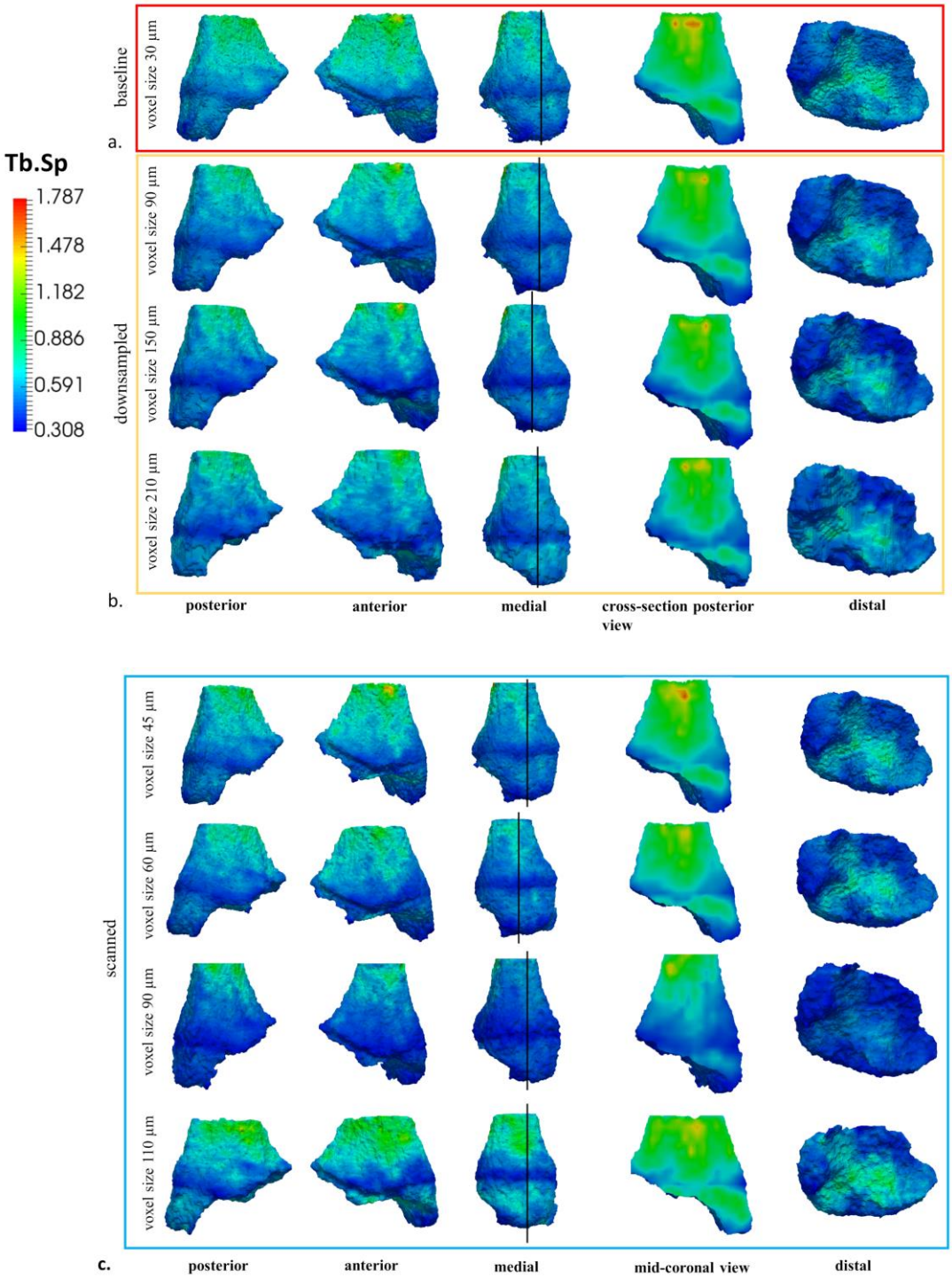

Figure S3.2: Distal tibia model of Tb.Sp distribution of tested *Gorilla* individual for baseline scan (a), downsampled voxel sizes of 90, 150, and 210 µm (b), and scan voxel sizes of 45 – 110 µm (c). Vertical lines through the medial view show where the slices are positions for the cross-section mid-coronal view. Dark red represents the highest and dark blue the lowest Tb. Sp values. All colourmaps were scaled to baseline scan data range.

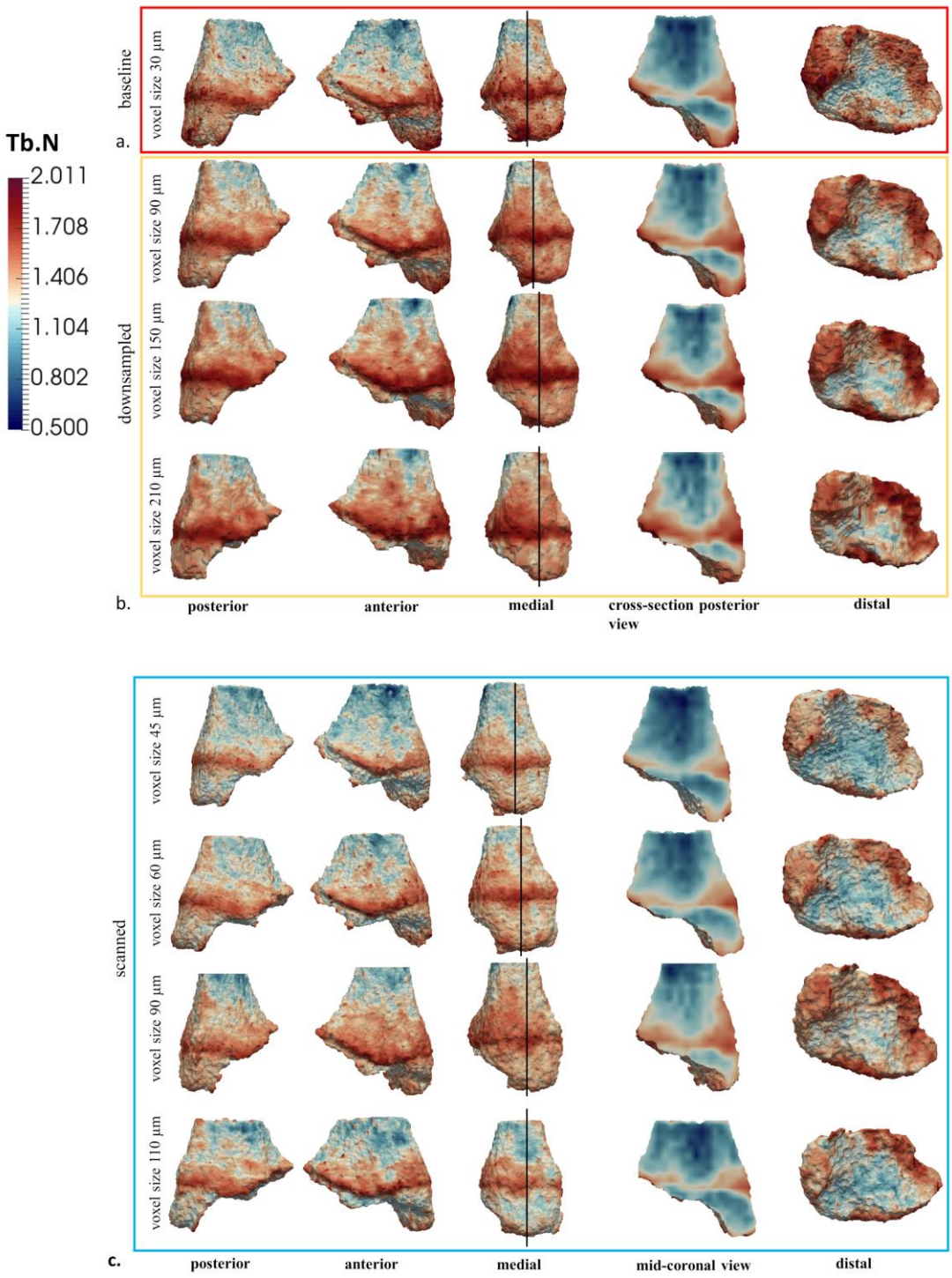

Figure S3.3: Distal tibia model of Tb.N distribution of tested *Gorilla* individual for baseline scan (a), downsampled voxel sizes of 90, 150, and 210 µm (b), and scan voxel sizes of 45 – 110 µm (c). Vertical lines through the medial view show where the slices are positions for the cross-section mid-coronal view. Dark red represents the highest and dark blue the lowest Tb.N values. All colourmaps were scaled to baseline scan data range.

Group	Resolution
A	30
B	60
C	90
D	120
E	150
F	180
G	210

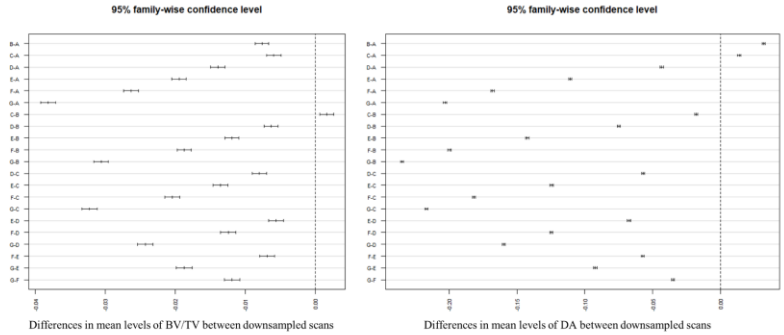

Differences in mean levels of BV/TV between downsampled scans

Differences in mean levels of DA between downsampled scans

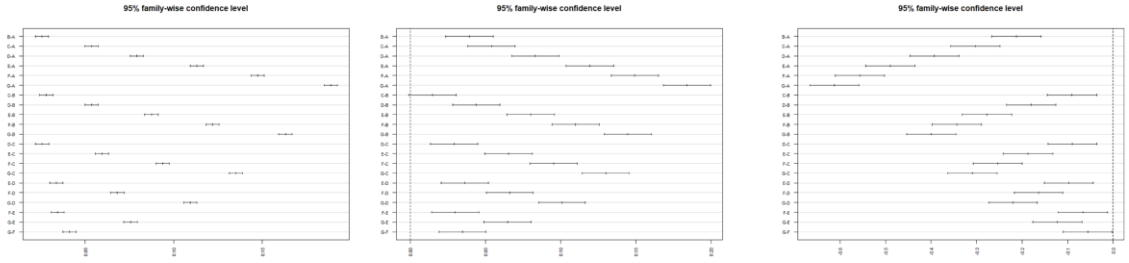

Differences in mean levels of Tb.Th between downsampled scans

Differences in mean levels of Tb.Sp between downsampled scans

Differences in mean levels of Tb.N between downsampled scans

Group	Resolution
A	30
B	45
C	60
D	90
E	110

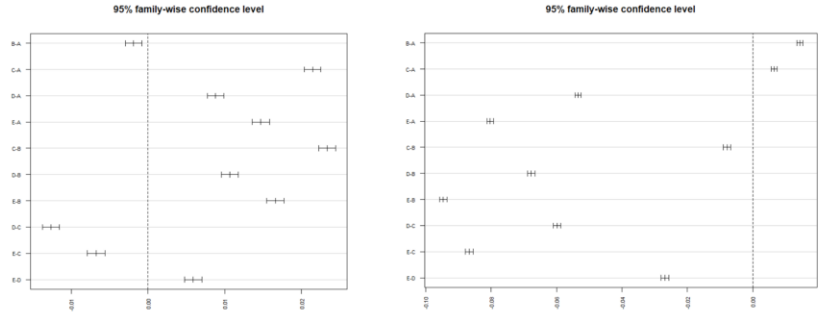

Differences in mean levels of BV/TV between scanned images

Differences in mean levels of DA between scanned images

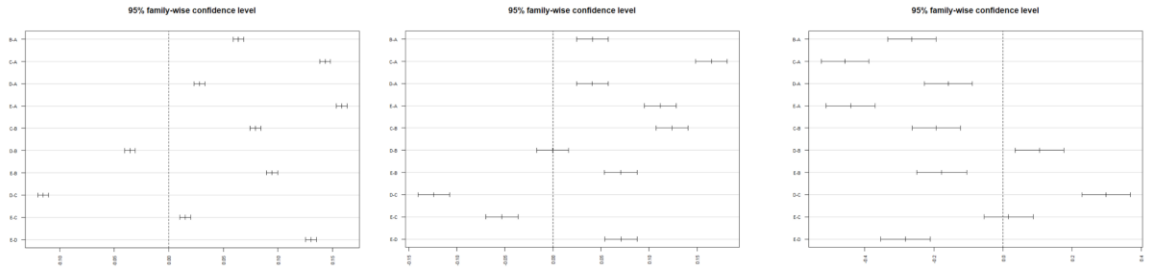

Differences in mean levels of Tb.Th between scanned images

Differences in mean levels of Tb.Sp between scanned images

Differences in mean levels of Tb.N between scanned images

Figure S3.4: Differences in mean levels of each tested parameter for all downsampled and scanned voxel sizes.

4 TRABECULAR ARCHITECTURE OF THE DISTAL FEMUR IN EXTANT HOMINIDS

Published article: Lukova, A., Dunmore, C. J., Bachmann, S., Synek, A., Pahr, D. H., Kivell, T. L., & Skinner, M. M. (2024). Trabecular architecture of the distal femur in extant hominids. *Journal of Anatomy*.

4.1 Abstract

Extant great apes are characterized by a wide range of locomotor, postural and manipulative behaviours that each require the limbs to be used in different ways. In addition to external bone morphology, comparative investigation of trabecular bone, which (re-)models to reflect loads incurred during life, can provide novel insights into bone functional adaptation. Here, we use canonical holistic morphometric analysis (cHMA) to analyze the trabecular morphology in the distal femoral epiphysis of *Homo sapiens* (n=26), *Gorilla gorilla* (n=14), *Pan troglodytes* (n=15), and *Pongo* spp. (n=9). We test two predictions: (1) that differing locomotor behaviours will be reflected in differing trabecular architecture of the distal femur across *Homo*, *Pan*, *Gorilla*, and *Pongo*; (2) that trabecular architecture will significantly differ between male and female *Gorilla* due to their different levels of arboreality but not between male and female *Pan* or *Homo* based on previous studies of locomotor behaviours. Results indicate that trabecular architecture differs among extant great apes based on their locomotor repertoires. The relative bone volume and degree of anisotropy patterns found reflect habitual use of extended knee postures during bipedalism in *Homo*, and habitual use of flexed knee posture during terrestrial and arboreal locomotion in *Pan* and *Gorilla*. Trabecular architecture in *Pongo* is consistent with a highly mobile knee joint that may vary in posture from extension to full flexion. Within *Gorilla*, trabecular architecture suggests a different loading of knee in extension/flexion between females and males, but no sex differences were found in *Pan* or *Homo*, supporting our predictions. Inter- and intra-specific variation in trabecular architecture of distal femur provides a comparative context to interpret knee postures and, in turn, locomotor behaviours in fossil hominins.

4.2 Introduction

Understanding how variation in skeletal morphology, both external shape and internal bone structure, may reflect differences in loading during habitual behaviours in extant apes is critical to reconstructing behaviour in fossil hominoid taxa. Extant apes are characterized by a wide range of locomotor, postural and manipulative behaviours linked to their respective ecological niches, subsistence strategies and social organization, which require each species to use their limbs in different ways. Though African apes also engage in arboreal suspension and climbing, they spend the majority of their time terrestrially knuckle-walking, in which the knee is flexed to varying degrees (Ankel-Simons, 2010; Georgiou et al., 2018; Isler, 2005; Lee et al., 2012). Orangutans engage in slow-moving, torso-orthograde locomotion, often supported by multiple limbs (Cant, 1987; Thorpe and Crompton, 2005), in which load is distributed across both upper and lower limb joints. Humans are the only living obligate bipedal ape and are unique among primates in that both the hips and knees remain relatively extended during the gait cycle. In this study we build on previous research (Georgiou et al., 2018; Sukhdeo et al., 2020; Sylvester and Terhune, 2017) to examine the link between habitual joint postures of the knee and trabecular architecture in the distal femur of extant great apes, including humans.

Although the structure of trabecular bone is also influenced by several factors, including genetics, hormones, diet, sex, age, body size, and physical activity (Turner et al., 2000; Loewen et al., 2001; Paternoster et al., 2013), (re-)modeling is at its peak during ontogeny and persists (although at a reduced rate) throughout adulthood (Barak, 2019; Glatt et al., 2007; Halloran et al., 2002; Saers, Ryan and Stock, 2020; Seeman, 2003; Wallace et al., 2013). It has been previously demonstrated that joint load is transferred from the subchondral bone of the epiphyses toward the diaphyseal cortical bone (Barak et al., 2008). Patterns between cortical bone features and different types of locomotion among great apes have been previously found. For example, Carlson (2005) found that African apes that engage more frequently in arboreal locomotion have more circular femoral cross-sections compared with those that engage more in terrestrial locomotion. Ruff (2002) also found a relationship between locomotor activities in great apes and cross-sectional properties of forelimb and hindlimb bones. Asian apes, show relatively stronger forelimb shafts than hindlimb shafts compared to African apes, and within African apes, more arboreal *Pan* shows relatively higher ratios of forelimb to hindlimb strength compared to more terrestrial *Gorilla* (Ruff, 2002). Moreover, cross-sectional differences between humans and non-human apes reflecting differences in locomotor loading have been

found in the femoral neck (Lovejoy, 1988; Ohman et al. 1997; Rafferty, 1998) and in the distal tibia and talus (Tsegai et al., 2017).

Trabecular bone models in response to loading through either an increase or decrease of bone tissue and/or reconfiguration of the shape and structure of trabecular struts in order to reduce strain and prevent fracture (Barak et al., 2011; Biewener et al., 1996; Harrison et al., 2011; Mittra et al., 2005; Pontzer et al., 2006; Rodan, 1997; Ruff et al., 2006; Sinclair et al., 2013). Thus, it is expected that trabecular bone structure within the epiphysis of the distal femur will reflect variation in loaded knee joint postures among extant great apes. The ratio of bone volume to total volume (BV/TV) is the proportion of trabecular bone of the total volume in a given region. In places where stress is lower, there is a gradual decline in the amount of trabecular bone, resulting in a weaker structure; conversely, in places where stress is higher, there is a gradual increase in trabecular bone deposition to help resist loads (Pontzer et al., 2006; Barak, 2011; Sinclair et al., 2013). Degree of anisotropy (DA) describes the trabecular alignment in 3D space, with high DA indicating greater alignment (trabeculae tend to be oriented in specific direction) or an anisotropic structure, and low DA (values closer to 0) reflecting less alignment (trabeculae tend to be more randomly oriented) and an isotropic structure. BV/TV and DA can together explain up to 97% of the variation in elastic properties of trabecular bone (Homminga et al., 2003; Maquer et al., 2015; Van Rietbergen et al., 1998; Zysset et al., 2003). BV/TV and DA have been shown to reflect the presumed predominant direction and relative magnitude that joints are loaded in, during different locomotor and manipulative behaviours; in previous landmark studies (Dunmore et al., 2019; 2020; Sylvester & Terhune, 2017), throughout an entire bone or epiphysis (Kuo at al., 2022; Ryan at al., 2019; Saers et al., 2022; Skinner et al., 2013; Stephens et al., 2016; Tsegai et al., 2018), or by using holistic morphometric approaches (Bachmann et al., 2022; DeMars et al., 2022; Dunmore et al, 2023). Recent methodological advancements allow comprehensive statistical analysis of trabecular bone structure within and between species, particularly those that vary in external bone shape (Bachmann et al., 2022; Gross et al., 2014). Here we investigate the trabecular structure in the entire distal femoral epiphysis of extant humans and other great apes to explore how potential variation might reflect differences in knee joint loading during locomotor behaviours.

Several previous studies have examined trabecular structure in the lower limbs of primates, including the pelvis/innominate (Dalstra et al., 1993; Eriksen et al., 1984; Volpato et al., 2008; Zaharie & Phillips, 2018), proximal femur (Cazenave et al., 2019; Coelho et al., 2009; Demes et al., 2000; Georgiou et al., 2019; Georgiou et al., 2020; Ruff et al., 2013; Ryan & Ketcham,

2002; Ryan & Walker, 2010; Volpato et al., 2008), proximal tibia (Kamibayashi et al., 1995; Mazurier et al., 2010; Novitskaya et al., 2014; Saers et al., 2016; Sugiyama et al., 2012; Thomsen et al., 2005) as well as the ankle and foot (DeSilva, 2009; DeSilva & Devlin, 2012; Su et al., 2013; Tsegai et al., 2017). However, only two previous studies have specifically examined trabecular bone structure in the hominoid knee joint. Sylvester & Terhune (2017) describe a new geometric morphometric approach to analyze subchondral trabeculae of human distal femur. They found sex differences in subchondral trabecular spacing in the human knee, with males having more evenly spaced trabeculae compared to females. This study provided important insight into bone loading that might be overlooked with a centrally placed volume-of-interest methods, particularly in joints where trabecular structure is not homogenously distributed across epiphyses (Sylvester & Terhune, 2017). Georgiou et al. (2018) analyzed trabecular structure of distal femoral epiphysis of extant great apes and found that humans have higher BV/TV and DA on the posteroinferior margin of the condyles compared to non-human apes. Additionally, they showed that *Pan* and *Pongo* have higher BV/TV values in the posterior region of the condyles compared to other hominoids. This study revealed some functional signals in distal femur linked to locomotor behaviour of great apes, but they also found a large degree of overlap across some taxa. Their statistical comparisons between taxa were limited to *a priori* defined quadrants of each condyle, so trabecular patterns within each quadrant could only be analyzed qualitatively (Georgiou et al., 2018).

We build upon these previous studies with an expanded sample and the canonical holistic morphometric analysis (cHMA) method to statistically analyze trabecular patterns of the distal femur in extant apes, free of *a priori* subsampling. cHMA addresses the potential bias caused by interspecific differences in shape by computing canonical models representing the mean size, position, and morphology from a multispecies sample of individual bones. Moreover, cHMA treats each mesh cell as homologous when computing a canonical model and so geometric homology is achieved. Without geometric homology, quadrants are an arbitrary unit of analysis and the functional signal might be lost when trabecular concentration is divided. cHMA allows us to test whether the distribution of bone parameters differ statistically between (as well as within) different species. By using cHMA, we are able to build taxon-specific mean models (with standard deviations) and conduct multivariate comparisons with high statistical power as all homologous finite elements of each studied trabecular parameter could be compared across every individual in the sample (see more details below) (Bachmann et al., 2022).

4.3 External knee morphology and predicted knee postures during locomotion

Extant hominids exhibit anatomical variation of the knee joint, particularly regarding the relative size and shape of the femoral condyles, the size and shape of the patella, as well as the articulation of the femoral condyles and the tibial plateau at various angles of knee flexion. The knee joint experiences load from substrate reaction forces, but also from the action of muscles, tendons and ligaments during various locomotor activities. Additionally, soft tissue morphology of the knee joint in extant non-human great apes (hereafter, just 'great apes') differs in the degree to which it provides stability and mobility at different joint angles (Barak et al., 2011; Currey, 2003; 2012; Demes, 2007; Pearson & Lieberman, 2004; Rubin et al., 2002; Ruff et al., 2006; Shaw & Ryan, 2012). In comparison, the human knee joint has several bony and soft-tissue features that stabilize the knee especially in a fully extended posture (Desilva et al., 2018; Haile-Selassie et al., 2012; Harcourt-Smith et al., 2015; Harcourt-Smith, 2016; Lovejoy et al., 2009; Sylvester & Organ, 2010; Sylvester, 2013; Sylvester et al., 2011). These differences in hard- and soft-tissue morphology, discussed in more detail below, will influence load distribution across the femoral condyles and the tibial plateau, which in turn should influence trabecular (re-)modeling across hominids.

4.3.1 Shape of the distal femur, proximal tibia and associated soft tissue structures

In humans both condyles of the distal femur are approximately the same size, but in other great apes the medial condyle is larger than the lateral condyle (Sylvester, 2013; Sylvester & Pfisterer, 2012; Tardieu, 1999). The distal articular surface is square in humans (i.e., with relatively equal anteroposterior and mediolateral dimensions) and is more symmetrical around the parasagittal plane passing through the middle of trochlea than it is the great ape femur (Aiello & Dean, 1990) (Figure 4.1g). Both condyles are elliptical when viewed laterally in humans, which projects the patella anteriorly, thereby increasing the lever arm of quadriceps femoris, compared to great apes. Also, the lateral femoral condyle is flat in its sagittal plane (Figure 4.1g), which increases the contact area between the lateral femoral condyle and lateral tibial plateau when the knee is extended (Lovejoy, 2007; Tardieu, 1999). The more convex lateral condyle in great apes (Figure 4.1g) produces similar joint stress across all the joint positions and helps to reduce joint stress in the patellofemoral contact area during flexion (Lovejoy, 2007). In humans, the patellar groove of the femur is relatively deep and the lateral

lip of trochlea projects more anteriorly than the medial lip (Wanner, 1977). Stern & Susman (1983) suggested that the main function of the deep patellar groove and prominent lateral lip is to prevent patellar dislocation on the flexed knee due to the line of action of the quadriceps whose origin is laterally placed due to the higher valgus angle in humans compared to higher varus angle in non-human great apes.

In humans, the quadriceps femoris inserts on the proximal patellar surface, continues over the anterior surface, and inserts via the patellar ligament on the tibial tuberosity. Vastus medialis and lateralis insert on the medial and lateral margins of the patella, respectively, which helps to protect the knee from medial/lateral dislocation as quadriceps femoris extends the knee. When the knee is at its full extension, the patello-femoral joint contact occurs at the distal end of the patella (Supplementary Figure S4.1c). As flexion increases the patello-femoral contact area increases as well. During flexion the patella engages into the femoral trochlear groove, and the contact area spreads across the width of the patella and moves proximally (Aiello & Dean, 1990; Lovejoy, 2007; Tardieu, 1999) (Supplementary Figure S4.1a, b). Thus, with the higher articular area, the stress during knee flexion is reduced (Masouros et al., 2010). In great apes, the patella is both absolutely and relatively smaller than in humans due to the smaller quadriceps muscle. In all primates, the quadriceps muscles compress the patella against the femur during flexion, with subsequent joint stress depending on the size of the patellofemoral contact area (Lovejoy, 2007). The knee of great apes is more or less flexed during all locomotor activities compared to humans. A flatter trochlea then allows the patellofemoral surface to bear higher forces when the quadriceps press the patella against the femur (Lovejoy, 2007).

In humans, the menisci form a mobile unit on the tibial plateau that adapts to the sliding and rotating movements of the femoral condyles and function as an important secondary co-resistant to the cruciate ligaments. When the knee is flexed, the popliteus tendon pulls the menisci posteriorly and the contact point of femoral condyle and tibial plateau also moves posteriorly (Aiello & Dean, 1990; Lovejoy, 2007; Tardieu, 1999). Conversely, when the human knee is extended, the menisci again follow the femoral condyle and tibial plateau moving both anteriorly (e.g., Hirschmann & Müller, 2015). In great apes, the lateral meniscus has only a single point of attachment to the tibia. Additionally, the lateral meniscus is connected on its posterior surface to the Wrisberg ligament, which in turn attaches on the inside of the medial femoral condyle (this ligament is rarely found in humans) (Girgis et al., 1975). The anterior transverse ligament is absent, and the medial meniscus is not attached to the medial collateral

ligament, but it is separated from it by a bursa. These differences allow greater range of knee movements in great apes compared to humans (Girgis et al., 1975).

Due to the difference in weight transfer through the lower limb and size of femoral condyles, the relative size of the tibial condyles in great apes is opposite to that in humans. The medial tibial condyle is much larger and more convex than the lateral and the tibial plateau is supero-inferiorly compressed (Berger & Tobias, 1996) with a thin lateral epicondyle (Frelat et al., 2017). The posterior cruciate ligament attaches to the medial femoral condyle more anteriorly and nearer to the midline of the intercondylar notch in great apes than in humans (Aiello & Dean, 1990). The collateral ligaments control the side-to-side motions and the cruciate ligaments control both the slide of the femur and the medial rotation of the tibia as they do in humans (Figure 4.1a-f). However, because of the different attachment of the posterior cruciate ligament, medial rotation of the tibia is greater in great apes compared to humans.

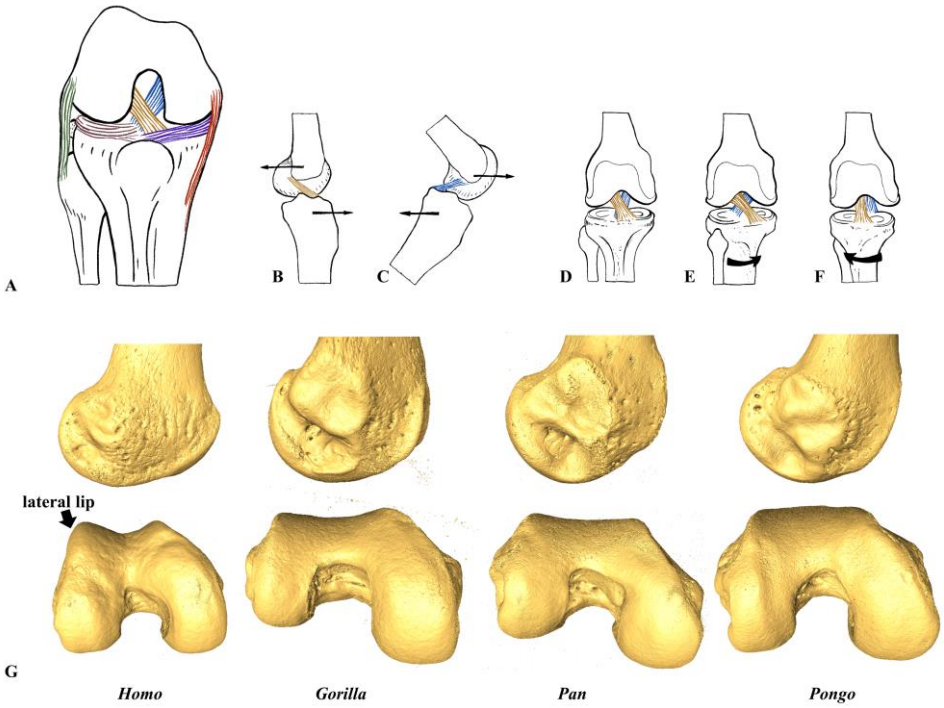

Figure 4.1: (A) Ligament attachments of the knee showing in inferior view. Gold, anterior cruciate ligament; blue, posterior cruciate ligament; green, lateral collateral ligament; red, medial collateral ligament; brown, lateral meniscus; purple, medial meniscus. The medial collateral ligament inserts at the medial epicondyle of the femur and attaches along the medial border of the tibial plateau and on the medial surface of the tibial shaft. The lateral collateral ligament inserts on the lateral femoral epicondyle and attaches on the head of fibula. (B) Anterior cruciate ligament position during forward tibia and backward femur movements. (C) Posterior cruciate ligament position during backward tibia and forward femur movements. Cruciate ligaments position during (D) neutral knee position; (E) medial knee rotation; (F) lateral knee rotation. The anterior cruciate ligament arises from the anterior intercondylar space on the tibial plateau, runs upwards and posteriorly and attaches on the inside of the lateral condyle of the femur. The posterior cruciate ligament arises from well back on the posterior intercondylar space, runs upwards and anteriorly and attaches on the inside of the medial condyle. (G) Surface models of right distal femur of *Homo*, *Gorilla*, *Pan* and *Pongo*. (G) Showing more elliptical shape of lateral condyle, square outline of distal surface and high lateral lip in humans compared to great apes.

4.4 Locomotor behaviour and biomechanics of knee posture during the gait cycle

Humans and great apes are characterized by a wide range of locomotor behaviours that vary in their frequency and knee postures, both across and within species. These differences influence knee load distribution and thus should affect trabecular (re-)modeling. Below, we discuss what is known about the biomechanical differences in knee joint posture and loading across our study species, which form the basis of our predictions about variation in trabecular structure.

4.4.1 Humans

Humans are primarily bipedal walkers but also often engage in other activities such as running, jumping, or squatting, in which the knee position may vary substantially (Racic et al., 2009; Mann & Hagy, 1980; Nilsson & Thorstensson, 1989). Human bipedal gait is at or close to full extension of the knee for most of its cycle (Javois et al., 2009; Landis & Karnick, 2006; Sylvester & Pfisterer, 2012; Tardieu, 1999; Organ & Ward, 2006) (Fig. S1D) and the variability in location of the resulting joint forces on the distal femur is limited (Preuschoft & Tardieu, 1996). Both the medial and lateral condyles are evenly loaded through the tibial plateau during locomotion (Lovejoy, 2007; Sylvester, 2013; Sylvester & Pfisterer, 2012; Tardieu, 1999). When the knee is flexed the range of motion is approximately 45 degrees of lateral and 25 degrees of medial rotation (Lovejoy, 2007). The amount of axial rotation (i.e., twisting of the knee relative to the tibia) depends on the amount of load, with high loads leading to low rotator flexibility and *vice versa* (Lovejoy, 2007). During extension, the patellar tendon moves to the center of rotation and the lever advantage of the quadriceps muscle increases in intensity (Loudon, 2016). Medial and lateral collateral ligaments tighten the knee joint in full extension and limit rotation and hyperextension. In flexion they are loose and allow more rotational knee movements. The medial collateral ligament is also tightened in lateral rotation and loose in medial rotation. The lateral collateral ligament is, by contraction of the quadriceps tendon, actively tightened during flexion-extension (Hirschmann & Muller, 2015). The posterior cruciate ligament is in tension when the knee is flexed and prevents the femur from sliding anteriorly off the tibial plateau (Figure 4.1c), whereas the anterior cruciate ligament is in tension when the knee is extended and prevents femur from sliding posteriorly off the tibial plateau (Figure 4.1b). Additionally, the cruciate ligaments limit medial rotation to the tibia in relation to the femur (Figure 4.1d, e). If tibia is rotated laterally, the cruciate ligaments untwist and have no limiting ability (Aiello & Dean, 1990) (Figure 4.1f).

4.4.2 Pan

Great apes practice a variety of locomotor behaviours depending on their habitat, body size, sex and age (although we focus only on adults in this study). In this study, *Pan* is represented only by *Pan troglodytes verus* from the Taï National Forest, Ivory Coast. Doran (1993) found that Taï adult *Pan* spend approximately 15-18% of their daily time in locomotion and, within this locomotor time, they engage on average in 16% arboreal and in 84% terrestrial locomotion. Both lower limbs are often exposed to external forces (substrate reaction forces) where the knee is flexed and the hip is abducted to varying degrees during both terrestrial and arboreal locomotion (Ankel-Simons, 2010; D'Aoŭt et al., 2004; Georgiou et al., 2018; Isler, 2005; Lee at al., 2012; Pontzer et al., 2009) (Fig. S1E). During climbing, *Pan* may utilize their full flexion-extension range at the knee (D'Aoŭt et al., 2002; Isler, 2005). The single meniscal attachment of the lateral meniscus facilitates medial and lateral rotation of the knee (Javois et al., 2009; Landis & Karnick, 2006; Tardieu, 1999). Characteristic flattening of the femoral trochlea allows free patellar movements during knee rotation associated with foot grasping during arboreal behaviour (Tardieu, 1999). During terrestrial knuckle-walking in zoo-housed chimpanzees, knee flexion ranges from ~161.4º at foot touchdown to ~117.4º at toe-off, and there is inter-individual variation in vertical ground reaction force (Finestone et al., 2018; Kozma et al., 2018). Even though there is an evident lateral rotation movement during extension in *Pan*, the knee is still mostly loaded in flexed and varus postures during terrestrial locomotion (Lovejoy, 2007). The differing size between femoral condyles causes mediolateral knee rotation during all phases of terrestrial quadrupedal locomotion. Additionally, the medial condyle is loaded more than the lateral condyle (Sylvester, 2013; Tardieu, 1999; Sylvester & Pfisterer, 2012). There are no significant sex differences in the overall frequency of arboreal and terrestrial locomotion (Doran, 1993). However, there are significant sex differences in the type of arboreal locomotor behaviors used, with adult male *Pan* using significantly less quadrupedalism (males 23.4%, females 60.6%) and more vertical climbing (males 60.2%, females 52.4%) than females (Doran, 1993).

4.4.3 Gorilla

Gorilla also engage most frequently in terrestrial knuckle-walking and the frequency of arboreality depends mostly on their habitat and body size (Doran, 1996; Doran, 1997; Isler, 2005; Remis, 1994; Tocheri et al., 2011). In this study, *Gorilla* is represented only by *Gorilla gorilla gorilla*, for which locomotor behavior in wild has only been studied in one group (Bia Hokou, Central African Republic; Remis, 1994). During terrestrial knuckle-walking, the knee

is flexed, as in *Pan*, and the hip is in abduction to varying degrees (Supplementary Figure S4.1e) (Finestone et al., 2018). Compared to *Pan*, zoo-housed *Gorilla* are found to extend their limbs more during terrestrial locomotion and vertical climbing (Crompton et al., 2008; Finestone et al., 2018; Kozma et al., 2018; Hofstetter & Niemitz, 1998; Isler, 2005). The knee angles vary from ~163.2º at foot touchdown to ~126.6 º at toe-off (Kozma et al., 2018). Hip abduction is a clear advantage in climbing and in *Gorilla* it is necessary to accommodate their large belly, which limits hip flexion in its sagittal plane during climbing as well as in quadrupedal postures (Preuschoft & Tardieu, 1996). However, flexion-extension range at the hip has been shown to differ more than 30º between sexes, with higher range of motion in females (Hammond, 2014), which could additionally rotate the knee more medially. Isler (2005) reported that maximal extension of the hip and knee during vertical climbing is significantly higher in the captive adult female *Gorilla* (approximately 135° knee extension) compared to males (approximately 100° knee extension). Additionally, Isler (2005) found that males exhibit a smaller range of motion at the knee during vertical climbing (approximately 55° knee range of motion) compared to females (approximately 65-85° knee range of motion).

4.4.4 Pongo

Pongo is the most arboreal of all the great apes. They are characterized by greater joint mobility than other hominids due to their diverse locomotor behaviour where all limbs are used variously to achieve balance (Payne et al., 2006; Thorpe et al., 2009; Thorpe & Crompton, 2006). In this study, *Pongo* is represented by *Pongo pygmaeus* and *Pongo abelii.* During terrestrial locomotion, the *Pongo* knee posture in zoo-housed individuals does not differ to that of African apes (Kozma et al., 2018). During terrestrial locomotion, *Pongo* is found to have a similar degree of knee extension to that of female *Gorilla*, but with a larger range of hip joint motion (Isler, 2005; Morbeck & Yihlman, 1988). However, during arboreal locomotion, their knee postures range from hyper-flexed to extended postures (Isler, 2005; Morbeck & Zihlman, 1988; Payne et al., 2006; Thorpe & Crompton, 2005; 2006; 2009) and thus the range of knee motion is significantly larger compared to *Pan* and *Gorilla* (Supplementary Figure S4.1f). Previous studies have found female Bornean *Pongo* to be more arboreal compared to their male counterparts (Cant, 1987; Galdikas, 1988). However, no sex differences in the frequency of arboreality have been found in Sumatran *Pongo* (e.g., Thorpe & Crompton, 2005; Thorpe & Crompton, 2006). Unfortunately, we are not able to test sex differences within *Pongo* in this study as we have only two males in our sample.

4.5 Hypotheses and predictions

In this study we test two hypotheses. **The first hypothesis** is that trabecular architecture of the distal femur will reflect differences in knee postures and presumed loading during locomotor behaviours across *Homo*, *Pan/Gorilla*, and *Pongo*. We predict that:

1A) *Homo* will exhibit the highest BV/TV posteroinferiorly in the condyles due to their habitual extended knee posture. BV/TV on the patellar surface of femur will be higher laterally due to the higher loading of lateral knee compartment. BV/TV will be greater in the lateral condyle compared to medial condyle, reflecting the resistance of the knee adduction moment provided by the quadriceps and gastrocnemius muscles. *Homo* will exhibit the highest DA in anterior and posteroinferior/superior regions of both condyles (consistent with low variability in loading direction) resulting from the stereotypical loading of these regions during extended knee postures during all phases of bipedal locomotion.

1B) *Pan* and *Gorilla* will exhibit the highest BV/TV posterosuperiorly on the condyles within their knee due to their more flexed knee position compared to *Homo*. BV/TV will be higher medially on patellar surface of femur due to the higher loading of medial knee compartment. *Pan* and *Gorilla* will display the highest DA in the posteroinferior/superior regions of the condyles (consistent with low variability in loading direction) due to their higher loading of the posterior regions during stereotypically flexed knee postures during arboreal and terrestrial locomotor behaviours.

1C) *Pongo* will exhibit a more homogenous distribution of BV/TV across the condyles and patellar surface of femur relative to other great apes due to their more variable knee joint postures during locomotion (which may vary from full extension to full flexion). *Pongo* will exhibit the highest DA in the posterior regions of condyles (consistent with low variability in loading direction) in a similar pattern as *Pan* and *Gorilla* due to their higher loading of the posterior regions in mostly flexed knee postures particularly during terrestrial locomotion. However, due to more varied postures/loading in *Pongo*, we predict that DA will be the lowest (consistent with high variability in loading direction) and the most homogenous across the distal femora of all studied taxa.

The second hypothesis is that trabecular architecture will reflect sex differences (or lack thereof) in the locomotor behaviours and, in particular, the frequency of arboreality between female and males in our study taxa. Note, we cannot test for sex differences in *Pongo* due to sample size restrictions. We predict that:

2A) If trabecular morphology reflects variation in frequency of terrestrial versus arboreal locomotion, we expect female *Gorilla* to show more flexed knee-posture loading than males due to greater frequency of climbing. If trabecular morphology reflects variation in the level of knee flexion/extension, we expect female *Gorilla* to have higher BV/TV in the lateral condyle, as well as in the lateral part of patellar surface and in the lateral epicondyle, compared to males due to their greater degrees of knee extension (particularly when climbing) and male *Gorilla* to have relatively higher BV/TV in the medial condyle and epicondyle because of their higher degree of flexion and thus higher loading of medial knee compartment (particularly when climbing).

2B) If trabecular morphology reflects variation in frequency of terrestrial versus arboreal locomotion, we expect to find no significant differences in BV/TV and DA between female and male *Pan*, since no significant sex differences in the overall frequency of arboreal and terrestrial locomotion has been found in the Taï chimpanzees (Doran, 1993). Furthermore, even though sex differences in the types of arboreal locomotion have been reported in *Pan,* with adult male *Pan* using significantly less quadrupedalism (males 23.4%, females 60.6%) and more vertical climbing (males 60.2%, females 52.4%) than females (Doran, 1993), the variation in the level of knee flexion/extension between sexes have not been previously described. Thus, if trabecular morphology reflects variation in the level of knee flexion/extension, there is no reason to predict these sex differences in the trabeculae of the knee in *Pan*. Similarly, we expect to find no significant differences in BV/TV and DA between female and male *Homo* as they are both obligate bipedal walkers.

4.6 Materials and methods

4.6.1 Study sample and scanning

4.6.1.1 Study sample

The study sample consists of complete distal femora of *Homo sapiens* (n = 26 individuals), *Gorilla gorilla gorilla* (n = 14 individuals), *Pan troglodytes verus* (n = 15 individuals), and *Pongo* spp. (n = 9 individuals). Research involving non-human great apes plays a vital role in many anthropological and medical studies as their close phylogenetic relationship to humans makes them a useful model for reconstructing locomotor (and other) behaviours in hominin fossil record. The studied species were chosen as a representative sample of primates that use locomotor behaviours potentially found within the locomotor repertoires of fossil hominins. Details of the study sample are shown in Table 4.1. All great apes were wild born with no

obvious signs of pathologies within their postcranial skeleton. The *Gorilla* sample is curated at the Powell-Cotton Museum in Birchington-on-Sea, UK, of which 13 individuals are from Cameroon and one is from the Democratic Republic of the Congo. The *Pan* sample is from the Taï Forest National Park, curated at the Max Planck Institute for Evolutionary Anthropology in Leipzig, Germany. The *Pongo* sample is from the Bavarian State Collection for Zoology in Munich, Germany and from the Natural History Museum in Berlin, Germany. Six individuals are *Pongo pygmaeus*, two are *P. abelii* and the species of one individual is unknown. Fifteen individuals of our human sample are from the W.M. Bass femoral collection from the Forensic Anthropology Centre at the University of Tennessee, USA and originate from diverse post-industrial populations. Eleven individuals are crew members of the Mary Rose ship from early 16th century (Barker, 1992) curated at the Portsmouth Museum, Portsmouth, UK. The Mary Rose sample comprises young adult males and are considered to represent high activity levels (e.g., Scorrer et al., 2021; Stirland et al., 1997). Both human samples showed no obvious signs of pathologies within their postcranial skeleton. For most of our sample (91%) we used the right distal femur. However, when it was not possible due to preservation or methodological issues (such as low resolution of the CT scan), the mirrored left distal femur was used.

Table 4.1: Femur sample composition and voxel size range.

			Sex		Voxel size (mm)	
Taxon	Locomotor behaviour	N	female	male	min	max
Homo sapiens (1.0 kya - present)	Bipedal	15	unknown		0.030	0.037
Homo sapiens (Mary Rose)	Bipedal	11	0	11	0.030	0.037
Gorilla gorilla gorilla	Terrestrial knucle-walker	14	7	7	0.048	0.058
Pan troglodytes verus	Arboreal/knuckle-walker	15	8	7	0.029	0.030
Pongo spp.	Arboreal/Suspensory	9	7	2	0.027	0.030
Total		64				

4.6.1.2 MicroCT scanning

All distal femora were scanned via high-resolution micro-computed tomography (microCT) using a BIR ACTIS 225/300, Diondo D3 or Skyscan 1172 scanner housed at the Department of Human Evolution, Max Planck Institute for Evolutionary Anthropology (Leipzig, Germany), a Phoenix Nanotom S – X-ray tomograph at the Department of Micro-CT Laboratory, Museum of Natural History (Berlin, Germany), a Nikon 225/XTH scanner at the Cambridge Biotomography Centre, University of Cambridge (Cambridge, UK), or with the Diondo D1 scanner at the Imaging Centre for Life Sciences at the University of Kent (Canterbury, UK). The scan parameters included acceleration voltages of 100–160 kV and 100–140 µA using a

0.2 to 0.5 mm copper or brass filter. Scan resolution ranged between 0.024 mm to 0.058 mm depending on the size of the bone (Table 4.1). Images were reconstructed as 16-bit TIFF stacks.

4.6.2 Data processing and trabecular bone analysis

Each distal femur was rotated into a standard anatomical orientation and non-bone inclusions were removed from the scans in Avizo Lite 9.0.0 (Visualization Sciences Group, SAS) (Fig. 2A). Scans were subsequently segmented using the medical image analysis (MIA) clustering method (Dunmore et al., 2018) (Figure 4.2b). This method requires the definition of a grid size, which was selected by measuring the thickness of the thickest trabeculae in a cross-section and selecting a slightly higher value for each individual. A maximum of three classes were used across all individuals. MIA allows more accurate separation of trabeculae and offers more flexibility to deal with surrounding non-bone inclusions than other bone segmentation methods (Dunmore et al., 2018). The outer and inner layer of the cortex was defined using Medtool v 4.5 (www.dr-pahr.at/medtool), following published protocols (Gross et al., 2014; Pahr & Zysset, 2009). This involves morphological filters to fill the bone and use of a ray-casting method to isolate the external and internal edge of the cortex in 3D, resulting in a mask of the internal bone volume and outer cortex (Figure 4.2c).

4.6.2.1 Canonical holistic morphometric analysis

cHMA, combining holistic morphometric analysis (HMA) and statistical free-form deformation model (SDM), approach was used to analyze the patterns of trabecular bone distribution within whole epiphysis following published protocols (Bachmann et al., 2022). SDM operates on masked images of bones, where all images are registered onto a randomly chosen reference image using a similarity transform. All similarity transformations are then averaged, and the center of rotation is fixed. All images are then registered onto the aligned reference image and a free-form deformation is applied using a cubic B-spline transformation. The steps of registering and averaging can be repeated several times until the model has congregated. The last reference image is used as the canonical bone image for further steps of the analysis. The degree to which this may affect the results has been tested in Bachmann et al. (2022). In brief, cHMA creates a canonical bone from all the samples and then registers all samples onto that canonical bone. To create a canonical bone, we used fifteen humans, fourteen gorillas, fifteen chimpanzees and nine orangutan individuals to create canonical bone representing all species as much as possible. The canonical bone refers to the mean meshwork of bones formed from all the studied samples. All left sided femora were mirrored in Avizo Lite 9.0.0 (Visualization Sciences Group, SAS) to resemble right sided femora. All bones were then aligned into a mean

position by translation and rotation in the image space and scaled to the mean bone size. Then, an SDM (Rueckert et al., 2003; Steiner, Synek & Pahr, 2021) was used to create a canonical bone in 3D space representing the sample's mean internal and external bone morphology (in our case morphology of right distal femur) (Figure 4.2d). To produce the canonical atlas of the internal bone, the internal volume of each individual bone is used (Figure 4.2e). The canonical bone registration was run in Python 3.7.10, while required pre- and postprocessing steps were performed in Medtool v 4.5 (www.dr-pahr.at/medtool). A 3D rectangular background grid with a grid size of 2.5mm was built around each individual segmented volume and a sampling sphere (VOI) of 5mm in diameter was used to measure BV/TV and DA across the entire bone in Medtool. Once these trabecular quantities were interpolated onto individual meshes the meshes were deformed to the canonical mesh to allow for homologous volumetric comparisons.

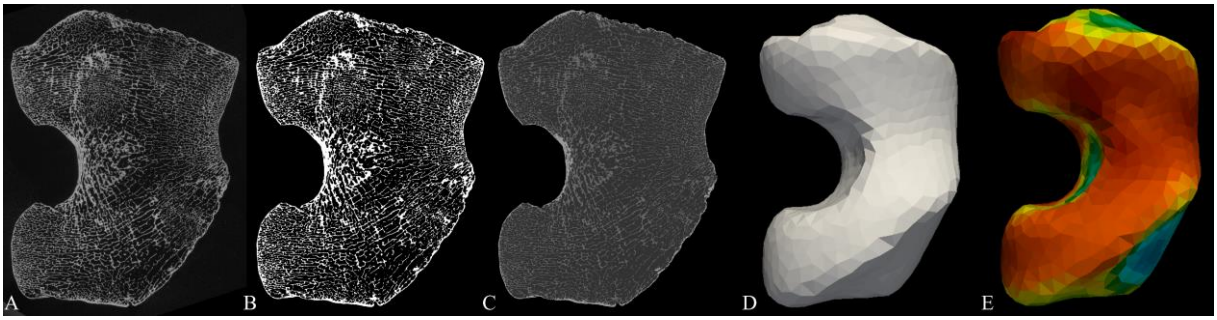

Figure 4.2: Processing steps of distal femur of a *Homo* specimen showing in inferior view. A) Original high-res micro-CT image. B) Micro-CT image segmented by MIA (Dunmore et al., 2018). C) MaskSeg defined by Medtool (Pahr & Zysset, 2009) showing the distinction between inner trabecular area and outer cortex. D) Outer canonical atlas representing sample's mean size, position, and external right distal femur morphology computed by cHMA (Bachmann et al., 2022). E) Inner mesh representing rBV/TV distribution in human sample computed by cHMA (Bachmann, et al., 2022).

DA was calculated using the mean-intercept-length method (Odgaard, 1997; Whitehouse, 1974). The value of DA is zero if the minor and major orientations are of equal magnitude, i.e., isotropic, and is one if the minor and major orientations are maximal different, i.e., anisotropic. Three-dimensional tetrahedral meshes of all specimens were created with CGAL 4.4 (CGAL, Computational Geometry, http://www.cgal.org), using the segmented trabecular structure and a characteristic mesh size of 3 mm. The morphometric values at each node of the background grid were then interpolated to the tetrahedral elements (back onto the canonical mesh) and the resulting BV/TV and DA distribution maps were visualized using Paraview 4.8.2 (Ahrens et al., 2005). Since data were collected from the canonical mesh, the datum collected at each node in the 3D grid is homologous between individuals. The BV/TV value for each mesh-element was used to calculate the mean BV/TV for each individual. To compensate for potential systematic differences between selected taxa and to analyse bone volume distribution while

controlling the magnitude, the BV/TV of each tetrahedron was divided by the overall average for that individual to give a measure of relative bone volume (rBV/TV). rBV/TV demonstrates where bone volume has increased or decreased relative to the mean allowing for comparisons between individuals and species that may differ in absolute BV/TV (Dunmore et al., 2019; Sukhdeo at al., 2020).

Femoral insertions of cruciate and collateral ligaments and of gastrocnemius muscle were located in the canonical distal femur shape (thus hereafter, just 'presumed insertions') based on their anatomical location for each studied species. Trabecular distribution under all ligament and muscle attachments of each individual were checked using HMA of Medtool.

4.6.2.2 Statistical analysis

All quantitative comparisons of measured variables and statistical analyses were conducted on the data generated from cHMA (Bachman et al., 2022). All specimens have the same number of tetrahedral elements and the same topology. Only the position of the vertices changes. Thus, homology is accounted for by the topology of the canonical mesh and the tetrahedral elements of each specimen can be considered geometrically homologous (Bachmann et al., 2022). To analyse the distribution of trabecular bone in each species, principal component analyses (PCA) were run, creating two PCA models for rBV/TV and DA separately using the scalars associated with tetrahedral elements (including the geometry) of the canonical mesh as an input variable. This allows for visual comparison of the differences in genus-specific rBV/TV and DA patterns in distal femur. To demonstrate the loadings of each PC, we chose three standard deviations to represent 99.7% of the available variation. All values of the trabecular volumes were coloured by the signed loadings at three standard deviations of each principal component and thresholded at the 70th percentile of the rBV/TV or DA range. All PCA plots were done in R v3.4.1 using the rgl package (R Core Team, 2017). To explore if interspecific allometry is driving species separation on PC1 of rBV/TV in our results, i.e. the potential that *Gorilla* has a different trabecular distribution because they have a larger body mass than *Pan*, we ran a regression of PC1 on "bone volume" in all studied individuals (Supplementary Figure S4.8). To explore potential intraspecific allometry, we ran a regression of PC1 on bone volume for each taxon separately (Supplementary Figure S4.9-S4.11). We measured 3D bone size as the solid volume of the whole object, here the distal femur (as all femora were cut at a homologous location). This whole "bone volume" (note this is not BV/TV in any sense) was measured for each of our individuals as a proxy for individual size. PC1 (as our sample species separate on PC1) could then be regressed on this bone volume.

4.7 Results

4.7.1 Mean species trabecular bone distribution

4.7.1.1 Relative bone volume in distal femur

4.7.1.1.1 Patellar surface and femoral condyles

In *Homo*, high rBV/TV (indicating the highest 30% of rBV/TV values, the regions assumed to be loaded the most) is concentrated in the posteroinferior volumes of both condyles, with higher values in the lateral condyle and on the patellar articular surface of the femur (Figure 4.3). In *Gorilla*, higher rBV/TV is found to extend from the inferior margin of the patellar articulation to the posteriosuperior region of both condyles, again with higher values in the lateral condyle. *Gorilla* lacks trabecular concentration at the anterior regions of both condyles (i.e., regions assumed to be loaded in an extended knee). Posterosuperior and posteroinferior regions of both condyles exhibit lower rBV/TV concentrations in the deeper trabecular network of *Gorilla* and are evenly distributed between medial and lateral condyles compared to *Homo* (Figure 4.3). *Pan* exhibits a similar, but more spatially homogenous, rBV/TV distribution between the medial and lateral condyles as *Gorilla*. In *Pan*, rBV/TV is low in the anterior regions of both condyles as well; the low rBV/TV extends almost to the posteroinferior part of medial condyle, which differs from the pattern found in *Gorilla* (Figure 4.3). The most homogenous rBV/TV concentration is found in *Pongo*, with, again, low rBV/TV in anterior regions of both condyles. In *Pongo*, as in *Pan*, low rBV/TV almost reaches the posteroinferior part of medial condyle, however, the posteroinferior region of lateral condyle exhibits higher rBV/TV values compared to *Pan* (Figure 4.3).

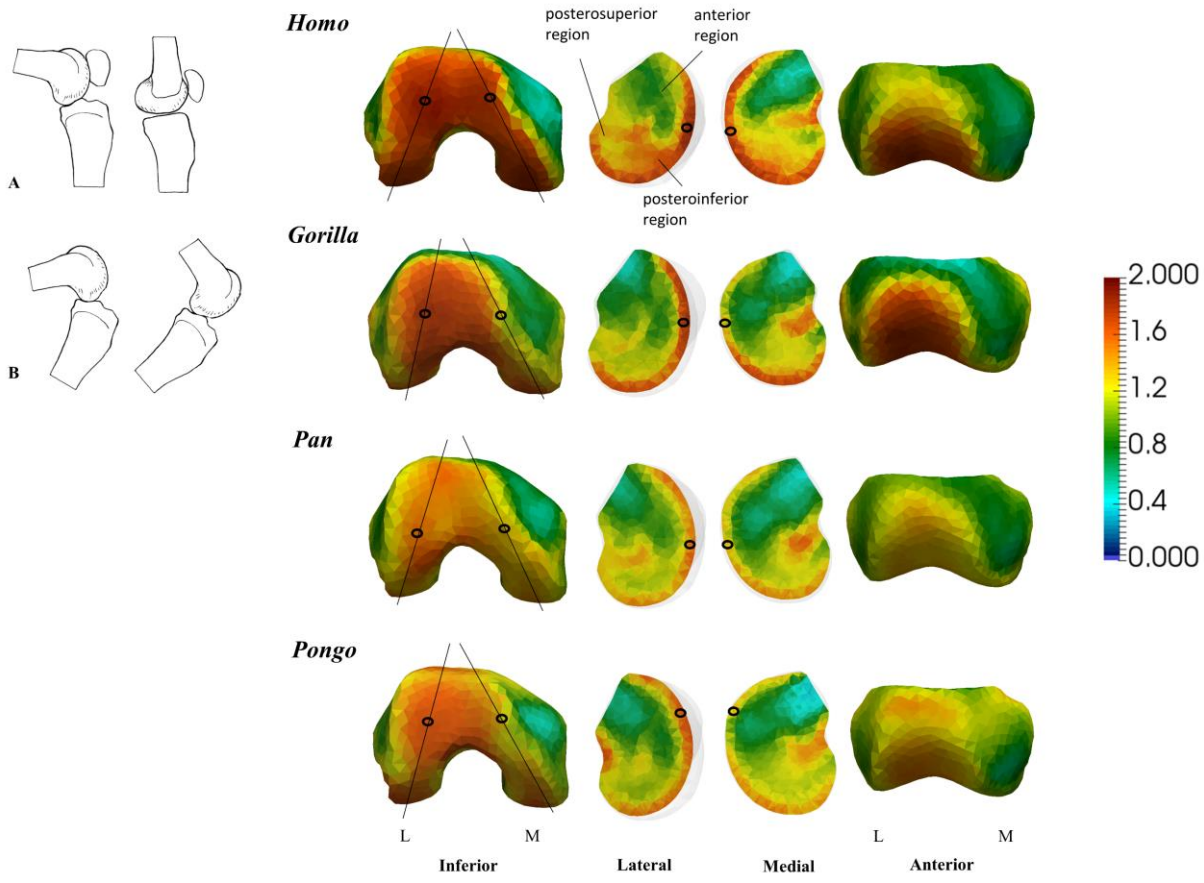

Figure 4.3: Species mean models of rBV/TV distribution in the patellar articular surface and femoral condyles of the distal femur of *Homo*, *Gorilla*, *Pan*, and *Pongo*. Vertical lines through the inferior view mean models show where the slices are positioned. Cross sections were positioned in the middle of lateral and medial condyle. (A) Showing approximate patellar and condyle position during flexed (90°) and extended knee position in humans in medial view; (B) showing approximate condyle position during flexed and extended knee position in great apes. L, lateral; M, medial.

4.7.1.1.2 Femoral insertions of cruciate and collateral ligaments

Even though approximate positions of ligaments and tendon insertion sites are well-known in humans and, to a lesser extent, great apes, the locations are necessarily artificial on the canonical models used in our study. Therefore, we state 'presumed' location to reflect our qualitative assessment of these insertions sites when interpreting the colour maps.

Homo exhibits high rBV/TV in the presumed insertions of cruciate ligaments, particularly for the posterior cruciate ligament in which high rBV/TV reaches to the middle of medial condyle (Figure 4.4). However, compared to medial condyle, rBV/TV under the anterior cruciate ligament does not penetrate as deeply into the trabecular network in lateral condyle (Figure 4.4). *Gorilla* also exhibits high rBV/TV in the presumed insertions of the cruciate ligaments, although not to the same degree as seen in *Homo*. rBV/TV under either cruciate insertion does not extend deeply into the epiphysis in *Gorilla* (Figure 4.4). *Pan* and *Pongo* show higher

rBV/TV under the presumed insertions of both the posterior (medial condyle) and anterior (lateral condyle) cruciate ligaments than in *Gorilla*. rBV/TV under both insertions extends deeper into the epiphyses in *Pan* and *Pongo* compared to *Gorilla* or *Homo* (Figure 4.4) and in both taxa, rBV/TV under the posterior cruciate ligament extends deeper compared to that of the anterior cruciate ligament, particularly in *Pongo* (Figure 4.4).

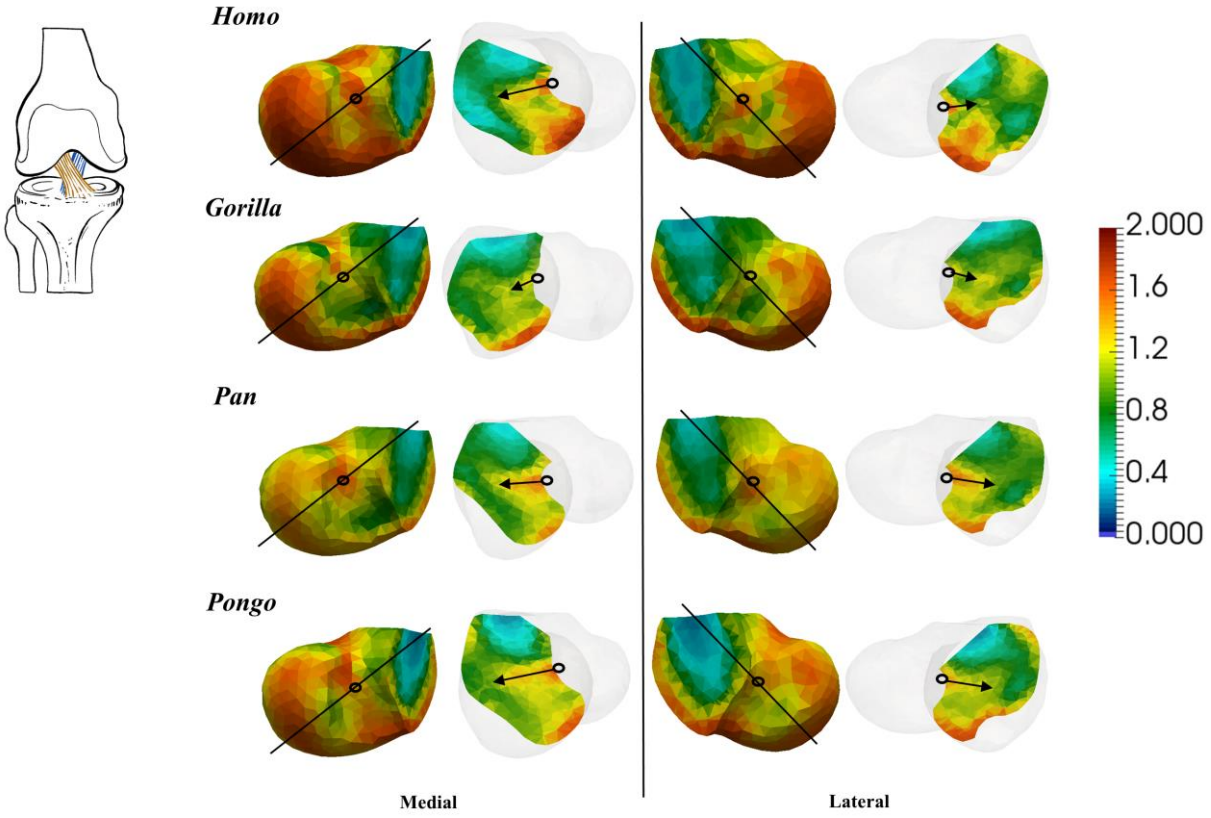

Figure 4.4: Species mean models of rBV/TV distribution under the presumed insertion of cruciate ligaments of the distal femur of *Homo*, *Gorilla*, *Pan*, and *Pongo*. Vertical lines through the medial and lateral mean models show where the slices are positioned. Cross sections were positioned in the middle of presumed insertions of cruciate ligaments. Knee model shows anterior cruciate ligaments during neutral knee position in the anterior view.

High rBV/TV concentrations under the presumed insertions of collateral ligaments are present in all taxa. In *Homo*, the lateral epicondyle shows higher rBV/TV than the medial epicondyle. However, in neither case does the rBV/TV concentration extend deeply into the epiphysis (Figure 4.5). In great apes, relatively higher concentrations of rBV/TV are present under the medial epicondyle and the concentration within the lateral and medial epicondyles is more similar and extends slightly deeper into the epiphysis (especially in the region of the presumed medial collateral ligament insertion) compared to *Homo* (Figure 4.5).

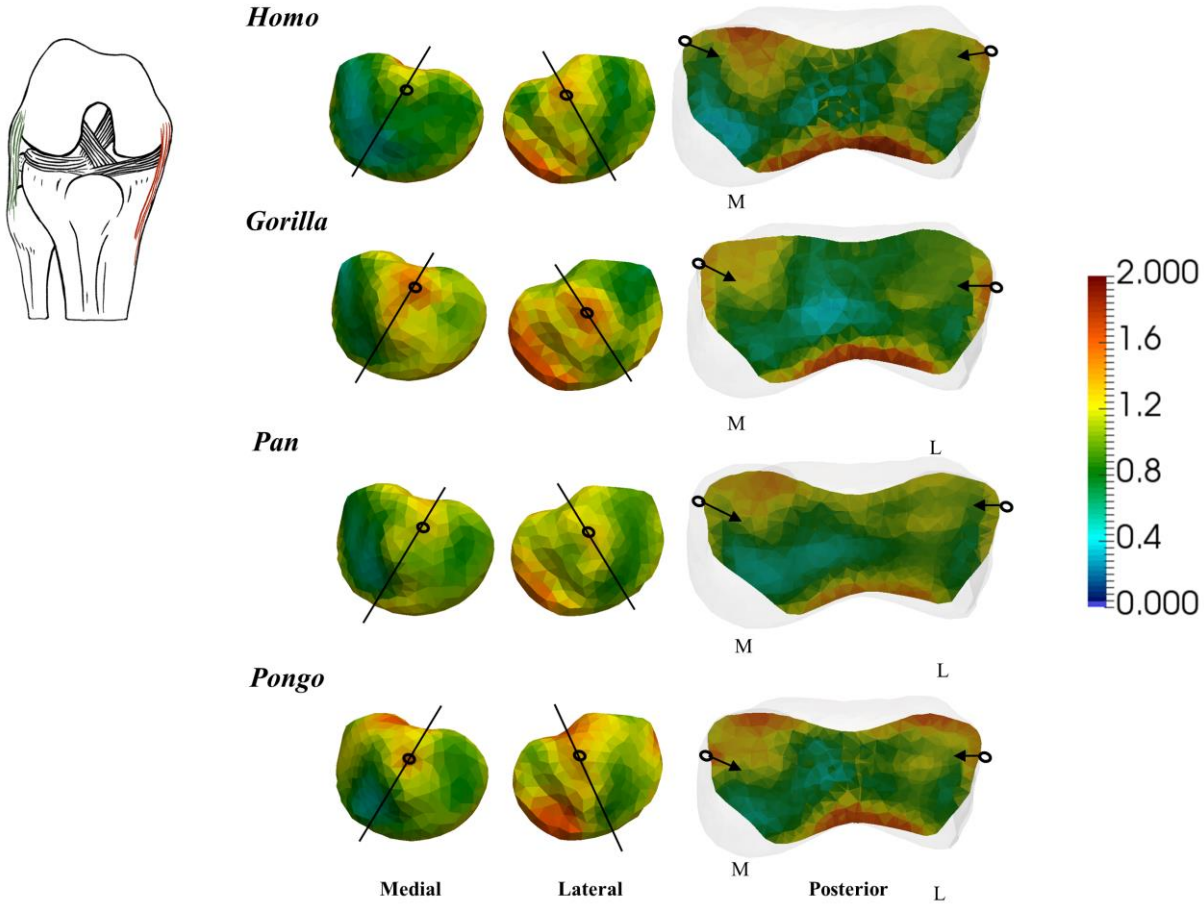

Figure 4.5: Species mean models of rBV/TV distribution under the presumed insertions of collateral ligaments of the distal femur of *Homo*, *Gorilla*, *Pan*, and *Pongo*. Vertical lines through the medial and lateral mean models show where the slices are positioned. Cross sections were positioned in the middle of presumed insertions of collateral ligaments. Knee model shows lateral collateral ligaments attachments. L, lateral; M, medial.

4.7.1.1.3 Femoral insertions of gastrocnemius muscle

When looking at the posterior view of distal femur, high rBV/TV concentrations under the presumed insertions of gastrocnemius muscle are present in all taxa. In all taxa, the concentration under the presumed medial head goes deep inside the medial condyle; however, its presumed lateral head (with the highest values in *Pongo*) does not extend as deeply, especially in *Gorilla* (Figure 4.6). We found the most homogenous distribution under both presumed insertions of gastrocnemius in *Pan* and *Pongo*, but with lower values in *Pan* (Figure 4.6).

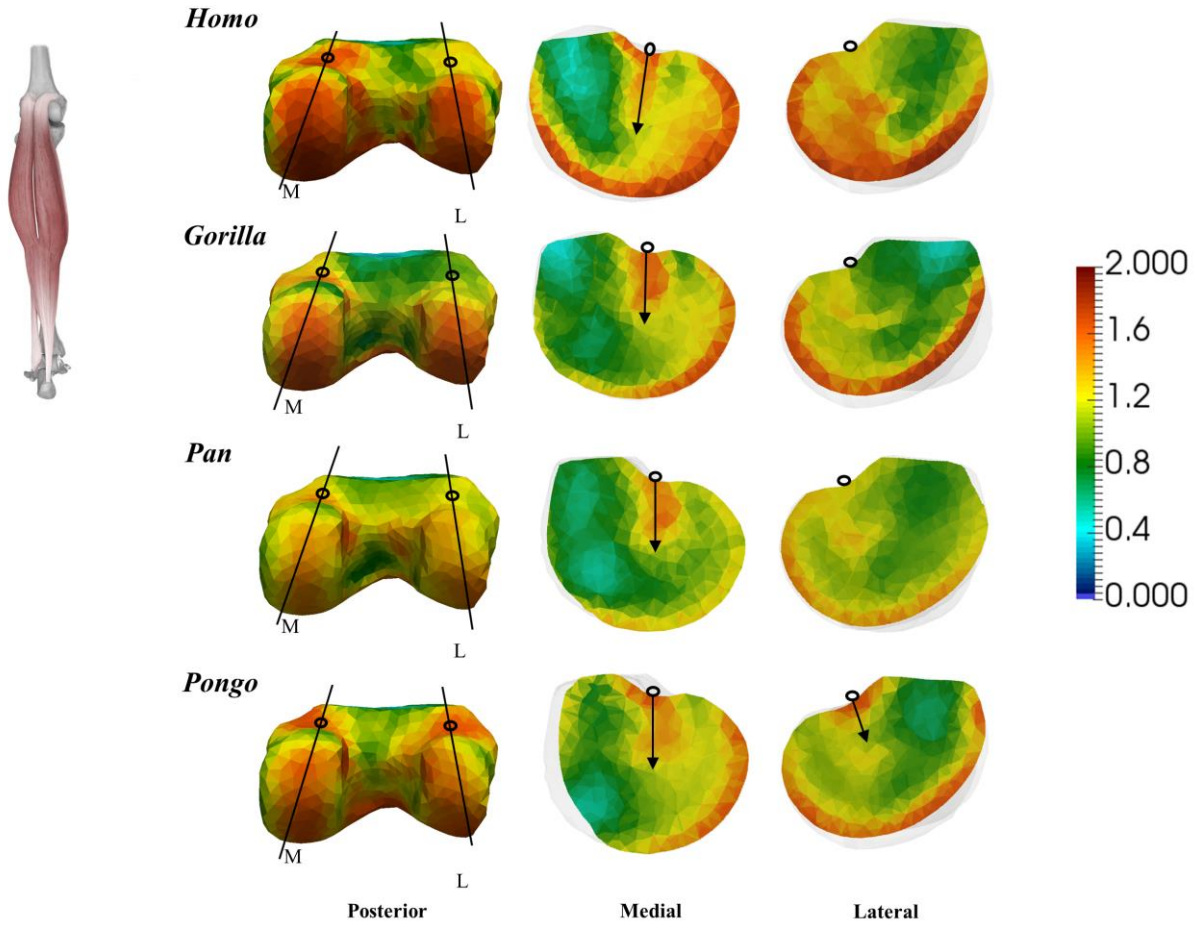

Figure 4.6: Species mean models of rBV/TV distribution under the presumed gastrocnemius muscle attachments of the distal femur of *Homo*, *Gorilla*, *Pan*, and *Pongo*. Vertical lines through the posterior mean models show where the slices are positioned. Cross sections were positioned in the middle of presumed gastrocnemius attachments. Lower limb model shows gastrocnemius attachments. L, lateral; M, medial.

4.7.1.2 Degree of anisotropy in the distal femur

4.7.1.2.1 Patellar surface, femoral condyles, and femoral insertions of gastrocnemius muscle

The *Homo* mean distribution shows more anisotropic values in the posterosuperior/inferior regions of both condyles and under the patellar surface, with higher DA values in the lateral condyle (Figure 4.7). In *Gorilla*, DA is higher under the patellar surface on its medial side and more isotropic above the intercondylar fossa. Posterior regions of the *Gorilla* medial condyle are more anisotropic compared to posterior regions of lateral condyle. This pattern in the condyles is also found in *Pan* and *Pongo*, but posterior regions of lateral condyle are more anisotropic compared to that of *Gorilla* (Figure 4.7). The patellar surface of *Pan* shows more isotropic DA in the middle than on its medial or lateral side. This pattern is even more visible in *Homo* where DA values on the medial and lateral sides of patellar surface are even higher

(Figure 4.7). *Pongo* exhibits a more homogenous distribution of moderate DA values; the most anisotropic values are in the posterior region of medial condyle and under the presumed insertions of cruciate ligaments relative to the patellar surface. In *Pongo*, DA values in both condyles are more homogenous compared to *Pan* (Figure 4.7). All taxa showed high DA values at the presumed insertions of gastrocnemius muscle (Figure 4.7).

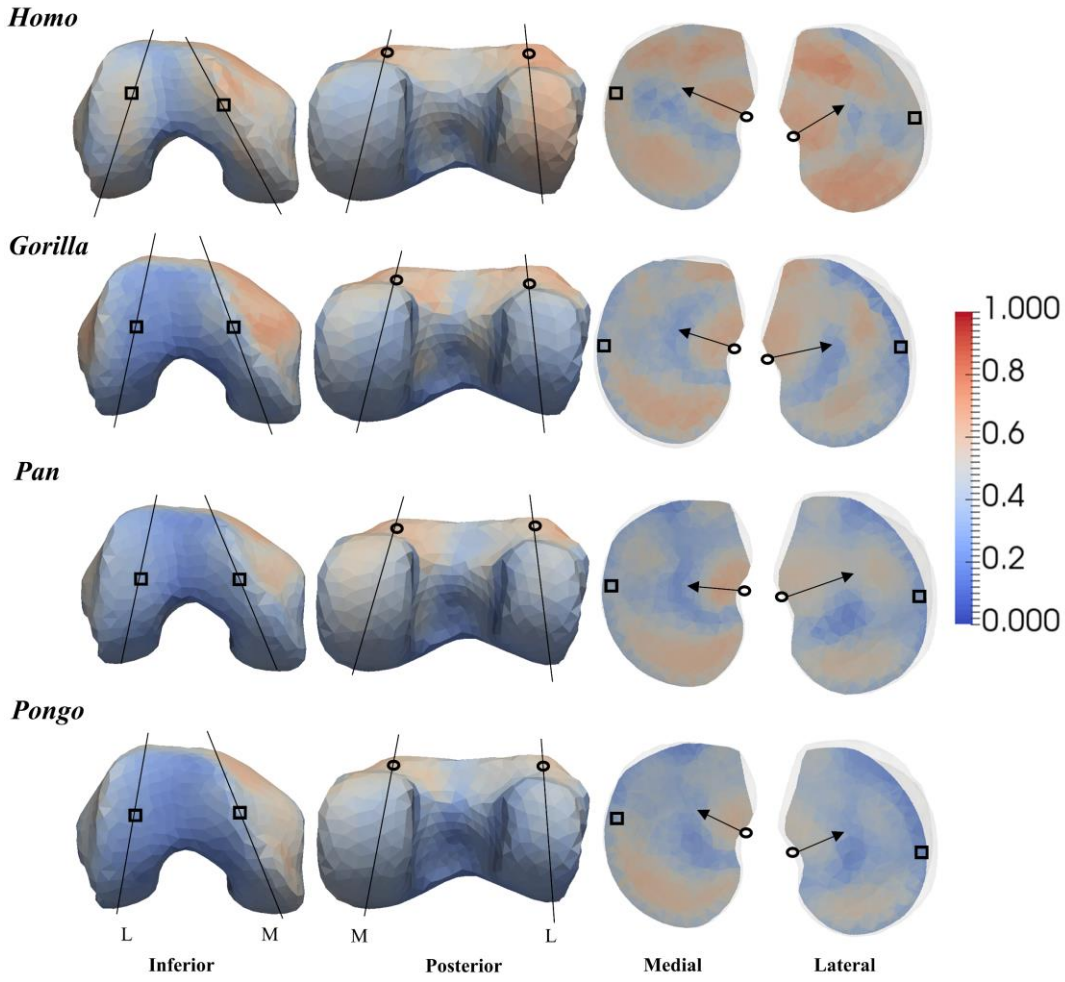

Figure 4.7: Species mean models of DA distribution in the patellar articular surface (marked with square) and in the presumed insertions of gastrocnemius muscle attachments (marked with circle) of the distal femur of *Homo*, *Gorilla*, *Pan*, and *Pongo*. Vertical lines through the inferior view mean models show where the slices are positioned. Cross sections were positioned in the middle of lateral and medial condyle. L, lateral; M, medial.

Segmented images of each individual can be linked with the anisotropic/isotropic parts of the bone presented in the mean colour maps. Figure 4.8 shows one representative individual of *Homo* and *Gorilla* to demonstrate the pattern of high DA in the lateral condyle, and beneath the presumed medial head of gastrocnemius muscle in *Homo* (Figure 4.8a), as well as high DA in the medial condyle of *Gorilla* (Figure 4.8b). Note that the signal within each individual might not be strong, while the mean colour maps are a representation of all individuals within a specific taxon.

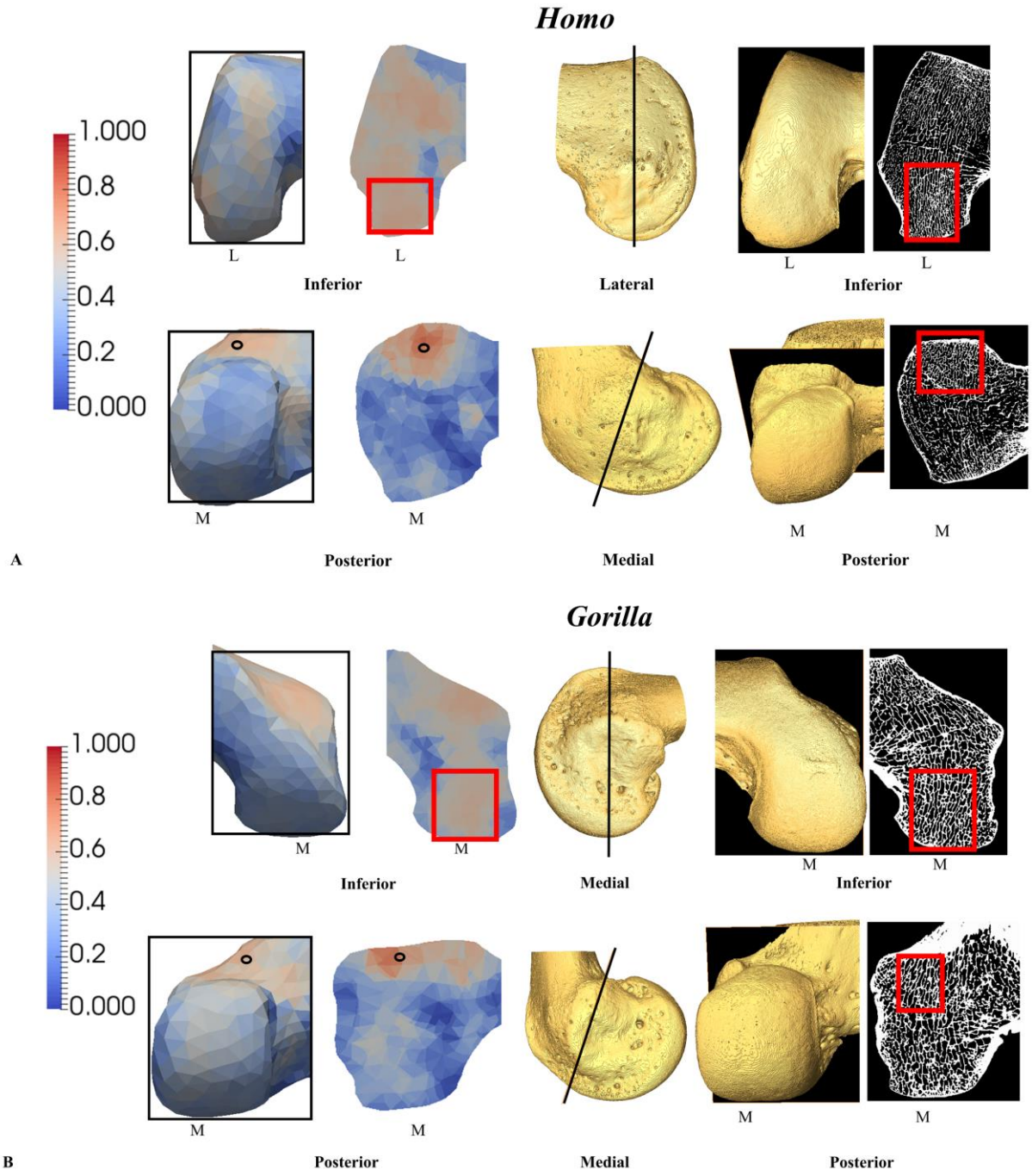

Figure 4.8: HMA and segmented models showing high DA concentration in the lateral/medial condyle and under the presumed insertions of gastrocnemius muscle attachments (marked with circle) of the distal femur of (A) *Homo* and (B) *Gorilla* individual. Vertical lines/squares show where the slices are positioned. L, lateral; M, medial.

4.7.2 Principal component analyses

Figure 4.9 presents the results of a principal component analysis of rBV/TV distribution in the distal femur. PC1 explained 21.4% of the variation in rBV/TV values at each mesh cell. PC1 separates *Homo* from great apes with positive PC1 scores associated with higher rBV/TV on the patellar surface of the femur and on its medial distal articular surface. Negative PC1 scores, associated with the great apes, are associated with higher rBV/TV under the medial and lateral epicondyles and in the posteroinferior region of lateral condyle. PC2 accounted for 9.1% of the variation in rBV/TV values and separates *Pan* and *Pongo* from *Gorilla*. Positive PC2 distinguishes *Gorilla* due to a different pattern under the patellar surface but also especially due to higher rBV/TV under both presumed insertions of gastrocnemius muscle. Negative PC2 separates *Pan* and *Pongo* mostly due to their higher lateral loading of patellar surface and the rBV/TV concentration in the anterior part of lateral condyle. However, because all taxa share a similar rBV/TV concentration on the patellar surface (Figure 4.3), the separation on PC2 more likely reflects the low rBV/TV concentration at the presumed insertions of gastrocnemius muscle in *Pan* and *Pongo* compared to *Gorilla*.

The PCA of DA values reveals separation among the different taxa in distal femur (Figure 4.10). PC1 accounted for 22.2% of the variation in DA values. Positive PC1 separates *Homo*, with highly aligned trabeculae on the lateral side of the patellar surface, in the presumed insertion of the lateral head of gastrocnemius and by higher DA in the posteroinferior region of the lateral condyle (Figure 4.10). Negative PC1 separates great apes, with high DA under the presumed insertions of vastus lateralis and medialis, under the presumed insertion of medial head of gastrocnemius, and in the medial condyle, where we see highly align trabeculae in posterosuperior/inferior regions (Figure 4.10). PC2 explained 7.3% of the variation in DA values. Positive PC2 separates *Gorilla* and *Pan* from *Pongo* with highly aligned trabeculae where vastus lateralis and medialis cross the femur. In contrast, negative PC2 separates *Pongo* from *Gorilla* and *Pan* by high DA in the posterosuperior/inferior regions of lateral and medial condyles (Figure 4.10).

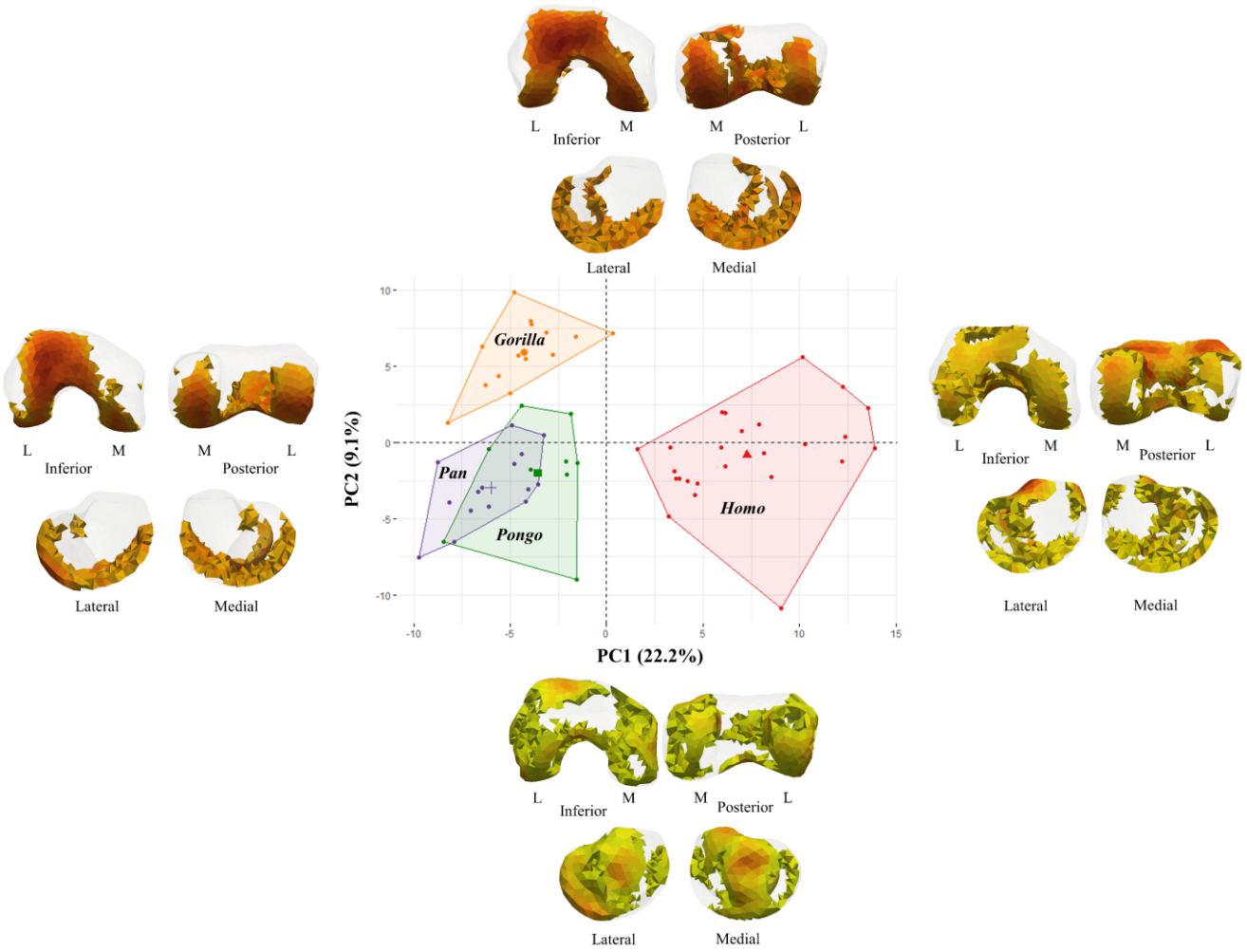

Figure 4.9: PCA of rBV/TV distribution in the distal femur of *Homo*, *Gorilla*, *Pan*, and *Pongo* showing separation among studied taxa. Thresholding models represent high 30% of the range of rBV/TV values for negative and positive PCAs. Models demonstrate the highest loading causing the separation between humans (negative PC1-3SD) and great apes (positive PC1+3SD); between *Pongo*, *Pan* (negative PC2-3SD) and *Gorilla* (positive PC2+3SD). L, lateral; M, medial.

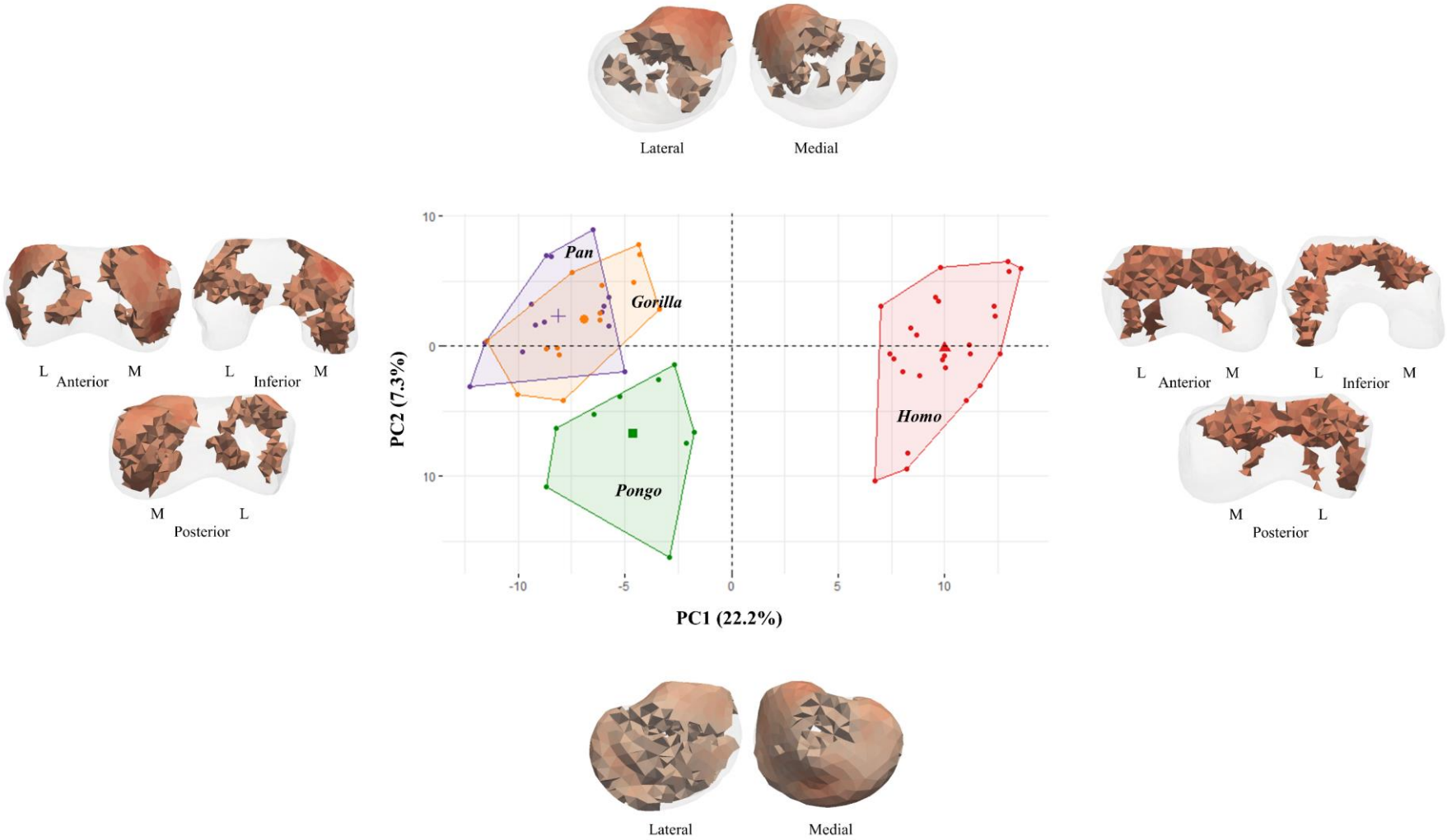

Figure 4.10: PCA of DA distribution in the distal femur of *Homo*, *Gorilla*, *Pan*, and *Pongo* showing separation among studied taxa. Thresholding models represent high 30% of the range of DA values for negative and positive PCAs. Models demonstrate the highest loading causing the separation between humans (positive PC1+3SD) and great apes (negative PC1-3SD); between *Gorilla*, *Pan* (positive PC2+3SD) and *Pongo* (negative PC2-3SD). L, lateral; M, medial.

4.7.3 Trabecular bone distribution in *Homo*, *Gorilla* and *Pan* by sex

Figure 4.11a shows PCA of rBV/TV distribution in *Gorilla*. Female and male *Gorilla* do not separate on PC1 (explaining 15.5% of the variation). PC2 accounted for 14.6% of the variation in rBV/TV values. Thresholded mean models show that females separate from males (positive PC2) due to higher rBV/TV on the lateral side of patellar surface and on the articular surface of medial and lateral condyles. Female *Gorilla* also show higher rBV/TV in the lateral epicondyle and in the posteroinferior region of lateral condyle compared to males. In contrast, in male *Gorilla*, high rBV/TV values extend to the medial side of patellar surface and are more homogeneous across the patellar surface. Figure 4.11b shows PCA of DA distribution in *Gorilla*. PC1 accounted for 22.3% of the variation in DA values. Positive PC1 distinguishes *Gorilla* males due to higher DA values under the presumed insertions of vastus lateralis and medialis muscles and negative PC1 distinguishes females due to higher values inside the medial condyle and under the presumed insertion of medial head of gastrocnemius (Figure 4.11b). We found no separation in rBV/TV and DA distribution between the sexes in *Pan* (Figure 4.11a, b).

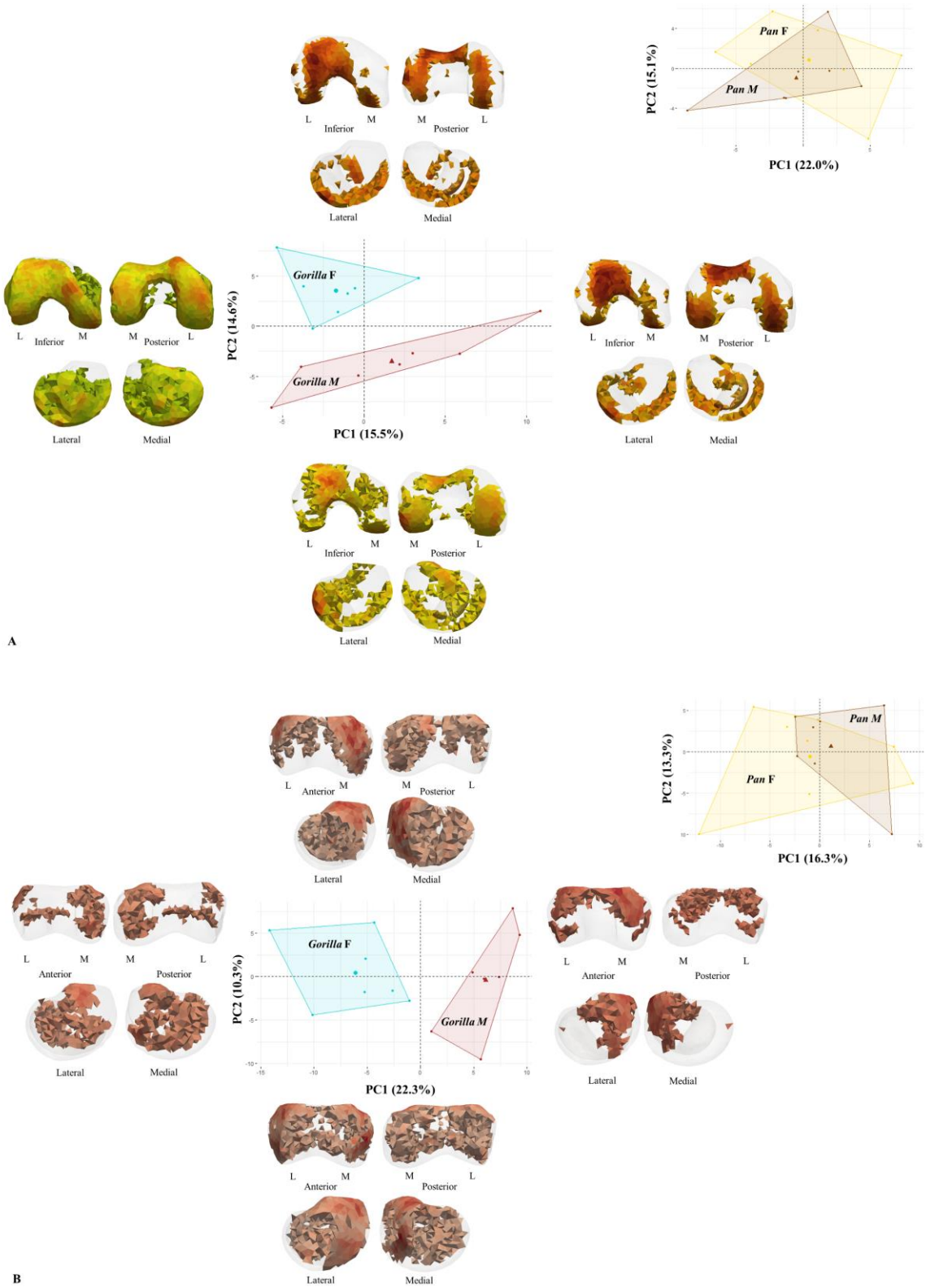

Figure 4.11: PCA of rBV/TV and DA distribution in the distal femur of *Gorilla* and *Pan*. (A) PCA of rBV/TV distribution of *Gorilla* and *Pan* showing separation between sexes in *Gorilla* and no separation in *Pan*. (B) PCA of DA distribution of *Gorilla* and *Pan* showing separation between sexes in *Gorilla* and no separation in *Pan*. Thresholding models represent high 30% of the range of rBV/TV and DA values for negative and positive PCs. Models demonstrate the highest loading causing the separation between female and male gorillas. L, lateral; M, medial; *F*, female; *M*, male.

Supplementary Figure S4.7 shows that the relative PC1 positions for rBV/TV (explaining 21.4% of the variation) and PC1 positions for DA (explaining 22.2% variation) remained constant when we divided the *Homo* sample by population (Mary Rose sample is represented by 11 male individuals) for a PCA. Note, that we could have not test sex differences across whole human sample as sex is known only for 11 (male) of the 26 individuals.

4.7.4 Allometry in our sample

We found no significant relationship between PC1 and bone volume (R^2 = 0.002, p = 0.890) across our sample (Supplementary Figure S4.8). We found no significant relationship (R^2 = 0.007, p = 0.740) in *Gorilla* (sexes pooled; Supplementary Figure S4.9). However, male *Gorilla* showed a stronger negative, if non-significant, relationship (R^2 = 0.490, p = 0.110) compared to females (R^2 = 0.090, p = 0.710) (Supplementary Figure S4.9). We found a significant negative relationship (R^2 = 0.292, p = 0.011) in *Pan*, but no significant relationship within each sex, although females had a stronger relationship (R^2 = 0.436, p = 0.059) than males (R^2 = 0.212, p = 0.069) (Supplementary Figure S4.10). Lastly, as our human sample is predominantly male, we explored potential allometric differences between populations. We found no significant relationship across all humans (R^2 = 0.058, p = 0.170) and neither in the sedentary population (R^2 = 0.221, p = 0.280) or the active population (R^2 = 0.012, p = 1.000) (Supplementary Figure S4.11).

4.8 Discussion

This study investigated trabecular variation in the distal femur of great apes and *Homo*. We expected trabecular architecture to differ based on different types of locomotion and predicted differences in habitual knee joint postures in extant hominid taxa. Also, we expected to find differences in trabecular architecture between female and male *Gorilla*, due to higher female arboreality, and to find no sex differences within *Pan* and *Homo*. We found general support for all our predictions.

4.8.1 Trabecular bone structure of the distal femur in human bipedal walking

We predicted that *Homo* would be significantly differ from other great apes in having a trabecular structure of the distal femur that reflected habitual use of extended knee postures during bipedalism. This prediction was supported. High rBV/TV values in posteroinferior regions of both condyles (Figure 4.3) were consistent with the extended knee postures during

all gait phases of human walking. High rBV/TV concentration in lateral condyle (Figure 4.3) was consistent with the resistance, provided by the quadriceps and gastrocnemius muscles and medial collateral ligament, of the knee adduction moment (when the tibia medially rotates on the knee joint in the frontal plane) and with valgus knee postures (Nordin & Frankel, 2001; Racic et al., 2009). High rBV/TV concentration in the lateral condyle is consistent with human bipedal heel strike and subsequently transferring weight from the lateral side of the foot to the medial side (Elftman & Manter, 1935; Napier, 1967). The distinct rBV/TV distribution in patellar surface in *Homo* compared to great apes (Figure 4.3) most likely reflected a more convex trochlea, such loading is distributed, with flatter trochlea, more evenly across the patellar articular surface in great apes. We found high rBV/TV values on the patellar articular surface being extended more mediolaterally, reflecting the patella's more extensive articulation with the lateral part of the trochlea than with its medial part (Figure 4.3). Moreover, high rBV/TV was also found beneath the presumed insertions of gastrocnemius and those of the femoral ligaments (Figure 4.3-4.6) (see below). The human distal femur was more anisotropic posterosuperiorly/inferiorly in both condyles and under the patellar articular surface than in great apes (Figure 4.7). This DA pattern was also consistent with what we would expect from loading during human's stereotypical extended knee postures. Furthermore, high DA was also found beneath the presumed insertions of gastrocnemius and vastus lateralis and medialis muscles (Figure 4.7-4.8; Supplementary Figure S4.5) (see below). Overall, the trabecular distribution patterns found in our human sample are consistent with variation in trabecular structure found in previous studies of the proximal (Cazenave et al., 2019; Georgiou et al., 2019; Georgiou et al., 2020; Ruff et al., 2013; Ryan & Ketcham, 2002; Ryan & Walker, 2010; Volpato et al., 2008) and distal (Georgiou et al., 2018; Sylvester & Terhune, 2017) femur and with our current biomechanical understanding of human walking cycle (Alexander, 1991; 2004; Elftman & Manter, 1935; Javois et al., 2009; Landis & Karnick, 2006; Napier, 1967; Sylvester & Pfisterer, 2012; Tardieu, 1999; Organ & Ward, 2006).

4.8.2 African ape trabecular bone structure and locomotor behaviour

We predicted that *Pan* and *Gorilla* would significantly differ from *Homo* and *Pongo*, but not from each other, in having a trabecular structure of the distal femur that reflected habitual use of a flexed knee posture during terrestrial and arboreal locomotion. This prediction was not fully supported. Compared to higher rBV/TV in the inferior patellar articulation in *Homo*, we found rBV/TV concentration posterosuperiorly in the condyles and mediolaterally on the patellar articulation in African apes (Figure 4.3). This trabecular pattern is consistent with

higher and more uniaxial loading of the distal femur in a flexed knee posture, which is used during quadrupedal knuckle-walking and vertical climbing in both taxa (D'Aoŭt et al., 2002; 2004; Georgiou et al., 2020; Isler, 2005). However, we also found some trabecular patterns that separate *Gorilla* from *Pan* (Figure 4.3; Figure 4.9). The more homogenous rBV/TV distribution between and within both condyles of distal femur in *Pan* compared to *Gorilla* (Figure 4.3) may reflect the more variable knee loading that has been documented during climbing in captive *Pan* (Isler, 2005). However, the trabecular pattern under the patellar articular surface in *Pan* (Figure 4.9) suggested an opposite functional signal, with higher lateral loading of the patellar articular surface, which might be related to the quadriceps muscles that are active regardless of climbing posture and thus always pulling on the patella in the same way. Moreover, high rBV/TV was also found beneath the presumed insertions of gastrocnemius and under the presumed insertions of femoral ligaments (Figure 4.4-4.6) (see below). *Gorilla* and *Pan* both displayed the highest DA in the posteroinferior/superior regions of (especially) the medial condyle (Figure 4.7), which is again consistent with their stereotypically flexed knee postures and higher loading of medial knee compartment (Ankel-Simons, 2010; Crompton, Vereecke and Thorpe, 2008; D'Août et al., 2004; Georgiou et al., 2018; Hofstetter & Niemitz, 1998; Isler, 2005; Kozma et al., 2018; Lee at al., 2012; Pontzer et al., 2009). High DA was also found at the presumed insertion sites of muscle tendons (Figure 4.7-4.8; Supplementary Figure S4.5) (see below).

4.8.3 *Pongo* trabecular bone structure and locomotor behaviour

We predicted that *Pongo* would exhibit the most homogenous trabecular distribution across the distal femur compared to other apes due to their more variable knee joint postures during locomotion. This prediction was not fully supported. Even though *Pongo* trabecular structure was found to be quite homogenous, *Pan* also exhibited a similar pattern (Figure 4.3). Like African apes, *Pongo* did not show trabecular concentrations at the anterior regions of both condyles (Figure 4.3). *Pongo* shared with *Pan* low rBV/TV in the posteroinferior region of the medial condyle but had higher rBV/TV in the posteroinferior region of the lateral condyle (Figure 4.3). This pattern may suggest higher lateral loading during knee extension or higher degree of knee extension in *Pongo* compared with *Pan*. Posterior regions of both condyles were anisotropic as in African apes in *Pongo*. Moreover, we found rBV/TV concentration beneath the presumed insertions of gastrocnemius and under the presumed insertions of femoral ligaments (Figure 4.4-4.6) (see below). As in *Homo* and African apes, highly aligned trabeculae were also found at the presumed insertion sites of muscle tendons (Figure 4.7; Supplementary

Figure S4.5) (see below). *Pongo* is thought to have the most variable knee range of motion (Payne et al., 2006; Pina et al., 2014; Zihlman et al., 2011), together, these results are consistent with the highly mobile knee joint (Morbeck & Zihlman, 1988) that enables more variable loading during a diverse locomotor repertoire (Cant, 1987; Thorpe 2009; Thorpe & Crompton, 2006; Thorpe et al., 2007).

4.8.4 Sex differences in *Gorilla*

We predicted that female and male *Gorilla* would significantly differ from each other due to higher arboreality and/or more extended knee posture when climbing in females (e.g., Hammond, 2014; Isler, 2005). This prediction was supported. We found distinct sex differences in our *Gorilla* sample, with females showing higher rBV/TV concentration in the posterior regions of lateral condyle, laterally on patellar surface, and medially above intercondylar fossa (Figure 4.11A). In contrast, *Gorilla* males had higher rBV/TV concentrations in the medial epicondyle (Figure 4.11A). This sex pattern could suggest that in females there is higher lateral knee compartment loading and/or a more extended knee posture, as previously discussed in some studies (Crompton et al., 2008; Hofstetter & Niemitz, 1998; Isler, 2005; Kozma et al., 2018) compared to more flexed knee position and/or greater lateral knee rotation during extension in males. Lateral knee rotation during extension has been previously discussed in *Pan* (Lovejoy, 2007), but it is currently unknown if this rotation is also found in *Gorilla*. Additionally, it is possible that low degree of extension (more common in males) is compensated for by the lateral rotation, but when the knee is highly extended, there may be more medial knee rotation (more common in females). Alternatively, when the knee flexes, posterior regions of the femoral condyles are expected to resist continuous compression, resulting in denser bone in these regions (Georgiou et al., 2018; Sylvester & Terhune, 2017). Thus, rBV/TV values potential higher increase in medial condyle compared to lateral condyle, as seen in our *Gorilla* male sample, could also suggest higher knee flexion in males compared to females. Moreover, we found females separating from males due to the higher anisotropy under both presumed insertions of gastrocnemius muscle (Figure 4.11b) (see below). However, the discussion of locomotor behaviour of lowland *Gorilla* is limited by lack of locomotor data in wild populations; with the exception of Remis (1994, 1995), all other locomotor studies derive from mountain gorillas (e.g., Doran, 1997; Thompson et al., 2018).

4.8.5 Can trabecular structure underlying ligament/tendon attachments inform loading?

Our analysis also highlighted clear concentrations of rBV/TV at the presumed insertion sites of muscle tendons and knee joint ligaments (Figure 4.4-4.6) and high DA at the presumed insertion sites of muscle tendons in all taxa (Figure 4.7-4.8; Supplementary Figure S4.5). High rBV/TV values in the presumed insertions of cruciate ligaments illustrate that loading of these ligaments is resulting in modelling of underlying trabecular bone. Higher bone density at both cruciate ligaments insertion sites in all taxa (Figure 4.4) likely reflects the need to protect and stabilize the femur from dislocation throughout its range of motion. However, at both ligament insertion sites, *Pan* and *Pongo* showed higher trabecular density that extended deeper into the epiphysis compared with *Gorilla* (Figure 4.4), which may reflect more variable knee loading in the former. Potential support for this hypothesis would be more well-developed trabeculae under the cruciate ligament sites in female *Gorilla* compared to males, which we did find (Figure 4.11a). In addition, loading of the collateral ligaments also appears to stimulate increased rBV/TV under their insertion points in all taxa. Collateral ligaments, in theory, should be loose when the knee is flexed to allow more rotational movements, and tightened when the knee is extended. Here it seems they are equally loaded in African apes, which could suggest a certain degree of medial and lateral knee rotation when knee is not in full flexion (eventually when knee is extended). Lateral knee rotation during knee extension has been previously discussed in *Pan*. However, this would imply higher bone density under the insertion of medial collateral ligament compared to lateral collateral ligament. The separation of *Homo* from great apes was driven primarily by differences in trabecular structure at both collateral ligament insertion sites (Figure 4.9), suggesting different loading when knee is in extension and/or flexion.

In humans, gastrocnemius is a complex muscle that is involved in running, jumping and other fast movements of the leg, and to a lesser degree in walking and standing (e.g., Huijing, 1985; Ishikawa et al., 2007; Maganaris, 2003; Muramatsu et al., 2001). The distribution of rBV/TV beneath the insertions of gastrocnemius in *Homo* could result from forceful extension of knee and/or the hip joint in our sample (Anderson & Pandy, 2001; Baltzopoulos, 1995; Georgiou et al., 2020; Hardt, 1978; Simpson & Pettit, 1997; Taylor et al., 2004; Zheng et al., 1998). The specific activation of this muscle during different locomotor and postural activities in *Homo* is not known (Ishikawa et al., 2007), but the highly aligned trabeculae in the presumed insertions of gastrocnemius suggest that this region of the bone is loaded frequently and in a similar direction. Although Stern & Susman (1981) did not measured the activity of the gastrocnemius

muscle, they found activation of the gluteus medius and, to a lesser extent, the gluteus superficialis muscles to be similar in African ape climbing as in humans during bipedality. Since gastrocnemius is in action during most of the hindlimb activities in *Homo* (Georgiou et al., 2018; Ishikawa et al., 2007; Lichtwark et al., 2006; Neptune et al., 2001), it is presumably actively involved during arboreal locomotion in African apes as well. It has been previously found that gastrocnemius muscle becomes an extensor at highly flexed postures of the knee (Goh et al., 2017). Both *Pan* and *Gorilla* are characterized by flexed knee postures during quadrupedalism (Finestone et al., 2018) and particularly during climbing (Crompton et al., 2008; D' D'Août et al., 2002; Hofstetter & Niemitz, 1998; Isler, 2005; Kozma et al., 2018) and thus, we would not expect they would separate from each other based on both presumed gastrocnemius insertions. We suggest that this could be the case of either more robust quadriceps muscle in *Gorilla* (e.g., Zihlman et al., 2011) or this muscle is somehow involved more during locomotion in *Gorilla* compared to *Pan.* The separation of female *Gorilla* from male *Gorilla* due to the higher anisotropy under both presumed insertions of gastrocnemius muscle suggests more stereotypical loading of gastrocnemius muscle in females compared to males and that perhaps this muscle is more active during climbing, which female *Gorilla* are thought to do more frequently than males (Isler, 2005; Kozma et al., 2018). The high rBV/TV and DA values in both presumed insertions of gastrocnemius muscle in *Pongo* could be the result of the involvement of this muscle during suspension by the lower limbs, which is common in *Pongo* (Thorpe & Crompton, 2006).

We also found that *Gorilla* and *Pan* are distinguished from *Pongo,* and likewise male *Gorilla* from female *Gorilla*, in their much more aligned trabecular structure at the presumed insertions of vastus lateralis and medialis. In quadrupedal primates, vastus lateralis and medialis are pulled towards the joint as the knee is flexed, causing the moment arm to decrease with increasing flexion (Krevolin et al., 2004; Spoor & Van Leeuwen, 1992; Visser et al., 1990). Thus, this might be a result of higher knee flexion in African apes compared to *Pongo* and of higher knee flexion in male *Gorilla* compared to female *Gorilla*. However, it is not clear if this anisotropy is caused by the contraction of vastus medialis and lateralis or/and joint reaction forces experienced by the femoral condyles towards the shaft.

4.8.6 Trabecular bone and body mass

Although current research on allometry has not yielded consistent results (e.g., Barak et al., 2011; Cotter et al., 2009; Doube et al., 2011; Ryan & Shaw, 2013), one of the factors affecting trabecular bone structure is body mass. Thus, comparative research incorporating taxa of variable body mass should consider the effects of allometry when interpreting biomechanical and behavioral signals (Ruff et al., 2006). As body size increases, the gravitational forces also increase and thus the loads imposed upon the joints are higher (Doube et al., 2011). As bones get longer, they tend to become more robust in overall external shape (Doube et al., 2011). Altering any of several properties of trabecular bone such as its volume, thickness or number can be an effective way to resist increasing joint loads caused by increasing body mass (Currey, 2003; Doube et al., 2011). Trabecular thickness, spacing, connectivity and number has been shown to significantly correlate with body mass such that trabeculae are thinner, more widely spaced and more numerous in smaller mammals compared to larger mammals (e.g., Barak et al., 2013; Cotter et al. 2009; Doube et al. 2011; Ryan & Shaw, 2013; Saers et al., 2019). In contrast, BV/TV and DA show no significant correlation with body mass and are considered to be relatively constant across species of various sizes (Barak et al., 2013; Cotter et al. 2009; Doube et al. 2011; Ryan & Shaw, 2013). However, Barak et al. (2013) also noted that BV/TV can increase through different mechanisms depending on body mass; in humans (70 kg), BV/TV increased via increases in trabecular thickness while in rodents (e.g., 40 g and orders of magnitude smaller), BV/TV increased via increases in trabecular number (Barak et al., 2013).

In our study, average body mass varies from 36 kg (female *Pongo*) to 170 kg (male *Gorilla*; Smith & Jungers, 1997) and previous studies of extant hominid trabecular bone structure confirm no significant allometric effect on the variables (BV/TV and DA) that we analysed (e.g., Barak et al., 2013; Cotter et al., 2009; Ryan & Shaw, 2013). We found no significant allometric relationship on interspecific level across our sample and only a weak significant negative relationship in *Pan* (sexes pooled) on the intraspecific level. Thus, we consider allometry to have little to no effect on our results of rBV/TV distribution and species separation. However, future investigation on intraspecific allometric effects on larger samples of females and males within each taxon, particularly for highly sexually dimorphic taxa, would be interesting to explore in more detail.

4.8.7 Limitations

There are some limitations to this study that should be acknowledged. Firstly, the colour maps of DA show regions with high/low anisotropy, but do not show the direction in which the trabeculae are oriented (Figure 4.7-4.8; Supplementary Figure S4.3-S4.5). The technical limitation of cHMA is that vectors and tensors cannot (yet) be transformed into the canonical space. Thus, we did not quantitatively explore the direction of loading in the highly anisotropic parts of distal femur (especially under the presumed insertions of vastus lateralis and medialis tendons). We suggest that future studies of trabecular structure should explore difference in the direction of trabecular orientation in extant primates; this may provide more informed functional interpretations of how the ligaments and muscles are involved in knee movements during specific types of locomotion. In addition, our functional interpretations are also limited by a lack of kinetic and kinematic data of the knee in non-human great apes, and most notably in wild populations.

Secondly, our study also found that *Pongo* has the most homogenous trabecular distribution, which is expected but also may be the result of the conflation of two *Pongo* species. The difficulty in obtaining high-resolution CT scans of complete adult *Pongo* distal femur also resulted in a lower sample size for this group and thus we were not able to explore sex differences. Future analysis of a larger *Pongo* sample could lead to a better understanding of knee postures/loading of this taxon.

Lastly, analyses of sex differences of *Homo* were limited by the lack of sex information for most of the sample. Sex for only 11 (male) individuals was known. These individuals are from Mary Rose population only and thus sex differences could have been tested only by splitting *Homo* populations. However, even though we see partial separation between the populations, the relative PCA positions for rBV/TV and DA remained constant when PCA for studied species was split by *Homo* population (Supplementary Figure S4.7).

4.9 Conclusion

This study provided a holistic approach of trabecular bone architecture within the hominid distal femur. We showed that trabecular pattern distinguishes taxa based on their locomotor repertoires. Trabecular structure in *Homo* reflects habitual use of extended knee postures during bipedalism, habitual use of flexed knee posture during terrestrial and arboreal locomotion in African apes, and the highly mobile knee joint in *Pongo*. Moreover, our results reflect differences in the level of knee extension/flexion between female and male *Gorilla*, which is consistent with our current understanding of greater arboreality in female *Gorilla*. Trabecular structure was not significantly different between sexes in *Pan* or *Homo*, which also reflects greater similarity in their locomotor behavior between sexes. The emergence and form of bipedality in fossil hominins remains a central research focus in paleoanthropology (Barak et al., 2013; Carey & Crompton, 2005; Fajardo et al., 2007; Griffin et al., 2010; Raichlen et al., 2010; Ryan & Ketcham, 2002; Saparin et al., 2011; Shaw & Ryan, 2012; Skinner et al., 2015; Stern & Susman, 1983; Susman, 1991; Susman et al., 1984) and extant great apes are often used to model aspects of fossil hominin locomotor repertoire, including the frequency of arboreality and types of bipedalism (e.g., facultative versus obligate). This study offers a comparative sample of trabecular structure in the hominoid distal femur and can contribute to future studies of locomotion in extinct taxa.

4.10 Supplementary material

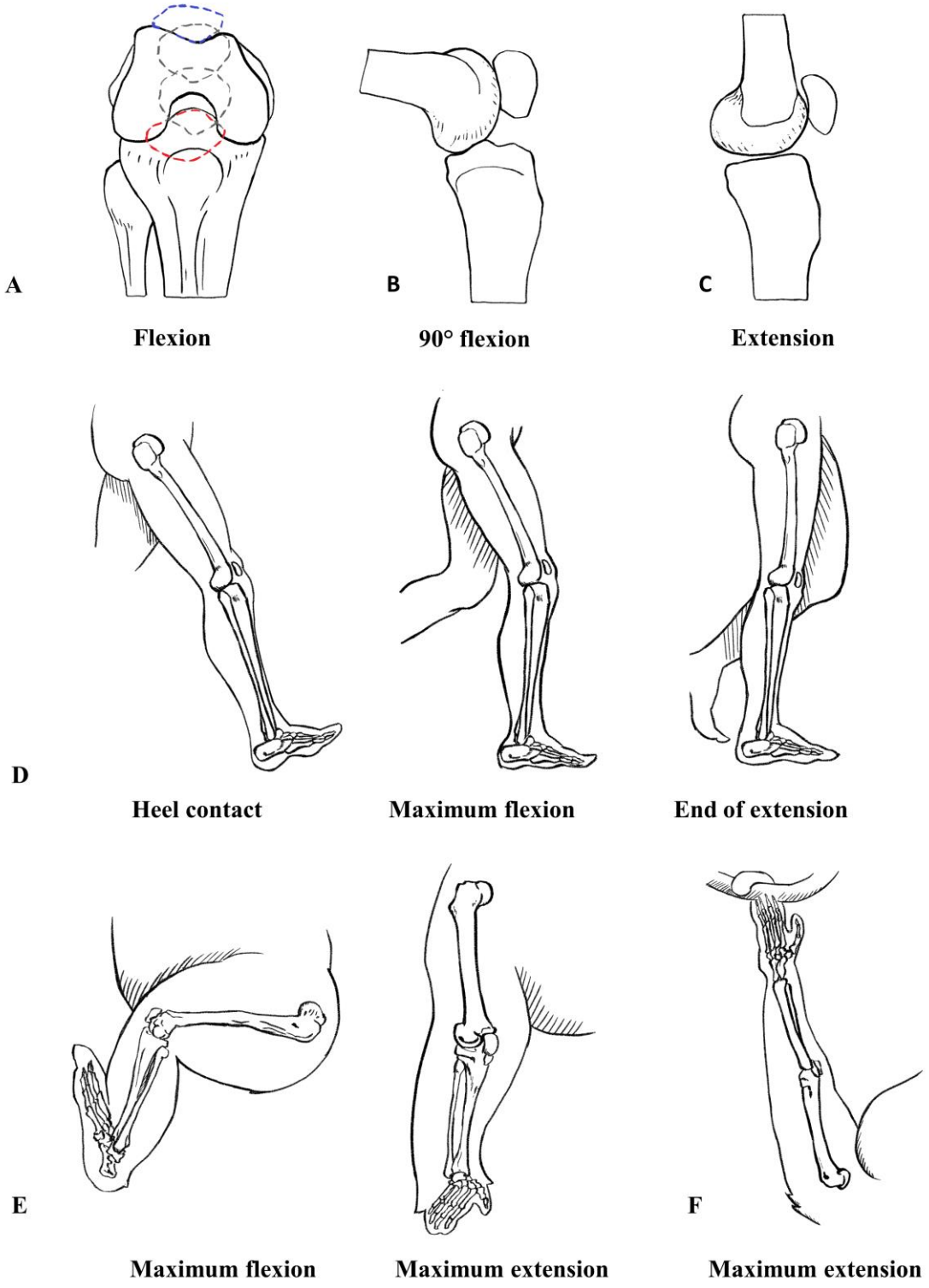

Figure S4.1: (A) Patella position during the range of flexed-extended knee showing in inferior view; red, maximum flexion; blue, maximum extension. (B) Patella position during 90° knee flexion showing in medial view. (C) Patella position during maximum knee extension in medial view. (D) Expected human knee posture during bipedal walking. (E) Expected *Gorilla* and *Pan* knee posture in maximum flexion during vertical climbing and maximum extension during terrestrial knuckle-walking. (F) Expected *Pongo* knee posture during arboreal locomotion.

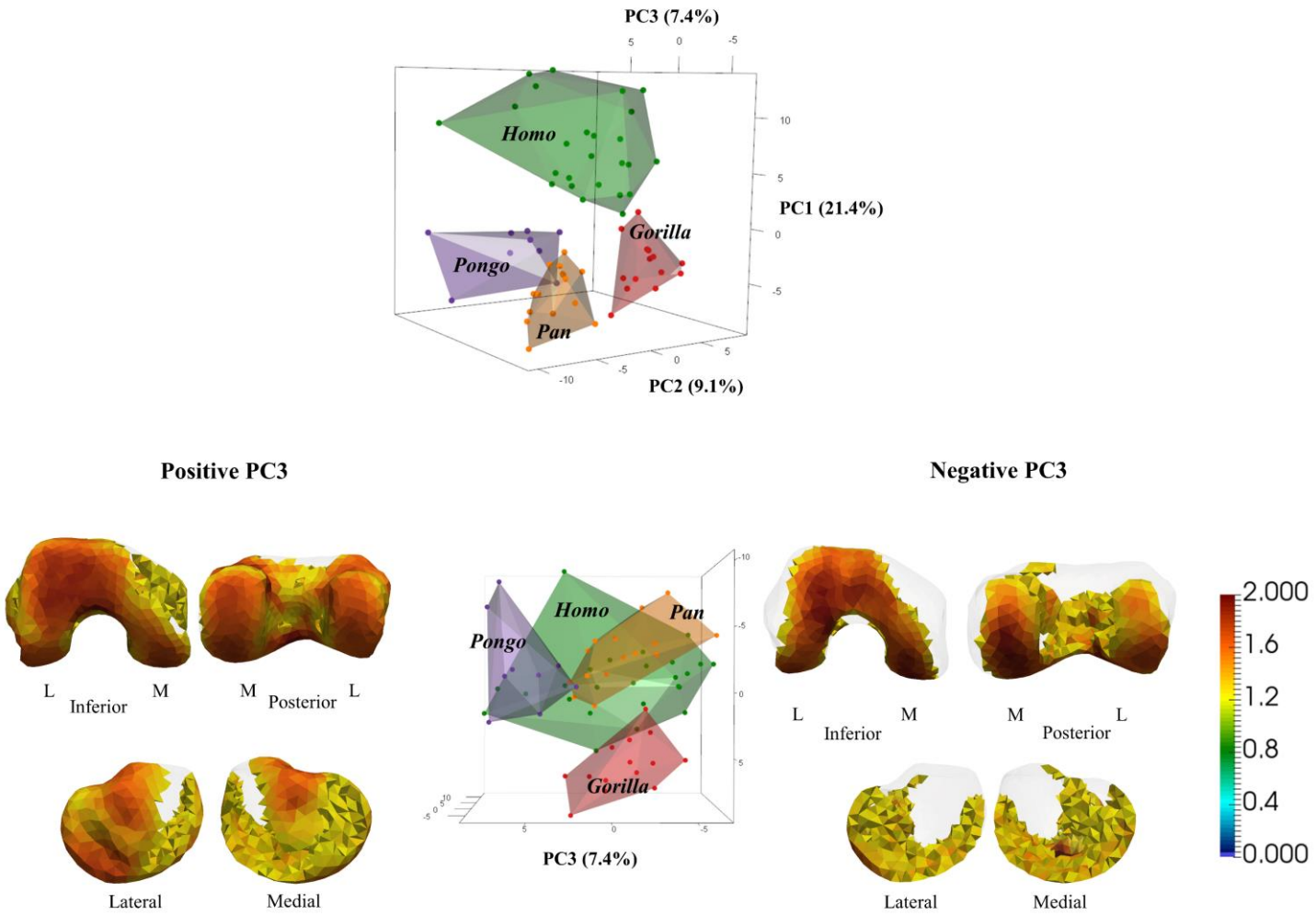

Figure S4.2: PCA of rBV/TV distribution in the distal femur of *Homo*, *Gorilla*, *Pan*, and *Pongo* showing separation among studied taxa. Thresholding models represent high 30% of the range of rBV/TV values for negative and positive PC3. Models demonstrate the highest loading causing the separation between *Pongo* (positive PC3+3SD) and *Gorilla*, *Pan* (negative PC3-3SD). L, lateral; M, medial; D, distal; P, posterior; I, inferior; S, superior.

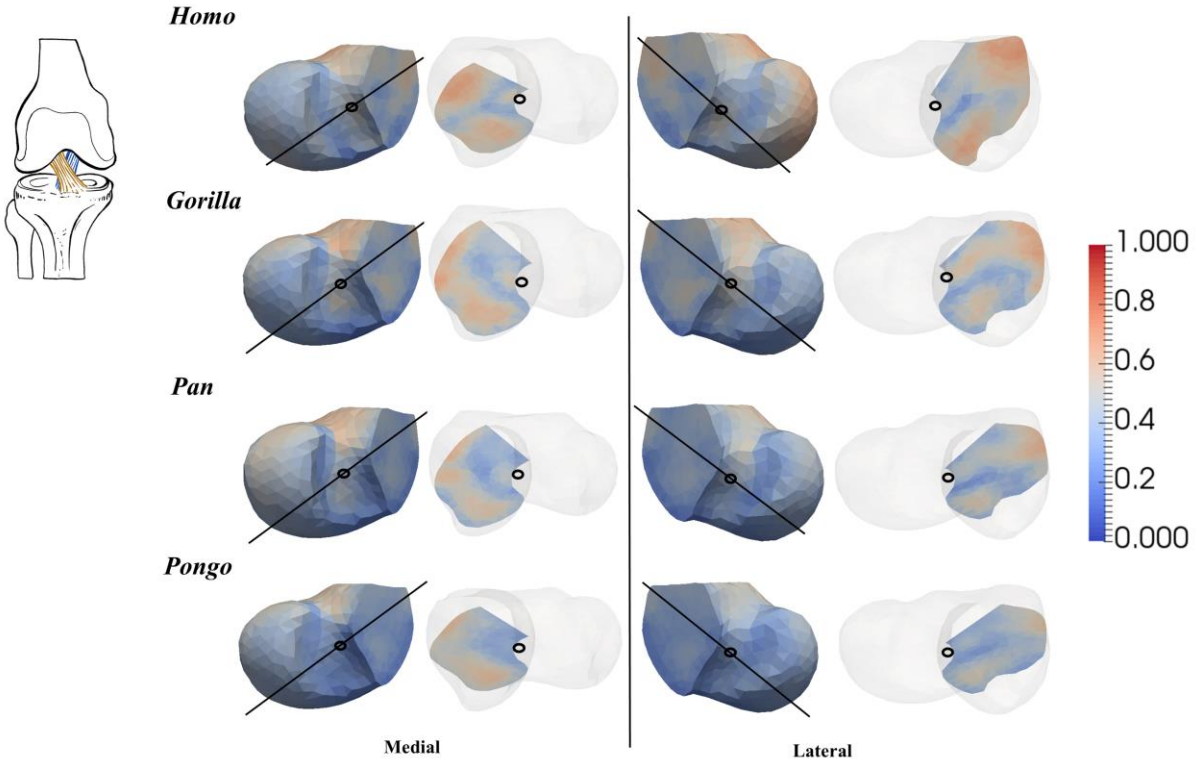

Figure S4.3: Species mean models of DA distribution under the presumed insertions of cruciate ligaments of the distal femur of *Homo*, *Gorilla*, *Pan*, and *Pongo*. Vertical lines through the mean medial and lateral models show where the slices are positioned. Cross sections were positioned in the middle of presumed insertions of cruciate ligaments. Knee model shows cruciate ligaments during neutral knee position. D, distal; P, posterior; I, inferior; S, superior.

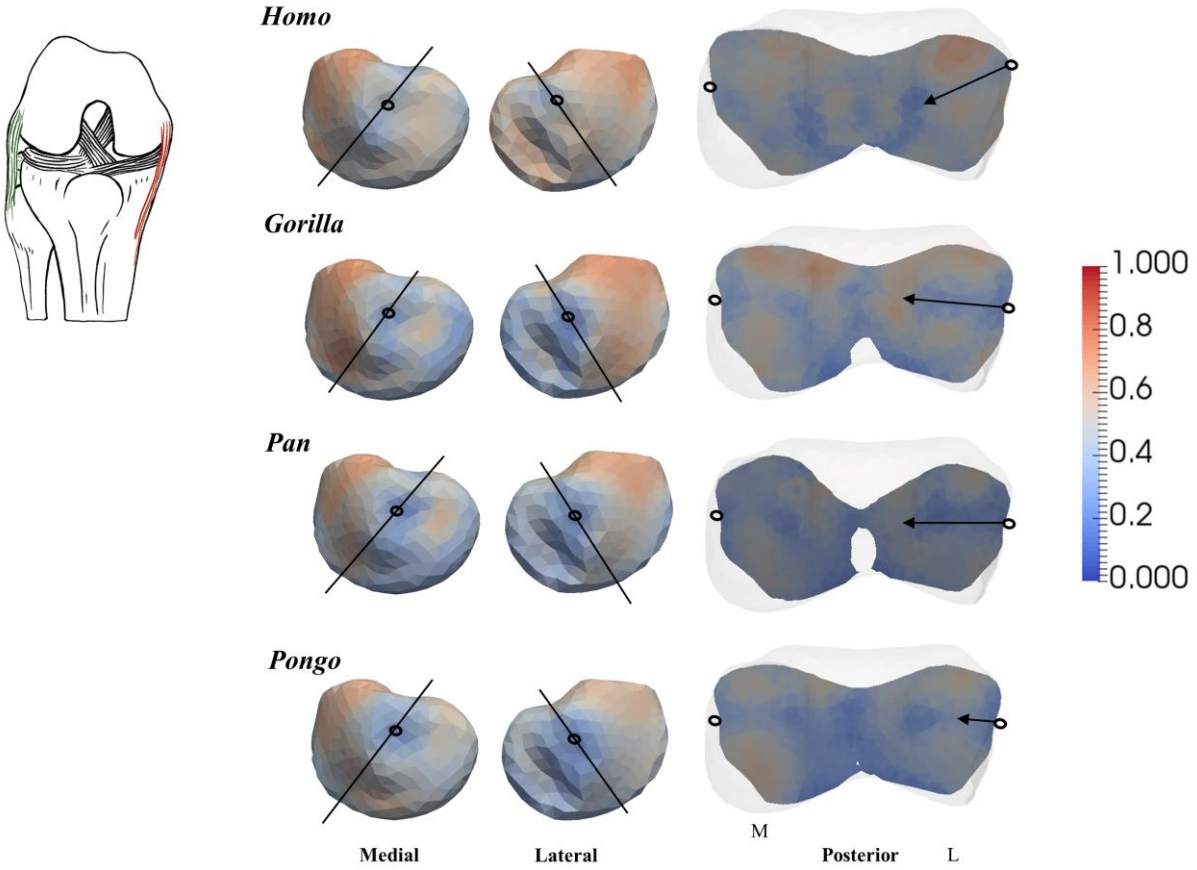

Figure S4.4: Species mean models of DA distribution under the presumed insertions of collateral ligaments of the distal femur of *Homo, Gorilla, Pan,* and *Pongo.* Vertical lines through the mean medial and lateral models show where the slices are positioned. Cross sections were positioned in the middle of presumed insertions of collateral ligaments. Knee model shows collateral ligaments attachments in the inferior view. L, lateral; M, medial; D, distal; P, posterior; I, inferior; S, superior.

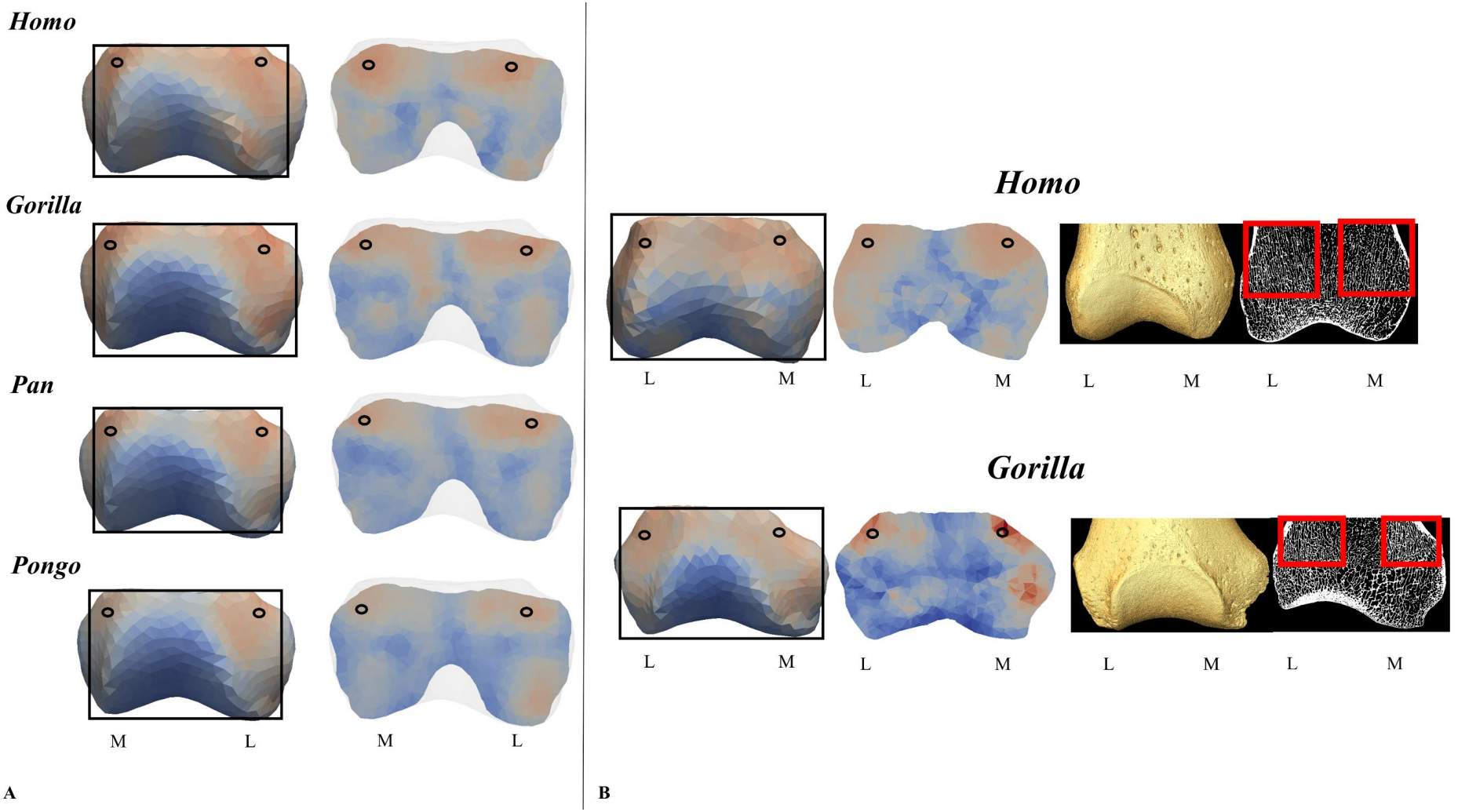

Figure S4.5: (A) Species mean models of DA distribution in the anterior view of distal femur of *Homo*, *Gorilla*, *Pan*, and *Pongo*. (B) HMA and segmented models showing high DA concentration above the condyles of the right distal femur of *Homo* and *Gorilla* individual in the anterior view. Squares show where the slices are positioned. L, lateral condyle; M, medial condyle.

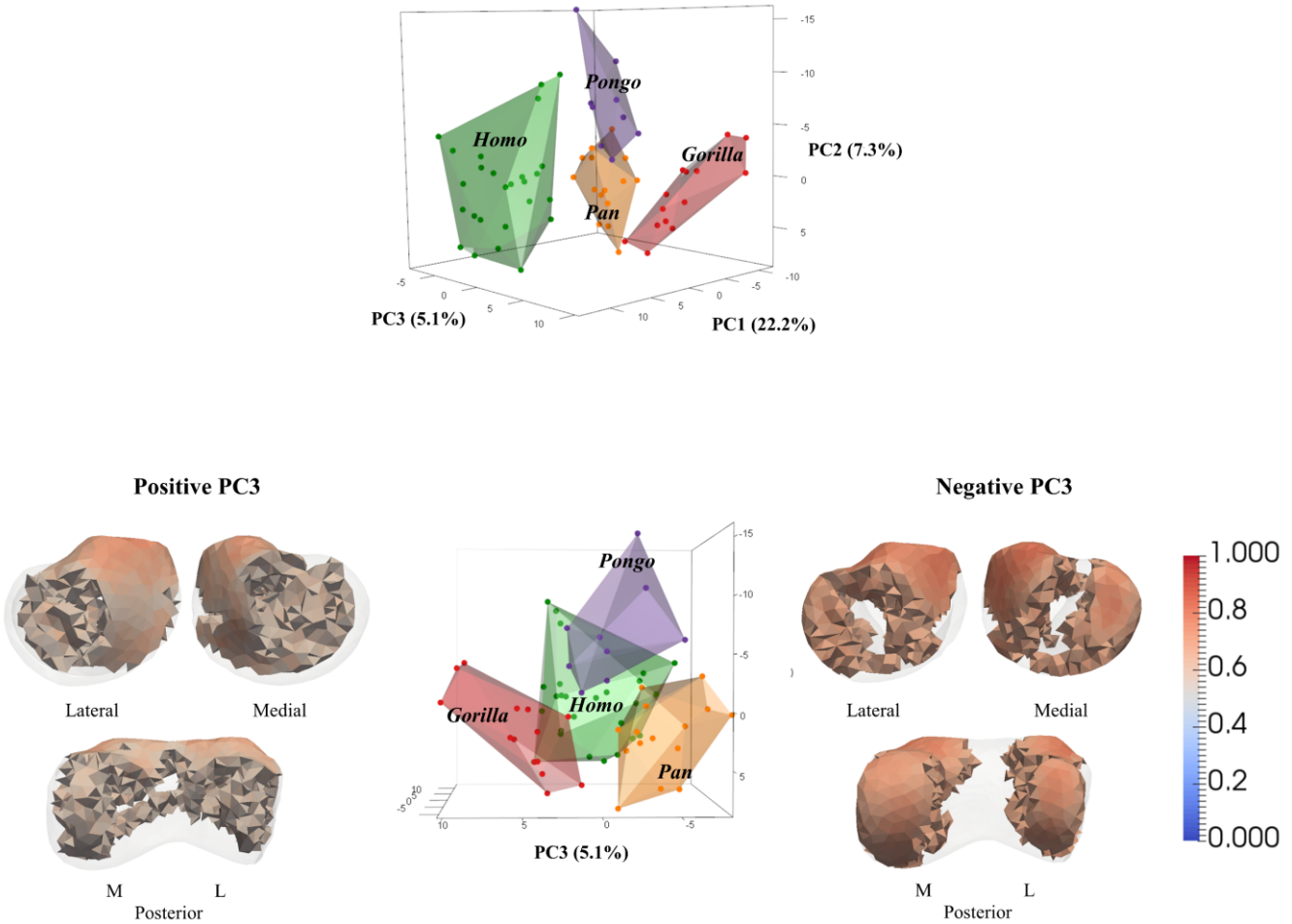

Figure S4.6: PCA of DA distribution in the distal femur of *Homo*, *Gorilla*, *Pan*, and *Pongo* showing separation among studied taxa. Thresholding models represent high 30% of the range of DA values for negative and positive PC3. Models demonstrate the highest loading causing the separation between *Gorilla* (positive PC3+3SD) and *Pan* (negative PC3-3SD). L, lateral; M, medial; D, distal; P, posterior; I, inferior; S, superior.

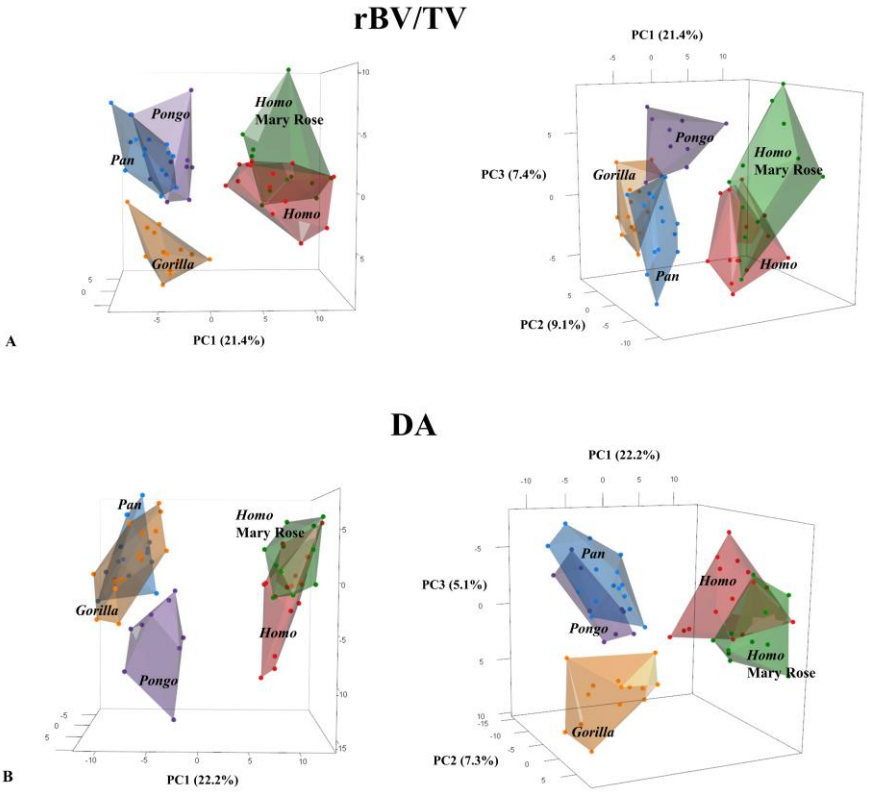

Figure S4.7: PCA of rBV/TV and DA distribution in the distal femur *Homo*. (A) PCA of rBV/TV distribution of *Homo* showing partial separation between Mary Rose (males) and rest of human sample (sex unknown). (B) PCA of DA distribution of *Homo* showing partial separation between Mary Rose (males) and rest of human sample (sex unknown).

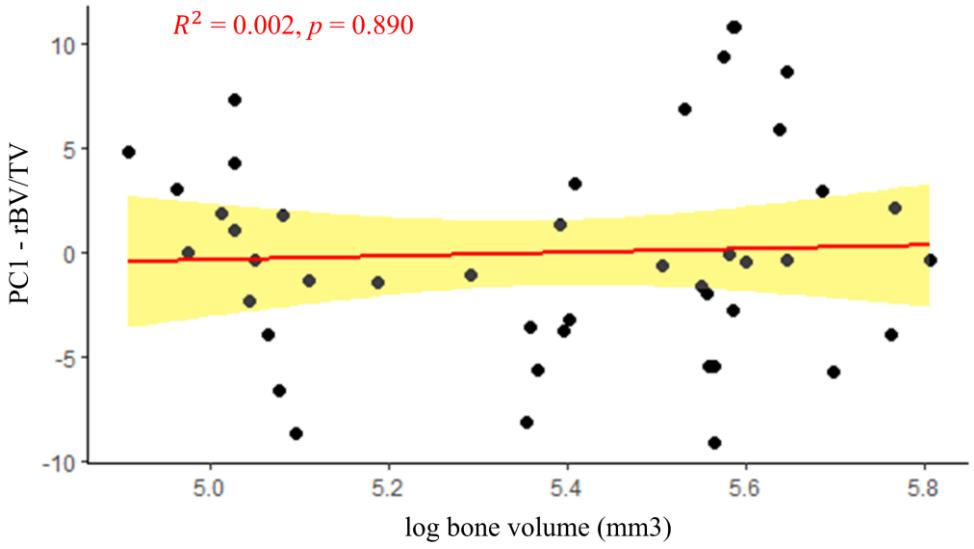

Figure S4.8: Covariation between PC1 of rBV/TV and bone volume in the distal femur of *Homo*, *Gorilla*, *Pan*, and *Pongo* showing no significant positive relationship between the variables.

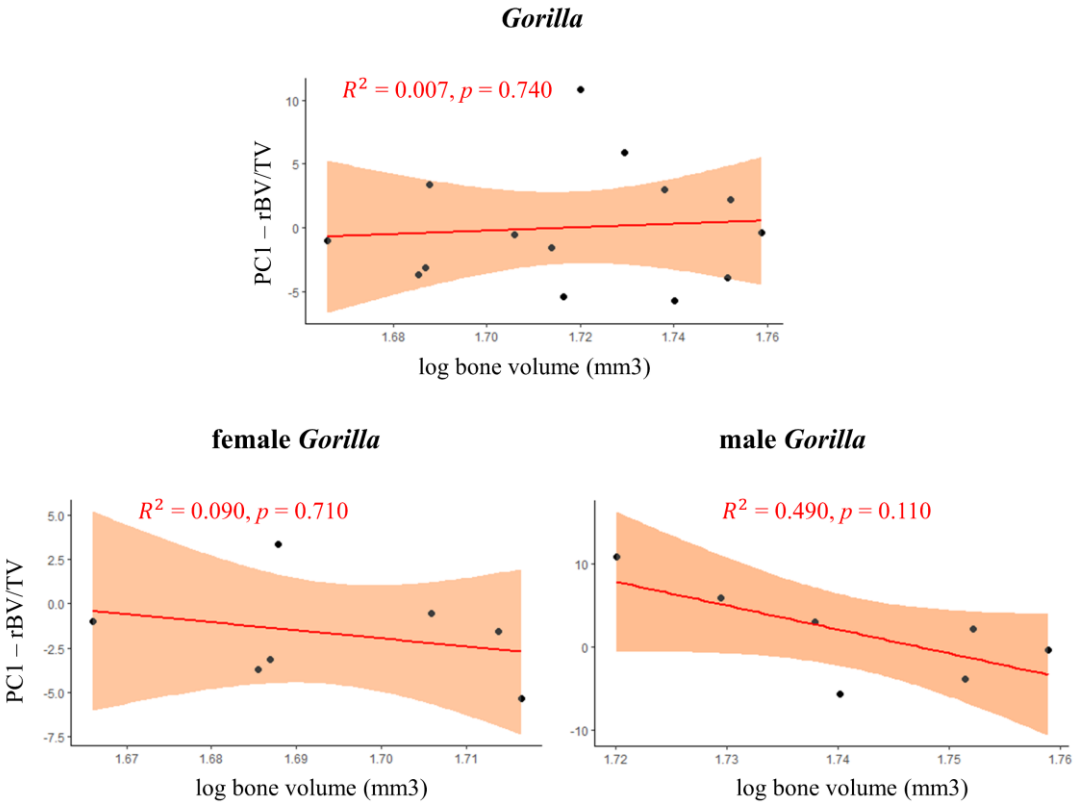

Figure S4.9: Covariation between PC1 of rBV/TV and bone volume in *Gorilla*, female *Gorilla* and male *Gorilla* showing no significant positive relationship in *Gorilla* and no significant negative relationship in female and male *Gorilla* between the variables.

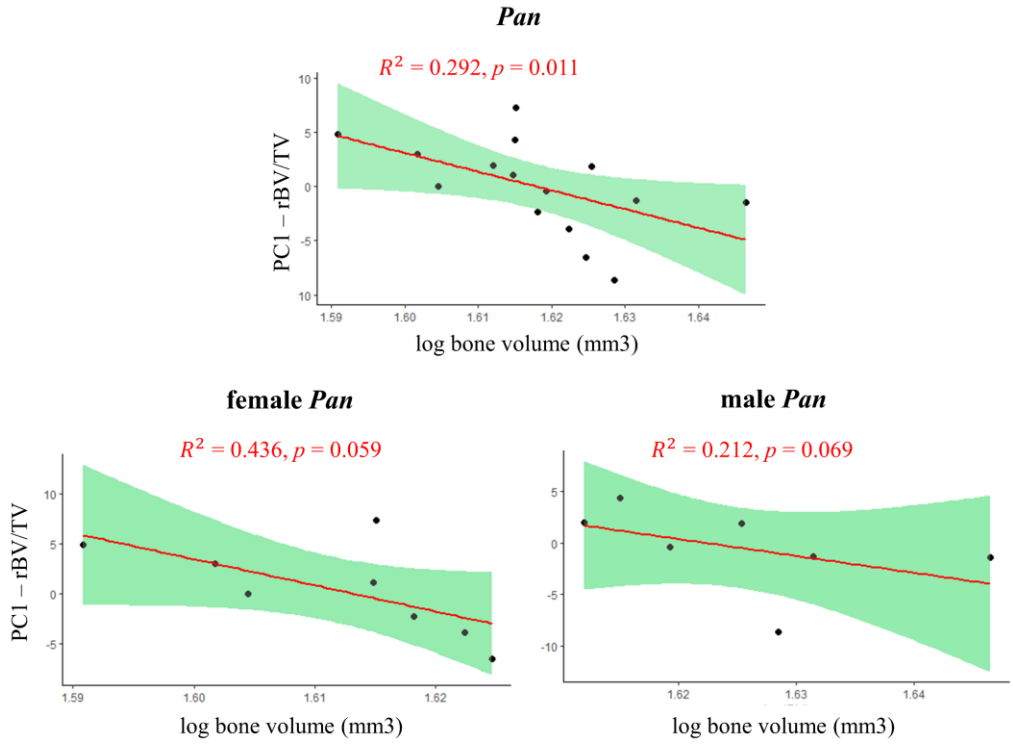

Figure S4.10: Covariation between PC1 of rBV/TV and bone volume in *Pan*, female *Pan* and male *Pan* showing significant weak negative relationship in *Pan* and no significant weak negative relationship in female and male *Pan* between the variables.

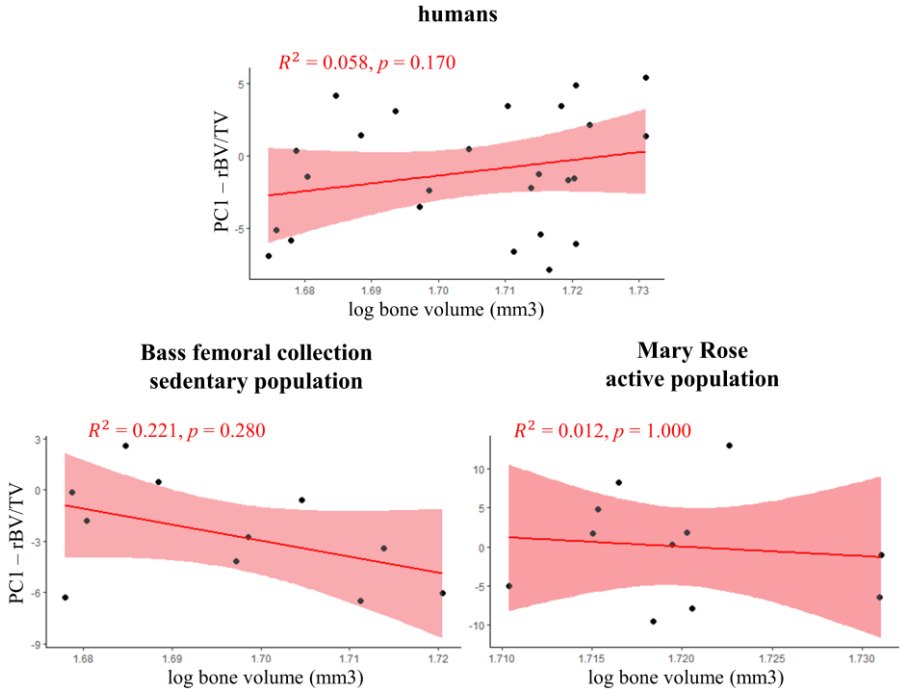

Figure S4.11: Covariation between PC1 of rBV/TV and bone volume in humans and separately for the studied human populations showing non-significant weak positive relationship in humans, no significant weak negative relationship in sedentary and in active populations between the variables.

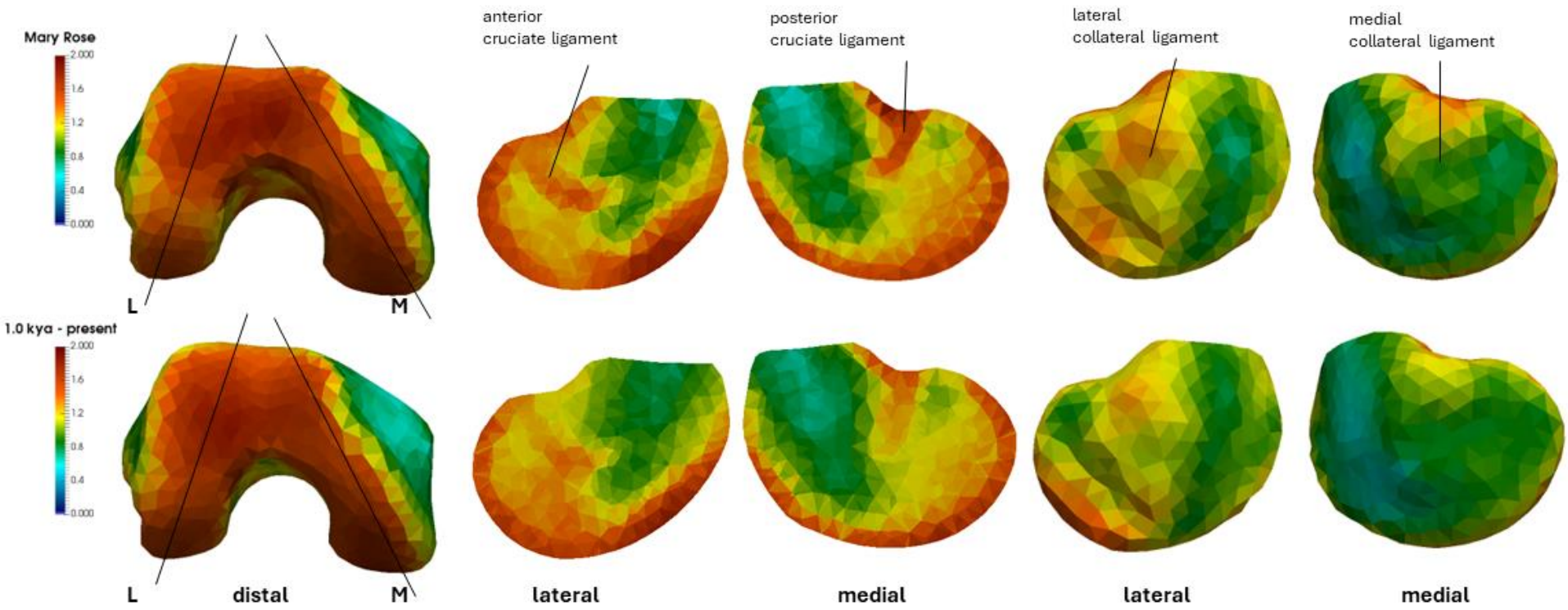

Figure S4.12: Mean models of rBV/TV distribution in the distal femur of human sample separated by populations. Mary Rose represents an active population while other individuals were taken from the sedentary population. Oblique slices are in the centre of the lateral and medial condyles. Vertical lines through the distal view mean models show where the slices are positioned. L, lateral condyle; M, medial condyle.

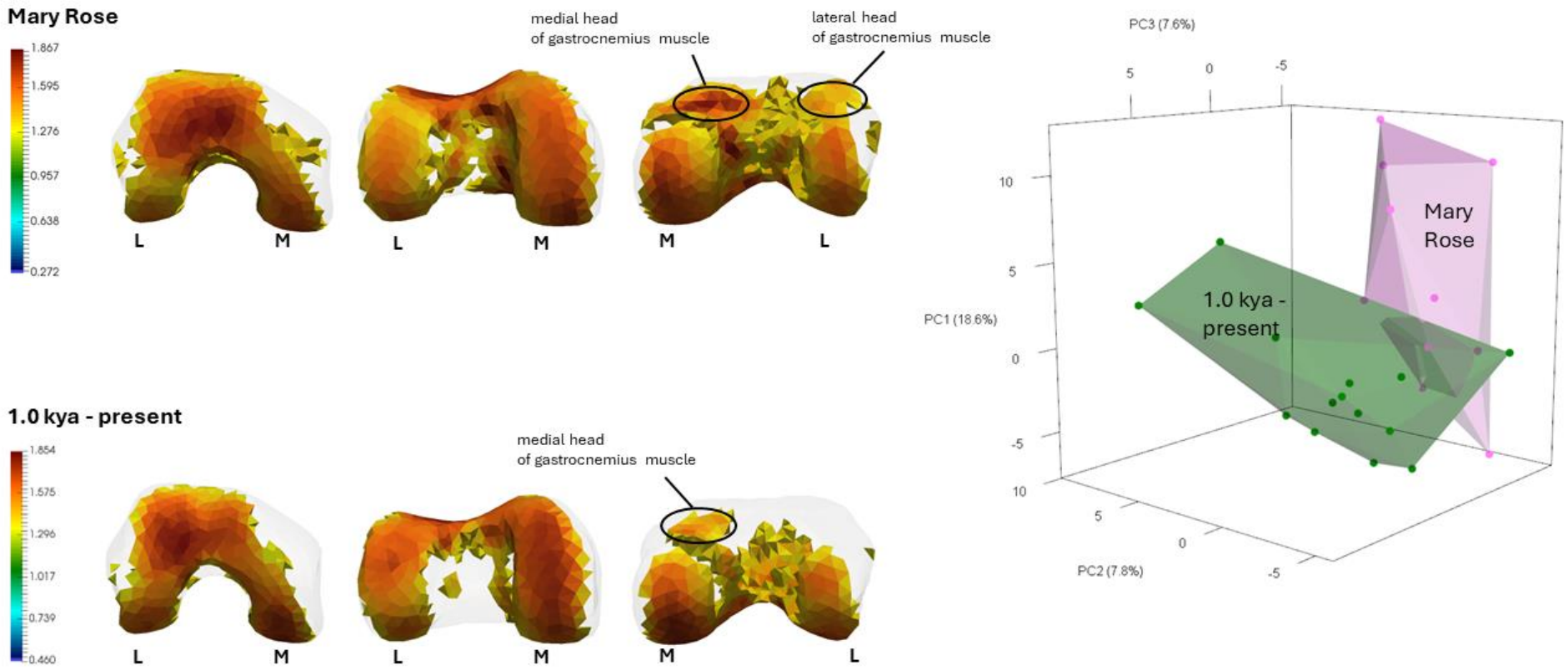

Figure S4.13: PCA of rBV/TV distribution in the distal femur of human sample showing separation between an active population (Mary Rose) and sedentary population (1.0 kya-present). Thresholding models represent a high 40 % of the range of rBV/TV values for the mean model of each group. Models demonstrate locations of the highest loadings causing the separation. L, lateral condyle; M, medial condyle.

5 TRABECULAR ARCHITECTURE OF THE PROXIMAL TIBIA IN EXTANT HOMINIDS

Article in review: Lukova, A., Bachmann, S., Synek, A., Pahr, D.H, Kilbourne, B., Dunmore, C.J., Kivell T.L, & Skinner, M.M. (2024). Trabecular architecture of the proximal tibia in extant hominids. *American Journal of Biological Anthropology*.

5.1 Abstract

Extant apes are characterized by a wide range of locomotor and postural behaviours that require each to use their limbs in different ways. Comparative investigation of trabecular bone can provide novel insights into bone functional adaptation related to limb use. Previous studies have examined trabecular bone structure in the hominoid knee joint but have focused on the distal femur only. This study is the first to examine trabecular structure of the proximal tibia in extant apes. We analyse the trabecular morphology of proximal tibial epiphysis of *Homo sapiens* (n=25), *Gorilla gorilla* (n=13), *Pan troglodytes* (n=15) and *Pongo* spp. (n=7). Trabecular bone was imaged using high-resolution microtomography and bone tissues were segmented using the medical image analysis clustering method. Canonical holistic morphometric analysis was used to analyse relative bone volume fraction and degree of anisotropy. Patterns of trabecular bone distribution within and between taxa were investigated via principal component analysis. Results indicate that trabecular distribution is consistent with habitual use of extended knee postures during bipedalism in *Homo*, and habitual use of flexed knee postures during terrestrial and arboreal locomotion in other great apes. Trabecular architecture within *Gorilla* suggests a higher degree of habitual knee extension in females compared to males, while *Pan* and *Homo* do not show significant sex differences in knee extension/flexion (*Pongo* sex differences could not be tested). We demonstrate that trabecular structure of the proximal tibia is consistent with habitual locomotor loading in extant hominids, which provides the comparative context to interpret knee posture and loading and, in turn, locomotor behaviours in fossil hominids.

5.2 Introduction

Extant primates are characterized by a wide range of locomotor behaviours and as such are often used as models to help reconstruct behaviour in fossil hominoid taxa (Cazenave & Kivell, 2023; Skinner et al., 2015; Tsegai et al., 2013; Vereecke, D'Aout & Aarts, 2011; Williams et al., 2014). Particularly, the morphology of the hindlimb has played a central role for understanding the emergences and the forms of hominin bipedality (Berillon et al., 2010; Carey & Crompton, 2005; Georgiou et al., 2020; Lovejoy & McCollum, 2010; O`Neill et al., 2015; Sockol, Raichlen & Pontzer, 2007; Stern & Susman, 1983; Susman, Stern & Jungers, 1984). Studying the morphology of the knee specifically, including how this joint is loaded during different types of locomotion in extant apes, can provide information about how early hominins walked bipedally, as well as other potential locomotor behaviours in which they may have engaged (Carey & Crompton, 2005; Lovejoy & McCollum, 2010; Stern & Susman, 1983; Susman, et al., 1984). Associations between extant hominid lower limb morphology and locomotor mode have been previously studied. For example, Carlson (2005) found more circular femoral cross-sections in apes that engage more frequently in arboreal locomotion compared to those who engage more in terrestrial locomotion. Ruff (2002) reported that more arboreal species show relatively stronger forelimb shafts than hindlimb shafts compared to more terrestrial species. Moreover, internal bone structure differences between humans and non-human apes, that most likely reflect differences in bone loading during different locomotion repertoires, have been found in the femoral neck (Cazenave et al., 2022; Demes et al., 2000; Lovejoy, 1988; Ohman et al. 1997; Rafferty, 1998), femoral head/proximal femur (Cazenave et al., 2019; Chirchir, 2016; Coelho et al., 2009; Georgiou et al., 2020; Volpato et al., 2008) and in the distal tibia and talus (Chirchir, 2016; DeSilva, 2009; DeSilva & Devlin, 2012; Su et al., 2013; Sorrentino et al., 2021; Tsegai et al., 2017).

Only three previous studies have specifically examined trabecular bone structure within the knee joint in a sample of extant primates (Georgiou et al., 2018; Lukova et al., 2024; Sylvester & Terhune, 2017), and all of these focused only on the distal femur. Trabecular structure in the proximal tibia has been investigated exclusively in humans (Kamibayashi et al., 1995; Novitskaya et al., 2014; Saers et al., 2016; Sugiyama et al., 2012; Thomsen et al., 2005), with the exception of Mazurier et al. (2010) who compared humans with non-human primates; however, their focus was only on the cortico-trabecular complex underlying the tibial plateau.

Functional interpretations of external bone morphology ca be complicated by phylogenetic inertia, in which some morphological traits may be more the result of common ancestry among

closely related species and less the result of biomechanical demand (Briggs, 2017; Cubo et al., 2008; Griffin et al., 2019; Rickman et al., 2023; Ward, 2002; Wund, 2012). Internal bone structure also can be influenced by genetic factors or phylogeny (Cubo et el., 2005; Lieberman, 1997). However, experimental studies have previously demonstrated that cortical and, in particular, trabecular bone are able to functionally adapt their structure to the magnitude and direction of joint load (Barak et al., 2008; Currey, 2006; Pontzer et al., 2006; Barak et al., 2011). Thus, trabecular and internal cortical bone can be informative for reconstructing locomotor behaviour during life (Dunmore et al., 2023; Chirchir et al., 2017; Georgiou et al., 2018; Georgiou et al., Skinner, 2019; Raichlen et al., 2015; Ryan & Shaw, 2012; Ryan & Van Rietbergen, 2005; Saers et al., 2022; Skinner et al., 2015; Tsegai et al., 2018). A relationship between trabecular patterns and assumed lower limb loading during locomotion has been previously found in the hip (Cazenave et al., 2019; Coelho et al., 2009; Dalstra et a., 1993; Demes et al., 2000; Georgiou et al., 2020; Saers et al., 2016; Volpato et al., 2008; Zaharie & Phillips, 2018), knee (Georgiou et al., 2018; Kamibayashi et al., 1995; Lukova et al., 2024; Mazurier et al., 2010; Novitskaya et al., 2014; Saers et al., 2016; Sylvester & Terhune, 2017; Thomsen et al., 2005) and ankle joints (Barak et al., 2013; Saers et al., 2016; Su et al., 2013; Su et al., 2017; Sylvester & Terhune, 2017; Tsegai et al., 2017). Moreover, previous studies have shown an association between trabecular bone (re-)modelling and the gait changes that occur with the development of bipedalism in humans (Barak, 2019; Gosman & Ketcham, 2009; Milovanovic et al., 2017; Raichlen et al., 2015; Ryan & Krovitz, 2006). In this study, we investigate trabecular bone patterning in the proximal tibiae of extant apes in relation to knee joint posture during locomotion.

Some studies that focused exclusively on a single region within the epiphyses of lower limb bones have not consistently detected clear postural or locomotor signal in the knee (Barak et al., 2011; Carlson et al., 2008; Ryan & Walker, 2010; Shaw & Ryan, 2012; Wallace et al., 2013). In mouse models, the absence of significant differences in trabecular parameters in the distal femur, as observed by Carlson et al. (2008), has been attributed to the knee joint specialization for flexion/extension, which may inherently limit mediolateral movements and reduce the impact of cutting maneuvers on trabecular structure. Conversely, Wallace et al. (2013) reported differences in the proximal humerus trabeculae of mice to enhanced mediolateral and anteroposterior movements, indicating that trabecular bone responds more in joints with greater range of motion. These findings underscore the importance of considering species with different locomotor regimes. While these studies highlight methodological

differences, they also suggest that the degree of joint motion, especially in the anteroposterior plane, plays a critical role in (re-)modelling trabecular architecture. This is further supported by Barak et al. (2011), who observed changes in trabecular parameters in the distal tibiae of sheep in response to altered ankle flexion. Moreover, Polk et al. (2008) found that variations in loading conditions significantly influenced trabecular bone parameters in the sheep knee joint. Increased loading particularly in anteroposterior plane, led to noticeable changes in trabecular density and architecture.

Range of motion can lead to varied loading patterns across the joint surface. This variability in loading can result in a more complex and heterogenous trabecular structure as the bone adapts to the different stresses it encounters. For example, Ryan & Shaw (2012) demonstrated that the variation in knee flexion and extension among primates is reflected in the trabecular architecture of the distal femur. Species that habitually engage in more extended postures tend to have trabecular structure aligned with the primary axis of loading, suggesting adaptation to a more consistent pattern of force application in the anteroposterior plane. Similarly, Su et al. (2013) found that the femoral midshaft in humans, which experiences forces primarily along the long axis during bipedal walking, exhibits a more regular trabecular pattern compared to non-human primates. These studies suggest that in species with more extended limb postures, such as bipedal humans, trabecular bone may reflect more consistent loading patterns, leading to a more uniform trabecular architecture. Conversely, in species with more flexed limb postures, such as arboreal primates, trabecular bone is likely to be more variable in its density and structural characteristics, reflecting the greater diversity of forces experienced during locomotion.

A number of studies have demonstrated that analyzing a single sub-region of trabecular bone within an epiphysis (and away from the articular surface) fails to identify trabecular patterning related to habitual joint posture (e.g., Fajardo & Muller, 2001; Kivell et al., 2011; Skinner et al., 2015; Stephens et al., 2016; Sylvester & Terhune, 2017; Tsegai et al., 2013; Tsegai et al., 2018). Conversely, a whole-epiphysis approach which has been facilitated by recent developments in analytical software (e.g., Gross et al., 2014), can offer a more comprehensive understanding of how trabecular structure is modelled to reflect posturel and locomotor loading. We build upon these previous studies with a canonical holistic morphometric analysis (cHMA) approach to statistically analyse trabecular patterns free of *a priori* (Bachmann et al., 2022). In this study, we examine the trabecular structure of the entire proximal tibial epiphysis in modern

humans and other great apes (*Pan*, *Gorilla*, and *Pongo*) to explore how variations in knee joint loading during locomotion might influence trabecular architecture.

Differences in joint kinematics and frequency of specific types of locomotion, as well as variation in knee joint morphology across human and non-human primates, may influence load distribution across the tibial epiphysis and, in turn, affect trabecular bone (re-)modelling (Barak, 2019). Thus, understanding how extant primates move and how they use their limbs during the locomotion is essential for the interpretation of trabecular structure. Modern humans (*Homo sapiens*) are defined by their obligatory bipedal locomotion, where the knee remains fully or nearly fully extended for most of the walking cycle. During movement, the medial and lateral tibial condyles bear weight evenly across the tibial plateau (Figure 5.1) (Javois et al., 2009; Landis & Karnick, 2006; Lovejoy, 2007; Organ & Ward, 2006; Sylvester, 2013; Sylvester & Pfisterer, 2012; Tardieu, 1999). However, humans frequently participate in other activities, such as running, jumping, and squatting, where the knee's flexion-extension cycle varies (Mann & Hagy, 1980; Nilsson & Thorstensson, 1989; Racic et al., 2009). Both the medial and lateral tibial condyles are relatively evenly loaded through the tibial plateau during locomotion compared to other great apes. This even loading is due to the human knee adaptation for bipedalism, which emphasizes stability in upright posture and efficient energy transfer during gait (e.g., DeSilva, 2009; Richmond & Strait, 2000; Venkadesan et al., 2020). However, multiple studies have demonstrated that the medial compartment of the tibial plateau still experiences higher loads compared to the lateral compartment during various activities, with the highest medial compartment loading occurring during activities such as stair climbing (e.g., Andriacchi & Dyrby, 2005; D'Lima et al., 2006; Heinlein et al., 2009; Kutzner et al., 2010). The individual postural and locomotor activities habitually practised by our human skeletal sample are unknown. Therefore, we assume that all sampled individuals loaded their tibia primarily through bipedal walking but acknowledge that they likely engaged in other activities that may be reflected in the trabecular structure of proximal tibia as well.

Gorilla and *Pan* both engage most frequently in quadrupedal knuckle-walking but also engage in other terrestrial and arboreal locomotor activities (Bauer, 1977; Doran, 1993; Doran, 1996; Doran, 1997; Drummond-Clarke et al., 2022; Hunt, 1992; Isler, 2005; Remis, 1994; Tocheri et al., 2011). The knee is typically flexed to varying degrees during both terrestrial and arboreal locomotion (Ankel-Simons, 2010; D'Aoŭt et al., 2004; Finestone et al., 2018; Georgiou et al., 2018; Isler, 2005; Pontzer et al., 2009). In both *Gorilla* and *Pan*, the knee is mostly loaded in flexed and varus postures (Figure 5.1) where the medial tibial condyle is loaded more than the

lateral tibial condyle during both arboreal and terrestrial locomotion (Davis & Cummings, 2002; Richmond & Strait, 2000; Stern & Susman, 1983; Tardieu, 2002; Tardieu & Fritsch, 1991; Thorpe & Crompton, 2005). The differing size between femoral condyles in *Gorilla* and *Pan* causes mediolateral knee rotation (Freeman & Pinskerova, 2005; O'Neill et al., 2013; Tardieu, 1986) during all phases of terrestrial quadrupedal locomotion (Sylvester, 2013; Tardieu, 1999; Sylvester & Pfisterer, 2012). Previous studies have found that zoo-housed *Gorilla* extend their knees more during both terrestrial and arboreal locomotion (particularly vertical climbing) compared to *Pan* (Crompton et al., 2008; Finestone et al., 2018; Hofstetter & Niemitz, 1998; Isler, 2005; Kozma et al., 2018). In our study, *Gorilla* is represented only by *Gorilla gorilla gorilla* in which females show a greater range of motion at the hip and knee (Hammond, 2014; Isler, 2005). In *Pan*, the knee is mostly loaded in a flexed and varus posture, though lateral rotation of the knee occurs during extension, which increases load in the lateral knee compartment (Lovejoy, 2007). During climbing, *Pan* species may fully utilize the entire flexion-extension range of the knee (D'Aoŭt et al., 2002; Isler, 2005). In this study, *Pan* is represented exclusively by *Pan troglodytes verus* from the Taï National Forest in Ivory Coast. Previous research has found no significant sex differences in the overall frequency of arboreal and terrestrial locomotion within this community of chimpanzees (Doran, 1993).

Pongo is the most arboreal of the great apes, engaging most frequently in torso-orthrograde suspension, vertical climbing/descent and arboreal quadrupedal/tripedal walking (Thorpe & Crompton, 2006). *Pongo* also uses bipedality and hindlimb suspension during arboreal locomotion in which their knee posture ranges from hyper-flexed to extended (Isler, 2005; Morbeck & Zihlman, 1988; Payne et al., 2006; Thorpe & Crompton, 2006; Thorpe et al., 2009). However, during arboreal locomotion, flexion-extension range of motion at the knee in zoo-housed *Pongo* does not differ significantly from that of African apes (Isler, 2005; Morbeck & Zihlman, 1988; Tuttle & Cortright, 1988). However, during terrestrial locomotion, zoo-housed *Pongo* flexion-extension range of motion at the knee is similar to that of African apes (Kozma et al., 2018). In this study, *Pongo* is represented by *Pongo pygmaeus* and *Pongo abelii*. In both subspecies, females have been found to be more arboreal compared to males (Cant, 1987; Galdikas, 1988).

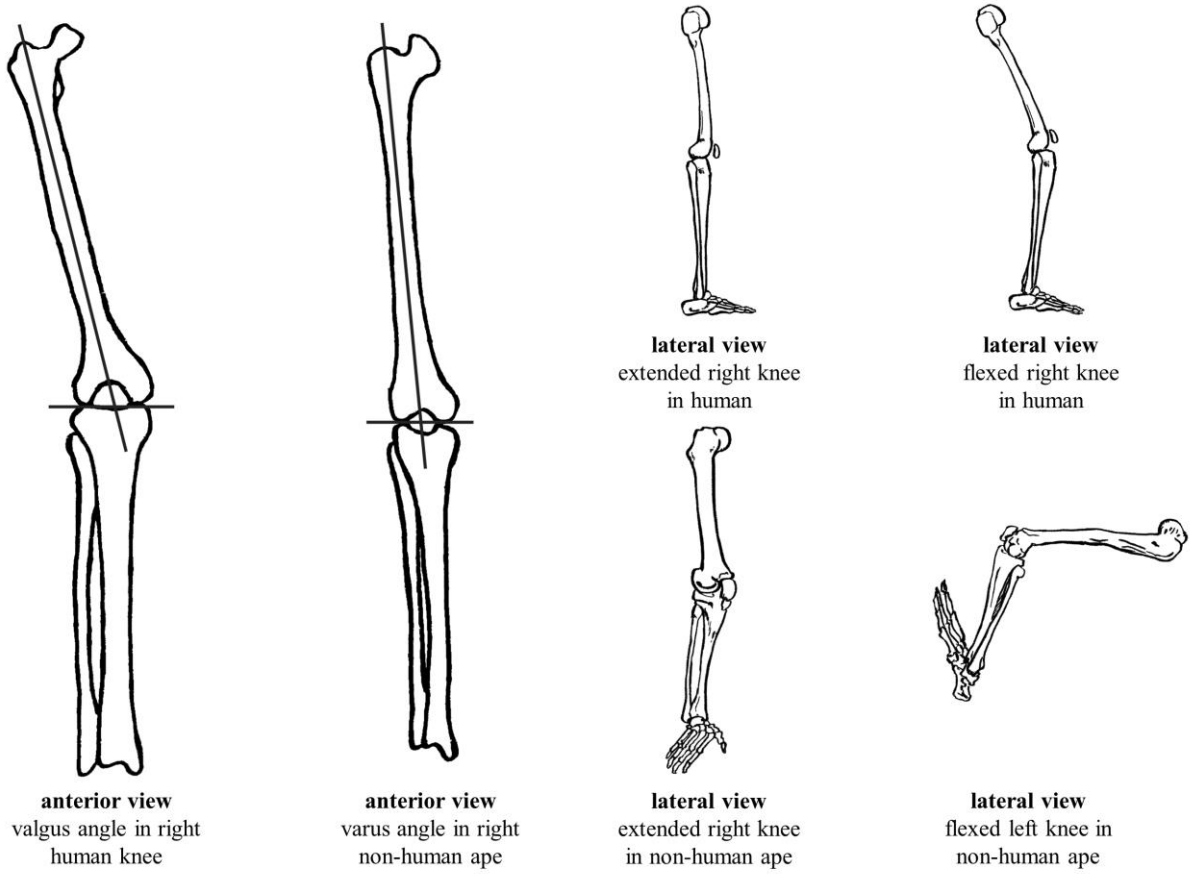

Figure 5.1: Knee angles and postures in humans and non-human apes in anterior and lateral view. Lines in the anterior views represent the anatomical axis of the femur.

5.3 Hypotheses and predictions

In this study, we quantify relative trabecular bone volume (bone volume/total volume, BV/TV) and trabecular alignment (degree of anisotropy, DA) throughout the proximal tibia epiphysis. In this first application of the cHMA method to the proximal tibia we restrict our analysis to these variables as they have been shown to explain up to 97% of the variation in elastic properties of trabecular bone in humans (Homminga et al., 2003; Maquer et al., 2015; Van Rietbergen et al., 1998; Zysset, 2003). cHMA can be used to examine additional trabecular bone variables (e.g., trabecular thickness, spacing and number) but these will be the focus of future work. Below we outline three hypotheses based on the current published literature of knee joint kinematics in extant humans and apes reviewed above.

The first hypothesis is that trabecular architecture of the proximal tibia will reflect differences in frequently observed knee postures and presumed loading during locomotor behaviours across humans (*Homo*), *Pan*/*Gorilla*, and *Pongo*. We predict that:

1A) *Homo* will exhibit the lowest differences in mean BV/TV values between medial and lateral tibial condyles compared to other great apes due to their relatively evenly loaded proximal tibia during bipedal locomotion. Additionaly, we predict that BV/TV on the tibial plateau will be concentrated in the anteroposterior centre of each condyle due to an extended knee posture during most of bipedal walking cycle.

1B) *Pan* and *Gorilla* will exhibit the highest BV/TV in the medial tibial condyle due higher medial knee compartment loading. BV/TV under the tibial plateau will be concentrated more medially on the medial condyle due to their more flexed knee position and varus knee angle (compared to *Homo*) during all types of locomotion. Moreover, based on the previous studies of zoo-housed *Gorilla* locomotion, we expect to find a signal that might reflect higher lateral condyle loading in *Gorilla* compared to *Pan*.

1C) *Pongo* will exhibit a more homogenous spatial arrangement of BV/TV values across the proximal tibia relative to other great apes due to their more variable knee postures (that vary from full extension to full flexion) and loading during locomotion. However, higher mean BV/TV in the medial condyle is still expected due to the higher medial knee compartment loading (caused by varus knee angle) in *Pongo*. Although, the differences will be lower compared to *Pan* and *Gorilla*.

1D) We expect to find high BV/TV values under the insertions of the patellar tendon (tibial tuberosity) in all studied taxa. High BV/TV in the non-human great apes is expected due to the stress that knee experiences under the patellar tendon during the deep flexion (e.g., D'Aoŭt et al., 2002; Sylvester, 2013. High BV/TV in *Homo* is expected due to the stress that the knee experiences when the patellar tendon facilitates the extension of the knee joint. The patellar tendon transmits the force generated by the quadriceps muscle group to the tibia, allowing for the straightening of the leg. This is essential for activities such as walking but also running, jumping, squatting etc. We also expect to find high BV/TV values under the tibiofibular joint articulation in all taxa as the joint must experience high stress during all types of locomotion (e.g., Holowka et al., 2017; Crompton et al., 2010; Sarma et al., 2015; Pietrobelli et al., 2023).

1E) In the regions of high loading, the trabeculae will be oriented with a dominant principal alignment (high DA), while regions with diffuse loading will be oriented without any principal alignment (low DA). Thus, we expect DA to be the lowest on the margins of the tibial plateau and high in the centre of each articular surface where the condyles predominantly articulate. We expect *Homo* to exhibit higher DA directly beneath both condyles in relation to the other taxa due to their stereotypically extended knee loading and relatively higher body mass loading during bipedal walking.

The second hypothesis is that trabecular structure will reflect sex differences (or lack thereof) in the locomotor behaviours of *Homo*, *Pan*, and *Gorilla* (we cannot test for sex differences in *Pongo* due to sample size; Table A1). We predict that:

2A) Female *Gorilla* will exhibit higher BV/TV and higher DA in the lateral tibial condyle compared to males due to their greater range of motion at the hip and knee, which would lead to increased knee extension and thus higher loading of the knee lateral compartment, particularly when climbing.

2B) There will be no sex differences in BV/TV and DA in *Pan* or *Homo* related to function since significant sex differences in the locomotor repertoire or knee posture have not been previously documented in these taxa.

For our **third hypothesis** we analyse BV/TV in the tibial plateau separately (Figure 5.2c, d) and hypothesize that there will be significant differences in mean BV/TV across our sample taxa. We predict that:

3A) Based on the previous studies of BV/TV in human lower and upper limbs (Chirchir et al., 2015; DeMars et al., 2021; Ryan & Shaw, 2015; Saers et al., 2016, Tsegai et al., 2018), we expect to find lower mean BV/TV in the tibial plateau in *Homo* compared to *Gorilla* and *Pan*.

3B) We expect to find higher mean BV/TV in the medial condyle compared to the lateral condyle of the tibial plateau in *Gorilla, Pan,* and *Pongo* due to their higher medial knee compartment loading, while we expect more similar mean BV/TV between medial and lateral condyles in *Homo* due to a r relatively evenly loaded proximal tibia during bipedal locomotion.

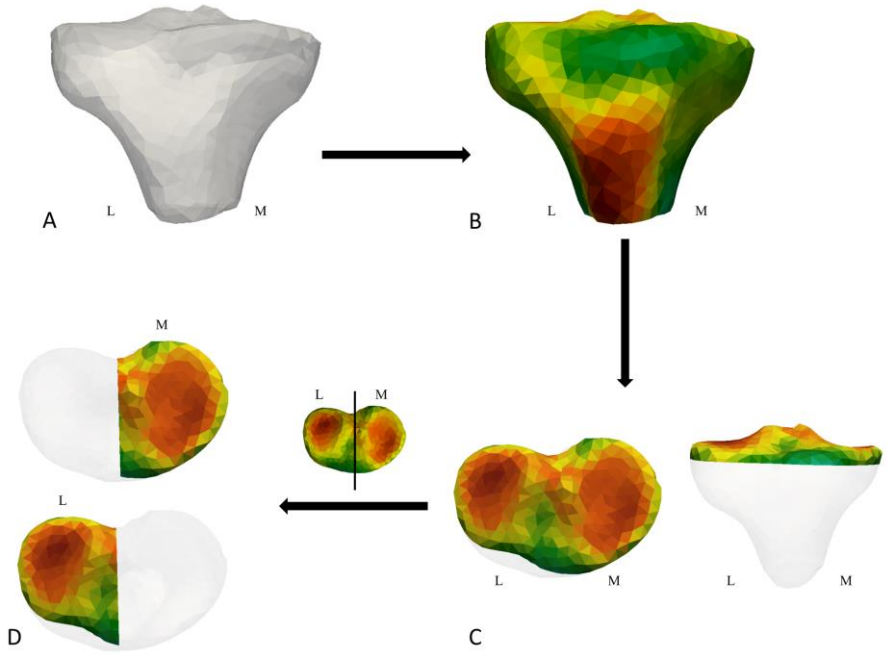

Figure 5.2: A) Model of outer canonical model showing orientation and external morphology of the right proximal tibia computed by cHMA. B) Inner mesh showing rBV/TV distribution in the whole proximal tibia of the human sample computed by cHMA. Note that the inner mesh of rBV/TV, as well as DA distribution, was generated for each taxon. C) The cropped tibial plateau used to test for differences in BV/TV between taxa. D) This tibial plateau sub-section was then cropped again in the sagittal plane to test for differences in BV/TV between the medial and lateral condyles.

5.3.1 Materials and methods

5.3.1.1 Study sample, scanning and segmentation

The study sample consists of complete proximal tibiae of *Homo sapiens* (n=25), *Gorilla gorilla gorilla* (n=13), *Pan troglodytes verus* (n=15) and *Pongo* spp. (n=7). Details of the study sample are shown in Tables 5.1 and A1. A similar sample size (or smaller) was used in many previous lower limb trabecular studies investigating locomotor repertoires in extant primates (see e.g., Cazenave et al., 2019; Georgiou et al., 2020; Mazurier et al., 2010; Su et al., 2013; Sylvester & Terhune, 2017). All non-human great apes (hereafter, 'great apes') were wild born with no obvious signs of pathologies within their postcranial skeleton. The *Gorilla* sample (n=7

females; n=6 males) is from Cameroon and curated at the Powell-Cotton Museum in Birchington-on-Sea, UK. The *Pan* sample (n=9 females; n=6 males) is from the Taï Forest National Park, Ivory Coast and curated at the Max Planck Institute for Evolutionary Anthropology in Leipzig, Germany. The *Pongo* sample consists of five individuals of *P. pygmaeus* (n=3 females; n=2 males), one *P. abelii* (female) and the taxon of one individual (female) is unknown. Human specimens were drawn from three populations. Nine individuals (n=3 females; n=6 males) of our human sample originate from diverse post-industrial populations (Table 5.1) and are assumed to represent comparatively low levels of activity. Ten individuals (all males) were crew members of the Mary Rose ship from early 16th century (Barker, 1992). The Mary Rose sample comprises young adult males and are considered to represent high activity levels (e.g., Scorrer et al., 2021; Stirland et al., 1997). Six individuals (n=3 females; n=2 males; n=1 unknown) are from the Medieval period (11th to 16th centuries AD) excavated from St Gregory's Priory in Canterbury, UK and also assumed to have engaged in higher activity levels compared with our post-industrial human sample. There are currently no known associations with living descendants/communities in our human sample. All data collection was conducted in line with the ethical guidelines of each curatorial institution (i.e., Johann-Friedrich-Blumenbach Institute for Zoology and Anthropology, Mary Rose Trust, and Skeletal Biology Research Centre at the University of Kent). All human samples showed no obvious signs of pathologies within their postcranial skeleton. For most of our sample we used the right proximal tibia (n=37). However, when it was not possible due to preservation the mirrored left proximal tibia (n=23) was used.

Specimens were scanned using a BIR ACTIS 225/300 or Diondo D3 high-resolution micro-CT scanner housed at the Department of Human Evolution, Max Planck Institute for Evolutionary Anthropology (Leipzig, Germany), a Phoenix Nanotom S – X-ray tomograph at the Department of Micro-CT Laboratory, Museum of Natural History (Berlin, Germany), a Nikon 225/XTH scanner at the Cambridge Biotomography Centre, University of Cambridge (Cambridge, UK), or with a Diondo D1 scanner at the Imaging Centre for Life Sciences at the University of Kent (Canterbury, UK). The scan parameters included acceleration voltages of 100–160 kV and 100–140 μA using a 0.2 to 0.5 mm copper or brass filter. Scan resolution ranged between 0.027 mm to 0.058 mm depending on the size of the bone and scanner used (Table 5.1; Supplementary Table S5.1; Table A1). Images were reconstructed as 16-bit TIFF stacks. All images were then segmented into a binary phase of background and bone using the MIA-clustering algorithm (Dunmore et al., 2018).

Table 5.1: Tibia sample composition and voxel size range.

			Sex			Voxel size (mm)	
Taxon	Locomotor behaviour	N	female	male	unknown	min	max
Homo sapiens (GAUG-Inden)*	Bipedal	9	3	6	0	0.036	0.036
Homo sapiens (Mary Rose)**	Bipedal	10	0	10	0	0.033	0.038
Homo sapiens (NGA)***	Bipedal	6	3	2	1	0.030	0.036
Gorilla gorilla gorilla	Terrestrial knuckle-walker	13	7	6	0	0.048	0.058
Pan troglodytes verus	Arboreal/knuckle-walker	15	9	6	0	0.029	0.030
Pongo spp.	Arboreal/Ratcheting	7	5	2	0	0.027	0.030
Total		60					

* University of Göttingen, Göttingen, Germany.

** Mary Rose Trust, Portsmouth, United Kingdom.

*** University of Kent, Canterbury, United Kingdom.

5.3.1.2 Trabecular bone analysis

BV/TV is the proportion of trabecular bone within the total volume in each region. Regions with high BV/TV are assumed to reflect higher or more frequent loading following the concept of bone functional adaptation (Pontzer et al., 2006; Ruff et al., 2006). However, absolute values of BV/TV have previously been argued to show systemic differences across extant hominids (Dunmore et al., 2023; Saers et al., 2016; Tsegai et al., 2018; Ryan & Shaw, 2012) and so relative measures have often been used to test for interspecific differences in trabecular bone volume distribution (e.g., Dunmore et al., 2019; Dunmore et al., 2020; Dunmore et al., 2023; Sukhdeo et al., 2020). Here, to compensate for potential systemic differences across our sample taxa and to analyse bone volume distribution while controlling for the bone volume density, the BV/TV of each tetrahedron was divided by overall average for that individual to give a measure of relative bone volume (rBV/TV). Relative BV/TV demonstrates where bone volume is higher or lower relative to the mean, allowing for comparisons of trabecular bone volume distribution between individuals and species that may differ in absolute BV/TV (Dunmore et al., 2019; 2023; Sukhdeo at al., 2020).

Degree of anisotropy (DA) describes the degree to which struts are similarly alighned in 3D space, with high DA indicating greater similarity in alignment and low DA indicationg a lack of similarity in alignment (Harrigan & Mann, 1984). DA was calculated using the mean-intercept-length method (Odgaard, Kabel, Van Rietberger, Dalstra & Huiskes 1997; Whitehouse, 1974). The value of DA is zero if the minor and major orientations are of equal magnitude, i.e., isotropic, and is one if the minor and major orientations are maximally different, i.e., anisotropic.

Left proximal tibiae in the sample were mirrored to ensure all specimens were in the same orientation before further processing. cHMA was used to quantitatively analyse the BV/TV and DA values in the meshes of each proximal tibia following published protocols (Bachmann et al., 2022). In brief, this method first creates a canonical (i.e., average) proximal tibia from all the samples (all proximal tibia used in the sample), including both the outer shape as well as trabecular volume. Second, all individuals are registered onto this canonical bone to establish homology in orientation. To create a canonical bone for all taxa, we used 15 humans, 13 gorillas, 15 chimpanzees and 7 orangutans. We did not use the complete human sample (n=25) to avoid biasing the canonical bone towards a human shape of the proximal tibia and to better represent morphology of all the taxa in our sample. The 15 human specimens used to create the canonical bone model were chosen randomly across the human populations. The remaining 10

human individuals were used for all further analysis to increase statistical power. The same canonical bone mesh was used for all statistical analyses studying both inter-species and sex-differences. Additionally, the limited number of *Pongo* in our sample could potentially bias our results by creating the canonical tibia that is slightly less representative of *Pongo* than each other species in our sample. However, as the external morphology of proximal tibia is similar across non-human great apes, this should not generate any significant bias.

Analysis of trabecular bone was conducted in Medtool 4.5 (http://www.dr-pahr.at/medtool/) following published protocols (Gross et al., 2014; Pahr & Zysset, 2009; Tsegai et al., 2013). This process involves morphological filters to fill the bone and use of a ray-casting method to isolate the external and internal edge of the cortex in 3D, resulting in a mask of the internal bone volume and outer cortex. Using holistic morphometric analysis (HMA), the trabecular volume is analyzed using a rectangular background grid and overlapping spherical 5 mm volumes of interest (VOI), centred on each of the grid's 2.5 mm spaced vertices. The BV/TV and DA of each VOI is then calculated. These values are then linearly interpolated onto a tetrahedral mesh of the trabecular volume. BV/TV and DA values generated by HMA can be measured in individual CT images and then interpolated on the morphed canonical bone mesh. The individual morphed meshes can then be morphed back to the canonical shape with individual HMA values mapped to homologous tetrahedral elements in the mesh, allowing for geometrically homologous volumetric comparisons. All colour-coded meshes were then visualised in Paraview v4.4.0 for the qualitative comparison where red colours represent high values and blue colours represent low values of rBV/TV and DA.

Insertion of the patellar tendon and the tibiofibular joint articulation were identified (based on their anatomical location for each studied species) on the canonical tibia models rather than mean or individual models, and are therefore referred to as the ‘presumed insertion’ and ‘presumed articulation’, respectively. Trabecular concentrations found under all ligaments and joints of each undeformed individual bone were checked to see if the morphed model is similar to the original individual models using HMA of Medtool 4.5.

5.3.1.3 Statistical analysis

All quantitative comparisons of measured variables and statistical analyses were conducted on the data generated from cHMA as the tetrahedral can be considered geometrically homologous between individual bones (Bachman et al., 2022). To analyze the distribution of trabecular bone in each taxon, a principal component analysis (PCA) was run for rBV/TV and DA separately.

The values of these trabecular measures at each tetrahedral element of the canonical mesh were treated as input variables for the PCA. Loadings representing three signed standard deviations (SD) of each principal component (PC) were mapped to the canonical mesh situated at the positive and negative ends of each axis. Using these loadings, a proximal tibia model was built to visualize the extreme patterns of rBV/TV (showing regions loaded the most) and DA (showing regions loaded in the most stereotypical way) driving variance along the axes. Based on the rBV/TV and DA data distribution across the individuals in our sample, we thresholded the resultant models to only include those rBV/TV and DA values above 60th percentile of trabecular values. This allowed volumetric visualization of the tibia regions that most strongly drive the variation observed along each PC. Pairwise permutational MANOVAs were conducted on the first two principal components to test for quantitative inter- and intra-taxon (i.e., sex) differences in these patterns.

To test for significant differences in BV/TV in the tibial plateau only, we cropped the tibia just below the tibial plateau (Figure 5.2). Mean BV/TV of each specimen was calculated and then separately (divided at the intercondylar eminence) for the medial and lateral sides of the tibial plateau (Figure 5.2). Specimens were cropped in Paraview v4.40. This was done only for the tibial plateau as opposed to the whole proximal tibia to test our predictions about variation in tibial plateau loading between taxa due to a different locomotion and knee postures. To test for inter- and intra-taxon differences, we used Kruskal-Wallis and post-hoc Dunn's tests with a Bonferroni correction (Supplementary Table S5.2; Table 5.2). Significance was determined at α=0.05 for all statistical tests. All statistical tests, PCA plots and boxplots were done in R v4.2.2 (*R Core Team, 2017*).

5.4 Results

5.4.1 Relative bone volume in whole proximal tibia

The qualitative descriptions of rBV/TV distributions in the whole proximal tibia of each taxon are summarized below. Here we assume that regions of high rBV/TV (red color) reflect the positions in which the proximal tibia is loaded frequently and with high magnitude.

Figures 5.3 and 5.4 illustrate comparative rBV/TV colour maps of a mean model for each taxon. In *Homo,* the highest mean rBV/TV values were found at the tibial plateau (Figure 5.3) within the center of both the medial and lateral condyles. The anterior region of the tibial plateau had low rBV/TV values. In great apes, the highest mean rBV/TV values were also concentrated on the tibial plateau as a circular pattern in the center of the lateral condyle and medially on the medial condyle (Figure 5.3). In *Pongo*, rBV/TV values were lowest at the latero-anterior region of the tibial plateau compared with other taxa (Figure 5.3). In *Gorilla*, *Pan* and *Pongo*, the average rBV/TV of the medial condyle was higher compared to the average rBV/TV of the lateral condyle. *Pongo* showed the greatest discrepancy in rBV/TV values between the medial and lateral condyles. In *Gorilla*, and to a lesser degree in *Pan* and, high rBV/TV values extended deeply under both tibial condyles, while *Pongo* showed lower rBV/TV values in these regions (Figure 5.3).

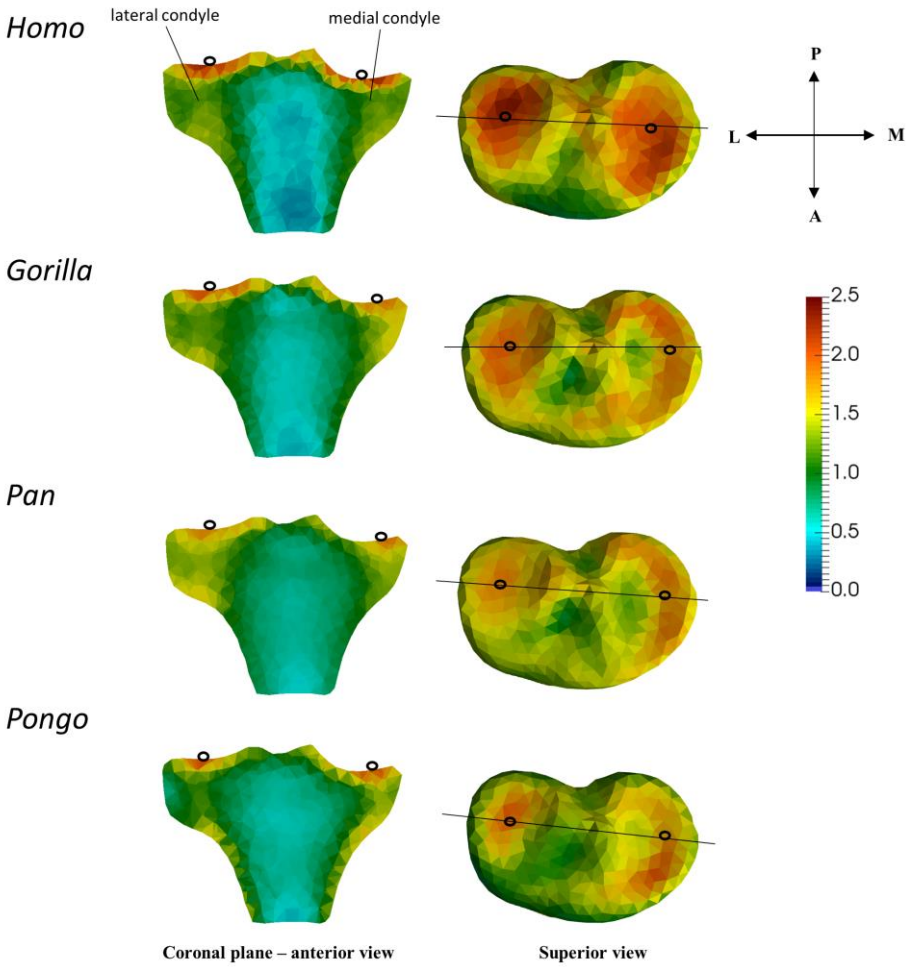

Figure 5.3: Coronal cross-sections of the rBV/TV mean models of the tibial plateau and tibial condyles. Horizontal black lines through the superior view mean models show where the cross-sectional coronal planes are positioned. Hollow black circles indicate section plane position. Red colour shows the highest rBV/TV magnitude and blue colour shows the lowest rBV/TV magnitude. L, lateral; M, medial; A, anterior; P, posterior.

All studied taxa showed high rBV/TV distribution under the insertion of patellar tendon; however, this concentration did not extend deep below the insertion site in any taxon (Figure 5.4). *Gorilla* showed the least variation under the presumed insertion of patellar tendon across all taxa (see standard deviation values in Supplementary Figure S5.1). Moreover, all taxa showed high rBV/TV values under the proximal tibiofibular joint (Figure 5.4). The rBV/TV values were highest in *Homo* and extended superiorly into the tibial plateau. However, in *Pan* and especially in *Pongo*, high rBV/TV did not extend into the lateral condyle as deeply, while *Gorilla* was intermediate between *Pan*/*Pongo* and *Homo* (Figure 5.4).

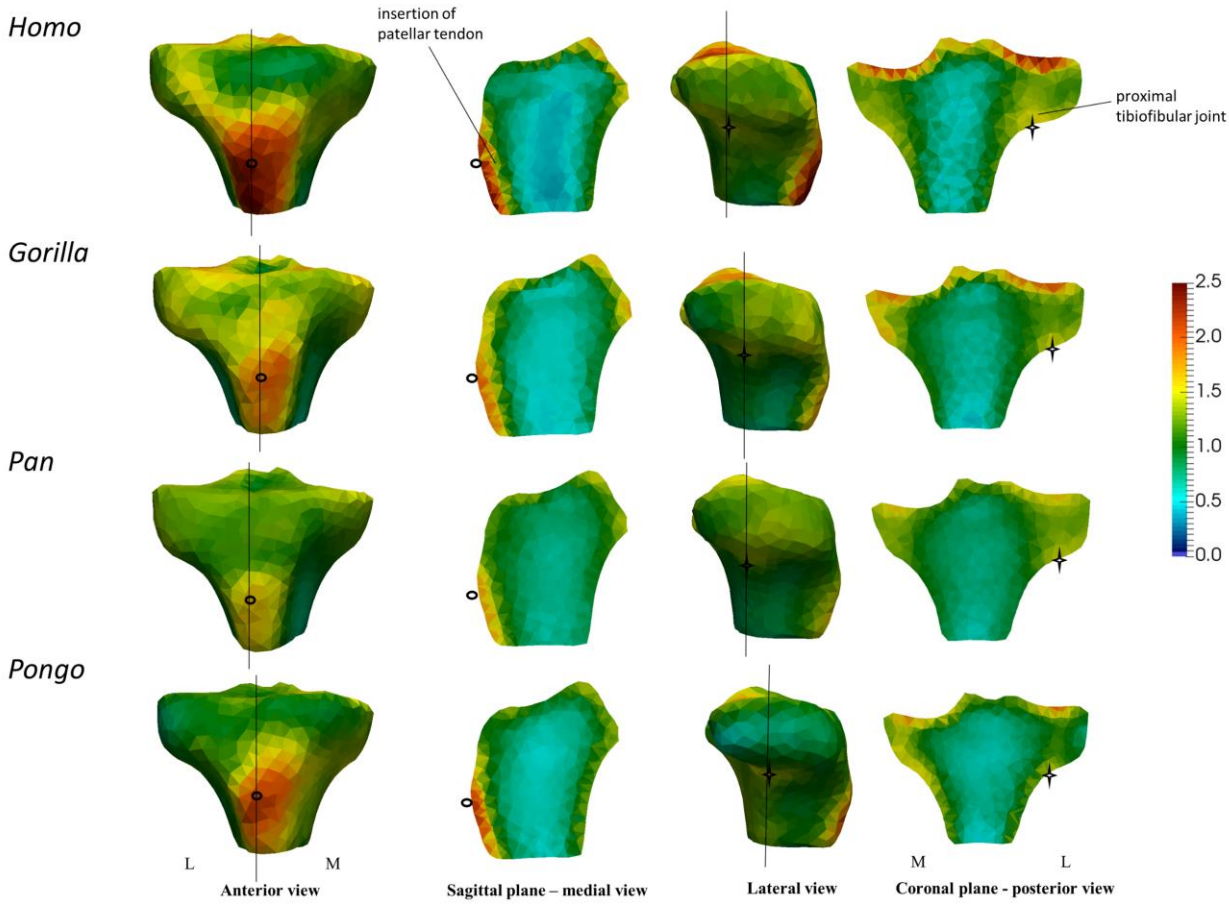

Figure 5.4: Sagittal (left middle) and coronal (right) cross-sections of the rBV/TV mean models under the insertion of patellar tendon and under the tibiofibular joint. Vertical black lines in the anterior and lateral views show where the cross-sectional coronal and sagittal planes are positioned. Hollow black circles in the anterior and medial views ad a black star I the lateral and posterior views indicate section plane position. Red colour shows the highest rBV/TV magnitude and blue colour shows the lowest rBV/TV magnitude. L, lateral; M, medial.

Figure 5.5 presents a principal component (PC) analysis of rBV/TV distribution in the proximal tibia. PC1 explained 24.9% of the variation in rBV/TV and separated *Homo* from other great apes with positive PC1 scores (see the loading models along PC1 axes in Figure 5) associated with higher rBV/TV in the middle of the lateral and medial condyles and under the insertion of patellar tendon (although rBV/TV was highly variable under the insertion of patellar tendon [Supplementary Figure S5.1] in *Homo*). Negative PC1 scores were associated with higher rBV/TV values found anteriorly on the tibial plateau and on the medial aspect of the medial condyle in great apes (see the loading models along PC1 axes in Figure 5.5).

PC2 accounted for 12.1% of the variation in rBV/TV values and separated *Pongo* from *Gorilla* (Figure 5.5), due to a different distribution on the tibial plateau and under the insertion of patellar tendon. In *Pongo*, the higher rBV/TV values were found in the posterior lateral condyle and along the anterior margin of the medial condyle whereas in *Gorilla* the highest rBV/TV values were along the posterior medial margin (see also Supplementary Figure S5.2). In *Gorilla*, rBV/TV under the insertion of patellar tendon extends posteriorly (reaching both sides of the tibial plateau), which differed from a distally located distribution under this tendon in *Pongo*. PC3 accounted for 7.6% of the variation in rBV/TV values and separated *Pongo* from *Pan* due to a different distribution on the tibial plateau and in the lateral condyle (see the loading models along PC3 azes in Supplementary Figure S5.2). *Pan* showed homogenous rBV/TV values across the lateral condyle and lacked a marked concentration anteriorly on the medial condyle. In contrast, *Pongo* rBV/TV values were found centrally on the lateral condyle and along the medial aspect of the medial condyle on the tibial plateau. *Pan* also showed higher rBV/TV values at the lateral condyle (negative PC3) compared to *Pongo* (see the loadinf models along PC3 axes in Supplementary Figure S5.2).

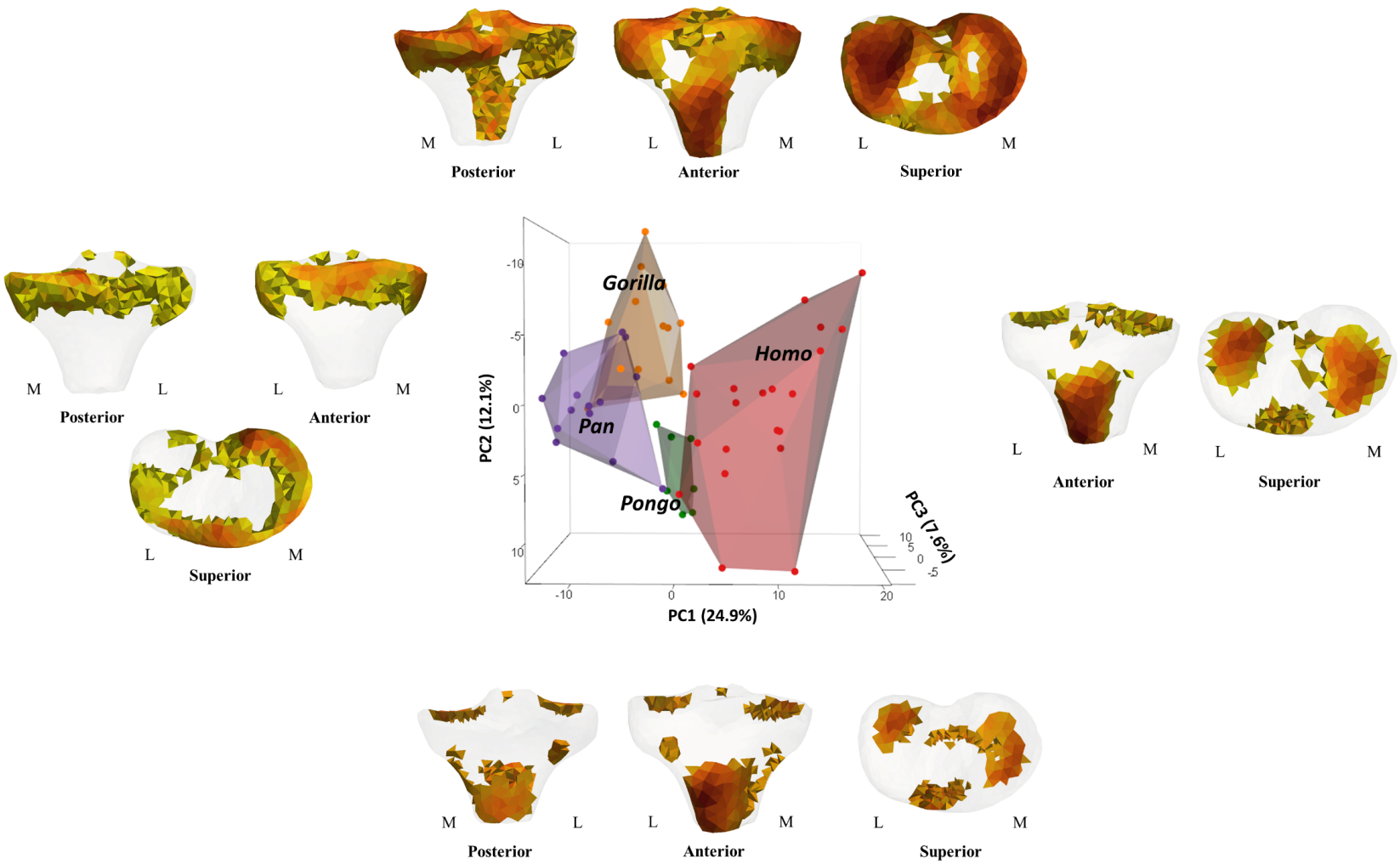

Figure 5.5: PCA of rBV/TV distribution in the proximal tibia. Thresholded models at each end of PC1 and PC2 identify the regions of high rBV/TV that are plus/minus 3 SD of variance along each axis. Humans are separated from non-huma apes along PC1 and *Pongo* is separated from *Gorilla* along PC2. L, lateral; M, medial.

Permutational pairwise MANOVAs found no significant difference in rBV/TV distributions between *Homo* and *Pongo* and between *Gorilla* and *Pan* (Table 5.2). All other pairwise comparisons were significant (Table 5.2). These results reflect species positions on PC1 and PC2 (Figure 5.5).

Table 5.2: Interspecific and intraspecific pairwise permutational MANOVAs on the first two principal components of rBV/TV (green) and DA (blue) distribution.

	Homo	*Gorilla*	*Pan*	*Pongo*		*Gorilla* F	*Gorilla* M
Homo		**<0.001**	**<0.012**	>0.999	*Gorilla* M		**<0.001**
Gorilla	**<0.001**		0.999	**<0.001**	*Gorilla* F	**<0.001**	
Pan	**<0.001**	0.999		0.235			
Pongo	0.865	**<0.001**	**0.001**				

5.4.2 Degree of anisotropy in the whole proximal tibia

The qualitative descriptions of DA distributions in the whole proximal tibia of each taxon are summarized below. Here we assume that regions of high DA (red color) reflect the positions in which the proximal tibia is the most stereotypically loaded.

Figures 5.6 and 5.7 present mean models of DA distribution for each taxon, together with a single cross-section of a segmented image in a representative individual for each taxon to show the trabecular structure. We found a common pattern across all taxa of more isotropic values just beneath the tibial plateau but more anisotropic values deeper within the epiphysis (Figure 5.6). In *Homo*, DA values were more similar between the medial and lateral condyles and higher compared to great apes (Figure 5.6). In contrast, in great apes, we found higher DA values in the medial condyle compared to the lateral condyle (Figure 5.6). In *Homo* and *Pongo*, the anterior side of the medial condyle was most variable in DA values (Supplementary Figure S5.3). We found high DA under the insertion of patellar tendon in all taxa, with the highest values in *Gorilla* and the lowest in *Pongo* (Figure 5.7).

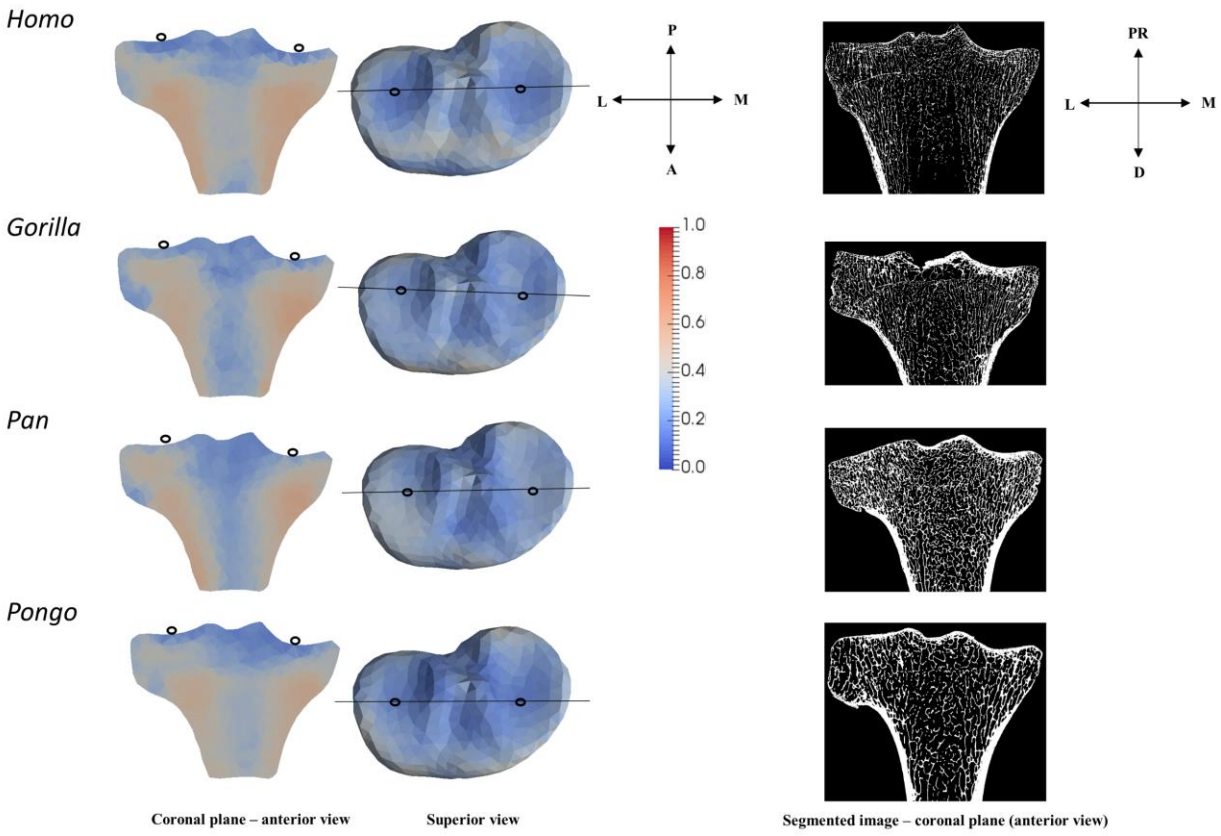

Figure 5.6: Coronal cross-sections (left) of the DA mean models of the proximal tibia. Black lines in the superior view (middle) show where the cross-sectional coronal planes and segmented microCT images (right) are positioned. Hollow black circles in the anterior and superior views indicate section plane position. Red colour shows the highest DA magnitude and blue colour shows the lowest DA magnitude. Orientation axes represent the orientation for the superior view and of the segmented images. L, lateral; M, medial; A, anterior; P, posterior; PR, proximal; D, distal.

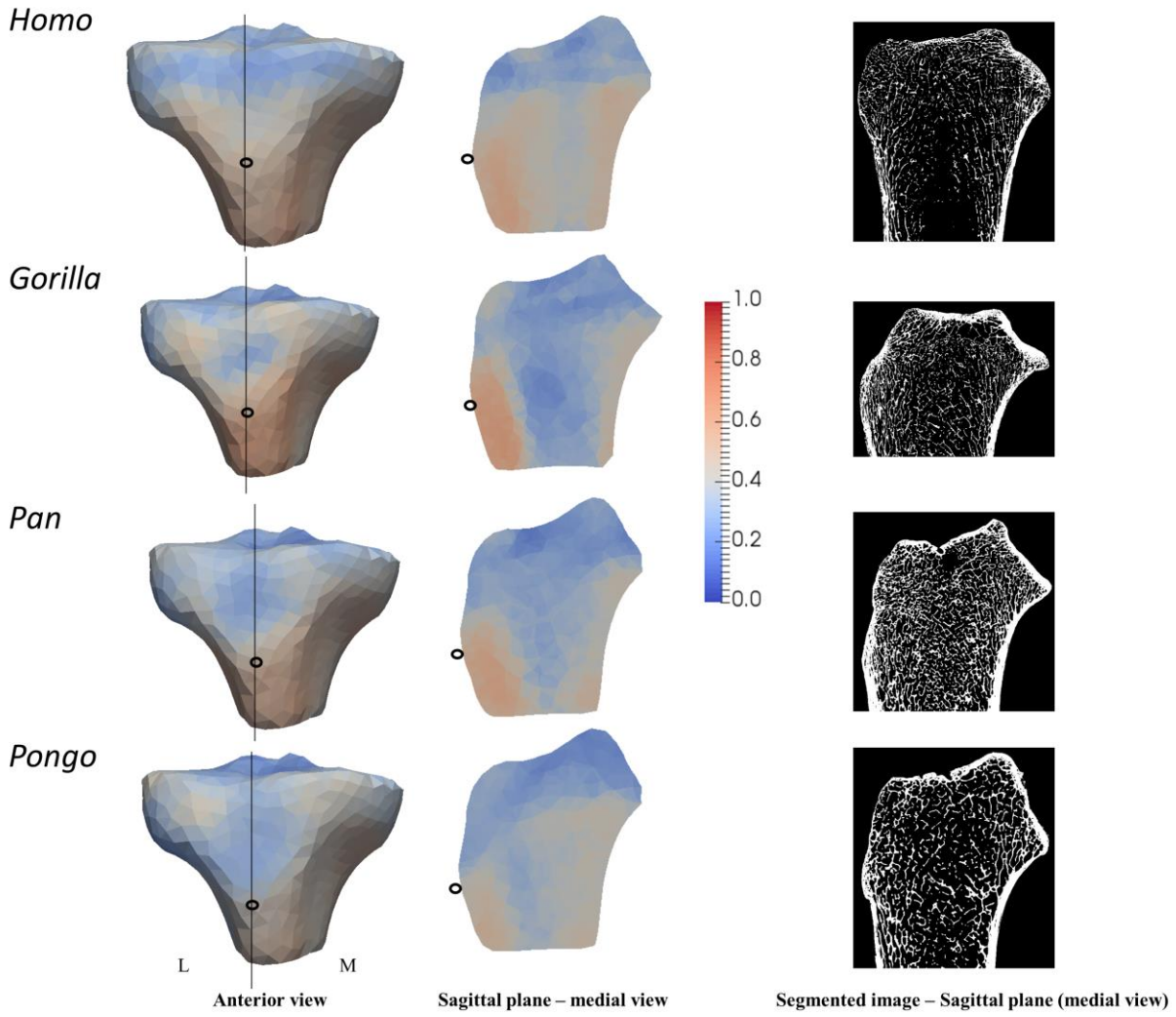

Figure 5.7: Sagittal cross-sections (middle) of the DA mean models under the insertion of patellar tendon. Black lines in the anterior view (left) show where the cross-sectional sagittal planes and segmented images are positioned. Hollow black circles in the anterior and medial views indicate section plane position. Red colour shows the highest DA magnitude and blue colour shows the lowest DA magnitude. L, lateral; M, medial.

Figure 5.8 presents a principal component analysis of DA values in the proximal tibia. PC1 explained 36.6% of the variation in DA values at each mesh element and did not separate taxa from each other (Figure 5.8). PC2 accounted for 8.8% of the variation in DA values and separated *Gorilla* from *Homo* and *Pongo*. Negative PC2 distinguished *Gorilla* due to higher DA values under the insertion of patellar tendon (see the loading models along PC2 axes in Figure 5.8). PC3 accounted for 5.1% of the variation in DA values and did not show any separation between studied taxa (Supplementary Figure S5.4).

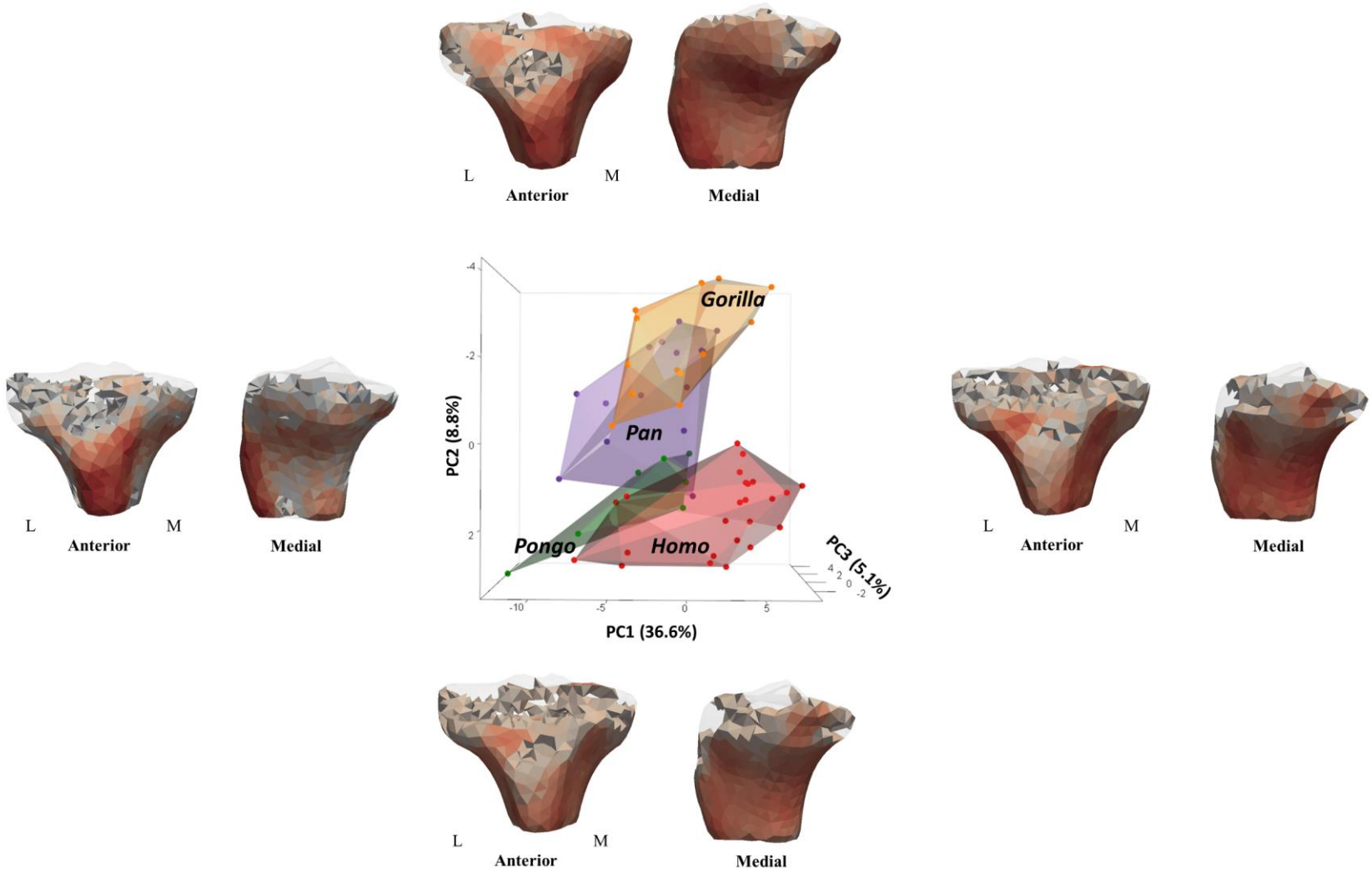

Figure 5.8: PCA of variation in DA among the study taxa. There is no separation between taca on PC1, while *Gorilla* separates from *Homo/Pongo* on PC2. Thresholded models at the end of each PC axis represent the regions of high DA variance along PC1 and PC2. L, lateral; M, medial.

Permutational pairwise MANOVAs found no significant difference in DA distributions between *Homo* and *Pongo,* between *Gorilla* and *Pan,* and between *Pan* and *Pongo* (Table 5.2). All other pairwise comparisons were significant (Table 5.2). These results are consistent with species positions on PC1 and PC2 (Figure 5.8).

5.4.3 Sex differences in mean trabecular architecture in the whole proximal tibia

Figure 5.9 shows a PCA of rBV/TV distribution in *Gorilla*. Female and male *Gorilla* did not separate completely on PC1 (explaining 22.6% of the variation) or on PC2 (explaining 15.5% of the variation) (Supplementary Figure S5.5). However, most female and male specimens were distinguished from each other, with the variation that separates them distributed across the first three PCs, with PC3 accounting for 12.2% of the variation. Thresholded mean loading models showed that female *Gorilla* separated from males (positive PC3) due to higher rBV/TV values on the anterior side of the tibial plateau and due to the different distribution on the posterior side of the medial aspect of the tibial plateay. In contrast, in male *Gorilla* (negative PC3), high rBV/TV values were more in the centre of lateral tibial condyle and under the presumed insertion of patellar tendon (see the loading models along PC3 axes in Figure 5.9). On PC3, one male individual shows higher concentration on the anterior side of the tibial plateau compared to other male individuals in the sample. Thus, this male outlier plots on the positive PC3, overlapping with females. Additionally, high rBV/TV values penetrated deeper into the trabecular network of the lateral condyle in males compared to females (Supplementary Figure S5.5). We found no separation in rBV/TV distribution between sexes in *Pan* and *Homo* (Supplementary Figure S5.6).

Permutational pairwise MANOVAs found significant differences between rBV/TV distributions of female and male *Gorilla* (Table 5.2), which is consistent with distribution of specimens on PC3 (Figure 5.9).

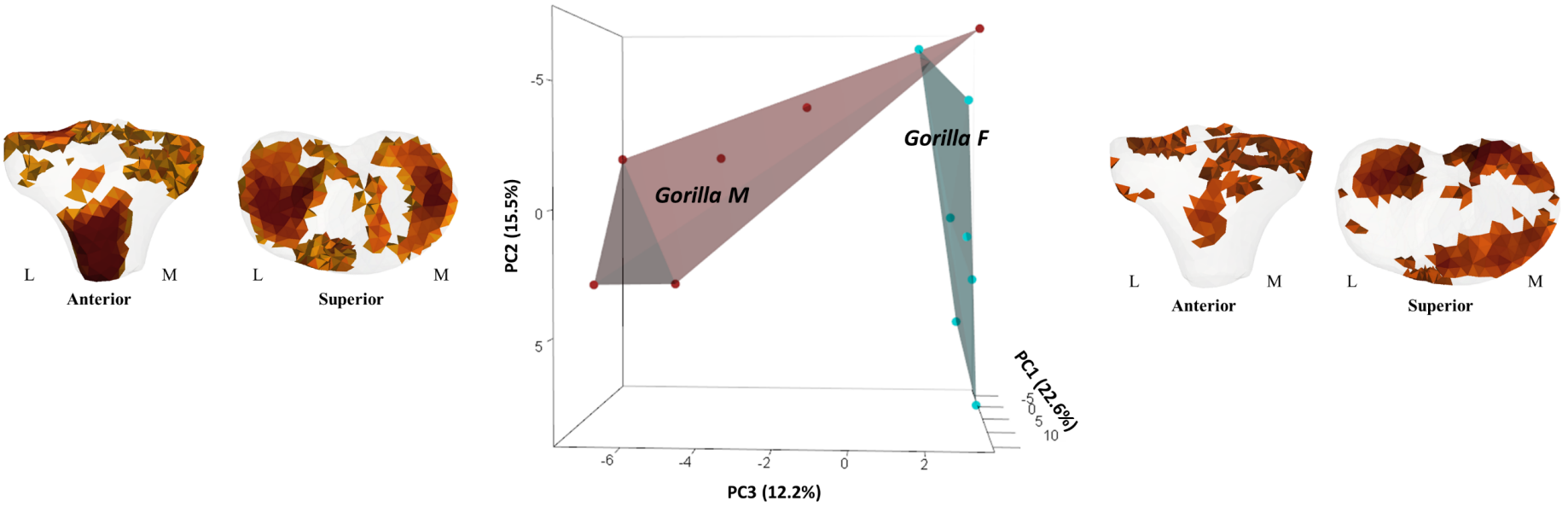

Figure 5.9: PCA of rBV/TV in the proximal tibia of *Gorilla* males and females. Thresholded models at each end of PC3 axis represent the regions of high rBV/TV that are plus/minus 3 SD along PC3, which broadly separates male and female *Gorilla*. L, lateral; M, medial; F, female; M, male.

Figure 5.10 shows a PCA of DA distribution in *Gorilla*. PC1 accounted for 37.9% of the variation in DA values. Negative PC1 distinguished female *Gorilla* due to lower DA values under the presumed insertion of patellar tendon and in both condyles and positive PC1 distinguished male *Gorilla* due to higher DA values inside both tibial condyles (see the loading models along PC1 axes in Figure 5.10). PC2 (explaining 13.8% of the variation) and PC3 (explaining 9% of the variation) did not show any separation with separation of specimens on PC1 between female and male *Gorilla* (Supplementary Figure S5.7). We found no separation in DA distribution between sexes in *Pan* and *Homo* (Supplementary Figure S5.8).

Permutational pairwise MANOVAs found significant differences between DA distributions of female and male *Gorilla* (Table 5.2), which is consistent with distribution of specimens on PC1 (Figure 5.10).

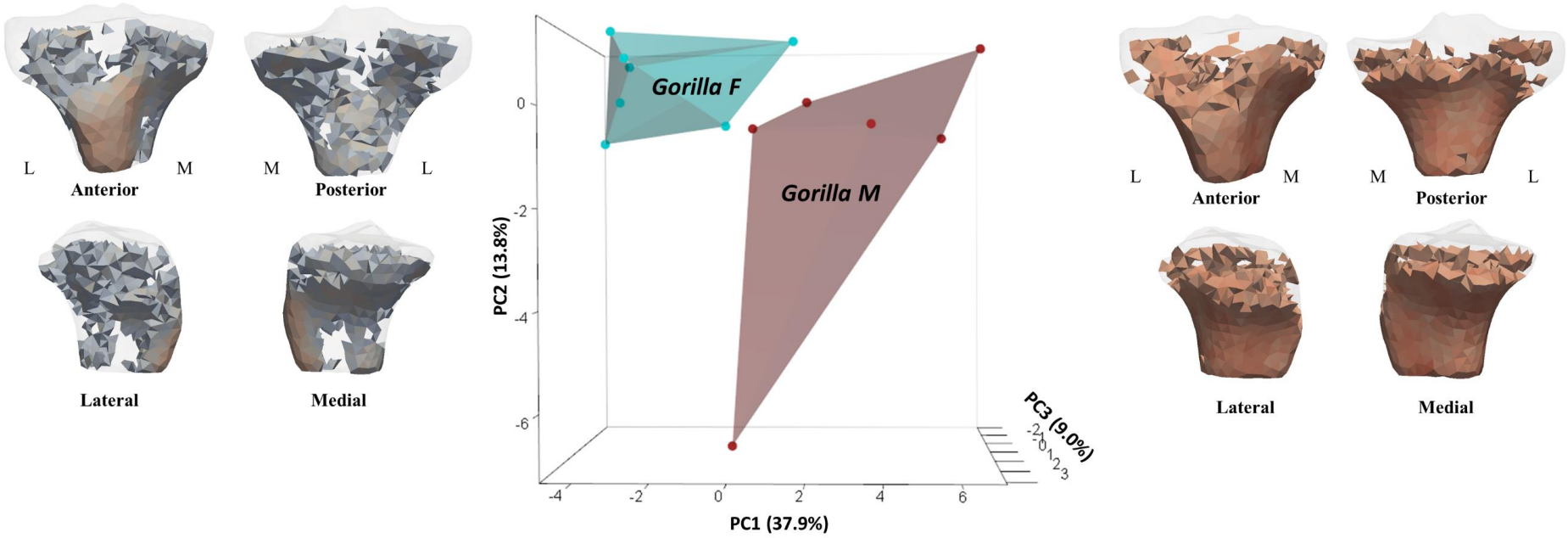

Figure 5.10: PCA of DA showing sex differences within *Gorilla* on PC1. Thresholded models at the end of each axis represent the regions of high DA that are plus/minus 3 SD along PC1. L, lateral; M, medial; F, female; M, male.

5.4.4 Trabecular bone volume fraction in the cropped tibial plateau

Dunn's tests showed mean BV/TV in the tibial plateau to be significantly higher in *Gorilla* and *Pan* compared to *Homo* (p-values<0.001), in *Gorilla* compared to *Pongo* (p-value=0.008) and in *Pan* compared to *Pongo* (p-value<0.010; Table 5.3; Figure 5.11a). *Gorilla* and *Pan* did not differ significantly from each other (p-value=0.999). *Homo* was found to have the lowest mean BV/TV and the most variable BV/TV distribution in the tibial plateau and did not differ significantly from *Pongo* (p-value=0.999 [Table 5.3; Figure 5.11a]). In *Homo*, mean BV/TV in the lateral side was non-significantly higher than the medial side of the tibial plateau, while the opposite pattern was found in great apes where the mean BV/TV in the medial side of the tibial plateau was significantly higher (Figure 5.11b; Table 5.3). In the lateral side only, mean BV/TV was significantly higher in *Gorilla* and *Pan* compared to *Homo* (p-values<0.003) and in *Gorilla* and *Pan* compared to *Pongo* (p-values<0.007). In the medial side only, mean BV/TV was significantly higher in *Gorilla* and *Pan* compared to *Homo* (p-values<0.001), in *Gorilla* compared to *Pongo* (p-value=0.010) and in *Pan* compared to *Pongo* (p-value<0.021 [Table 5.3; Figure 5.11b]).

Table 5.3: Dunn's tests for interspecific differences in mean BV/TV throughout the tibial plateau (orange), the lateral side of the tibial plateau (green), and the medial side of the tibial plateau (blue). Dunn's tests for intraspecific differences in mean BV/TV between the medial and the lateral side of the tibial plateau (yellow).

	Homo	*Gorilla*	*Pan*	*Pongo*	*Homo*	*Gorilla*	*Pan*	*Pongo*		medial vs. lateral
Homo						**<0.001**	**<0.001**	0.999	*Homo*	0.999
Gorilla	**<0.001**				**<0.003**		0.999	**0.01**	*Gorilla*	**0.001**
Pan	**<0.001**	0.999			**<0.003**	0.999		**<0.021**	*Pan*	**0.031**
Pongo	0.999	**0.008**	**<0.010**		0.999	**<0.007**	**<0.007**		*Pongo*	**0.001**

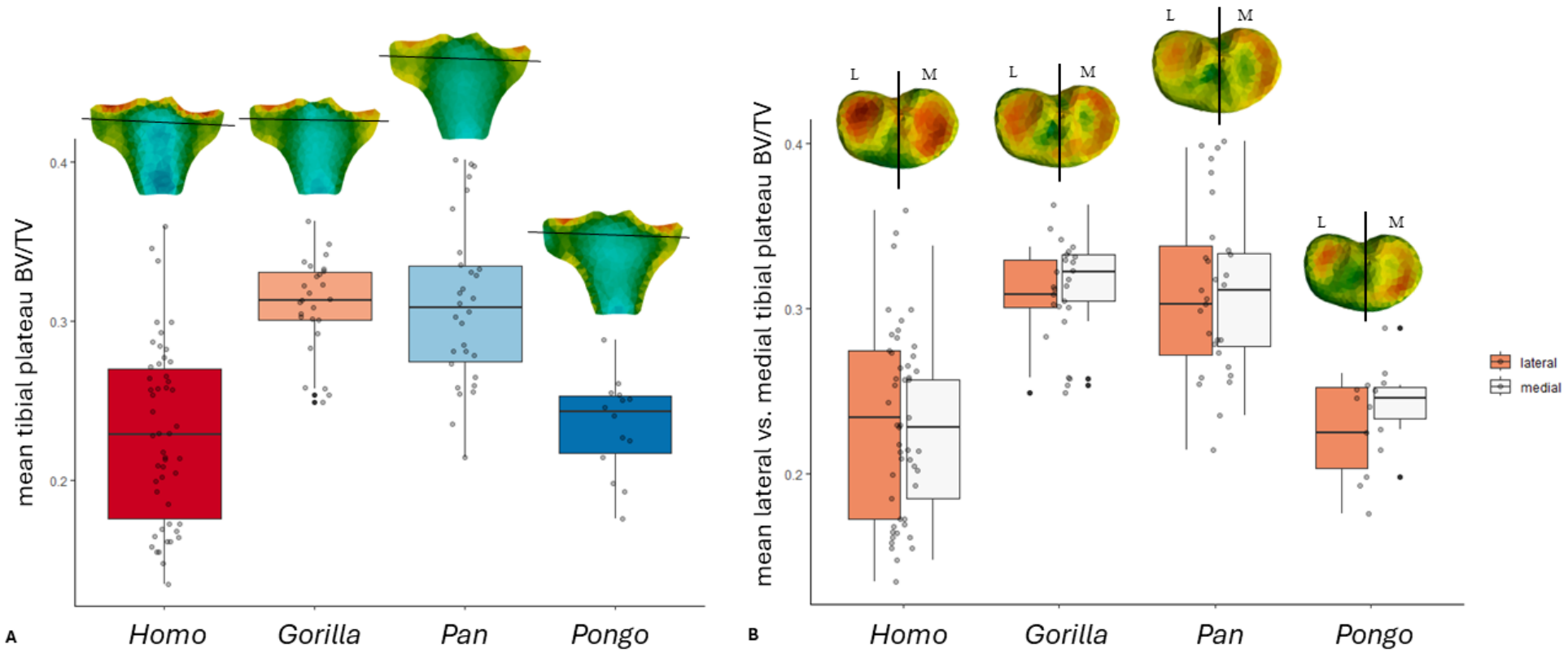

Figure 5.11: (A) Mean tibial plateau BV/TV (measured as everything superior to the horizontal black line) by taxon, and (B) between lateral and medial sides of the tibial plateau (black line shows where the medial and lateral condyle were divided). Mean BV/TV is higher in lateral side of tibial plateau compared to medial side in humans and higher in medial side of tibial plateau compared to lateral side in all non-human apes. L, lateral; M, medial.

5.5 Discussion

5.5.1 Trabecular architecture variation among humans and great apes

We predicted that *Homo* would differ from great apes in having a trabecular structure of the proximal tibia that reflected habitual use of extended knee postures during bipedalism. This prediction would be supported bythe lowest mean rBV/TV differences between both tibial condyles, by a concentration of rBV/TV in the anteroposterior center of each condyle, and by comparatively high DA across both condyles in *Homo* compared with the other taxa in our sample. This prediction was supported. We found high rBV/TV values in the anteroposterior center of each condyle on the tibial plateau (Figures 5.3 and 5.5) and DA to be comparatively higher in *Homo* than in great apes across both condyles (Figures 5.6 and 5.7). Moreover, we found no separation by rBV/TV distribution in the proximal tibia between the different human populations in our sample (Supplementary Figure S5.9). However, the post-industrial sample assumed to represent low levels of activity (Göttingen) and the Medieval sample assumed to represent higher levels of activity (NGA) show the greatest variability of rBV/TV values in the tibial plateau, and in its lateral and medial side separately, compared with the Mary Rose sample. The rBV/TV pattern of the Mary Rose sample of young, active male adults was closest to the great ape sample (Supplementary Figure S5.9). We did find separation between our human populations in DA distribution; the Göttingen and Mary Rose populations showed comparatively higher DA values in both condyles compared to Medieval sample, which showed higher DA values under the tibial tuberosity (see models of PCs loadings in Supplementary Figure S5.14). Some previous research has suggested that loading through the medial and lateral femoral and tibial condyles are nearly equal in humans (e.g., Preuschoft, 1971; Sylvester, 2013), which is also supported by our results, while other studies have found differences between lateral and medial knee compartment loading (e.g., Holder et al., 2023; Kuntzner et al., 2009; Mündermann et al., 2008).

In general, the trabecular architecture of the human proximal tibia was found to be the most consistent with loading during bipedal locomotion and with a stereotypically extended knee position during all phases of human walking. The trabecular structure of the human proximal tibia is also consistent with that of the distal femur (Lukova et al., 2024). In our previous study, we found high rBV/TV values in the posteroinferior regions of both femoral condyles reflecting more extended knee postures during all gait phases of walking compared to non-human great apes. We also found higher rBV/TV values in the lateral femoral condyle compared to medial

condyle. We suggested that this pattern in the distal femur was consistent with the extended knee posture combined with a valgus knee angle (Lukova et al., 2024).

We predicted that *Pan* and *Gorilla* would differ from humans and *Pongo* in having trabecular structure of the proximal tibia that reflected habitual use of flexed knee postures during terrestrial and arboreal locomotion. This prediction would be supported by higher rBV/TV in the medial tibial condyle compared to the lateral condyle. Additionally, we predicted that *Pan* and *Gorilla* would differ from *Homo* in having trabecular structure of the proximal tibia that reflected varus knee angle. This prediction would be supported by rBV/TV under the tibial plateau to be concentrated more medially on the medial condyle. Both predictions were supported. We found rBV/TV to be higher in the medial condyle and on the medial side of the tibial plateau (Figure 5.3) in *Pan* and *Gorilla* compared to humans and *Pongo*. In both African apes, the highest rBV/TV values were found along the medial edge of the medial condyle while rBV/TV was highest in the center of lateral condyle (Figure 5.3; Figure 5.5). This rBV/TV concentration in *Pan* and *Gorilla* is consistent with higher medial knee compartment loading and flexed knee postures during locomotion, distinguishing the African apes from *Homo* and *Pongo* (Figures 5.5). When the knee is flexed, and thus tke medial knee compartment is loaded more, it might be expected that medial femoral condyle is pushing on the proximal margin of the medial tibial condyle, such that the trabeculae (re-)model along the medial edge as we found in our *Gorilla* and *Pan* sample. In both taxa, high DA values were found across both condyles and low DA values were found on the tibial plateau (Figure 5.6). The trabecular structure of the proximal tibia in African apes is also consistent with high rBV/TV values posterosuperiorly in both femoral condyles and mediolaterally on the patellar articulation of the femur, which also reflects loading of the distal femur in a flexed knee posture (Lukova et al., 2024).

We predicted that *Pongo* would significantly differ from other great apes due to more variable knee postures and loading during arboreal locomotion, as well as their higher medial knee compartment loading (due to their varus knee angle). This prediction would be supported by a more homogenous spatial arrangement of rBV/TV across the proximal tibia compared to other great apes and by higher mean rBV/TV values (but lower than in African apes) in the medial compared to the lateral condyle. This prediction was partially supported. We found rBV/TV to be concentrated medially on the medial side of the tibial plateau as in African apes, however, this concentration extended more anteriorly in *Pongo* (Figure 5.3). We suggest that this pattern is consistent with loading of the knee in extended as well as flexed knee postures while the medial knee compartment is loaded more than the lateral knee compartment. As mentioned

above, when the knee is flexed and more medially loaded, the trabeculae become denser proximally on the medial side of the tibial plateau. However, the more the knee is extended, the bone becomes denser anteriorly as well. Thus, this could be a signal of higher knee extension in *Pongo* compared to African apes. In general, the trabecular architecture in the proximal tibia of *Pongo* suggests knee loading in flexed postures. However, as the results of the cropped tibial plateau suggest (see below), the knee is most likely loaded in the way that differs from African apes. A previous study of trabecular architecture in the distal femur found that *Pongo* did not differ significantly to *Pan*, but did separate from *Gorilla* (Georgiou et al., 2019). However, our more recent study of trabecular architecture in distal femora, which incorporated the more quantitative and statistical tools of cHMA, found a greater degree of separation between both *Pongo* and *Pan* and *Pongo* and *Gorilla* (Lukova et al., 2024).

We predicted high rBV/TV under the insertion of patellar tendon (tibial tuberosity) and under the presumed articulation of the proximal tibiofibular joint in all taxa. These predictions were supported. In *Homo*, the patellar tendon plays a crucial role in the biomechanics of the knee joint (Bergmann & Bender, 2006; Fitzgerald & Piva, 2009; Henderson & Schindler, 2005; Wand & Huang, 2018). The patellar tendon helps to stabilize the knee joint by fixing the patella in place. When the quadriceps contract, it pulls on the patella via the quadriceps tendon, which in turn pulls on the patellar tendon. This transmission of force from the quadriceps to the tibia is significant during activities such as walking, running, jumping, and squatting (Nilsson & Thorstensson, 1989; Racic et al., 2009). Similar to humans, the great ape patellar tendon helps stabilize the knee joint by keeping the patella aligned, which is crucial for the effective functioning of the knee during movement. In great apes, as in humans, the contraction of the quadriceps exerts force through the quadriceps tendon, which then pulls on the patella. This force is transmitted through the patellar tendon to the tibia, enabling knee extension. Non-human great apes experience dynamic loading of the patellar tendon during the various activities but especially during the activities where the knee is in deep flexion (D'Aoŭt et al., 2002; Sylvester, 2013). This mechanical importance is reflected in our results as we found high rBV/TV values under the patellar tendon in all taxa.

In *Homo*, the proximal fibula needs to resist repeated forces transmitted through the tibiofibular joints during bipedalism (Lambert, 1971; Ogden, 1974; Pietrobelli et al., Preuschoft, 1971), thus the articulation is less mobile compared to non- human great apes (Eichenblat & Nathan, 1983; Ogden, 1974; Pietrobelli et al., 2023; Sarma et al., 2015). This more stable articulation is reflected in our results, as the rBV/TV under the presumed proximal tibiofibular joint is the

highest in *Homo* compared to the remaining taxa of our sample. The proximal tibiofibular articulation in great apes is more mobile compared to humans, allowing for greater ankle dorsiflexion, particularly during arboreal locomotion (DeSilva, 2009; Orgen, 1974). While earlier studies suggested that *Pan* uses relatively high ankle joint dorsiflexion compared to humans across various types of locomotion (DeSilva, 2009), more recent research by Holowka et al. (2017) demonstrated that *Pan* exhibits dorsiflexion capabilities that are more similar to humans, including during vertical climbing. This closer similarity has been further supported by Venkataraman et al. (2013), who found comparable dorsiflexion abilities in human climbers. Additionally, previous studies have shown that *Pan* has greater flexibility in the tibiofibular joint compared to *Gorilla* and *Pongo* (Crompton et al., 2010; Orden, 1974). This increased flexibility has been linked to the need to prevent anterior displacement of the fibula and accommodate wider bicondylar angles during knee flexion (Lovejoy, 2007), as well as the need in *Pongo* to stabilize the knee during extension while walking bipedally in the trees (Thorpe et al., 2009). However, we were not able to find any significant differences between great apes under the proximal tibiofibular joint that could reflect differences in mobility found in previous studies.

5.5.1.1 Sex differences in trabecular architecture in Homo, Gorilla, and Pan

We predicted that trabecular structure would reflect sex differences in locomotor behaviors of *Gorilla* but not that of *Pan* and *Homo*. We expected female *Gorilla* to show higher rBV/TV and higher DA in the lateral tibial condyle compared to males, as a previous study reported higher lateral compartment loading in female *Gorilla* compared to males when climbing (Beaudet & Chouinard, 2020; Falk & Towne, 2004; Jungers & Schmitt, 2009; Manning & Richmond, 2003; Tardieu & Fritsch, 1991); likely due to a greater range of motion at the hip and knee (Hammond, 2014; Isler, 2005). Our hypothesis of a sex difference was supported by the result was the opposite of our prediction with males, rather than females, exhibiting higher rBV/TV values in the lateral condyle (Figure 9). Moreover, we found higher rBV/TV values anteriorly on the medial side of the tibial plateau in female compared to male *Gorilla*, and higher rBV/TV under the tibial tuberosity in males compared to females (Figure 9). We found DA values to be comparatively higher in both tibial condyles in males (Figure 10). The medial tibial condyle of the male *Gorilla* is more concave compared to that of females (as in *Pan*) possibly due to the differences in body mass and/or differences in locomotor behavior (Sylvester, 2013), which could potentially allow female *Gorilla* to have greater range of knee motion. Partial separation between female and male *Gorilla* in our PCA results suggested a

more extended (and flexed) knee postures along with higher medial knee compartment loading (compared to lateral knee compartment loading) and a less stereotypically loaded proximal tibia in females compared to males. A higher level of knee extension and a generally higher range of motion at the knee was previously found in zoo-housed adult female *Gorilla* compared to males, particularly during vertical climbing (Isler, 2005). This was supported by our recent examination of trabecular structure in distal femur with females showing higher rBV/TV values in the posterior regions of lateral condyle, laterally on patellar surface, and medially above intercondylar fossa (Lukova et al., 2024). In contrast, *Gorilla* males had higher rBV/TV values in the medial condyle (Lukova et al., 2024). Compared to males, wild female *Gorilla* are more arboreal but also smaller in body mass (Remis, 1997). *Homo* body size dimorphism approaches that of *Pan* (Smith & Jungers, 1997). However, we did not find any sex differences in proximal tibia loading in these taxa (although small sample sizes necessitate additional examination of this finding). Thus, sex differences found in the proximal tibia in *Gorilla* might be driven by differences in body mass, the degree of arboreality and/or by differences in knee loading. Further investigation of *Gorilla* locomotor kinematics and kinetics, particularly in wild communities, and larger skeletal samples are needed to address whether sex differences in trabecular structure exist in *Gorilla*.

5.5.2 Trabecular bone volume fraction in the cropped tibial plateau

We predicted *Homo* to have lower BV/TV and the most similar BV/TV between the medial and lateral tibial plateau compared to *Gorilla* and *Pan*. These predictions were supported. The mean BV/TV in the human (together with *Pongo*) tibial plateau was found to be the lowest of all studied taxa, and to significantly differ from *Gorilla* and *Pan* (Figure 5.11; Table 5.3). Moreover, in humans, mean BV/TV in the lateral side of the tibial plateau was non-significantly higher than that of the medial side. This differs to the pattern we found in great apes where the mean BV/TV in the medial side of the tibial plateau was significantly higher (Figure 5.11; Table 5.3). Our results in *Homo* suggest that the lateral condyle experiences higher stress compared to medial condyle during bipedal walking and/or that slightly higher BV/TV in the lateral condyle is caused by valgus angle at the knee in humans compared to great apes. However, considering that the medial knee compartment has greater proportional area of articular surface than the lateral one (although this difference in minimal compared to other great apes) and that the difference in mean BV/TV is small, loading might still be considered relatively equal between the knee compartments.

Even though humans are obligate bipeds, previous studies have documented low BV/TV in the lower (and upper) limb of recent human populations, which has been linked to decreased loading due to sedentism relative to more mobile or active Pleistocene and Holocene populations (Chirchir et al., 2015; DeMars et al., 2021; Ryan & Shaw, 2015). However, this potentially systemic pattern of reduced BV/TV of the lower limb appears to characterize both forager and agricultural human populations (Saers et al., 2016) and thus the factors producing low BV/TV may be more complex. Tsegai et al. (2018) suggested that lower BV/TV in recent human populations compared to *P. troglodytes* across anatomical sites is at least partially systemic. BV/TV could be influenced by a pleiotropic effect of reducing loading of the upper limb, or related to the changes in diet, disease prevalence, hormonal differences or by other factors (e.g., Chavassieux et al., 2007; Chirchir, 2015; Chirchir, 2021; Dawson-Hughes et al., 1997; Riggs & Melton, 1986; Robling et al., 2006; Weber & Zemel, 2011). In general, the trabecular architecture of the human tibial plateau was found to be the most consistent with loading during bipedal locomotion and with a stereotypically extended knee position during all phases of human walking.

We expected to find higher mean BV/TV in the medial condyle compared to the lateral condyle of the tibial plateau in *Gorilla*, *Pan*, and *Pongo*. This prediction was supported. In *Pan* and *Gorilla*, the single attachment of lateral meniscus of the knee allows a greater range of motion compared to two attachments of the medial meniscus, which make the medial knee compartment more stable (Tardieu, 1981). Previous studies have demonstrated that soft tissue differences, together with a varus knee angle, allow the axis of internal/external rotation to pass through the medial tibial condyle in African apes and leads to the higher medial knee compartment loading (Churchill et al., 1998; Freeman & Pinskerova, 2005; Schipplein & Andriacchi, 1991; Sylvester, 2013). Thus, the medial concentration of high BV/TV on the medial condyle that we found may reflect loading of the more stable medial knee compartment in the flexed position and varus angle. Tardieu (1981) showed that *Pan* (and we also assume *Gorilla*) has a greater range of internal/external rotation of the flexed knee compared to humans. The greater range of rotation at the knee could be useful especially during the frequent arboreal locomotion practiced in *Pan* and *Gorilla* (Doran, 1996; Doran, 1997; Remis, 1995; Remis, 1998). Kinematic studies in humans have shown the relationship between knee flexion and internal/external rotation during deep squatting (e.g., Dahlkvist et al., 1982; Dyrby et al., 1997). Moreover, Dahlkvist et al. (1982) demonstrated that the tibiofemoral forces are 4.7 to 5.6 times body weight in the mediolateral direction and 2.9 to 3.5 times body weight in the anteroposterior

direction on the knee during deep squatting. These forces are much larger (although more static) than those incurred during normal walking in humans (Mikosz et al., 1988; Morrison, 1970; Schipplein & Andriacchi, 1991; Seireg & Arvikar, 1975; Taylor et al., 2004; Wang et al., 2014). Additionally, Nagura et al. (2002) showed that the human knee experiences increased stress on the patellar tendon and posterior side of the tibial plateau during deep flexion. While the elastic properties of the patellar tendons in African apes and humans may differ (Alexander & Ker, 1990; Fukashiro & Hayashi, 1997; Lichtwark & Wilson, 2006; Schmidt & Alford, 2003; Seymour & Schilling, 2018), if we assume the proximal tibia in African apes to experience similar stress as found in humans during deep knee flexion (considering the differences in knee angle and size and shape of femoral condyles in great apes compared to humans), we would expect trabecular structure to re-model in a way supported by our results in *Gorilla* and *Pan*. Respectively, we would expect to find higher BV/TV values under the patellar tendon and on the medial condyle of the tibial plateau, specifically on its posterior side and all along the medial edge of the tibial plateau of the medial condyle (due to the varus knee angle) in African apes. These predictions were supported. Higher BV/TV values along the medial edge of the tibial plateau of the medial condyle was also found in our Mary Rose sample (i.e., active young males) compared to other humans in our sample and thus, it could be used as a potential explanation for why Mary Rose is plotting the closest to our non-human great ape taxa. Despite humans exhibiting stereotypical knee loading patterns compared to other great apes, the concentration of medial BV/TV could stem from frequent behaviours in our active human population sample. These behaviors include climbing stairs, sitting, squatting, or running, all of which involve varying degrees of knee flexion angles (Hardt 1978; Baltzopoulos, 1995; Anderson & Pandy, 2001; Kellis, 2001). Changes in knee angle have been observed to influence joint reaction force and contact area. For instance, more flexed knee postures lead to increased forces on the articular surface (Taylor et al. 2004; Kutzner et al. 2010) and a larger contact area at the posterior end of the condyles (von Eisenhart-Rothe et al. 2004).

Like African apes, the lateral meniscus in *Pongo* also has only one attachment site on the knee, facilitating a greater range of motion at the knee (i.e., knee posture can vary from full extension to full flexion) and thus the medial knee compartment might then experience higher loading in a similar way as in *Pan* and *Gorilla* (Girgis et al., 1975). This hypothesis is supported by our results where we found higher BV/TV distribution on the medial side of the tibial plateau compared to the lateral side (Figure 5.11). In general, the trabecular architecture in the proximal tibia of *Pongo* also suggests knee loading in flexed postures based on the BV/TV concentration

pattern found in the tibial plateau (Figure 5.11). However, the tibial plateau loading differs significantly from *Pan* and *Gorilla* but not from *Homo* (Figure 5.11; Table 5.3). This might be due to the more homogenous distribution between the lateral and medial side of the tibial plateau in *Pongo* compared to African apes as the knee has a greater range of motion and can be loaded in full flexion as well as full extension frequently. Moreover, *Pongo* and *Homo* show much lower mean BV/TV values in the tibial plateau compared to the African apes (Figure 5.11). As mentioned above, absolute values of BV/TV have previously been argued to show systemic differences across extant hominids (Dunmore et al., 2023; Saers et al., 2016; Tsegai et al., 2018; Ryan & Shaw, 2012) and thus this can be also the case when testing mean BV/TV values in the tibial plateau only and/or we did not find the significant differences between *Pongo* and *Homo* due to the limited sample size of our *Pongo* sample.

5.6 Conclusion

This study is an examination of trabecular bone architecture within the hominid proximal tibia. Trabecular architecture in *Homo* indicates habitual use of extended knee postures during bipedalism and significantly differs from African apes. However, despite *Homo* loading only the lower limb during locomotion, mean BV/TV was significantly lower on the tibial plateau than that of great apes. Trabecular architecture of African apes indicates higher medial knee compartment loading and use of flexed knee posture during terrestrial and arboreal locomotion and significantly differs from *Homo* and *Pongo*. Trabecular architecture of the proximal tibia suggests a greater amount of knee extension in *Pongo* compared to African apes and in female *Gorilla* compared to male *Gorilla*. Trabecular structure was not substantially different between sexes in *Pan* or *Homo*, reflecting greater presumed similarity in proximal tibia loading between sexes in these taxa. This study offers a comparative context of trabecular structure in the hominoid proximal tibia and can contribute to future studies of locomotion in extinct taxa.

5.7 Supplementary material

Table S5.1: Descriptive statistics of BV/TV distribution in tibial plateau.

Taxa	Region	n	mean	SD	min	max	median
Homo	tibial plateau	25	0.237	0.056	0.147	0.353	0.236
	lateral		0.235	0.061	0.135	0.359	0.234
	medial		0.224	0.050	0.148	0.338	0.228
Gorilla	tibial plateau	13	0.317	0.030	0.258	0.352	0.323
	lateral		0.305	0.028	0.249	0.337	0.309
	medial		0.315	0.032	0.254	0.363	0.322
Pan	tibial plateau	15	0.317	0.051	0.239	0.402	0.311
	lateral		0.310	0.053	0.215	0.302	0.397
	medial		0.311	0.050	0.236	0.401	0.311
Pongo	tibial plateau	7	0.239	0.029	0.192	0.281	0.237
	lateral		0.225	0.032	0.176	0.261	0.225
	medial		0.243	0.027	0.198	0.288	0.246

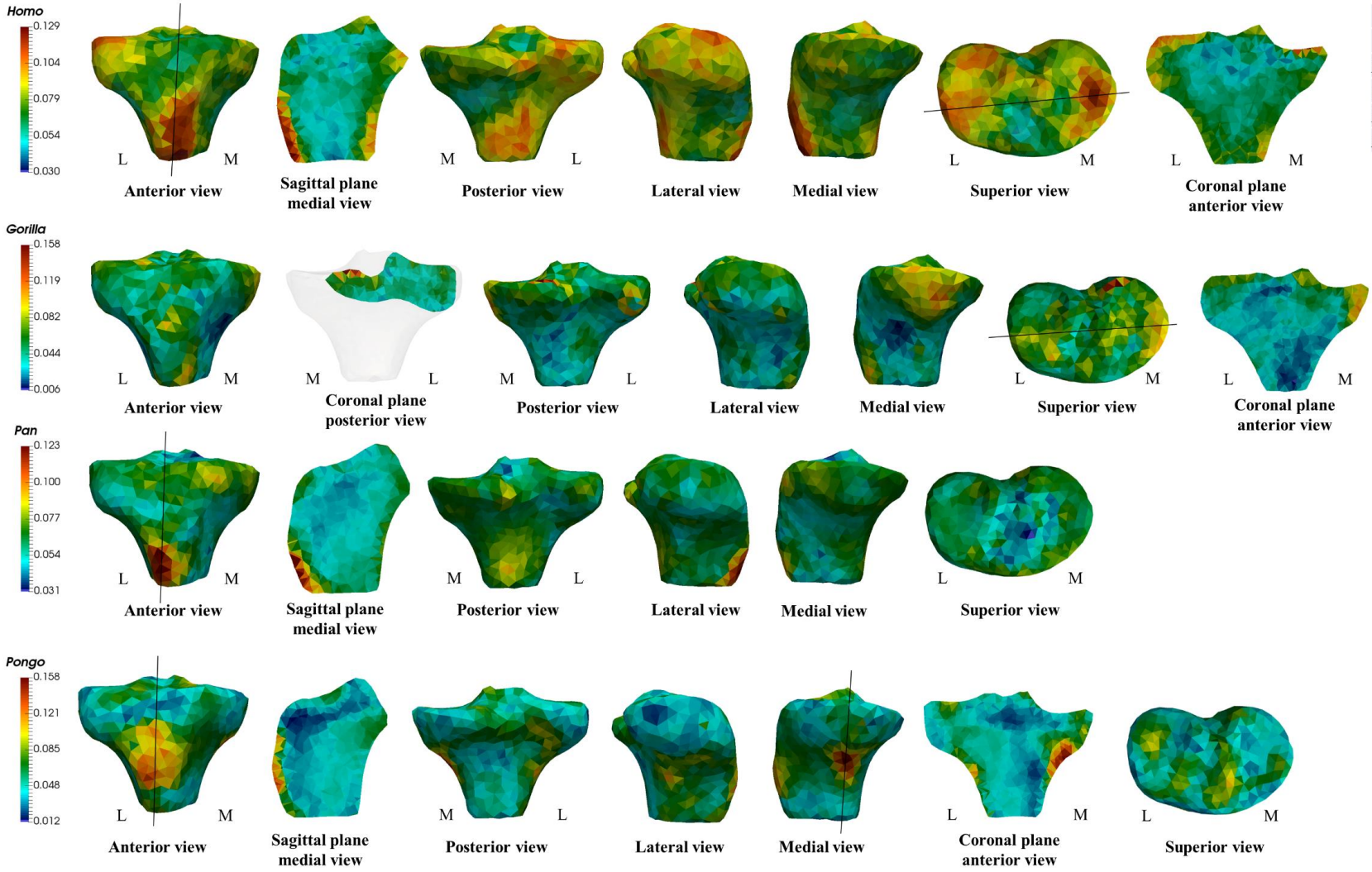

	Proximal tibia	
	Mean	SD
Homo	0.201	0.129
Gorilla	0.254	0.158
Pan	0.278	0.123
Pongo	0.216	0.158

Figure S5.1: Taxa standard deviation models of rBV/TV values in the proximal tibia of *Homo*, *Gorilla*, *Pan*, and *Pongo*. Vertical and horizontal lines through the SD models show where the cross-sectional sagittal and coronal planes are positioned. Red colour shows the highest variability in the rBV/TV values and blue colour shows the lowest variability in the rBV/TV values. L, lateral; M, medial.

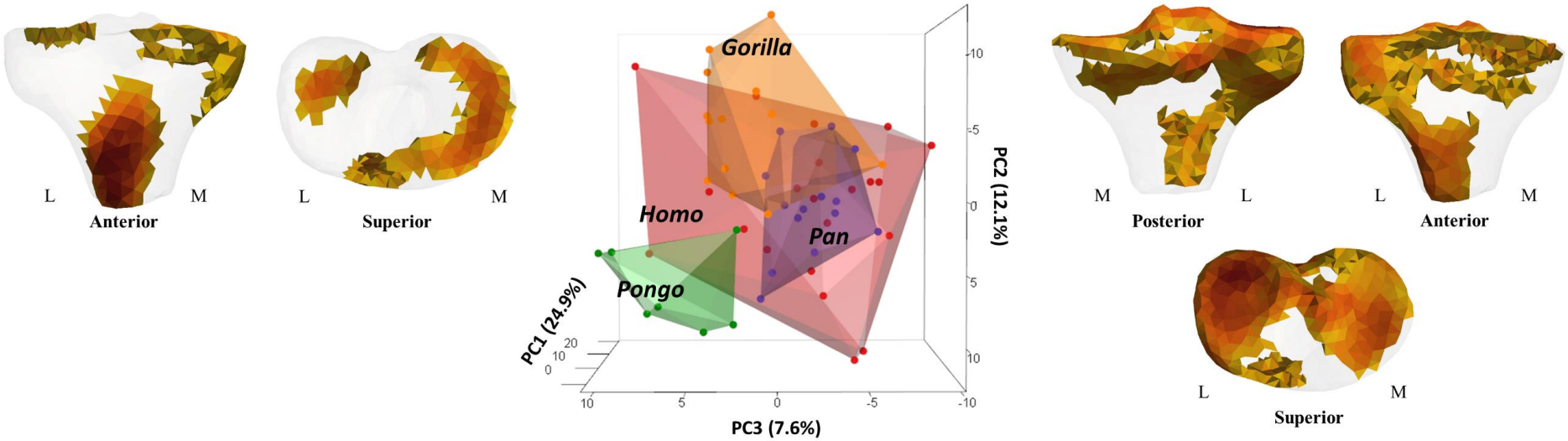

Figure S5.2: PC3 of rBV/TV distribution in proximal femur of *Homo*, *Gorilla*, *Pan*, and *Pongo* showing separation among studied taxa. Models at the end of each axis represent the regions of high rBV/TV driving variance along PC3. Models demonstrate the rBV/TV values separating between *Pongo* (positive PC3+3SD) and *Pan* (negative PC3-3SD). L, lateral; M, medial.

	Proximal tibia	
	Mean	SD
Homo	0.404	0.176
Gorilla	0.380	0.157
Pan	0.370	0.125
Pongo	0.350	0.152

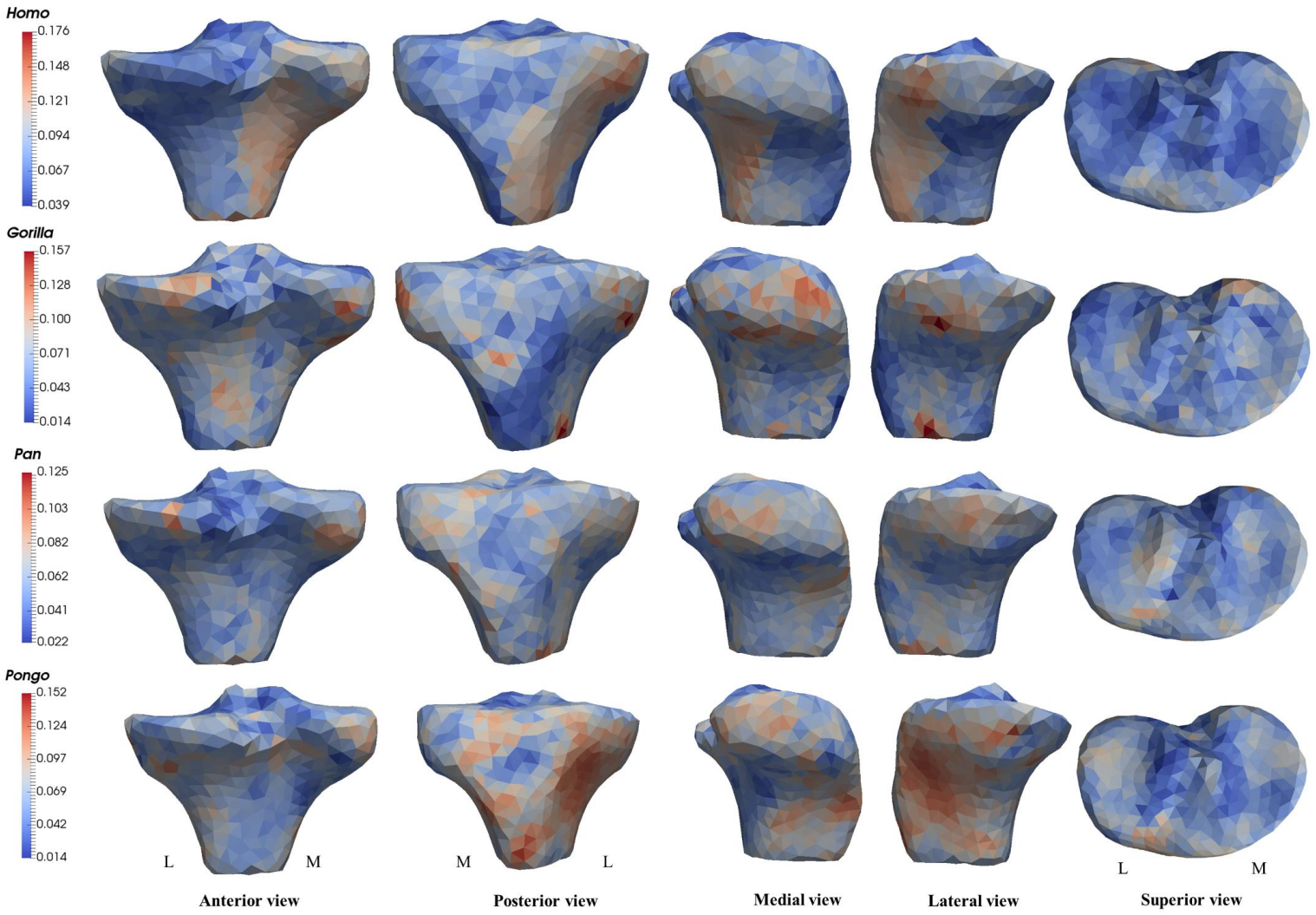

Figure S5.3: Taxa SD models of DA distribution of the proximal tibia of *Homo*, *Gorilla*, *Pan*, and *Pongo*. Red colour shows the highest variability in the DA values and blue colour shows the lowest variability in the DA values. L, lateral; M, medial.

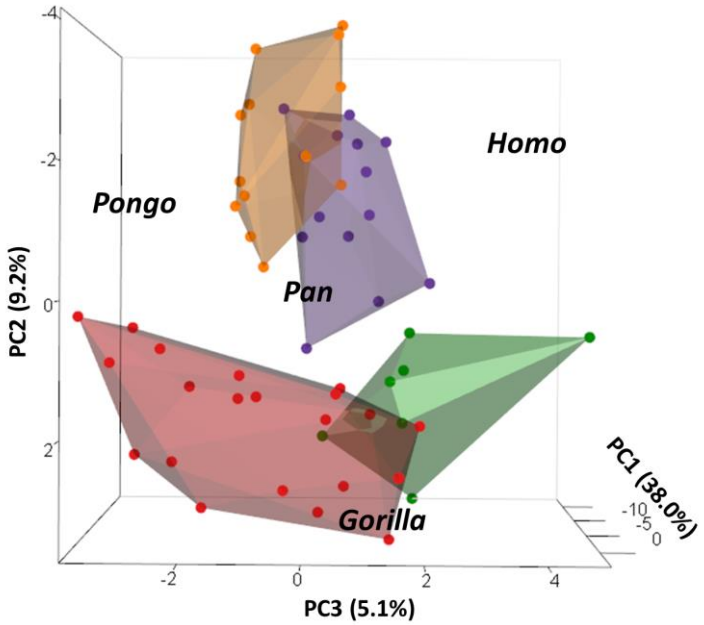

Figure S5.4: PCA of DA distribution in the proximal tibia of *Homo*, *Gorilla*, *Pan*, and *Pongo* on PC3.

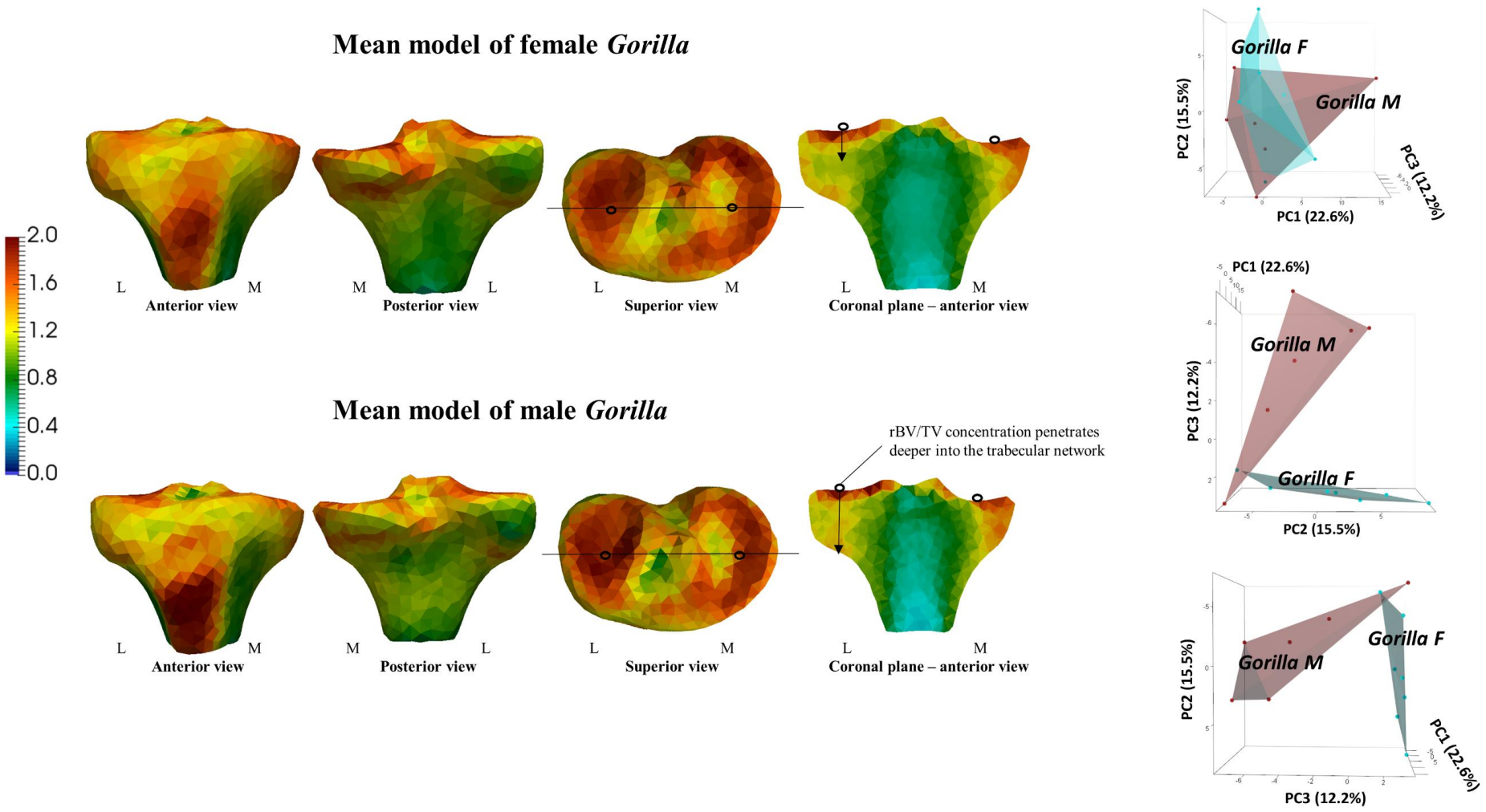

Figure S5.5: *Gorilla* mean models and PCA of rBV/TV distribution in the proximal tibia of *Gorilla* showing no separation on PC1 and partial separation on PC2 and PC3. Horizontal lines through the superior view mean models show where the cross-sectional coronal planes are positioned. Circles in the superior and anterior views represent the homologous locations. F, female; M, male.

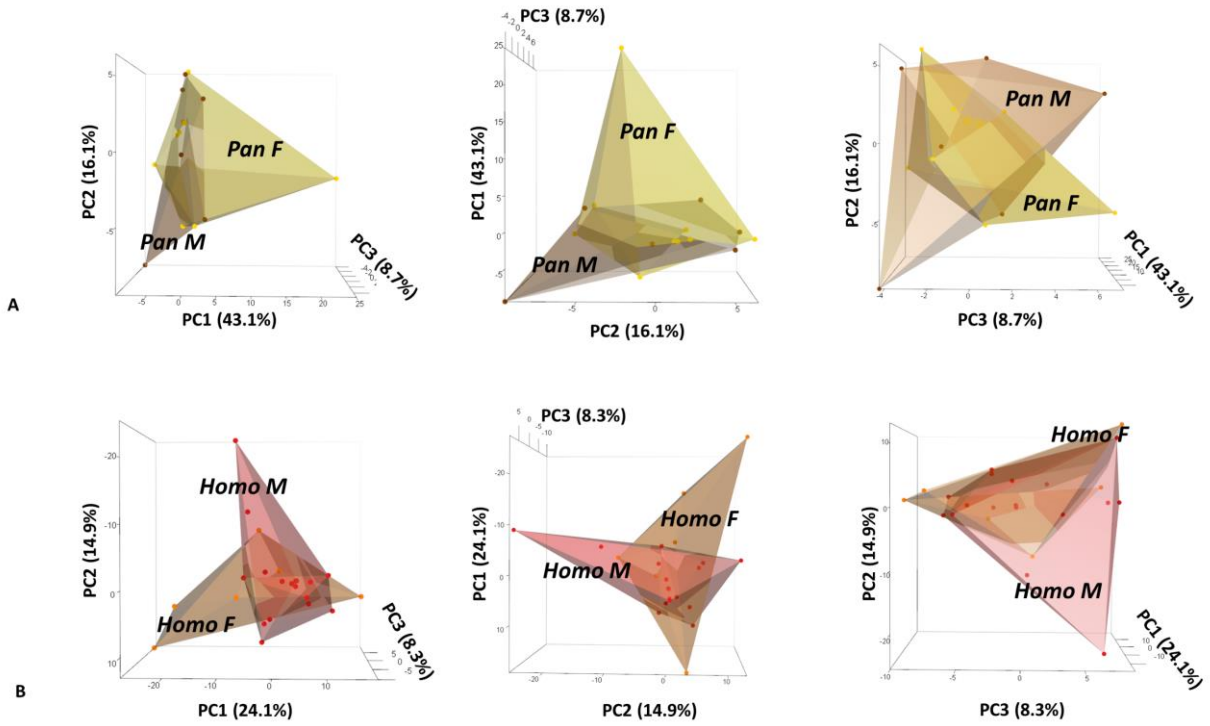

Figure S5.6: PCA of rBV/TV distribution in the proximal tibia of (A) *Pan* and (B) *Homo* showing no separation between sexes. F, female; M, male.

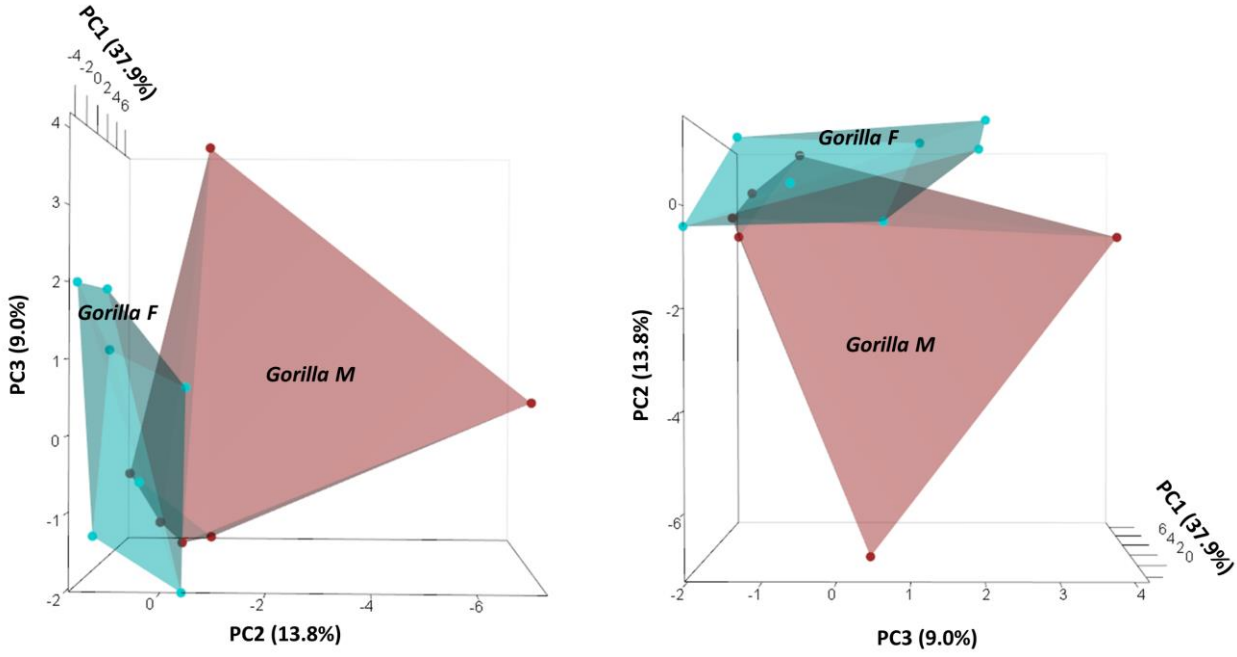

Figure S5.7: PCA of DA distribution in proximal tibia of *Gorilla* showing no separation between sexes on PC2 and PC3. F, female; M, male.

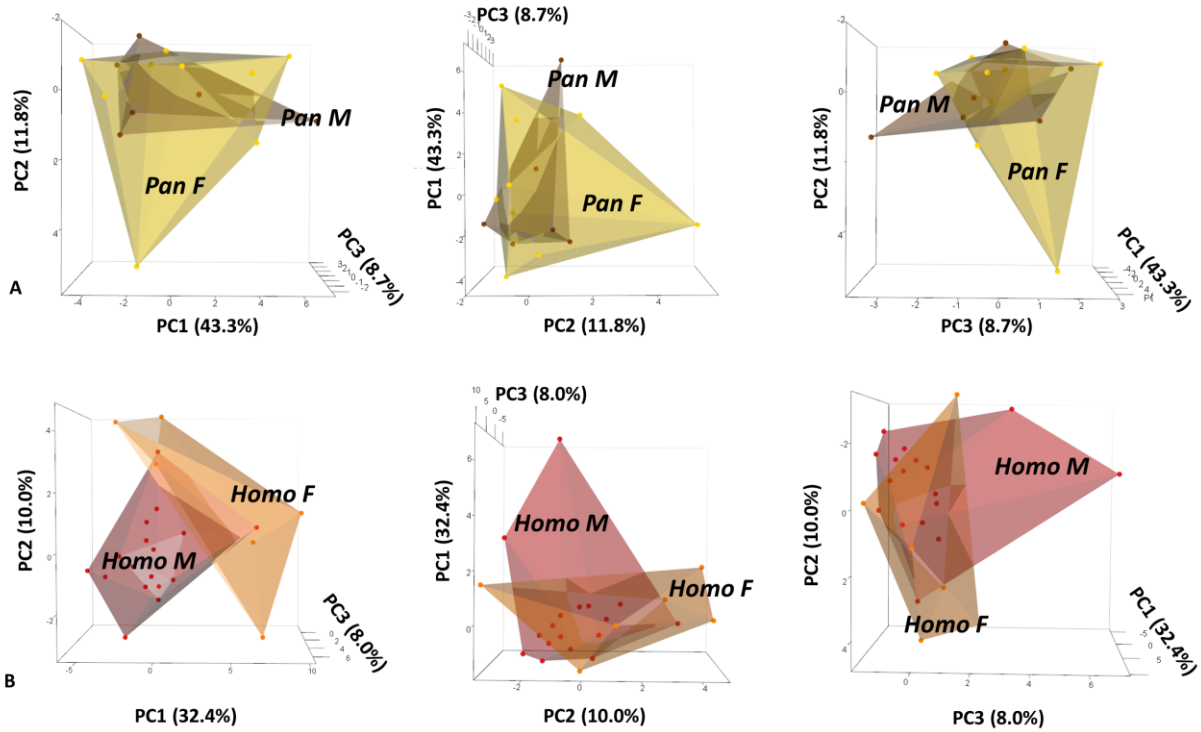

Figure S5.8: PCA of DA distribution in proximal tibia of (A) *Pan*, and (B) *Homo* showing no separation between sexes. F, female; M, male.

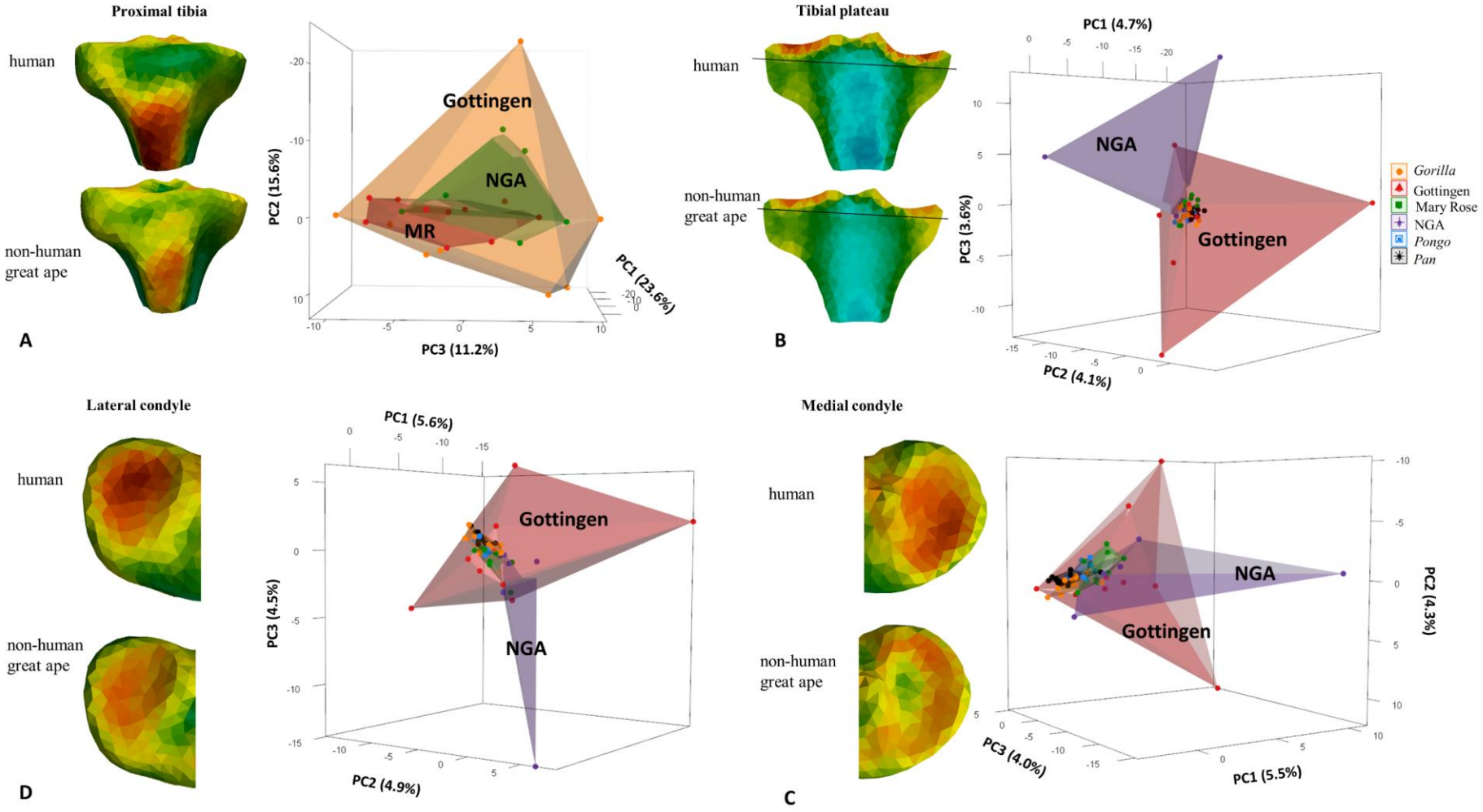

Figure S5.9: PCA of rBV/TV distribution in the whole proximal tibia (A) of *Homo* showing no separation between populations; in the tibial plateau (above the line) (B); in the medial side of tibial plateau (C); in the lateral side of tibial plateau (D) showing the highest variability of rBV/TV values in the post-industrial population assumed to represent low levels of activity (Gottingen) and in the population from the Medieval period (11th to 16th centuries) assumed to represent higher levels of activity (NGA). Sample of young active male adults (Mary Rose/MR) is within the non-human ape sample.

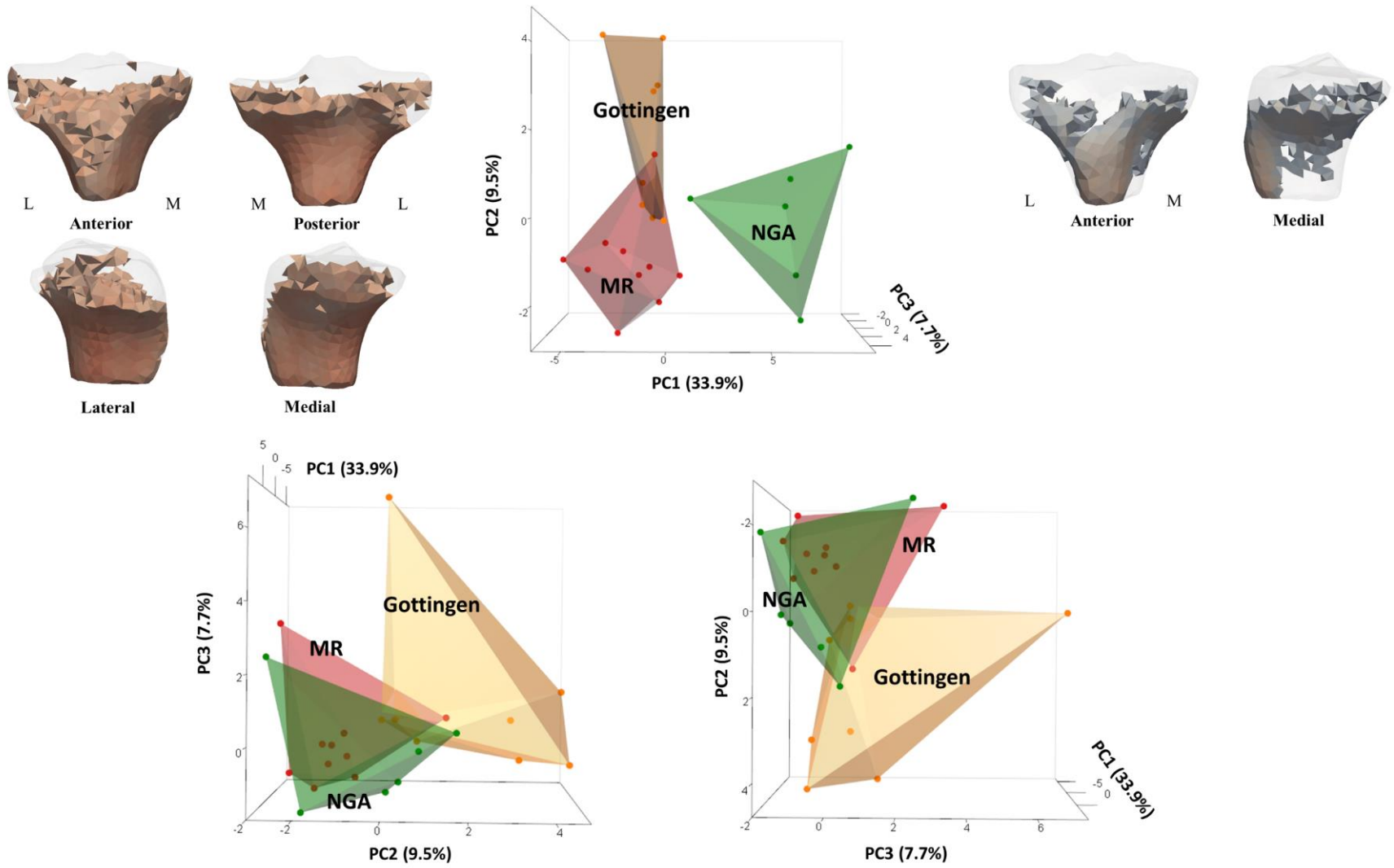

Figure S5.10: PCA of DA distribution in the proximal tibia of *Homo* showing separation between populations on PC1 and no separation on PC2 and PC3. Models at the end of each axis represent the regions of high DA driving variance along PC1. Models demonstrate the regions loaded in the most stereotypical way causing the separation between Gottingen and MR populations (negative PC1-3SD) and NGA population (positive PC1+3SD). L, lateral; M, medial.

6 TRABECULAR ARCHITECTURE OF THE DISTAL FEMUR AND PROXIMAL TIBIA IN FOSSIL HOMININS

6.1 Abstract

This study investigates the internal morphology of fossilized distal femora and proximal tibia from *Australopithecus* and *Homo* species, analyzing their implications for bipedalism and locomotor behavior. The valgus knee, commonly cited as evidence for bipedalism in *Australopithecus*, has been central to debates regarding the retention of climbing abilities in *Australopithecus afarensis*. External morphological variations, such as the anterior projection of the lateral patellar lip and differences in the patellar surface, distinguish members of the *Australopithecus* genus from one another and from *Homo*. However, reliance on external morphology alone may obscure subtle differences in knee biomechanics. This study uses micro-CT scanning and medical image analysis to examine trabecular bone structure in a comparative sample of *Homo sapiens* (femora N=26; tibiae N=25), *Gorilla gorilla* (femora N=14; tibiae N=13), *Pan troglodytes verus* (femora N=15; tibiae N=15), and *Pongo spp.* (femora N=9; tibiae N=7), alongside fossil specimens from *Australopithecus africanus* (StW 318, TM 1513), *Australopithecus sediba* (U.W. 88-63), *Homo floresiensis* (LB1-8, LB1-13), and *Homo neanderthalensis* (D322-15). Canonical holistic morphometric and principal component analyses were applied to compare trabecular architecture across species. Results reveal that the lateral femoral condyle in *StW 318* exhibits bone structure consistent with bipedal walking and frequent knee flexion, whereas *TM 1513* displays an ape-like distribution, indicating more diverse joint postures. The trabecular architecture of *Australopithecus sediba* suggests extended knee postures with flexion distinct from that of *Australopithecus africanus* and extant non-human apes. In *Homo floresiensis*, a combination of features suggests both extended and flexed knee postures, potentially indicating a unique form of bipedalism involving more flexed knees than in *Homo sapiens*. Finally, the trabecular structure of *Homo neanderthalensis* supports its status as an obligate biped with locomotion similar to modern humans. These findings underscore the diversity of locomotor adaptations among South African hominins and reveal distinct biomechanical patterns within the genus *Homo*.

6.2 Introduction

Bipedalism stands as a defining trait of the hominin lineage, with skeletal adaptations for this mode of locomotion evolving over the past six million years (e.g., Senut et al., 2001; Pickford et al., 2002; Crompton et al., 2008; Almecija et al., 2013). These adaptations are reflected throughout the skeleton, but the knee joint is particularly crucial for understanding how load is distributed through the lower limb. In modern humans, adaptations for bipedal locomotion include flat, ellipsoid femoral condyles and a distally elevated patellar lip (Heiple & Lovejoy, 1971; Tardieu, 1981). In contrast, African apes possess more circular distal femoral condyles, which are suited for both terrestrial and arboreal quadrupedal locomotion (Heiple & Lovejoy, 1971; Tardieu, 1981). Detecting bipedal adaptations in fossil hominins is key to placing them within the evolutionary lineage, although identifying such features in the earliest fossil hominins, like *Sahalenthropus*, *Orrorin* and *Ardipithecus*, remains debated (e.g., Pickford et al., 2002; Wolpoff et al., 2002; Zollikofer et al., 2005; Crompton et al., 2008; Lovejoy et al., 2009; Ohman et al., 2005; Almecija et al., 2013). In contrast, later hominins, such as *Australopithecus*, show more definitive evidence of obligate bipedalism (e.g., Ward et al., 1999; Lovejoy et al., 2002; Ward, 2013).

A. afarensis, for instance, exhibits an elongated femoral neck and a femoral muscular organization that resembles that of modern humans, alongside distal femoral characteristics indicative of habitual bipedality (Lovejoy, 2005; Lovejoy & Heiple, 1970; Tardieu, 1981). Lovejoy (2007) outlined several similarities and differences between the knee of *A. afarensis* and modern humans: 1) tibiofemoral force likely exceeds patellofemoral force during most locomotor activities, suggesting tibial knee dominance (i.e., tibia experiences greater loads and forces compared to the femur during various locomotor activities) in *A. afarensis* compared to earlier hominins, a trait shared with humans; 2) the bicondylar angle is higher than in modern humans and decreases with increasing flexion in *A. afarensis* contradicting the hypothesis proposed by some authors (e.g., Crompton et al., 1998; Jungers, 1988; Sockol et al., 2007; Crompton et al., 2018) that *A. afarensis* employs an exclusively 'bent hip/bent knee' gait, as this would not allow for the necessary knee extension to develop such a bicondylar angle; 3) the tibial plateau is more elliptical in *A. afarensis* compared to a more circular tibial plateau observed in quadrupedal primates; 4) both tibial condyles display anterior extension of the tibial plateau in *A. afarensis*, similar to humans, although the anteroposterior elongation of the patellar portion of the medial and lateral femoral condyles is not as pronounced in *A. afarensis* as in humans (Lovejoy, 2007). *A. africanus* shares similar knee morphology traits with *A.*

afarensis, including adaptations indicative of committed terrestrial bipedality. For example, the foot morphology of *A. afarensis* provides clear evidence of habitual bipedalism (Ward et al., 2011). Moreover, *Australopithecus* species display distinctive anatomical features at the knee joint. Notably, they possess a unique single anterior attachment for the lateral meniscus (Frelat et al., 2017). This singular attachment facilitates greater medial and lateral rotation of the knee joint (Tardieu, 1999; Landis & Karnick, 2006; Javois et al., 2009), a trait that would also support climbing activities. Additionally, *Australopithecus* possess a relatively straight and unprojected tibial tuberosity, a feature shared with apes (Frelat et al., 2017). In contrast to apes, however, *Australopithecus* display more equal-sized femoral and tibial condyles akin to humans. This equality suggests a similar weight transfer through the condyles, a feature theorized to enhance joint stability during bipedal locomotion (e.g., Tardieu, 1999; Landis & Karnick, 2006; Organ & Ward, 2006; Javois et al., 2009; Sylvester & Pfisterer, 2012; Sylvester, 2013).

Latimer (1991) proposed that the hand of *A. afarensis* was primarily adapted for manipulation rather than arboreality. According to this view, traits conducive to climbing might be evolutionary remnants from a common ancestor adapted to arboreal life, rather than features actively maintained by selection for climbing. This argument is based on the idea that traits beneficial for bipedality and manipulation would be stabilized by selection, unlike those for arboreality. Critics argue that the relatively short fingers of *A. afarensis*—in comparison to those of non-human great apes—are not optimal for effective arboreal grasping. Thus, these critics suggest that the hand's morphology reflects selective pressures favoring manipulation abilities over climbing (Latimer, 1991; Alba et al., 2003). In contrast, Susman (1983) suggested that bipedalism did not evolve as a single, isolated adaptation but rather as a complex response to a changing environment and a combination of selective pressures acting on our ancestors over millions of years. He highlighted features such as the shape of the pelvis, the position of the foramen magnum, the structure of the foot, and the alignment of the spine, all of which are characteristic of bipedalism and distinguish humans from other primates and suggested that these anatomical changes likely evolved gradually over time in response to the selective pressures associated with bipedal locomotion (Susman, 1983; Susman et al., 1984). The mixture of human and ape-like external traits found in *Australopithecus* has sparked significant debate about the nature of bipedalism and the extent of arboreal behavior within this genus (e.g., Stern & Susman, 1983; Susman et al., 1984; Berge, 1994; Carey & Crompton, 2005; Lovejoy & McCollum, 2010; Raichlen et al., 2010). While species such as *H. erectus* and later hominins like *H. neanderthalensis* are generally recognized as fully bipedal, the timeline for the transition

to obligate bipedalism is still debated (e.g., Susman et al., 1984; Wood & Collard, 1999; Berillon, 2004; Bramble & Lieberman, 2004; Harcourt-Smith & Aiello, 2004). Traditional studies of fossil hominin bipedalism have focused primarily on external morphological traits (e.g., Stern & Susman, 1983; Lovejoy & Heiple, 1970; Tardieu, 1981; Lovejoy, 2005; 2007; Harmon, 2009; Lovejoy et al., 2009; Senut et al., 2018). However, to gain a deeper understanding of past behaviors, functional analyses that emphasize traits influenced by function are essential. For example, trabecular bone architecture has become a key tool in reconstructing past behaviors, as it reflects habitual postures and locomotion patterns throughout an individual's life (e.g., Macchiarelli et al., 1999; DeSilva & Devlin, 2012; Barak et al., 2013; Tsegai et al., 2013; Skinner et al., 2015; Stephens et al., 2016; Ryan et al., 2018).

Chapter 4 and **5** investigated the trabecular bone structure of the distal femur and proximal tibia in extant great apes. These chapters linked the patterns of trabecular bone distribution with the distinct habitual locomotor behaviours exhibited by each of the extant taxa. By testing and demonstrating this connection between trabecular bone morphology and locomotor repertoires, a comparative framework was established to infer locomotor behaviours in fossil hominins. This chapter discusses the locomotor repertoires of *A. africanus*, *A. sediba*, *H. floresiensis*, and *H. neanderthalensis* based on the trabecular distribution of the distal femur (Table 6.1). In the case of *H. floresiensis*, the analysis also included the proximal tibia (Table 6.1). This was particularly interesting as the femur and tibia are associated with the same individual of *H. floresiensis* (LB1) which allowed me to analyse and discuss the knee of *H. floresiensis* from a more holistic perspective. The same methodological approach described in **Chapter 2** was applied to the fossil sample to explore the trabecular bone structure of their distal femur/proximal tibia. Any adjustments made to the method of analysis for a specific species or specimen are detailed in methodology subsection of this chapter.

In this chapter, I conducted a comparative analysis of the trabecular bone distribution in the distal femoral condyles and proximal tibial condyles, where trabecular bone strength is generally higher within the bones during locomotion (Harada et al., 1988), across modern humans, *Gorilla*, *Pan*, and *Pongo* (Table 2.1). I examined two fossil hominin specimens from Sterkfontein, South Africa (*A. africanus*; distal femora StW 318 and TM 1513), one fossil hominin specimen from Malapa, South Africa (*A. sediba*; distal femur U.W. 88-63), one fossil hominin specimen from Liang Bua, Indonesia (*H. floresiensis*; distal femur LB1-8 and proximal tibia LB1-13), and one fossil hominin specimen from Kleine Feldhofer Grotte, Germany (*H. neanderthalensis*; distal femur D322-15) (Table 6.1). This analysis utilized a canonical holistic

morphometric analysis (cHMA) with a whole-epiphysis approach. Detailed information about this method can be found in **Chapter 2**.

The first aim of this chapter was to test whether the trabecular architecture of the distal femur in *A. africanus*, *A. sediba*, *H. floresiensis*, and *H. neanderthalensis* reflects rather ape-like (i.e., flexed knee postures) or a modern *Homo*-like (i.e., extended knee postures) morphology. An ape-like distribution would be supported by high bone volume fraction (BV/TV) posterosuperiorly in the femoral condyles, medially on the patellar surface of the femur, and by higher BV/TV in the medial femoral condyle compared to lateral femoral condyle. This distribution pattern reflects higher medial knee compartment loading, compared to humans, due to habitual flexed knee postures in non-human apes as discussed in **Chapter 4**.

A modern *Homo*-like distribution would be supported by high BV/TV posteroinferiorly in the femoral condyles, laterally on the patellar surface of the femur, and by higher BV/TV in the lateral femoral condyle compared to medial femoral condyle. This distribution pattern reflects higher lateral knee compartment loading, compared to non-human great apes, due to humans' habitual extended knee posture as discussed in **Chapter 4**.

The second aim of this chapter was to test whether the trabecular architecture of the proximal tibia in *H. floresiensis* reflects rather ape-like or modern *Homo*-like morphology. Again, to objectively assess which functional interpretations the analyses of internal structure of the proximal tibia supports, no specific predictions were made for *H. floresiensis*. An ape-like distribution would be supported by higher BV/TV in the medial tibial condyle, and by BV/TV under the tibial plateau concentrated more medially on the medial condyle. This distribution pattern reflects higher medial knee compartment loading and more flexed knee position and varus knee angle (compared to *Homo*) during all types of locomotion in non-human apes as discussed in **Chapter 5**.

A modern *Homo*-like distribution would be supported by homogenous distribution of BV/TV across both tibial condyles compared to other great apes, and by BV/TV on the tibial plateau concentrated in the anteroposterior centre of each tibial condyle. This distribution pattern reflects relatively evenly loaded proximal tibia and extended knee posture during most of bipedal walking cycle as discussed in **Chapter 5**.

Table 6.1: Sample composition of the fossil sample used in this study.

		bone (n)			sex		
Extinct sample	**specimen**	**femur**	**tibia**	**Side**	**female**	**male**	**unknown**
Australopithecus africanus	StW 318	1	0	L	0	0	1
	TM 1513	1	0	R	0	0	1
Australopithecus sediba	MH2 U.W. 88-63	1	0	R	1	0	0
Homo floresiensis	LB1-8	1	0	R	1	0	0
	LB1-13	0	1	R	1	0	0
Homo neanderthalensis	Neanderthal-1 D322-15	1	0	L	0	0	1

6.3 Methodology

Chapter 2 provides detailed information about the external and internal bone preservation of each fossil in the sample. Unfortunately, not all fossils described in **Chapter 2** were included in the trabecular bone analysis. Fossil StW 129 was excluded due to the presence of a growth plate in the trabecular structure indicating this specimen is not adult (Figure 2.1) and fossils LB1-9 (Figure 2.5), and LB8-1 (Figure 2.7) were excluded from the sample due to their poor trabecular bone preservation.

Firstly, each fossil was segmented using the medical image analysis (MIA) clustering algorithm (Dunmore et al., 2018) with an individualised protocol to produce the best segmentation with minimal manual cleaning to avoid subjective decision making of the cleaning which decreases the reproducibility of results. Although in some fossils manual cleaning was applied (Appendix A; Figure A1 – A5). **Chapter 2** provides detailed information about the MIA segmentation and its implementation. Secondly, all fossil specimens included in the trabecular bone analysis (Table 6.1) were registered to the canonical bone of the distal femur or proximal tibia using individual landmark sets. Further information on the creation of the canonical bone and the implementation of cHMA can be found in **Chapter 2**. Initially, homologous landmarks across the fossil specimens and canonical bone were placed in Avizo 6.3 (Figure 6.1). Information about the landmarks locations for a specimen is described in Table 6.2. This ensured that the fossil was appropriately rigidly transformed to the canonical bone during registration, allowing for further analysis and comparison with the extant sample. For the subsequent step of meshing, the canonical mesh created from the extant sample was utilized. In other words, the transformation data from the extant sample were used to warp the tetrahedral canonical mesh of the extant sample onto the individual fossil data. Finally, morphometry (HMA) was

performed on the original images and then interpolated on the warped canonical mesh. BV/TV was initially measured in the same manner as described in **Chapter 2**. The presumed location (based on the anatomical location of extant primates) of femoral/tibial insertions of ligaments and tendons were located in the canonical distal femur/proximal tibia shape (thus hereafter, just 'insertions').

Table 6.2: Positions of the individual landmark sets used for the cHMA registration of the fossil sample. The landmarks used differ between specimens due to the variable preservation of the external surface of the fossils.

specimen	landmark number	landmark position
StW-318	1	The most proximal point of the lateral patellar lip.
	2	The middle of the proximal border of the patellar surface.
	3	The middle of the distal border of the patellar surface.
	4	The most postero-proximal point of the lateral condyle.
	5	Below the lateral epicondyle; in the popliteal groove.
TM-1513 U.W. 88-63	1	The most proximal point of the lateral patellar lip.
	2	The most proximal point of the medial patellar lip.
	3	The middle of the patellar surface.
	4	The middle of the intercondylar fossa.
	5	The middle of the inferior border of the medial condyle.
	6	The most postero-proximal point of the lateral condyle.
	7	Below the lateral epicondyle; in the popliteal groove.
LB1-8	1	The most proximal point of the lateral patellar lip.
	2	On the patellar surface.
	3	Proximo-lateral border of the lateral condyle.
	4	The most distal point of the lateral condyle in the lateral view.
	5	The most postero-proximal point of the lateral condyle.
	6	The middle of the posterior border of the medial condyle.
	7	Above the medial epicondyle.
LB1-13	1	The middle of the lateral side of the tibial plateau.
	2	The middle of the medial side of the tibial plateau.
	3	The most anterior point of the tibial plateau.
	4	The middle of the tibial tuberosity.
	5	Postero-medial side below the tibial plateau.
	6	Postero-lateral side below the tibial plateau.
	7	Lateral border below the lateral tibial condyle.
	8	Medial border below the medial tibial condyle.
Neanderthal-1 D322-15	1	The most proximal point of the lateral patellar lip.
	2	The most proximal point of the medial patellar lip.
	3	The middle of the patellar surface.
	4	The middle of the intercondylar fossa.
	5	The most postero-proximal point of the medial condyle.
	6	The most postero-proximal point of the lateral condyle.
	7	Centre of the lateral epicondyle.
	8	Centre of the medial epicondyle.

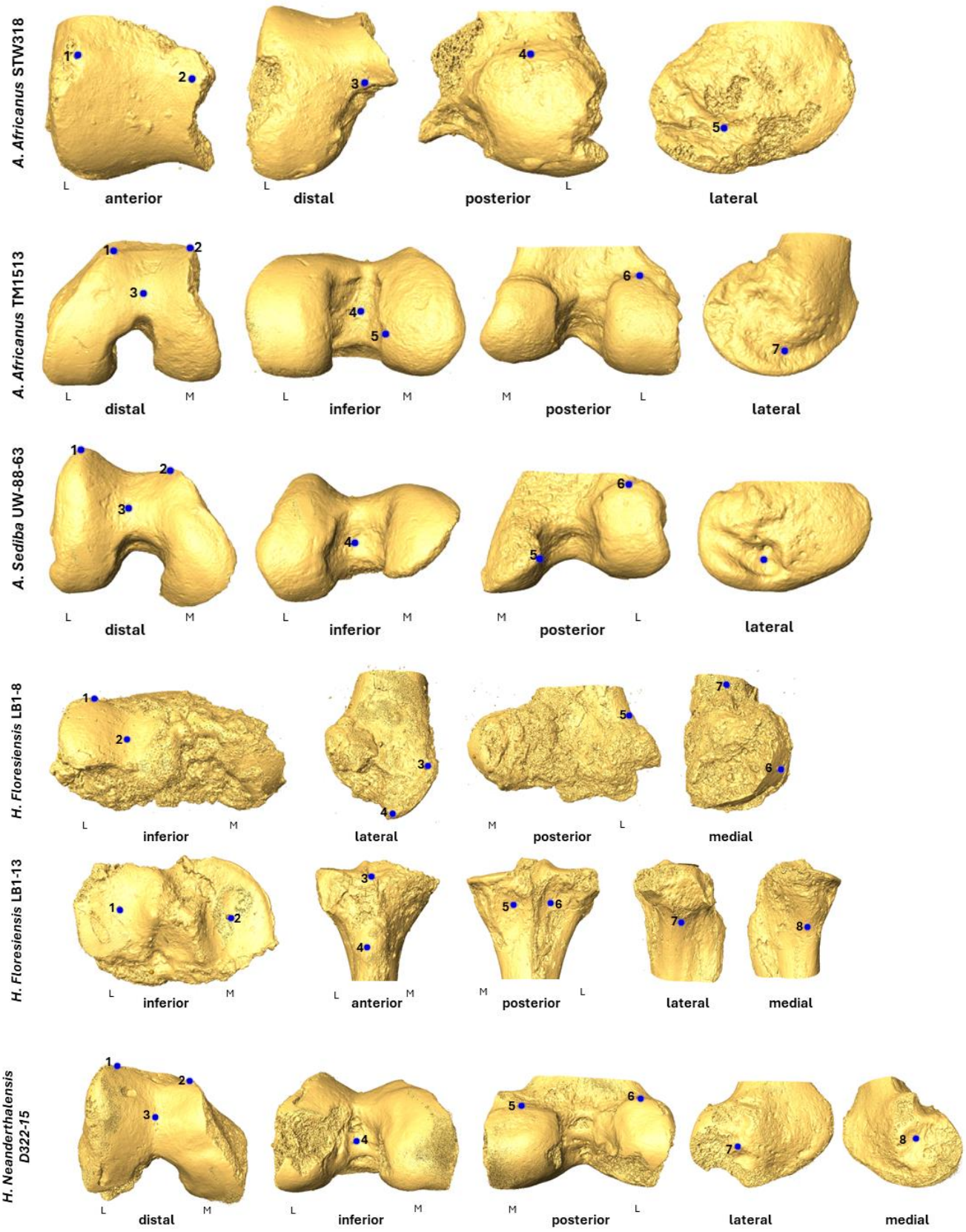

Figure 6.1: Positions of the individual landmark sets used for the cHMA registration of the fossil sample. L, lateral; M, medial.

Due to fossil fragmentation and poor trabecular bone preservation across the fossils, a script in Medtool was developed to detect only tetrahedral elements containing preserved trabeculae. This script analyses individual images and uses the mesh to count the number of non-zero voxels inside each tetrahedral element. As the canonical mesh is overlapping the voxel image, the centroid (i.e., its coordinate) of each voxel for each tetrahedral element is examined. If the centroid is outside of the tetrahedral element, it is flagged. The output is a .csv file containing the number of non-zero voxels within each element, along with a mesh displaying the same information. This allows for the removal of all tetrahedral elements with non-zero voxels where bone (or marrow) is not expected, using Paraview. As cHMA creates a geometicaly homologous canonical mesh into which the data are interpolated (for more details see **Chapter 2**), this process can be applied to all individuals in the sample, enabling further analysis such as Principal Component Analysis (PCA) to be implemented only on cells with preserved trabecular structure. Information about which cells were removed for a specimen/species is described within that subsection of this chapter.

6.4 Results

6.4.1 Australopithecus africanus

6.4.1.1 StW 318

Figure 6.2 shows the relative bone volume (rBV/TV) distribution in the lateral femoral condyle of StW 318. The highest 30% of rBV/TV values were considered as high and locations with these values were assumed to be subjected to the most habitual load. High rBV/TV values are predominantly located in the posteroinferior volume of the lateral condyle. Particularly elevated values are observed on the patellar articular surface of the femur and beneath the presumed insertions of the cruciate ligaments and gastrocnemius muscle (Figure 6.2). In contrast, the rBV/TV values in the lateral epicondyle represent the medium 50% of rBV/TV values. The lowest rBV/TV values were found in the distal volume of lateral condyle (see the cross-section lateral view; Figure 6.2). The elements with no information due to missing fossil bone, depicted in dark blue (Figure 6.2a), were removed for further analysis (Figure 6.2b).

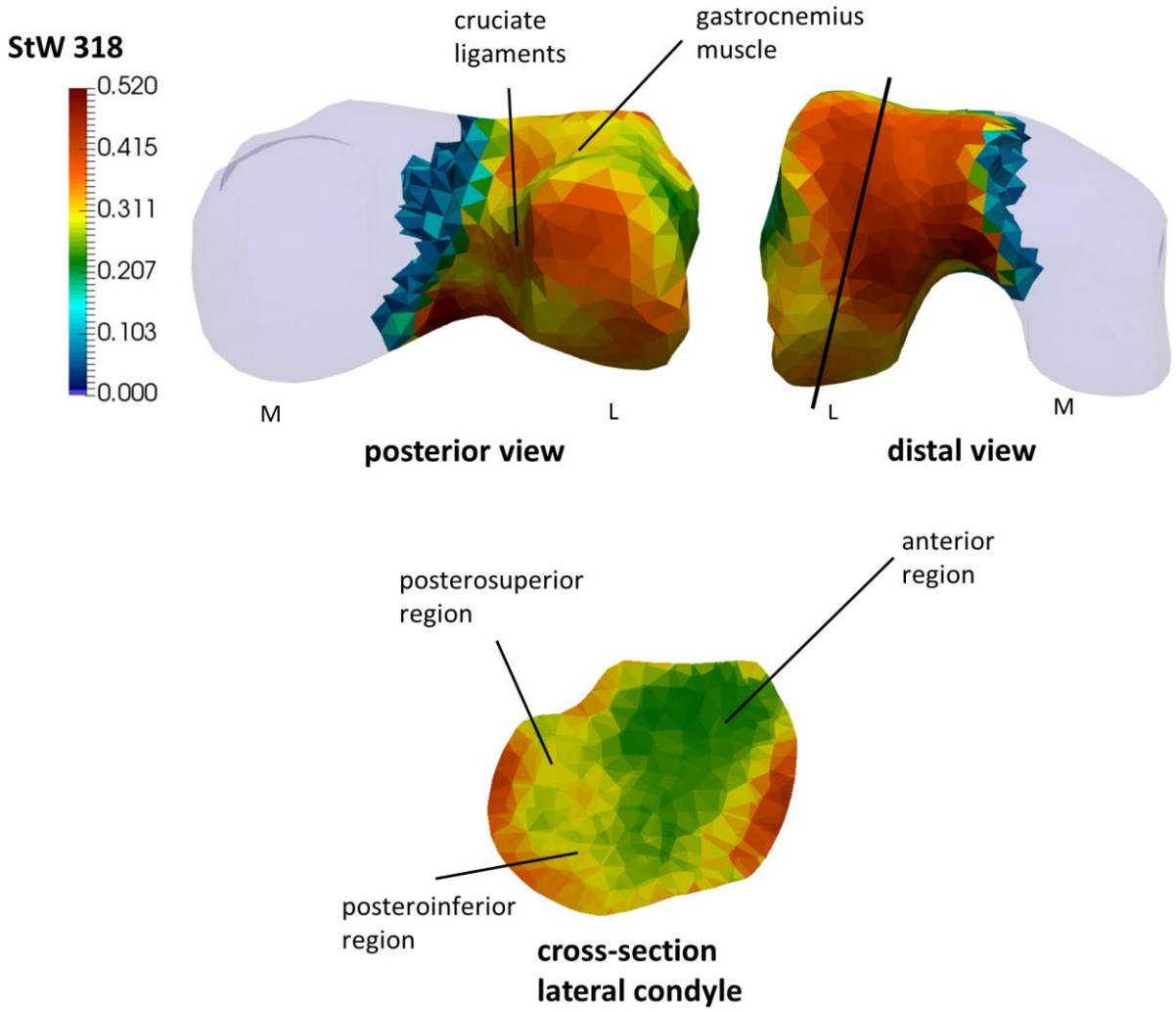

Figure 6.2: BV/TV distribution in the lateral condyle of *A. africanus* StW 318 specimen. Vertical line in the distal view shows where the cross-section is positioned. L, lateral; M, medial.

Figure 6.3 displays the outcomes of PCA of the rBV/TV distribution in the lateral condyle, compared to the extant sample. PC1 explains 20% of the variation in rBV/TV values across mesh cells. It effectively segregates *Homo* from great apes, as positive PC1 scores are driven by higher rBV/TV on the patellar surface of the femur, while negative PC1 scores, associated with non-human great apes, are linked to higher rBV/TV under the lateral epicondyle and in the posteroinferior region of the lateral condyle (Figure 6.4). StW 318 plots equidistant from *Pan* and *Homo* centroids and plots closest to *Pongo* and *Gorilla* on PC1, although one human individual in the sample also falls within this distribution (Figure 6.4).

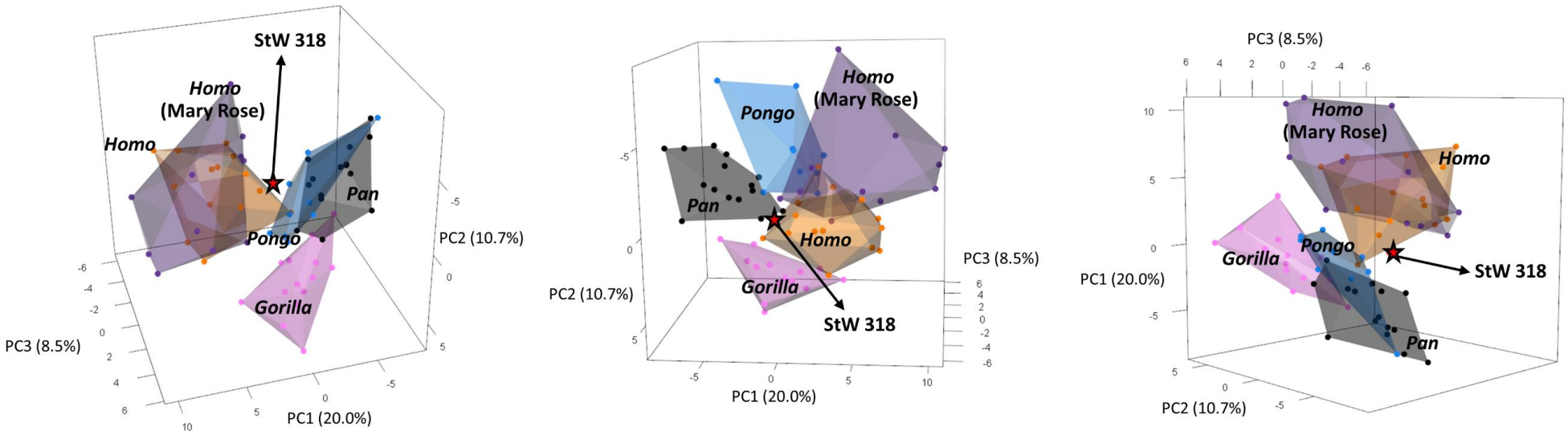

Figure 6.3: PCA of the rBV/TV distribution in the lateral femoral condyle of *A. africanus* StW 318 specimen (red star), *Homo*, *Gorilla*, *Pan*, and *Pongo* showing in the different views.

PC2, accounting for 10.7% of the variation in rBV/TV values, distinctly separates *Gorilla* from the other taxa. Positive PC2 values distinguish *Gorilla* due to a distinct pattern under the patellar surface, lateral epicondyle, and in the posteroinferior region of the lateral condyle (Figure 6.4). Conversely, negative PC2 values differentiate the other taxa from *Gorilla*, primarily due to high rBV/TV values under the presumed insertion sites of the gastrocnemius muscle and cruciate ligaments, as well as due to the concentrated area of high rBV/TV above the patellar surface of the femur, visible in anterior view (Figure 6.4). StW 318 is separated completely from the range of *Gorilla* distribution however, it is somewhere between *Pan, Pongo,* and *Homo* sample (Figure 6.3; Figure 6.4). PC3 accounted for 8.5% of the variation in rBV/TV and did not separate the taxa from each other (Figure 6.3).

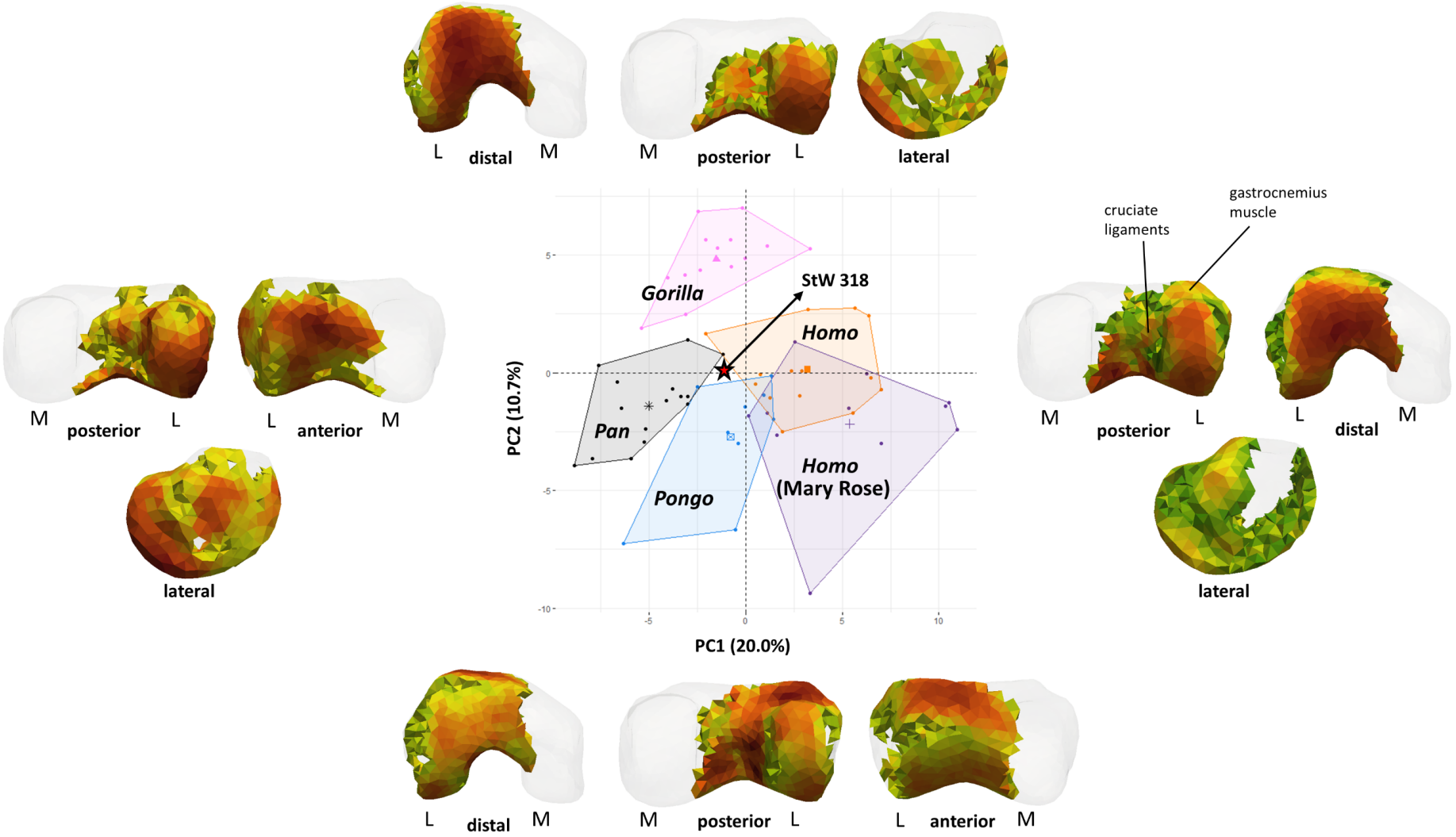

Figure 6.4: Loading models of PC1 and PC2 of the rBV/TV distribution in the lateral femoral condyle of *A. africanus* StW 318 specimen (red star), *Homo*, *Gorilla*, *Pan*, and *Pongo*.

6.4.1.2 TM 1513

Figure 6.5 shows the rBV/TV distribution in the femoral condyles of TM 1513 specimen. The areas with high rBV/TV values are predominantly located in the posteroinferior volume of both femoral condyles. Particularly higher values are observed on the medial side of the patellar articular surface and beneath the presumed insertions of the cruciate ligaments and gastrocnemius muscle, and in the distal volume of medial condyle (Figure 6.5). In contrast, the rBV/TV values in the lateral epicondyle represent the interquartile range of rBV/TV values, medial epicondyle is missing. The lowest rBV/TV values were found in the distal volume of lateral condyle, however, deeper in the trabecular alignment of this region, high rBV/TV was found (see the cross-section view of the lateral condyle; Figure 6.5a). The elements with no information, depicted in dark blue (Figure 6.5a) were removed for further analysis (Figure 6.5b).

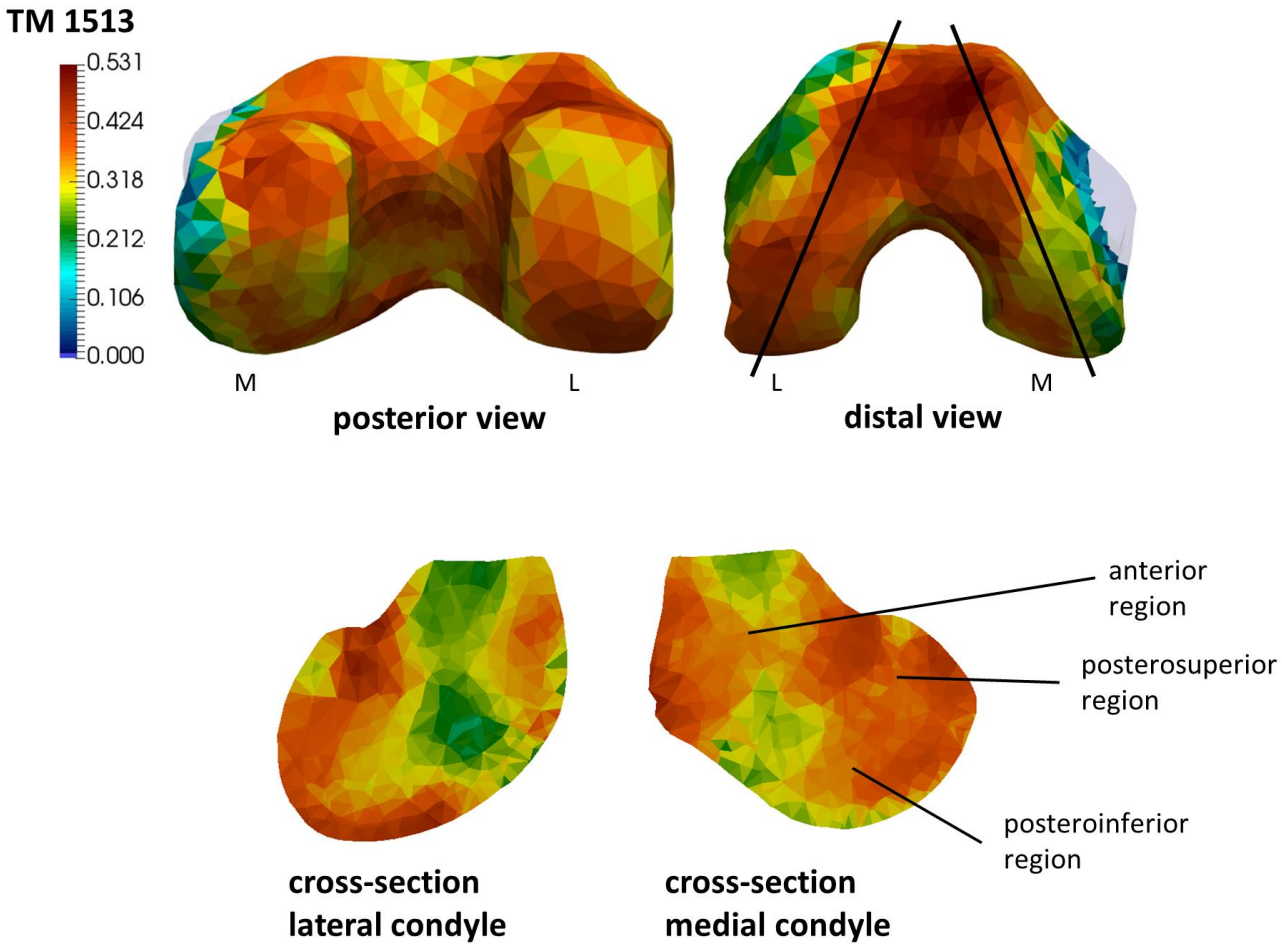

Figure 6.5: BV/TV distribution in both femoral condyles of *A. africanus* TM 1513 specimen. Vertical lines in the distal view show where the cross-sections are positioned. L, lateral; M, medial.

Figure 6.6 displays the outcomes of PCA of the rBV/TV distribution in both femoral condyles (excluding the medial epicondyle), compared to the extant sample. PC1 explained 19.9% of the variation in rBV/TV values at each mesh cell. It effectively segregates *Homo* from other great apes, as positive PC1 scores correlate with higher rBV/TV on the patellar surface of the femur and under the presumed insertion of the medial head of gastrocnemius muscle and medial and lateral cruciate ligaments. While negative PC1 scores, associated with great apes, are linked to higher rBV/TV under the lateral epicondyle, in the posteroinferior region of the lateral condyle and on the lateral side of the patellar surface (Figure 6.7). TM 1513 separates from humans with the great apes and plots closest to *Pan* and *Pongo* on PC1. (Figure 6.7).

PC2, accounting for 9.4% of the variation in rBV/TV values, distinctly separates *Gorilla* from the other taxa. Positive PC2 values distinguish *Gorilla* due to a distinct pattern under the patellar surface, lateral epicondyle, and in the posteroinferior region of the lateral condyle (Figure 6.7). Conversely, negative PC2 values differentiate the other taxa from *Gorilla*, primarily due to high rBV/TV under the presumed insertion of both sites of the gastrocnemius muscle and cruciate ligaments, as well as a concentrated area of high rBV/TV above the patellar surface, visible in anterior view (Figure 6.7). TM 1513 is separated completely from the range of *Gorilla* distribution on PC2. TM 1513 is within the range of *Pongo*, however, not far from *Pan* as well (Figure 6.6; Figure 6.7). PC3 accounted for 7.5% of the variation in rBV/TV and did not separate the taxa from each other (Figure 6.6).

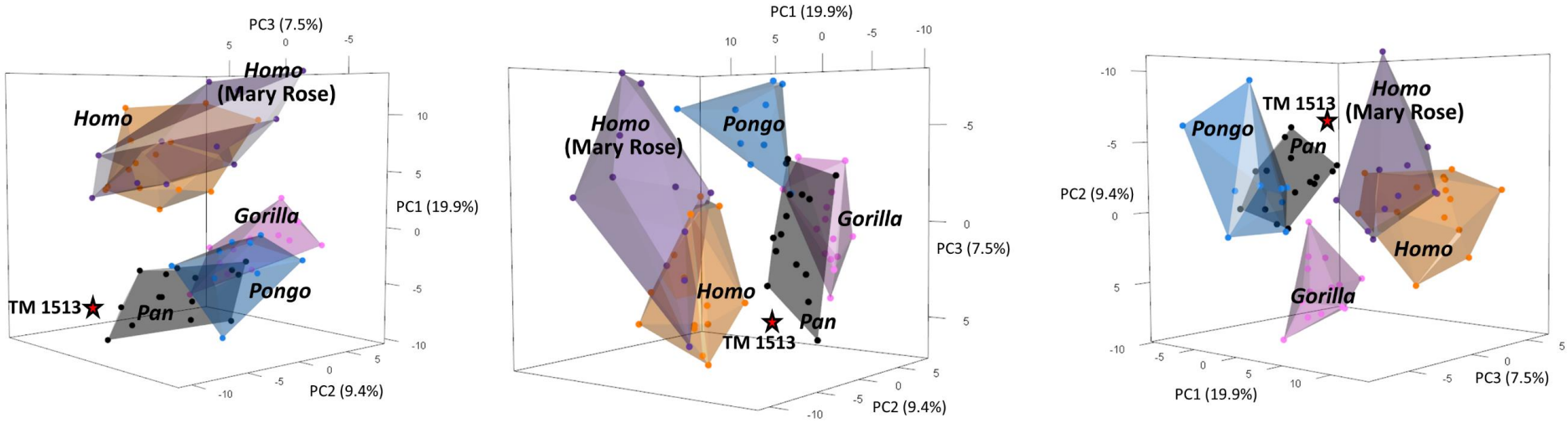

Figure 6.6: PCA of the rBV/TV distribution in both femoral condyles of *A. africanus* TM 1513 specimen (red star), *Homo*, *Gorilla*, *Pan*, and *Pongo* showing in the different views.

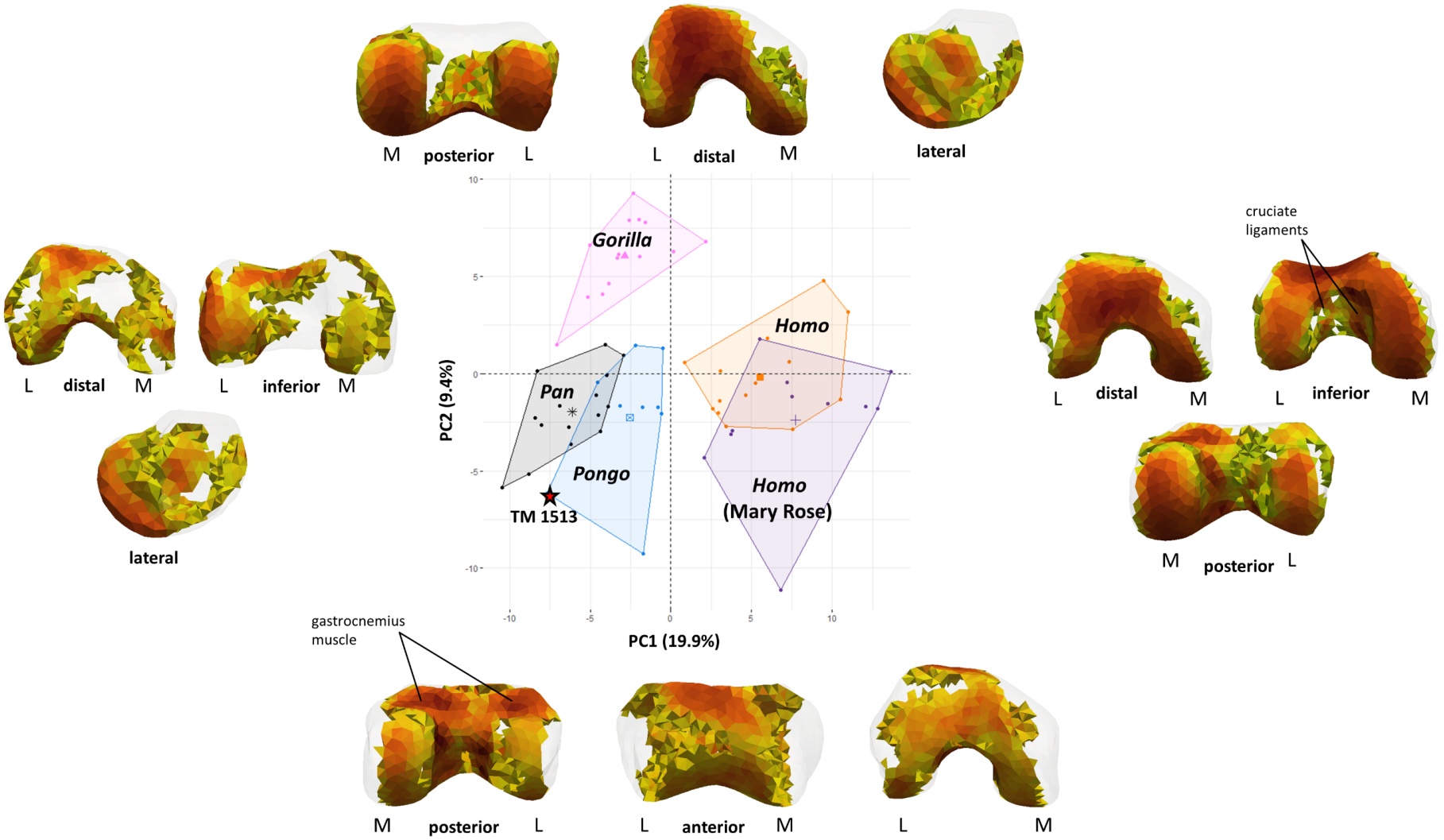

Figure 6.7: Loading models of PC1 and PC2 of the rBV/TV distribution in both femoral condyles of *A. africanus* TM 1513 specimen (red star), *Homo*, *Gorilla*, *Pan*, and *Pongo*.

Figure 6.8 shows the PCA of the rBV/TV distribution in the lateral condyle for both *A. africanus* specimens. Preserved elements of StW 318 specimen were used as an input for PCA. PC1 explains 19.9%, PC2 10.5% and PC3 8.4% of the variation in rBV/TV values at each mesh cell. StW 318 is still plotting somewhere between the range of *Gorilla* and *Pongo* distribution on PC1, while TM 1513 is again closer to the range of *Pan* distribution (Figure 6.8).

In this analysis of the lateral condyle only (Figure S6.1), the Canonical Variates Analysis (CVA) was performed using the first three principal components, as these components explain the greatest amount of variance with the fewest dimensions. The first two canonical variates account for 66.7% (CV1) and 33.3% (CV2) of the variance in the dataset. The results indicate that modern *Homo* and *Pongo* tend to cluster toward negative scores on CV1, while *Gorilla* and *Pan* cluster toward the positive side of CV1. For CV2, *Homo* and *Gorilla* are positioned in the negative range, whereas *Pan* and *Pongo* mostly plot towards positive CV2 scores. The fossil *A. africanus* specimen StW 318 is located nearest to *Pongo* and *Homo*, whereas TM 1513 falls within the *Pan* range. Typicality probability analysis shows that StW 318 is most likely associated with *Pongo* (47% probability), and TM 1513 with *Pan* (69% probability).

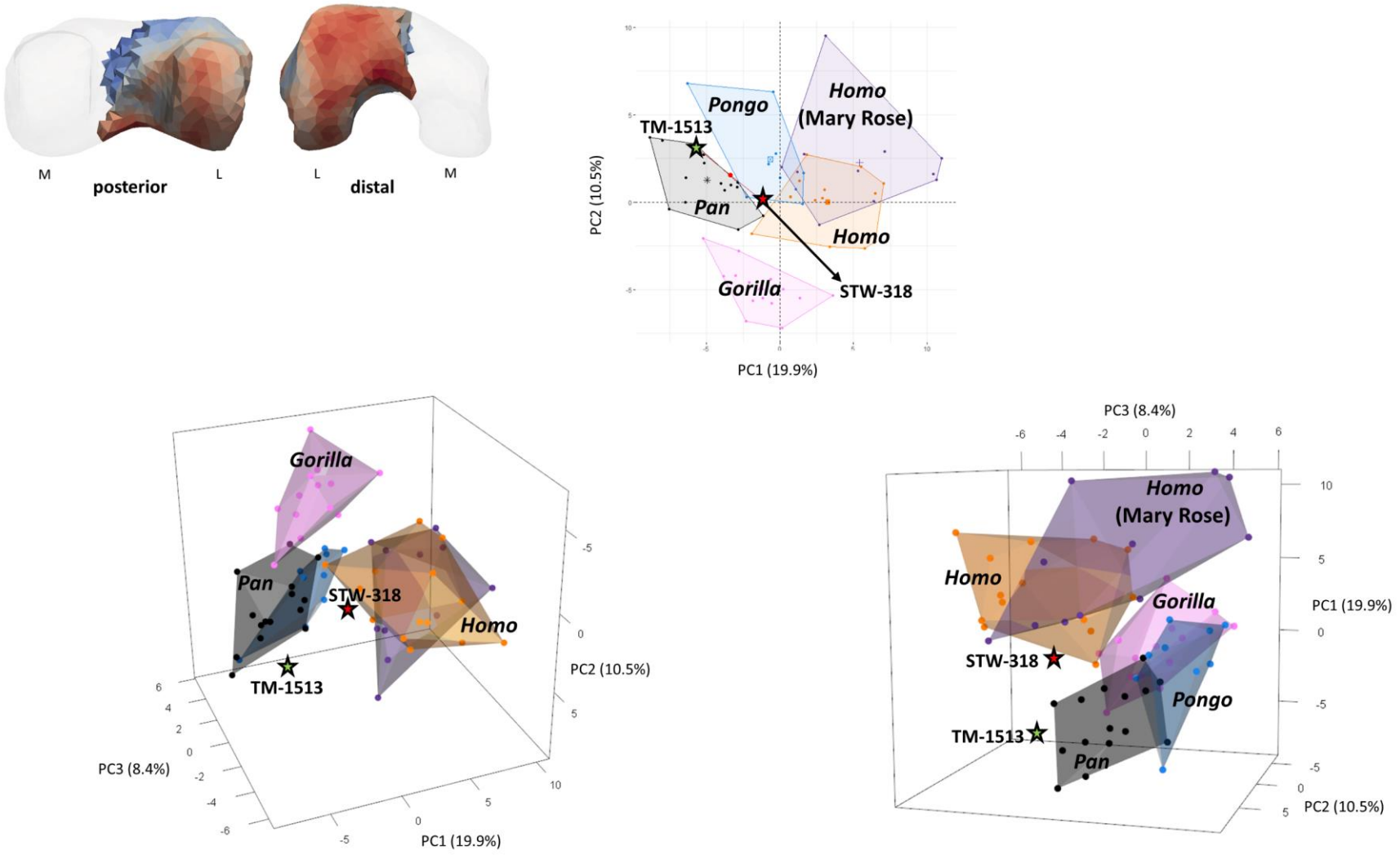

Figure 6.8: PCA of the rBV/TV distribution in the lateral femoral condyle of *A. africanus* StW 318 (red star) and TM 1513 (green star) specimens, *Homo*, *Gorilla*, *Pan*, and *Pongo* showing in the different views. The sub-setting model shows which cells were used for the PCA. Note that the preserved elements of StW 318 were used for PCA, thus only the lateral condyle was analysed.

6.4.2 Australopithecus sediba

Figure 6.9 shows the rBV/TV distribution under the femoral patellar surface in U.W. 88-63. The areas with high rBV/TV values are predominantly located medially on the patellar surface and in the posteroinferior volume of the medial condyle. In contrast, the rBV/TV values on the lateral side of the patellar surface were lower compared to its medial side. The lowest rBV/TV values were found in the distal volumes of both condyles. However, most of the trabecular bone was not preserved in other parts of the bone (Figure 6.9). The elements with no information, depicted in dark blue (Figure 6.9a) were removed for further analysis (Figure 6.9b).

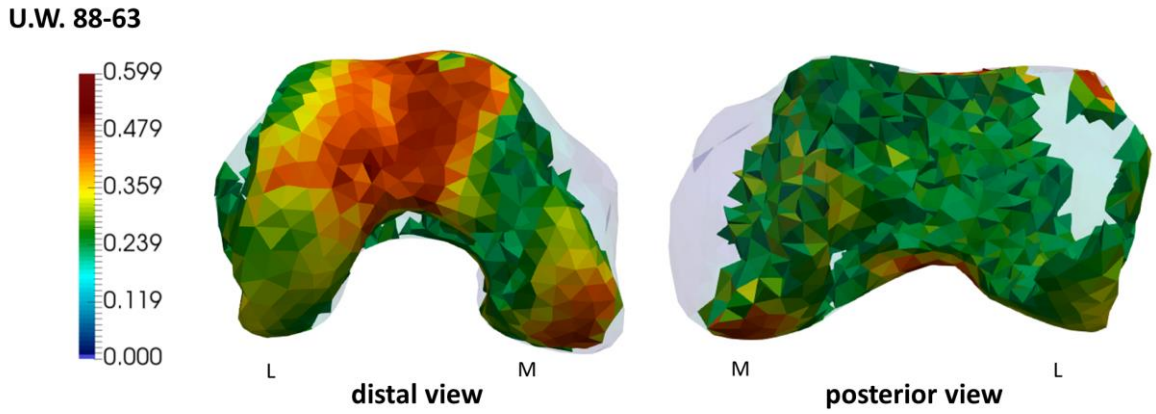

Figure 6.9: BV/TV distribution under the femoral patellar surface of *A. sediba* U.W. 88-63 specimen. L, lateral; M, medial.

Figure 6.10 displays the PCA of rBV/TV distribution under the femoral patellar surface, compared to the extant sample. PC1 explains 23.0% of the variation in rBV/TV values at each mesh cell. It effectively segregates *Homo,* and partially *Gorilla*, from other great apes, as positive PC1 scores correlate with higher rBV/TV on the patellar surface of the femur. While negative PC1 scores, associated with other great apes (especially *Pan* and *Pongo*), are linked to higher rBV/TV above the patellar surface and in the posteroinferior region of the lateral condyle (Figure 6.11). U.W. 88-63 separates from humans, along with *Pan* and *Pongo*, and plots closest to *Pongo* on PC1 (Figure 6.11).

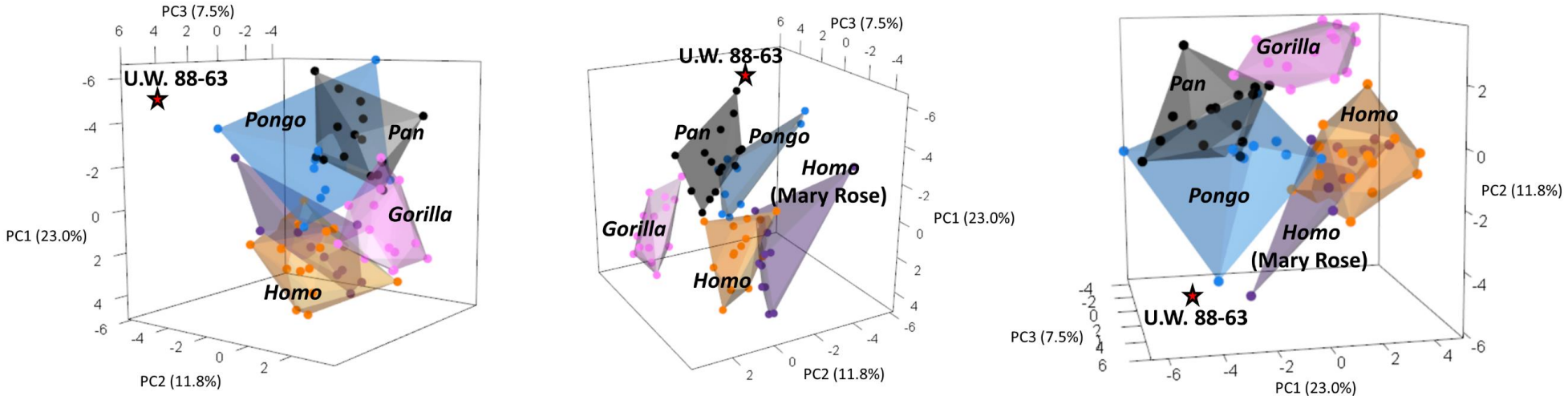

Figure 6.10: PCA of the rBV/TV distribution under the femoral patellar surface of *A. sediba* U.W. 88-63 specimen (red star), *Homo*, *Gorilla*, *Pan*, and *Pongo* showing in the different views.

PC2, accounting for 11.8% of the variation in rBV/TV values and separates *Gorilla* (and partially *Pan*) from the other taxa. Positive PC2 values distinguish *Gorilla* due to a distinct pattern under the patellar surface and in the posteroinferior region of the lateral condyle (Figure 6.11). Additionally, negative PC2 values differentiate the other taxa from *Gorilla*, due to a concentrated area of high rBV/TV above the patellar surface, visible in anterior view (Figure 6.11). U.W. 88-63 is separated rom the range of *Gorilla* distribution on PC1 and PC2, and it is again closest to *Pongo* on PC2 (Figure 6.10; Figure 6.11). PC3 accounts for 7.5% of the variation in rBV/TV and did not separate the taxa from each other (Figure 6.10).

Figure 6.12 shows the outcomes of PCA of the rBV/TV distribution under the femoral patellar surface for both *A. sediba* U.W. 88-63 and *A. africanus* TM 1513 specimens. Preserved elements of U.W. 88-63 specimen was used as an input for PCA. PC1 explains 23.3%, PC2 11.7% and PC3 7.5% of the variation in rBV/TV values at each mesh cell. U.W. 88-63 is still plotting closest to *Pongo* distribution. While TM 1513 is now withing the *Pongo* range on PC1 and within *Pan* and *Homo* on PC2 and PC3 (Figure 6.12).

CVA was also applied using the first three principal components of the femoral patellar surface distribution (Figure S6.2). The CV1 contributing 84.33% and CV2 contributing 15.67% to the variance. The analysis showed that *Homo* clusters towards the positive end of CV1, while *Gorilla* and *Pan* tend to cluster towards the negative side, with *Pongo* positioned between them. Regarding CV2, *Gorilla* is primarily in the negative range, whereas *Pan* and *Pongo* group towards positive CV2 values, with *Homo* overlapping across the dataset. The fossil specimen *A. africanus* (TM 1513) plots within the *Pongo* range, and *A. sediba* (U.W. 88-63) occupies a distinct morphospace in the positive CV2 range. Typicality probabilities suggest TM 1513 has a 17% likelihood of being associated with *Pongo*, while U.W. 88-63 is not definitively assigned to any species in the sample (Figure S6.2).

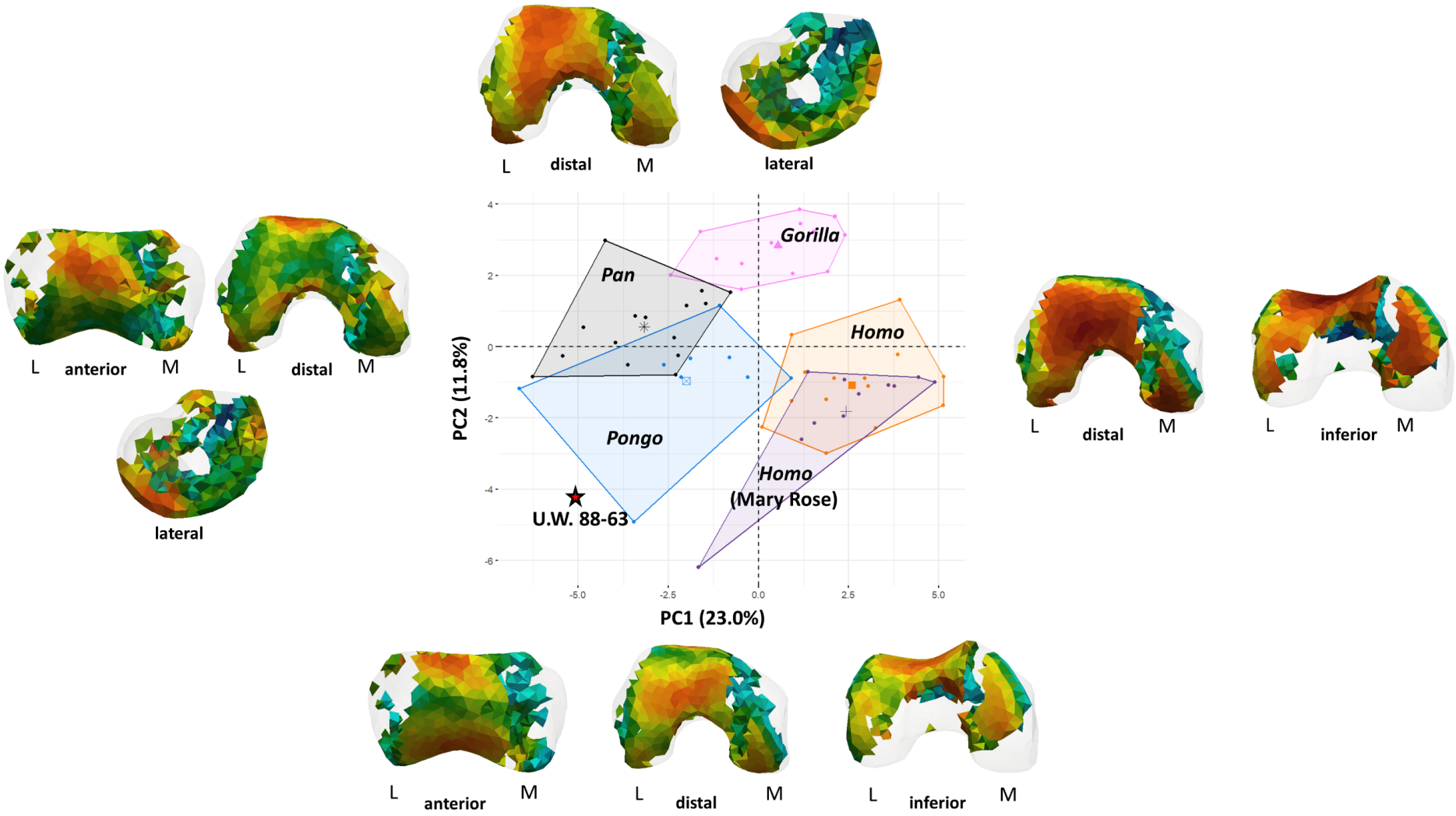

Figure 6.11: Loading models of PC1 and PC2 of the rBV/TV distribution under the femoral patellar surface of *A. sediba* U.W. 88-63 specimen (red star), *Homo*, *Gorilla*, *Pan*, and *Pongo*.

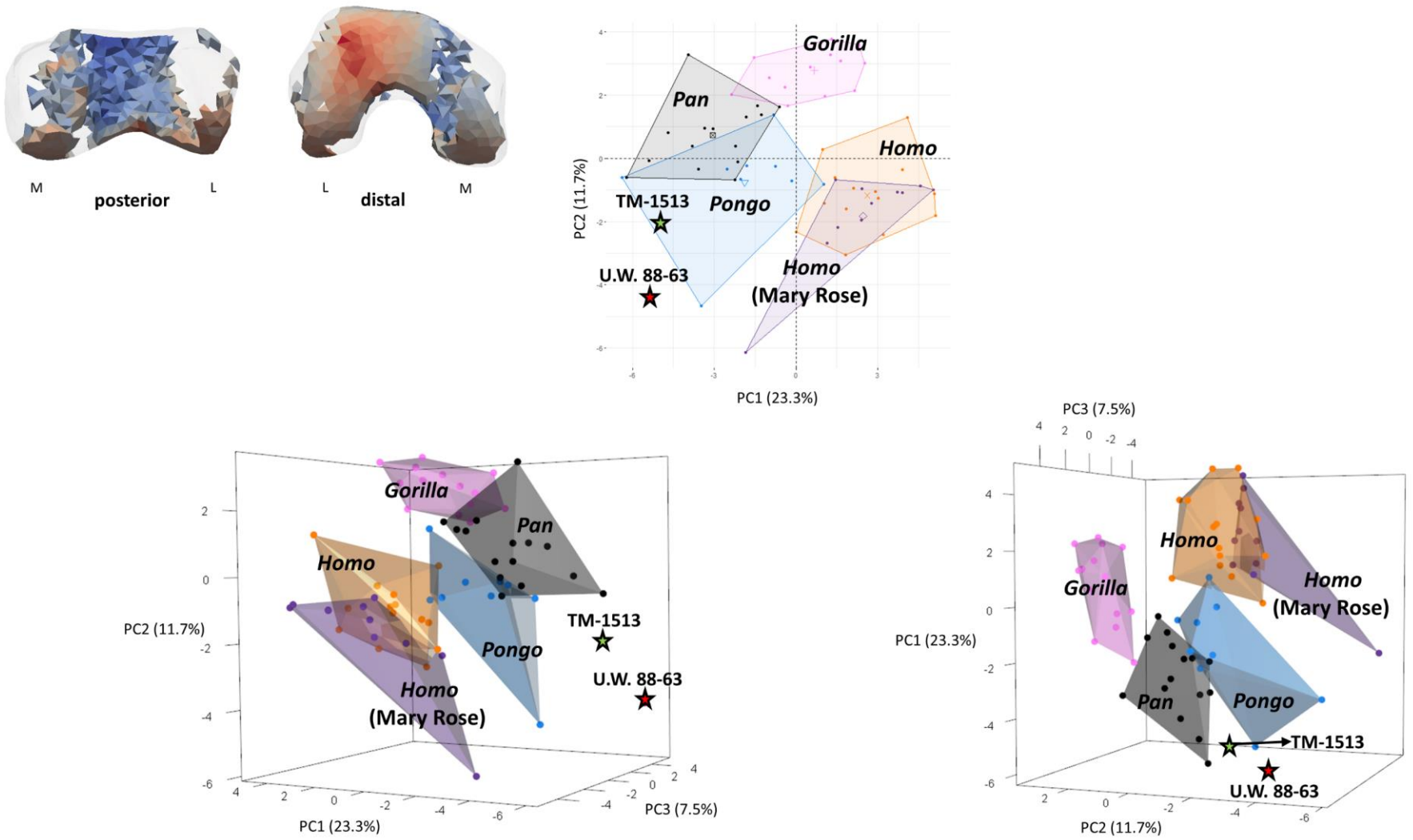

Figure 6.12: PCA of the rBV/TV distribution under the femoral patellar surface of *A. sediba* U.W. 88-63 (red star) and *A. africanus* TM 1513 (green star) specimens, *Homo*, *Gorilla*, *Pan*, and *Pongo* showing in the different views. The sub-setting model shows which cells were used for the PCA. Note that the preserved elements of U.W. 88-63 were used for PCA, thus only lateral condyle was analysed.

6.4.3 Homo floresiensis

6.4.3.1 LB1-8

Figure 6.13 shows the rBV/TV distribution in both femoral condyles of LB1-8 specimen, however, significant parts of both condyles are missing (Figure 6.13). The areas with high rBV/TV values are predominantly located laterally on the patellar surface, in the lateral epicondyle, under the presumed lateral head of the gastrocnemius muscle, and in the distal volume of the lateral condyle. However, the posteroinferior volumes were not preserved. In contrast, the rBV/TV values were low inferiorly on the medial condyle, under the presumed insertions of the cruciate ligaments compared to the inferior region of the lateral condyle (Figure 6.13). The elements with no information, depicted in dark blue (Figure 6.13a) were removed for further analysis (Figure 6.13b).

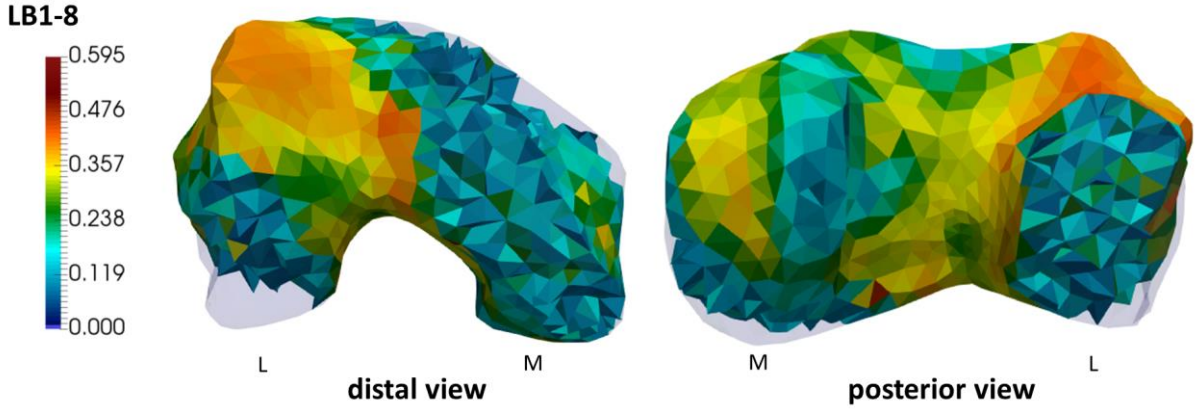

Figure 6.13: BV/TV distribution in both femoral condyles of *H. floresiensis* LB1-8 specimen. L, lateral; M, medial.

Figure 6.14 displays the outcomes of PCA of the rBV/TV distribution in both femoral condyles of LB1-8. PC1 explained 21.7% of the variation in rBV/TV values at each mesh cell. It effectively segregates *Homo* from other great apes, as positive PC1 scores correlate with higher rBV/TV on the lateral side of the patellar surface of the femur, under the presumed insertions of cruciate ligaments and lateral head of gastrocnemius muscle. While negative PC1 scores, associated with non-human great apes, are linked to higher rBV/TV in the lateral epicondyle and to distinctive rBV/TV distribution on the lateral side of the patellar surface (Figure 6.15). LB1-8 separates from humans, along with other great apes, and plots closest to *Pan* on PC1 (Figure 6.15).

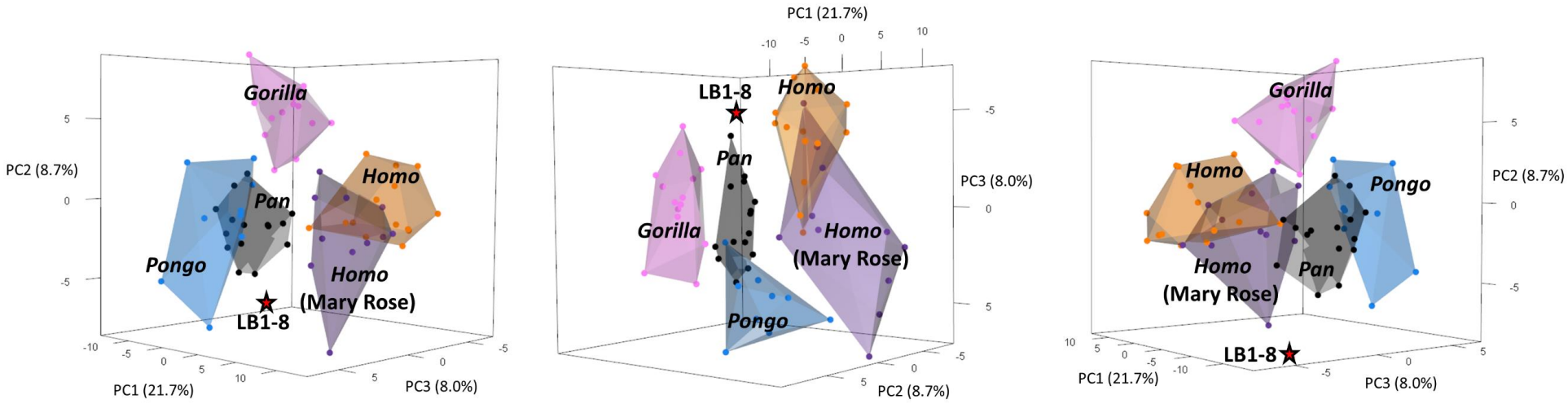

Figure 6.14: PCA of the rBV/TV distribution in both femoral condyles of *H. floresiensis* LB1-8 specimen (red star), *Homo*, *Gorilla*, *Pan*, and *Pongo* showing in the different views.

PC2, accounting for 8.7% of the variation in rBV/TV values and separates *Gorilla* from the other taxa. Positive PC2 values distinguish *Gorilla* due to a distinct pattern under the patellar surface, in the posteroinferior region of the lateral condyle and in the lateral epicondyle (Figure 6.15). In contrast, negative PC2 values differentiate the other taxa from *Gorilla*, due to a concentrated area of high rBV/TV above the patellar surface, visible in anterior view, and under the presumed insertion of both cruciate ligaments and both heads of gastrocnemius muscle (Figure 6.15). LB1-8 is separated completely from the range of *Gorilla* distribution on PC2, and it is close to *Pan, Pongo*, and the "active" (Mary Rose) population of the human sample (Figure 6.14; Figure 6.15). PC3 accounted for 7.5% of the variation in rBV/TV and did not separate the taxa from each other (Figure 6.14).

CVA was conducted using the first three principal components, with CV1 accounting for 78.82% and CV2 for 21.18% of the variance (Figure S6.3). The results indicated that *Homo* clustered towards the positive end of CV1, while *Gorilla*, *Pan*, and *Pongo* were grouped towards the negative end. On CV2, *Gorilla* remained in the negative range, whereas *Pan* and *Pongo* were positioned on the positive side, with *Homo* overlapping the dataset. The fossil specimen *H. floresiensis* (LB1-8) occupied a unique morphospace in the positive CV2 range but was not classified with any of the species in the sample (Figure S6.4).

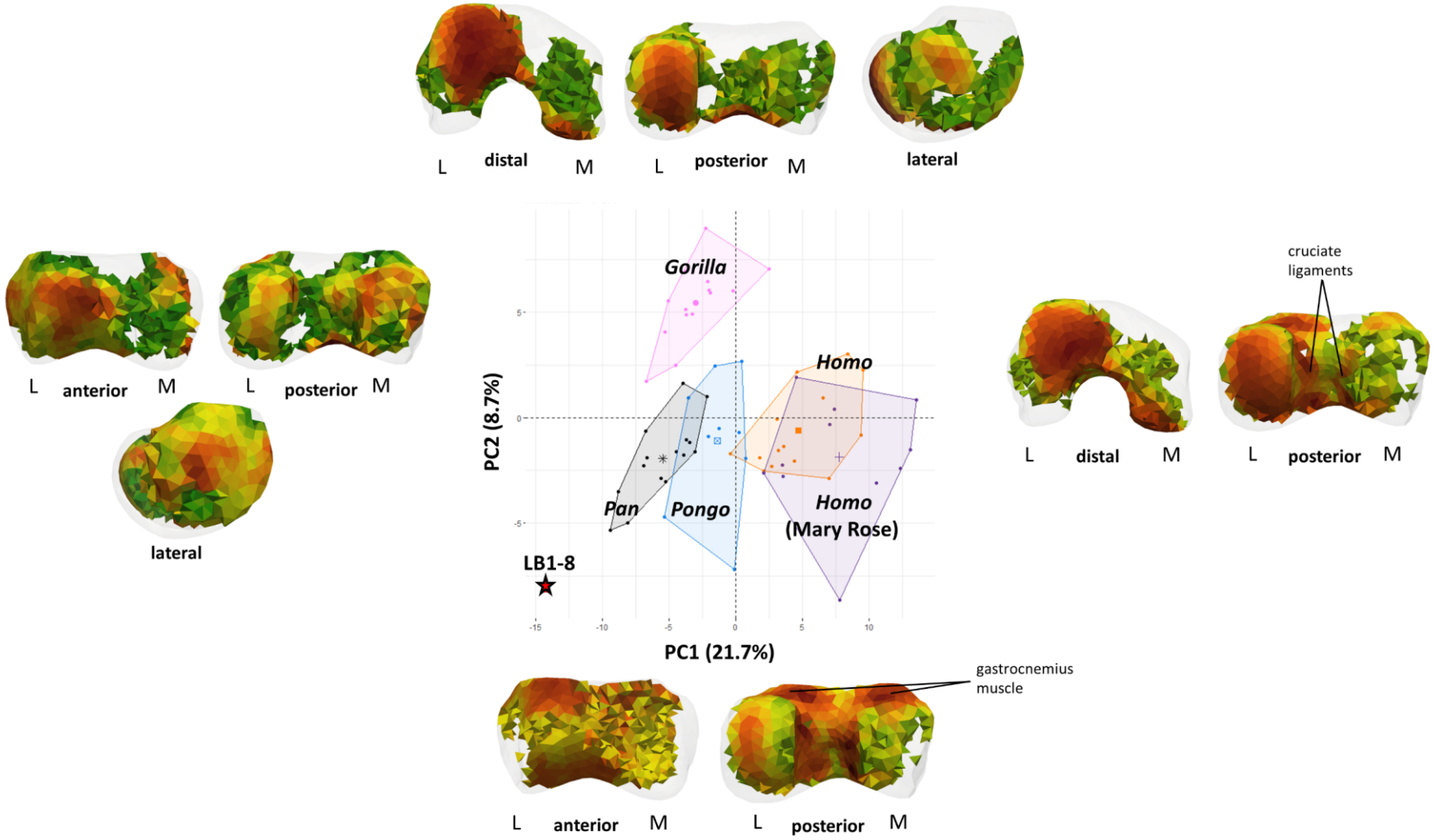

Figure 6.15: Loading models of PC1 and PC2 of the rBV/TV distribution in both femoral condyles of *H. floresiensis* LB1-8 specimen (red star), *Homo*, *Gorilla*, *Pan*, and *Pongo*.

6.4.3.2 LB1-13

Figure 6.16 shows the rBV/TV distribution in both tibial condyles of LB1-13 specimen. The highest rBV/TV values were concentrated at the lateral side of the tibial plateau and anteriorly at the medial side of the tibial plateau. Contrarily, rBV/TV concentration was the lowest medially on the tibial plateau of the medial condyle (Figure 6.16). In the cross-section view, rBV/TV was higher across the whole lateral condyle compared to the medial condyle. High rBV/TV values extended deep inferiorly under both tibial condyles (Figure 6.16). The elements with no information were removed for further analysis (Figure 6.16b). Moreover, high rBV/TV distribution was found under the presumed insertion of patellar tendon; this concentration extended deep below the insertion site, and under the proximal tibiofibular joint. The rBV/TV values at this region extended superiorly into the tibial plateau (Figure 6.16).

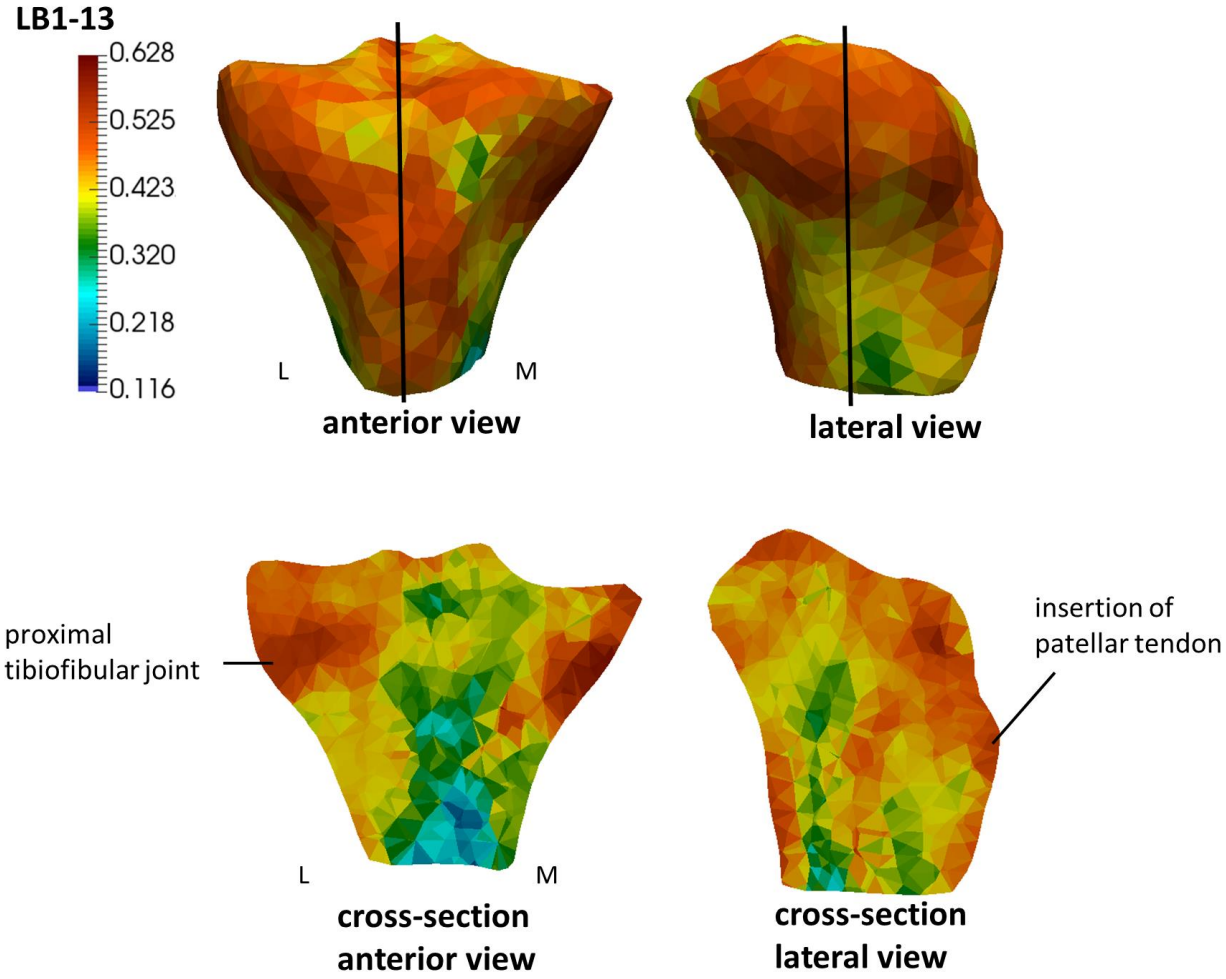

Figure 6.16: BV/TV distribution in both tibial condyles of *H. floresiensis* LB1-13 specimen. Vertical lines in the anterior, lateral and medial views show where the cross-sections are positioned. L, lateral; M, medial.

Figure 6.17 presents a PCA of rBV/TV distribution in the proximal tibia of LB1-13 and the extant sample. PC1 explains 17.8% of the variation in rBV/TV values at each mesh element. PC1 separated *Homo* and *Pongo* from *Gorilla* and (partially) *Pan* with negative PC1 scores associated with higher rBV/TV in the middle of the lateral and medial condyles and under the presumed insertion of the patellar tendon (although rBV/TV was highly variable under the insertion of patellar tendon [Supplementary Figure S5.8] in *Homo*). Positive PC1 scores were associated with higher rBV/TV concentrated anteriorly on the tibial plateau and on the medial and posterior aspect of the medial condyle in *Gorilla* and *Pan* (Figure 6.18). LB1-13 separated completely from the range of *Gorilla* distribution on PC1, but only partially from *Pan* and between the distribution of *Pongo, Pan* and *Homo* (Figure 6.17; Figure 6.18).

PC2 accounts for 14.6% of the variation in rBV/TV values and does not separate extant taxa from each other. However, LB1-13 is separated from the extant sample on PC2. Positive PC2 distinguished the extant sample due to a different distribution on the tibial plateau and under the presumed insertion of patellar tendon (Figure 6.18). In LB1-13, higher rBV/TV concentration was found in the lateral side of the tibial plateau. Besides, the rBV/TV was concentrated rather around the medial lip of the tibial plateau where in other taxa this concentration was on the tibial plateau in the middle of the medial condyle (Figure 6.18). PC3 accounts for 7.6% of the variation in rBV/TV and did not separate the taxa from each other (Figure 6.17).

CVA was performed using the first three principal components, with CV1 explaining 85.52% and CV2 accounting for 14.48% of the variance (Figure S6.4). The analysis showed that *Gorilla*, *Pan,* and *Pongo* clustered towards negative CV1 scores, while *Homo* was positioned towards positive CV1 scores. On CV2, *Pan* and *Pongo* were mostly located in the negative range, while *Gorilla* tended to be in the positive range, with *Homo* overlapping both ranges along CV2. The fossil specimen *H. floresiensis* (LB1-13) occupied a distinct morphospace in the positive CV2 range and had the highest probability (16%) of being assigned to *Pan* (Figure S6.4).

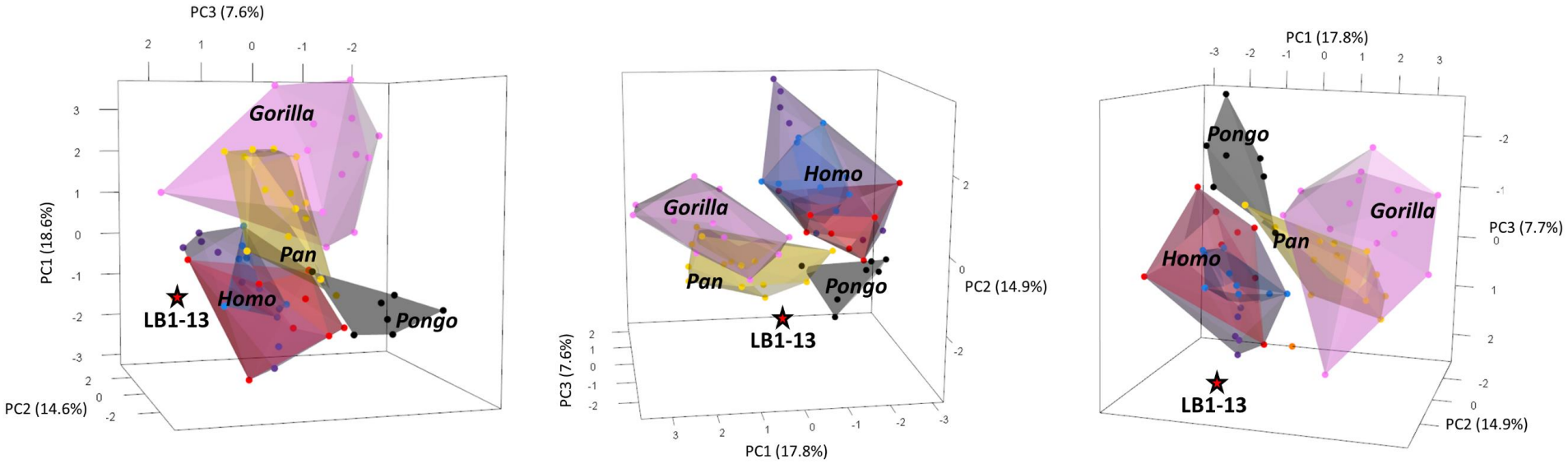

Figure 6.17: PCA of the rBV/TV distribution in both tibial condyles of *H. floresiensis* LB1-13 specimen (red start), *Homo*, *Gorilla*, *Pan*, and *Pongo* showing in the different views.

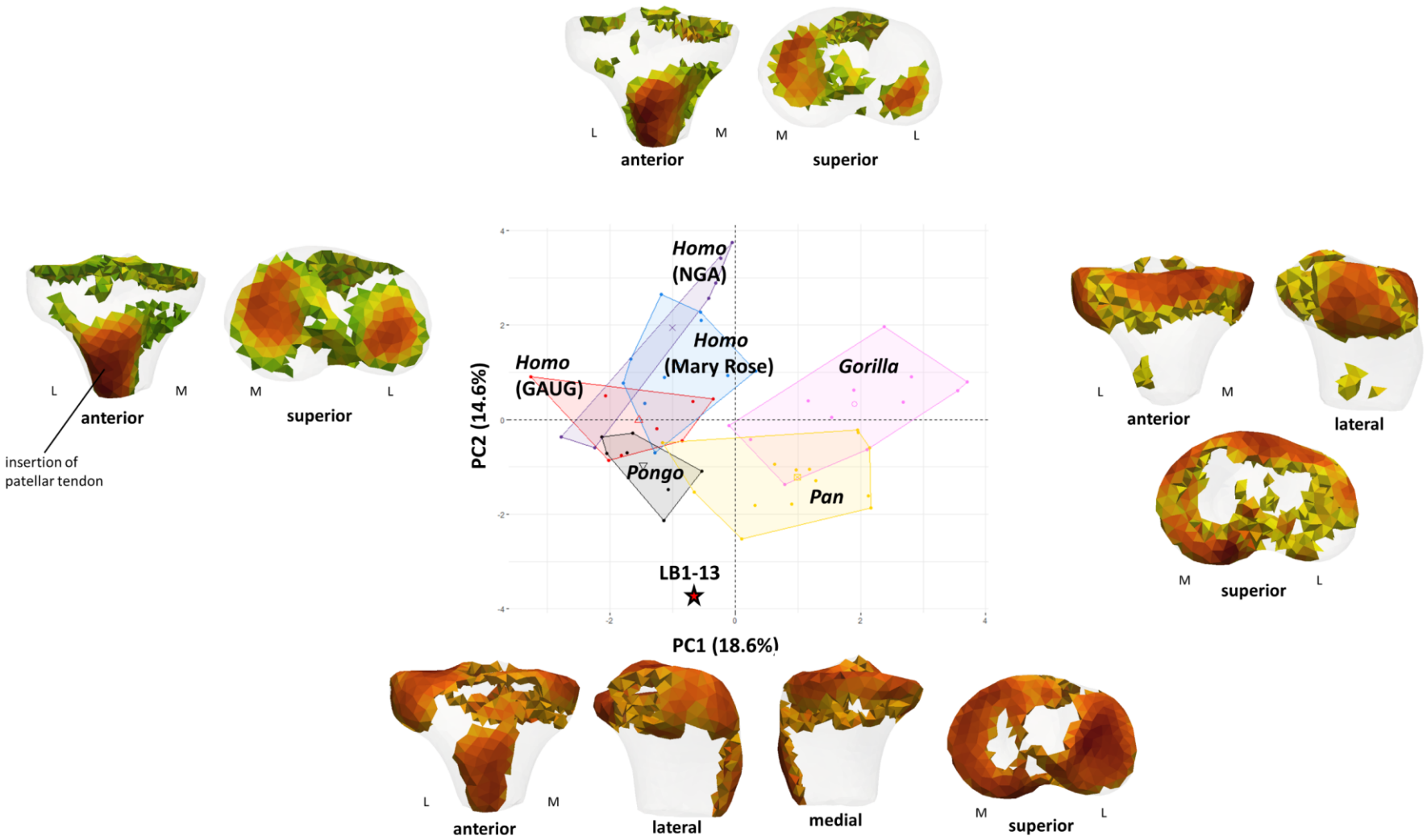

Figure 6.18: Loading models of PC1 and PC2 of the rBV/TV distribution in both tibial condyles of *H. floresiensis* LB1-13 specimen (red star), *Homo*, *Gorilla*, *Pan*, and *Pongo*.

6.4.4 Homo neanderthalensis

Figure 6.19 shows the rBV/TV distribution in both femoral condyles in D322-15 specimen. The areas with high rBV/TV are predominantly located on the patellar surface and posteroinferior/superior volumes of both condyles (Figure 6.19a). Also, high rBV/TV is located under the presumed insertion of the medial head of gastrocnemius muscle and both cruciate ligaments (Figure 6.19a). In contrast, the distal volumes of both condyles lack high rBV/TV concentration, with later condyle having higher values compared to the medial condyle (Figure 6.19a). Few elements with no information, depicted in dark blue (Figure 6.19a) were removed for further analysis (Figure 6.19b).

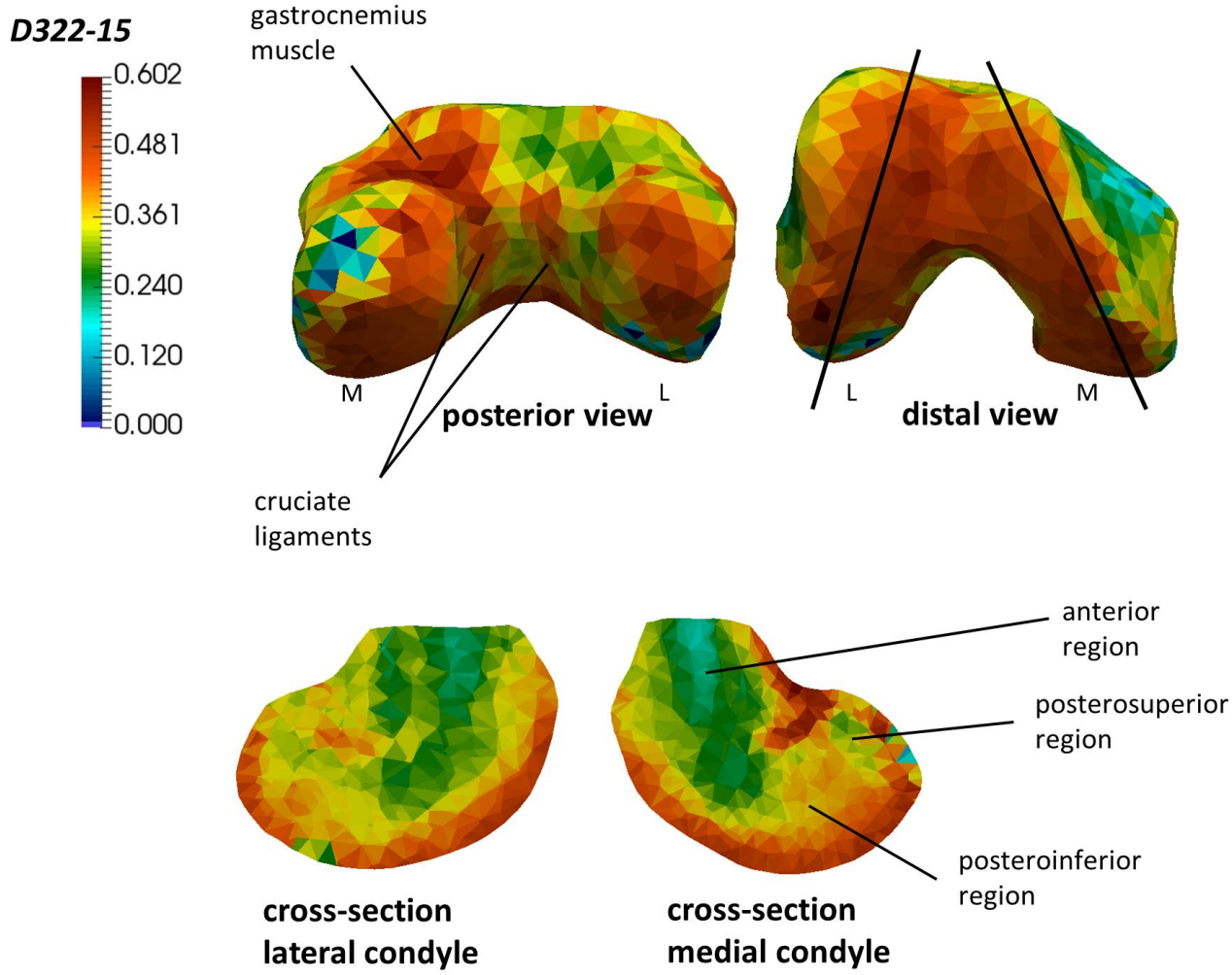

Figure 6.19: BV/TV distribution in both femoral condyles of *H. neanderthalensis* D322-15 specimen. Vertical lines in the distal view show where the cross-sections are positioned. L, lateral; M, medial.

Figure 6.20 displays the PCA of rBV/TV distribution in both femoral condyles, compared to the extant sample. PC1 explains 21.1% of the variation in rBV/TV values. It effectively separates *Homo,* from other great apes, as negative PC1 scores correlate with higher rBV/TV on the patellar surface of the femur, under both cruciate ligaments and medial head of the gastrocnemius muscle (Figure 6.21). While positive PC1 scores, associated with non-human great apes, are linked to higher rBV/TV in both femoral epicondyles, in the posteroinferior volume of the lateral condyle and to a different distribution under the patellar surface of the femur (Figure 6.21). D322-15 specimen separates from non-human great apes and plots closest to the human sample on PC1 (Figure 6.21).

PC2, accounting for 9.0% of the variation in rBV/TV values and separates *Gorilla* from the other taxa. Positive PC2 values distinguish *Gorilla* due to a distinct pattern under the patellar surface (Figure 6.21). Additionally, negative PC2 values differentiate the other taxa from *Gorilla*, due to a concentrated area of high rBV/TV above the patellar surface, visible in anterior view (Figure 6.21). D322-15 separates completely from the range of *Gorilla* distribution on PC2, and it is closest to human and *Pan* and *Pongo* distribution range (Figure 6.20; Figure 6.21). PC3 accounted for 7.4% of the variation in rBV/TV and did not separate the taxa from each other (Figure 6.20).

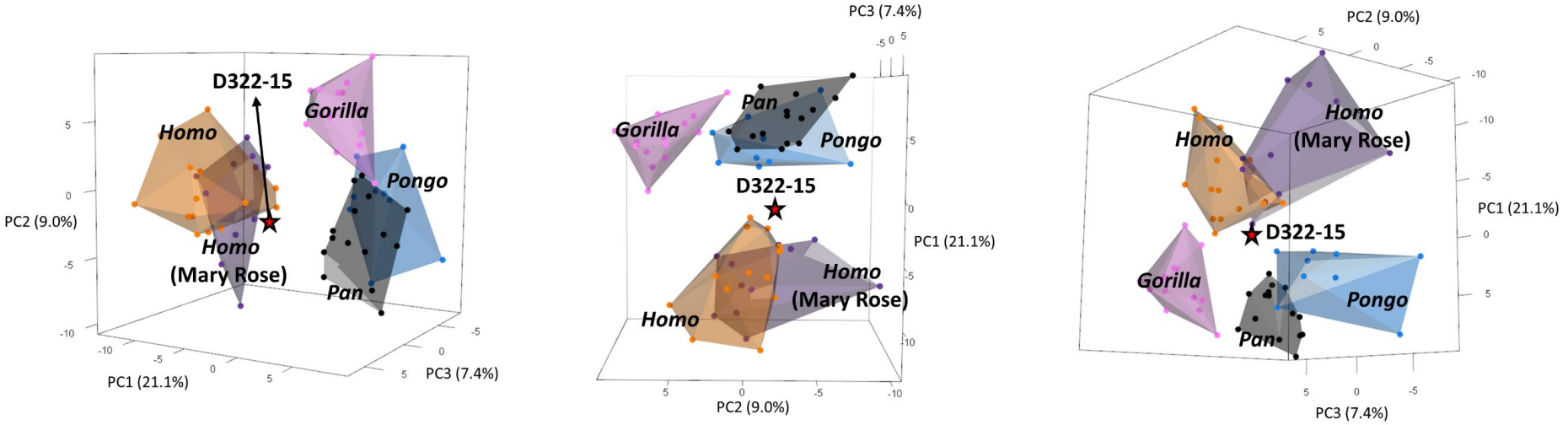

Figure 6.20: PCA of the rBV/TV distribution in both femoral condyles of *H. neanderthalensis* D322-15 specimen (red star), *Homo*, *Gorilla*, *Pan*, and *Pongo* showing in the different views.

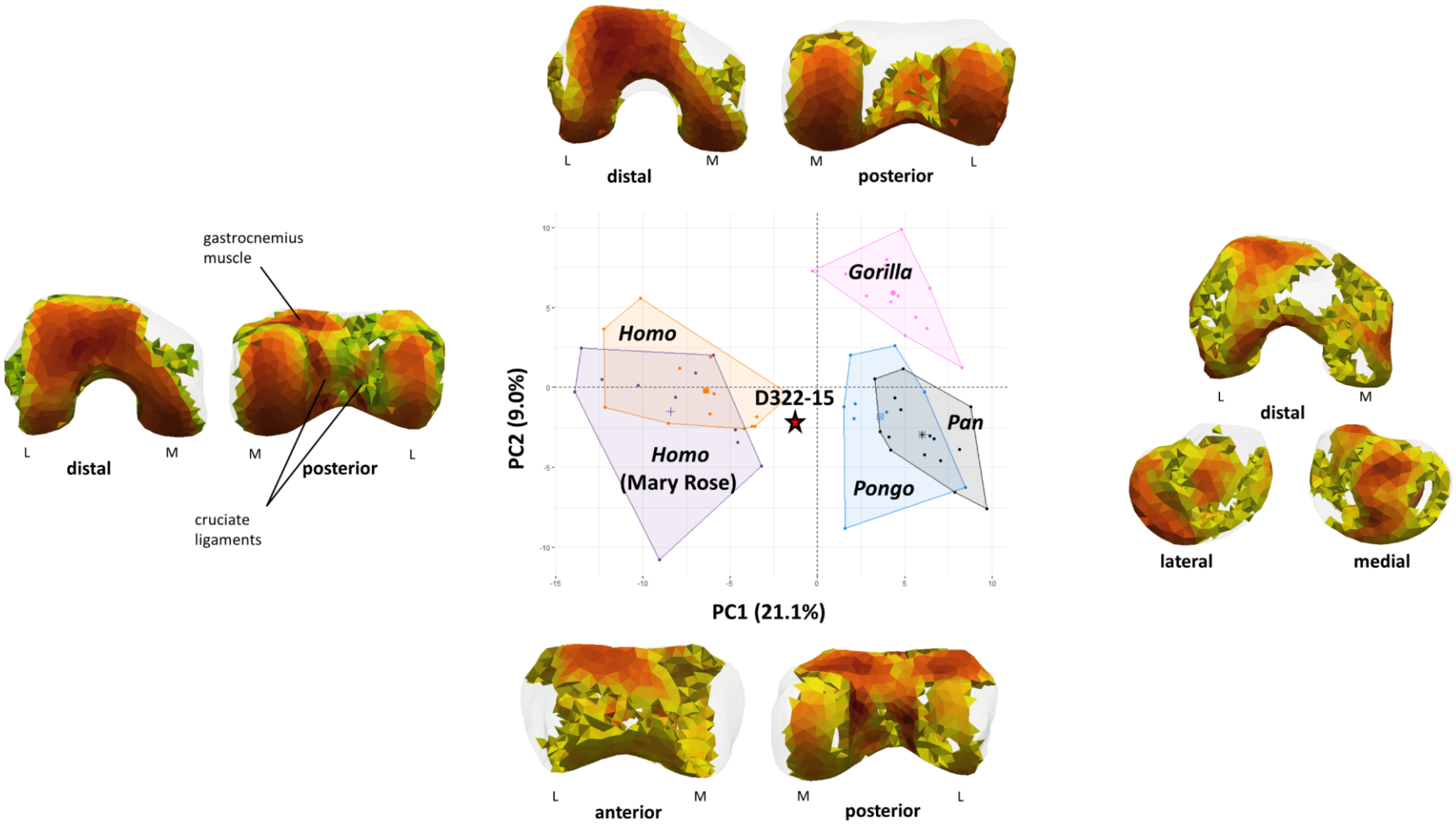

Figure 6.21: Loading models of PC1 and PC2 of the rBV/TV distribution in both femoral condyles of *H. neanderthalensis* D322-15 specimen (red star), *Homo*, *Gorilla*, *Pan*, and *Pongo*.

Figure 6.22 shows the PCA of rBV/TV distribution in the lateral femoral condyle for two *A. africanus* StW 318 and TM 1513 specimens, and for *H. neanderthalensis* D322-15 specimen. Preserved elements of StW 318 specimen were used as an input for PCA. PC1 explained 23.3%, PC2 11.7% and PC3 8.3% of the variation in rBV/TV values at each mesh cell. D322-15 and StW 318 are the closest to the human range distribution and withing the range of *Gorilla* and *Pongo* on PC1, while TM1513 is within the range of *Pan* on PC1 (Figure 6.22).

Figure 6.23 shows the PCA of rBV/TV distribution under the patellar surface of the femur of one *A. africanus* TM 1513 specimen, one *A. sediba* U.W. 88-63 specimen and one *H. neanderthalensis* D322-15 specimen. Preserved elements of U.W. 88-63 specimen were used as an input for PCA.PC1 explained 23.0%, PC2 11.6% and PC3 7.4% of the variation in rBV/TV values at each mesh cell. D322-15 and TM1513 are within the range of *Pongo*, while D322-15 is closer to the human sample. U.W. 88-63 is the closest to *Pongo*, however further from its distribution than D322-15 and TM1513 specimens (Figure 6.23).

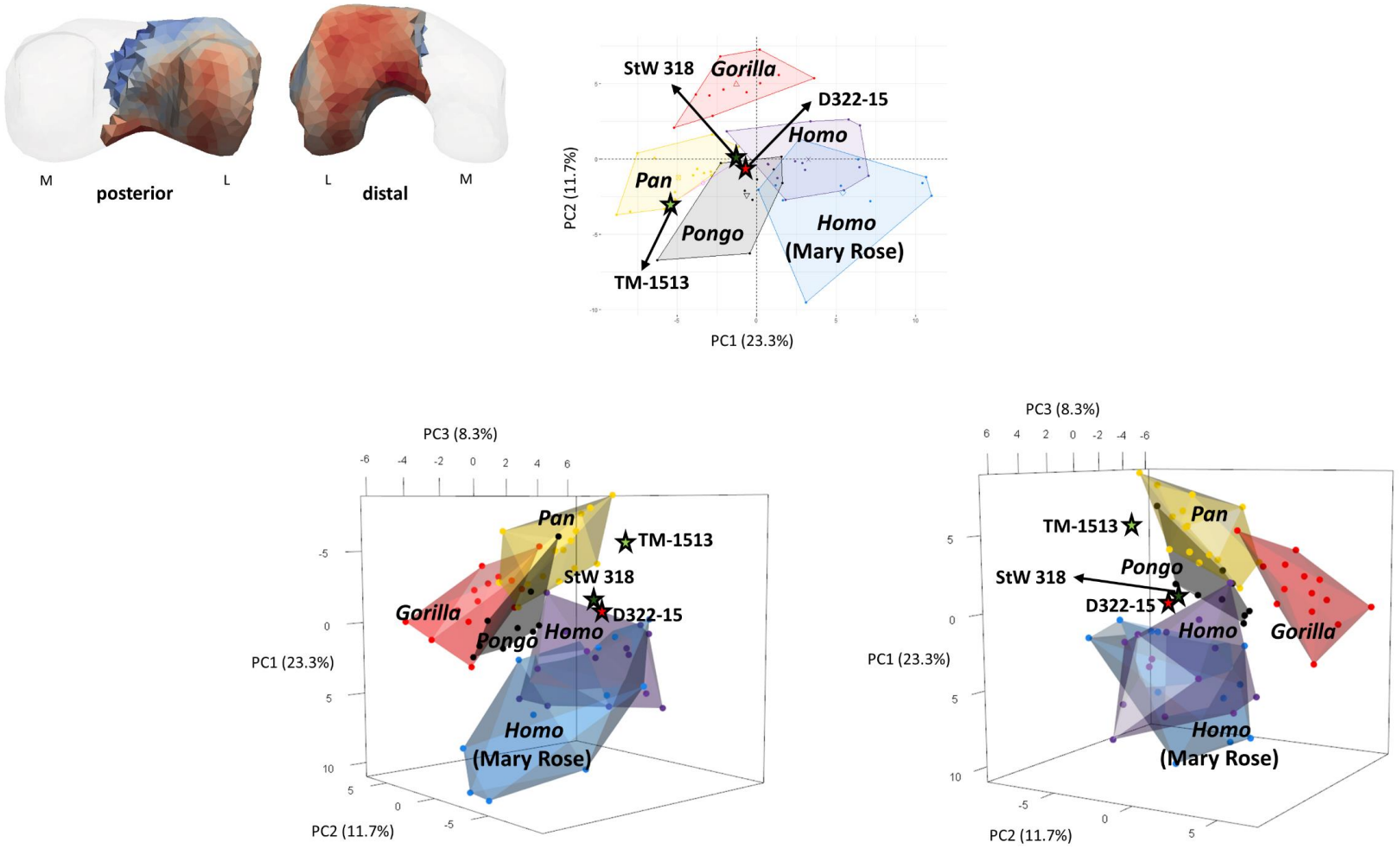

Figure 6.22: PCA of the rBV/TV distribution in the lateral femoral condyle of *A. africanus* StW 318 (dark green star), TM 1513 (light green star) and *H. neanderthalensis* D322-15 (red star) specimens, *Homo*, *Gorilla*, *Pan*, and *Pongo* showing in the different views. The sub-setting model shows which cells were used for the PCA. Note that the preserved elements of StW 318 were used for PCA, thus only lateral condyle was analysed.

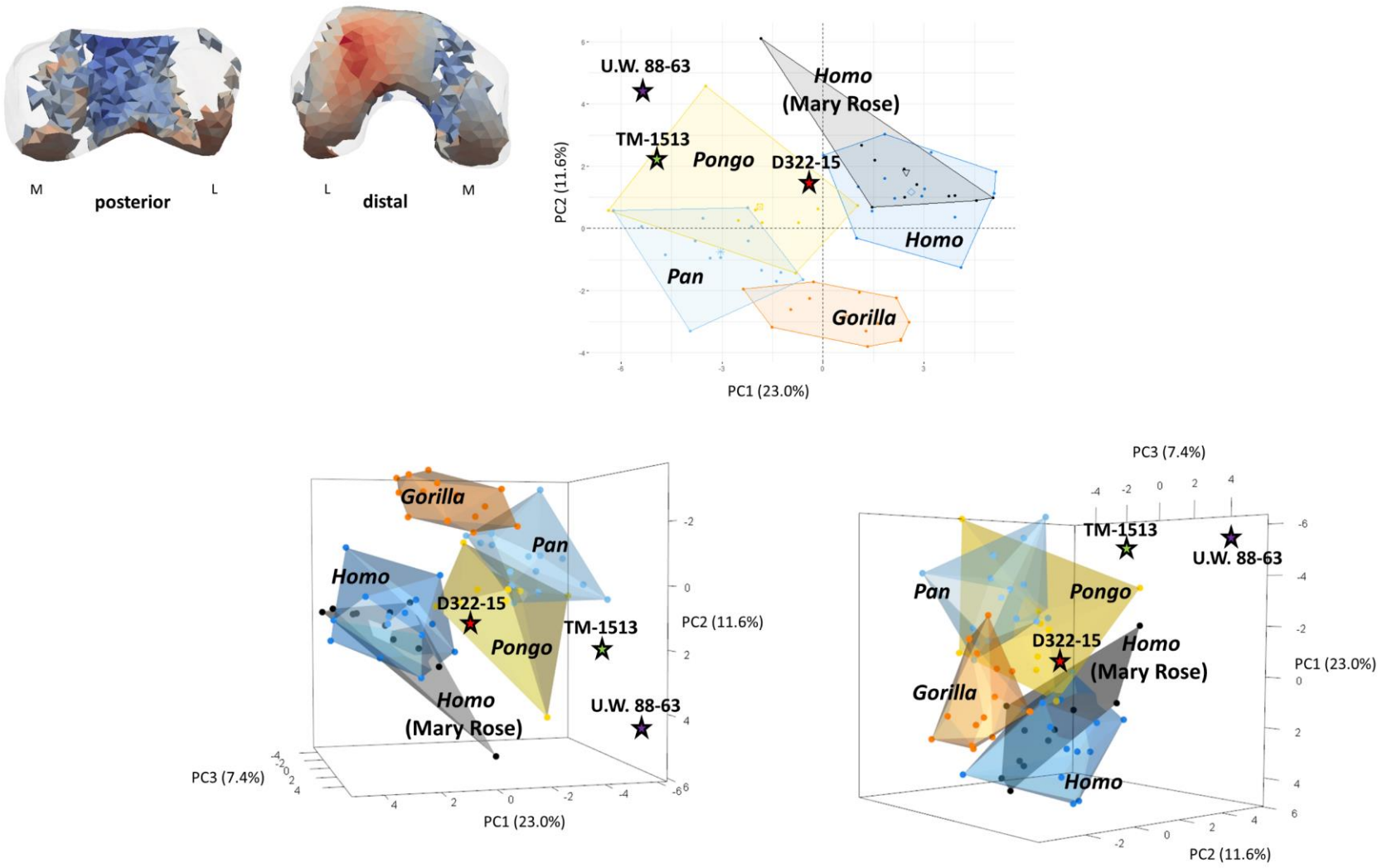

Figure 6.23: PCA of the rBV/TV distribution under the femoral patellar surface of *A. sediba* U.W. 88-63 (brown star), *A. africanus* TM 1513 (green star), and *H. neanderthalensis* D322-15 (red star) specimens, *Homo*, *Gorilla*, *Pan*, and *Pongo* showing in the different views. The sub-setting model shows which cells were used for the PCA. Note that the preserved elements of U.W. 88-63 were used for PCA, thus only lateral condyle was analysed.

6.5 Discussion

6.5.1 Locomotor signals in the trabecular bone distribution of South African fossil hominins

The lateral femoral condyle of StW 318, attributed to *A. africanus*, exhibits a trabecular distribution under the patellar surface of the femur, in the lateral epicondyle, and in the posteroinferior volumes of the lateral condyle, falling somewhere between *Pan* and *Pongo* but not distinctly different from *H. sapiens* (Figure 4.3, Figure 6.2, and Figure 6.4). However, the distribution beneath the presumed lateral head of gastrocnemius muscle resembles that of *H. sapiens* to the exclusion of the great apes (Figure 4.6, Figure 6.2, and Figure 6.4). The gastrocnemius muscle in humans primarily functions in plantarflexion of the foot and ankle joint, which involves pointing the foot downward. It also assists in knee flexion when the foot is dorsiflexed, aiding in bending the knee joint. This muscle plays a key role in activities such as running, jumping, and other fast leg movements (e.g., Huijing, 1985; Ishikawa et al., 2007; Maganaris, 2003; Muramatsu et al., 2001). While its involvement in walking and standing is less pronounced, its contribution to these activities should not be overlooked. These functions have been extensively studied and documented in scientific literature (e.g., Huijing, 1985; Ishikawa et al., 2007; Maganaris, 2003; Muramatsu et al., 2001). Furthermore, the distribution of rBV/TV beneath the insertions of the gastrocnemius in *Homo* may be influenced by forceful flexion of the knee and/or hip joint (e.g., Anderson & Pandy, 2001; Baltzopoulos, 1995; Georgiou et al., 2020; Hardt, 1978; Simpson and Pettit, 1997; Taylor et al., 2004; Zheng et al., 1998).

The specific activation pattern of the gastrocnemius muscle during different locomotor and postural activities in *Homo* remains unclear (Ishikawa et al., 2007). Although Stern & Susman (1981) did not directly measure gastrocnemius activity, they observed that the activation patterns of the gluteus medius and, to a lesser extent, the gluteus superficialis were similar between African apes during climbing and humans during bipedal walking. Since the gastrocnemius is involved in most hindlimb activities in humans (Ishikawa et al., 2007; Lichtwark et al., 2006; Neptune et al., 2001), it is likely also plays a significant role in arboreal locomotion in African apes. The human-like distribution of rBV/TV under the lateral head of the gastrocnemius in StW 318 could suggest a comparable level of involvement during bipedal walking or an increased degree of knee extension compared to non-human great apes. However, this inference is based on observations from the lateral condyle alone, as the medial condyle is not preserved, and thus, should be interpreted with caution.

TM 1513 shows high rBV/TV in the distal volumes of both femoral condyles, suggesting extended knee postures (Figure 6.5). However, the higher rBV/TV values in the medial condyle compared to the lateral condyle are consistent with higher medial knee compartment loading, typical for great apes (Figure 4.3). Moreover, the rBV/TV concentration under the presumed insertions of the gastrocnemius muscle is again more similar to that of *H. sapiens*, (Figure 4.6 and Figure 6.7; Supplementary Figure S4.12). Overall, TM 1513 shows trabecular structure more like that of non-human great apes due to medial rBV/TV concentration but there are individual features (rBV/TV concentration under the insertions and in the distal volumes of both femoral condyles) that are more modern *Homo*-like. The general trabecular pattern of TM 1513 distal femur is more like that of non-human great apes than StW 318. Variations in knee angle have been shown to affect both joint reaction forces and contact areas. In particular, more flexed knee positions result in greater forces on the articular surface and expand the contact area toward the posterior portion of the condyles. Therefore, even though TM 1513 most likely loaded knees in extended postures in a similar way as humans, the knee was likely more frequently loaded in flexed positions than in most humans as well. TM 1513 shows similar rBV/TV concentration under the patellar surface to the Mary Rose population. rBV/TV concentration is more medial on the patellar surface in Mary Rose individuals compared to other human individuals in the sample, where the highest values were found on the lateral side of the patellar surface (Supplementary Figure S4.12). Moreover, trabecular bone concentration under the insertions of both cruciate ligaments is higher in Mary Rose individuals compared to other human individuals (Supplementary Figure S4.12). Posterosuperior/inferior regions of both condyles exhibit high values compared to other regions in both human samples. However, Mary Rose individuals show slightly higher values in the medial condyle and lower values in the lateral condyle (as it is in TM 1513) compared to other human individuals, where higher values are present in the lateral and lower values in the medial condyle (Supplementary Figure S4.12). The lateral epicondyle exhibits higher values compared to the medial epicondyle in both samples, however, with higher rBV/TV values in Mary Rose individuals (Supplementary Figure S4.12). Additionally, there is a higher rBV/TV concentration under the insertions of the posterior cruciate ligaments and the medial head of the gastrocnemius muscle in the Mary Rose sample compared to other human individuals, which is again consistent with the rBV/TV distribution in TM 1513 specimen (Supplementary Figure S4.13; Figure 6.5). Although humans exhibit distinctive knee-loading patterns compared to other great apes, the increased medial rBV/TV concentration in the distal femur could be attributed to behaviors common in the active human population. Activities such as climbing stairs, sitting, squatting, and running involve

various knee flexion angles, which may contribute to this observed increase in medial rBV/TV. These activities can impose different mechanical stresses on the knee joint, potentially influencing trabecular bone distribution and contributing to the observed differences in bone density.

Trabecular structure is poorly preserved in the *A. sediba* U.W. 88-63 specimen and analysis were restricted to under the patellar surface, where U.W. 88-63 exhibits a trabecular distribution falling between *Pan* and *Pongo*, and not far from Mary Rose human sample (Figure 4.3, Figure 6.10, Figure 6.11). Trabecular bone structure under the patellar surface of the femur shows similar distribution as found in TM 1513 specimen and the Mary Rose human sample, where rBV/TV is concentrated more medially (but still more laterally than non-human apes) on the patellar surface compared to human individuals from sedentary population (Figure 4.6, Figure 6.7, Figure 6.9, Supplementary Figure S6.1), supporting the functional interpretation of extended knee postures during bipedal locomotion with a degree of knee flexion that differs from *A. africanus* and extant non-human apes. However, this conclusion is based solely on the trabecular distribution under the patellar surface, as rest of the trabecular structure of the distal femur was in poor condition, thus requires caution in interpretation.

To date, resolving the debate on the evolution of hominin bipedalism has proven challenging, despite extensive research into external skeletal morphology. Numerous studies have scrutinized external features to understand early hominin locomotion, yet questions persist about their precise locomotor behaviors (e.g. Stern & Susman, 1983; Susman et al. 1984; Ward, 2002; Carey & Crompton, 2005; Ohman et al. 2005; Lovejoy et al. 2009a, b; Lovejoy & McCollum, 2010; Raichlen et al. 2010). This thesis offers new insights by examining trabecular bone to reconstruct the locomotion and postural behaviors of South African hominins from the early Pleistocene. The trabecular bone distribution in StW 318, an *A. africanus* individual, reveals extensive knee movements consistent with earlier findings (e.g., Ward et al. 1999; Ward et al. 2001; Lovejoy et al. 2002). The *Homo*-like trabecular morphology observed in the proximal femur of *A. africanus* aligns with previous research (Georgiou et al., 2018), suggesting that climbing was not the sole locomotor strategy for this species. This supports earlier studies showing Homo-like traits in the pelvis and knee of *A. africanus* (Napier, 1964; Lovejoy & Heiple, 1970; Tardieu, 1981; Häusler & Berger, 2001; Haeusler, 2002).

In contrast, TM 1513 shows a more ape-like trabecular pattern in the distal femur. This pattern is consistent with paleoenvironmental reconstructions that suggest significant tree cover and cyclical wet and dry phases in the Sterkfontein region during the Early Pleistocene (Reynolds

& Kibii, 2011; Pickering et al., 2018). The trabecular distribution in TM 1513 resembles that observed in StW 567, a distal tibia specimen from the Member 5 East infill. While Barak et al. (2013) noted *Homo*-like trabecular orientation in StW 567, suggesting less dorsiflexed ankles, the trabecular parameters were not distinctly *Homo*-like. The BV/TV in StW 567 was higher compared to *H. sapiens* or *P. troglodytes*, though the taxonomic uncertainty surrounding StW 567, which includes both *P. robustus* and early *Homo* fossils, complicates the interpretation of these results.

The trabecular bone distribution of U.W. 88-63 reveals that this *A. sediba* individual loaded their knees in extended postures possibly during a unique bipedal gait that differs somehow from another *Australopithecus* and the *Homo* genus. This functional interpretation is supported by external morphology of the distal femur in U.W. 88-63. *A. sediba* exhibits unique anatomical characteristics compared to other members of the genus, such as a significantly more pronounced lateral patellar lip, a lower relative notch height similar to that of humans, and a more squared distal epiphyseal shape. These features have led to the suggestion that *A. sediba* has developed distinctive gait exerted increased lateral forces on the knee joint, contributing to the development of the larger lateral patellar lip (DeSilva et al., 2013). According to Miller & DeSilva (2024), *A. sediba* also had anteriorly expanded femoral condyles, which may have enhanced the patellar moment arm, improving quadriceps efficiency. If that was the case, the results of this chapter suggest that this unique external knee morphology led to the higher medial knee compartment loading. Higher medial knee compartment loading is typical for non-human great apes due to their knee flexion during (especially) arboreal locomotion. However, in case of *A. sediba*, the knee might have been loaded in a higher degree of flexion compared to humans due to this unique external knee morphology rather than climbing. These variations among individuals within the *Australopithecus* imply the potential for diverse bipedal gaits utilized by different species in this genus. The results highlight the diversity of locomotor behaviours in South African hominins around 2 million years ago.

6.5.2 Locomotor signals in the trabecular bone distribution of *Homo floresiensis*

The distal femoral condyles of LB1-8 and proximal tibial condyles of LB1-13 are attributed to one female individual of *H. floresiensis*. The mixture of features in the trabecular structure found in the distal femur and proximal tibia of LB1, suggesting both extended and flexed knee postures LB1-8 exhibits a trabecular distribution under the patellar surface of the femur, in the lateral epicondyle, and in the distal volume of the lateral condyle, falling closest to the range of

Pan (Figure 4.3, Figure 6.15). However, the distribution beneath the presumed lateral and medial heads of the gastrocnemius muscle resembles that of *H. sapiens* (Figure 4.6, Figure 6.15). The role of the gastrocnemius muscle in human locomotion has been previously discussed. In humans, as well as in African apes, the medial and lateral collateral ligaments stabilize the knee joint in full extension, preventing excessive rotation and hyperextension. These ligaments loosen when the knee is flexed, allowing for greater rotational movement (e.g., Nagai et al., 2021). The medial collateral ligament tightens during external rotation and relaxes with internal rotation, while the lateral collateral ligament is actively tightened during the flexion-extension cycle by the contraction of the biceps tendon (Hirschmann & Muller, 2015). It has also been observed that loading of the collateral ligaments leads to increased rBV/TV beneath their attachment points in all primates (for further details, see Chapter 4). The collateral ligaments are thought to remain loose during knee flexion, allowing for greater rotational movements, and become taut during knee extension. However, results of rBV/TV concentration in both femoral epicondyles suggest that both collateral ligaments are equally loaded in African apes (Figure 4.9). This observation suggests that there may be some degree of medial and lateral rotation of the knee when it is not fully flexed. Previous research has noted that *Pan* exhibits lateral knee rotation during knee extension (e.g., Lovejoy, 2007). However, this would typically result in higher bone density around the insertion of the medial collateral ligament compared to the lateral collateral ligament, a pattern not observed in *Pan* (Figure 4.9). Furthermore, this hypothesis cannot be tested in LB1-8 due to the exclusion of the medial femoral epicondyle from the analysis. Nevertheless, similar distribution in the lateral femoral epicondyle in LB1-8 to that found in *Pan* suggests similar involvement of the lateral collateral ligament during locomotion in both species.

LB1-13 exhibits a modern *Homo*-like trabecular distribution in the centre of the lateral side of the tibial plateau, suggesting higher lateral knee compartment loading (compared to great apes) typical during bipedalism in humans. Moreover, a modern *Homo*-like trabecular distribution was also found under the presumed insertion of the patellar tendon. During knee extension in humans, the patellar tendon moves to the centre of rotation, enhancing the lever advantage of the quadriceps muscle due to the anterior projection and supero-inferior extension of the tibial tuberosity. As extension is completed, slight mediolateral rotation stabilizes the knee (Tardieu, 1999). However, the stress that the knee experiences under the patellar tendon is higher during deep flexion (Racic et al., 2009). In humans, typical activities causing this are running, jumping, squatting, etc. (e.g., Nilsson & Thorstensson, 1989; Racic et al., 2009). However, this is also

expected in non-human great apes due to the stress that the knee experiences during deep flexion, especially during arboreal locomotion (e.g., D'Aoŭt et al., 2002; Sylvester, 2013). Additionally, trabecular distribution along the lateral and medial margins of the tibial plateau exhibit rather *Pongo*-like distribution suggesting a high range of knee movements. rBV/TV was concentrated medially on the medial side of the tibial plateau in all non-human great apes (Figure 5.3). However, this concentration extended more anteriorly in *Pongo* (Figure 5.3) and LB1-13 (Figure 6.16, Figure 6.18). As described in **Chapter 5**, I suggest that this anterior concentration is consistent with loading of the knee in extended knee postures. When the knee is flexed and more medially loaded, the trabeculae become denser proximally on the medial side of the tibial plateau. However, the more the knee is extended, the denser the bone becomes anteriorly as well. This could thus be a signal of higher knee extension in *Pongo* and LB1-13 compared to African apes. As the results suggest, LB1-13 is most likely loaded during the knee flexion in the way that differs from African apes, especially *Gorilla* as the distribution in *Pan* was found to be more like that of *Pongo* compared to *Gorilla*.

To date, research on external morphology of the lower limb of *H. floresiensis* is limited indicating adaptations for bipedal locomotion, albeit with some unique features that distinguish it from both earlier hominins and modern humans. In their initial description of *H. floresiensis*, Brown et al. (2004) emphasized several postcranial elements of the hind limb. The femur of the specimen LB1 was described as robust, circular in cross-section, and lacking a pilaster. It featured a compressed anteroposterior femoral neck and a relatively high bicondylar angle, around 14 degrees. The muscle attachments were not well-developed, though the lesser trochanter and intertrochanteric crest were notably prominent. The LB1 tibia was also robust, with a slight curve along its length and an oval cross-section at the midshaft. Overall, the hind-limb morphology suggested a modern, *Homo*-like form of obligate bipedalism (Brown et al., 2004). In a follow-up study, Morwood et al. (2005) described another tibia (LB8) from a smaller individual, which also exhibited robustness and an oval midshaft cross-section. For the first time, the inter-limb proportions were analyzed with the discovery of the humerus (LB1), revealing similarities to *Australopithecus* and differences from both modern humans and early *H. erectus*. The major limb bones were considered robust relative to their lengths, suggesting adaptations for bipedalism (Morwood et al., 2005).

Jacob et al. (2006) attempted to dismiss these findings, suggesting that the new fossils were pathological humans. They described the long bones as very porous, with weak muscle attachment sites indicating severe muscle hypotonia. Claims were made about pathologically

asymmetrical proximal femora and patellae, and interpretations were made regarding compromised tibial cross-sections due to weak muscle development (Jacob et al., 2006). Argue et al. (2006) highlighted that the skeletal anatomy and body proportions of LB1 did not match individuals diagnosed with primordial dwarfism. The long bones of LB1 lacked metaphyseal flaring or triangular epiphyses and were not thin. However, another proposed pathological diagnosis for the unusual skeletal features of *H. floresiensis* was put forward by Hershkovitz et al. (2007), suggesting LB1 may have suffered from Laron Syndrome, a congenital deficiency of insulin-like growth factor. However, their claims lacked quantitative support, and subsequent challenges were raised (Falk et al., 2009). Based on the personal observation, the lower limb long bones of *H. floresiensis*, display a uniquely porous cortex. The reason behind this porosity remains unclear; however, it is established that increased porosity in cortical bone diminishes its mechanical strength under load (e.g., Yeni et al., 1997; Augat & Schorlemmer, 2006). This could potentially impact both the performance of trabecular bone under mechanical stress and the locomotor behaviors of *H. floresiensis*.

Some researchers have proposed that they may have retained some adaptations for climbing or arboreal behaviour, given the environment of the island of Flores, which was characterized by dense forest and rugged terrain (e.g., Farisi & Higuchi, 2017; Setiawan, 2021). This could explain the mixture of features in the trabecular structure found in the distal femur and proximal tibia of LB1, suggesting both extended and flexed knee postures. However, the extent to which *H. floresiensis* relied on arboreal locomotion remains uncertain and is subject to ongoing research and debate (e.g., Blaszczuk & Vaughan, 2007; Kramer & Sylvester, 2009; Van Heteren, 2012). Another possible explanation could be that *H. floresiensis* exhibited a distinctive form of bipedalism, possibly characterized by a more flexed knee posture compared to modern humans. However, both hypotheses remain speculative and require further evidence to support them.

6.5.3 Locomotor signals in the trabecular bone distribution of *Homo neanderthalensis*

The distal femoral condyles of specimen D322-15, attributed to *H. neanderthalensis*, display a trabecular distribution beneath the patellar surface and in both femoral condyles similar to that of *H. sapiens* (Figure 4.3, Figure 6.19, Figure 6.21). Additionally, D322-15 shows a trabecular distribution beneath the presumed attachment sites of both cruciate ligaments and the gastrocnemius muscle, akin to the Mary Rose population (Figure 4.6, Figure 6.19, Figure 6.21). This suggests higher or more variable knee joint loading, which is consistent with the physical

demands expected of hunter-gatherer populations, in contrast to sedentary groups. High rBV/TV concentration under the gastrocnemius muscle is present in all taxa as this muscle is involved during different types of locomotion, however, mostly when the knee is flexed. Thus, in humans, higher rBV/TV under this muscle is found in active populations rather than in sedentary populations. Similarly, high rBV/TV is found under the insertions of cruciate ligaments of all taxa. However, when the knee is flexed, the posterior cruciate ligament (PCL) is under tension, resulting in higher rBV/TV beneath the PCL compared to the anterior cruciate ligament (ACL) in non-human great apes. Conversely, during knee extension when the ACL is in tension, humans exhibit higher rBV/TV under the ACL relative to the PCL (see **Chapter 4** for detailed analysis). This pattern is also evident in the Mary Rose population, where higher rBV/TV was observed under the PCL compared to the ACL, suggesting more frequent knee flexion. Similarly, D322-15 shows a comparable pattern, indicating habitual loading in flexed positions more prevalent than in sedentary populations. The increased bone density at both cruciate ligament insertion sites across all taxa (Figure 4.4) likely reflects the necessity to protect and stabilize the femur throughout its range of motion. Despite these findings, the trabecular structure and external femoral morphology of *H. neanderthalensis* are very similar to those of modern *H. sapiens* (e.g., Trinkaus, 1976; Hershkovitz et al., 1995; Trinkaus & Jelínek, 1997; De Groote, 2011), indicating that *H. neanderthalensis* employed a bipedal gait similar to that of modern humans.

6.6 Conclusion

This study provided a holistic examination of trabecular bone architecture within the distal femur of *A. africanus* (StW 318, TM 1513), *A. sediba* (U.W. 88-63), *H. floresiensis* (LB1-8) and *H. neanderthalensis* (D322-15) and within the proximal tibia of *H. floresiensis* (LB1-13). Trabecular architecture of the lateral femoral condyle in StW 318 reveals that its bone structure was consistent with joint posture of bipedal walking with knee being frequently loaded in flexed positions as well. Trabecular architecture of the distal femur in TM 1513, however, reveals rather ape-like distribution pattern in distal femur or/and the knee being loaded in more diverse joint postures. Trabecular architecture under the patellar surface of the femur in *A. sediba* supports the functional interpretation of extended knee postures during bipedal locomotion with a degree of knee flexion that differs from *A. africanus* and extant non-human apes. The results highlight the diversity of locomotor behaviours in South African hominins. Trabecular architecture of the distal femur and proximal tibia in *H. floresiensis* exhibits a mixture of features suggesting both extended and flexed knee postures. Alongside a unique external lower

limb morphology, this could indicate that *H. floresiensis* exhibited a distinctive form of bipedalism, possibly characterized by a more flexed knee posture compared to *H. sapiens*. Trabecular architecture of the distal femur in *H. neanderthalensis* shows that *H. neanderthalensis* were obligate bipedal hominins with locomotion similar to that of *H. sapiens*.

6.7 Supplementary material

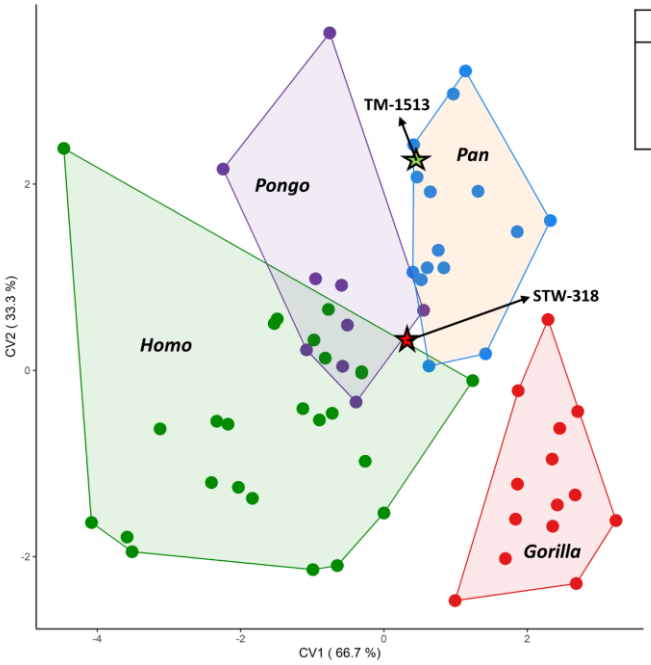

Typical probability	Human	*Pan*	*Gorilla*	*Pongo*	Assignment
A. africanus (StW 318)	0.111	0.381	0.047	0.466	*Pongo*
A. africanus (TM 1513)	0.002	0.688	0.000	0.215	*Pan*

Figure S6.1: A bi-variate plot was generated based on the first two components from the CVA, which was conducted using the first three principal components of trabecular bone distribution in the lateral femoral condyle. The table includes the cross-validated typicality probabilities, indicating the likelihood of fossil specimens being assigned to each extant taxon, based on their canonical variate scores.

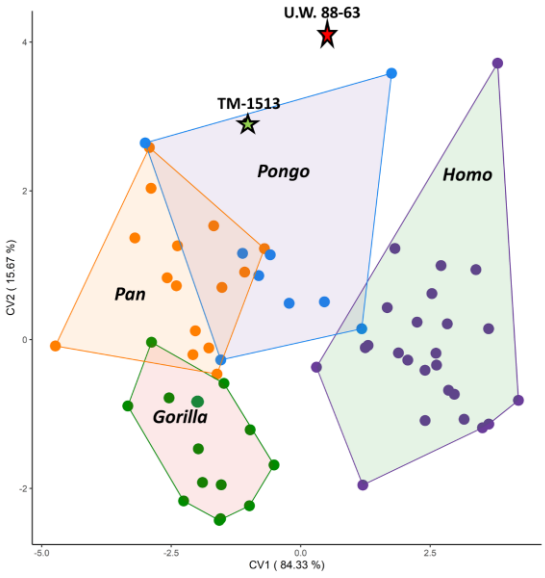

Typical probability	Human	*Pan*	*Gorilla*	*Pongo*	Assignment
A. sediba (UW 8863)	0.000	0.001	0.000	0.008	none
A. africanus (TM 1513)	0.000	0.055	0.000	0.171	*Pongo*

Figure S6.2: A bi-variate plot was generated based on the first two components from the CVA, which was conducted using the first three principal components of trabecular bone distribution under the patellar femoral surface. The table includes the cross-validated typicality probabilities, indicating the likelihood of fossil specimens being assigned to each extant taxon, based on their canonical variate scores.

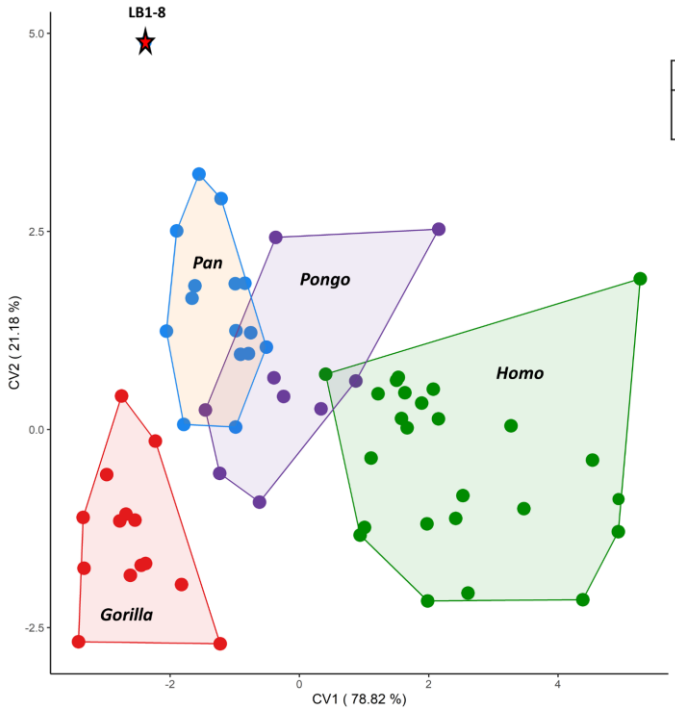

Typical probability	Human	*Pan*	*Gorilla*	*Pongo*	Assignment
H. floresiensis (LB1-8)	0.000	0.000	0.000	0.000	none

Figure S6.3: A bi-variate plot was generated based on the first two components from the CVA, which was conducted using the first three principal components of trabecular bone distribution in the distal femur. The table includes the cross-validated typicality probabilities, indicating the likelihood of fossil specimens being assigned to each extant taxon, based on their canonical variate scores.

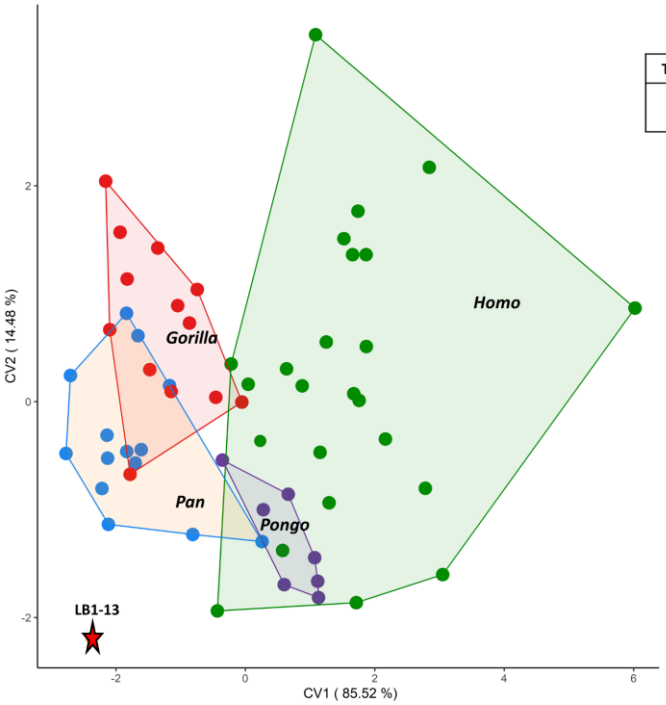

Typical probability	Human	*Pan*	*Gorilla*	*Pongo*	Assignment
H. floresiensis (LB1-13)	0.000	0.163	0.008	0.007	*Pan*

Figure S6.4: A bi-variate plot was generated based on the first two components from the CVA, which was conducted using the first three principal components of trabecular bone distribution in the proximal tibia. The table includes the cross-validated typicality probabilities, indicating the likelihood of fossil specimens being assigned to each extant taxon, based on their canonical variate scores.

7 GENERAL DISCUSSION AND CONCLUSION

The primary goal of this thesis was to explore trabecular bone architecture in the distal femur and proximal tibia of extant hominids and to investigate how these patterns relate to locomotion. Specifically, the thesis aimed to determine whether trabecular bone structures corresponded with inferred locomotion types in *Australopithecus africanus*, *Australopithecus sediba*, *Homo floresiensis*, and *Homo neanderthalensis*. Trabecular bone analysis provides a deeper understanding of extinct species' behaviours than external morphology alone, as bone structure continually remodels in response to mechanical loading throughout the life of an individual (e.g., Barak et al., 2011; Pontzer et al., 2006; Volpato et al., 2008). Therefore, analyzing trabecular patterns in living apes is crucial for interpreting the behavior of extinct hominins. Extant great apes, with their close genetic relationships to humans and diverse locomotor behaviors, serve as important analogs for reconstructing the locomotion of extinct hominins (e.g., Tuttle, 1969; Doran, 1996; 1997; Isler, 2005; Thorpe & Crompton, 2005; 2006).

This thesis employed canonical holistic morphometric analysis (cHMA) to examine trabecular architecture in the entire distal femur and proximal tibia. The investigation was conducted in three main chapters:

- **Chapter 4**: Analyzed trabecular architecture in the distal femur of extant apes to identify locomotor-related patterns in the knee.
- **Chapter 5**: Analyzed trabecular architecture in the proximal tibia of extant apes to identify locomotor-related patterns in the knee.
- **Chapter 6**: Used the trabecular patterns observed in extant apes to infer habitual loading patterns in the distal femur and proximal tibia of extinct hominins, including *A. africanus*, *A. sediba*, *H. floresiensis*, and *H. neanderthalensis*.

The following sections provide a detailed review and interpretation of the key findings from these chapters, offering insights into the evolution of hominin bipedalism and how these findings contribute to our broader understanding of locomotor evolution.

7.1 Trabecular bone knee structure in human bipedal walking

This study predicted that modern humans would exhibit significant differences in trabecular bone structure in both the distal femur **(Chapter 4)** and proximal tibia **(Chapter 5)** compared to other great apes, reflecting their habitual use of extended knee postures during bipedal locomotion. These predictions were supported.

In particular, we observed high relative bone volume (rBV/TV) in the posteroinferior regions of both femoral condyles (Figure 4.3) and in the anteroposterior centers of each tibial condyle on the tibial plateau (Figure 5.3, Figure 5.5). These findings align with the extended knee postures characteristic of all phases of human gait. Additionally, the human distal femur displayed greater anisotropy posterosuperiorly and inferiorly in both femoral condyles, as well as under the patellar articular surface of the femur (Figure 4.7), and across both tibial condyles compared to non-human great apes (Figure 5.6, Figure 5.7). This pattern of high degree of anisotropy (DA) is consistent with the loading expected during the extended knee postures typical of human walking.

The knee experiences varying degrees of loading depending on the specific phase of the gait cycle of human walking (Figure 1.4d). However, the knee is loaded in extension during most of the cycle. In the initial contact phase, when the foot first contacts the ground, the knee is typically in a slightly flexed position, which helps absorb the impact forces generated by the body weight. As the stance phase progresses, the knee straightens gradually, reaching full extension during midstance, when the body weight is directly over the supporting leg. At this point, the (extended) knee experiences maximum loading as it bears the full weight of the body. During the terminal stance and pre-swing phases, as the body prepares to lift the foot off the ground, the knee begins to flex again, relieving some of the loading. Finally, in the swing phase, the knee remains in a flexed position as the leg swings forward, minimizing loading until the foot contacts the ground again to initiate the next gait cycle (e.g., Nisell, 1985; Martin & Brown, 2009; Earp et al., 2014; Wang, 2022).

Higher rBV/TV concentration observed in the lateral femoral condyle compared to the medial femoral condyle (Figure 4.3) aligns with the biomechanical concept of knee adduction moment and valgus knee postures (e.g., Nordin & Frankel, 2001; Racic et al., 2009). The knee adduction moment describes the torque acting around the knee joint in the frontal plane during weight-bearing activities, such as walking. This moment tends to move the knee inward or medially, particularly during the stance phase. Factors influencing the knee adduction moment include lower limb bone alignment, muscle activity, and joint morphology.

An increased knee adduction moment is associated with higher stress on the medial compartment of the knee joint. Muscles on the inner side of the thigh and leg, such as the adductor group, gracilis, and sartorius, contribute to this inward movement, while muscles on the outer hip, like the gluteus medius and minimus, control the pelvis and femur position, indirectly affecting the knee adduction moment. The medial collateral ligament helps stabilize

the knee and resist excessive inward movement, while the anterior cruciate ligament primarily prevents forward tibial movement but also stabilizes the knee against rotational forces. When considering the valgus angle of the knee, an adduction moment places additional stress on the lateral aspect of the knee joint, whereas a varus knee would stress the medial aspect (e.g., Zhang & Wang, 2001; Kutzner et al., 2013; Van den Noort et al., 2013; Ogaya et al., 2014).

The results from the proximal tibia support this higher lateral knee compartment loading. High rBV/TV concentration in the lateral tibial condyle is consistent with the human bipedal gait, particularly the heel strike and the subsequent transfer of weight from the lateral to the medial side of the foot (e.g., Elftman & Manter, 1935; Napier, 1967). Additionally, the mean bone volume fraction (BV/TV) was higher in the lateral condyle compared to the medial condyle of the tibial plateau (Figure 5.11). This suggests that the lateral condyle experiences higher stress during bipedal walking and/or that the valgus angle of the knee in humans contributes to this higher BV/TV in the lateral condyle. However, considering that the medial knee compartment has a larger proportional articular surface area compared to the lateral compartment, and given the relatively small difference in mean BV/TV, the loading between the knee compartments might be considered relatively balanced.

The more laterally distributed rBV/TV beneath the patellar surface in *Homo* compared to other great apes (Figure 4.3) likely reflects a more concave trochlea. Modern humans possess a well-developed, deep trochlear groove, which is essential for stabilizing the patella during bipedal locomotion. In contrast, non-human great apes have a relatively shallow and flat trochlear groove. The elevated rBV/TV values observed across the patellar articular surface of the femur extend more mediolaterally, indicating greater articulation of the patella with the lateral part of the trochlea than with the medial part (Figure 4.3). The lateral and medial patellar facets are two distinct articular surfaces on the posterior aspect of the patella that articulate with the femur within the trochlear groove (Hirschmann & Müller, 2015). The lateral patellar facet is the larger of the two facets in humans. It typically exhibits a more convex or rounded shape compared to the medial facet and bears a greater proportion of the load during activities that involve knee extension, such as walking and running in humans (Hirschmann & Müller, 2015).

In humans, rBV/TV under the proximal tibiofibular joint was found to be the highest of all great apes (Figure 5.4). The proximal tibiofibular joint allows for slight movement, primarily rotation, and translation of the fibula relative to the tibia. While the range of motion at this joint is limited compared to non-human great apes (e.g., Eichenblat, & Nathan, 1983; Ogden, 1974; Pietrobelli et al., 2023; Sarma et al., 2015), it plays a role in distributing forces between the

tibia and fibula during bipedal locomotion (e.g., Lambert, 1971; Ogden, 1974; Pietrobelli et al., Preuschoft, 1971) and allows for slight rotational movement of the fibula during ankle dorsiflexion and plantarflexion (e.g., Marchetti et al., 2017).

The high rBV/TV and DA observed beneath the insertion of the gastrocnemius muscle in humans (Figures 4.3, 4.7, and 4.8) reflect the significant role this muscle in various locomotor and postural activities. The gastrocnemius, primarily responsible for plantarflexion of the foot, also assists in knee flexion, particularly when the foot is dorsiflexed. This muscle is crucial in actions such as running, jumping, and fast leg movements, and to a lesser extent in walking and standing (e.g., Huijing, 1985; Ishikawa et al., 2007; Maganaris, 2003; Muramatsu et al., 2001). The observed high rBV/TV and DA in this region of the femur may be related to the frequent and forceful flexion of the knee and/or hip joint, which engages the gastrocnemius muscle. This aligns with the muscle's role in stabilizing and assisting movements during activities that involve significant knee flexion (e.g., Anderson & Pandy, 2001; Baltzopoulos, 1995; Georgiou et al., 2020; Hardt, 1978; Simpson & Pettit, 1997; Taylor et al., 2004; Zheng et al., 1998). Notably, the high alignment of trabeculae under the presumed insertion points of the gastrocnemius suggests consistent directional loading of this region. While the specific activation pattern of the gastrocnemius during different locomotor and postural activities in humans remains under-explored (Ishikawa et al., 2007), the trabecular architecture beneath its insertion sites provides valuable insight into the forces and activities influencing bone structure. The alignment of trabecular bone in these areas indicates that the femur experiences frequent loading in the direction of muscle force, which is consistent with the known functional roles of the gastrocnemius in human movement.

The human sample of this thesis consists of sedentary and active populations (for more details about the human sample see **Chapter 2**). When examining intraspecific differences within the human sample, rBV/TV concentration was found to be higher in the medial region of the patellar surface of the femur in the active population (Mary Rose) compared to the more sedentary population (Figure 6.2). Additionally, individuals from the Mary Rose population exhibited higher rBV/TV values in both the medial femoral condyle and epicondyle, as well as medially under the patellar surface of the femur, compared to those in the more sedentary population (but still not to the extent of non-human apes). Furthermore, rBV/TV concentration under the insertions of both cruciate ligaments and the medial head of the gastrocnemius muscle was found to be higher in the Mary Rose population compared to those individuals in the more sedentary population. However, no differences between the populations were found when

exploring trabecular distribution in the proximal tibia. These findings suggest a greater loading of the medial knee compartment across individuals in the Mary Rose population, indicative of higher levels of activity such as squatting, running, jumping, or other movements involving a flexed knee posture.

The trabecular bone distribution patterns observed in the distal femur and proximal tibia of the modern human sample are consistent with previous research on trabecular structure in both the proximal (Cazenave et al., 2019; Georgiou et al., 2019; Georgiou et al., 2020; Ruff et al., 2013; Ryan & Ketcham, 2002; Ryan & Walker, 2010; Volpato et al., 2008) and distal (Georgiou et al., 2018; Sylvester & Terhune, 2017) femur. This agreement with earlier studies underscores the reliability of these findings.

The observed patterns align with our current biomechanical understanding of the human walking cycle (Alexander, 1991; 2004; Elftman & Manter, 1935; Javois et al., 2009; Landis & Karnick, 2006; Napier, 1967; Sylvester & Pfisterer, 2012; Tardieu, 1999; Organ & Ward, 2006). Specifically:

- **High rBV/TV in posterior regions**: The high rBV/TV in the posteroinferior regions of the femoral condyles reflects the loading patterns during the stance phase of walking and extended knee postures.
- **Increased anisotropy**: The higher DA observed in the posteroinferior regions is consistent with the biomechanical demands of human walking, which involve significant directional loading.
- **Lateral vs. medial condyle differences**: The higher rBV/TV in the lateral femoral condyle compared to the medial condyle and the corresponding patterns in the tibia are in line with the mechanical loading associated with bipedal gait and valgus knee postures.
- **Gastrocnemius muscle loading**: The high rBV/TV and DA beneath the gastrocnemius muscle insertion sites support its role in knee flexion and forceful movements, reflecting consistent directional loading in these areas.

These findings collectively contribute to our understanding of how human trabecular bone adapts to habitual bipedal locomotion and further support the use of trabecular bone analysis to infer locomotor behaviors in extinct species.

7.2 Trabecular bone knee structure and locomotor behaviour in African apes

The predictions that *Pan* and *Gorilla* would differ significantly from *Homo* and *Pongo* in trabecular structure of the distal femur and proximal tibia, reflecting habitual use of a flexed knee posture during terrestrial and arboreal locomotion, were indeed supported. Here is a summary of the findings:

- ***Pan*** and ***Gorilla*** exhibit trabecular bone patterns in both the distal femur and proximal tibia that align with habitual flexed knee postures. This is consistent with their arboreal and terrestrial locomotor behaviors, which often involve maintaining the knee in a flexed position during various activities.
- ***Homo*** and ***Pongo*** display distinct trabecular patterns that are indicative of different habitual loading conditions related to their bipedalism and suspensory locomotion, respectively. The trabecular architecture of ***Homo*** reflects the extended knee postures typical of bipedal walking, while ***Pongo*** shows adaptations for suspensory behaviors.
- The trabecular structures of ***Pan*** and ***Gorilla*** were found to be similar to each other, suggesting that their adaptations for flexed knee postures are comparable. This similarity reflects their shared adaptations for climbing and other arboreal activities, which require frequent knee flexion.

Specifically, high rBV/TV values posterosuperiorly in the femoral condyles, mediolaterally on the patellar articulation of the femur (Figure 4.3), along the medial edge of the medial tibial condyle and in the center of the lateral tibial condyle (Figure 5.3) were consistent with higher medial knee compartment loading and flexed knee postures during locomotion (e.g., Hofstetter & Niemitz, 1998; D'Aoŭt et al., 2002; 2004; Isler, 2005; Crompton et al., 2008; Pontzer et al., 2009; Ankel-Simons, 2010; Lee at al., 2012; Georgiou et al., 2018; 2020; Kozma et al., 2018), distinguishing the African apes from *Homo* and *Pongo* (Figures 5.5). This functional interpretation was also supported by higher mean BV/TV in the medial side compared to the lateral side of the tibial plateau in *Gorilla* and *Pan* (and *Pongo*). The distal femur of African apes was more anisotropic in the posteroinferior/superior regions of (especially) the medial femoral condyle (Figure 4.7), while proximal tibia was more anisotropic across both tibial condyles (Figure 5.6). This DA pattern was also consistent with what we would expect from loading the knee in flexed postures.

During terrestrial locomotion, African apes adopt a quadrupedal gait, where they walk on all fours with the body weight supported by the limbs. The knee positions during terrestrial walking cycles typically involve bending and straightening of the knees as the ape moves each limb forward and backward. When the limb is in contact with the ground (stance phase), the knee is usually bent to absorb shock and support the body weight. As the ape propels itself forward, the knee extends to push off the ground and move the limb into the swing phase, where it moves forward to take the next step. Thus, the knee positions in terrestrial locomotion are adapted for stability, weight support, and efficient forward propulsion on flat or uneven terrain. In contrast, during arboreal locomotion, African apes exhibit a range of knee positions depending on the specific behaviors and movements involved in navigating tree branches and arboreal environments. When climbing, the knees may be flexed to grip branches and maintain stability while ascending or descending. However, during brachiation, the knees may be more extended as the ape reaches and grasps onto branches with the arms while the legs trail behind. Arboreal locomotion often requires rapid changes in knee position to adapt to the dynamic and three-dimensional nature of the canopy environment (e.g., Hofstetter & Niemitz, 1998; D'Aoŭt et al., 2002; 2004; Isler, 2005; Crompton et al., 2008; Pontzer et al., 2009; Ankel-Simons, 2010; Lee at al., 2012; Georgiou et al., 2018; 2020; Kozma et al., 2018).

In *Pan* and *Gorilla*, the single attachment of lateral meniscus of the knee allows a greater range of motion compared to two attachments of the medial meniscus, which make the medial knee compartment more stable (Tardieu, 1981). Previous studies have demonstrated that soft tissue differences, together with a varus knee angle, allow the axis of internal/external rotation to pass through the medial tibial condyle in African apes and leads to the higher medial knee compartment loading (e.g., Churchill et al., 1998; Freeman & Pinskerova, 2005; Schipplein & Andriacchi, 1991; Sylvester, 2013). Additionally, considering the stress, on the patellar tendon and posterior side of the tibial plateau, experienced by the human knee during deep flexion, as demonstrated by Nagura et al. (2002), we can anticipate similar patterns in African apes. Specifically, we would expect to observe higher concentrations of rBV/TV along the medial edge of the tibial plateau, particularly on the medial condyle, in African apes which aligns with the findings in *Gorilla* and *Pan*. Additionally, the Mary Rose sample, consisting of active young males, exhibited higher rBV/TV concentrations along the medial edge of the tibial plateau compared to other human individuals in the sample. This observation may help explain why the Mary Rose sample somewhat closely resembles our non-human great ape taxa in our analyses (see above). Studies in the past have demonstrated that changes in knee angle can significantly

impact joint reaction force and contact area. Specifically, knee postures that are more flexed have been shown to increase forces exerted on the articular surface and enlarge the contact area, particularly at the posterior end of the condyles (Taylor et al., 2004; Kutzner et al., 2010).

As in *Homo*, high rBV/TV under the tendon attachment site of the proximal tibiofibular joint was found in *Gorilla* and *Pan*. In African apes, the proximal tibiofibular joint helps distribute forces between the tibia and fibula, ensuring proper alignment and stability of the lower leg. Compared with humans, the non-human great ape proximal tibiofibular articulation is more mobile to accommodate higher degrees of ankle dorsiflexion during arboreal locomotion (Orgen, 1974; DeSilva, 2009). When climbing or moving through trees, *Gorilla* displays dorsiflexion of the ankle joint to accommodate the curvature and irregularities of branches and trunks. This dorsiflexion helps them maintain contact with the substrate, enhance grip, and navigate through the forest canopy. *Pan* exhibits a wider range of ankle dorsiflexion compared to *Gorilla*. When climbing vertically or horizontally along branches, *Pan* often dorsiflexes their ankles to grasp and manipulate the substrate effectively. This dorsiflexion allows them to flexibly adjust their foot placement and maintain stability while navigating complex arboreal environments (e.g., DeSilva, 2009; Crompton et al., 2010, Holowka et al., 2017). However, results of this thesis have not shown any significant differences between *Gorilla* and *Pan* under the proximal tibiofibular joint that could reflect differences in mobility found in previous studies.

Furthermore, *Gorilla* and *Pan* exhibit a more aligned trabecular structure at the sites associated with the vastus lateralis and medialis compared to *Pongo*. This alignment suggests a specific adaptation in these apes for resisting forces associated with knee extension, which is a major function of the quadriceps femoris muscle group. These muscles play essential roles in various locomotor behaviours, supporting both terrestrial and arboreal movement patterns. During terrestrial locomotion, the vastus lateralis helps to generate the necessary force for propelling the body forward and maintaining stability. In arboreal locomotion, particularly during climbing or brachiation, the vastus lateralis assists in stabilizing the knee joint and supporting the body's weight as the ape navigates through trees and branches. Like the vastus lateralis, vastus medialis primary function is knee extension, contributing to the straightening of the leg during movement. The vastus medialis also plays a role in stabilizing the patella and preventing lateral displacement during knee extension, promoting proper tracking of the patella within the femoral groove. During activities that involve deep knee flexion, such as climbing, the vastus medialis helps support the knee joint and provides stability, allowing the ape to maintain

balance and control while navigating arboreal environments. As the knee bends, both muscles are drawn toward the joint, which leads to a reduction in the moment arm with increased flexion (e.g., Visser et al., 1990; Spoor & Van Leeuwen, 1992; Krevolin et al., 2004). Consequently, the pronounced trabecular alignment observed may be attributed to greater knee flexion in African apes compared to Pongo. However, this thesis did not conclusively determine whether this anisotropy is due to the contraction of the vastus medialis and lateralis or the joint reaction forces exerted on the femoral condyles relative to the shaft.

In African apes, the medial knee compartment experiences loading primarily during locomotor activities. However, the specific patterns of medial knee compartment loading may differ between these two species due to variations in their locomotor behaviors. Differences in the trabecular structure of the distal femur were observed between *Gorilla* and *Pan*. In *Pan*, the distribution of rBV/TV was more uniform across both femoral condyles compared to *Gorilla* (Figure 4.3). This uniformity could indicate the greater variability in knee loading experienced during climbing, as noted in studies of captive *Pan* (Isler, 2005). *Gorilla*, with their large body size and predominantly terrestrial quadrupedal locomotion, may experience more consistent knee loading during activities such as terrestrial knuckle-walking. Their knee joints endure substantial forces associated with supporting their body weight and propelling themselves on the ground, leading to relatively consistent loading patterns (Isler, 2005). On the other hand, *Pan*, which exhibits more diverse locomotor behaviours including quadrupedalism, arboreal climbing, and occasional bipedalism, may experience more variable knee loading. Arboreal locomotion, in particular, involves navigating through complex and varied environments, leading to dynamic shifts in knee loading as *Pan* adapts to different substrates and modes of movement (Isler, 2005). Overall, while both *Gorilla* and *Pan* experience variations in knee loading, the extent and patterns of variability may differ between the two species based on their unique locomotor adaptations and ecological contexts.

Moreover, differences between *Gorilla* and *Pan* have been found in the trabecular alignment under both cruciate ligament insertion sites at the femur (Figure 4.4). *Pan* (and *Pongo*) exhibited higher trabecular density at both cruciate ligament insertion sites, with this density extending further into the epiphysis compared to *Gorilla* (Figure 4.4). This pattern may reflect the more variable knee loading experienced by *Pan* during arboreal locomotion, as *Pan* is more arboreal than *Gorilla* (Remis, 1999; Isler, 2005). This interpretation is supported by the observation of more robust trabeculae at the cruciate ligament sites in female *Gorilla* compared to males (Figure 4.11a), as females are more arboreal than males (as discussed below).

Overall, the trabecular distribution patterns observed in the distal femur and proximal tibia of the African ape sample align with the flexed knee postures seen during quadrupedalism (Finestone et al., 2018) and, more specifically, during climbing (Crompton et al., 2008; D' D'Août et al., 2002; Hofstetter & Niemitz, 1998; Isler, 2005; Kozma et al., 2018).

7.2.1 Sex differences in trabecular bone knee structure in *Gorilla*

It was anticipated that the trabecular structure of the distal femur **(Chapter 4)** and proximal tibia **(Chapter 5)** in female *Gorilla* would differ from that in males, owing to females' higher levels of arboreal activity and/or more extended knee postures during climbing (e.g., Hammond, 2014; Isler, 2005). These expectations were confirmed. Female *Gorilla* displayed a greater concentration of rBV/TV in specific areas: the posterior regions of the lateral femoral condyle, the lateral patellar surface of the femur, medially above the intercondylar fossa (Figure 4.11a), and anteriorly on the medial side of the tibial plateau (Figure 5.9), compared to males. This pattern aligns with increased lateral knee compartment loading and/or more extended knee postures (Hofstetter & Niemitz, 1998; Isler, 2005; Crompton et al., 2008; Kozma et al., 2018). Additionally, the greater anisotropy observed in female *Gorilla* at the presumed insertion sites of the gastrocnemius muscle indicates more consistent loading of this muscle in females relative to males, possibly suggesting that the muscle is more actively engaged during climbing. This is consistent with the idea that female *Gorilla* engage in climbing more frequently than males (Isler, 2005; Kozma et al., 2018). During walking, the gastrocnemius muscle contracts to plantarflex the ankle joint, pushing off the ground with each step. This action helps propel *Gorilla* forward and provides stability during the stance phase of walking (Macalister, 1870; Hepburn, 1892; Goh et al., 2017). In addition to walking, the gastrocnemius muscle is also important for climbing and brachiation. During these activities, the muscle contracts to maintain grip and stability, especially when supporting the body weight while climbing vertically or during the suspensory postures (Macalister, 1870; Hepburn, 1892; Goh et al., 2017).

In contrast, male *Gorilla* exhibited higher rBV/TV concentrations in the medial femoral epicondyle (Figure 4.11A) and beneath the tibial tuberosity (Figure 5.9), which supports the idea that males experience more flexed knee positions and/or increased lateral knee rotation during extension. Additionally, the tibial condyles in males showed greater anisotropy compared to females (Figure 5.10), indicating a more consistent loading pattern in the proximal tibia for males. As the knee flexes, the posterior regions of the femoral condyles are subject to sustained compression, which leads to increased bone density in these areas (Georgiou et al., 2018; Sylvester & Terhune, 2017). Therefore, the higher rBV/TV values observed in the medial

femoral and tibial condyles relative to the lateral condyles in the male *Gorilla* sample may also suggest greater knee flexion in males compared to females. The medial tibial condyle of the male *Gorilla* is more concave compared to that of females possibly due to the differences in body mass and/or differences in locomotor behavior (Sylvester, 2013), which could potentially allow male *Gorilla* to extend their knees less than males.

A higher level of knee extension and a generally higher range of motion at the knee was previously found in zoo-housed adult female *Gorilla* compared to males, particularly during vertical climbing (Isler, 2005). Compared to males, wild female *Gorilla* are more arboreal but also smaller in body mass (Remis, 1997). Thus, sex differences found in the distal femur and proximal tibia in *Gorilla* might be driven by differences in body mass, the degree of arboreality and/or by differences in knee loading. Further investigation of *Gorilla* locomotor kinematics and kinetics, particularly in wild communities, and larger skeletal samples are needed to address whether sex differences in trabecular structure exist in *Gorilla*. The analysis of locomotor behavior in lowland *Gorilla* is particularly constrained by the lack of data from wild populations. Most studies on locomotion focus on mountain *Gorilla* (e.g., Doran, 1997; Thompson et al., 2018), with the notable exception of Remis (1994, 1995), who provided insights into the locomotion of lowland *Gorilla*.

7.3 Trabecular bone knee structure and locomotor behaviour in *Pongo*

It was anticipated that *Pongo* would show significant differences from *Hom*o and African apes, particularly in having the most uniform trabecular structure in the distal femur **(Chapter 4)** and proximal tibia **(Chapter 5)** due to their more variable knee joint postures during arboreal locomotion. This hypothesis was not entirely supported by the distal femur findings but was confirmed for the proximal tibia.

Although *Pongo's* trabecular structure in the distal femur was relatively spatially homogeneous, *Pan* displayed a similar pattern (Figure 4.3). Both *Pongo* and *Pan* had low rBV/TV in the posteroinferior region of the medial femoral condyle, but *Pongo* showed higher rBV/TV in the posteroinferior region of the lateral femoral condyle (Figure 4.3). This distribution could indicate greater lateral loading during knee extension or a more extended knee posture in *Pongo* compared to *Pan*. This functional interpretation aligns with the findings for the proximal tibia, where rBV/TV was concentrated medially on the medial side of the tibial plateau, similar to African apes, but in *Pongo*, this concentration extended more anteriorly (Figure 5.3, Figure

5.11). As described above, when the knee is flexed and experiences higher medial loading, trabeculae are getting denser proximally on the medial side of the tibial plateau. However, as the knee extends further, there is an increase in bone density anteriorly as well. Contrary to the prediction that *Pongo* would exhibit the highest degree of isotropy, this taxon demonstrates a similar level of isotropy to that observed in African apes in both distal femur and proximal tibia. This suggests that despite their highly variable joint positioning (Cant, 1987; Morbeck & Zihlman, 1988; Thorpe & Crompton, 2006; Thorpe et al., 2007; Thorpe, 2009), the degree to which trabeculae are similarly oriented in *Pongo* is not distinctly different from that of African apes.

In *Pongo*, the knee positions during a gait cycle differ between terrestrial and arboreal locomotion due to the unique locomotor behaviours and environments associated with each mode of movement. During terrestrial locomotion, orangutans primarily use a quadrupedal gait, walking on all fours with the body weight supported by the limbs. The knee positions during terrestrial walking cycles involve flexion and extension as the orangutan moves each limb forward and backward. When the limb is in contact with the ground (stance phase), the knee is typically flexed to absorb shock and support the body weight. As *Pongo* propels itself forward, the knee extends to push off the ground and move the limb into the swing phase, where it moves forward to take the next step. In contrast, during arboreal locomotion, *Pongo* exhibits a variety of knee positions depending on the specific behaviours and movements involved. When climbing, the knees may be flexed to grip branches and maintain stability while ascending or descending. However, during suspensory locomotion, such as brachiation, the knees may be more extended as the orangutan reaches and grasps branches with their feet or with the arms while the legs trail behind (e.g., Cant, 1987; Morbeck & Zihlman, 1988; Thorpe & Crompton, 2006; Thorpe et al., 2007; Thorpe, 2009).

Overall, the trabecular architecture in the proximal tibia of *Pongo* indicates knee loading in flexed postures, as suggested by the pattern of BV/TV concentration observed in the tibial plateau (Figure 5.11). However, while the loading pattern in *Pongo* differs significantly from that of *Pan* and *Gorilla*, it does not differ significantly from *Homo* (Figure 5.11; Table 5.3). This discrepancy may arise from the more uniform distribution of BV/TV between the lateral and medial sides of the tibial plateau in *Pongo* compared to African apes. This suggests that the knee in *Pongo* has a greater range of motion and can experience loading across a wider spectrum of flexion and extension angles (e.g., Cant, 1987; Morbeck & Zihlman, 1988; Thorpe & Crompton, 2006; Thorpe et al., 2007; Thorpe, 2009).

Moreover, both *Pongo* and *Homo* exhibited much lower mean BV/TV values in the tibial plateau compared to African apes (Figure 5.11). As discussed in **Chapter 1**, previous research has highlighted potential systemic differences in BV/TV values across extant hominids (e.g., Ryan & Shaw, 2012; Saers et al., 2016; Tsegai et al., 2018; Dunmore et al., 2023). Therefore, the lack of significant differences between *Pongo* and *Homo* in BV/TV concentration observed in the tibial plateau may be attributed to either the limited sample size of the *Pongo* sample (see below) or the inherent variation in trabecular bone density across hominid species.

7.4 How do the trabecular patterns of the extinct hominins compare to those of the extant taxa?

Chapter 6 examined the trabecular patterns in the distal femur of two *A. africanus* specimens (StW 318 and TM 1513), one *A. sediba* specimen (U.W. 88-63), one *H. floresiensis* specimen (LB1-8), and one *H. neanderthalensis* specimen (D322-15). In that chapter, I also analyzed the trabecular patterns in the proximal tibia of another *H. floresiensis* specimen (LB1-13). The primary objective was to compare these trabecular structures with those of extant apes and humans to infer the locomotion of these ancient hominins.

Among the *A. africanus* specimens, notable variability in trabecular patterns was observed, reflecting differences in locomotor behavior. The trabecular distribution in the lateral femoral condyle of StW 318 was intermediate between that of *Pan* and *Pongo* but did not significantly differ from that of *H. sapiens*. This suggests that StW 318 engaged in locomotion involving both extended and flexed knee positions. TM 1513 distal femoral epiphysis also exhibited some *Homo*-like trabecular features, particularly high rBV/TV beneath the presumed insertion sites of the gastrocnemius muscle. However, the elevated rBV/TV across the medial condyle points to medial knee compartment loading and flexed knee postures, similar to non-human great apes. The gastrocnemius muscle, which assists with plantarflexion of the foot and flexion of the knee joint, likely played an important role in the locomotion of *Australopithecus* genus. Although direct evidence is sparse, its function is inferred from the anatomy of related species and the biomechanics of bipedalism (e.g., Huijing, 1985; Ishikawa et al., 2007; Maganaris, 2003; Muramatsu et al., 2001). In *Australopithecus*, the gastrocnemius muscle would have been important for maintaining stability and propulsion during bipedal walking. It likely contributed to pushing off the ground during the toe-off phase of the gait cycle, helping to propel the body forward. Additionally, the gastrocnemius muscle may have been involved in stabilizing the knee joint during walking and running by providing tension to the Achilles tendon, which helps

support the body weight and absorb impact forces (e.g., Huijing, 1985; Ishikawa et al., 2007; Maganaris, 2003; Muramatsu et al., 2001). Overall, while specific details about the size and function of the gastrocnemius muscle in *Australopithecus* are speculative, it is reasonable to infer that it played a significant role in their bipedal locomotion, similar to its function in modern humans. However, more research is needed to know how exactly this muscle is involved during different types of locomotion as high rBV/TV was found in all primates regardless of their locomotion repertoires. Thus, the *Homo*-like rBV/TV concentration under the lateral head of this muscle in StW 318 and under both heads of this muscle in TM 1513 could suggest a similar level of involvement during bipedal walking. However, this conclusion is limited by lack of information about the specific function of the gastrocnemius muscle across primates and thus requires caution in interpretation. Overall, the general trabecular pattern of TM 1513 distal femur is more like that of non-human great apes than StW 318.

Unfortunately, most of the trabecular structure in distal femur of *A. sediba* is not preserved and thus the functional interpretations of how the knee was involved during the locomotion is based solely on a trabecular distribution under the patellar surface of the femur. U.W. 88-63 exhibits a trabecular distribution, under the patellar surface, falling somewhere between *Pan* and *Pongo*. Trabecular bone structure under the patellar surface of the femur shows similar distribution as found in TM 1513, where rBV/TV is concentrated more medially on the patellar surface compared to human individuals from sedentary population. *A. sediba* exhibits a unique combination of primitive and derived features in its postcranial skeleton, suggesting a mosaic of arboreal and bipedal adaptations (e.g., Meyer et al., 2017; Rein et al., 2017). While it likely retained some arboreal capabilities, *A. sediba* shows anatomical traits indicative of habitual bipedalism, such as a more modern *Homo*-like pelvis and lower limbs compared to earlier australopiths. In terms of the patellar surface loading, it is important to consider the role of the patella in transmitting forces between the femur and tibia during locomotion. In bipedal species like humans, the patellar surface experiences significant loading during activities like walking, running, and climbing stairs, as it helps to distribute forces and stabilize the knee joint. However, in species with more arboreal behaviours, the loading patterns on the patellar surface may differ. Arboreal primates often use a variety of knee positions and movements, including flexion, extension, and rotation, to navigate through trees and branches. This may result in different loading patterns on the patellar surface compared to habitual bipedalism. The results of this thesis suggest that the patellar surface of *A. sediba* was loaded more similar to *Pan* and *Pongo* than to that of modern humans. However, the unique shape of the distal femur of *A.*

sediba could lead to a different loading pattern than we would expect in bipedal hominins. It has been previously suggested that the distinctive gait of *A. sediba* exerted increased lateral forces on the knee joint, contributing to the pronounced lateral patellar lip (DeSilva et al., 2013). According to Miller & DeSilva (2024), *A. sediba* may have had anteriorly expanded femoral condyles, which would enhance the patellar moment arm, improving quadriceps efficiency. If this were the case, the findings of this thesis suggest that this external knee morphology may have resulted in greater loading on the medial knee compartment and that the knee could have been subjected to higher degrees of flexion during bipedal walking compared to modern humans. These individual differences within australopiths suggest the possibility of varied bipedal gaits across different species in the genus.

The distal femur (LB1-8) and proximal tibia (LB1-13) of one *H. floresiensis* individual have been analysed to infer the trabecular pattern in the knee. LB1-8 exhibits a trabecular distribution somewhere between *Pan* and *Homo*. The distribution under the patellar surface of the femur and in the lateral condyle shows rather *Pan*-like pattern while the rBV/TV concentration under the gastrocnemius muscle recalls that of *H. sapiens*. LB1-13 on the other hand exhibits a modern *Homo*-like trabecular distribution suggesting an extended knee postures during bipedal walking. However, rBV/TV was also found to be concentrated along the lateral and medial margins of the tibial plateau suggesting a certain level of knee flexion. This concentration was more like that of *Pongo* suggesting knee flexion in a way that differed from African apes. The results of this thesis indicate that *H. floresiensis* may have retained adaptations for climbing or arboreal behaviour during which the knee was loaded in the flexed positions or/and that *H. floresiensis* exhibited a distinctive form of bipedalism, possibly characterized by a more flexed knee posture compared to modern humans.

The trabecular patterns in the distal femur of the *H. neanderthalensis* specimen (D322-15) were analyzed with the aim of comparing them to those of modern humans. As expected, this specimen displayed a trabecular distribution similar to that of modern *H. sapiens*, confirming its adaptation to obligate bipedal locomotion. Specifically, this specimen, like modern *H. sapiens*, showed high rBV/TV in the posteroinferior regions of the femoral condyles, laterally on the patellar surface, and in the lateral femoral condyle compared to the medial femoral condyle (Figure 6.19-6.21). These characteristics are associated with the typical loading patterns observed in specialized bipedal locomotion and are distinct to modern *Homo* specimens. The findings from **Chapter 6**, together with those from **Chapter 4**, support the idea

that the trabecular pattern in the distal femur of obligate bipedal taxa is a distinguishing feature among apes.

This thesis highlights the value of analyzing trabecular structure across entire epiphyses rather than limiting the focus to isolated sub-volumes, as seen in some previous studies (e.g., Ryan & Ketcham, 2002; Ryan & Shaw, 2002; Scherf, 2008; Ryan et al., 2018). By examining the distribution of trabecular parameters throughout the epiphyses, this approach provides a more thorough understanding of locomotor behaviors. The thesis advocates for a comprehensive analysis of trabecular architecture, offering new insights into the locomotor signals present in the trabecular structures of the distal femur and proximal tibia in both extant and extinct hominins.

7.5 Limitations

This study has several limitations that should be noted. First and foremost, the functional interpretations are constrained by the absence of kinetic and kinematic data for the knee in non-human great apes, particularly in wild populations. Secondly, the *Pongo* sample was smaller than all other taxa in this thesis and comprised two (rather than one) species. These sample limitations meant that sex differences could have not been explored in trabecular structure in *Pongo* and that potential locomotor signals may be obscured by the inclusion of two species and only two males. Similarly, only 9 individuals for distal femur and 7 individuals for proximal tibia of *Pongo* were used to create the canonical bone of the distal femur/proximal tibia. This could have potentially bias the results, creating the canonical femur/tibia that is slightly less representative of *Pongo* than each other species in the sample. However, it did not appear to generate any significant bias in this study, likely as the gross external morphology of distal femur/proximal tibia is similar across non-human great apes (most of the sample). Thirdly, our study of proximal tibia found that *Pongo* has the most homogenous trabecular distribution, which is expected but also may be the result of the conflation of two *Pongo* species. Thirdly, the analysis of sex differences in the human distal femur was restricted by the lack of sex information for the majority of the sample, with known sex data available for only 11 individuals (all male) from the Mary Rose population. Consequently, sex differences could only be examined by comparing *Homo* populations. Although a partial separation between populations was observed, the relative positions of rBV/TV and DA in principal component analysis (PCA) remained consistent when the PCA was divided by *Homo* populations (Supplementary Figure S4.7). Finally, while the color maps of DA indicate regions with varying levels of anisotropy, they do not reveal the orientation of the trabecular structures. A technical

limitation of cHMA is that vectors and tensors cannot currently be transformed into canonical space, making it impossible to quantitatively assess the direction of loading in the highly anisotropic regions of the distal femur and proximal tibia.

7.6 Future directions

Firstly, understanding the localized functional adaptations across complex multi-joined bones is hindered by the limitations associated with whole-bone measures of DA. A deeper comprehension of the roles playes by femoral and tibial ligaments and muscles during various locomotor activities would greatly benefit from such analyses. Confirming differences in trabecular orientation among extant primates could provide valuable insights into how ligaments and muscles contribute to knee movements during specific locomotion types. Advancing techniques to study trabecular anisotropy presents a major opportunity for future research. At present, although tools like Medtool allow for visualization of the primary eigenvector and its associated eigenvalue as a scalar, there is a gap in statistical methods for analyzing principal trabecular directions in three dimensions. Developing such methods could significantly enhance our understanding of trabecular structure and its functional implications.

Secondly, given the biomechanical complexity of the knee joint, incorporating advanced modeling techniques could enhance our understanding of how forces are transmitted through the knee and how these forces might be interpreted in fossil hominins. Reconstructing behaviors of extinct hominins often relies on analogs from living species, yet it remains challenging to understand how loads are distributed across morphologies that differ from any extant analogs. Finite element modeling, which estimates stress and strain experienced by structures under various loading conditions, has been predominantly applied to *H. sapiens*. This method requires detailed inputs on loading conditions, including the geometry and Young's modulus of both hard and soft tissues, ligament attachment sites, and substrate reaction forces. Understanding how articular cartilage affects load dissipation and force transfer through the knee is particularly important. The role of articular cartilage in trabecular adaptation is not well understood but could be crucial for explaining why areas with ligamentous attachments exhibit notably thick cortices. Before applying finite element modeling to non-human hominid knees, additional basic biomechanical data must be gathered through in vivo research. Another promising technique for future paleoanthropological research is 4D CT, which captures and reconstructs multiple high-resolution x-rays during movement. Although its use in non-human hominids may be constrained by practical and ethical considerations, further research could utilize this technology to explore the human knee across various locomotor behaviors.

Lastly, while this study focused on BV/TV and DA distribution, analyzing other parameters such as trabecular thickness (Tb.Th), trabecular spacing (Tb.Sp), and trabecular number (Tb.N) using cHMA could yield valuable insights. BV/TV and DA are commonly reported trabecular parameters that facilitate easy comparison across studies. However, breaking down BV/TV into its constituent components (Tb.Th, Tb.Sp, and Tb.N) could enhance our understanding of trabecular knee structure in extant primates. This comprehensive approach would offer a more nuanced perspective on how trabecular bone adapts to various locomotor behaviors and environmental conditions across primate species.

7.7 Conclusion

This thesis provided a novel analysis of the trabecular bone architecture in the distal femur and proximal tibia of hominids. It demonstrated that trabecular structure distinguishes extant and fossil taxa correlates with known (extant) or inferred (fossil) locomotor behaviors. In *Homo*, trabecular architecture reflects habitual use of extended knee postures during bipedalism, whereas African apes show habitual use of flexed knee postures during terrestrial and arboreal locomotion, and *Pongo* exhibits a highly mobile knee joint. Additionally, our findings indicate differences in knee extension/flexion levels between female and male *Gorilla*, aligning with greater arboreality in female *Gorilla*. Trabecular structure did not significantly differ between sexes in *Pan* or *Homo*, suggesting similar locomotor behaviors between sexes in these species. The thesis comprehensively examines trabecular bone architecture in the distal femur of *A. africanus* (StW 318, TM 1513), *A. sediba* (U.W. 88-63), *H. floresiensis* (LB1-8), and *H. neanderthalensis* (D322-15), and in the proximal tibia of *H. floresiensis* (LB1-13). Trabecular architecture in the lateral femoral condyle of StW 318 suggests bipedal walking with frequent knee loading in flexed positions. Conversely, TM 1513 exhibits an ape-like distribution pattern in the distal femur, indicating more diverse knee joint postures. Trabecular architecture under the patellar surface of the femur in *A. sediba* supports interpretations of extended knee postures during bipedal locomotion, differing from *A. africanus* and extant non-human apes. These results underscore the locomotor diversity among South African hominins around 2 million years ago. In *H. floresiensis*, trabecular architecture in the distal femur and proximal tibia suggests a blend of features indicative of both extended and flexed knee postures. Coupled with unique lower limb morphology, this suggests a distinctive form of bipedalism, possibly characterized by a more flexed knee posture compared to *H. sapiens*. Trabecular architecture in the distal femur of *H. neanderthalensis* aligns with interpretations of obligate bipedalism similar to that of *H. sapiens*.

REFERENCES

Ahrens, J., Geveci, B., Law, C., Hansen, C., & Johnson, C. (2005). Paraview: an end-user tool for large-data visualization. *The Visualization Handbook, 717*, 50038-1.

Ahrens, J., Heitmann, K., Habib, S., Ankeny, L., McCormick, P., Inman, J., ... & Ma, K. L. (2006). Quantitative and comparative visualization applied to cosmological simulations. *Journal of Physics: Conference Series*, *46*, 526.

Aiello, L., & Dean, C. (1990). *An Introduction to Human Evolutionary Anatomy*. Academic Press.

Alba, D. M., Moyà-Solà, S., & Köhler, M. (2003). Morphological affinities of the *Australopithecus afarensis* hand on the basis of manual proportions and relative thumb length. *Journal of Human Evolution*, *44*, 225-254.

Alemseged, Z. (2023). Reappraising the palaeobiology of *Australopithecus*. *Nature*, *617*, 45-54.

Alexander, R. McN. (1991). Characteristics and advantages of human bipedalism. In: Rayner, J. M. V., & Wooton, R. J., (eds.) *Biomechanics and Evolution*, 255–266.

Alexander, R. M. (2004). Bipedal animals, and their differences from humans. *Journal of Anatomy*, *204*, 321-330.

Alexander, R. M., & Ker, R. F. (1990). The architecture of leg muscles. In: Winters, J. M., & Woo, S. L., (eds.) *Multiple Muscle Systems: Biomechanics and Movement Organization*, 568-577.

Almecija, S., Moya-Sola, S., & Alba, D. M. (2010). Early origin for human-like precision grasping: a comparative study of pollical distal phalanges in fossil hominins. *PLoS One*, 5, 11-727.

Almécija, S., Tallman, M., Alba, D. M., Pina, M., Moyà-Solà, S., & Jungers, W. L. (2013). The femur of *Orrorin tugenensis* exhibits morphometric affinities with both Miocene apes and later hominins. *Nature Communications*, *4*, 1-12.

Anderson, F. C., & Pandy, M. G. (2001). Dynamic optimization of human walking. *Journal of Biomechanical Engineering*, *123*, 381-390.

Andriacchi, T. P., & Dyrby, C. O. (2005). Interactions between kinematics and loading during walking for the normal and ACL deficient knee. *Journal of Biomechanics*, *38*, 293-298.

Ankel-Simons, F. (2010). *Primate Anatomy: an Introduction*. Academic Press.

Arnason, U., Gullberg, A., & Janke, A. (1998). Molecular timing of primate divergences as estimated by two nonprimate calibration points. *Journal of Molecular Evolution*, *47*, 718-727.

Augat, P., & Schorlemmer, S. (2006). The role of cortical bone and its microstructure in bone strength. *Age and Ageing*, *35*, 27-31.

Auger, J. D., Frings, N., Wu, Y., Marty, A. G., & Morgan, E. F. (2020). Trabecular architecture and mechanical heterogeneity effects on vertebral body strength. *Current Osteoporosis Reports*, *18*, 716-726.

Bachmann, S., Dunmore, C. J., Skinner, M. M., Pahr, D. H., & Synek, A. (2022). A computational framework for canonical holistic morphometric analysis of trabecular bone. *Scientific Reports*, *12*, 51-87.

Bachmann, S., Pahr, D. H., & Synek, A. (2023). A density-dependent target stimulus for inverse bone (re) modeling with homogenized finite element models. *Annals of Biomedical Engineering*, *51*, 925-937.

Bagge, M. (2000). A model of bone adaptation as an optimization process. *Journal of Biomechanics, 33*, 49-57.

Baltzopoulos, V. (1995). A videofluoroscopy method for optical distortion correction and measurement of knee-joint kinematics. *Clinical Biomechanics*, *10*, 85-92.

Barak, M. M. (2019). Bone modeling or bone remodeling: That is the question. *American Journal of Physical Anthropology, 172*, 53-55.

Barak, M. M., Lieberman, D. E., & Hublin, J. J. (2011). A Wolff in sheep's clothing: trabecular bone adaptation in response to changes in joint loading orientation. *Bone*, *49*, 41-51.

Barak, M. M., Lieberman, D. E., & Hublin, J. J. (2013a). Of mice, rats and men: trabecular bone architecture in mammals scales to body mass with negative allometry. *Journal of Structural Biology, 183*, 123-131.

Barak, M. M., Lieberman, D. E., Raichlen, D., Pontzer, H., Warrener, A. G., & Hublin, J. J. (2013b). Trabecular evidence for a human-like gait in *Australopithecus africanus*. *PloS One, 8*, 76-87.

Barak, M. M., Weiner, S., & Shahar, R. (2008). Importance of the integrity of trabecular bone to the relationship between load and deformation of rat femora: an optical metrology study. *Journal of Materials Chemistry, 18*, 55-64.

Barker, R. (1992). Shipshape for discoveries, and return. *The Mariner's Mirror, 78*, 433-447.

Barker, S. (1996). The Mary Rose revisited: Tudor myth, popular history and" the tears that England owes". *Journal of Popular Culture, 29*, 51.

Basmajian, J. V. (1967). Electromyography: its structural and neural basis. *International Review of Cytology, 21*, 129-140.

Bauer, H. R. (1977). Chimpanzee bipedal locomotion in the Gombe National Park, East Africa. *Primates, 18*, 913-921.

Beaudet, A. M., & Chouinard, A. (2020). Sexual Dimorphism in the Skeletal Adaptations to Climbing in Great Apes. *Journal of Anatomy, 237*, 79-90.

Begun, D. R. (1992). Miocene fossil hominids and the chimp-human clade. *Science, 257*, 29-33.

Belcastro, M. G., Mariotti, V., Pietrobelli, A., Sorrentino, R., García-Tabernero, A., Estalrrich, A., & Rosas, A. (2020). The study of the lower limb entheses in the Neanderthal sample from El Sidrón (Asturias, Spain): How much musculoskeletal variability did Neanderthals accumulate? *Journal of Human Evolution, 141*, 27-46.

Berge, C. (1984). Multivariate analysis of the pelvis for hominids and other extant primates: implications for the locomotion and systematics of the different species of australopithecines. *Journal of Human Evolution, 13*, 555-562.

Berge, C. (1991). Size-and locomotion-related aspects of hominid and anthropoid pelves: an osteometrical multivariate analysis. *Journal of Human Evolution, 6*, 365-376.

Berge, C. (1994). How did the australopithecines walk? A biomechanical study of the hip and thigh of *Australopithecus afarensis*. *Journal of Human Evolution, 26*, 259-273.

Berge, C., & Kazmierczak, J. B. (1986). Effects of size and locomotor adaptations on the hominid pelvis: evaluation of australopithecine bipedality with a new multivariate method. *Folia Primatologica, 46*, 185-204.

Berger, L. R., De Ruiter, D. J., Churchill, S. E., Schmid, P., Carlson, K. J., Dirks, P. H., & Kibii, J. M. (2010). *Australopithecus sediba*: a new species of *Homo*-like australopith from South Africa. *Science, 328*, 195-204.

Berger, L. R., & Tobias, P. V. (1996). A chimpanzee-like tibia from Sterkfontein, South Africa and its implications for the interpretation of bipedalism in *Australopithecus africanus*. *Journal of Human Evolution, 30*, 343-348.

Bergmann, G., & Bender, A. (2006). The Patellar Tendon and Its Biomechanical Impact on Knee Joint Function. *Clinical Biomechanics, 21*, 792-798.

Berillon, G. (2004). In what manner did they walk on two legs? An architectural perspective for the functional diagnostics of the early hominid foot. In: Meldrum, D. J., & Hilton, C. E., (eds.) *From Biped to Strider: The Emergence of Modern Human Walking, Running, and Resource Transport*, 85-100.

Berillon, G., Daver, G., D'août, K., Nicolas, G., de La Villetanet, B., Multon, F., ... & Dubreuil, G. (2010). Bipedal versus quadrupedal hind limb and foot kinematics in a captive sample of *Papio anubis*: setup and preliminary results. *International Journal of Primatology, 31*, 159-180.

Bird, E. E., Kivell, T. L., Dunmore, C. J., Tocheri, M. W., & Skinner, M. M. (2024). Trabecular bone structure of the proximal capitate in extant hominids and fossil hominins with implications for midcarpal joint loading and the dart-thrower's motion. *American Journal of Biological Anthropology, 183*, 24-824.

Bird, E. E., Kivell, T. L., & Skinner, M. M. (2021). Cortical and trabecular bone structure of the hominoid capitate. *Journal of Anatomy, 239*, 351-373.

Blackburn, T. A., & Craig, E. (1980). Knee anatomy: a brief review. *Physical therapy, 60*, 56-60.

Blaszczyk, M. B., & Vaughan, C. L. (2007). Re-interpreting the evidence for bipedality in Homo floresiensis. *South African Journal of Science, 103*, 409-414.

Bloch, J. I., & Boyer, D. M. (2003). Response to comment on *"Grasping Primate Origins". Science, 300*, 741-741.

Bouxsein, M. L., Boyd, S. K., Christiansen, B. A., Guldberg, R. E., Jepsen, K. J., & Müller, R. (2010). Guidelines for assessment of bone microstructure in rodents using micro–computed tomography. *Journal of Bone and Mineral Research, 25*, 68-86.

Boyer, D. M., Yapuncich, G. S., Butler, J. E., Dunn, R. H., & Seiffert, E. R. (2015). Evolution of postural diversity in primates as reflected by the size and shape of the medial tibial facet of the talus. *American Journal of Physical Anthropology, 157*, 134-177.

Bramble, D. M., & Lieberman, D. E. (2004). Endurance running and the evolution of *Homo*. *Nature, 432*, 345-352.

Briggs, D. E. (2017). Seilacher, konstruktions-morphologie, morphodynamics, and the evolution of form. *Journal of Experimental Zoology Part B: Molecular and Developmental Evolution, 328*, 197-206.

Brown, P., Sutikna, T., Morwood, M. J., Soejono, R. P., Jatmiko, Wayhu Saptomo, E., & Awe Due, R. (2004). A new small-bodied hominin from the Late Pleistocene of Flores, Indonesia. *Nature, 431*, 55-61.

Buzug, T. M. (2011). Computed tomography. In *Springer Handbook of Medical Technology*, 311-342.

Cant, J. G. (1987). Positional behavior of female Bornean orangutans (*Pongo pygmaeus*). *American Journal of Primatology, 12*, 71-90.

Carey, T. S., & Crompton, R. H. (2005). The metabolic costs of 'bent-hip, bent-knee'walking in humans. *Journal of Human Evolution, 48*, 25-44.

Carlson, K. J. (2005). Investigating the form-function interface in African apes: Relationships between principal moments of area and positional behaviors in femoral and humeral diaphyses. *American Journal of Physical Anthropology, 127*, 312-334.

Carlson, K. J., Lublinsky, S., & Judex, S. (2008). Do different locomotor modes during growth modulate trabecular architecture in the murine hind limb? *Integrative and Comparative Biology, 48*, 385-393.

Carrier, D. R., Kapoor, A. K., Kimura, T., Nickels, M. K., Satwanti, Scott, E. C., ... & Trinkaus, E. (1984). The energetic paradox of human running and hominid evolution. *Current Anthropology, 25*, 483-495.

Cartmill, M., Lemelin, P., & Schmitt, D. (2002). Support polygons and symmetrical gaits in mammals. *Zoological Journal of the Linnean Society, 136*, 401-420.

Cazenave, M., Braga, J., Oettlé, A., Pickering, T. R., Heaton, J. L., Nakatsukasa, M., ... & Macchiarelli, R. (2019). Cortical bone distribution in the femoral neck of Paranthropus robustus. *Journal of Human Evolution, 135*, 26-66.

Cazenave, M., & Kivell, T. L. (2023). Challenges and perspectives on functional interpretations of australopith postcrania and the reconstruction of hominin locomotion. *Journal of Human Evolution, 175*, 103-304.

Cazenave, M., Kivell, T. L., Pina, M., Begun, D. R., & Skinner, M. M. (2022). Calcar femorale variation in extant and fossil hominids: Implications for identifying bipedal locomotion in fossil hominins. *Journal of Human Evolution, 167*, 103-183.

Cazenave, M., Oettlé, A., Pickering, T. R., Heaton, J. L., Nakatsukasa, M., Thackeray, J. F., ... & Macchiarelli, R. (2021). Trabecular organization of the proximal femur in *Paranthropus robustus*: Implications for the assessment of its hip joint loading conditions. *Journal of Human Evolution, 153*, 102-964.

Cazenave, M., Pina, M., Hammond, A. S., Böhme, M., Begun, D. R., Spassov, N., & Wood, B. (2024). Postcranial evidence does not support habitual bipedalism in Sahelanthropus tchadensis: a reply to Daver et al. (2022). *Journal of Human Evolution*, 103557.

Chakeres, D. W. (1984). Clinical significance of partial volume averaging of the temporal bone. *American Journal of Neuroradiology, 5*, 297-302.

Chavassieux, P., Seeman, E., & Delmas, P. D. (2007). Insights into material and structural basis of bone fragility from diseases associated with fractures: How determinants of the biomechanical properties of bone are compromised by disease. *Endocrine Reviews, 28*, 151-164.

Chen, G., Pettet, G. J., Pearcy, M., & McElwain, D. L. S. (2007). Modelling external bone adaptation using evolutionary structural optimisation. *Biomechanics and Modeling in Mechanobiology, 6*, 275-285.

Chirchir, H. (2015). A comparative study of trabecular bone mass distribution in cursorial and non-cursorial limb joints. *The Anatomical Record*, *298*, 797-809.

Chirchir, H. (2016). Limited trabecular bone density heterogeneity in the human skeleton. *Anatomy Research International*, *92*, 53-83.

Chirchir, H. (2021). Trabecular bone in domestic dogs and wolves: Implications for understanding human self-domestication. *The Anatomical Record*, *304*, 31-41.

Chirchir, H., Kivell, T. L., Ruff, C. B., Hublin, J. J., Carlson, K. J., Zipfel, B., & Richmond, B. G. (2015). Recent origin of low trabecular bone density in modern humans. *Proceedings of the National Academy of Sciences*, *112*, 366-371.

Chirchir, H., Zeininger, A., Nakatsukasa, M., Ketcham, R. A., & Richmond, B. G. (2017). Does trabecular bone structure within the metacarpal heads of primates vary with hand posture? *Comptes Rendus Palevol*, *16*, 533-544.

Churchill, S. E., Green, D. J., Feuerriegel, E. M., Macias, M. E., Matthews, S., Carlson, K. J., ... & Berger, L. R. (2018). *Australopithecus sediba* - The Shoulder, Arm, and Forearm of *Australopithecus sediba*. *PaleoAnthropology*, *2018*, 234-281.

Churchill, S. E., Holliday, T. W., Carlson, K. J., Jashashvili, T., Macias, M. E., Mathews, S., ... & Berger, L. R. (2013). The upper limb of *Australopithecus sediba*. *Science*, *340*, 34-77.

Churchill, D. L., Incavo, S. J., Johnson, C. C., & Beynnon, B. D. (1998). The transepicondylar axis approximates the optimal flexion axis of the knee. *Clinical Orthopaedics and Related Research*, *356*, 111-118.

Clarke, R. J., & Tobias, P. V. (1995). Sterkfontein Member 2 foot bones of the oldest South African hominid. *Science*, *269*, 521-524.

Choi, K., & Goldstein, S. A. (1992). A comparison of the fatigue behavior of human trabecular and cortical bone tissue. *Journal of Biomechanics*, *25*, 1371-1381.

Coelho, P. G., Fernandes, P. R., Rodrigues, H. C., Cardoso, J. B., & Guedes, J. M. (2009). Numerical modeling of bone tissue adaptation - a hierarchical approach for bone apparent density and trabecular structure. *Journal of Biomechanics*, *42*, 830-837.

Conradi, S. H., Lutey, B. A., Atkinson, J. J., Wang, W., Senior, R. M., & Gierada, D. S. (2010). Measuring small airways in transverse CT images: Correction for partial volume averaging and airway tilt. *Academic Radiology*, *17*, 1525-1534.

Cotter, M. M., Simpson, S. W., Latimer, B. M., & Hernandez, C. J. (2009). Trabecular microarchitecture of hominoid thoracic vertebrae. *The Anatomical Record: Advances in Integrative Anatomy and Evolutionary Biology*, *292*, 1098-1106.

Cowin, S. C. (1984). Mechanical modeling of the stress adaptation process in bone. *Calcified Tissue International*, *36*, 98-103.

Crompton, R. H., McClymont, J., Thorpe, S., Sellers, W., Heaton, J., Pickering, T. R., ... & Clarke, R. (2018). Functional anatomy, biomechanical performance capabilities and potential niche of StW 573: an *Australopithecus* skeleton (circa 3.67 Ma) from Sterkfontein Member 2, and its significance for the last common ancestor of the African apes and for hominin origins. *BIoRxiv*, 481556.

Crompton, R. H., Sellers, W. I., & Thorpe, S. K. (2010). Arboreality, terrestriality and bipedalism. *Philosophical Transactions of the Royal Society B: Biological Sciences*, *365*, 3301-3314.

Crompton, R. H., Vereecke, E. E., & Thorpe, S. K. (2008). Locomotion and posture from the common hominoid ancestor to fully modern hominins, with special reference to the last common panin/hominin ancestor. *Journal of Anatomy*, *212*, 501-543.

Crompton, R. H., Weijie, L. Y. W., Günther, M., & Savage, R. (1998). The mechanical effectiveness of erect and "bent-hip, bent-knee" bipedal walking in *Australopithecus afarensis*. *Journal of Human Evolution*, *35*, 55-74.

Cubo, J., Legendre, P., De Ricqlès, A., Montes, L., De Margerie, E., Castanet, J., & Desdevises, Y. (2008). Phylogenetic, functional, and structural components of variation in bone growth rate of amniotes. *Evolution & Development*, *10*, 217-227.

Cubo, J., Ponton, F., Laurin, M., De Margerie, E. D., & Castanet, J. (2005). Phylogenetic signal in bone microstructure of sauropsids. *Systematic Biology*, *54*, 562-574.

Currey, J. D. (2002). *Bones: structure and Mechanics*. Princeton university press.

Currey, J. D. (2003). The many adaptations of bone. *Journal of Biomechanics*, *36*, 1487-1495.

Currey, J. D. (2012). The structure and mechanics of bone. *Journal of Materials Science, 47*, 41-54.

Dainton, M., & Macho, G. A. (1999). Did knuckle walking evolve twice? *Journal of Human Evolution, 36*, 171-194.

Dahlkvist, N. J., Mayo, P., & Seedhom, B. B. (1982). Forces during squatting and rising from a deep squat. *Engineering in Medicine, 11*, 69-76.

Dalstra, M., Huiskes, R., Odgaard, A. V., & Van Erning, L. (1993). Mechanical and textural properties of pelvic trabecular bone. *Journal of Biomechanics*, *26*, 523-535.

D'Août, K., Aerts, P., De Clercq, D., De Meester, K., & Van Elsacker, L. (2002). Segment and joint angles of hind limb during bipedal and quadrupedal walking of the bonobo (*Pan paniscus*). *American Journal of Physical Anthropology, 119*, 37-51.

D'Août, K., Vereecke, E., Schoonaert, K., De Clercq, D., Van Elsacker, L., & Aerts, P. (2004). Locomotion in bonobos (*Pan paniscus*): differences and similarities between bipedal and quadrupedal terrestrial walking, and a comparison with other locomotor modes. *Journal of Anatomy, 204*, 353-361.

Darwin, C. (1859). Origin of the species. In *British Politics and the Environment in the Long Nineteenth Century, 2023*, 47-55.

Daver, G., Guy, F., Mackaye, H. T., Likius, A., Boisserie, J. R., Moussa, A., & Clarisse, N. D. (2022). Postcranial evidence of late Miocene hominin bipedalism in Chad. *Nature*, *609*, 94-100.

Davis, J. C., & Cummings, J. T. (2002). Knee Loading in Primates: A Comparative Study of *Gorilla* and *Pan*. *Journal of Experimental Biology, 205*, 1899-1911.

Dawson-Hughes, B., Harris, S. S., & Krall, E. A. (1997). Effect of calcium and vitamin D supplementation on bone density in men and women 65 years of age or older. *The New England Journal of Medicine*, 337, 670-676.

De Groote, I. (2011). Femoral curvature in Neanderthals and modern humans: a 3D geometric morphometric analysis. *Journal of Human Evolution*, *60*, 540-548.

DeMars, L. J., Kuo, S., Saers, J. P., Stock, J. T., & Ryan, T. M. (2022). Trabecular Bone Structural Variation of the Human Distal Tibia, Talus, and Calcaneus. *The FASEB Journal*, *36*.

DeMars, L. J., Stephens, N. B., Saers, J. P., Gordon, A., Stock, J. T., & Ryan, T. M. (2021). Using point clouds to investigate the relationship between trabecular bone phenotype and behavior: An example utilizing the human calcaneus. *American Journal of Human Biology*, *33*, 34-68.

Demes, B. (2007). In vivo bone strain and bone functional adaptation. *American journal of Physical Anthropology*, *133*, 717-722.

Demes, B., Jungers, W. L., & Walker, C. (2000). Cortical bone distribution in the femoral neck of strepsirhine primates. *Journal of Human Evolution*, *39*, 367-379.

Demes, B., Larson, S. G., Stern Jr, J. T., Jungers, W. L., Biknevicius, A. R., & Schmitt, D. (1994). The kinetics of primate quadrupedalism:" hindlimb drive" reconsidered. *Journal of Human Evolution*, *26*, 353-374.

Dempster, D. W. (2003). Bone microarchitecture and strength. *Osteoporosis International*, *14*, 54-56.

DeSilva, J. M. (2009). Functional morphology of the ankle and the likelihood of climbing in early hominins. *Proceedings of the National Academy of Sciences*, *106*, 6567-6572.

DeSilva, J. M., Churchill, S. E., Zipfel, B., Walker, C. S., Sylvester, A. D., McNutt, E. J., ... & Berger, L. R. (2018). *Australopithecus sediba* - The Anatomy of the Lower Limb Skeleton of *Australopithecus sediba*. *PaleoAnthropology*, *2018*, 357-405.

DeSilva, J. M., & Devlin, M. J. (2012). A comparative study of the trabecular bony architecture of the talus in humans, non-human primates, and *Australopithecus*. *Journal of Human Evolution*, *63*, 536-551.

DeSilva, J., & Grabowski, M. (2020). Femur. In: Zipfel, B., Richmond, B., & Ward, C., (eds.) *Hominin Postcranial Remains from Sterkfontein, South Africa*. *Oxford University Press*, *19*, 36-95.

DeSilva, J. M., Holt, K. G., Churchill, S. E., Carlson, K. J., Walker, C. S., Zipfel, B., & Berger, L. R. (2013). The lower limb and mechanics of walking in *Australopithecus sediba*. *Science*, *340*, 1232999.

DeSilva, J. A., Tecuapetla, F., Paixão, V., & Costa, R. M. (2018). Dopamine neuron activity before action initiation gates and invigorates future movements. *Nature*, *554*, 244-248.

Dirks, P. H., Kibii, J. M., Kuhn, B. F., Steininger, C., Churchill, S. E., Kramers, J. D., ... & Berger, L. R. (2010). Geological setting and age of *Australopithecus sediba* from southern Africa. *Science*, *328*, 205-208.

D'Lima, D. D., Patil, S., Steklov, N., Chien, S., & Colwell, C. W. (2006). In vivo knee forces during recreation and exercise after knee arthroplasty. *Clinical Orthopaedics and Related Research*, *452*, 172-181.

Doershuk, L. J., Saers, J. P., Shaw, C. N., Jashashvili, T., Carlson, K. J., Stock, J. T., & Ryan, T. M. (2019). Complex variation of trabecular bone structure in the proximal humerus and femur of five modern human populations. *American Journal of Physical Anthropology*, *168*, 104-118.

Dolan, P., Earley, M., & Adams, M. A. (1994). Bending and compressive stresses acting on the lumbar spine during lifting activities. *Journal of Biomechanics*, *27*, 1237-1248.

Doran, D. M. (1993). Comparative locomotor behavior of chimpanzees and bonobos: the influence of morphology on locomotion. *American Journal of Physical Anthropology*, *91*, 83-98.

Doran, D. M. (1996). Comparative positional behavior of the African apes. In: McGrew, W., Marchant, L., Nishida, T., (eds.) *Great Ape Societies. Cambridge: Cambridge University Press.* 213-224.

Doran, D. M. (1997). Ontogeny of locomotion in mountain gorillas and chimpanzees. *Journal of Human Evolution*, *32*, 323-344.

Doran, D. M., & McNeilage, A. (1998). *Gorilla* ecology and behavior. *Evolutionary Anthropology: Issues, News, and Reviews, 6*, 120-131.

Doube, M., Kłosowski, M. M., Wiktorowicz-Conroy, A. M., Hutchinson, J. R., & Shefelbine, S. J. (2011). Trabecular bone scales allometrically in mammals and birds. *Biological Sciences*, *278*, 3067-3073.

Dougherty, R., & Kunzelmann, K. H. (2007). Computing local thickness of 3D structures with ImageJ. *Microscopy and Microanalysis*, *13*, 1678-1679.

Duncan, A. S., Kappelman, J., & Shapiro, L. J. (1994). Metatarsophalangeal joint function and positional behavior in *Australopithecus afarensis*. *American Journal of Physical Anthropology*, *93*, 67-81.

Dunmore, C. J., Bardo, A., Skinner, M. M., & Kivell, T. L. (2020). Trabecular variation in the first metacarpal and manipulation in hominids. *American Journal of Physical Anthropology*, *171*, 219-241.

Dunmore, C. J., Kivell, T. L., Bardo, A., & Skinner, M. M. (2019). Metacarpal trabecular bone varies with distinct hand-positions used in hominid locomotion. *Journal of Anatomy*, *235*, 45-66.

Dunmore, C. J., Skinner, M. M., Bardo, A., Berger, L. R., Hublin, J. J., Pahr, D. H., ... & Kivell, T. L. (2020). The position of *Australopithecus sediba* within fossil hominin hand use diversity. *Nature Ecology & Evolution*, *4*, 911-918.

Dunmore, C. J., Wollny, G., & Skinner, M. M. (2018). MIA-Clustering: a novel method for segmentation of paleontological material. *PeerJ*, *6*, 43-74.

Dyrby, C. O., Toney, M. K., & Andriacchi, T. P. (1997). Relation between knee flexion and tibial-femoral rotation during activities involving deep flexion. *Gait & Posture*, *2*, 179.

Earp, J. E., Newton, R. U., Cormie, P., & Blazevich, A. J. (2014). The influence of loading intensity on muscle–tendon unit behavior during maximal knee extensor stretch shortening cycle exercise. *European Journal of Applied Physiology*, *114*, 59-69.

Eichenblat, M., & Nathan, H. (1983). The proximal tibio fibular joint: an anatomical study with clinical and pathological considerations. *International Orthopaedics*, *7*, 31-39.

Ehrlich, P. J., & Lanyon, L. E. (2002). Mechanical strain and bone cell function: a review. *Osteoporosis international*, *13*, 688.

Elftman, H., & Manter, J. (1935). The evolution of the human foot, with especial reference to the joints. *Journal of Anatomy*, *70*, 56.

Emerson, S. B., & Bramble, D. M. (1993). Scaling, allometry, and skull design. *The skull*, *3*, 384-421.

Eriksen, E. F., Melsen, F., & Mosekilde, L. (1984). Reconstruction of the resorptive site in iliac trabecular bone: a kinetic model for bone resorption in 20 normal individuals. *Metabolic Bone Disease and Related Research*, *5*, 235-242.

Eriksen, E. F., Mosekilde, L., & Melsen, F. (1986). Trabecular bone remodeling and balance in primary hyperparathyroidism. *Bone*, *7*, 213-221.

Eriksen, E. F., Hodgson, S. F., Eastell, R., Riggs, B. L., Cedel, S. L., & O'Fallon, W. M. (1990). Cancellous bone remodelling in type I (postmenopausal) osteoporosis: quantitative assessment of rates of formation, resorption, and bone loss at tissue and cellular levels. *Journal of Bone and Mineral Research, 5,* 311-319.

Eriksen, E. F. (2010). Cellular mechanisms of bone remodeling. *Reviews in Endocrine and Metabolic Disorders, 11*, 219-227.

Eriksen, E. F., Melsen, F., & Mosekilde, L. (1984). Reconstruction of the resorptive site in iliac trabecular bone: a kinetic model for bone resorption in 20 normal individuals. *Metabolic Bone Disease and Related Research, 5*, 235-242.

Fajardo, R. J., & Müller, R. (2001). Three-dimensional analysis of nonhuman primate trabecular architecture using micro-computed tomography. *American Journal of Physical Anthropology*, *115*, 327-336.

Fajardo, R. J., Müller, R., Ketcham, R. A., & Colbert, M. (2007). Nonhuman anthropoid primate femoral neck trabecular architecture and its relationship to locomotor mode. *The Anatomical Record: Advances in Integrative Anatomy and Evolutionary Biology, 290*, 422-436.

Falk, D., Hildebolt, C., Smith, K., Jungers, W., Larson, S., Morwood, M., ... & Prior, F. (2009). The type specimen (LB1) of *Homo floresiensis* did not have Laron syndrome. *American Journal of Physical Anthropology, 140*, 52-63.

Falk, D., & Towne, B. (2004). Functional Morphology and Evolution of the Great Apes. *American Journal of Physical Anthropology*, *124*, 140-156.

Farisi, G. H., & Higuchi, H. (2017). Landscape characteristics of oriental honey buzzards wintering in western part of Flores island based on satellite-tracking data. *Earth and Environmental Science, 91*, 12-31.

Fennell, K. J., & Trinkaus, E. (1997). Bilateral femoral and tibial periostitis in the La Ferrassie 1 Neanderthal. *Journal of Archaeological Science, 24*, 985-995.

Fields, A. J., Eswaran, S. K., Jekir, M. G., & Keaveny, T. M. (2009). Role of trabecular microarchitecture in whole-vertebral body biomechanical behavior. *Journal of Bone and Mineral Research, 24*, 1523-1530.

Finestone, E. M., Brown, M. H., Ross, S. R., & Pontzer, H. (2018). Great ape walking kinematics: Implications for hominoid evolution. *American Journal of Physical Anthropology, 166,* 43-55.

Fitzgerald, G. K., & Piva, S. R. (2009). Role of the Patellar Tendon in the Biomechanics of the Knee During Gait and Exercise. *Journal of Biomechanics, 42,* 1648-1655.

Fleagle, J. G., Stern, J. T., Jungers, W. L., Susman, R. L., Vangor, A. K., & Wells, J. P. (1981). Climbing: a biomechanical link with brachiation and with bipedalism. In *Symp Zool Soc Lond, 48*, 359-375.

Foster, A. D., Raichlen, D. A., & Pontzer, H. (2013). Muscle force production during bent-knee, bent-hip walking in humans. *Journal of Human Evolution, 65,* 294-302.

Freeman, M. A., & Pinskerova, V. (2005). The movement of the normal tibio-femoral joint. *Journal of Biomechanics, 38,* 197-208.

Frelat, M. A., Shaw, C. N., Sukhdeo, S., Hublin, J. J., Benazzi, S., & Ryan, T. M. (2017). Evolution of the hominin knee and ankle. *Journal of Human Evolution, 108*, 147-160.

Fukashiro, S., & Hayashi, K. (1997). Differences in the mechanical properties of human and animal tendons: a review. *Journal of Biomechanics, 30*, 833-842.

Galdikas, B. M. (1988). Orangutan diet, range, and activity at Tanjung Puting, Central Borneo. *International Journal of Primatology, 9*, 1-35.

Gebo, D. L. (2004). Functional Morphology of the Primate Foot and Ankle. *In: Primate Locomotion: A Comparative Approach,* 239-256.

Gebo, D. L. (2010). Locomotor function across primates (including humans). *A Companion to Biological Anthropology,* 530-544.

Georgiou, L., Dunmore, C. J., Bardo, A., Buck, L. T., Hublin, J. J., Pahr, D. H., ... & Skinner, M. M. (2020). Evidence for habitual climbing in a Pleistocene hominin in South Africa. *Proceedings of the National Academy of Sciences, 117,* 8416-8423.

Georgiou, L., Kivell, T. L., Pahr, D. H., & Skinner, M. M. (2018). Trabecular bone patterning in the hominoid distal femur. *PeerJ, 6,* 51-56.

Georgiou, L., Kivell, T. L., Pahr, D. H., Buck, L. T., & Skinner, M. M. (2019). Trabecular architecture of the great ape and human femoral head. *Journal of Anatomy, 234*, 679-693.

Geurts, J., Patel, A., Hirschmann, M. T., Pagenstert, G. I., Müller-Gerbl, M., Valderrabano, V., & Hügle, T. (2016). Elevated marrow inflammatory cells and osteoclasts in subchondral osteosclerosis in human knee osteoarthritis. *Journal of Orthopaedic Research, 34*, 262-269.

Girgis, F. G., Marshall, J. L., & Jem, A. A. M. (1975). The cruciate ligaments of the knee joint: anatomical, functional and experimental analysis. *Clinical Orthopaedics and Related Research, 106*, 216-231.

Glatt, V., Canalis, E., Stadmeyer, L., & Bouxsein, M. L. (2007). Age-related changes in trabecular architecture differ in female and male C57BL/6J mice. *Journal of Bone and Mineral Research, 22*, 1197-1207.

Goh, C., Blanchard, M. L., Crompton, R. H., Gunther, M. M., Macaulay, S., & Bates, K. T. (2017). A 3D musculoskeletal model of the western lowland gorilla hind limb: moment arms and torque of the hip, knee and ankle. *Journal of Anatomy, 231*, 568-584.

Goldstein, L., Prasher, S. O., & Ghoshal, S. (2007). Three-dimensional visualization and quantification of non-aqueous phase liquid volumes in natural porous media using a medical X-ray Computed Tomography scanner. *Journal of Contaminant Hydrology, 93*, 96-110.

Gosman, J. H., & Ketcham, R. A. (2009). Patterns in ontogeny of human trabecular bone from SunWatch Village in the Prehistoric Ohio Valley: general features of microarchitectural change. *American Journal of Physical Anthropology, 138*, 318-332.

Green, D. J., & Alemseged, Z. (2012). *Australopithecus afarensis* scapular ontogeny, function, and the role of climbing in human evolution. *Science, 338*, 514-517.

Green, D. J., & Gordon, A. D. (2008). Metacarpal proportions in *Australopithecus africanus*. *Journal of Human Evolution, 54*, 705-719.

Green, D. J., Gordon, A. D., & Richmond, B. G. (2007). Limb-size proportions in *Australopithecus afarensis* and *Australopithecus africanus*. *Journal of Human Evolution, 52*, 187-200.

Griffin, C. T., Bano, L. S., Turner, A. H., Smith, N. D., Irmis, R. B., & Nesbitt, S. J. (2019). Integrating gross morphology and bone histology to assess skeletal maturity in early

dinosauromorphs: new insights from Dromomeron (Archosauria: Dinosauromorpha). *PeerJ*, *7*, 6331.

Griffin, N. L., D'Août, K., Ryan, T. M., Richmond, B. G., Ketcham, R. A., & Postnov, A. (2010). Comparative forefoot trabecular bone architecture in extant hominids. *Journal of Human Evolution, 59*, 202-213.

Gross, T., Kivell, T. L., Skinner, M. M., Nguyen, N. H., & Pahr, D. H. (2014). A CT-image-based framework for the holistic analysis of cortical and trabecular bone morphology. *Paleontol Electron 17*, 17333.

Gruss, L. T., & Schmitt, D. (2015). The evolution of the human pelvis: changing adaptations to bipedalism, obstetrics and thermoregulation. *Biological Sciences, 370*, 20140063.

Haile-Selassie, Y., Saylor, B. Z., Deino, A., Levin, N. E., Alene, M., & Latimer, B. M. (2012). A new hominin foot from Ethiopia shows multiple Pliocene bipedal adaptations. *Nature, 483*, 565-569.

Halloran, B. P., Ferguson, V. L., Simske, S. J., Burghardt, A., Venton, L. L., & Majumdar, S. (2002). Changes in bone structure and mass with advancing age in the male C57BL/6J mouse. *Journal of Bone and Mineral Research, 17*, 1044-1050.

Hammond, A. S. (2014). In vivo baseline measurements of hip joint range of motion in suspensory and nonsuspensory anthropoids. *American Journal of Physical Anthropology*, *153*, 417-434.

Harada, Y., Wevers, H. W., & Cooke, T. D. V. (1988). Distribution of bone strength in the proximal tibia. *The Journal of Arthroplasty*, *3*, 167-175.

Harcourt-Smith, W. (2016). Early hominin diversity and the emergence of the genus *Homo*. *Journal of Anthropolpgocal Sciences*, *94*, 19-27.

Harcourt-Smith, W. E., & Aiello, L. C. (2004). Fossils, feet and the evolution of human bipedal locomotion. *Journal of Anatomy, 204*, 403-416.

Harcourt-Smith, W. E., Throckmorton, Z., Congdon, K. A., Zipfel, B., Deane, A. S., Drapeau, M. S., ... & DeSilva, J. M. (2015). The foot of *Homo naledi*. *Nature Communications*, *6*, 4-32.

Hardt, D. E. (1978). Determining muscle forces in the leg during normal human walking - an application and evaluation of optimization methods. *Journal of Biomechanical Engineering, 100*, 72-78.

Harmon, E. H. (2009). The shape of the early hominin proximal femur. *American Journal of Physical Anthropology, 139*, 154-171.

Harper, C. M., & Patel, B. A. (2024). Trabecular bone variation in the gorilla calcaneus. *American Journal of Biological Anthropology, 24*, 9-39.

Harrigan, T. P., & Mann, R. W. (1984). Characterization of microstructural anisotropy in orthotropic materials using a second rank tensor. *Journal of Materials Science, 19*, 761-767.

Hart, N. H., Nimphius, S., Rantalainen, T., Ireland, A., Siafarikas, A., & Newton, R. U. (2017). Mechanical basis of bone strength: influence of bone material, bone structure and muscle action. *Journal of Musculoskeletal & Neuronal Interactions, 17*, 114.

Hart, R. T., Thongpreda, N., & Van Buskirk, W. C. (1988). Supercomputer use in orthopaedic biomechanics research: focus on functional adaptation of bone. *IEEE Engineering in Medicine and Biology Magazine, 7*, 39-43.

Haxton, H. (1945). A comparison of the action of extension of the knee and elbow joints in man. *The Anatomical Record, 93*, 279-286.

He, J., Chen, S., Zhang, H., Tao, X., Lin, W., Zhang, S., Ma, J. (2021). Downsampled imaging geometric modeling for accurate CT reconstruction via deep learning. *IEEE Transactions on Medical Imaging, 40,* 2976–2985.

Heinlein, B., Kutzner, I., Graichen, F., Bender, A., Rohlmann, A., Halder, A. M., Beier, A., & Bergmann, G. (2009). ESB clinical biomechanics award 2008: Complete data of total knee joint replacement loading for level walking and stair climbing measured in vivo with a mobile knee prosthesis. *Clinical Biomechanics, 24*, 315-326.

Heiple, K. G., & Lovejoy, C. O. (1971). The distal femoral anatomy of *Australopithecus*. *American Journal of Physical Anthropology, 35*, 75-84.

Henderson, G. I., & Schindler, A. G. (2005). The Role of the Patellar Tendon in Knee Joint Biomechanics: A Review of Function and Implications for Injury. *Journal of Orthopaedic Research, 23*, 1028-1036.

Hepburn, D. (1892). Comparative anatomy of the muscles and nerves of the superior and inferior extremities of the anthropoid apes: Part II. *Journal of Anatomy and Physiology*, *26*, 324.

Hernandez, C. J., Loomis, D. A., Cotter, M. M., Schifle, A. L., Anderson, L. C., Elsmore, L., ... & Latimer, B. (2009). Biomechanical allometry in hominoid thoracic vertebrae. *Journal of Human Evolution*, *56*, 462-470.

Hershkovitz, I., Kornreich, L., & Laron, Z. (2007). Comparative skeletal features between *Homo floresiensis* and patients with primary growth hormone insensitivity (Laron Syndrome). *American Journal of Physical Anthropology*, *134*, 198-208.

Hershkovitz, I., Speirs, M. S., Frayer, D., Nadel, D., Wish-Baratz, S., & Arensburg, B. (1995). Ohalo II H2: A 19,000-year-old skeleton from a water-logged site at the Sea of Galilee, Israel. *American Journal of Physical Anthropology*, *96*, 215-234.

Hildebrand, T., & Rüegsegger, P. (1997). A new method for the model-independent assessment of thickness in three-dimensional images. *Journal of Microscopy*, *185*, 67-75.

Hirschmann, M. T., & Müller, W. (2015). Complex function of the knee joint: the current understanding of the knee. *Knee Surgery, Sports Traumatology, Arthroscopy*, *23*, 80-88.

Hofstetter, A. M., Niemitz, C. (1998). Comparative gait analyses in apes. *Folia Primatologica, 69*, 233-234.

Hogervorst, T., Bouma, H. W., & De Vos, J. (2009). Evolution of the hip and pelvis. *Acta orthopaedica*, *80*, 1-39.

Homminga, J., Mccreadie, B. R., Weinans, H., & Huiskes, R. (2003). The dependence of the elastic properties of osteoporotic cancellous bone on volume fraction and fabric. *Journal of Biomechanics*, *36*, 1461-1467.

Hora, M., & Sladek, V. (2014). Influence of lower limb configuration on walking cost in Late Pleistocene humans. *Journal of Human Evolution*, *67*, 19-32.

Huijing, P. A. (1985). Architecture of the human gastrocnemius muscle and some functional consequences. *Cells Tissues Organs*, *123*, 101-107.

Hunt, K. D. (1991). Mechanical implications of chimpanzee positional behavior. *American Journal of Physical Anthropology*, *86*, 521-536.

Hunt, K. D. (1992). Positional behavior of *Pan troglodytes* in the Mahale mountains and Gombe stream national parks, Tanzania. *American Journal of Physical Anthropology*, *87*, 83-105.

Hunt, K. D., Dunevant, S. E., Yohler, R. M., & Carlson, K. J. (2021). Femoral bicondylar angles among dry-habitat chimpanzees (*Pan troglodytes schweinfurthii*) resemble those of humans: implications for knee function, australopith sexual dimorphism, and the evolution of bipedalism. *Journal of Anthropological Research*, *77*, 303-337.

Isaksson, H., Prantner, V., & Jurvelin, J. S. (2011). AGE related variation in BMD and trabecular architecture differs between the proximal femur and calcaneus in men. In *Summer Bioengineering Conference. American Society of Mechanical Engineers, 54587*, 1079-1080.

Ishikawa, M., Pakaslahti, J., & Komi, P. V. (2007). Medial gastrocnemius muscle behavior during human running and walking. *Gait & Posture*, *25*, 380-384.

Isler, K. (2002). Characteristics of vertical climbing in African apes. *Senckenbergiana Lethaea, 82*, 115-124.

Isler, K. (2005). 3D-kinematics of vertical climbing in hominoids. *American Journal of Physical Anthropology, 126*, 66-81.

Isler, K., & Thorpe, S. K. (2003). Gait parameters in vertical climbing of captive, rehabilitant and wild Sumatran orangutans (*Pongo pygmaeus abelii*). *Journal of Experimental Biology*, *206*, 4081-4096.

Ito, M., Ejiri, S., Jinnai, H., Kono, J., Ikeda, S., Nishida, A., ... & Hayashi, K. (2003). Bone structure and mineralization demonstrated using synchrotron radiation computed tomography (SR-CT) in animal models: preliminary findings. *Journal of Bone and Mineral Metabolism*, *21*, 287-293.

Jacobs, C. R. (2000). The mechanobiology of cancellous bone structural adaptation. *Journal of Rehabilitation Research and Development, 37*, 209-216.

Jacob, T., Indriati, E., Soejono, R. P., Hsü, K., Frayer, D. W., Eckhardt, R. B., ... & Henneberg, M. (2006). Pygmoid Australomelanesian *Homo sapiens* skeletal remains from Liang Bua, Flores: population affinities and pathological abnormalities. *Proceedings of the National Academy of Sciences*, *103*, 13421-13426.

Janis, C. M., Shoshitaishvili, B., Kambic, R., & Figueirido, B. (2012). On their knees: distal femur asymmetry in ungulates and its relationship to body size and locomotion. *Journal of Vertebrate Paleontology, 32*, 433-445.

Javois, C., Tardieu, C., Lebel, B., Seil, R., Hulet, C., & Société française d'arthroscopie. (2009). Comparative anatomy of the knee joint: effects on the lateral meniscus. *Orthopaedics & Traumatology: Surgery & Research, 95*, 49-59.

Jensen, K. S., Mosekilde, L., & Mosekilde, L. (1990). A model of vertebral trabecular bone architecture and its mechanical properties. *Bone, 11*, 417-423.

Johanson, D. C., & Taieb, M. (1976). Plio-pleistocene hominid discoveries in Hadar, Ethiopia. *Nature, 260*, 293-297.

Johanson, D. C., & White, T. D. (1979). A systematic assessment of early African hominids. *Science, 203*, 321-330.

Jungers, W. L. (1988). Relative joint size and hominoid locomotor adaptations with implications for the evolution of hominid bipedalism. *Journal of Human Evolution, 17*, 247-265.

Jungers, W. L., Larson, S. G., Harcourt-Smith, W., Morwood, M. J., Sutikna, T., Awe, R. D., & Djubiantono, T. (2009). Descriptions of the lower limb skeleton of *Homo floresiensis*. *Journal of Human Evolution, 57*, 538-554.

Kamibayashi, L., Wyss, U. P., Cooke, T. D. V., & Zee, B. (1995). Trabecular microstructure in the medial condyle of the proximal tibia of patients with knee osteoarthritis. *Bone, 17*, 27-35.

Kaplan, E. B. (1962). Some aspects of functional anatomy of the human knee joint. *Clinical Orthopaedics and Related Research, 23*, 18-29.

Keaveny, T. M., Morgan, E. F., Niebur, G. L., & Yeh, O. C. (2001). Biomechanics of trabecular bone. *Annual Review of Biomedical Engineering, 3*, 307-333.

Kellis, E. (2001). Tibiofemoral joint forces during maximal isokinetic eccentric and concentric efforts of the knee flexors. *Clinical Biomechanics, 16*, 229-236.

Kersh, M. E., Martelli, S., Zebaze, R., Seeman, E., & Pandy, M. G. (2018). Mechanical loading of the femoral neck in human locomotion. *Journal of Bone and Mineral Research, 33*, 1999-2006.

Kim, D. G., Hunt, C. A., Zauel, R., Fyhrie, D. P., & Yeni, Y. N. (2007). The effect of regional variations of the trabecular bone properties on the compressive strength of human vertebral bodies. *Annals of Biomedical Engineering, 35*, 1907-1913.

Kinney, J. H., & Ladd, A. J. C. (1998). The relationship between three-dimensional connectivity and the elastic properties of trabecular bone. *Journal of Bone and Mineral Research, 13*, 839-845.

Kivell, T. L., Davenport, R., Hublin, J. J., Thackeray, J. F., & Skinner, M. M. (2018). Trabecular architecture and joint loading of the proximal humerus in extant hominoids, *Ateles*, and *Australopithecus africanus*. *American Journal of Physical Anthropology, 167*, 348-365.

Kivell, T. L., Ostrofsky, K. R., Richmond, B. G., & Drapeau, M. S. (2020). Metacarpals and manual phalanges. *Hominin Postcranial Remains from Sterkfontein, South Africa, 106, 1936-1995*.

Kivell, T. L., Skinner, M. M., Lazenby, R., & Hublin, J. J. (2011). Methodological considerations for analyzing trabecular architecture: an example from the primate hand. *Journal of Anatomy, 218*, 209-225.

Kivell, T. L. (2016). A review of trabecular bone functional adaptation: what have we learned from trabecular analyses in extant hominoids and what can we apply to fossils? *Journal of Anatomy, 228*, 569-594.

Kivell, T. L., & Schmitt, D. (2009). Independent evolution of knuckle-walking in African apes shows that humans did not evolve from a knuckle-walking ancestor. *National Academy of Sciences, 106*, 14241-14246.

Klawitter, J. J., & Hulbert, S. F. (1971). Application of porous ceramics for the attachment of load bearing internal orthopedic applications. *Journal of Biomedical Materials Research, 5*, 161-229.

Kothari, M., Keaveny, T. M., Lin, J. C., Newitt, D. C., Genant, H. K., & Majumdar, S. (1998). Impact of spatial resolution on the prediction of trabecular architecture parameters. *Bone, 22*, 437-443.

Kozma, E. E., Webb, N. M., Harcourt-Smith, W. E., Raichlen, D. A., D'Août, K., Brown, M. H., ... & Pontzer, H. (2018). Hip extensor mechanics and the evolution of walking and climbing

capabilities in humans, apes, and fossil hominins. *National Academy of Sciences, 115*, 4134-4139.

Kramer, P. A., & Sylvester, A. D. (2009). Bipedal form and locomotor function: understanding the effects of size and shape on velocity and energetics. *PaleoAnthropology*, *2009*, 238-251.

Krevolin, J. L., Pandy, M. G., & Pearce, J. C. (2004). Moment arm of the patellar tendon in the human knee. *Journal of Biomechanics*, *37*, 785-788.

Kuo, S., Saers, J. P., Scott, R. S., & Ryan, T. M. (2022). Trabecular and Cortical Bone Morphology of the Distal Radius in Humans, Chimpanzees, Cercopithecids, and Anteaters. *The FASEB Journal*, *36*.

Kuroda, S., Nishihara, T., Suzuki, S., & Oko, R. A. (1996). Sympatric chimpanzees and gorillas in the Ndoki Forest, Congo. *Great Ape Societies*, *71*, 81.

Kutzner, I., Trepczynski, A., Heller, M. O., & Bergmann, G. (2013). Knee adduction moment and medial contact force–facts about their correlation during gait. *PloS One*, *8*, 81036.

Lambert, K. L. (1971). The weight-bearing function of the fibula: a strain gauge study. *Journal of Bone and Joint Surgery*, *53*, 507-513.

Landis, E. K., & Karnick, P. (2006). A three-dimensional analysis of the geometry and curvature of the proximal tibial articular surface of hominoids. In *Three-Dimensional Image Capture and Applications VII*, *6056*, 189-200.

Larson, S. G. (2013). Shoulder morphology in early hominin evolution. *The Paleobiology of Australopithecus*, 247-261.

Larson, S. G., Jungers, W. L., Morwood, M. J., Sutikna, T., Saptomo, E. W., Due, R. A., & Djubiantono, T. (2007). *Homo floresiensis* and the evolution of the hominin shoulder. *Journal of Human Evolution*, *53*, 718-731.

Larson, S. G., Jungers, W. L., Tocheri, M. W., Orr, C. M., Morwood, M. J., Sutikna, T., ... & Djubiantono, T. (2009). Descriptions of the upper limb skeleton of *Homo floresiensis*. *Journal of Human Evolution*, *57*, 555-570.

Larson, S. G., Schmitt, D., Lemelin, P., & Hamrick, M. (2001). Limb excursion during quadrupedal walking: how do primates compare to other mammals? *Journal of Zoology*, *255*, 353-365.

Latimer, B., & Lovejoy, C. O. (1989). The calcaneus of *Australopithecus afarensis* and its implications for the evolution of bipedality. *American Journal of Physical Anthropology, 78*, 369-386.

Latimer, B., Ohman, J. C., & Lovejoy, C. O. (1987). Talocrural joint in African hominoids: implications for *Australopithecus afarensis*. *American Journal of Physical Anthropology, 74*, 155-175.

Lazenby, R. A., Skinner, M. M., Kivell, T. L., & Hublin, J. J. (2011). Scaling VOI size in 3D μCT studies of trabecular bone: A test of the over-sampling hypothesis. *American Journal of Physical Anthropology, 144*, 196-203.

Lee, L. F., O'Neill, M. C., Demes, B., LaBoda, M. D., Thompson, N. E., Larson, S. G., ... & Umberger, B. R. (2012). Joint kinematics in chimpanzee and human bipedal walking. *Hip*, *20*, 10.

Lichtwark, G. A., & Wilson, A. M. (2006). Elastic energy storage in tendons: the key to understanding the mechanics of jumping and running. *Journal of Experimental Biology, 209*, 2500-2511.

Lieberman, D. E. (1997). Making behavioral and phylogenetic inferences from hominid fossils: considering the developmental influence of mechanical forces. *Annual Review of Anthropology, 26*, 185-210.

Loewen, N., Fautsch, M. P., Peretz, M., Bahler, C. K., Cameron, J. D., Johnson, D. H., & Poeschla, E. M. (2001). Genetic modification of human trabecular meshwork with lentiviral vectors. *Human Gene Therapy, 12*, 2109-2119.

Loudon, J. K. (2016). Biomechanics and pathomechanics of the patellofemoral joint. *International Journal of Sports Physical Therapy, 11*, 820.

Lovejoy, C. O. (1988). Evolution of human walking. *Scientific American, 259*, 118-125.

Lovejoy, C. O. (2005). The natural history of human gait and posture: Part 2. Hip and thigh. *Gait & posture, 21*, 113-124.

Lovejoy, C. O. (2007). The natural history of human gait and posture: Part 3. The knee. *Gait & posture, 25*, 325-341.

Lovejoy, C. O., & Heiple, K. G. (1970). A reconstruction of the femur of *Australopithecus africanus*. *American Journal of Physical Anthropology, 32*, 33-40.

Lovejoy, C. O., McCollum, M. A., Reno, P. L., & Rosenman, B. A. (2003). Developmental biology and human evolution. *Annual Review of Anthropology, 32*, 85-109.

Lovejoy, C. O., & McCollum, M. A. (2010). Spinopelvic pathways to bipedality: why no hominids ever relied on a bent-hip–bent-knee gait. *Biological Sciences, 365*, 3289-3299.

Lovejoy, C. O., Meindl, R. S., Ohman, J. C., Heiple, K. G., & White, T. D. (2002). The Maka femur and its bearing on the antiquity of human walking: applying contemporary concepts of morphogenesis to the human fossil record. *American Journal of Physical Anthropology, 119*, 97-133.

Lovejoy, C. O., Simpson, S. W., White, T. D., Asfaw, B., & Suwa, G. (2009). Careful climbing in the Miocene: the forelimbs of *Ardipithecus ramidus* and humans are primitive. *Science, 326*, 70-78.

Lovejoy, C. O., Suwa, G., Spurlock, L., Asfaw, B., & White, T. D. (2009). The pelvis and femur of *Ardipithecus ramidus*: the emergence of upright walking. *Science, 326*, 71-76.

Lukova, A., Dunmore, C. J., Bachmann, S., Synek, A., Pahr, D. H., Kivell, T. L., & Skinner, M. M. (2024). Trabecular architecture of the distal femur in extant hominids. *Journal of Anatomy*.

Macalister, A. (1870). The muscular anatomy of the gorilla. *Proceedings of the Royal Irish Academy. Science, 1*, 501-506.

Macchiarelli, R., Bondioli, L., Galichon, V., & Tobias, P. V. (1999). Hip bone trabecular architecture shows uniquely distinctive locomotor behaviour in South African australopithecines. *Journal of Human Evolution, 36*, 211-232.

Maga, M., Kappelman, J., Ryan, T. M., & Ketcham, R. A. (2006). Preliminary observations on the calcaneal trabecular microarchitecture of extant large-bodied hominoids. *American Journal of Physical Anthropology, 129*, 410-417.

Maganaris, C. N. (2003). Force-length characteristics of the in vivo human gastrocnemius muscle. *Clinical Anatomy, 16*, 215-223.

Magland, J. F., & Wehrli, F. W. (2008). Trabecular bone structure analysis in the limited spatial resolution regime of in vivo MRI. *Academic Radiology, 15,* 1482-1493.

Maquer, G., Musy, S. N., Wandel, J., Gross, T., & Zysset, P. K. (2015). Bone volume fraction and fabric anisotropy are better determinants of trabecular bone stiffness than other morphological variables. *Journal of Bone and Mineral Research, 30,* 1000-1008.

Marchetti, D. C., Moatshe, G., Phelps, B. M., Dahl, K. D., Ferrari, M. B., Chahla, J., ... & LaPrade, R. F. (2017). The proximal tibiofibular joint: a biomechanical analysis of the anterior and posterior ligamentous complexes. *American Journal of Sports Medicine, 45,* 1888-1892.

Mann, R. A., & Hagy, J. (1980). Biomechanics of walking, running, and sprinting. *American Journal of Sports Medicine, 8,* 345-350.

Manduell, K. L., Harrison, M. E., & Thorpe, S. K. (2012). Forest structure and support availability influence orangutan locomotion in Sumatra and Borneo. *American Journal of Primatology, 74,* 1128-1142.

Manning, P. L., & Richmond, B. G. (2003). Locomotor Adaptations of Orangutans: A Comparative Study of Posture and Knee Joint Loading. *American Journal of Physical Anthropology, 120,* 394-402.

Martin, J. C., & Brown, N. A. (2009). Joint-specific power production and fatigue during maximal cycling. *Journal of Biomechanics, 42,* 474-479.

Martinón-Torres, M. (2003). Quantifying trabecular orientation in the pelvic cancellous bone of modern humans, chimpanzees, and the Kebara 2 Neanderthal. *American Journal of Human Biology, 15,* 647-661.

Masouros, S. D., Bull, A. M. J., & Amis, A. A. (2010). Biomechanics of the knee joint. *Orthopaedics and Trauma, 24,* 84-91.

Masouros, S. D., McDermott, I. D., Amis, A. A., & Bull, A. M. J. (2008). Biomechanics of the meniscus-meniscal ligament construct of the knee. *Knee Surgery, Sports Traumatology, Arthroscopy, 16,* 1121-1132.

Matarazzo, S. A. (2015). Trabecular architecture of the manual elements reflects locomotor patterns in primates. *PLoS One, 10,* 120-436.

Mazurier, A., Nakatsukasa, M., & Macchiarelli, R. (2010). The inner structural variation of the primate tibial plateau characterized by high-resolution microtomography. Implications for the reconstruction of fossil locomotor behaviours. *Comptes Rendus Palevol, 9*, 349-359.

McCabe, L., Britton, R. A., & Parameswaran, N. (2015). Prebiotic and probiotic regulation of bone health: role of the intestine and its microbiome. *Current Osteoporosis Reports, 13*, 363-371.

McCalden, R.W., & McGeough, J.A. (1997) Age-related changes in the compressive strength of cancellous bone. The relative importance of changes in density and trabecular architecture. *Journal of Bone and Joint Surgery*, 79, 421–427.

McHenry, H. M. (1983). The capitate of *Australopithecus afarensis* and *A. africanus*. *American Journal of Physical Anthropology, 62*, 187-198.

McHenry, H. M. (1986). The first bipeds: a comparison of the *A. afarensis* and *A. africanus* postcranium and implications for the evolution of bipedalism. *Journal of Human Evolution, 15*, 177-191.

McHenry, H. M. (1991). Femoral lengths and stature in Plio-Pleistocene hominids. *American Journal of Physical Anthropology, 85*, 149-158.

McHenry, H. M., & Berger, L. R. (1998). Body proportions in *Australopithecus afarensis* and *A. africanus* and the origin of the genus *Homo*. *Journal of Human Evolution, 35*, 1-22.

Meyer, M. R., Jung, J. P., Spear, J. K., Araiza, I. F., Galway-Witham, J., & Williams, S. A. (2023). Knuckle-walking in Sahelanthropus? Locomotor inferences from the ulnae of fossil hominins and other hominoids. *Journal of Human Evolution, 179*, 103355.

Meyer, M. R., Williams, S. A., Schmid, P., Churchill, S. E., & Berger, L. R. (2017). The cervical spine of *Australopithecus sediba*. *Journal of Human Evolution, 104*, 32-49.

Mikosz, R. P., Andriacchi, T., & Andersson, G. B. J. (1988). Model analysis of factors influencing the prediction of muscle forces at the knee. *Journal of Orthopaedic Research, 6*, 205-214.

Miller, C. K., & DeSilva, J. M. (2024). A review of the distal femur in *Australopithecus*. *Evolutionary Anthropology: Issues, News, and Reviews, 33*, 22012.

Miller, Z., Fuchs, M. B., & Arcan, M. (2002). Trabecular bone adaptation with an orthotropic material model. *Journal of Biomechanics, 35*, 247-256.

Miller, J. A., & Gross, M. M. (1998). Locomotor advantages of Neandertal skeletal morphology at the knee and ankle. *Journal of Biomechanics, 31*, 355-361.

Milovanovic, P., Djonic, D., Hahn, M., Amling, M., Busse, B., & Djuric, M. (2017). Region-dependent patterns of trabecular bone growth in the human proximal femur: A study of 3D bone microarchitecture from early postnatal to late childhood period. *American Journal of Physical Anthropology, 164*, 281-291.

Mittra, E., Rubin, C., & Qin, Y. X. (2005). Interrelationship of trabecular mechanical and microstructural properties in sheep trabecular bone. *Journal of Biomechanics, 38*, 1229-1237.

Morbeck, M. E., & Zihlman, A. L. (1989). Body size and proportions in chimpanzees, with special reference to *Pan troglodytes schweinfurthii* from Gombe National Park, Tanzania. *Primates, 30*, 369-382.

Mogg, J. A. (2018). Refining locomotory style in the fossil record through use of 3D Geometric Morphometrics and muscle attachment sites in the fossil species *Australopithecus afarensis Doctoral dissertation, University of Sheffield*.

Morrison, J. B. (1970). The mechanics of the knee joint in relation to normal walking. *Journal of Biomechanics, 3*, 51-61.

Morwood, M. J., Brown, P., Jatmiko, Sutikna, T., Wahyu Saptomo, E., Westaway, K. E., ... & Djubiantono, T. (2005). Further evidence for small-bodied hominins from the Late Pleistocene of Flores, Indonesia. *Nature, 437*, 1012-1017.

Muramatsu, T., Muraoka, T., Takeshita, D., Kawakami, Y., Hirano, Y., & Fukunaga, T. (2001). Mechanical properties of tendon and aponeurosis of human gastrocnemius muscle in vivo. *Journal of Applied Physiology, 90*, 1671-1678.

Müller, R., Koller, B., Hildebrand, T., Laib, A., Gianolini, S., & Rüegsegger, P. (1996). Resolution dependency of microstructural properties of cancellous bone based on three-dimensional μ-tomography. *Technology and Health Care, 4*, 113-119.

Müller, R., Van Campenhout, H., Van Damme, B., Van der Perre, G., Dequeker, J., Hildebrand, T., & Rüegsegger, P. (1998). Morphometric analysis of human bone biopsies: a quantitative

structural comparison of histological sections and micro-computed tomography. *Bone*, *23*, 59-66.

Myatt, J. P., Crompton, R. H., & Thorpe, S. K. (2011). Hindlimb muscle architecture in non-human great apes and a comparison of methods for analysing inter-species variation. *Journal of Anatomy, 219*, 150-166.

Nagai, K., Nakanishi, Y., Kamada, K., Hoshino, Y., & Kuroda, R. (2021). Anatomy and biomechanics of the collateral ligaments of the knee. *Orthopaedic Biomechanics in Sports medicine*, 311-320.

Nakatsukasa, M. (1996). Locomotor differentiation and different skeletal morphologies in mangabeys (*Lophocebus* and *Cercocebus*). *Folia Primatologica, 66*, 15-24.

Napier, J. (1967). The antiquity of human walking. *Scientific American, 216*, 56-67.

Neaux, D., Bienvenu, T., Guy, F., Daver, G., Sansalone, G., Ledogar, J. A., & Brunet, M. (2017). Relationship between foramen magnum position and locomotion in extant and extinct hominoids. *Journal of Human Evolution, 113*, 1-9.

Newitt, D. C., Majumdar, S., Van Rietbergen, B., Von Ingersleben, G., Harris, S. T., Genant, H. K., ... & MacDonald, B. (2002). In vivo assessment of architecture and micro-finite element analysis derived indices of mechanical properties of trabecular bone in the radius. *Osteoporosis International, 13*, 6-17.

Nilsson, J., & Thorstensson, A. (1987). Adaptability in frequency and amplitude of leg movements during human locomotion at different speeds. *Acta Physiologica Scandinavica, 129*, 107-114.

Nilsson, J., & Thorstensson, A. (1989). Ground reaction forces at different speeds of human walking and running. *Acta Physiologica Scandinavica, 136*, 217-227.

Nicholson, E. K., Stock, S. R., Hamrick, M. W., & Ravosa, M. J. (2006). Biomineralization and adaptive plasticity of the temporomandibular joint in myostatin knockout mice. *Archives of Oral Biology, 51*, 37-49.

Nikander, R., Sievänen, H., Heinonen, A., & Kannus, P. (2005). Femoral neck structure in adult female *Athletes* subjected to different loading modalities. *Journal of Bone and Mineral Research, 20*, 520-528.

Nikander, R., Sievänen, H., Uusi-Rasi, K., Heinonen, A., & Kannus, P. (2006). Loading modalities and bone structures at nonweight-bearing upper extremity and weight-bearing lower extremity: a pQCT study of adult female athletes. *Bone, 39*, 886-894.

Nikander, R., Kannus, P., Dastidar, P., Hannula, M., Harrison, L., Cervinka, T., ... & Sievänen, H. (2009). Targeted exercises against hip fragility. *Osteoporosis International, 20*, 1321-1328.

Nisell, R. (1985). Mechanics of the knee: a study of joint and muscle load with clinical applications. *Acta Orthopaedica Scandinavica*, *56*, 1-42.

Nordin, M., & Frankel, V. H. (2001). In: *Basic Biomechanics of the Musculoskeletal System*. 3rd. Philadelphia, Pa: Lippincott Williams & Wilkins.

Novitskaya, E., Zin, C., Chang, N., Cory, E., Chen, P., D'Lima, D., ... & McKittrick, J. (2014). Creep of trabecular bone from the human proximal tibia. *Materials Science and Engineering: C*, *40*, 219-227.

Ocobock, C., Lacy, S., & Niclou, A. (2021). Between a rock and a cold place: Neanderthal biocultural cold adaptations. *Evolutionary Anthropology: Issues, News, and Reviews*, *30*, 262-279.

Odgaard, A. (1997). Three-dimensional methods for quantification of cancellous bone architecture. *Bone, 20*, 315-328.

Ogaya, S., Naito, H., Iwata, A., Higuchi, Y., Fuchioka, S., & Tanaka, M. (2014). Knee adduction moment and medial knee contact force during gait in older people. *Gait & Posture, 40*, 341-345.

Ogden, J. A. (1974). The anatomy and function of the proximal tibiofibular joint. *Clinical Orthopaedics and Related Research (1976-2007), 101*, 186-191.

Ohman, J. C., Krochta, T. J., Lovejoy, C. O., Mensforth, R. P., & Latimer, B. (1997). Cortical bone distribution in the femoral neck of hominoids: implications for the locomotion of *Australopithecus afarensis*. *American Journal of Physical Anthropology*, *104*, 117-131.

Ohman, J. C., Lovejoy, C. O., & White, T. D. (2005). Questions about *Orrorin* femur. *Science*, *307*, 845-845.

O'Neill, M. C., Lee, L. F., Demes, B., Thompson, N. E., Larson, S. G., Stern Jr, J. T., & Umberger, B. R. (2015). Three-dimensional kinematics of the pelvis and hind limbs in

chimpanzee (*Pan troglodytes*) and human bipedal walking. *Journal of Human Evolution*, *86*, 32-42.

O'Neill, M. C., Lee, L. F., Larson, S. G., Demes, B., Stern Jr, J. T., & Umberger, B. R. (2013). A three-dimensional musculoskeletal model of the chimpanzee (*Pan troglodytes*) pelvis and hind limb. *Journal of Experimental Biology*, *216*, 3709-3723.

Organ, J. M., & Ward, C. V. (2006). Contours of the hominoid lateral tibial condyle with implications for *Australopithecus*. *Journal of Human Evolution, 51*, 113-127.

Orr, C. M., Tocheri, M. W., Burnett, S. E., Awe, R. D., Saptomo, E. W., Sutikna, T., ... & Jungers, W. L. (2013). New wrist bones of *Homo floresiensis* from liang Bua (Flores, Indonesia). *Journal of Human Evolution*, *64*, 109-129.

Ott, S. M. (2002). Histomorphometric analysis of bone remodeling. *Principles of Bone Biology*, 303-XXIII.

Ott, S. M. (2002). Histomorphometric analysis of bone remodeling. In: Bilezikian, J. P., Raisz, L. G., & Rodan, G. A., (eds.) *Principles of Bone Biology*. Academic Press, 2002; 303–319.

Oxnard, C. E. (1975). The place of the australopithecines in human evolution: grounds for doubt? *Nature, 258*, 389-395.

Pahr, D. H., & Zysset, P. K. (2009). From high-resolution CT data to finite element models: development of an integrated modular framework. *Computer Methods in Biomechanics and Biomedical Engineering*, *12*, 45-57.

Parfitt, A. M. (2000). The mechanism of coupling: a role for the vasculature. *Bone*, *26*, 319-323.

Paternoster, L., Lorentzon, M., Lehtimäki, T., Eriksson, J., Kähönen, M., Raitakari, O., ... & Ohlsson, C. (2013). Genetic determinants of trabecular and cortical volumetric bone mineral densities and bone microstructure. *PLoS Genetics, 9*, 32-47.

Payne, R. C., Crompton, R. H., Isler, K., Savage, R., Vereecke, E. E., Günther, M. M., ... & D'Août, K. (2006). Morphological analysis of the hindlimb in apes and humans. I. Muscle architecture. *Journal of Anatomy, 208*, 709-724.

Pearson, O. M., Cordero, R. M., & Busby, A. M. (2006). How different were Neanderthals' habitual activities? A comparative analysis with diverse groups of recent humans. *Neanderthals Revisited: New Approaches and Perspectives*, 135-156.

Pearson, O. M., & Lieberman, D. E. (2004). The aging of Wolff's "law": ontogeny and responses to mechanical loading in cortical bone. *American Journal of Physical Anthropology, 125*, 63-99.

Pélabon, C., Firmat, C., Bolstad, G. H., Voje, K. L., Houle, D., Cassara, J., ... & Hansen, T. F. (2014). Evolution of morphological allometry. *Annals of the New York Academy of Sciences, 1320*, 58-75.

Pettermann, H. E., Reiter, T. J., & Rammerstorfer, F. G. (1997). Computational simulation of internal bone remodeling. *Archives of Computational Methods in Engineering, 4*, 295-323.

Phillips, J., & Coetsee, M. F. (2007). Incidence of non-traumatic anterior knee pain among 11-17-years-olds. *South African Journal of Sports Medicine, 19*, 60-64.

Pickford, M., Senut, B., Gommery, D., & Treil, J. (2002). Bipedalism in *Orrorin tugenensis* revealed by its femora. *Comptes Rendus Palevol, 1*, 191-203.

Pickering, T. R., Heaton, J. L., Clarke, R. J., & Stratford, D. (2018). Hominin hand bone fossils from Sterkfontein Caves, South Africa (1998–2003 excavations). *Journal of Human Evolution, 118*, 89-102.

Pickford, M., Senut, B., Gommery, D., & Treil, J. (2002). Bipedalism in *Orrorin tugenensis* revealed by its femora. *Comptes Rendus Palevol, 1*, 191-203.

Pietrobelli, A., Sorrentino, R., Benazzi, S., Belcastro, M. G., & Marchi, D. (2023). Linking the proximal tibiofibular joint to hominid locomotion: A morphometric study of extant species. *American Journal of Biological Anthropology, 184*, 24696.

Pina, M., Almecija, S., Alba, D. M., O'Neill, M. C., & Moya-Sola, S. (2014). The Middle Miocene ape *Pierolapithecus catalaunicus* exhibits extant great ape-like morphometric affinities on its patella: Inferences on knee function and evolution. *PLoS One, 9*, 91944.

Plewes, D. B., & Dean, P. B. (1981). The influence of partial volume averaging on sphere detectability in computed tomography. *Physics in Medicine & Biology, 26*, 913.

Polk, J. D. (2002). Adaptive and phylogenetic influences on musculoskeletal design in cercopithecine primates. *Journal of Experimental Biology, 205*, 3399-3412.

Polk, J. D., Blumenfeld, J., & Ahluwalia, D. (2008). Knee posture predicted from subchondral apparent density in the distal femur: an experimental validation. *The Anatomical Record: Advances in Integrative Anatomy and Evolutionary Biology, 291*, 293-302.

Pontzer, H., Lieberman, D. E., Momin, E., Devlin, M. J., Polk, J. D., Hallgrimsson, B., & Cooper, D. M. L. (2006). Trabecular bone in the bird knee responds with high sensitivity to changes in load orientation. *Journal of Experimental Biology, 209*, 57-65.

Pontzer, H., Raichlen, D. A., & Sockol, M. D. (2009). The metabolic cost of walking in humans, chimpanzees, and early hominins. *Journal of Human Evolution, 56*, 43-54.

Preuschoft, H. (1971). Body posture and mode of locomotion in early Pleistocene hominids. *Folia Primatologica, 14*, 209-240.

Preuschof, H., & Tardieu, C. (1996). Biomechanical reasons for the divergent morphology of the knee joint and the distal epiphyseal suture in hominoids. *Folia Primatologica, 66*, 82-92.

Provine, R. R. (2004). Walkie-talkie evolution: Bipedalism and vocal production. *Behavioral and Brain Sciences, 27*, 520-521.

Pyka, G., Kerckhofs, G., Schrooten, J., & Wevers, M. (2014). The effect of spatial micro-CT image resolution and surface complexity on the morphological 3D analysis of open porous structures. *Materials Characterization, 87*, 104-115.

Racic, V., Pavic, A., & Brownjohn, J. M. W. (2009). Experimental identification and analytical modelling of human walking forces: Literature review. *Journal of Sound and Vibration, 326*, 1-49.

Rafferty, K. L. (1998). Structural design of the femoral neck in primates. *Journal of Human Evolution, 34*, 361-383.

Raichlen, D. A., Gordon, A. D., Foster, A. D., Webber, J. T., Sukhdeo, S. M., Scott, R. S., ... & Ryan, T. M. (2015). An ontogenetic framework linking locomotion and trabecular bone architecture with applications for reconstructing hominin life history. *Journal of Human Evolution, 81*, 1-12.

Raichlen, D. A., Gordon, A. D., Harcourt-Smith, W. E., Foster, A. D., & Haas Jr, W. R. (2010). Laetoli footprints preserve earliest direct evidence of human-like bipedal biomechanics. *PloS One*, *5*, 9769.

Reginster, J. Y., & Burlet, N. (2006). Osteoporosis: a still increasing prevalence. *Bone*, *38*, 4-9.

Rein, T. R., Harrison, T., Carlson, K. J., & Harvati, K. (2017). Adaptation to suspensory locomotion in *Australopithecus sediba*. *Journal of Human Evolution*, *104*, 1-12.

Remis, M. J. (1994). Feeding ecology and positional behavior of western lowland gorillas (*Gorilla gorilla gorilla*) in the Central African Republic. *Doctoral dissertation, Yale University*.

Remis, M. (1995). Effects of body size and social context on the arboreal activities of lowland gorillas in the Central African Republic. *American Journal of Physical Anthropology*, *97*, 413-433.

Remis, M. J. (1997). Western lowland gorillas (*Gorilla gorilla gorilla*) as seasonal frugivores: use of variable resources. *American Journal of Primatology*, *43*, 87-109.

Remis, M. J. (1998). The gorilla paradox: the effects of body size and habitat on the positional behavior of lowland and mountain gorillas. *Primate Locomotion: Recent Advances*, 95-106.

Reynolds, T. R. (1985). Stresses on the limbs of quadrupedal primates. *American Journal of Physical Anthropology*, *67*, 351-362.

Reznikov, N., Chase, H., Brumfeld, V., Shahar, R., & Weiner, S. (2015). The 3D structure of the collagen fibril network in human trabecular bone: relation to trabecular organization. *Bone*, *71*, 189-195.

Richmond, B. G., Begun, D. R., & Strait, D. S. (2001). Origin of human bipedalism: the knuckle-walking hypothesis revisited. *American Journal of Physical Anthropology*, *116*, 70-105.

Richmond, B. G., & Jungers, W. L. (2008). *Orrorin tugenensis* femoral morphology and the evolution of hominin bipedalism. *Science*, *319*, 1662-1665.

Richmond, B. G., Roach, N. T., & Ostrofsky, K. R. (2016). Evolution of the early hominin hand. *The Evolution of the Primate Hand: Anatomical, Developmental, Functional, and Paleontological Evidence*, 515-543.

Richmond, B. G., & Strait, D. S. (2000). Evidence that humans evolved from a knuckle-walking ancestor. *Nature, 404*, 382-385.

Ricklan, D. E. (1987). Functional anatomy of the hand of *Australopithecus africanus*. *Journal of Human Evolution, 16*, 643-664.

Rickman, J., Burtner, A. E., Linden, T. J., Santana, S. E., & Law, C. J. (2023). Size and locomotor ecology have differing effects on the external and internal morphologies of squirrel (*Rodentia: Sciuridae*) limb bones. *Integrative Organismal Biology, 17*.

Riggs, B. L., & Melton, L. J. (1986). Involutional osteoporosis. *The New England Journal of Medicine, 314*, 1676-1686.

Robling, A. G., Castillo, A. B., & Turner, C. H. (2006). Biomechanical and molecular regulation of bone remodeling. *Annual Review of Biomedical Engineering*, 8, 455-498.

Rook, L., Renne, P., Benvenuti, M., & Papini, M. (2000). News and Views Geochronology of Oreopithecus-bearing succession at Baccinello (Italy) and the extinction pattern of European Miocene hominoids. *Journal of Human Evolution, 39*, 577-582.

Rosas, A., Rodriguez-Perez, F. J., Bastir, M., Estalrrich, A., Huguet, R., García-Tabernero, A., ... & de la Rasilla, M. (2016). Adult Neandertal clavicles from the El Sidrón site (Asturias, Spain) in the context of *Homo* pectoral girdle evolution. *Journal of Human Evolution, 95*, 55-67.

Rubin, C., Turner, A. S., Bain, S., Mallinckrodt, C., & McLeod, K. (2001). Low mechanical signals strengthen long bones. *Nature, 412*, 603-604.

Rubin, C., Turner, A. S., Mallinckrodt, C., Jerome, C., McLeod, K., & Bain, S. (2002). Mechanical strain, induced noninvasively in the high-frequency domain, is anabolic to cancellous bone, but not cortical bone. *Bone, 30*, 445-452.

Rueckert, D., Frangi, A. F., Schnabel, J. A. (2003). Automatic construction of 3-D statistical deformation models of the brain using nonrigid registration. *IEEE transactions on medical imaging, 22*, 1014-1025.

Ruff, C. (1988). Hindlimb articular surface allometry in *Hominoide*a and *Macaca*, with comparisons to diaphyseal scaling. *Journal of Human Evolution, 17*, 687-714.

Ruff, C. B. (2018). Biomechanical analyses of archaeological human skeletons. *Biological Anthropology of the Human Skeleton*, 189-224.

Ruff, C. B. (2002). Long bone articular and diaphyseal structure in Old World monkeys and apes. I: Locomotor Effects. *American Journal of Physical Anthropology*, *119*, 305-342.

Ruff, C. B., Burgess, M. L., Bromage, T. G., Mudakikwa, A., & McFarlin, S. C. (2013). Ontogenetic changes in limb bone structural proportions in mountain gorillas (*Gorilla beringei beringei*). *Journal of Human Evolution*, *65*, 693-703.

Ruff, C., Holt, B., & Trinkaus, E. (2006). Who's afraid of the big bad Wolff? "Wolff's law" and bone functional adaptation. *American Journal of Physical Anthropology, 129*, 484-498.

Ryan, T. M., Carlson, K. J., Gordon, A. D., Jablonski, N., Shaw, C. N., & Stock, J. T. (2018). Human-like hip joint loading in *Australopithecus africanus* and *Paranthropus robustus*. *Journal of Human Evolution, 121*, 12-24.

Ryan, T. M., & Ketcham, R. A. (2002a). The three-dimensional structure of trabecular bone in the femoral head of strepsirrhine primates. *Journal of Human Evolution, 43*, 1-26.

Ryan, T. M., & Ketcham, R. A. (2002b). Femoral head trabecular bone structure in two omomyid primates. *Journal of Human Evolution*, *43*, 241-263.

Ryan, T. M., & Ketcham, R. A. (2005). Angular orientation of trabecular bone in the femoral head and its relationship to hip joint loads in leaping primates. *Journal of Morphology*, *265*, 249-263.

Ryan, T. M., & Krovitz, G. E. (2006). Trabecular bone ontogeny in the human proximal femur. *Journal of Human Evolution*, *51*, 591-602.

Ryan, T. M., & Shaw, C. N. (2012). Unique suites of trabecular bone features characterize locomotor behavior in human and non-human anthropoid primates. *PloS One*, *7*, 41037.

Ryan, T. M., & Shaw, C. N. (2013). Trabecular bone microstructure scales allometrically in the primate humerus and femur. *Proceedings of the Royal Society B: Biological Sciences, 280*, 20130172.

Ryan, T. M., & Shaw, C. N. (2015). Gracility of the modern *Homo sapiens* skeleton is the result of decreased biomechanical loading. *Proceedings of the National Academy of Sciences*, *112*, 372-377.

Ryan, T. M., Stephens, N., Doershuk, L. J., Saers, J. P., Jashashvili, T., Carlson, K. J., ... & Gordon, A. D. (2019). Trabecular bone structural variation in the human postcranial skeleton. *The FASEB Journal*, *33*, 19-20.

Ryan, T. M., & Van Rietbergen, B. (2005). Mechanical significance of femoral head trabecular bone structure in Loris and Galago evaluated using micromechanical finite element models. *American Journal of Physical Anthropology*, *126*, 82-96.

Ryan, T. M., & Walker, A. (2010). Trabecular bone structure in the humeral and femoral heads of anthropoid primates. *The Anatomical Record: Advances in Integrative Anatomy and Evolutionary Biology*, *293*, 719-729.

Saers, J. P., Cazorla-Bak, Y., Shaw, C. N., Stock, J. T., & Ryan, T. M. (2016). Trabecular bone structural variation throughout the human lower limb. *Journal of human evolution*, *97*, 97-108.

Saers, J. P., Gordon, A. D., Ryan, T. M., & Stock, J. T. (2022). Trabecular bone ontogeny tracks neural development and life history among humans and non-human primates. *Proceedings of the National Academy of Sciences*, *119*, 2208772119.

Saers, J. P., Ryan, T. M., & Stock, J. T. (2019). Trabecular bone structure scales allometrically in the foot of four human groups. *Journal of Human Evolution*, *135*, 102654.

Saers, J. P., Ryan, T. M., & Stock, J. T. (2020). Baby steps towards linking calcaneal trabecular bone ontogeny and the development of bipedal human gait. *Journal of Anatomy*, *236*, 474-492.

Sanders, W. J. (1998). Comparative morphometric study of the australopithecine vertebral series Stw-H8/H41. *Journal of Human Evolution*, *34*, 249-302.

Saparin, P., Scherf, H., Hublin, J. J., Fratzl, P., & Weinkamer, R. (2011). Structural adaptation of trabecular bone revealed by position resolved analysis of proximal femora of different primates. *The Anatomical Record: Advances in Integrative Anatomy and Evolutionary Biology*, *294*, 55-67.

Sarma, A., Borgohain, B., & Saikia, B. (2015). Proximal tibiofibular joint: Rendezvous with a forgotten articulation. *Indian Journal of Orthopaedics*, *49*, 489-495.

Sarringhaus, L. A., MacLatchy, L. M., & Mitani, J. C. (2014). Locomotor and postural development of wild chimpanzees. *Journal of Human Evolution*, *66*, 29-38.

Scherf, H. (2008). Locomotion-related femoral trabecular architectures in primates - high resolution computed tomographies and their implications for estimations of locomotor preferences of fossil primates. *Anatomical Imaging: Towards a New Morphology*, 39-59.

Scherf, H., Harvati, K., & Hublin, J. J. (2013). A comparison of proximal humeral cancellous bone of great apes and humans. *Journal of Human Evolution*, *65*, 29-38.

Scherf, H., Wahl, J., Hublin, J. J., & Harvati, K. (2016). Patterns of activity adaptation in humeral trabecular bone in Neolithic humans and present-day people. *American Journal of Physical Anthropology*, *159*, 106-115.

Schilling, A. M., Tofanelli, S., Hublin, J. J., & Kivell, T. L. (2014). Trabecular bone structure in the primate wrist. *Journal of Morphology*, *275*, 572-585.

Schipplein, O. D., & Andriacchi, T. P. (1991). Interaction between active and passive knee stabilizers during level walking. *Journal of Orthopaedic Research*, *9*, 113-119.

Schmitt, D. (1994). Forelimb mechanics as a function of substrate type during quadrupedalism in two anthropoid primates. *Journal of Human Evolution*, *26*, 441-457.

Schmitt, D. (2003). Insights into the evolution of human bipedalism from experimental studies of humans and other primates. *Journal of Experimental Biology*, *206*, 1437-1448.

Schmidt, M. A., & Alford, C. M. (2003). Comparative analysis of tendon properties in primates. *Journal of Anatomy*, *203*, 133-142.

Schmitt, D., & Lemelin, P. (2002). Origins of primate locomotion: gait mechanics of the woolly opossum. *American Journal of Physical Anthropology*, *118*, 231-238.

Schmitz, A., & Noehren, B. (2014). What predicts the first peak of the knee adduction moment? *The Knee*, *21*, 1077-1083.

Schulte, F. A., Ruffoni, D., Lambers, F. M., Christen, D., Webster, D. J., Kuhn, G., & Müller, R. (2013). Local mechanical stimuli regulate bone formation and resorption in mice at the tissue level. *PloS One*, *8*, 62172.

Scorrer, J., Faillace, K. E., Hildred, A., Nederbragt, A. J., Andersen, M. B., Millet, M. A., ... & Madgwick, R. (2021). Diversity aboard a Tudor warship: investigating the origins of the Mary Rose crew using multi-isotope analysis. *Royal Society Open Science*, *8*, 202106.

Seeman, E. (2003). Reduced bone formation and increased bone resorption: rational targets for the treatment of osteoporosis. *Osteoporosis International, 14*, 2-8.

Seireg, A., & Arvikar, R. J. (1975). The prediction of muscular load sharing and joint forces in the lower extremities during walking. *Journal of Biomechanics, 8*, 89-102.

Sellers, W. I., Dennis, L. A., W.-J, W., & Crompton, R. H. (2004). Evaluating alternative gait strategies using evolutionary robotics. *Journal of Anatomy, 204*, 343-351.

Senut, B. (2002). From apes to humans: locomotion as a key feature for phylogeny. *Zeitschrift für Morphologie und Anthropologie*, 351-360.

Senut, B. (2012). Fifty years of debate on the origins of human bipedalism. *Journal of Biological Research-Bollettino della Società Italiana di Biologia Sperimentale, 85*.

Senut, B., Pickford, M., Gommery, D., Mein, P., Cheboi, K., & Coppens, Y. (2001). First hominid from the Miocene (Lukeino formation, Kenya). *Comptes Rendus de l'Académie des Sciences-Series IIA-Earth and Planetary Science*, *332*, 137-144.

Senut, B., Pickford, M., Gommery, D., & Ségalen, L. (2018). Palaeoenvironments and the origin of hominid bipedalism. *Historical Biology*, *30*, 284-296.

Setiawan, R. M. K. (2021). Spatial distribution and landscape characteristics of Flores Hawk-Eagle (Nisaetus Floris) habitat in Flores Island. *Journal of Natural Resources and Environmental Management*, *11*, 542-549.

Seymour, N., & Schilling, N. (2018). Adaptations in tendon mechanics in response to different locomotor behaviors. *Journal of Experimental Biology*, *221*, 159730.

Shapiro, D. (2009). The Hominid Status of Sahelanthropus tchadensis and Orrorin tugenensis (Doctoral dissertation).

Shaw, C. N., & Ryan, T. M. (2012). Does skeletal anatomy reflect adaptation to locomotor patterns? Cortical and trabecular architecture in human and nonhuman anthropoids. *American Journal of Physical Anthropology, 147*, 187-200.

Sievänen, H., Józsa, L., Järvinen, M., Järvinen, T. A., Kannus, P., & Järvinen, T. L. (2007). Fragile external phenotype of modern human proximal femur in comparison with medieval bone. *Journal of Bone and Mineral Research*, *22*, 537-543.

Silva, M. J., Brodt, M. D., Lynch, M. A., Stephens, A. L., Wood, D. J., & Civitelli, R. (2012). Tibial loading increases osteogenic gene expression and cortical bone volume in mature and middle-aged mice. *PloS One, 7*, 34980.

Simpson, K. J., & Pettit, M. (1997). Jump distance of dance landings influencing internal joint forces: II. Shear forces. *Medicine and Science in Sports and Exercise, 29*, 928-936.

Sinclair, K. D., Farnsworth, R. W., Pham, T. X., Knight, A. N., Bloebaum, R. D., & Skedros, J. G. (2013). The artiodactyl calcaneus as a potential 'control bone'cautions against simple interpretations of trabecular bone adaptation in the anthropoid femoral neck. *Journal of Human Evolution, 64*, 366-379.

Singh, I. (1978). The architecture of cancellous bone. *Journal of Anatomy*, *127*, 305.

Skinner, M. M., Stephens, N. B., Tsegai, Z. J., Foote, A. C., Nguyen, N. H., Gross, T., ... & Kivell, T. L. (2015). Human-like hand use in *Australopithecus africanus*. *Science, 347*, 395-399.

Skinner, M., Tsegai, Z. J., Kivell, T. L., Gross, T., Nguyen, N. H., Pahr, D. H., & Smaers, J. B. (2013). Trabecular Bone Structure Correlates with Hand Posture and Use in Hominoids. *PLoS One*, *8*.

Smith, R. J., & Jungers, W. L. (1997). Body mass in comparative primatology. *Journal of Human evolution, 32*, 523-559.

Smit, T. H., Odgaard, A., & Schneider, E. (1997). Structure and function of vertebral trabecular bone. *Spine*, *22*, 2823-2833.

Sockol, M. D., Raichlen, D. A., & Pontzer, H. (2007). Chimpanzee locomotor energetics and the origin of human bipedalism. *Proceedings of the National Academy of Sciences*, *104*, 12265-12269.

Sode, M., Burghardt, A. J., Kazakia, G. J., Link, T. M., & Majumdar, S. (2010). Regional variations of gender-specific and age-related differences in trabecular bone structure of the distal radius and tibia. *Bone, 46*, 1652-1660.

Sode, M., Burghardt, A. J., Nissenson, R. A., & Majumdar, S. (2008). Resolution dependence of the non-metric trabecular structure indices. *Bone, 42*, 728-736.

Sorrentino, R., Stephens, N. B., Marchi, D., DeMars, L. J., Figus, C., Bortolini, E., ... & Benazzi, S. (2021). Unique foot posture in Neanderthals reflects their body mass and high mechanical stress. *Journal of Human Evolution*, *161*, 103093.

Spoor, C. W., & Van Leeuwen, J. L. (1992). Knee muscle moment arms from MRI and from tendon travel. *Journal of Biomechanics*, *25*, 201-206.

Stamos, P. A., & Alemseged, Z. (2023). Hominin locomotion and evolution in the Late Miocene to Late Pliocene. *Journal of Human Evolution*, *178*, 103332.

Stanley, S. M. (1992). An ecological theory for the origin of Homo. *Paleobiology*, *18*, 237-257.

Steiner, L., Synek, A., & Pahr, D. H. (2021). Femoral strength can be predicted from 2D projections using a 3D statistical deformation and texture model with finite element analysis. *Medical Engineering & Physics*, *93*, 72-82.

Stephens, N. B., Kivell, T. L., Gross, T., Pahr, D. H., Lazenby, R. A., Hublin, J. J., ... & Skinner, M. M. (2016). Trabecular architecture in the thumb of *Pan* and *Homo*: implications for investigating hand use, loading, and hand preference in the fossil record. *American Journal of Physical Anthropology*, *161*, 603-619.

Stern Jr, J. T. (2000). Climbing to the top: a personal memoir of *Australopithecus afarensis*. *Evolutionary Anthropology: Issues, News, and Reviews*, *9*, 113-133.

Stern Jr, J. T., & Susman, R. L. (1981). Electromyography of the gluteal muscles in *Hylobates*, *Pongo*, and *Pan*: implications for the evolution of hominid bipedality. *American Journal of Physical Anthropology*, *55*, 153-166.

Stern Jr, J. T., & Susman, R. L. (1983). The locomotor anatomy of *Australopithecus afarensis*. *American Journal of Physical Anthropology*, *60*, 279-317.

Stephens, N. B., Kivell, T. L., Gross, T., Pahr, D. H., Lazenby, R. A., Hublin, J. J., ... & Skinner, M. M. (2016). Trabecular architecture in the thumb of *Pan* and *Homo*: implications for investigating hand use, loading, and hand preference in the fossil record. *American Journal of Physical Anthropology*, *161*, 603-619.

Stephens, N. B., Kivell, T. L., Pahr, D. H., Hublin, J. J., & Skinner, M. M. (2018). Trabecular bone patterning across the human hand. *Journal of Human Evolution*, *123*, 1-23.

Stirland, A. J., & Waldron, T. (1997). Evidence for Activity Related Markers in the Vertebrae of the Crew of theMary Rose. *Journal of archaeological science*, *24*(4), 329-335.

Su, A., Wallace, I. J., & Nakatsukasa, M. (2013). Trabecular bone anisotropy and orientation in an Early Pleistocene hominin talus from East Turkana, Kenya. *Journal of Human Evolution*, *64*, 667-677.

Sugardjito, J., & Van Hooff, J. A. R. A. M. (1986). Age-sex class differences in the positional behaviour of the Sumatran orangutan (*Pongo pygmaeus abelii*) in the Gunung Leuser National Park, Indonesia. *Folia Primatologica*, *47*, 14-25.

Sugiyama, T., Neuhaus, M., Cole, R., Giles-Corti, B., & Owen, N. (2012). Destination and route attributes associated with adults' walking: a review. *Medicine and Science in Sports and Exercise*, *44*, 1275-1286.

Sugiyama, T., Price, J. S., & Lanyon, L. E. (2010). Functional adaptation to mechanical loading in both cortical and cancellous bone is controlled locally and is confined to the loaded bones. *Bone*, *46*, 314-321.

Sukhdeo, S., Parsons, J., Niu, X. M., & Ryan, T. M. (2020). Trabecular bone structure in the distal femur of humans, apes, and baboons. *The Anatomical Record*, *303*, 129-149.

Susman, R. L. (1983). Evolution of the human foot: evidence from Plio-Pleistocene hominids. *Foot & Ankle*, *3*, 365-376.

Susman, R. L. (1991). Who made the Oldowan tools? Fossil evidence for tool behavior in Plio-Pleistocene hominids. *Journal of Anthropological Research*, *47*, 129-151.

Susman, R. L., & Stern, J. T. (1982). Functional morphology of *Homo habilis*. *Science*, *217*, 931-934.

Susman, R. L., Stern, J. T., & Jungers, W. L. (1984). Arboreality and bipedality in the Hadar hominids. *Folia Primatologica*, *43*, 113-156.

Sutikna, T., Tocheri, M. W., Morwood, M. J., Saptomo, E. W., Jatmiko, Awe, R. D., ... & Roberts, R. G. (2016). Revised stratigraphy and chronology for *Homo floresiensis* at Liang Bua in Indonesia. *Nature*, *532*, 366-369.

Sylvester, A. D. (2013). A geometric morphometric analysis of the medial tibial condyle of African hominids. The Anatomical Record, 296(10), 1518-1525.

Sylvester, A. D., Mahfouz, M. R., & Kramer, P. A. (2011). The effective mechanical advantage of AL 129-1a for knee extension. *The Anatomical Record: Advances in Integrative Anatomy and Evolutionary Biology*, *294*, 1486-1499.

Sylvester, A. D., & Organ, J. M. (2010). Curvature scaling in the medial tibial condyle of large bodied hominoids. *The Anatomical Record: Advances in Integrative Anatomy and Evolutionary Biology*, *293*, 671-679.

Sylvester, A. D., & Pfisterer, T. (2012). Quantifying lateral femoral condyle ellipticalness in chimpanzees, gorillas, and humans. *American Journal of Physical Anthropology*, *149*, 458-467.

Sylvester, A. D., & Terhune, C. E. (2017). Trabecular mapping: Leveraging geometric morphometrics for analyses of trabecular structure. *American Journal of Physical Anthropology*, *163*, 553-569.

Synek, A., & Pahr, D. H. (2018). Plausibility and parameter sensitivity of micro-finite element-based joint load prediction at the proximal femur. *Biomechanics and Modeling in Mechanobiology*, *17*, 843-852.

Tabor, Z. (2004). Analysis of the influence of image resolution on the discriminating power of trabecular bone architectural parameters. *Bone*, *34*, 170-179.

Tardieu, C. (1981). Morpho-functional analysis of the articular surfaces of the knee-joint in primates. In *Primate Evolutionary Biology: Selected Papers (Part A) of the VIIIth Congress of the International Primatological Society, Florence, 7–12 July, 1980*, 68-80.

Tardieu, C. (1999). Ontogeny and phylogeny of femoro-tibial characters in humans and hominid fossils: functional influence and genetic determinism. *American Journal of Physical Anthropology*, *110*, 365-377.

Tardieu, C. (2002). Functional Morphology of the Primate Knee Joint. *Journal of Anatomy*, *200*, 183-194.

Tardieu, C., & Fritsch, G. (1991). Knee Kinematics and Loadings in Great Apes. *American Journal of Physical Anthropology*, *84*, 313-322.

Taylor, W. R., Heller, M. O., Bergmann, G., & Duda, G. N. (2004). Tibio-femoral loading during human gait and stair climbing. *Journal of Orthopaedic Research*, *22*, 625-632.

Thompson, N. E., Ostrofsky, K. R., McFarlin, S. C., Robbins, M. M., Stoinski, T. S., & Almecija, S. (2018). Unexpected terrestrial hand posture diversity in wild mountain gorillas. *American Journal of Physical Anthropology*, *166*, 84-94.

Thomsen, J. S., Laib, A., Koller, B., Prohaska, S., Mosekilde, L. I., & Gowin, W. (2005). Stereological measures of trabecular bone structure: comparison of 3D micro computed tomography with 2D histological sections in human proximal tibial bone biopsies. *Journal of Microscopy*, *218*, 171-179.

Tocheri, M. W., Solhan, C. R., Orr, C. M., Femiani, J., Frohlich, B., Groves, C. P., ... & Jungers, W. L. (2011). Ecological divergence and medial cuneiform morphology in gorillas. *Journal of Human Evolution, 60*, 171-184.

Thorpe, S. K., & Crompton, R. H. (2005). Locomotor ecology of wild orangutans (*Pongo pygmaeus abelii*) in the Gunung Leuser Ecosystem, Sumatra, Indonesia: A multivariate analysis using log-linear modelling. *American Journal of Physical Anthropology, 127*, 58-78.

Thorpe, S. K., & Crompton, R. H. (2006). Orangutan positional behavior and the nature of arboreal locomotion in *Hominoidea*. *American Journal of Physical Anthropology, 131*, 384-401.

Thorpe, S. K., Holder, R. L., & Crompton, R. H. (2007). Origin of human bipedalism as an adaptation for locomotion on flexible branches. *Science, 316*, 1328-1331.

Thorpe, S. K., Holder, R., & Crompton, R. H. (2009). Orangutans employ unique strategies to control branch flexibility. *Proceedings of the National Academy of Sciences, 106*, 12646-12651.

Tocheri, M. W., Orr, C. M., Jacofsky, M. C., & Marzke, M. W. (2008). The evolutionary history of the hominin hand since the last common ancestor of *Pan* and *Homo*. *Journal of Anatomy, 212*, 544-562.

Tocheri, M. W., Orr, C. M., Larson, S. G., Sutikna, T., Jatmiko, Saptomo, E. W., ... & Jungers, W. L. (2007). The primitive wrist of *Homo floresiensis* and its implications for hominin evolution. *Science, 317*, 1743-1745.

Trinkaus, E. (1976). The evolution of the hominid femoral diaphysis during the Upper Pleistocene in Europe and the Near East. *Zeitschrift für Morphologie und Anthropologie*, 291-319.

Trinkaus, E., & Jelínek, J. (1997). Human remains from the Moravian Gravettian: the Dolní Věstonice 3 postcrania. *Journal of Human Evolution, 33*, 33-82.

Tsegai, Z. J., Kivell, T. L., Gross, T., Nguyen, N. H., Pahr, D. H., Smaers, J. B., & Skinner, M. M. (2013). Trabecular bone structure correlates with hand posture and use in hominoids. *PloS One, 8*, 78781.

Tsegai, Z. J., Skinner, M. M., Gee, A. H., Pahr, D. H., Treece, G. M., Hublin, J. J., & Kivell, T. L. (2017). Trabecular and cortical bone structure of the talus and distal tibia in *Pan* and *Homo*. *American Journal of Physical Anthropology, 163*, 784-805.

Tsegai, Z. J., Stephens, N. B., Treece, G. M., Skinner, M. M., Kivell, T. L., & Gee, A. H. (2017). Cortical bone mapping: an application to hand and foot bones in hominoids. *Comptes Rendus Palevol, 16*, 690-701.

Tocheri, M. W., Solhan, C. R., Orr, C. M., Femiani, J., Frohlich, B., Groves, C. P., ... & Jungers, W. L. (2011). Ecological divergence and medial cuneiform morphology in gorillas. *Journal of Human Evolution, 60*, 171-184.

Trinkaus, E., Churchill, S. E., Ruff, C. B., & Vandermeersch, B. (1999). Long bone shaft robusticity and body proportions of the Saint-Césaire 1 Châtelperronian Neanderthal. *Journal of Archaeological Science, 26*, 753-773.

Tsegai, Z. J., Kivell, T. L., Gross, T., Nguyen, N. H., Pahr, D. H., Smaers, J. B., & Skinner, M. M. (2013). Trabecular bone structure correlates with hand posture and use in hominoids. *PloS One, 8*, 78781.

Tsegai, Z. J., Skinner, M. M., Pahr, D. H., Hublin, J. J., & Kivell, T. L. (2018a). Ontogeny and variability of trabecular bone in the chimpanzee humerus, femur and tibia. *American Journal of Physical Anthropology, 167*, 713-736.

Tsegai, Z. J., Skinner, M. M., Pahr, D. H., Hublin, J. J., & Kivell, T. L. (2018b). Systemic patterns of trabecular bone across the human and chimpanzee skeleton. *Journal of Anatomy, 232*, 641-656.

Turnquist, J. E., & Hong, N. (1995). Functional morphology. In *Nonhuman Primates in Biomedical Research*, 49-76. Academic Press.

Turner, C. H., Hsieh, Y. F., Müller, R., Bouxsein, M. L., Baylink, D. J., Rosen, C. J., ... & Beamer, W. G. (2000). Genetic regulation of cortical and trabecular bone strength and microstructure in inbred strains of mice. *Journal of Bone and Mineral Research, 15*, 1126-1131.

Tuttle, R. H. (1969). Knuckle-Walking and the Problem of Human Origins: Studies on the hands of great apes and man lead to reevaluation of theories on hominoid evolution. *Science, 166*, 953-961.

Tuttle, R. H. (1981). Evolution of hominid bipedalism and prehensile capabilities. *Philosophical Transactions of the Royal Society of London. B, Biological Sciences, 292*, 89-94.

Tuttle, R., Butzer, K. W., & Blumenberg, B. (1974). Darwin's apes, dental apes, and the descent of man: normal science in evolutionary anthropology. *Current Anthropology, 15*, 389-426.

Tuttle, R.H., Cortright, W. (1988). Positional behaviour, adaptive complexes, and evolution. In: Schwartz, J. H., (eds.) *Orangutan Biology. Oxford: Oxford University Press*, 311-330.

Tward, D. J., & Siewerdsen, J. H. (2009). Noise aliasing and the 3D NEQ of flat-panel cone-beam CT: Effect of 2D/3D apertures and sampling. *Medical Physics*, *36*, 3830–3843.

Uhthoff, H. K., Poitras, P., & Backman, D. S. (2006). Internal plate fixation of fractures: short history and recent developments. *Journal of Orthopaedic Science, 11*, 118-126.

Van den Noort, J. C., Schaffers, I., Snijders, J., & Harlaar, J. (2013). The effectiveness of voluntary modifications of gait pattern to reduce the knee adduction moment. *Human Movement Science, 32*, 412-424.

Van Heteren, A. H. (2012). The hominins of Flores: Insular adaptations of the lower body. *Comptes Rendus Palevol*, *11*, 169-179.

Van Rietbergen, B., Müller, R., Ulrich, D., Rüegsegger, P., & Huiskes, R. (1999). Tissue stresses and strain in trabeculae of a canine proximal femur can be quantified from computer reconstructions. *Journal of Biomechanics, 32*, 165-173.

Van Rietbergen, B., Odgaard, A., Kabel, J., & Huiskes, R. (1998). Relationships between bone morphology and bone elastic properties can be accurately quantified using high-resolution computer reconstructions. *Journal of Orthopaedic Research, 16*, 23-28.

Vásárhelyi, L., Kónya, Z., Kukovecz, Á., & Vajtai, R. (2020). Microcomputed tomography–based characterization of advanced materials: a review. *Materials Today Advances*, *8*, 100084.

Venkadesan, M., Yawar, A., Eng, C. M., Matson, A., & Bandi, M. M. (2020). The evolutionary biomechanics of the human knee. *Journal of Experimental Biology*, *223*, jeb217083.

Vereecke, E. E., D'Août, K., & Aerts, P. (2011). Studying captive ape locomotion: past, present, and future. *Primate Locomotion: Linking Field and Laboratory Research*, 29-46.

Visser, J. J., Hoogkamer, J. E., Bobbert, M. F., & Huijing, P. A. (1990). Length and moment arm of human leg muscles as a function of knee and hip-joint angles. *European Journal of Applied Physiology and Occupational Physiology*, *61*, 453-460.

Volpato, V., Viola, T. B., Nakatsukasa, M., Bondioli, L., & Macchiarelli, R. (2008). Textural characteristics of the iliac-femoral trabecular pattern in a bipedally trained Japanese macaque. *Primates*, *49*, 16-25.

Vrba, E. S. (1979). A new study of the scapula of *Australopithecus africanus* from Sterkfontein. *American Journal of Physical Anthropology*, *51*, 117-129.

Wallace, I. J., Kwaczala, A. T., Judex, S., Demes, B., & Carlson, K. J. (2013). Physical activity engendering loads from diverse directions augments the growing skeleton. *Journal of Musculoskelet Neuronal Interact*, *13*, 283-8.

Wallace, I. J., Demes, B., & Judex, S. (2017). 10 Ontogenetic and Genetic Influences on Bone's Responsiveness to Mechanical Signals. *Building Bones: Bone Formation and Development in Anthropology*, *77*, 233.

Wang, S. (2022). Biomechanical analysis of the human knee joint. *Journal of Healthcare Engineering*, *2022*, 9365362.

Wang, W. J., Crompton, R. H., Li, Y., & Gunther, M. M. (2003). Energy transformation during erect and 'bent-hip, bent-knee'walking by humans with implications for the evolution of bipedalism. *Journal of Human Evolution*, *44*, 563-579.

Wang, Y., Fan, Y., & Zhang, M. (2014). Comparison of stress on knee cartilage during kneeling and standing using finite element models. *Medical Engineering & Physics*, *36*, 439-447.

Wanner, J. A. (1977). Variations in the anterior patellar groove of the human femur. *American Journal of Physical Anthropology*, *47*, 99-102.

Ward, C. V. (2002). Interpreting the posture and locomotion of *Australopithecus afarensis*: where do we stand? *American Journal of Physical Anthropology*, *119*, 185-215.

Ward, C. V. (2013). Postural and locomotor adaptations of *Australopithecus* species. *The Paleobiology of Australopithecus*, 235-245.

Ward, C. V., Kimbel, W. H., & Johanson, D. C. (2011). Complete fourth metatarsal and arches in the foot of *Australopithecus afarensis*. *Science, 331*, 750-753.

Ward, C. V., Leakey, M. G., Brown, B., Brown, F., Harris, J., & Walker, A. (1999). South Turkwel: a new Pliocene hominid site in Kenya. *Journal of Human Evolution, 36*, 69-95.

Ward, C. V., Tocheri, M. W., Plavcan, J. M., Brown, F. H., & Manthi, F. K. (2014). Early Pleistocene third metacarpal from Kenya and the evolution of modern human-like hand morphology. *Proceedings of the National Academy of Sciences, 111*, 121-124.

Washburn, S. L. (1967). Behaviour and the origin of man. *Proceedings of the Royal Anthropological Institute of Great Britain and Ireland, 1967*, 21-27.

Watson, J., Payne, R., Chamberlain, A., Jones, R., & Sellers, W. I. (2009). The kinematics of load carrying in humans and great apes: implications for the evolution of human bipedalism. *Folia Primatologica, 80*, 309-328.

Weber, D. R., & Zemel, B. S. (2011). Bone health in childhood chronic disease: A practical guide to assessment and treatment. *Frontiers in Endocrinology, 2*, 42.

White, T. D., Asfaw, B., Beyene, Y., Haile-Selassie, Y., Lovejoy, C. O., Suwa, G., & WoldeGabriel, G. (2009). *Ardipithecus ramidus* and the paleobiology of early hominids. *Science, 326*, 64-86.

White, T. D., & Suwa, G. (1987). Hominid footprints at Laetoli: facts and interpretations. *American Journal of Physical Anthropology, 72*, 485-514.

Whitehouse, W. J., & Dyson, E. D. (1974). Scanning electron microscope studies of trabecular bone in the proximal end of the human femur. *Journal of Anatomy, 118*, 417.

Wickham, H., & Wickham, H. (2016). Data analysis. *Springer International Publishing*, 189-201.

Williams, M., Zalasiewicz, J. A., Waters, C. N., & Landing, E. (2014). Is the fossil record of complex animal behaviour a stratigraphical analogue for the Anthropocene? *Geological Society, London, Special Publications, 395*, 143-148.

Wolpoff, M. H., Senut, B., Pickford, M., & Hawks, J. (2002). *Sahelanthropus* or '*Sahelpithecus*'? *Nature*, *419*, 581-582.

Wood, B., & Collard, M. (1999). The human genus. *Science*, *284*, 65-71.

Wroe, S., Parr, W. C., Ledogar, J. A., Bourke, J., Evans, S. P., Fiorenza, L., ... & Yokley, T. R. (2018). Computer simulations show that Neanderthal facial morphology represents adaptation to cold and high energy demands, but not heavy biting. *Proceedings of the Royal Society B: Biological Sciences*, *285*, 20180085.

Wund, M.A. (2012). Assessing the impacts of phenotypic plasticity on evolution. *Integrative and Comparatove Biology, 52*, 5–15.

Yeni, Y. N., Brown, C. U., Wang, Z., & Norman, T. L. (1997). The influence of bone morphology on fracture toughness of the human femur and tibia. *Bone*, *21*, 453-459.

Zaharie, D. T., & Phillips, A. T. (2018). Pelvic construct prediction of trabecular and cortical bone structural architecture. *Journal of Biomechanical Engineering*, *140*, 091001.

Zhang, L. Q., & Wang, G. (2001). Dynamic and static control of the human knee joint in abduction–adduction. *Journal of Biomechanics, 34*, 1107-1115.

Zheng, N., Fleisig, G. S., Escamilla, R. F., & Barrentine, S. W. (1998). An analytical model of the knee for estimation of internal forces during exercise. *Journal of Biomechanics*, *31*, 963-967.

Zihlman, A. L., Mcfarland, R. K., & Underwood, C. E. (2011). Functional anatomy and adaptation of male gorillas (*Gorilla gorilla gorilla*) with comparison to male orangutans (*Pongo pygmaeus*). *The Anatomical Record: Advances in Integrative Anatomy and Evolutionary Biology*, *294*, 1842-1855.

Zipfel, B., & Berger, L. R. (2009). Partial hominin tibia (StW 396) from Sterkfontein, South Africa. *Palaeontologia Africana*, *44*, 71-75.

Zipfel, B., DeSilva, J. M., Kidd, R. S., Carlson, K. J., Churchill, S. E., & Berger, L. R. (2011). The foot and ankle of *Australopithecus sediba*. *Science*, *333*, 1417-1420.

Zollikofer, C. P., Ponce de León, M. S., Lieberman, D. E., Guy, F., Pilbeam, D., Likius, A., ... & Brunet, M. (2005). Virtual cranial reconstruction of *Sahelanthropus tchadensis*. *Nature*, *434*, 755-759.

Zysset, P. K. (2003). A review of morphology–elasticity relationships in human trabecular bone: theories and experiments. *Journal of Biomechanics*, *36*, 1469-1485.

Appendix A: Sample composition

Table A1: Detailed information of sample composition.

taxonomy	specimen	ontoitem	side	voxel size (mm)	sex	age	dated	curatorial institution
Homo sapiens	UT-15_08D	distal femur	R	0.037	N/A	adult	1.0 kya - present	University of Tennessee, US
Homo sapiens	UT-93_06D	distal femur	R	0.036	N/A	adult	1.0 kya - present	University of Tennessee, US
Homo sapiens	UT_8_92D	distal femur	R	0.037	N/A	adult	1.0 kya - present	University of Tennessee, US
Homo sapiens	UT_40_08D	distal femur	R	0.037	N/A	adult	1.0 kya - present	University of Tennessee, US
Homo sapiens	UT_50_07_D	distal femur	R	0.037	N/A	adult	1.0 kya - present	University of Tennessee, US
Homo sapiens	UT_38_05_D	distal femur	R	0.037	N/A	adult	1.0 kya - present	University of Tennessee, US
Homo sapiens	UT_82_07D	distal femur	R	0.037	N/A	adult	1.0 kya - present	University of Tennessee, US
Homo sapiens	UT-1_86A	distal femur	R	0.037	N/A	adult	1.0 kya - present	University of Tennessee, US
Homo sapiens	UT-2_86D	distal femur	R	0.036	N/A	adult	1.0 kya - present	University of Tennessee, US
Homo sapiens	UT-99_06	distal femur	R	0.037	N/A	adult	1.0 kya - present	University of Tennessee, US
Homo sapiens	UT-45_06	distal femur	R	0.037	N/A	adult	1.0 kya - present	University of Tennessee, US
Homo sapiens	UT_47_06D	distal femur	R	0.037	N/A	adult	1.0 kya - present	University of Tennessee, US
Homo sapiens	NGA-88_SK-766	distal femur	R	0.030	M	adult	1.0 kya - present	University of Kent, Canterbury, UK
Homo sapiens	NGA-88_SK-911	distal femur	R	0.030	F	adult	1.0 kya - present	University of Kent, Canterbury, UK
Homo sapiens	NGB-89_SK-15	distal femur	R	0.030	N/A	adult	1.0 kya - present	University of Kent, Canterbury, UK
Homo sapiens	MRT_FCS73	distal femur	R	0.046	M	adult	1.0 kya - present	Mary Rose Trust, Portsmouth, UK
Homo sapiens	MRT_FCS52	distal femur	R	0.040	M	adult	1.0 kya - present	Mary Rose Trust, Portsmouth, UK
Homo sapiens	MRT_FCS47	distal femur	R	0.043	M	adult	1.0 kya - present	Mary Rose Trust, Portsmouth, UK
Homo sapiens	MRT_FCS26	distal femur	R	0.040	M	adult	1.0 kya - present	Mary Rose Trust, Portsmouth, UK
Homo sapiens	MRT_FCS79	distal femur	R	0.039	M	adult	1.0 kya - present	Mary Rose Trust, Portsmouth, UK
Homo sapiens	MRT_FCS35	distal femur	R	0.040	M	adult	1.0 kya - present	Mary Rose Trust, Portsmouth, UK
Homo sapiens	MRT_FCS50	distal femur	R	0.043	M	adult	1.0 kya - present	Mary Rose Trust, Portsmouth, UK
Homo sapiens	MRT_FCS8	distal femur	R	0.041	M	adult	1.0 kya - present	Mary Rose Trust, Portsmouth, UK

Homo sapiens	MRT_FCS11	distal femur	R	0.041	M	adult	1.0 kya - present	Mary Rose Trust, Portsmouth, UK
Homo sapiens	MRT_FCS40	distal femur	R	0.039	M	adult	1.0 kya - present	Mary Rose Trust, Portsmouth, UK
Homo sapiens	MRT_FCS6	distal femur	R	0.052	M	adult	1.0 kya - present	Mary Rose Trust, Portsmouth, UK
Pan troglodytes verus	MPITC_11785	distal femur	R	0.030	M	adult	1.0 kya - present	Max Planck Institute for Evolutionary Anthropology, Leipzig, Germany
Pan troglodytes verus	MPITC_15012	distal femur	R	0.030	M	adult	1.0 kya - present	Max Planck Institute for Evolutionary Anthropology, Leipzig, Germany
Pan troglodytes verus	MPITC_11781	distal femur	R	0.030	M	adult	1.0 kya - present	Max Planck Institute for Evolutionary Anthropology, Leipzig, Germany
Pan troglodytes verus	MPITC_15014	distal femur	R	0.030	M	adult	1.0 kya - present	Max Planck Institute for Evolutionary Anthropology, Leipzig, Germany
Pan troglodytes verus	MPITC_15004	distal femur	R	0.030	F	adult	1.0 kya - present	Max Planck Institute for Evolutionary Anthropology, Leipzig, Germany
Pan troglodytes verus	MPITC_15013	distal femur	R	0.030	F	adult	1.0 kya - present	Max Planck Institute for Evolutionary Anthropology, Leipzig, Germany
Pan troglodytes verus	MPITC_15023	distal femur	R	0.030	F	adult	1.0 kya - present	Max Planck Institute for Evolutionary Anthropology, Leipzig, Germany
Pan troglodytes verus	MPITC_11778	distal femur	R	0.030	F	adult	1.0 kya - present	Max Planck Institute for Evolutionary Anthropology, Leipzig, Germany
Pan troglodytes verus	MPITC_11793	distal femur	R	0.029	M	adult	1.0 kya - present	Max Planck Institute for Evolutionary Anthropology, Leipzig, Germany
Pan troglodytes verus	MPITC_15019	distal femur	R	0.030	M	adult	1.0 kya - present	Max Planck Institute for Evolutionary Anthropology, Leipzig, Germany
Pan troglodytes verus	MPITC_11786	distal femur	R	0.030	F	adult	1.0 kya - present	Max Planck Institute for Evolutionary Anthropology, Leipzig, Germany
Pan troglodytes verus	MPITC_15001	distal femur	R	0.030	F	adult	1.0 kya - present	Max Planck Institute for Evolutionary Anthropology, Leipzig, Germany
Pan troglodytes verus	USNM_220063	distal femur	L	0.030	F	adult	1.0 kya - present	Smithsonian National Museum of Natural History, US
Pan troglodytes verus	USNM_220064	distal femur	R	0.030	F	adult	1.0 kya - present	Smithsonian National Museum of Natural History, US
Pan troglodytes verus	USNM_176228	distal femur	L	0.030	M	adult	1.0 kya - present	Smithsonian National Museum of Natural History, US
Gorilla gorilla gorilla	PC_MER_96	distal femur	L	0.058	F	adult	1.0 kya - present	Powell-Cotton Museum, Birchington-on-Sea, UK
Gorilla gorilla gorilla	PC_MER_372	distal femur	R	0.063	M	adult	1.0 kya - present	Powell-Cotton Museum, Birchington-on-Sea, UK

Gorilla gorilla gorilla	PC_MER_329	distal femur	L	0.058	F	adult	1.0 kya - present	Powell-Cotton Museum, Birchington-on-Sea, UK
Gorilla gorilla gorilla	PC_MER_720	distal femur	R	0.058	M	adult	1.0 kya - present	Powell-Cotton Museum, Birchington-on-Sea, UK
Gorilla gorilla gorilla	PC_MER_840	distal femur	L	0.058	F	adult	1.0 kya - present	Powell-Cotton Museum, Birchington-on-Sea, UK
Gorilla gorilla gorilla	PC_MER_95	distal femur	L	0.053	F	adult	1.0 kya - present	Powell-Cotton Museum, Birchington-on-Sea, UK
Gorilla gorilla gorilla	PC_MER_135	distal femur	R	0.057	M	adult	1.0 kya - present	Powell-Cotton Museum, Birchington-on-Sea, UK
Gorilla gorilla gorilla	PC_MER_264	distal femur	L	0.058	M	adult	1.0 kya - present	Powell-Cotton Museum, Birchington-on-Sea, UK
Gorilla gorilla gorilla	PC_MER_300	distal femur	R	0.052	F	adult	1.0 kya - present	Powell-Cotton Museum, Birchington-on-Sea, UK
Gorilla gorilla gorilla	PC_MER_729	distal femur	R	0.057	M	adult	1.0 kya - present	Powell-Cotton Museum, Birchington-on-Sea, UK
Gorilla gorilla gorilla	PC_MER_798	distal femur	L	0.048	F	adult	1.0 kya - present	Powell-Cotton Museum, Birchington-on-Sea, UK
Gorilla gorilla gorilla	PC_MER_856	distal femur	R	0.049	F	adult	1.0 kya - present	Powell-Cotton Museum, Birchington-on-Sea, UK
Gorilla gorilla gorilla	PC_CAMI_106	distal femur	L	0.089	M	adult	1.0 kya - present	Powell-Cotton Museum, Birchington-on-Sea, UK
Gorilla gorilla gorilla	PC_FC_123	distal femur	L	0.058	M	adult	1.0 kya - present	Powell-Cotton Museum, Birchington-on-Sea, UK
Pongo pygmaeus pygmaeus	ZSM_1909_0801	distal femur	R	0.029	F	adult	1.0 kya - present	Bavarian State Collection of Zoology, Munich, Germany
Pongo pygmaeus pygmaeus	ZSM_1907_0331	distal femur	L	0.028	F	adult	1.0 kya - present	Bavarian State Collection of Zoology, Munich, Germany
Pongo pygmaeus pygmaeus	ZSM_1907_0483	distal femur	L	0.028	F	adult	1.0 kya - present	Bavarian State Collection of Zoology, Munich, Germany
Pongo pygmaeus pygmaeus	ZSM_1955_0228	distal femur	L	0.028	F	adult	1.0 kya - present	Bavarian State Collection of Zoology, Munich, Germany
Pongo sp.	ZSM_1982_0092	distal femur	R	0.028	F	adult	1.0 kya - present	Bavarian State Collection of Zoology, Munich, Germany
Pongo pygmaeus pygmaeus	ZSM_1907_0633b	distal femur	R	0.028	F	adult	1.0 kya - present	Bavarian State Collection of Zoology, Munich, Germany
Pongo abelii	ZSM_1973_0270	distal femur	R	0.028	F	adult	1.0 kya - present	Bavarian State Collection of Zoology, Munich, Germany

Pongo pygmaeus pygmaeus	ZSM_1966_0203	distal femur	R	0.029	M	adult	1.0 kya - present	Bavarian State Collection of Zoology, Munich, Germany
Pongo pygmaeus pygmaeus	ZMB_MAN_83213	distal femur	R	0.029	M	adult	1.0 kya - present	Natural History Museum, Berlin, Germany
Homo sapiens	GAUG-Inden_101	proximal tibia	R	0.036	F	adult	1.0 kya - present	University of Göttingen, Göttingen, Germany
Homo sapiens	GAUG-Inden_113	proximal tibia	L	0.036	M	adult	1.0 kya - present	University of Göttingen, Göttingen, Germany
Homo sapiens	GAUG-Inden_117	proximal tibia	L	0.036	M	adult	1.0 kya - present	University of Göttingen, Göttingen, Germany
Homo sapiens	GAUG-Inden_118	proximal tibia	R	0.036	F	adult	1.0 kya - present	University of Göttingen, Göttingen, Germany
Homo sapiens	GAUG-Inden_166	proximal tibia	R	0.036	M	adult	1.0 kya - present	University of Göttingen, Göttingen, Germany
Homo sapiens	GAUG-Inden_243	proximal tibia	R	0.036	M	adult	1.0 kya - present	University of Göttingen, Göttingen, Germany
Homo sapiens	GAUG-Inden_311	proximal tibia	L	0.036	M	adult	1.0 kya - present	University of Göttingen, Göttingen, Germany
Homo sapiens	GAUG-Inden_91	proximal tibia	R	0.036	M	adult	1.0 kya - present	University of Göttingen, Göttingen, Germany
Homo sapiens	GAUG-Inden_93	proximal tibia	R	0.036	F	adult	1.0 kya - present	University of Göttingen, Göttingen, Germany
Homo sapiens	NGA-88_SK-1047	proximal tibia	R	0.030	F	adult	1.0 kya - present	University of Kent, Canterbury, UK
Homo sapiens	NGA-88_SK-766	proximal tibia	R	0.030	M	adult	1.0 kya - present	University of Kent, Canterbury, UK
Homo sapiens	NGA-88_SK-825	proximal tibia	L	0.030	F	adult	1.0 kya - present	University of Kent, Canterbury, UK
Homo sapiens	NGA-88_SK-880	proximal tibia	L	0.030	M	adult	1.0 kya - present	University of Kent, Canterbury, UK
Homo sapiens	NGA-88_SK-911	proximal tibia	L	0.030	F	adult	1.0 kya - present	University of Kent, Canterbury, UK
Homo sapiens	NGB-89_SK-15	proximal tibia	R	0.036	N/A	adult	1.0 kya - present	University of Kent, Canterbury, UK
Homo sapiens	MRT_FCS73	proximal tibia	R	0.038	M	adult	1.0 kya - present	Mary Rose Trust, Portsmouth, UK
Homo sapiens	MRT_FCS47	proximal tibia	L	0.036	M	adult	1.0 kya - present	Mary Rose Trust, Portsmouth, UK
Homo sapiens	MRT_FCS26	proximal tibia	L	0.036	M	adult	1.0 kya - present	Mary Rose Trust, Portsmouth, UK
Homo sapiens	MRT_FCS79	proximal tibia	R	0.035	M	adult	1.0 kya - present	Mary Rose Trust, Portsmouth, UK
Homo sapiens	MRT_FCS35	proximal tibia	L	0.038	M	adult	1.0 kya - present	Mary Rose Trust, Portsmouth, UK
Homo sapiens	MRT_FCS50	proximal tibia	L	0.033	M	adult	1.0 kya - present	Mary Rose Trust, Portsmouth, UK
Homo sapiens	MRT_FCS8	proximal tibia	L	0.038	M	adult	1.0 kya - present	Mary Rose Trust, Portsmouth, UK
Homo sapiens	MRT_FCS11	proximal tibia	L	0.034	M	adult	1.0 kya - present	Mary Rose Trust, Portsmouth, UK
Homo sapiens	MRT_FCS40	proximal tibia	L	0.034	M	adult	1.0 kya - present	Mary Rose Trust, Portsmouth, UK
Homo sapiens	MRT_FCS6	proximal tibia	R	0.038	M	adult	1.0 kya - present	Mary Rose Trust, Portsmouth, UK

Pan troglodytes verus	MPITC_15001	proximal tibia	R	0.030	F	adult	1.0 kya - present	Max Planck Institute for Evolutionary Anthropology, Leipzig, Germany
Pan troglodytes verus	MPITC_11778	proximal tibia	R	0.030	F	adult	1.0 kya - present	Max Planck Institute for Evolutionary Anthropology, Leipzig, Germany
Pan troglodytes verus	MPITC_11781	proximal tibia	R	0.030	M	adult	1.0 kya - present	Max Planck Institute for Evolutionary Anthropology, Leipzig, Germany
Pan troglodytes verus	MPITC_11785	proximal tibia	R	0.030	M	adult	1.0 kya - present	Max Planck Institute for Evolutionary Anthropology, Leipzig, Germany
Pan troglodytes verus	MPITC_11786	proximal tibia	R	0.030	F	adult	1.0 kya - present	Max Planck Institute for Evolutionary Anthropology, Leipzig, Germany
Pan troglodytes verus	MPITC_11793	proximal tibia	R	0.030	M	adult	1.0 kya - present	Max Planck Institute for Evolutionary Anthropology, Leipzig, Germany
Pan troglodytes verus	MPITC_15012	proximal tibia	R	0.030	M	adult	1.0 kya - present	Max Planck Institute for Evolutionary Anthropology, Leipzig, Germany
Pan troglodytes verus	MPITC_15013	proximal tibia	R	0.030	F	adult	1.0 kya - present	Max Planck Institute for Evolutionary Anthropology, Leipzig, Germany
Pan troglodytes verus	MPITC_15014	proximal tibia	R	0.030	M	adult	1.0 kya - present	Max Planck Institute for Evolutionary Anthropology, Leipzig, Germany
Pan troglodytes verus	MPITC_15019	proximal tibia	R	0.030	M	adult	1.0 kya - present	Max Planck Institute for Evolutionary Anthropology, Leipzig, Germany
Pan troglodytes verus	MPITC_15023	proximal tibia	R	0.030	F	adult	1.0 kya - present	Max Planck Institute for Evolutionary Anthropology, Leipzig, Germany
Pan troglodytes verus	MPITC_15004	proximal tibia	R	0.030	F	adult	1.0 kya - present	Max Planck Institute for Evolutionary Anthropology, Leipzig, Germany
Pan troglodytes verus	MPITC_11775	proximal tibia	R	0.030	F	adult	1.0 kya - present	Max Planck Institute for Evolutionary Anthropology, Leipzig, Germany
Pan troglodytes verus	MPITC_11800	proximal tibia	R	0.030	F	adult	1.0 kya - present	Max Planck Institute for Evolutionary Anthropology, Leipzig, Germany
Pan troglodytes verus	MPITC_14994	proximal tibia	R	0.030	F	adult	1.0 kya - present	Max Planck Institute for Evolutionary Anthropology, Leipzig, Germany
Gorilla gorilla gorilla	PC_CAMI_106	proximal tibia	L	0.050	M	adult	1.0 kya - present	Powell-Cotton Museum, Birchington-on-Sea, UK
Gorilla gorilla gorilla	PC_FC_123	proximal tibia	L	0.063	M	adult	1.0 kya - present	Powell-Cotton Museum, Birchington-on-Sea, UK
Gorilla gorilla gorilla	PC_MER_329	proximal tibia	L	0.058	F	adult	1.0 kya - present	Powell-Cotton Museum, Birchington-on-Sea, UK
Gorilla gorilla gorilla	PC_MER_720	proximal tibia	R	0.056	M	adult	1.0 kya - present	Powell-Cotton Museum, Birchington-on-Sea, UK

Gorilla gorilla gorilla	PC_MER_840	proximal tibia	L	0.055	F	adult	1.0 kya - present	Powell-Cotton Museum, Birchington-on-Sea, UK
Gorilla gorilla gorilla	PC_MER_856	proximal tibia	R	0.034	F	adult	1.0 kya - present	Powell-Cotton Museum, Birchington-on-Sea, UK
Gorilla gorilla gorilla	PC_MER_798	proximal tibia	L	0.034	F	adult	1.0 kya - present	Powell-Cotton Museum, Birchington-on-Sea, UK
Gorilla gorilla gorilla	PC_MER_372	proximal tibia	R	0.043	M	adult	1.0 kya - present	Powell-Cotton Museum, Birchington-on-Sea, UK
Gorilla gorilla gorilla	PC_MER_300	proximal tibia	R	0.043	F	adult	1.0 kya - present	Powell-Cotton Museum, Birchington-on-Sea, UK
Gorilla gorilla gorilla	PC_MER_135	proximal tibia	R	0.045	M	adult	1.0 kya - present	Powell-Cotton Museum, Birchington-on-Sea, UK
Gorilla gorilla gorilla	PC_MER_96	proximal tibia	L	0.040	F	adult	1.0 kya - present	Powell-Cotton Museum, Birchington-on-Sea, UK
Gorilla gorilla gorilla	PC_M36_264	proximal tibia	R	0.050	M	adult	1.0 kya - present	Powell-Cotton Museum, Birchington-on-Sea, UK
Gorilla gorilla gorilla	PC_MER_95	proximal tibia	L	0.038	F	adult	1.0 kya - present	Powell-Cotton Museum, Birchington-on-Sea, UK
Pongo pygmaeus pygmaeus	ZMB_MAN_83213	proximal tibia	L	0.029	M	adult	1.0 kya - present	Natural History Museum, Berlin, Germany
Pongo sp.	ZSM_1982_0092	proximal tibia	R	0.030	F	adult	1.0 kya - present	Bavarian State Collection of Zoology, Munich, Germany
Pongo pygmaeus pygmaeus	ZSM_1907_0633b	proximal tibia	R	0.025	F	adult	1.0 kya - present	Bavarian State Collection of Zoology, Munich, Germany
Pongo pygmaeus pygmaeus	ZSM_1907_0489	proximal tibia	L	0.028	F	adult	1.0 kya - present	Bavarian State Collection of Zoology, Munich, Germany
Pongo pygmaeus pygmaeus	ZSM_1966_0203	proximal tibia	L	0.030	M	adult	1.0 kya - present	Bavarian State Collection of Zoology, Munich, Germany
Pongo abelii	ZSM_1973_0270	proximal tibia	R	0.025	F	adult	1.0 kya - present	Bavarian State Collection of Zoology, Munich, Germany
Pongo pygmaeus pygmaeus	ZSM_1909_0801	proximal tibia	R	0.030	F	adult	1.0 kya - present	Bavarian State Collection of Zoology, Munich, Germany
Australopithecus africanus	STW-318	distal femur	R	0.030	N/A	adult	~1.8-5.0 mya	University of Witwatersrand, Johannesburg, South Africa
Australopithecus africanus	STW-129	distal femur	L	0.030	N/A	subadult	~1.8-5.0 mya	University of Witwatersrand, Johannesburg, South Africa
Australopithecus africanus	TM-1513	distal femur	L	0.036	N/A	adult	~1.8-5.0 mya	University of Witwatersrand, Johannesburg, South Africa

Australopithecus sediba	MH2_U.W. 88-63	distal femur	R	0.060	F	adult	~1.98 mya	University of Witwatersrand, Johannesburg, South Africa
Homo floresiensis	LB1-8	distal femur	R	0.034	F	adult	~100-60 kya	National Archeology Institute, Jakarta, Indonesia
Homo floresiensis	LB1-9	distal femur	L	0.026	F	adult	~100-60 kya	National Archeology Institute, Jakarta, Indonesia
Homo floresiensis	LB1-13	proximal tibia	R	0.028	F	adult	~100-60 kya	National Archeology Institute, Jakarta, Indonesia
Homo floresiensis	LB8-1	proximal tibia	R	0.031	F	adult	~100-60 kya	National Archeology Institute, Jakarta, Indonesia
Homo neanderthalensis	Neanderthal 1_D322-16	distal femur	L	0.038	N/A	adult	~42 kya	State Museum, Bonn, Germany

3

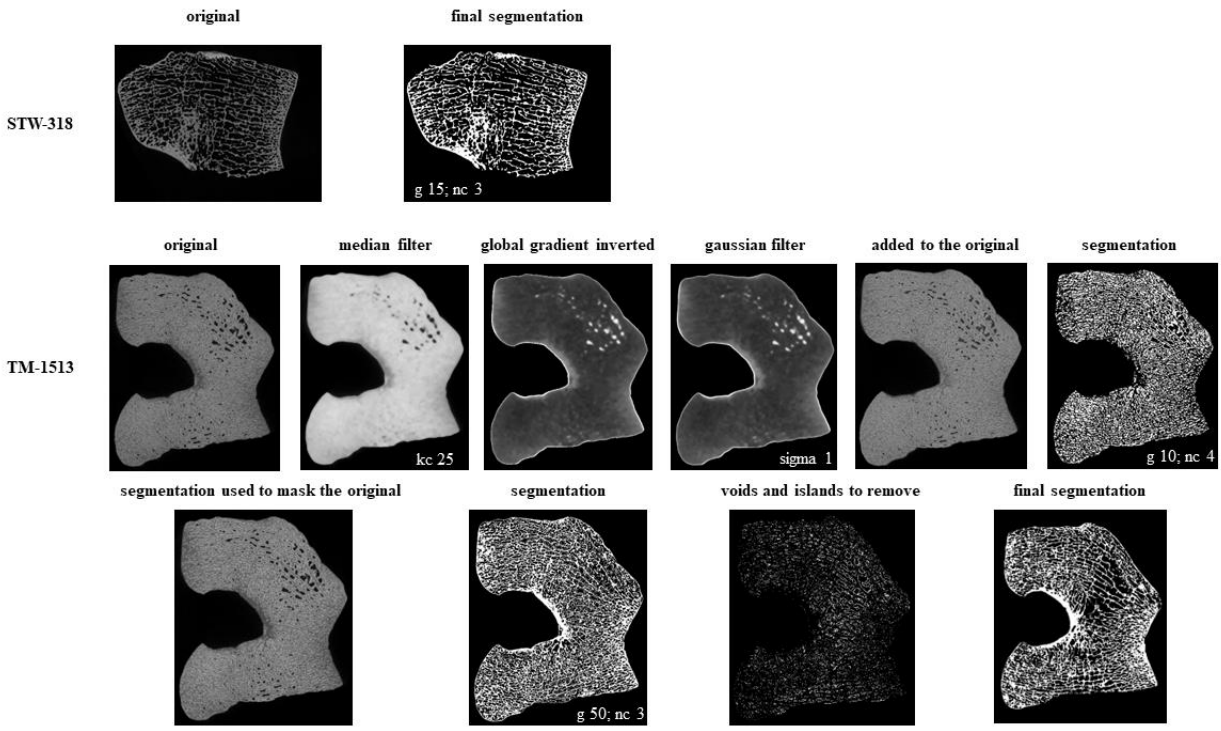

Figure A1: Segmentation steps of *A. africanus* specimens. g; grid size; nc; number of classes; kc; kernel size.

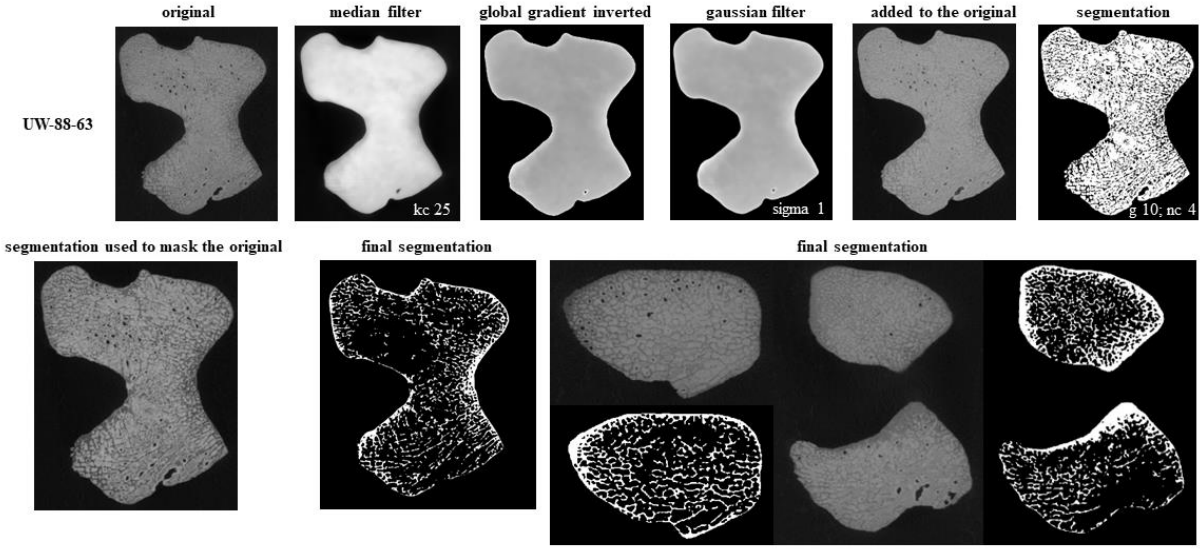

Figure A2: Segmentation steps of *A. sediba* specimen. g; grid size; nc; number of classes; kc; kernel size; L; probability filter. Final segmentation: g 5 --nc=3, L99 + g90, nc3, L80 + g 150 –nc=3, L75. All segmentations were binarized, combined, and manually cleaned in Avizo to ger the final segmentation.

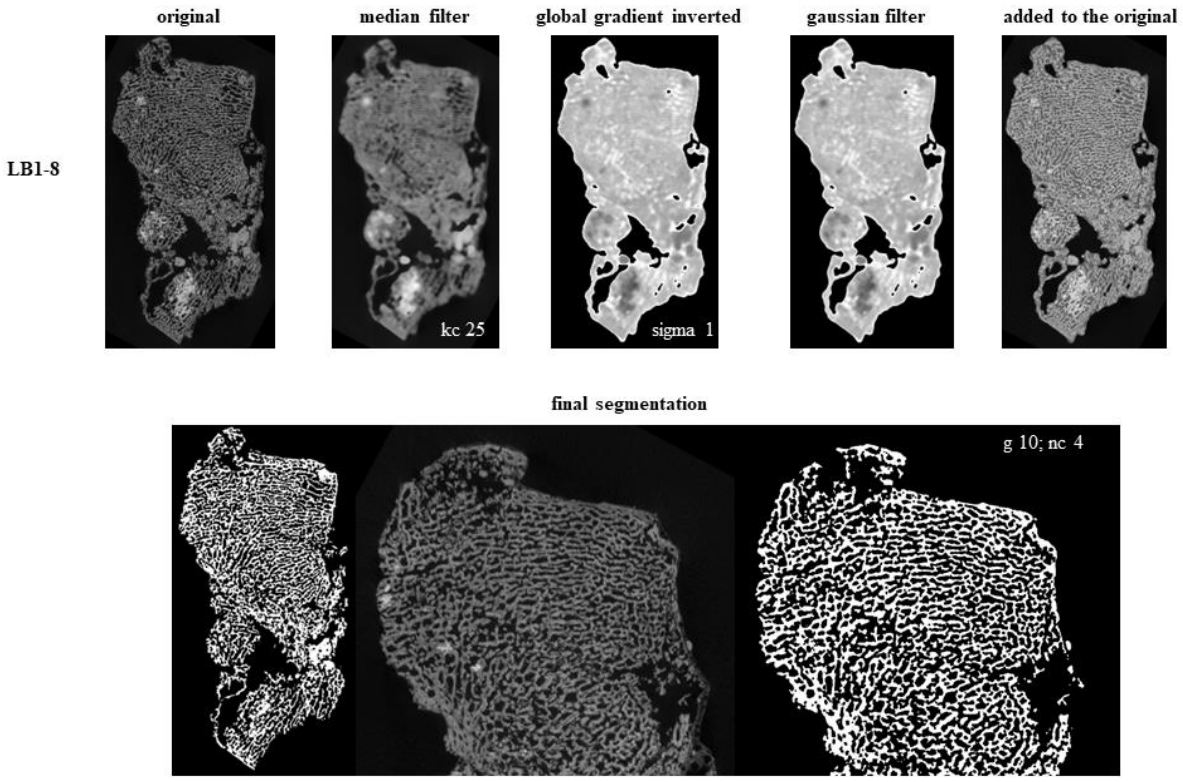

Figure A3: Segmentation steps of *H. floresiensis* specimens. g; grid size; nc; number of classes; kc; kernel size.

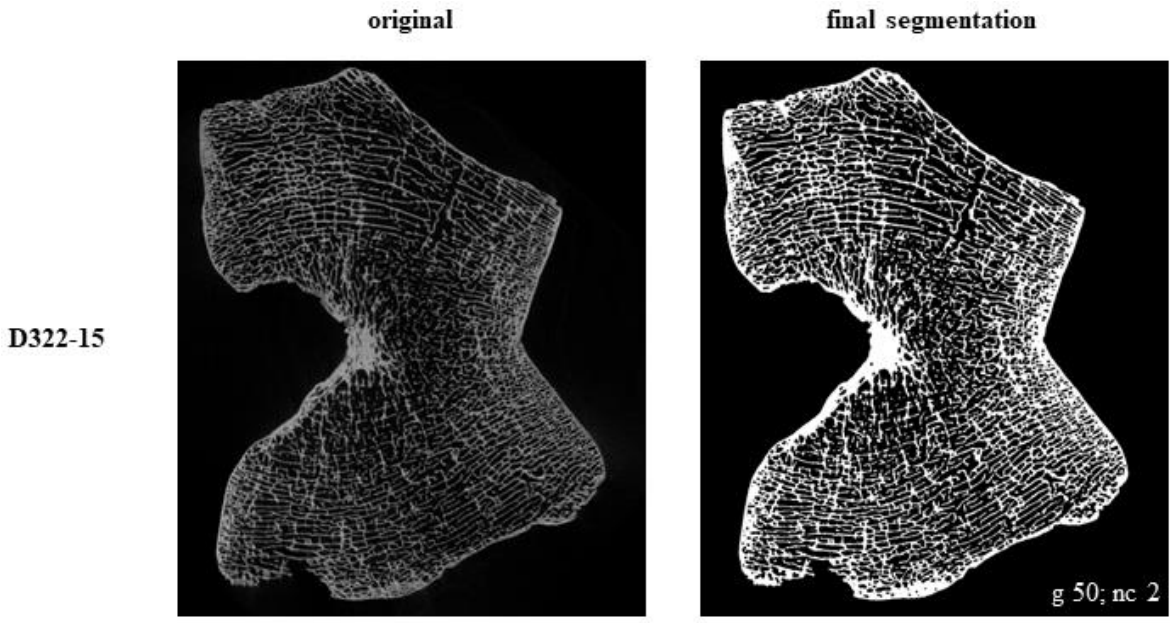

Figure A4: Segmentation steps of *H. neanderthalensis* specimen.

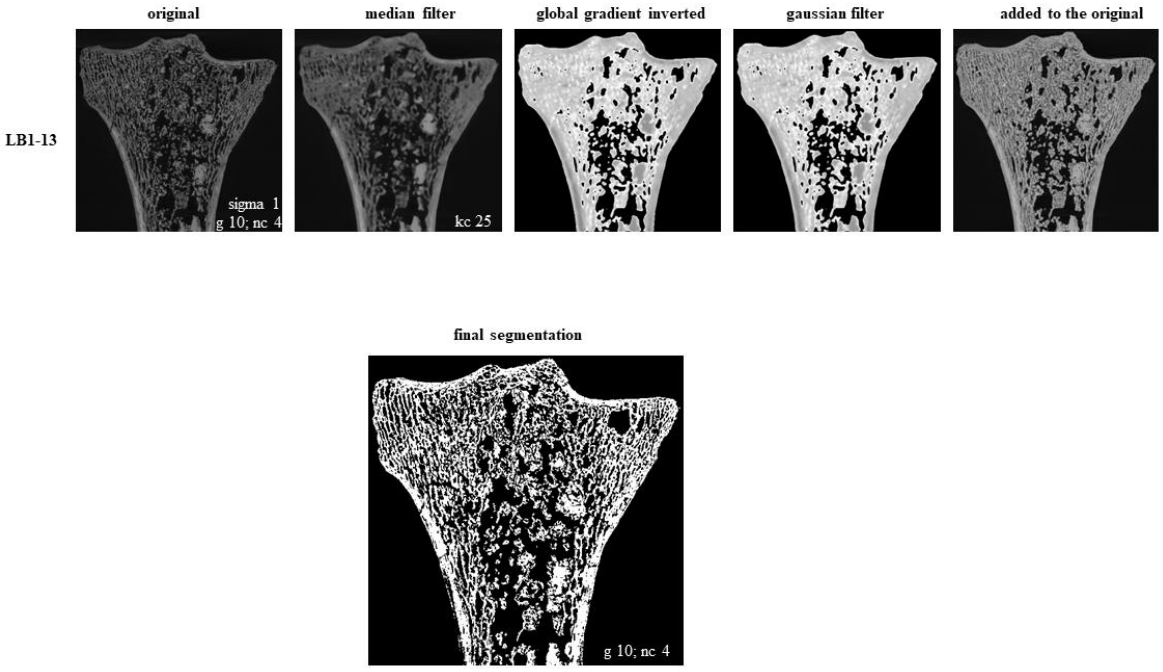

Figure A5: Segmentation steps of *H. floresiensis* specimens. g; grid size; nc; number of classes; kc; kernel size.

Appendix B: Published work

Received: 22 May 2024 | Revised: 12 August 2024 | Accepted: 18 August 2024

DOI: 10.1002/ajpa.25023

TECHNICAL NOTE

AMERICAN JOURNAL OF BIOLOGICAL ANTHROPOLOGY

WILEY

Technical note: Does scan resolution or downsampling impact the analysis of trabecular bone architecture?

Andrea Lukova[1,2] | Christopher J. Dunmore[1] | Zewdi J. Tsegai[3] | Sebastian Bachmann[4] | Alexander Synek[4] | Matthew M. Skinner[2]

[1]Skeletal Biology Research Centre, School of Anthropology and Conservation, University of Kent, Canterbury, UK

[2]Human Origins, Max Planck Institute for Evolutionary Anthropology, Leipzig, Germany

[3]Department of Organismal Biology and Anatomy, University of Chicago, Chicago, Illinois, USA

[4]Computatioal Biomechanics, Institute of Lightweight Design and Structural Biomechanics, Wien, Austria

Correspondence
Andrea Lukova, Max Planck Institute for Evolutionary Anthropology, Leipzig, Germany.
Email: andrea_lukova@eva.mpg.de

Funding information
Marie Skłodowska-Curie Action, Grant/Award Number: 101025719; European Union's Horizon 2020, Grant/Award Number: 819960

Abstract

The "gold standard" for the assessment of trabecular bone structure is high-resolution micro-CT. In this technical note, we test the influence of initial scan resolution and post hoc downsampling on the quantitative and qualitative analysis of trabecular bone in a *Gorilla* tibia. We analyzed trabecular morphology in the right distal tibia of one *Gorilla gorilla* individual to investigate the impact of variation in voxel size on measured trabecular variables. For each version of the micro-CT volume, trabecular bone was segmented using the medical image analysis method. Holistic morphometric analysis was then used to analyze bone volume (BV/TV), anisotropy (DA), trabecular thickness (Tb.Th), spacing (Tb.Sp), and number (Tb.N). Increasing voxel size during initial scanning was found to have a strong impact on DA and Tb.Th measures, while BV/TV, Tb.Sp, and Tb.N were found to be less sensitive to variations in initial scan resolution. All tested parameters were not substantially influenced by downsampling up to 90 µm resolution. Color maps of BV/TV and DA also retained their distribution up to 90 µm. This study is the first to examine the effect of variation in micro-CT voxel size on the analysis of trabecular bone structure using whole epiphysis approaches. Our results indicate that microstructural variables may be measured for most trabecular parameters up to a voxel size of 90 µm for both scan and downsampled resolutions. Moreover, if only BV/TV, Tb.Sp or Tb.N is measured, even larger voxel sizes might be used without substantially affecting the results.

KEYWORDS
anisotropy, bone volume, resolution, trabecular bone, trabecular number, trabecular spacing, trabecular thickness, voxel size

1 | INTRODUCTION

Trabecular bone is a porous tissue found in the epiphyses of long, short, and irregular bones (Keaveny et al., 2001). Although the structure of trabecular bone is partially genetically determined (Loewen et al., 2016; Paternoster et al., 2013; Turner et al., 2000), (re)modeling is at its peak during growth and gradually declines into adulthood (Glatt et al., 2007; Halloran et al., 2002; Saers et al., 2020; Seeman, 2003; Su et al., 2013). Trabecular bone tissue is thought to respond to biomechanical forces and functionally adapt to its mechanical environment (Ruff et al., 2006). In places where incurred load is lower, there is thought to be a reduction in the amount of trabecular

bone, resulting in a weaker structure (Schulte et al., 2013). Conversely, in places where stress is higher, there should be an increase in trabecular tissue, resulting in a stronger bone structure (Barak et al., 2011; Pontzer et al., 2006; Schulte et al., 2013; Sinclair et al., 2013). These changes in trabecular bone architecture can include the thickness of trabecular struts, their spacing, and their orientation. Therefore, analysis of trabecular structure can provide insights into the biomechanical loads incurred by bones during life. It can be used to understand the skeletal morphology of living taxa and reconstruct behavior in fossil taxa (Kivell, 2016; Komza, & Skinner, 2019; Ryan & Shaw, 2012; Saers et al., 2020).

The traditional method of analyzing trabecular structure in 3D is to quantify trabecular bone in a volume of interest (VOI). The main advantage of the VOI method is that it allows for the extraction and quantification of a portion of a complex structure from a much larger micro-CT data set. However, defining a homologous VOI, both its size and location, is far from straightforward, especially across taxa and/or an ontogenetic series where there can be substantial differences in both size and morphology (Gross et al., 2014; Kivell et al., 2011; Lazenby et al., 2011). Moreover, the region of trabecular structure that differs most amongst the study sample could be outside of the VOI region when determined a priori. More recently, several studies have placed multiple VOIs throughout an anatomical region, revealing the presence of regional differences in trabecular bone structsure (DeSilva & Devlin, 2012; Griffin, 2018; Su et al., 2013). Some studies used geometric morphometrics (GM), where sliding semilandmarks are used to define homologous locations across surfaces in order to place multiple VOIs, to assess trabecular variation beneath the articular surfaces of the talus and distal femur (Sylvester & Terhune, 2017), in the metacarpals (e.g., Dunmore et al., 2019; Dunmore, Bardo, Skinner, & Kivell, Dunmore, Bardo, et al., 2020) and in the proximal femur (Georgiou et al., 2020). Furthermore, a method originally developed for finite-element material-mapping (Pahr & Zysset, 2009), has been adapted for analyses of high-resolution trabecular bone across primates (Gross et al., 2014; Tsegai et al., 2013). Holistic morphometric analysis (HMA) quantifies trabecular morphology through the entire epiphysis rather than in one or a few sub-surface VOIs. Recently, Bachmann et al. (2022), developed HMA with a canonical holistic approach (cHMA), which allows for statistical comparisons of trabecular patterns between groups, free of a priori subsampling, by calculating mean models that contain homologous spatial units of analysis.

Studies of trabecular bone architecture often analyze scans with different resolutions across the studied species and/or individuals (Cazenave et al., 2019; Georgiou et al., 2018; Lukova et al., 2024; Sylvester & Terhune, 2017). This can be due to collection of micro-CT scans by different researchers with different protocols, due to specimen size limiting resolution on different CT systems, or scans may be downsampled (i.e., process of reducing the resolution or dimensions of a digital image by decreasing the number of pixels in the image) after collection due to the computational limitations of processing large datasets. Previous studies have shown that downsampling can impact the accuracy and precision of measurements of trabecular architecture. For example, trabecular thickness (Tb.Th) (Isaksson et al., 2011; Kothari et al., 1998; Majumdar et al., 1996; Muller et al., 1996; Sode et al., 2008) or measures of anisotropy can be highly sensitive to voxel size (Isaksson et al., 2011; Kothari et al., 1998; Sode et al., 2008). In general, it is expected that lower resolutions (the lower resolution the larger voxel size) create blur in the scan images making some features hard to segment and may lead to loss of thin trabeculae, that is, if the feature is smaller than the voxel size it may well be averaged out in favor of another phase such as background (partial volume averaging). Majumdar et al. (1996) showed that Tb.Th tends to be increasingly overestimated at lower resolutions when analyzing magnetic resonance (MR) and micro-CT images. Similarly, Müller et al. (1996) found that trabecular spacing and number can be precisely measured at resolutions up to 175 µm, however, Tb.Th required a much higher resolution for accurate assessment. Moreover, Isaksson et al. (2011), using micro-CT scans, found that with decreasing resolution, the originally detected differences between normal and osteoporotic groups diminished. Kim et al. (2004) used three different scanning and voxel sizes a high-resolution voxel size (21 µm), a commonly used intermediate voxel size (50 µm), and a voxel size applicable to scans of whole human vertebral bodies (110 µm) to examine the effect of voxel size on stereological measures of human trabecular bone. They found that the error in stereological parameters ranged from 0.1% to 102% depending on the voxel size analyzed. Peyrin et al. (1998) examined a series of vertebral samples with voxel sizes of 1.4, 6.7, and 14 µm. They concluded that voxel sizes as large as 14 µm provide a reasonably accurate measurement of trabecular architecture. Christiansen (2016) investigated micro-CT scans of mouse trabecular bone measures with voxel sixes at 6–30 µm. They demonstrated that voxel size strongly affects connectivity density and Tb.Th. All these studies suggest that high resolution scans should be used, when possible, to accurately measure trabecular bone microstructure.

In this study, we test the impact of (1) scanning the same specimen at different resolutions and (2) downsampling a high-resolution scan of this specimen to lower resolutions using a whole-epiphysis approach. The trabecular variables tested include bone volume fraction (BV/TV), degree of anisotropy (DA), Tb.Th, trabecular spacing (Tb.Sp), and trabecular number (Tb.N). We also assess the impact of scan resolution and downsampling on material maps of BV/TV and DA, which are some of the most biomechanically informative aspects of trabecular architecture and are widely reported in the literature (Goldstein et al., 1993; Odgaard et al., 1997; Van Rietbergen et al., 1998).

2 | MATERIALS AND METHODS

The study sample of micro-CT scans of varying resolutions was created from scans of a complete right distal tibia of a *Gorilla gorilla* individual from Cameroon, curated at the Powell-Cotton Museum in Birchington-on-Sea, UK.

The specimen was scanned using a Diondo D1 scanner at the Imaging Centre for Life Sciences at the University of Kent (Canterbury, UK). The scan parameters included an acceleration voltage of 130 kV, a tube current of 130 µA and a 1.0 mm aluminium filter. Images were reconstructed as 16-bit TIFF stacks.

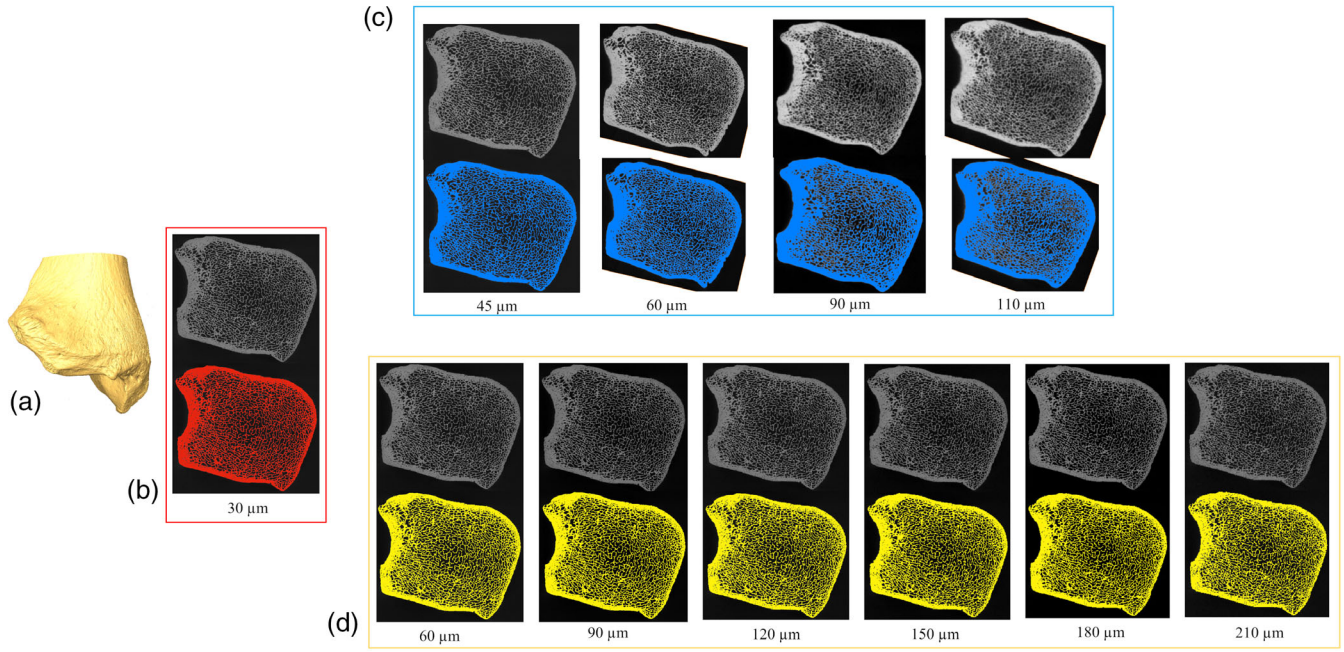

FIGURE 1 (a) Surface of the studied distal tibia region (anterior view); (b) unsegmented (raw) and overlapping segmented high-resolution scan (in distal view) with voxel size of 30 µm used as the baseline scan; (c) serial unsegmented and overlapping segmented images of the same distal tibia (in distal view) scanned under the lower resolution with four different voxel sizes of 45, 60, 90, and 110 µm; (d) the baseline scan downsampled to voxel size of 60, 90, 120, 150, 180, and 210 µm.

TABLE 1 Segmentation parameters.

Method	Resolution (µm)	Trabecular thickness (mm)*	Trabecular thickness/ resolution (mm/µm)	Grid size (px)	Number of classes	Probability filter
Baseline scan	30	0.27	9.0	10	2	None
Downsampled	60	0.28	4.7	5	2	None
Downsampled	90	0.31	3.4	5	2	None
Downsampled	120	0.33	2.8	5	2	None
Downsampled	150	0.35	1.9	5	2	None
Downsampled	180	0.37	2.0	5	2	None
Downsampled	210	0.37	1.8	5	2	None
Rescanned	45	0.40	8.9	10	2	None
Rescanned	60	0.32	5.3	10	2	None
Rescanned	90	0.39	4.3	5	2	None
Rescanned	110	0.45	4.1	5	2	None

*Measured in a 2D cross-section.

Two samples were created to test the impact of voxel resolution on the measurement and visualization of trabecular architecture. In the first, the tibia was rescanned four additional times to produce volumes with voxel sizes of 45, 60, 90, and 110 µm (Figure 1c). To create the second sample, a scan with a voxel size of 30 µm was downsampled to 60, 90, 120, 150, 180, and 210 µm (Figure 1d). Downsampling was conducted in medtool v4.5 (www.dr-pahr.at/medtool) using whole-integer factors only to avoid aliasing (for more details on aliasing, see for example, He et al., 2021; Tward & Siewerdsen, 2009; Yen et al., 1999; Zbijewski & Beekman, 2003). For example, when downsampling 30 to 60 µm eight (2^3) voxels are averaged and from 30 to 90 µm 27 (3^3) voxels are averaged.

All images were segmented into a binary phase of background and bone using the MIA-clustering algorithm (Dunmore et al., 2018). This method requires the definition of a grid size, which was selected by measuring the thickness of the thickest trabeculae in a 2D cross-section using Avizo to determine their width in pixels. The grid size was then set a few voxels larger then this measurement to ensure that the local segmentation focused on features within the phase of interest (Table 1) (Dunmore et al., 2018). Two classes were used for all

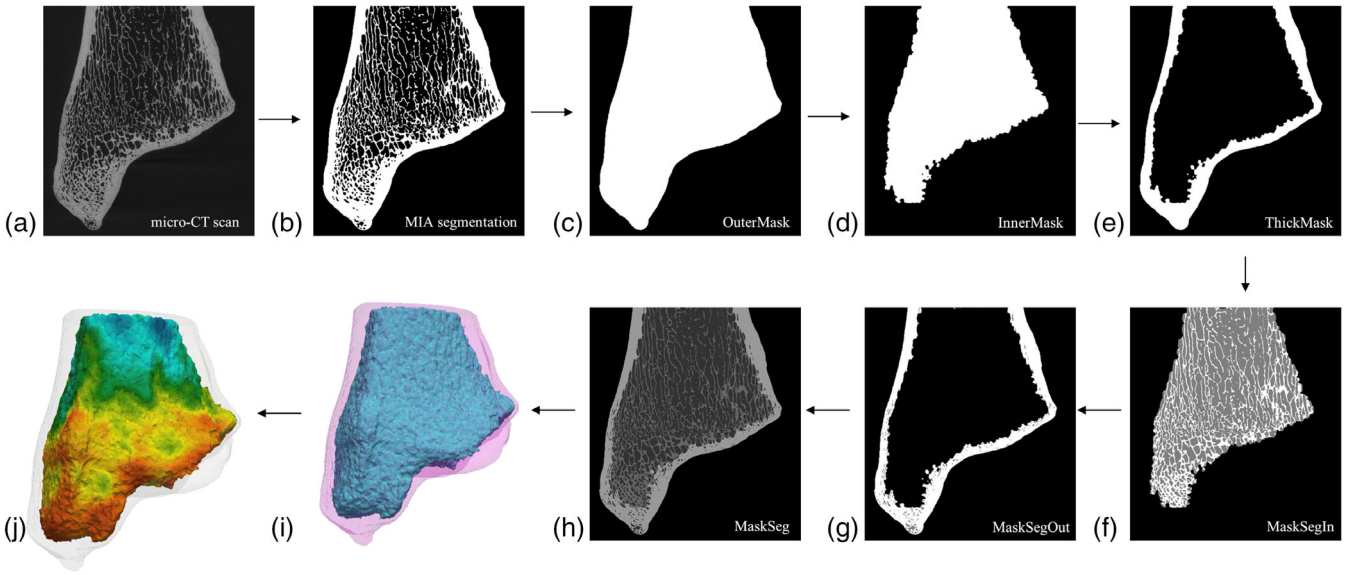

FIGURE 2 Workflow of medtool processing steps (posterior view). (a) Original micro-CT scan; (b) results of the MIA binary segmentation process; (c) *OuterMask*; (d) *InnerMask*; (e) *ThickMask*; (f) *MaskSegIn*; (g) *MaskSegOut*; (h) *MaskSeg*; (i) finite element model of the cortical (pink) and trabecular (blue) area; (j) BV/TV representation. BV/TV, bone volume.

scans (Table 1). To assess if the same volume of bone was segmented in each image stack, we measured segmented BV/TV for each scan in Avizo 6.3 (Visualization Science Group, SAS). Each segmented image was then used for further analysis of trabecular parameters (Figure 2).

The external and inner volumes of all images were defined using medtool v4.5 (www.dr-pahr.at/medtool) and taken from each other to produce the thick cortical bone shell, following published protocols (Gross et al., 2014; Pahr & Zysset, 2009; Tsegai et al., 2013). The binary images (in which bone voxels can be classified as 1 and non-bone voxels as 0) from MIA (Figure 2b) were used as inputs for medtool. The primary structure in the image was identified with a grayscale value of one (white voxels). Subsequently, any floating voxels that were not contiguous with the bone were set to zero or black. Morphological filters in medtool were then applied to fill the bone, thereby isolating the external and internal edges of the cortical bone in 3D. This process resulted in a mask delineating the internal BV/TV and outer cortical bone. During the bone filling process, small pores within the cortical bone were identified and filled based on the size of the kernel radius. This method ensured that the fine porosity of the cortical bone was preserved, while moderate gaps indicative of genuine variations in trabecular shape or separation were maintained. For this, a ray-casting method was used. Subsequently, closing, and opening operations were performed to fill in the gaps in the bone structure, resulting in the creation of the *OuterMask* (Figure 2c). To identify trabecular spaces, the same ray casting process was employed, but with a starting point at the edge of the *OuterMask* instead of the image edge. Rays terminated upon encountering air voxels rather than bone voxels. Closing and opening operations were then applied to fill in areas where rays had traversed directly through trabeculae, thus closing voids in the *InnerMask* (Figure 2d). The *OuterMask* delineated the overall geometry of the entire bone by detecting its outer contour using rays. Conversely, the *InnerMask* served a similar purpose to the *OuterMask*, but specifically defined the 3D geometric boundaries of the trabecular bone region within the entire bone structure. Once both masks were completed, medtool subtracted the *InnerMask* from the *OuterMask* and created a "*ThickMask*" (Figure 2e), which specifically represented the thickness of the cortical bone. Following the creation of *InnerMask*, *OuterMask*, and *ThickMask*, medtool generated three final volumes for subsequent analysis. *MaskSegIn* (Figure 2f) represented the trabecular bone and internal spaces. It was derived from *OuterMask* with *ThickMask* removed, focusing solely on the trabecular bone and internal spaces. *MaskSegOut* (Figure 2g) represented the cortical bone, including its pores. It was derived from *InnerMask* with *OuterMask* removed, isolating only the cortical bone. *MaskSeg* (Figure 2h) represented all elements including cortical bone, pores, trabeculae, and internal spaces. *MaskSeg* was created by combining *MaskSegIn* and *MaskSegOut*.

The CGAL (Computational Geometry Algorithms Library, https://www.cgal.org) 4.9 mesher was then applied to the *InnerMask* and *OuterMask* to create a tetrahedral mesh of both the trabecular volumes (Figure 2i). This mesh was created for each resolution separately and all meshes were later used for data visualization. Each mesh underwent optimization through a series of iterative processes to achieve a smooth boundary, ensuring there were no overlaps or holes between the tetrahedra. Tetrahedra were chosen over hexahedra because their geometry results in a smoother boundary, minimizing the loss of trabecular architectural information (Alberich-Bayarri et al., 2008; Müller, & Rüegsegger, 1996; Ulrich et al., 1999). To gather material property data, a 3D grid with 2.5 mm cells was placed as a bounding box over the *MaskSegIn*. Subsequently, a 5 mm sampling sphere moved between the grid nodes across the entire bounding box, iteratively measuring trabecular parameters. By aligning the finite element

mesh with the nodes of the sampling sphere, each of the trabecular parameters was interpolated onto the mesh. When all these steps were taken, HMA was completed, and trabecular parameters were measured within the bone. Trabecular parameters were measured by the mia-multi module in medtool. Medtool outputted quantitative data as well as options for the quantitative visualization of the data. These interpolated meshes are visualized in Paraview 4.8.2 (Ahrens et al., 2006) (Figure 2j).

The measure of BV/TV is the proportion of trabecular bone of the total volume in each region and was calculated as the ratio of bone voxels to non-bone voxels within the masked volume of each sampling sphere (VOI). DA in 3D was calculated using the mean-intercept-length method (Odgaard et al., 1997; Whitehouse, 1974). The value of DA is zero if the minor and major eigenvectors are of equal magnitude (i.e., isotropic), and is one if the minor and major eigenvectors are maximally different (i.e., anisotropic). A value between 0 and 1 is produced via the formula 1–(min. eigenvalue/max. eigenvalue) (Kivell et al., 2011). To calculate Tb.Th, medtool computed the distance map of the bone voxels of the *MaskSegIn* (Figure 2f) and extracted the distance ridge from which the average distance was calculated. Tb.Sp was calculated in a similar way by inverting bone and background labels. Tb.N was calculated using Tb.Th and Tb.Sp via the formula 1/(Tb.Th + Tb.Sp).

Boxplots and histograms summarizing the data distribution of each variable were generated directly from all VOIs of each respective scan. Shapiro–Wilk tests were used to assess normality and Levene's tests were used to assess equality of variance of each trabecular variable (Tables S1–S5 and Figure S4). Kruskal–Wallis and Dunn's post hoc tests were used to test if the means of a specific parameter differed significantly between datasets. The differences were tested between all combinations of groups within the downsampled images and then separately within the rescanned images. All statistical analyses were conducted in R v3.4.1 and plots were generated using the ggplot2 package (R Core Team, 2017; Wickham, 2016).

3 | RESULTS

3.1 | Total bone volume

The total segmented BV/TV for the 30 µm scan is 28,082 mm^3 (Table 2). When downsampling, the segmented BV/TV remains similar until 210 µm, at which point there is a reduction of 0.7% (27,897 mm^3) (Table 2). Rescanning the specimen results in a stepped increase at 45 (1.5%) and 60 (2.1%) µm, with the segmented volume then remaining similar in scans at 90 and 110 µm (Table 2).

3.2 | Bone volume fraction

Distributions of BV/TV values for each VOI of the background grid in the baseline scan, downsampled volumes and rescanned volumes are presented in Figure 3. The variance of BV/TV values remains relatively similar for all scans and any outliers represent the elements with both lowest and highest BV/TV values. When downsampling, there appears to be a slight decrease in median BV/TV values compared to the baseline scan (Figure 3a), however, the distributions strongly overlap. When rescanned at 45 µm, the median BV/TV is similar, but then increases slightly at voxel sizes of 60, 90, and 110 µm. Similarly, histograms of BV/TV values from each VOI show that the general data distribution pattern remains stable and not normally distributed across all voxel sizes using both downsampled and rescanned images (Figure 3b,c; Table S1). Table 3 shows that the mean BV/TV values (of the VOI's) gradually decrease with downsampling (reaching 12.1% at 210 µm). Rescanning at 45 µm results in a mean BV/TV decrease (0.64%), while there are increases in mean BV/TV at 60 (8.06%), 90 (3.87%), and 110 µm (5.81%) compared to the baseline scan (Table 3).

TABLE 2 Segmented bone volume for all tested CT scans.

Voxel size (µm)	Technique	Segmented bone volume (mm3)	Segmented bone volume change (%)
30	Baseline micro-CT scan	28,082	0.00
60	Downsampled	28,037	−0.16
90		28,058	−0.09
120		27,985	−0.35
150		28,061	−0.08
180		28,118	0.13
210		27,897	−0.66
45	Rescanned	28,505	1.51
60		28,674	2.11
90		28,682	2.14
110		28,700	2.20

The Kruskal–Wallis test shows a statistically significant difference in BV/TV within the downsampled and (separately) within the scanned images (Table 4). Additionally, a Dunn's post hoc test was performed to further explore these differences. The post hoc tests indicate that there are significant differences in BV/TV within all combinations of downsampled and scanned images (Table S6).

To understand if any of these outliers are spatially organized, and thus potentially affecting functional interpretations, we visualized the BV/TV distribution throughout the distal tibia for the baseline scan and all downsampled and rescanned volumes. Figure 4 shows the colourmaps, that is, interpolations of the values from the VOI's discussed above, of BV/TV distribution. Compared to the baseline scan (Figure 4a), the general pattern of BV/TV distribution is maintained in all downsampled images, up to a voxel size of 210 µm (Figure 4b). In this volume the region of highest BV/TV (in red) extends further above the malleolus and is more concentrated in the malleolar groove and, in the mid-coronal view, the region of highest BV/TV is concentrated more laterally and BV/TV is lower in the malleolar region

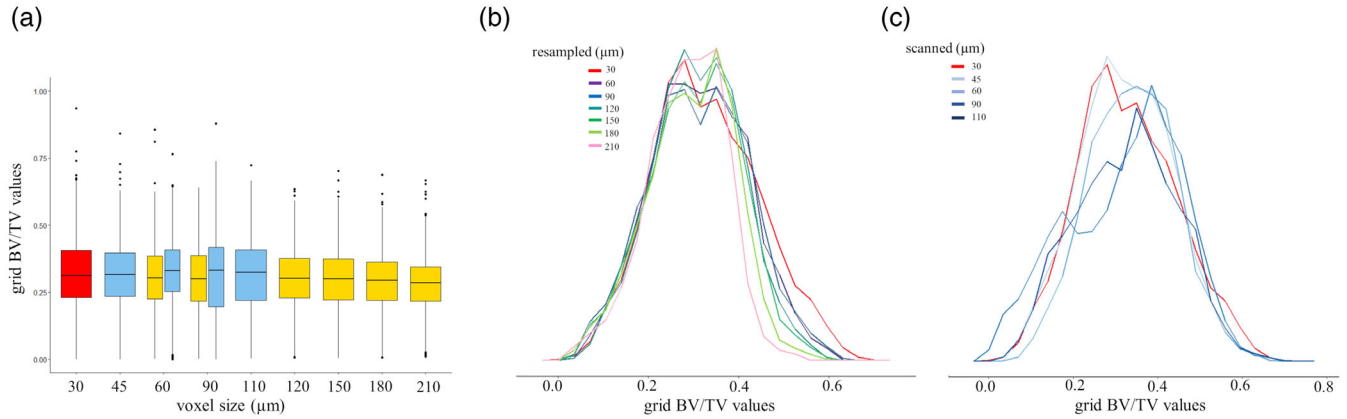

FIGURE 3 (a) Boxplots of the grid BV/TV values for each voxel size for the baseline scan (red), the downsampled data (yellow) and for the specimen scanned at different resolution (blue); (b) histogram of the grid BV/TV values for each voxel size for the baseline scan (red line) and the downsampled data; (c) histogram of the grid BV/TV values for each voxel size for the baseline scan (red line) and for the specimen scanned at different resolution. BV/TV, bone volume.

TABLE 3 The mean and SD values of all tested trabecular parameters.

Voxel size (μm)	Technique	Mean BV/TV (SD)	Mean DA (SD)	Mean Tb. Th (SD)	Mean Tb. Sp (SD)	Mean Tb. N (SD)	N of grid nodes*
30	Baseline micro-CT scan	0.313 (0.105)	0.470 (0.112)	0.272 (0.081)	0.759 (0.267)	1.001 (0.154)	734,423
60	Downsampled	0.301 (0.098)	0.498 (0.117)	0.291 (0.078)	0.786 (0.786)	0.954 (0.136)	648,989
90		0.302 (0.099)	0.479 (0.116)	0.316 (0.080)	0.802 (0.252)	0.916 (0.124)	646,690
120		0.299 (0.095)	0.421 (0.105)	0.338 (0.076)	0.818 (0.247)	0.885 (0.118)	683,156
150		0.293 (0.091)	0.353 (0.092)	0.370 (0.072)	0.846 (0.244)	0.840 (0.108)	535,414
180		0.284 (0.087)	0.296 (0.079)	0.404 (0.061)	0.873 (0.242)	0.799 (0.101)	527,357
210		0.275 (0.086)	0.261 (0.074)	0.446 (0.048)	0.905 (0.240)	0.754 (0.093)	573,089
45	Rescanned	0.311 (0.101)	0.488 (0.114)	0.295 (0.085)	0.783 (0.264)	0.954 (0.140)	699,828
60		0.335 (0.094)	0.481 (0.114)	0.336 (0.092)	0.777 (0.254)	0.918 (0.119)	668,455
90		0.322 (0.128)	0.420 (0.102)	0.427 (0.112)	0.921 (0.278)	0.768 (0.121)	682,908
110		0.328 (0.107)	0.391 (0.102)	0.442 (0.116)	0.859 (0.249)	0.781 (0.087)	583,379

*Number of intrenal grid nodes on which each VOI is centred.

(Figure 4b). The BV/TV concentration on the posterior side of the malleolus, as well as anteriorly and posteriorly on the articular surface, is also higher at the downsampled voxel size of 210 μm (see the distal view Figure 4b). Rescanning at 60 μm presents a broadly similar pattern of BV/TV on each surface and in the mid-coronal cross section (Figure 4c). However, after rescanning at 90 and 110 μm the distribution pattern is less consistent. The high BV/TV concentration along the malleolar region and under the articular surface is lost (see mid-coronal view in Figure 4c).

3.3 | Degree of anisotropy

Downsampling from the baseline to 60 and 90 μm does not result in a large change in DA values; however, there is a marked reduction in DA when downsampling between 120 and 210 μm (Figure 5). Similarly, rescanning at 45 and 60 μm does not result in a change in DA, but DA drops to a greater degree in scans at 90 and 110 μm. The general DA data distribution for the baseline scan is not normally distributed and overlaps across all scan voxel sizes (Figure 5b; Table S3), even in the downsampled voxel size of 90 μm (Figure 5b). However, the data moves towards an apparent positively skewed distribution pattern when downsampled to 120–210 μm (Figure 5b; Table S2). Table 3 shows that mean DA values are closest to the baseline scan at downsampled voxel sizes of 60 and 90 μm and the lowest mean DA values drop 44.5% from the baseline scan at 210 μm. The mean DA values are close to the baseline in rescans at 45 and 60 μm, while there is a 19.9% drop in DA when rescanned at 110 μm (Table 3).

The Kruskal–Wallis test shows a statistically significant difference in DA within the downsampled and scanned images (Table 4). Additionally, the Dunn's post hoc test indicates that there are significant differences in DA within all combinations of downsampled and scanned images (Table S6).

TABLE 4 The Kruskal-Wallis test for BV/TV, DA, Tb.Th, and Tb.Sp grid values within downsampled and scanned images.

Technique	Df	Chi-squared	*p*-value
BV/TV			
Downsampling	6	11,400	**<0.001**
Scanning	4	6025	**<0.001**
DA			
Downsampling	6	399,906	**<0.001**
Scanning	4	95,682	**<0.001**
Tb.Th			
Downsampling	6	16,247	**<0.001**
Scanning	4	7770	**<0.001**
Tb.Sp			
Downsampling	6	1907	**<0.001**
Scanning	4	864	**<0.001**
Tb.N			
Downsampling	6	6100	**<0.001**
Scanning	4	3352	**<0.001**

Note: Significance bold value represents $\alpha = 0.05$.

Figure 6 shows colourmaps of the DA distribution throughout the distal tibia for the baseline scan and all downsampled and rescanned volumes. The DA colourmaps are more impacted by voxel sizes compared to the BV/TV distribution maps. Compared to the baseline scan (Figure 6a), the general pattern of DA distribution is consistent in all downsampled images until the voxel size of 120 µm (Figure 6b). The general DA distribution pattern is visible even at the downsampled voxel size of 150 µm. However, in this volume the low DA (blue color) starts to be concentrated randomly above the articular surface where high DA is found in higher resolution scans (see mid-coronal view in Figure 6c). This is even more apparent in the larger voxel sizes of 180 and 210 µm. The general DA distribution pattern of the baseline scan disappears completely at a voxel size of 210 µm and high DA is inconsistently concentrated throughout the distal tibia (Figure 6b). Rescanning at 60 µm presents a broadly similar pattern of DA on each surface and in the cross-section (Figure 6c). However, after rescanning at 90 and 110 µm the distribution pattern becomes less consistent. The high DA values are lost laterally above the articular surface at a rescanning voxel size of 90 µm and medially above the malleolus at a voxel size of 110 µm (see mid-coronal view in Figure 6c).

3.4 | Trabecular thickness, spacing, and number

Distributions of Tb.Th, Tb.Sp, and Tb.N values for each VOI of the background grid for the baseline scan, downsampled, and rescanned volumes are presented in Figure 7. Voxel size changes in both rescanning and downsampling images has the strongest effect on the quantification of Tb.Th and a weaker effect on the quantification of Tb.Sp and Tb.N (Figure 7). The outliers represent the elements with the lowest/highest Tb.Th (Figure 7a), Tb.Sp (Figure 7b), and Tb.N (Figure 7c). In both downsampled and rescanned images, median values of Tb.Th and Tb.Sp increase gradually, while median values of Tb.N decrease gradually across all voxel sizes compared to baseline scan (Figure 7). When scanning at different resolutions, the Tb.Sp range remains approximately the same up to a voxel size of 60 µm compared to the baseline scan (Figure 7b), however, the distributions overlap across all voxel sizes.

Table 3 shows that mean Tb.Th values gradually increase with increasing voxel size in both downsampled (reaching 64.0% at 210 µm) and rescanned (reaching 62.5% at 110 µm) images. The mean Tb.Sp values are unstable with increasing voxel size in both downsampled (reaching highest increase 194.4% at 60 µm and highest decrease 11.1% at 210 µm) and rescanned (reaching highest increase 4.1% at 90 µm and highest decrease 6.7% at 110 µm) images compared to the baseline scan (Table 3). The mean Tb.N values gradually decrease with increasing voxel size in downsampled (reaching 24.7% at 210 µm) images compared to the baseline scan (Table 3). Mean Tb.N drops off 23.3% at a rescanned voxel size of 90 µm compared to the baseline scan and increases again at 110 µm (reaching 1.7%) compared to the 90 µm scan (Table 3).

The Kruskal–Wallis test shows a statistically significant difference in Tb.Th, Tb.Sp, and Tb.N within the downsampled and scanned images (Table 4). Additionally, the Dunn's post hoc test indicates that there are significant differences in Tb.Th, Tb.Sp, and Tb.N within most combinations of downsampled and scanned images (Table S7). There are no significant differences in Tb.Sp between the downsampled 60 and 90 µm datasets or between scanned voxel sizes of 45 and 90 µm. Moreover, there is no significant difference in Tb.N between scanned voxel sizes of 60 and 110 µm (Table S7).

Colourmaps of the Tb.Th, Tb.Sp, and Tb.N distribution are presented as supporting information (Figures S1–S3). Compared to the baseline scan, the general pattern of the Tb.Th distribution is consistent when downsampled to 150 µm and rescanned at 45 µm (Figure S1). Tb.Th values are higher in the malleolus and under the articular surface and lower above the articular surface when downsampled to 210 µm (see the cross-section mid-coronal view in the Figure S1b). Tb.Th values are lower across the entire distal tibia at rescanned voxel sizes of 90 and 110 µm (Figure S1c). The general pattern of the Tb.Sp distribution is consistent for all images up to a voxel size of 60 µm (Figure S2). The Tb.Sp values are lower in the malleolus and under the articular surface when rescanned at 90 µm compared to the baseline scan (Figure S2c). The Tb.Sp values in the malleolus are higher at 110 µm compared to the baseline scan (see the mid-coronal view in Figure S2c). The general pattern of Tb.N distribution is consistent when downsampled to 150 µm and rescanned at 110 µm (Figure S3). However, in both cases, high Tb.N values above the articular surface are spread more broadly across all voxel sizes compared to the baseline scan (see the mid-coronal view in the Figure S3).

4 | DISCUSSION

This study investigated the impact of voxel size (in downsampled and rescanned micro-CT volumes) on the quantification of trabecular bone

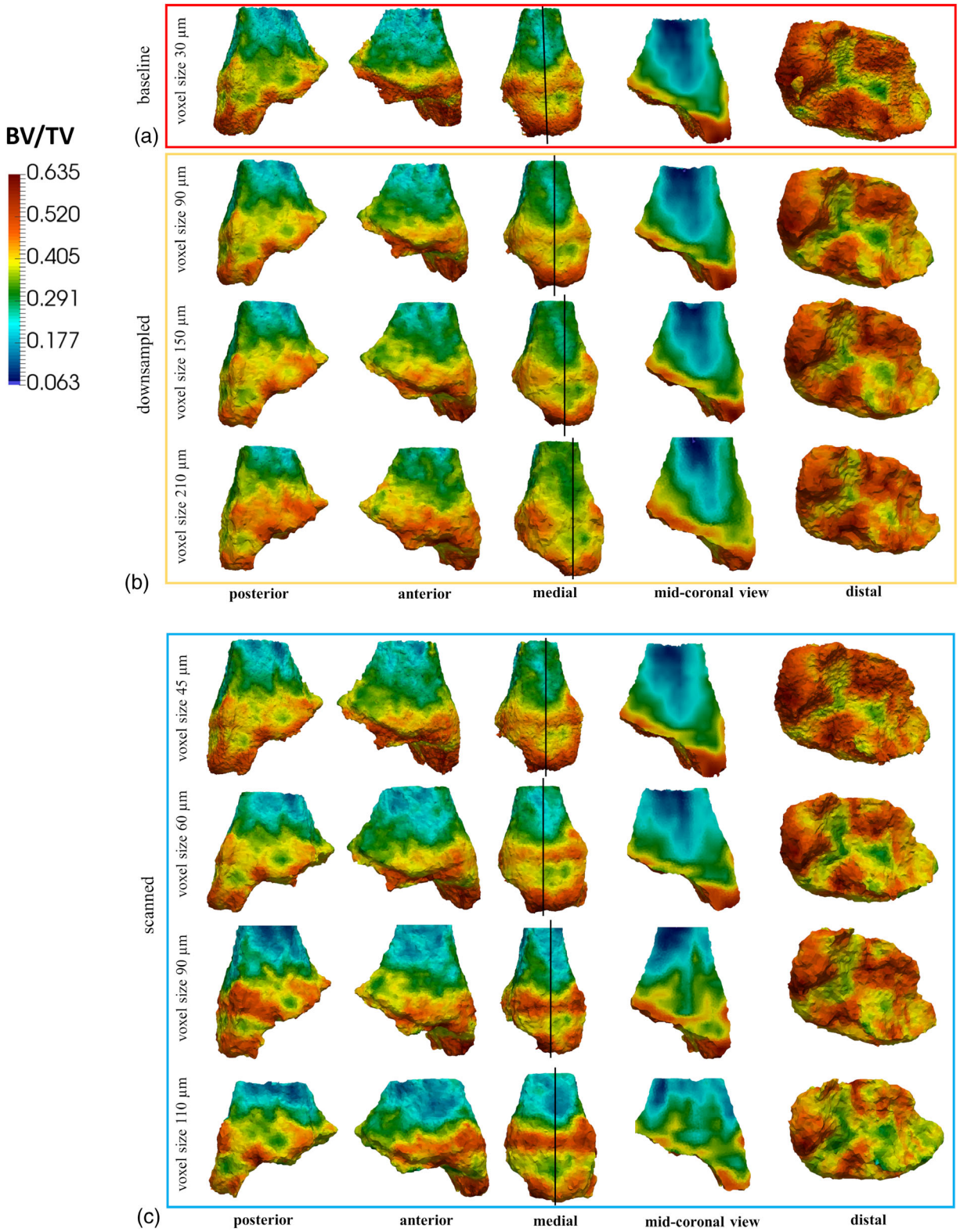

FIGURE 4 Distal tibia model of BV/TV distribution of tested *Gorilla* individual for baseline scan (a), downsampled voxel sizes of 90, 150, and 210 µm (b), and scan voxel sizes of 45–110 µm (c). Vertical lines through the medial view show where the slices are positions for the cross-section mid-coronal view. Dark red represents the highest and dark blue the lowest BV/TV values. All colourmaps were scaled to baseline scan data range. BV/TV, bone volume.

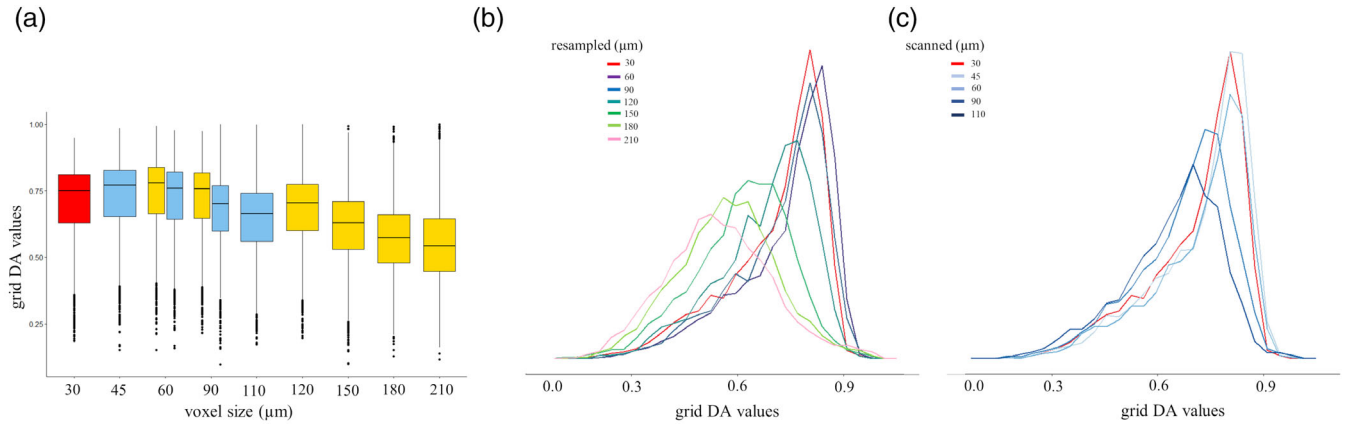

FIGURE 5 (a) Boxplots of the grid DA values for each voxel size for the baseline scan (red), the downsampled data (yellow) and for the specimen scanned at the different resolution (blue); (b) histogram of the grid DA values for each voxel size for the baseline scan (red line) and the downsampled data; (c) histogram of the grid DA values for each voxel size for the baseline scan (red line) and for the specimen scanned at different resolution. DA, degree of anisotropy.

morphology of the distal tibia of a *G. gorilla* individual. Rescanning was found to have a stronger effect on DA and Tb.Th, while BV/TV, Tb.Sp, and Tb.N remained relatively constant across all tested voxel sizes. Downsampling was found to have less of an effect on trabecular parameters compared to rescanning. However, a strong impact on trabecular parameters when downsampling was found in DA and Tb.Th, while BV/TV, Tb.Sp, and Tb.N were less sensitive to increasing voxel sizes.

Quantification of the total BV/TV after segmentation demonstrated differences in the number of bone voxels segmented in each protocol. This BV/TV changed more for rescanned voxel sizes compared to downsampled voxel sizes. However, the differences were below 5% compared to the baseline scan across all scans. When the baseline scan was downsampled to larger voxel sizes, the total segmented BV/TV decreased gradually. However, the opposite pattern was found in rescanned images where the total segmented BV/TV gradually increased with larger voxel sizes. Changes in total segmented BV/TV within the rescanned images often represented fundamental differences that could also be observed on visual inspection of the voxel data. With the lowest scanned resolution, a more substantial difference in volume was found, and the trabecular structure captured is less comparable to that at higher scan resolutions. However, for the results of the downsampled images, where the data captured was based on the voxel set acquired at a higher resolution, there was less divergence in BV/TV from the baseline scan.

Our results for Tb.Th and Tb.Sp imply that while the trabecular spacing remains relatively stable, Tb.Th increases at larger voxel sizes. Because Tb.Sp is higher than Tb.Th, it is less sensitive to scanning/downsampling at tested resolutions. This might suggest that the thickness of the trabeculae is overestimated, that is, trabeculae are segmented as thicker, in very low-resolution scans. Another explanation could be that small trabeculae are lost during the downsampling/rescanning to larger voxels and thus the distribution of the thickness changes more rapidly than it is the case for Tb.Sp. Partial volume averaging occurs when the boundaries of small structures within an image intersect multiple pixels or voxels. This can lead to a blurring effect, where the intensity values of different tissues or structures are averaged within the pixels or voxels. This can compromise the spatial resolution of the image and make it difficult to accurately delineate the small structures or detect fine details (Chakeres, 1984; Plewes & Dean, 1981). Downsampling/rescanning to larger voxel sizes can exacerbate the effects of partial volume averaging, especially if the original image already contains small structures that are near the limit of resolution. Thus, when an image is downsampled/rescanned, the smaller structures may be spread across even fewer pixels or voxels, increasing the degree of averaging, and further blurring the image, that is, downsampling/rescanning can amplify the problem of partial volume averaging by reducing the number of pixels or voxels available to represent small structures within an image (Chakeres, 1984; Conradi et al., 2010; Plewes & Dean, 1981). Thus, it is possible that in the end only the largest trabeculae persist, giving the impression that the average Tb.Th is as large as the maximum of the initial Tb.Th. Moreover, this partial volume averaging could also explain how BV/TV remains constant despite trabeculae getting thicker (on average). It must be emphasized that the trabecular parameters are measured on the segmented images and thus, the changes in the segmented images are another source of potential error in the measurement of trabecular parameters. As mentioned above, MIA is a voxel-size dependent segmentation method (Dunmore et al., 2018). Although we used the same protocol for each bone segmentation, ultimately any segmentation algorithm is limited by the size of the voxels it is classifying.

Our result suggests that the BV/TV, Tb.Sp, and Tb.N can be measured with reasonable precision up to 210 µm, as can DA and Tb.Th up to 90 µm, when downsampling. In contrast, the mean of BV/TV, DA, Tb.Sp, and Tb.N increases from 90 µm when rescanning. We found Tb.Th to be the most sensitive to voxel size changes, where the mean increased for scans above 45 µm. This is visible especially when looking at the colourmaps of the distribution patterns of all studied parameters. The discrepancies might be

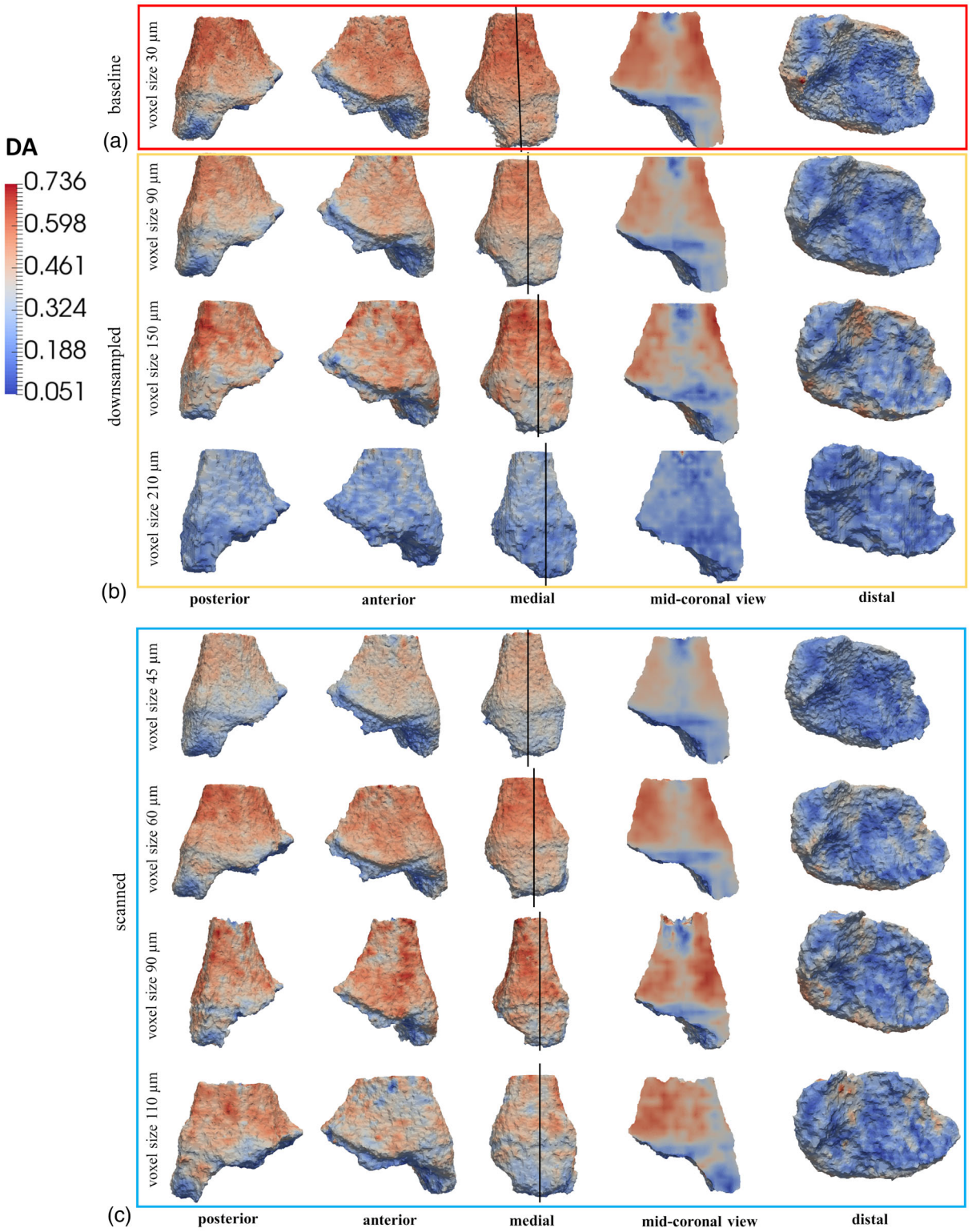

FIGURE 6 Distal tibia model of DA distribution of tested *Gorilla* individual for baseline scan (a), downsampled voxel sizes of 90, 150, and 210 µm (b), and scan voxel sizes of 45–110 µm (c). Vertical lines through the medial view show where the slices are positions for the cross-section mid-coronal view. Dark red represents the highest and dark blue the lowest DA values. All colourmaps were scaled to baseline scan data range. DA, degree of anisotropy.

due to the inconsistencies in the definition of the *InnerMask* as medtool uses morphological filters this is influenced by resolution due to kernel size. However, the morphological filter kernel sizes (in voxels) of the fill algorithm were adjusted for each resolution, so definition of the *OuterMask* and *InnerMask* was kept as consistent as possible.

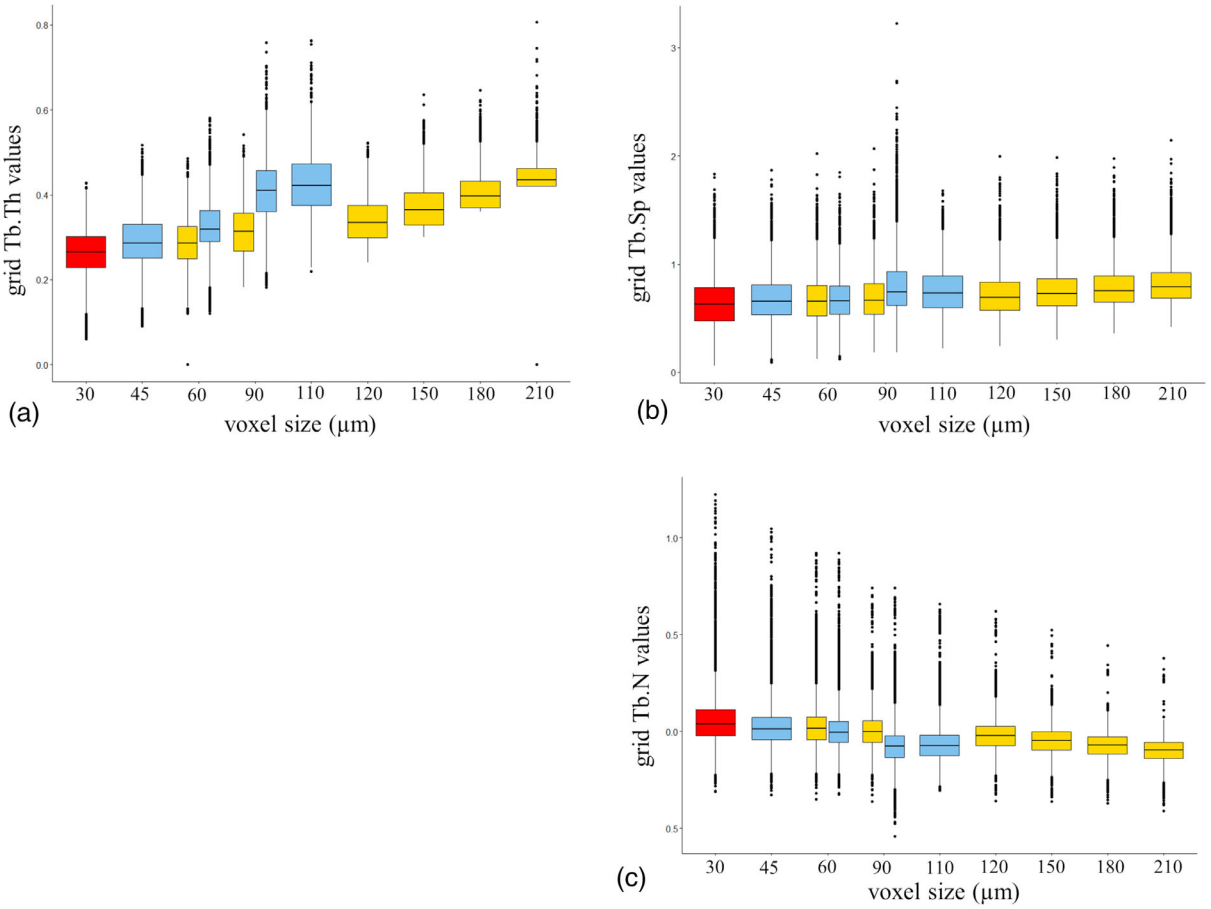

FIGURE 7 Boxplots of the grid Tb.Th (a), Tb.Sp (b), and Tb.N (c) values for each voxel size for the baseline scan (red), the downsampled data (yellow) and for the specimen scanned at the different resolution (blue). Tb.Sp, spacing;Tb.Th, trabecular thickness.

Previous studies of the impact of CT and micro-CT resolution on quantification of trabecular structure observed dependence of trabecular bone parameters on voxel size, consistent with our results. Isaksson et al. (2011) found BV/TV to be less dependent on the voxel sizes compared to DA, Tb.Sp, and Tb.N which were more sensitive to changes in voxel sizes. Similarly, Kim et al. (2004) found mean Tb.Th. and Tb.Sp to increase and Tb.N to decrease with larger voxel sizes which is again consistent with our results. However, they also found mean BV/TV to increase significantly with larger voxel sizes (Kim et al., 2004), which is not consistent with our results. Nevertheless, as supported by our study, Christiansen (2016) found mean BV/TV to be rather consistent within the voxel sizes and Tb.Th to be strongly affected by changes in voxel size. Overall, other studies that tested all or some of other trabecular parameters such as Tb.Th, Tb.Sp, and Tb.N have reported higher dependency on voxel size in all these parameters especially compared to BV/TV, and also compared to DA if included in the study (Isaksson et al., 2011; Kim et al., 2004; Kothari et al., 1998; Majumdar et al., 1996; Maquer et al., 2015; Müller et al., 1996; Peyrin et al., 1998; Sode et al., 2008; Stauber et al., 2006; Tabor, 2004).

This study is the first to show the effect of micro-CT voxel size using a whole-bone mapping approach to analyze trabecular bone morphology. Although this study only included a single specimen, and was not extended to other anatomical sites, we recommend using high-resolution if possible. To speed up trabecular analysis, downsampled images rather than low-resolution scans could be used for certain trabecular parameters. This is especially important if DA and Tb.Th are quantified. Our results suggest that trabecular structure may be more precisely measured by quantifying most trabecular parameters up to voxel size of 90 µm (excluding Tb.Th). Moreover, BV/TV, Tb.Sp, and Tb.N are more robust and can be quantified at even larger voxel sizes with a greater degree of certainty than the other parameters, which are more sensitive to voxel size changes.

Though it was beyond the scope of this study, there are additional factors, such as segmentation method and/or the use of multiple micro-CT scanners for sample acquisition that have the potential to impact quantification of trabecular architecture and may warrant future investigation. It is also possible that the effect of voxel size on trabecular bone is different for regions with higher or lower trabecular BV/TV fraction. Thus, including trabecular bone from taxa that differ in mean BV/TV, as well as BV/TV range, is an important future direction. For example, large primates, such as *Gorilla*, tend to have robust trabecular bone network to support their larger body mass. In contrast, small primates generally exhibit relatively less trabecular bone

structures compared to larger primates as their smaller body size results in lower mechanical loads on their bones, reducing the need for extensive trabecular bone networks (Ryan & Shaw, 2013; Saparin et al., 2011). Based on our results, it might be expected that relatively less trabecular bone structure would be more sensitive to the resolution changes. This could potentially lead to less sensitivity to the resolution changes in BV/TV and potentially other parameters as micro-CT scanning is generally more effective at detecting more gracile structures compared to less gracile structures (e.g., Pyka et al., 2014; Vásárhelyi et al., 2020). Overall, this diversity in sample selection would help address potential sensitivity to resolution changes, particularly in smaller/less more gracile structures, which may lead to a reduction in trabecular network visibility and subsequently affect measured trabecular parameters.

AUTHOR CONTRIBUTIONS

Andrea Lukova: Formal analysis (lead); methodology (lead). **Christopher J. Dunmore:** Formal analysis (equal); methodology (equal). **Zewdi J. Tsegai:** Formal analysis (equal); methodology (equal). **Sebastian Bachmann:** Formal analysis (equal); methodology (equal). **Alexander Synek:** Formal analysis (supporting); methodology (supporting). **Matthew M. Skinner:** Formal analysis (supporting); methodology (supporting).

ACKNOWLEDGMENTS

For access to the specimen, we thank Rachel Jennings, Powell-Cotton Museum, Birchington-on-sea, UK. We thank Dr Trudy Turner, the Editor-in-Chief, associated Editor and one anonymous reviewer for constructive comments that greatly improved our manuscript. This project received funding from the European Research Council (ERC) under the European Union's Horizon 2020 research and innovation programme grant agreement No. 819960 (MMS, SB, CJD) and Marie Skłodowska-Curie Action #101025719 (ZJT).

DATA AVAILABILITY STATEMENT

Copies of all scans are curated by the relevant curatorial institution that is responsible for the original specimen and access can be requested through their institution. The authors confirm that the data supporting the findings of this study are available from the corresponding author upon reasonable request.

ORCID

Andrea Lukova https://orcid.org/0009-0001-9843-336X
Christopher J. Dunmore https://orcid.org/0000-0002-8634-9777
Zewdi J. Tsegai https://orcid.org/0000-0001-9041-4829

REFERENCES

Ahrens, J., Heitmann, K., Habib, S., Ankeny, L., McCormick, P., Inman, J., … Ma, K. L. (2006). Quantitative and comparative visualization applied to cosmological simulations. *Journal of Physics: Conference Series*, *46*, 52–533.

Alberich-Bayarri, A., Marti-Bonmati, L., Sanz-Requena, R., Belloch, E., & Moratal, D. (2008). In vivo trabecular bone morphologic and mechanical relationship using high-resolution 3-T MRI. *American Journal of Roentgenology*, *191*, 721–726.

Bachmann, S., Dunmore, C. J., Skinner, M. M., Pahr, D. H., & Synek, A. (2022). A computational framework for canonical holistic morphometric analysis of trabecular bone. *Scientific Reports*, *12*, 5187.

Barak, M. M., Lieberman, D. E., & Hublin, J. J. (2011). A Wolff in sheep's clothing: Trabecular bone adaptation in response to changes in joint loading orientation. *Bone*, *49*, 1141–1151.

Cazenave, M., Braga, J., Oettlé, A., Pickering, T. R., Heaton, J. L., Nakatsukasa, M., … Macchiarelli, R. (2019). Cortical bone distribution in the femoral neck of Paranthropus robustus. *Journal of Human Evolution*, *135*, 102666.

Chakeres, D. W. (1984). Clinical significance of partial volume averaging of the temporal bone. *American Journal of Neuroradiology*, *5*, 297–302.

Christiansen, B. A. (2016). Effect of micro-computed tomography voxel size and segmentation method on trabecular bone microstructure measures in mice. *Bone Reports*, *5*, 136–140.

Conradi, S. H., Lutey, B. A., Atkinson, J. J., Wang, W., Senior, R. M., & Gierada, D. S. (2010). Measuring small airways in transverse CT images: Correction for partial volume averaging and airway tilt. *Academic Radiology*, *17*, 1525–1534.

DeSilva, J. M., & Devlin, M. J. (2012). A comparative study of the trabecular bony architecture of the talus in humans, non-human primates, and Australopithecus. *Journal of Human Evolution*, *63*, 536–551.

Dunmore, C. J., Bardo, A., Skinner, M. M., & Kivell, T. L. (2020). Trabecular variation in the first metacarpal and manipulation in hominids. *American Journal of Physical Anthropology*, *171*, 219–241.

Dunmore, C. J., Kivell, T. L., Bardo, A., & Skinner, M. M. (2019). Metacarpal trabecular bone varies with distinct hand-positions used in hominid locomotion. *Journal of Anatomy*, *235*, 45–66.

Dunmore, C. J., Skinner, M. M., Bardo, A., Berger, L. R., Hublin, J. J., Pahr, D. H., … Kivell, T. L. (2020). The position of Australopithecus sediba within fossil hominin hand use diversity. *Nature Ecology & Evolution*, *4*, 911–918.

Dunmore, C. J., Wollny, G., & Skinner, M. M. (2018). MIA-clustering: A novel method for segmentation of paleontological material. *PeerJ*, *6*, 4374.

Georgiou, L., Dunmore, C. J., Bardo, A., Buck, L. T., Hublin, J. J., Pahr, D. H., … Skinner, M. M. (2020). Evidence for habitual climbing in a Pleistocene hominin in South Africa. *Proceedings of the National Academy of Sciences*, *117*, 8416–8423.

Georgiou, L., Kivell, T. L., Pahr, D. H., & Skinner, M. M. (2018). Trabecular bone patterning in the hominoid distal femur. *PeerJ*, *6*, 5156.

Glatt, V., Canalis, E., Stadmeyer, L., & Bouxsein, M. L. (2007). Age-related changes in trabecular architecture differ in female and male C57BL/6J mice. *Journal of Bone and Mineral Research*, *22*, 1197–1207.

Goldstein, S. A., Goulet, R., & McCubbrey, D. (1993). Measurement and significance of three-dimensional architecture to the mechanical integrity of trabecular bone. *Calcified Tissue International*, *53*, 127–133.

Griffin, C. T. (2018). Pathological bone tissue in a late Triassic neotheropod fibula, with implications for the interpretation of medullary bone. *New Jersey State Museum Investigations*, *6*, 2–10.

Gross, T., Kivell, T. L., Skinner, M. M., Nguyen, N. H., & Pahr, D. H. (2014). A CT-image-based method for the holistic analysis of cortical and trabecular bone. *Submitted to pal Elec*, 17, 33A.

Halloran, B. P., Ferguson, V. L., Simske, S. J., Burghardt, A., Venton, L. L., & Majumdar, S. (2002). Changes in bone structure and mass with advancing age in the male C57BL/6J mouse. *Journal of Bone and Mineral Research*, *17*, 1044–1050.

He, J., Chen, S., Zhang, H., Tao, X., Lin, W., Zhang, S., … Ma, J. (2021). Downsampled imaging geometric modeling for accurate CT reconstruction via deep learning. *IEEE Transactions on Medical Imaging*, *40*, 2976–2985.

Isaksson, H., Töyräs, J., Hakulinen, M., Aula, A. S., Tamminen, I., Julkunen, P., … Jurvelin, J. S. (2011). Structural parameters of normal and osteoporotic human trabecular bone are affected differently by microCT image resolution. *Osteoporosis International*, *22*, 167–177.

Keaveny, T. M., Morgan, E. F., Niebur, G. L., & Yeh, O. C. (2001). Biomechanics of trabecular bone. *Annual Review of Biomedical Engineering*, *3*, 307–333.

Kim, D. G., Christopherson, G. T., Dong, X. N., Fyhrie, D. P., & Yeni, Y. N. (2004). The effect of microcomputed tomography scanning and reconstruction voxel size on the accuracy of stereological measurements in human cancellous bone. *Bone*, *35*, 1375–1382.

Kivell, T. L. (2016). A review of trabecular bone functional adaptation: What have we learned from trabecular analyses in extant hominoids and what can we apply to fossils? *Journal of Anatomy*, *228*, 569–594.

Kivell, T. L., Skinner, M. M., Lazenby, R., & Hublin, J. J. (2011). Methodological considerations for analyzing trabecular architecture: An example from the primate hand. *Journal of Anatomy*, *218*, 209–225.

Kothari, M., Keaveny, T. M., Lin, J. C., Newitt, D. C., Genant, H. K., & Majumdar, S. (1998). Impact of spatial resolution on the prediction of trabecular architecture parameters. *Bone*, *22*, 437–443.

Lazenby, R. A., Skinner, M. M., Kivell, T. L., & Hublin, J. J. (2011). Scaling VOI size in 3D μCT studies of trabecular bone: A test of the oversampling hypothesis. *American Journal of Physical Anthropology*, *144*, 196–203.

Loewen, T. N., Carriere, B., Reist, J. D., Halden, N. M., & Anderson, W. G. (2016). Linking physiology and biomineralization processes to ecological inferences on the life history of fishes. *Comparative Biochemistry and Physiology Part A: Molecular & Integrative Physiology*, *202*, 123–140.

Lukova, A., Dunmore, C. J., Bachmann, S., Synek, A., Pahr, D. H., Kivell, T. L., & Skinner, M. M. (2024). Trabecular architecture of the distal femur in extant hominids. *Journal of Anatomy*, *245*, 156–180.

Majumdar, S., Newitt, D., Mathur, A., Osman, D., Gies, A., Chiu, E., … Genant, H. (1996). Magnetic resonance imaging of trabecular bone structure in the distal radius: Relationship with X-ray tomographic microscopy and biomechanics. *Osteoporosis International*, *6*, 376–385.

Maquer, G., Musy, S. N., Wandel, J., Gross, T., & Zysset, P. K. (2015). Bone volume fraction and fabric anisotropy are better determinants of trabecular bone stiffness than other morphological variables. *Journal of Bone and Mineral Research*, *30*, 1000–1008.

Müller, R., Koller, B., Hildebrand, T., Laib, A., Gianolini, S., & Rüegsegger, P. (1996). Resolution dependency of microstructural properties of cancellous bone based on three-dimensional μ-tomography. *Technology and Health Care*, *4*, 113–119.

Müller, R., & Rüegsegger, P. (1996). Analysis of mechanical properties of cancellous bone under conditions of simulated bone atrophy. *Journal of Biomechanics*, *29*, 1053–1060.

Odgaard, A., Kabel, J., van Rietbergen, B., Dalstra, M., & Huiskes, R. (1997). Fabric and elastic principal directions of cancellous bone are closely related. *Journal of Biomechanics*, *30*, 487–495.

Pahr, D. H., & Zysset, P. K. (2009). From high-resolution CT data to finite element models: Development of an integrated modular framework. *Computer Methods in Biomechanics and Biomedical Engineering*, *12*, 45–57.

Paternoster, L., Lorentzon, M., Lehtimäki, T., Eriksson, J., Kähönen, M., Raitakari, O., … Ohlsson, C. (2013). Genetic determinants of trabecular and cortical volumetric bone mineral densities and bone microstructure. *PLoS Genetics*, *9*, 1003247.

Peyrin, F., Salome, M., Cloetens, P., Laval-Jeantet, A. M., Ritman, E., & Rüegsegger, P. (1998). Micro-CT examinations of trabecular bone samples at different resolutions: 14, 7 and 2 micron level. *Technology and Health Care*, *6*, 391–401.

Plewes, D. B., & Dean, P. B. (1981). The influence of partial volume averaging on sphere detectability in computed tomography. *Physics in Medicine & Biology*, *26*, 913–919.

Pontzer, H., Lieberman, D. E., Momin, E., Devlin, M. J., Polk, J. D., Hallgrimsson, B., & Cooper, D. M. L. (2006). Trabecular bone in the bird knee responds with high sensitivity to changes in load orientation. *Journal of Experimental Biology*, *209*, 57–65.

Pyka, G., Kerckhofs, G., Schrooten, J., & Wevers, M. (2014). The effect of spatial micro-CT image resolution and surface complexity on the morphological 3D analysis of open porous structures. *Materials Characterization*, *87*, 104–115.

Ruff, C., Holt, B., & Trinkaus, E. (2006). Who's afraid of the big bad Wolff?: "Wolff's law" and bone functional adaptation. *American Journal of Physical Anthropology*, *129*, 484–498.

Ryan, T. M., & Shaw, C. N. (2012). Unique suites of trabecular bone features characterize locomotor behavior in human and non-human anthropoid primates. *PLoS One*, *7*, e41037.

Ryan, T. M., & Shaw, C. N. (2013). Trabecular bone microstructure scales allometrically in the primate humerus and femur. *Proceedings of the Royal Society B: Biological Sciences*, *280*, 20130172.

Saers, J. P., Ryan, T. M., & Stock, J. T. (2020). Baby steps towards linking calcaneal trabecular bone ontogeny and the development of bipedal human gait. *Journal of Anatomy*, *236*, 474–492.

Saparin, P., Scherf, H., Hublin, J. J., Fratzl, P., & Weinkamer, R. (2011). Structural adaptation of trabecular bone revealed by position resolved analysis of proximal femora of different primates. *The Anatomical Record: Advances in Integrative Anatomy and Evolutionary Biology*, *294*, 55–67.

Schulte, F. A., Ruffoni, D., Lambers, F. M., Christen, D., Webster, D. J., Kuhn, G., & Müller, R. (2013). Local mechanical stimuli regulate bone formation and resorption in mice at the tissue level. *PLoS One*, *8*, 62172.

Seeman, E. (2003). Bone quality. *Osteoporosis International*, *14*, 3–7.

Sinclair, K. D., Farnsworth, R. W., Pham, T. X., Knight, A. N., Bloebaum, R. D., & Skedros, J. G. (2013). The artiodactyl calcaneus as a potential control bone cautions against simple interpretations of trabecular bone adaptation in the anthropoid femoral neck. *Journal of Human Evolution*, *64*, 366–379.

Sode, M., Burghardt, A. J., Nissenson, R. A., & Majumdar, S. (2008). Resolution dependence of the non-metric trabecular structure indices. *Bone*, *42*, 728–736.

Stauber, M., Rapillard, L., van Lenthe, G. H., Zysset, P., & Müller, R. (2006). Importance of individual rods and plates in the assessment of bone quality and their contribution to bone stiffness. *Journal of Bone and Mineral Research*, *21*, 586–595.

Su, A., Wallace, I. J., & Nakatsukasa, M. (2013). Trabecular bone anisotropy and orientation in an early Pleistocene hominin talus from East Turkana, Kenya. *Journal of Human Evolution*, *64*, 667–677.

Sylvester, A. D., & Terhune, C. E. (2017). Trabecular mapping: Leveraging geometric morphometrics for analyses of trabecular structure. *American Journal of Physical Anthropology*, *163*, 553–569.

Tabor, Z. (2004). Analysis of the influence of image resolution on the discriminating power of trabecular bone architectural parameters. *Bone*, *34*, 170–179.

Tsegai, Z. J., Kivell, T. L., Gross, T., Nguyen, N. H., Pahr, D. H., Smaers, J. B., & Skinner, M. M. (2013). Trabecular bone structure correlates with hand posture and use in hominoids. *PLoS One*, *8*, 78781.

Turner, C. H., Hsieh, Y. F., Müller, R., Bouxsein, M. L., Baylink, D. J., Rosen, C. J., … Beamer, W. G. (2000). Genetic regulation of cortical and trabecular bone strength and microstructure in inbred strains of mice. *Journal of Bone and Mineral Research*, *15*, 1126–1131.

Tward, D. J., & Siewerdsen, J. H. (2009). Noise aliasing and the 3D NEQ of flat-panel cone-beam CT: Effect of 2D/3D apertures and sampling. *Medical Physics*, *36*, 3830–3843.

Ulrich, D., Van Rietbergen, B., Laib, A., & Ruegsegger, P. (1999). The ability of three-dimensional structural indices to reflect mechanical aspects of trabecular bone. *Bone*, *25*, 55–60.

Van Rietbergen, B., Odgaard, A., Kabel, J., & Huiskes, R. (1998). Relationships between bone morphology and bone elastic properties can be

accurately quantified using high-resolution computer reconstructions. *Journal of Orthopaedic Research*, *16*, 23–28.

Vásárhelyi, L., Kónya, Z., Kukovecz, Á., & Vajtai, R. (2020). Microcomputed tomography–based characterization of advanced materials: A review. *Materials Today Advances*, *8*, 100084.

Whitehouse, W. J. (1974). The quantitative morphology of anisotropic trabecular bone. *Journal of Microscopy*, *101*, 153–168.

Wickham, H. (2016). *ggplot2: Elegant graphics for data analysis*. Springer-Verlag. https://ggplot2.tidyverse.org

Yen, S. Y., Yan, C. H., Rubin, G. D., & Napel, S. (1999). Longitudinal sampling and aliasing in spiral CT. *IEEE Transactions on Medical Imaging*, *18*, 43–58.

Zbijewski, W., & Beekman, F. J. (2003). Characterization and suppression of edge and aliasing artefacts in iterative x-ray CT reconstruction. *Physics in Medicine & Biology*, *49*, 145.

SUPPORTING INFORMATION

Additional supporting information can be found online in the Supporting Information section at the end of this article.

How to cite this article: Lukova, A., Dunmore, C. J., Tsegai, Z. J., Bachmann, S., Synek, A., & Skinner, M. M. (2024). Technical note: Does scan resolution or downsampling impact the analysis of trabecular bone architecture? *American Journal of Biological Anthropology*, e25023. https://doi.org/10.1002/ajpa.25023

Received: 10 July 2023 | Revised: 1 February 2024 | Accepted: 5 February 2024

DOI: 10.1111/joa.14026

Journal of Anatomy | ANATOMICAL SOCIETY WILEY

ORIGINAL ARTICLE

Trabecular architecture of the distal femur in extant hominids

Andrea Lukova[1] | Christopher J. Dunmore[1] | Sebastian Bachmann[2] | Alexander Synek[2] | Dieter H. Pahr[2,3] | Tracy L. Kivell[4] | Matthew M. Skinner[4]

[1]Skeletal Biology Research Centre, School of Anthropology and Conservation, University of Kent, Canterbury, UK

[2]Institute of Lightweight Design and Structural Biomechanics, TU Wien, Wien, Austria

[3]Department of Anatomy and Biomechanics, Division Biomechanics, Karl Landsteiner University of Health Sciences, Krems, Austria

[4]Department of Human Origins, Max Planck Institute for Evolutionary Anthropology, Leipzig, Germany

Correspondence
Andrea Lukova1, Skeletal Biology Research Centre, School of Anthropology and Conservation, University of Kent, Canterbury, UK.
Email: al646@kent.ac.uk

Funding information
European Union's Horizon 2020 research and innovation programme, Grant/Award Number: 819960

Abstract

Extant great apes are characterized by a wide range of locomotor, postural and manipulative behaviours that each require the limbs to be used in different ways. In addition to external bone morphology, comparative investigation of trabecular bone, which (re-)models to reflect loads incurred during life, can provide novel insights into bone functional adaptation. Here, we use canonical holistic morphometric analysis (cHMA) to analyse the trabecular morphology in the distal femoral epiphysis of *Homo sapiens* ($n = 26$), *Gorilla gorilla* ($n = 14$), *Pan troglodytes* ($n = 15$) and *Pongo* sp. ($n = 9$). We test two predictions: (1) that differing locomotor behaviours will be reflected in differing trabecular architecture of the distal femur across *Homo*, *Pan*, *Gorilla* and *Pongo*; (2) that trabecular architecture will significantly differ between male and female *Gorilla* due to their different levels of arboreality but not between male and female *Pan* or *Homo* based on previous studies of locomotor behaviours. Results indicate that trabecular architecture differs among extant great apes based on their locomotor repertoires. The relative bone volume and degree of anisotropy patterns found reflect habitual use of extended knee postures during bipedalism in *Homo*, and habitual use of flexed knee posture during terrestrial and arboreal locomotion in *Pan* and *Gorilla*. Trabecular architecture in *Pongo* is consistent with a highly mobile knee joint that may vary in posture from extension to full flexion. Within *Gorilla*, trabecular architecture suggests a different loading of knee in extension/flexion between females and males, but no sex differences were found in *Pan* or *Homo*, supporting our predictions. Inter- and intra-specific variation in trabecular architecture of distal femur provides a comparative context to interpret knee postures and, in turn, locomotor behaviours in fossil hominins.

KEYWORDS
bipedalism, functional morphology, *Gorilla*, human, knee, locomotor behaviour, *Pan*, *Pongo*

1 | INTRODUCTION

Understanding how variation in skeletal morphology, both external shape and internal bone structure, may reflect differences in loading during habitual behaviours in extant apes is critical to reconstructing behaviour in fossil hominoid taxa. Extant apes are characterized by a wide range of locomotor, postural and manipulative behaviours linked to their respective ecological niches,

subsistence strategies and social organization, which require each species to use their limbs in different ways. Although African apes also engage in arboreal suspension and climbing, they spend the majority of their time terrestrially knuckle-walking, in which the knee is flexed to varying degrees (Ankel-Simons, 2010; Georgiou et al., 2018; Isler, 2005; Lee et al., 2012). Orangutans engage in slow-moving, torso-orthograde locomotion, often supported by multiple limbs (Cant, 1987; Thorpe & Crompton, 2005), in which load is distributed across both upper and lower limb joints. Humans are the only living obligate bipedal ape and are unique among primates in that both the hips and knees remain relatively extended during the gait cycle. In this study we build on previous research (Georgiou et al., 2018; Sukhdeo et al., 2020; Sylvester & Terhune, 2017) to examine the link between habitual joint postures of the knee and trabecular architecture in the distal femur of extant great apes, including humans.

Although the structure of trabecular bone is also influenced by several factors, including genetics, hormones, diet, sex, age, body size and physical activity (Loewen et al., 2001; Paternoster et al., 2013; Turner et al., 2000), (re-)modelling is at its peak during ontogeny and persists (although at a reduced rate) throughout adulthood (Barak, 2019; Glatt et al., 2007; Halloran et al., 2002; Saers et al., 2020; Seeman, 2003; Wallace et al., 2013). It has been previously demonstrated that joint load is transferred from the subchondral bone of the epiphyses towards the diaphyseal cortical bone (Barak et al., 2008). Correlations between cortical bone features and different types of locomotion among great apes have been previously found. For example, Carlson (2005) found that African apes engaging more frequently in arboreal locomotion have more circular femoral cross-sections compared with those that engage more in terrestrial locomotion. Ruff (2002) also found a relationship between locomotor activities in great apes and cross-sectional properties of forelimb and hindlimb bones. Asian apes show relatively stronger forelimb shafts than hindlimb shafts compared to African apes and within African apes, more arboreal *Pan* shows relatively higher ratios of forelimb to hindlimb strength compared to more terrestrial *Gorilla* (Ruff, 2002). Moreover, cross-sectional differences between humans and non-human apes reflecting differences in locomotor loading have been found in the femoral neck (Lovejoy, 1988; Ohman et al., 1997; Rafferty, 1998) and in the distal tibia and talus (Tsegai et al., 2017).

Trabecular bone models in response to loading through either an increase or decrease of bone tissue and/or reconfiguration of the shape and structure of trabecular struts in order to reduce strain and prevent fracture (Barak et al., 2011; Biewener et al., 1996; Harrison et al., 2011; Mittra et al., 2005; Pontzer et al., 2006; Rodan, 1997; Ruff et al., 2006; Sinclair et al., 2013). Thus, it is expected that trabecular bone structure within the epiphysis of the distal femur will reflect variation in loaded knee joint postures among extant great apes. The ratio of bone volume to total volume (BV/TV) is the proportion of trabecular bone of the total volume in a given region. In places where stress is lower, there is a gradual decline in the amount of trabecular bone, resulting in a weaker structure; conversely, in places where stress is higher, there is a gradual increase in trabecular bone deposition to help resist loads (Barak et al., 2011; Pontzer et al., 2006; Sinclair et al., 2013). Degree of anisotropy (DA) describes the trabecular alignment in 3D space, with high DA indicating greater alignment (trabeculae tend to be oriented in specific direction) or an anisotropic structure, and low DA (values closer to 0) reflecting less alignment (trabeculae tend to be more randomly oriented) and an isotropic structure. BV/TV and DA can together explain up to 97% of the variation in elastic properties of trabecular bone (Homminga et al., 2003; Maquer et al., 2015; Van Rietbergen et al., 1998; Zysset, 2003). BV/TV and DA have been shown to reflect the presumed predominant direction and relative magnitude that joints are loaded in, during different locomotor and manipulative behaviours; in previous landmark studies (Dunmore et al., 2019, 2020; Sylvester & Terhune, 2017), throughout an entire bone or epiphysis (Kuo et al., 2022; Ryan et al., 2019; Saers et al., 2022; Skinner et al., 2013; Stephens et al., 2016; Tsegai et al., 2018) or by using holistic morphometric approaches (Bachmann et al., 2022; DeMars et al., 2022; Dunmore et al, 2023). Recent methodological advancements allow comprehensive statistical analysis of trabecular bone structure within and between species, particularly those that vary in external bone shape (Bachmann et al., 2022; Gross et al., 2014). Here we investigate the trabecular structure in the entire distal femoral epiphysis of extant humans and other great apes to explore how potential variation might reflect significant differences in knee joint loading during locomotor behaviours.

Several previous studies have examined trabecular structure in the lower limbs of primates, including the pelvis/innominate (Dalstra et al., 1993; Eriksen et al., 1984; Volpato et al., 2008; Zaharie & Phillips, 2018), proximal femur (Cazenave et al., 2019; Coelho et al., 2009; Demes et al., 2000; Georgiou et al., 2019; Georgiou et al., 2020; Ruff et al., 2013; Ryan & Ketcham, 2002; Ryan & Walker, 2010; Volpato et al., 2008), proximal tibia (Kamibayashi et al., 1995; Mazurier et al., 2010; Novitskaya et al., 2014; Saers et al., 2016; Sugiyama et al., 2012; Thomsen et al., 2005) as well as the ankle and foot (DeSilva, 2009; DeSilva & Devlin, 2012; Su et al., 2013; Tsegai et al., 2017). However, only two previous studies have specifically examined trabecular bone structure in the hominoid knee joint. Sylvester and Terhune (2017) describe a new geometric morphometric approach to analyse subchondral trabeculae of human distal femur. They found sex differences in subchondral trabecular spacing in the human knee, with males having more evenly spaced trabeculae compared to females. This study provided important insight into bone loading that might be overlooked with a centrally placed volume-of-interest methods, particularly in joints where trabecular structure is not homogenously distributed across epiphyses (Sylvester & Terhune, 2017). Georgiou et al. (2018) analysed trabecular structure of distal femoral epiphysis of extant great apes and found that humans have higher BV/TV and DA on the posteroinferior margin of the condyles compared to non-human apes. Additionally, they showed that *Pan* and *Pongo* have higher BV/TV

values in the posterior region of the condyles compared to other hominoids. This study revealed some functional signals in distal femur linked to locomotor behaviour of great apes, but they also found a large degree of overlap across some taxa. Their statistical comparisons between taxa were limited to a priori defined quadrants of each condyle, so trabecular patterns within each quadrant could only be analysed qualitatively (Georgiou et al., 2018).

We build upon these previous studies with an expanded sample and the canonical holistic morphometric analysis (cHMA) method to statistically analyse trabecular patterns of the distal femur in extant apes, free of a priori sub-sampling. cHMA addresses the potential bias caused by inter-specific differences in shape by computing canonical models representing the mean size, position and morphology from a multispecies sample of individual bones. Moreover, cHMA treats each mesh cell as homologous when computing a canonical model and so geometric homology is achieved. Without geometric homology, quadrants are an arbitrary unit of analysis and the functional signal might be lost when trabecular concentration is divided. cHMA allows us to test whether the distribution of bone parameters differ statistically between (as well as within) different species. By using cHMA, we are able to build taxon-specific mean models (with standard deviations) and conduct multivariate comparisons with high statistical power as all homologous finite elements of each studied trabecular parameter could be compared across every individual in the sample (see more details next) (Bachmann et al., 2022).

2 | EXTERNAL KNEE MORPHOLOGY AND PREDICTED KNEE POSTURES DURING LOCOMOTION

Extant hominids exhibit anatomical variation of the knee joint, particularly regarding the relative size and shape of the femoral condyles, the size and shape of the patella as well as the articulation of the femoral condyles and the tibial plateau at various angles of knee flexion. The knee joint experiences load not only from substrate reaction forces, but also from the action of muscles, tendons and ligaments during various locomotor activities. Additionally, soft tissue morphology of the knee joint in extant non-human great apes (hereafter, just 'great apes') differs in the degree to which it provides stability and mobility at different joint angles (Barak et al., 2011; Currey, 2003, 2012; Demes, 2007; Pearson & Lieberman, 2004; Rubin et al., 2002; Ruff et al., 2006; Shaw & Ryan, 2012). In comparison, the human knee joint has several bony and soft tissue features that stabilize the knee especially in a fully extended posture (DeSilva et al., 2018; Haile-Selassie et al., 2012; Harcourt-Smith et al., 2015; Harcourt-Smith, 2016; Lovejoy et al., 2009; Sylvester & Organ, 2010; Sylvester, 2013; Sylvester et al., 2011). These differences in hard and soft tissue morphology, discussed in more detail next, will influence load distribution across the femoral condyles and the tibial plateau, which in turn should influence trabecular (re-)modelling across hominids.

2.1 | Shape of the distal femur, proximal tibia and associated soft tissue structures

In humans both condyles of the distal femur are approximately the same size, but in other great apes the medial condyle is larger than the lateral condyle (Sylvester, 2013; Sylvester & Pfisterer, 2012; Tardieu, 1999). The distal articular surface is square in humans (i.e. with relatively equal anteroposterior and mediolateral dimensions) and is more symmetrical around the parasagittal plane passing through the middle of trochlea than it is the great ape femur (Figure 1g). Both condyles are elliptical when viewed laterally in humans, which projects the patella anteriorly, thereby increasing the lever arm of quadriceps femoris, compared to great apes. Also, the lateral femoral condyle is flat in its sagittal plane (Figure 1g), which increases the contact area between the lateral femoral condyle and lateral tibial plateau when the knee is extended (Lovejoy, 2007; Tardieu, 1999). The more convex lateral condyle in great apes (Figure 1g) produces similar joint stress across all the joint positions and helps to reduce joint stress in the patellofemoral contact area during flexion (Lovejoy, 2007). In humans, the patellar groove of the femur is relatively deep and the lateral lip of trochlea projects more anteriorly than the medial lip (Wanner, 1977). Stern Jr and Susman (1983) suggested that the main function of the deep patellar groove and prominent lateral lip is to prevent patellar dislocation on the flexed knee due to the line of action of the quadriceps whose origin is laterally placed due to the higher valgus angle in humans compared to higher varus angle in non-human great apes.

In humans, the quadriceps femoris inserts on the proximal patellar surface, continues over the anterior surface and inserts via the patellar ligament on the tibial tuberosity. Vastus medialis and lateralis insert on the medial and lateral margins of the patella, respectively, which helps to protect the knee from medial/lateral dislocation as quadriceps femoris extends the knee. When the knee is at its full extension, the patello-femoral joint contact occurs at the distal end of patella (Figure S1). As flexion increases, the patello-femoral contact area increases as well. During flexion, the patella engages into the femoral trochlear groove and the contact area spreads across the width of the patella and moves proximally (Lovejoy, 2007; Tardieu, 1999) (Figure S1). Thus, with the higher articular area, the stress during knee flexion is reduced (Masouros et al., 2010). In great apes, the patella is both absolutely and relatively smaller than in humans due to the smaller quadriceps muscle. In all primates, the quadriceps muscles compress the patella against the femur during flexion, with subsequent joint stress depending on the size of the patello-femoral contact area (Lovejoy, 2007). The knee of great apes is more or less flexed during all locomotor activities compared to humans. A flatter trochlea then allows the patello-femoral surface to bear higher forces when the quadriceps press the patella against the femur (Lovejoy, 2007).

In humans, the menisci form a mobile unit on the tibial plateau that adapts to the sliding and rotating movements of the femoral condyles and function as an important secondary co-resistant to

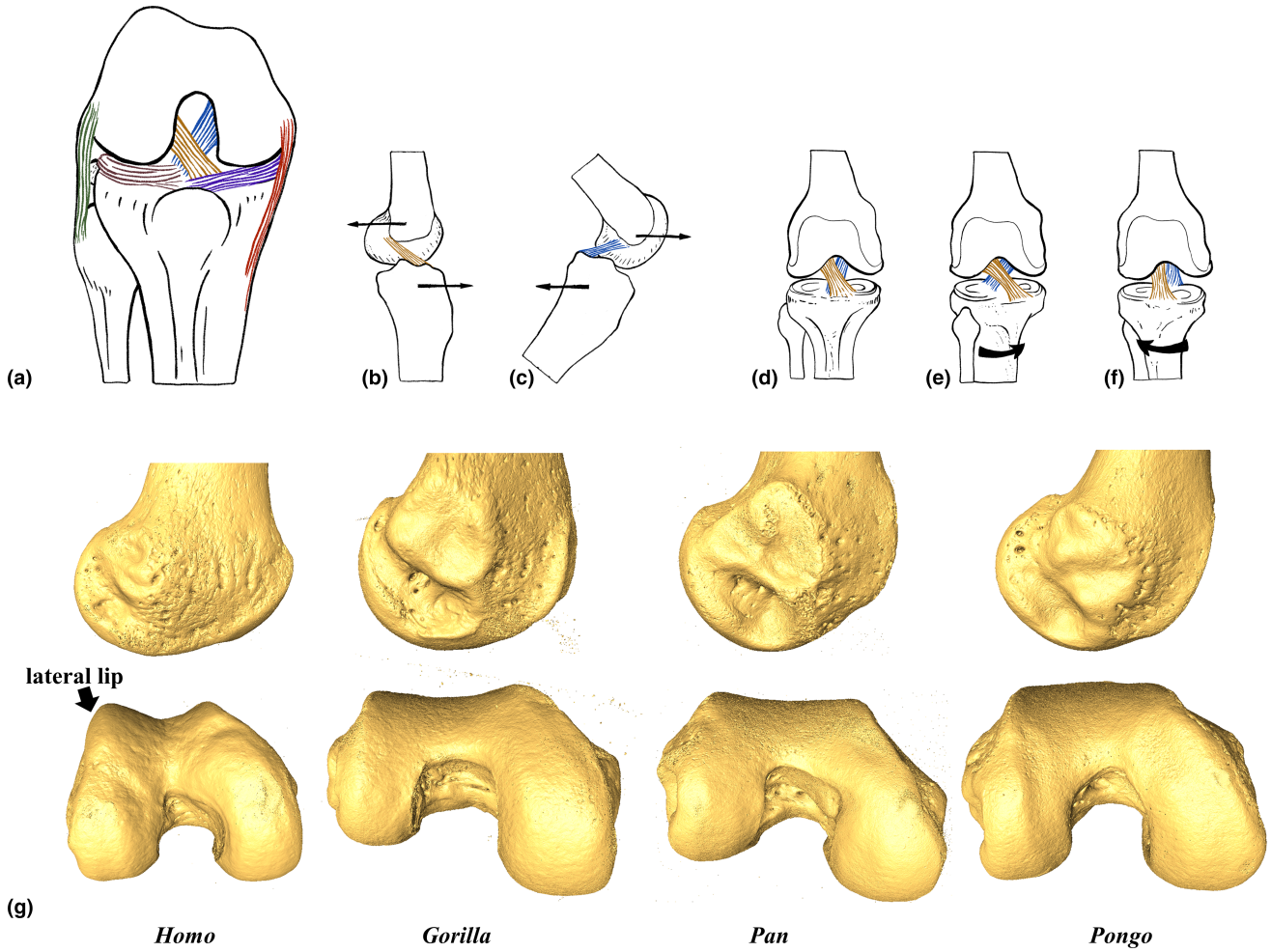

FIGURE 1 (a) Ligament attachments of the knee showing inferior view. Gold, anterior cruciate ligament; blue, posterior cruciate ligament; green, lateral collateral ligament; red, medial collateral ligament; brown, lateral meniscus; purple, medial meniscus. The medial collateral ligament inserts at the medial epicondyle of the femur and attaches along the medial border of the tibial plateau and on the medial surface of the tibial shaft. The lateral collateral ligament inserts on the lateral femoral epicondyle and attaches on the head of fibula. (b) Anterior cruciate ligament position during forward tibia and backward femur movements. (c) Posterior cruciate ligament position during backward tibia and forward femur movements. Cruciate ligaments position during (d) neutral knee position; (e) medial knee rotation; (f) lateral knee rotation. The anterior cruciate ligament arises from the anterior intercondylar space on the tibial plateau, runs upwards and posteriorly and attaches on the inside of the lateral condyle of the femur. The posterior cruciate ligament arises from well back on the posterior intercondylar space, runs upwards and anteriorly and attaches on the inside of the medial condyle. (g) Surface models of right distal femur of *Homo*, *Gorilla*, *Pan* and *Pongo*. Showing more elliptical shape of lateral condyle, square outline of distal surface and high lateral lip in humans compared to great apes.

the cruciate ligaments. When the knee is flexed, the popliteus tendon pulls the menisci posteriorly and the contact point of femoral condyle and tibial plateau also moves posteriorly (Lovejoy, 2007; Tardieu, 1999). Conversely, when the human knee is extended, the menisci again follow the femoral condyle and tibial plateau moving both anteriorly (e.g. Hirschmann & Müller, 2015). In great apes, the lateral meniscus has only a single point of attachment to the tibia. Additionally, the lateral meniscus is connected on its posterior surface to the Wrisberg ligament, which in turn attaches on the inside of the medial femoral condyle (this ligament is rarely found in humans) (Girgis et al., 1975). The anterior transverse ligament is absent, and the medial meniscus is not attached to the medial collateral ligament, but it is separated from it by a bursa. These differences allow greater range of knee movements in great apes compared to humans (Girgis et al., 1975).

Due to the difference in weight transfer through the lower limb and size of femoral condyles, the relative size of the tibial condyles in great apes is opposite to that in humans. The medial tibial condyle is much larger and more convex than the lateral and the tibial plateau is supero-inferiorly compressed (Berger & Tobias, 1996) with a thin lateral epicondyle (Frelat et al., 2017). The posterior cruciate ligament attaches to the medial femoral condyle more anteriorly and nearer to the midline of the intercondylar notch in great apes than in humans. The collateral ligaments control the side-to-side motions and the cruciate ligaments control both the slide of the femur and the medial rotation of the tibia as they do in humans (Figure 1a–f).

However, because of the different attachment of the posterior cruciate ligament, medial rotation of the tibia is greater in great apes compared to humans.

2.2 | Locomotor behaviour and biomechanics of knee posture during the gait cycle

Humans and great apes are characterized by a wide range of locomotor behaviours that vary in their frequency and knee postures, both across and within species. These differences influence knee load distribution and thus should affect trabecular (re-)modelling. Next, we discuss what is known about the biomechanical differences in knee joint posture and loading across our study species, which form the basis of our predictions about variation in trabecular structure.

2.2.1 | Humans

Humans not only are primarily bipedal walkers but also often engage in other activities such as running, jumping or squatting, in which the knee position may vary substantially (Mann & Hagy, 1980; Nilsson & Thorstensson, 1987; Racic et al., 2009). Human bipedal gait is at or close to full extension of the knee for most of its cycle (Javois et al., 2009; Landis & Karnick, 2006; Organ & Ward, 2006; Sylvester & Pfisterer, 2012; Tardieu, 1999) (Figure S1) and the variability in location of the resulting joint forces on the distal femur is limited (Preuschof & Tardieu, 1996). Both the medial and lateral condyles are evenly loaded through the tibial plateau during locomotion (Lovejoy, 2007; Sylvester, 2013; Sylvester & Pfisterer, 2012; Tardieu, 1999). When the knee is flexed, the range of motion is approximately 45° of lateral and 25° of medial rotation (Lovejoy, 2007). The amount of axial rotation (i.e. twisting of the knee relative to the tibia) depends on the amount of load, with high loads leading to low rotator flexibility and vice versa (Lovejoy, 2007). During extension, the patellar tendon moves to the centre of rotation and the lever advantage of the quadriceps muscle increases in intensity (Loudon, 2016). Medial and lateral collateral ligaments tighten the knee joint in full extension and limit rotation and hyperextension. In flexion, they are loose and allow more rotational knee movements. The medial collateral ligament is also tightened in lateral rotation and loose in medial rotation. The lateral collateral ligament is, by contraction of the quadriceps tendon, actively tightened during flexion–extension (Hirschmann & Müller, 2015). The posterior cruciate ligament is in tension when the knee is flexed and prevents the femur from sliding anteriorly off the tibial plateau (Figure 1c), whereas the anterior cruciate ligament is in tension when the knee is extended and prevents femur from sliding posteriorly off the tibial plateau (Figure 1b). Additionally, the cruciate ligaments limit medial rotation to the tibia in relation to the femur (Figure 1d,e). If tibia is rotated laterally, the cruciate ligaments untwist and have no limiting ability (Figure 1f).

2.2.2 | Pan

Great apes practice a variety of locomotor behaviours depending on their habitat, body size, sex and age (although we focus only on adults in this study). In this study, *Pan* is represented only by *Pan troglodytes verus* from the Taï National Forest, Ivory Coast. Doran (1993) found that Taï adult *Pan* spend approximately 15%–18% of their daily time in locomotion and, within this locomotor time, they engage on average in 16% arboreal and in 84% terrestrial locomotion. Both lower limbs are often exposed to external forces (substrate reaction forces) where the knee is flexed and the hip is abducted to varying degrees during both terrestrial and arboreal locomotion (Ankel-Simons, 2010; D'Août et al., 2004; Georgiou et al., 2018; Isler, 2005; Lee et al., 2012; Pontzer et al., 2009) (Figure S1). During climbing, *Pan* may utilize their full flexion–extension range at the knee (D'Août et al., 2002; Isler, 2005). The single meniscal attachment of the lateral meniscus facilitates medial and lateral rotation of the knee (Javois et al., 2009; Landis & Karnick, 2006; Tardieu, 1999). Characteristic flattening of the femoral trochlea allows free patellar movements during knee rotation associated with foot grasping during arboreal behaviour (Tardieu, 1999). During terrestrial knuckle-walking in zoo-housed chimpanzees, knee flexion ranges from ~161.4° at foot touchdown to ~117.4° at toe-off, and there is inter-individual variation in vertical ground reaction force (Finestone et al., 2018; Kozma et al., 2018). Even though there is an evident lateral rotation movement during extension in *Pan*, the knee is still mostly loaded in flexed and varus postures during terrestrial locomotion (Lovejoy, 2007). The differing size between femoral condyles causes mediolateral knee rotation during all phases of terrestrial quadrupedal locomotion. Additionally, the medial condyle is loaded more than the lateral condyle (Sylvester, 2013; Sylvester & Pfisterer, 2012; Tardieu, 1999). There are no significant sex differences in the overall frequency of arboreal and terrestrial locomotion (Doran, 1993). However, there are significant sex differences in the type of arboreal locomotor behaviours used, with adult male *Pan* using significantly less quadrupedalism (males 23.4%, females 60.6%) and more vertical climbing (males 60.2%, females 52.4%) than females (Doran, 1993).

2.2.3 | Gorilla

Gorilla also engages most frequently in terrestrial knuckle-walking and the frequency of arboreality depends mostly on their habitat and body size (Doran, 1996; Doran, 1997; Isler, 2005; Remis, 1994; Tocheri et al., 2011). In this study, *Gorilla* is represented only by *Gorilla gorilla gorilla*, for which locomotor behaviour in wild has only been studied in one group (Bia Hokou, Central African Republic; Remis, 1994). During terrestrial knuckle-walking, the knee is flexed, as in *Pan*, and the hip is in abduction to varying degrees (Figure S1) (Finestone et al., 2018). Compared to *Pan*, zoo-housed *Gorilla* are found to extend their limbs more during terrestrial locomotion and vertical climbing (Crompton et al., 2008; Finestone et al., 2018; Isler, 2005; Kozma et al., 2018). The knee

angles vary from ~163.2° at foot touchdown to ~126.6° at toe-off (Kozma et al., 2018). Hip abduction is a clear advantage in climbing, and in *Gorilla*, it is necessary to accommodate their large belly, which limits hip flexion in its sagittal plane during climbing as well as in quadrupedal postures (Preuschof & Tardieu, 1996). However, flexion–extension range at the hip has been shown to differ more than 30° between sexes, with higher range of motion in females (Hammond, 2014), which could additionally rotate the knee more medially. Isler (2005) reported that maximal extension of the hip and knee during vertical climbing is significantly higher in the captive adult female *Gorilla* (approximately 135° knee extension) compared to males (approximately 100° knee extension). Additionally, Isler (2005) found that males exhibit a smaller range of motion at the knee during vertical climbing (approximately 55° knee range of motion) compared to females (approximately 65–85° knee range of motion).

2.2.4 | Pongo

Pongo is the most arboreal of all the great apes. They are characterized by greater joint mobility than other hominids due to their diverse locomotor behaviour where all limbs are used variously to achieve balance (Payne et al., 2006; Thorpe et al., 2009; Thorpe & Crompton, 2006). In this study, *Pongo* is represented by *Pongo pygmaeus* and *Pongo abelii*. During terrestrial locomotion, the *Pongo* knee posture in zoo-housed individuals does not differ significantly to that of African apes (Kozma et al., 2018). During terrestrial locomotion, *Pongo* is found to have a similar degree of knee extension to that of female *Gorilla*, but with a larger range of hip joint motion (Isler, 2005; Morbeck & Zihlman, 1989). However, during arboreal locomotion, their knee postures range from hyper-flexed to extended postures (Isler, 2005; Morbeck & Zihlman, 1989; Payne et al., 2006; Thorpe & Crompton, 2005, 2006; Thorpe et al., 2009) and thus the range of knee motion is significantly larger compared to *Pan* and *Gorilla* (Figure S1). Previous studies have found female Bornean *Pongo* to be more arboreal compared to their male counterparts (Cant, 1987; Galdikas, 1988). However, no sex differences in the frequency of arboreality have been found in Sumatran *Pongo* (e.g. Thorpe & Crompton, 2005; Thorpe & Crompton, 2006). Unfortunately, we are not able to test sex differences within *Pongo* in this study as we have only two males in our sample.

3 | HYPOTHESES AND PREDICTIONS

In this study we test two hypotheses. The first hypothesis is that trabecular architecture of the distal femur will reflect differences in knee postures and presumed loading during locomotor behaviours across *Homo*, *Pan/Gorilla* and *Pongo*. We predict that:

(1A) *Homo* will exhibit the highest BV/TV posteroinferiorly in the condyles due to their habitual extended knee posture. BV/TV on the patellar surface of femur will be higher laterally due to the higher loading of lateral knee compartment. BV/TV will be greater in the lateral condyle compared to medial condyle, reflecting the resistance of the knee adduction moment provided by the quadriceps and gastrocnemius muscles. *Homo* will exhibit the highest DA in anterior and posteroinferior/superior regions of both condyles (consistent with low variability in loading direction) resulting from the stereotypical loading of these regions during extended knee postures during all phases of bipedal locomotion.

(1B) *Pan* and *Gorilla* will exhibit the highest BV/TV posterosuperiorly on the condyles within their knee due to their more flexed knee position compared to *Homo*. BV/TV will be higher medially on patellar surface of femur due to the higher loading of medial knee compartment. *Pan* and *Gorilla* will display the highest DA in the posteroinferior/superior regions of the condyles (consistent with low variability in loading direction) due to their higher loading of the posterior regions during stereotypically flexed knee postures during arboreal and terrestrial locomotor behaviours.

(1C) *Pongo* will exhibit a more homogenous distribution of BV/TV across the condyles and patellar surface of femur relative to other great apes due to their more variable knee joint postures during locomotion (which may vary from full extension to full flexion). *Pongo* will exhibit the highest DA in the posterior regions of condyles (consistent with low variability in loading direction) in a similar pattern as *Pan* and *Gorilla* due to their higher loading of the posterior regions in mostly flexed knee postures particularly during terrestrial locomotion. However, due to more varied postures/loading in *Pongo*, we predict that DA will be the lowest (consistent with high variability in loading direction) and the most homogenous across the distal femora of all studied taxa.

The second hypothesis is that trabecular architecture will reflect sex differences (or lack thereof) in the locomotor behaviours and, in particular, the frequency of arboreality between female and males in our study taxa. Note, we cannot test for sex differences in *Pongo* due to sample size restrictions. We predict that:

(2A) If trabecular morphology reflects variation in frequency of terrestrial versus arboreal locomotion, we expect female *Gorilla* to show more flexed knee-posture loading than males due to greater frequency of climbing. If trabecular morphology reflects variation in the level of knee flexion/extension, we expect female *Gorilla* to have higher BV/TV in the lateral condyle, as well as in the lateral part of patellar surface and in the lateral epicondyle, compared to males due to their greater degrees of knee extension (particularly when climbing) and male *Gorilla* to have relatively higher BV/TV in the medial condyle and epicondyle because of their higher degree of flexion and thus higher loading of medial knee compartment (particularly when climbing).

(2B) If trabecular morphology reflects variation in frequency of terrestrial versus arboreal locomotion, we expect to find no significant differences in BV/TV and DA between female and male *Pan*, since no significant sex differences in the overall frequency of arboreal and terrestrial locomotion has been found in the Taï chimpanzees (Doran, 1993). Furthermore, even though sex differences in the types of arboreal locomotion have been reported in *Pan*, with

adult male *Pan* using significantly less quadrupedalism (males 23.4%, females 60.6%) and more vertical climbing (males 60.2%, females 52.4%) than females (Doran, 1993), the variation in the level of knee flexion/extension between sexes have not been previously described. Thus, if trabecular morphology reflects variation in the level of knee flexion/extension, there is no reason to predict these sex differences in the trabeculae of the knee in *Pan*. Similarly, we expect to find no significant differences in BV/TV and DA between female and male *Homo* as they are both obligate bipedal walkers.

4 | MATERIALS AND METHODS

4.1 | Study sample and scanning

4.1.1 | Study sample

The study sample consists of complete distal femora of *Homo sapiens* ($n = 26$ individuals), *Gorilla gorilla gorilla* ($n = 14$ individuals), *Pan troglodytes verus* ($n = 15$ individuals) and *Pongo* spp. ($n = 9$ individuals). Research involving non-human great apes plays a vital role in many anthropological and medical studies as their close phylogenetic relationship to humans makes them a useful model for reconstructing locomotor (and other) behaviours in hominin fossil record. The studied species were chosen as a representative sample of primates that use locomotor behaviours potentially found within the locomotor repertoires of fossil hominins. Details of the study sample are shown in Table 1. All great apes were wild born with no obvious signs of pathologies within their postcranial skeleton. The *Gorilla* sample is curated at the Powell-Cotton Museum in Birchington-on-Sea, UK, of which 13 individuals are from Cameroon and one is from the Democratic Republic of the Congo. The *Pan* sample is from the Taï Forest National Park, curated at the Max Planck Institute for Evolutionary Anthropology in Leipzig, Germany. The *Pongo* sample is from the Bavarian State Collection for Zoology in Munich, Germany and from the Natural History Museum in Berlin, Germany. Six individuals are *Pongo pygmaeus*, two are *P. abelii* and the species of one individual is unknown. Fifteen individuals of our human sample are from the W.M. Bass femoral collection from the Forensic Anthropology Centre at the University of Tennessee, USA and originate from diverse post-industrial populations. Eleven individuals are crew members of the Mary Rose ship from early 16th century (Barker, 1992) curated at the Portsmouth Museum, Portsmouth, UK. The Mary Rose sample comprises young adult males and are considered to represent high activity levels (e.g. Scorrer et al., 2021; Stirland & Waldron, 1997). Both human samples showed no obvious signs of pathologies within their postcranial skeleton. For most of our sample (91%), we used the right distal femur. However, when it was not possible due to preservation or methodological issues (such as low resolution of the CT scan), the mirrored left distal femur was used.

4.1.2 | MicroCT scanning

All distal femora were scanned via high-resolution micro-computed tomography (microCT) using a BIR ACTIS 225/300, Diondo D3 or Skyscan 1172 scanner housed at the Department of Human Evolution, Max Planck Institute for Evolutionary Anthropology (Leipzig, Germany), a Phoenix Nanotom S – X-ray tomograph at the Department of Micro-CT Laboratory, Museum of Natural History (Berlin, Germany), a Nikon 225/XTH scanner at the Cambridge Biotomography Centre, University of Cambridge (Cambridge, UK) or with the Diondo D1 scanner at the Imaging Centre for Life Sciences at the University of Kent (Canterbury, UK). The scan parameters included acceleration voltages of 100–160 kV and 100–140 μA using a 0.2 to 0.5 mm copper or brass filter. Scan resolution ranged between 0.024 mm and 0.058 mm depending on the size of the bone (Table 1). Images were reconstructed as 16-bit TIFF stacks.

4.2 | Data processing and trabecular bone analysis

Each distal femur was rotated into a standard anatomical orientation and non-bone inclusions were removed from the scans in Avizo Lite 9.0.0 (Visualization Sciences Group, SAS) (Figure 2a). Scans were subsequently segmented using the medical image analysis (MIA) clustering method (Dunmore et al., 2018) (Figure 2b). This method requires the definition of a grid size, which was selected by measuring the thickness of the thickest trabeculae in a cross-section and selecting a slightly higher value for each individual. A maximum of three classes were used across all individuals. MIA allows more accurate separation of trabeculae and offers more flexibility to deal

TABLE 1 Sample composition and voxel size range.

			Sex		Voxel size (mm)	
Taxon	**Locomotor behaviour**	***N***	**Female**	**Male**	**Min**	**Max**
Homo sapiens (1.0 kya to present)	Bipedal	15	Unknown		0.030	0.037
Homo sapiens (Mary Rose)	Bipedal	11	0	11	0.030	0.037
Gorilla gorilla gorilla	Terrestrial knuckle-walker	14	7	8	0.048	0.058
Pan troglodytes verus	Arboreal/knuckle-walker	15	8	7	0.029	0.030
Pongo sp.	Arboreal/suspensory	9	7	2	0.027	0.030
Total		64				

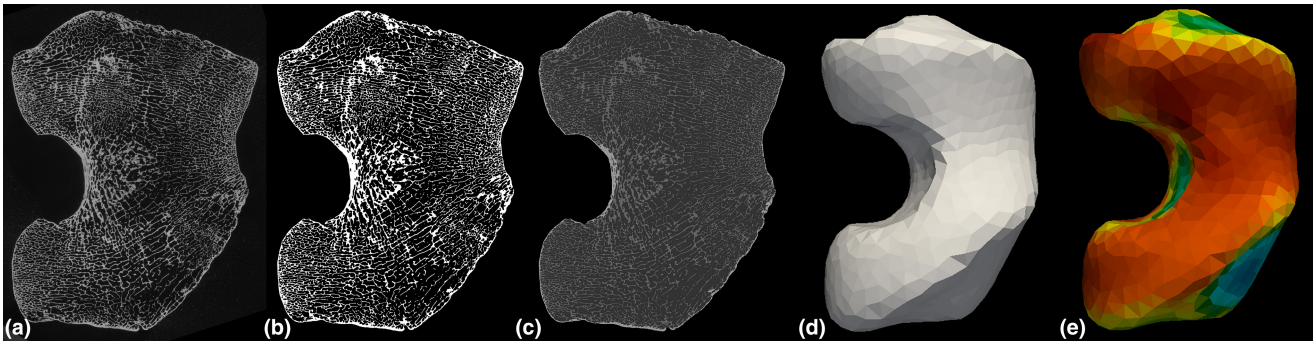

FIGURE 2 Processing steps of distal femur of a *Homo* specimen showing in inferior view. (a) Original high-res microCT image. (b) MicroCT image segmented by MIA (Dunmore et al., 2018). (c) MaskSeg defined by Medtool (Pahr & Zysset, 2009) showing the distinction between inner trabecular area and outer cortex. (d) Outer canonical atlas representing sample's mean size, position and external right distal femur morphology computed by cHMA (Bachmann et al., 2022). (e) Inner mesh representing rBV/TV distribution in human sample computed by cHMA (Bachmann et al., 2022).

with surrounding non-bone inclusions than other bone segmentation methods (Dunmore et al., 2018). The outer and inner layers of the cortex were defined using Medtool v 4.5 (www.dr-pahr.at/medtool), following published protocols (Gross et al., 2014; Pahr & Zysset, 2009). This involves morphological filters to fill the bone and use of a ray-casting method to isolate the external and internal edge of the cortex in 3D, resulting in a mask of the internal bone volume and outer cortex (Figure 2c).

4.2.1 | Canonical holistic morphometric analysis

A cHMA, combining HMA and statistical free-form deformation model (SDM), approach was used to analyse the patterns of trabecular bone distribution within whole epiphysis following published protocols (Bachmann et al., 2022). SDM operates on masked images of bones, where all images are registered onto a randomly chosen reference image using a similarity transform. All similarity transformations are then averaged and the centre of rotation is fixed. All images are then registered onto the aligned reference image and a free-form deformation is applied using a cubic B-spline transformation. The steps of registering and averaging can be repeated several times until the model has congregated. The last reference image is used as the canonical bone image for further steps of the analysis. The degree to which this may affect the results has been tested in Bachmann et al. (2022). In brief, cHMA creates a canonical bone from all the samples and then registers all samples onto that canonical bone. To create a canonical bone, we used 15 humans, 14 gorillas, 15 chimpanzees and 9 orangutan individuals to create canonical bone representing all species as much as possible. The canonical bone refers to the mean meshwork of bones formed from all the studied samples. All left-sided femora were mirrored in Avizo Lite 9.0.0 (Visualization Sciences Group, SAS) to resemble right-sided femora. All bones were then aligned into a mean position by translation and rotation in the image space and scaled to the mean bone size. Then, an SDM (Rueckert et al., 2003; Steiner et al., 2021) was used to create a canonical bone in 3D space representing the sample's mean internal and external bone morphology (in our case morphology of right distal femur) (Figure 2d). To produce the canonical atlas of the internal bone, the internal volume of each individual bone is used (Figure 2e). The canonical bone registration was run in Python 3.7.10, while required pre- and post-processing steps were performed in Medtool v 4.5 (www.dr-pahr.at/medtool). A 3D rectangular background grid with a grid size of 2.5 mm was built around each individual segmented volume and a sampling sphere (VOI) of 5 mm in diameter was used to measure BV/TV and DA across the entire bone in Medtool. Once these trabecular quantities were interpolated onto individual meshes, the meshes were deformed to the canonical mesh to allow for homologous volumetric comparisons.

DA was calculated using the mean intercept length method (Odgaard et al., 1997; Whitehouse, 1974). The value of DA is zero if the minor and major orientations are of equal magnitude, i.e. isotropic, and is one if the minor and major orientations are maximal different, i.e. anisotropic. Three-dimensional tetrahedral meshes of all specimens were created with CGAL 4.4 (CGAL, Computational Geometry, https://www.cgal.org), using the segmented trabecular structure and a characteristic mesh size of 3 mm. The morphometric values at each node of the background grid were then interpolated to the tetrahedral elements (back onto the canonical mesh) and the resulting BV/TV and DA distribution maps were visualized using Paraview 4.8.2 (Ahrens et al., 2005). Since data were collected from the canonical mesh, the datum collected at each node in the 3D grid is homologous between individuals. The BV/TV value for each mesh element was used to calculate the mean BV/TV for each individual. To compensate for potential systematic differences between selected taxa and to analyse bone volume distribution while controlling the magnitude, the BV/TV of each tetrahedron was divided by the overall average for that individual to give a measure of relative bone volume (rBV/TV). rBV/TV demonstrates where bone volume has increased or decreased relative to the mean allowing for comparisons between individuals and species that may differ in absolute BV/TV (Dunmore et al., 2019; Sukhdeo et al., 2020).

Femoral insertions of cruciate and collateral ligaments and of gastrocnemius muscle were located in the canonical distal femur shape (thus hereafter, just 'presumed insertions') based on their anatomical location for each studied species. Trabecular distribution under all ligament and muscle attachments of each individual was checked using the HMA of Medtool.

4.3 | Statistical analysis

All quantitative comparisons of measured variables and statistical analyses were conducted on the data generated from cHMA (Bachmann et al., 2022). All specimens have the same number of tetrahedral elements and the same topology. Only the position of the vertices changes. Thus, homology is accounted for by the topology of the canonical mesh and the tetrahedral elements of each specimen can be considered geometrically homologous (Bachmann et al., 2022). To analyse the distribution of trabecular bone in each species, principal component analyses (PCA) were run, creating two PCA models for rBV/TV and DA separately using the scalars associated with tetrahedral elements (including the geometry) of the canonical mesh as an input variable. This allows for visual comparison of the differences in genus-specific rBV/TV and DA patterns in distal femur. To demonstrate the loadings of each PC, we chose three standard deviations to represent 99.7% of the available variation. All values of the trabecular volumes were coloured by the signed loadings at three standard deviations of each principal component and thresholded at the 70th percentile of the rBV/TV or DA range. All PCA plots were done in R v3.4.1 using the rgl package (R Core Team, 2017). To explore if inter-specific allometry is driving species separation on PC1 of rBV/TV in our results, i.e. the potential that *Gorilla* has a different trabecular distribution because they have a larger body mass than *Pan*, we ran a regression of PC1 on 'bone volume' in all studied individuals (Figure S8). To explore potential intra-specific allometry, we ran a regression of PC1 on bone volume for each taxon separately (Figures S9–S11). We measured 3D bone size as the solid volume of the whole object, here the distal femur (as all femora were cut at a homologous location). This whole 'bone volume' (note this is not BV/TV in any sense) was measured for each of our individuals as a proxy for individual size. PC1 (as our sample species separate on PC1) could then be regressed on this bone volume.

5 | RESULTS

5.1 | Mean species trabecular bone distribution

5.1.1 | Relative bone volume in distal femur

Patellar surface and femoral condyles

In *Homo*, high rBV/TV (indicating the highest 30% of rBV/TV values, the regions assumed to be loaded the most) is concentrated in the posteroinferior volumes of both condyles, with higher values in the lateral condyle and on the patellar articular surface of the femur (Figure 3). In *Gorilla*, higher rBV/TV is found to extend from the inferior margin of the patellar articulation to the posterosuperior region of both condyles, again with higher values in the lateral condyle. *Gorilla* lacks trabecular concentration at the anterior regions of both condyles (i.e. regions assumed to be loaded in an extended knee). Posterosuperior and posteroinferior regions of both condyles exhibit lower rBV/TV concentrations in the deeper trabecular network of *Gorilla* and are evenly distributed between medial and lateral condyles compared to *Homo* (Figure 3). *Pan* exhibits a similar, but more spatially homogenous, rBV/TV distribution between the medial and lateral condyles as *Gorilla*. In *Pan*, rBV/TV is low in the anterior regions of both condyles as well; the low rBV/TV extends almost to the posteroinferior part of medial condyle, which differs from the pattern found in *Gorilla* (Figure 3). The most homogenous rBV/TV concentration is found in *Pongo*, with, again, low rBV/TV in anterior regions of both condyles. In *Pongo*, as in *Pan*, low rBV/TV almost reaches the posteroinferior part of medial condyle, however, the posteroinferior region of lateral condyle exhibits higher rBV/TV values compared to *Pan* (Figure 3).

Femoral insertions of cruciate and collateral ligaments

Note, even though approximate positions of ligaments and tendon insertion sites are well-known in humans and, to a lesser extent, great apes, the locations are necessarily artificial on the canonical models used in our study. Therefore, we state 'presumed' location to reflect our qualitative assessment of these insertions sites when interpreting the colour maps.

Homo exhibits high rBV/TV in the presumed insertions of cruciate ligaments, particularly for the posterior cruciate ligament in which high rBV/TV reaches to the middle of medial condyle (Figure 4). However, compared to medial condyle, rBV/TV under the anterior cruciate ligament does not penetrate as deeply into the trabecular network in lateral condyle (Figure 4). *Gorilla* also exhibits high rBV/TV in the presumed insertions of the cruciate ligaments, though not to the same degree as seen in *Homo*. rBV/TV under either cruciate insertion does not extend deeply into the epiphysis in *Gorilla* (Figure 4). *Pan* and *Pongo* show higher rBV/TV under the presumed insertions of both the posterior (medial condyle) and anterior (lateral condyle) cruciate ligaments than in *Gorilla*. rBV/TV under both insertions extends deeper into the epiphyses in *Pan* and *Pongo* compared to *Gorilla* or *Homo* (Figure 4) and in both taxa, rBV/TV under the posterior cruciate ligament extends deeper compared to that of the anterior cruciate ligament, particularly in *Pongo* (Figure 4).

High rBV/TV concentrations under the presumed insertions of collateral ligaments are present in all taxa. In *Homo*, the lateral epicondyle shows higher rBV/TV than the medial epicondyle. However, in neither case does the rBV/TV concentration extend deeply into the epiphysis (Figure 5). In great apes, relatively higher concentrations of rBV/TV are present under the medial epicondyle and the concentration within the lateral and medial epicondyles is more similar and extends slightly

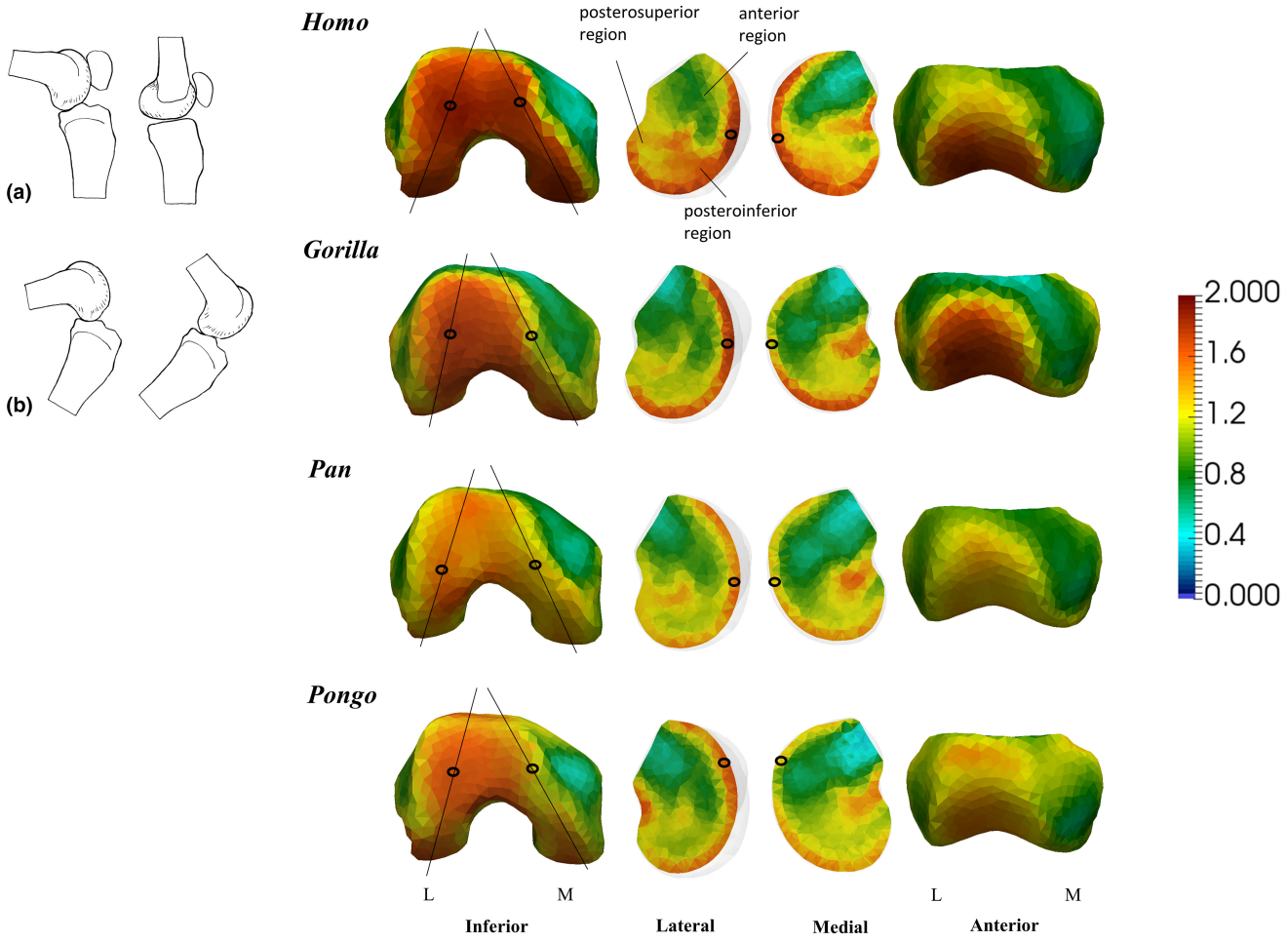

FIGURE 3 Species mean models of rBV/TV distribution in the patellar articular surface and femoral condyles of the distal femur of *Homo*, *Gorilla*, *Pan* and *Pongo*. Vertical lines through the inferior view mean models show where the slices are positioned. Cross sections were positioned in the middle of lateral and medial condyle. (a) Approximate patellar and condyle position during flexed (90°) and extended knee position in humans in medial view; (b) approximate condyle position during flexed and extended knee position in great apes. L, lateral; M, medial.

deeper into the epiphysis (especially in the region of the presumed medial collateral ligament insertion) compared to *Homo* (Figure 5).

Femoral insertions of gastrocnemius muscle

When looking at the posterior view of distal femur, high rBV/TV concentrations under the presumed insertions of gastrocnemius muscle are present in all taxa. In all taxa, the concentration under the presumed medial head goes deep inside the medial condyle; however, its presumed lateral head (with the highest values in *Pongo*) does not extend as deeply, especially in *Gorilla* (Figure 6). We found the most homogenous distribution under both presumed insertions of gastrocnemius in *Pan* and *Pongo*, but with lower values in *Pan* (Figure 6).

5.1.2 | Degree of anisotropy in the distal femur

Patellar surface, femoral condyles and femoral insertions of gastrocnemius muscle

The *Homo* mean distribution shows more anisotropic values in the posterosuperior/inferior regions of both condyles and under the patellar surface, with higher DA values in the lateral condyle (Figure 7). In *Gorilla*, DA is higher under the patellar surface on its medial side and more isotropic above the intercondylar fossa. Posterior regions of the *Gorilla* medial condyle are more anisotropic compared to posterior regions of lateral condyle. This pattern in the condyles is also found in *Pan* and *Pongo*, but posterior regions of lateral condyle are more anisotropic compared to that of *Gorilla* (Figure 7). The patellar surface of *Pan* shows more isotropic DA in the middle than on its medial or lateral side. This pattern is even more visible in *Homo* where DA values on the medial and lateral sides of patellar surface are even higher (Figure 7). *Pongo* exhibits a more homogenous distribution of moderate DA values; the most anisotropic values are in the posterior region of medial condyle and under the presumed insertions of cruciate ligaments relative to the patellar surface. In *Pongo*, DA values in both condyles are more homogenous compared to *Pan* (Figure 7). All taxa showed high DA values at the presumed insertions of gastrocnemius muscle (Figure 7).

Segmented images of each individual can be linked with the anisotropic/isotropic parts of the bone presented in the mean colour

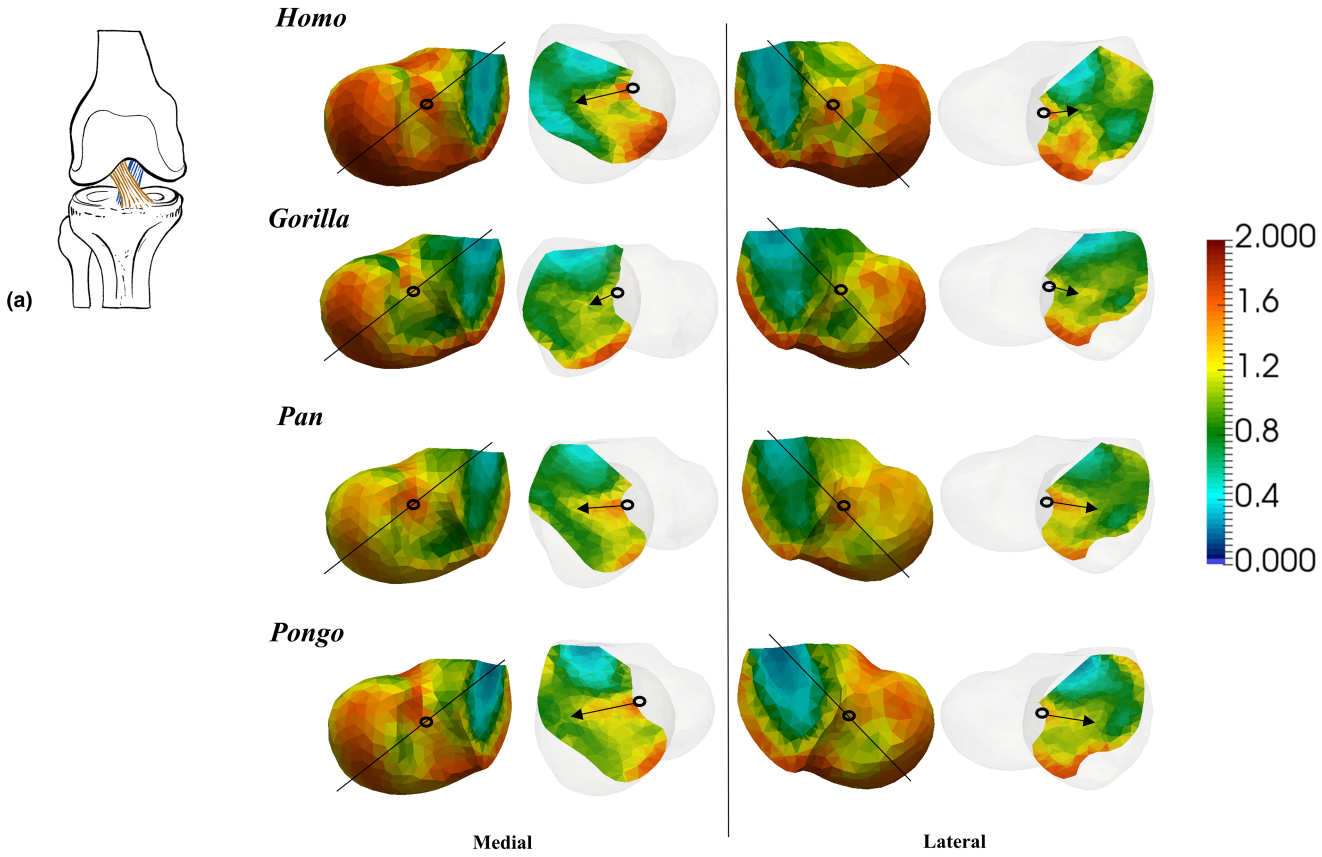

FIGURE 4 Species mean models of rBV/TV distribution under the presumed insertion of cruciate ligaments of the distal femur of *Homo*, *Gorilla*, *Pan* and *Pongo*. Vertical lines through the medial and lateral mean models show where the slices are positioned. Cross sections were positioned in the middle of presumed insertions of cruciate ligaments. (a) Anterior cruciate ligaments during neutral knee position in the anterior view.

maps. Figure 8 shows one representative individual of *Homo* and *Gorilla* to demonstrate the pattern of high DA in the lateral condyle, and beneath the presumed medial head of gastrocnemius muscle in *Homo* (Figure 8a), as well as high DA in the medial condyle of *Gorilla* (Figure 8b). Note that the signal within each individual might not be strong, while the mean colour maps are a representation of all individuals within a specific taxon.

5.2 | Principle component analyses

Figure 9 presents the results of a principal component analysis of rBV/TV distribution in the distal femur. PC1 explained 21.4% of the variation in rBV/TV values at each mesh cell. PC1 separates *Homo* from great apes with positive PC1 scores associated with higher rBV/TV on the patellar surface of the femur and on its medial distal articular surface. Negative PC1 scores, associated with the great apes, are associated with higher rBV/TV under the medial and lateral epicondyles and in the posteroinferior region of lateral condyle. PC2 accounted for 9.1% of the variation in rBV/TV values and separates *Pan* and *Pongo* from *Gorilla*. Positive PC2 distinguishes *Gorilla* not only due to a different pattern under the patellar surface but also especially due to higher rBV/TV under both presumed insertions of gastrocnemius muscle. Negative PC2 separates *Pan* and *Pongo* mostly due to their higher lateral loading of patellar surface and the rBV/TV concentration in the anterior part of lateral condyle. However, because all taxa share a similar rBV/TV concentration on the patellar surface (Figure 3), the separation on PC2 more likely reflects the low rBV/TV concentration at the presumed insertions of gastrocnemius muscle in *Pan* and *Pongo* compared to *Gorilla*.

The PCA of DA values reveals separation among the different taxa in distal femur (Figure 10). PC1 accounted for 22.2% of the variation in DA values. Positive PC1 separates *Homo*, with highly aligned trabeculae on the lateral side of the patellar surface, in the presumed insertion of the lateral head of gastrocnemius and by higher DA in the posteroinferior region of the lateral condyle (Figure 10). Negative PC1 separates great apes, with high DA under the presumed insertions of vastus lateralis and medialis, under the presumed insertion of medial head of gastrocnemius, and in the medial condyle, where we see highly align trabeculae in posterosuperior/inferior regions (Figure 10). PC2 explained 7.3% of the variation in DA values. Positive PC2 separates *Gorilla* and *Pan* from *Pongo* with highly aligned trabeculae where vastus lateralis and medialis cross the femur. In contrast, negative PC2 separates *Pongo* from *Gorilla* and *Pan* by high DA in the posterosuperior/inferior regions of lateral and medial condyles (Figure 10).

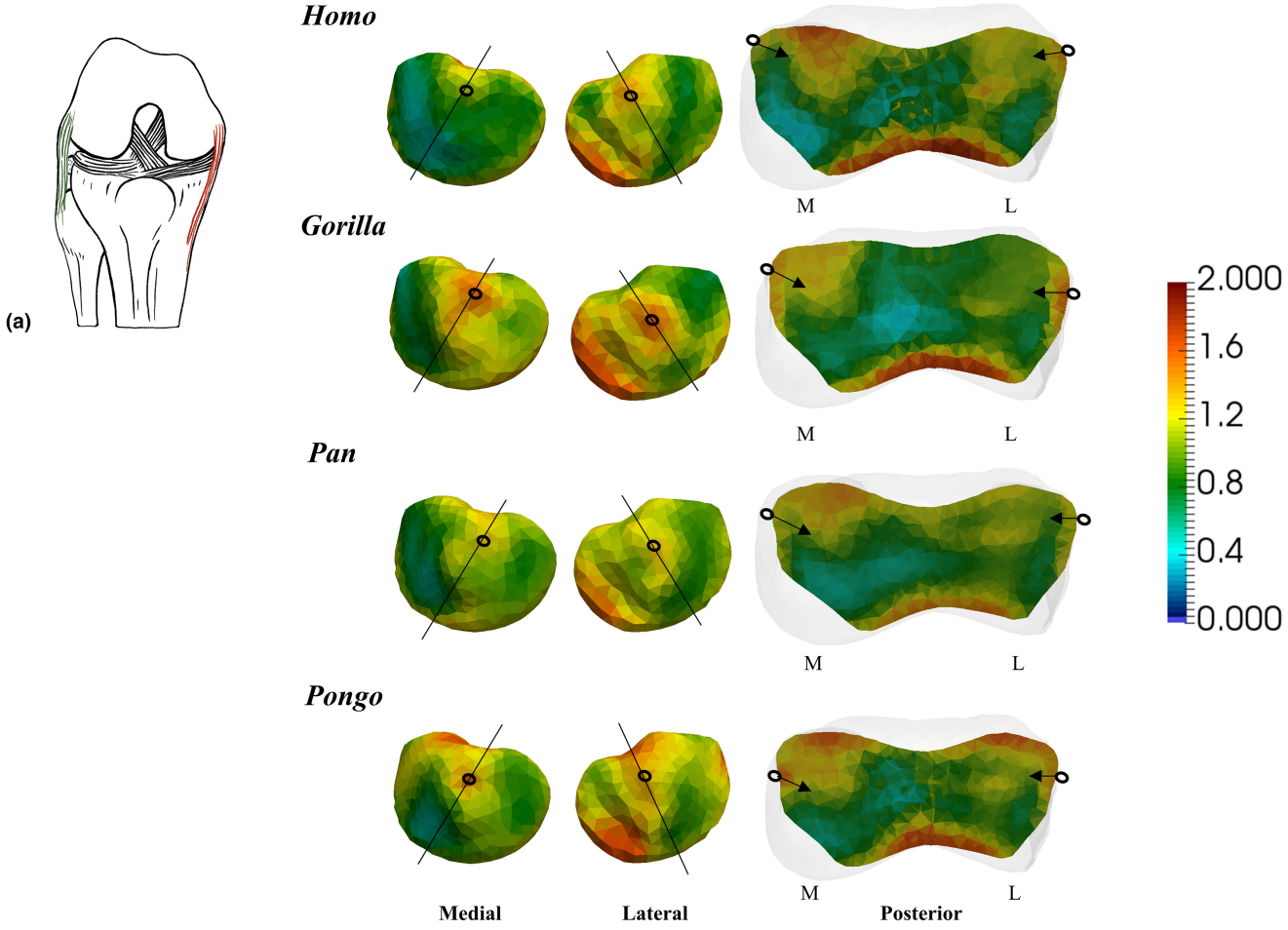

FIGURE 5 Species mean models of rBV/TV distribution under the presumed insertions of collateral ligaments of the distal femur of *Homo*, *Gorilla*, *Pan* and *Pongo*. Vertical lines through the medial and lateral mean models show where the slices are positioned. Cross sections were positioned in the middle of presumed insertions of collateral ligaments. (a) Lateral collateral ligaments attachments. L, lateral; M, medial.

5.3 | Trabecular bone distribution in *Homo*, *Gorilla* and *Pan* by sex

Figure 11a shows PCA of rBV/TV distribution in *Gorilla*. Female and male *Gorilla* do not separate on PC1 (explaining 15.5% of the variation). PC2 accounted for 14.6% of the variation in rBV/TV values. Thresholded mean models show that females separate from males (positive PC2) due to higher rBV/TV on the lateral side of patellar surface and on the articular surface of medial and lateral condyles. Female *Gorilla* also show higher rBV/TV in the lateral epicondyle and in the posteroinferior region of lateral condyle compared to males. In contrast, in male *Gorilla*, high rBV/TV values extend to the medial side of patellar surface and are more homogeneous across the patellar surface. Figure 11b shows PCA of DA distribution in *Gorilla*. PC1 accounted for 22.3% of the variation in DA values. Positive PC1 distinguishes *Gorilla* males due to higher DA values under the presumed insertions of vastus lateralis and medialis muscles and negative PC1 distinguishes females due to higher values inside the medial condyle and under the presumed insertion of medial head of gastrocnemius (Figure 11b). We found no separation in rBV/TV and DA distribution between the sexes in *Pan* (Figure 11a,b).

Figure S7 shows that the relative PC1 positions for rBV/TV (explaining 21.4% of the variation) and PC1 positions for DA (explaining 22.2% variation) remained constant when we divided the *Homo* sample by population (Mary Rose sample is represented by 11 male individuals) for a PCA. Note that we could have no test sex differences across whole human sample as sex is known only for 11 (male) of the 26 individuals.

5.4 | Allometry in our sample

We found no significant relationship between PC1 and bone volume (R^2 =0.002, p=0.890) across our sample (Figure S8). We found no significant relationship (R^2 =0.007, p=0.740) in *Gorilla* (sexes pooled; Figure S9). However, male *Gorilla* showed a stronger negative, if non-significant, relationship (R^2 =0.490, p=0.110) compared to females (R^2 =0.090, p=0.710) (Figure S9). We found a significant negative relationship (R^2 =0.292, p=0.011) in *Pan*,

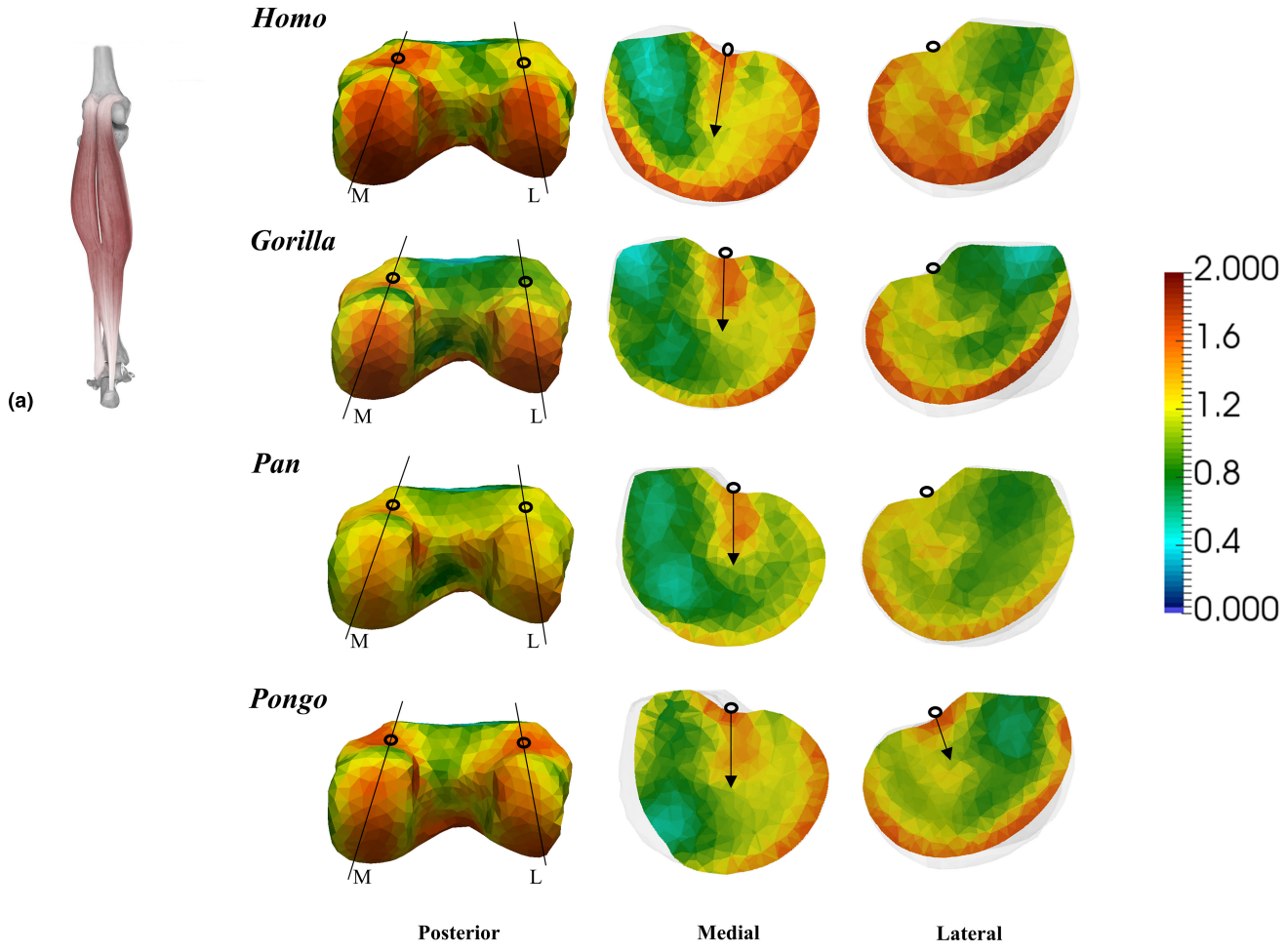

FIGURE 6 Species mean models of rBV/TV distribution under the presumed gastrocnemius muscle attachments of the distal femur of *Homo*, *Gorilla*, *Pan* and *Pongo*. Vertical lines through the posterior mean models show where the slices are positioned. Cross sections were positioned in the middle of presumed gastrocnemius attachments. (a) Gastrocnemius attachments. L, lateral; M, medial.

but no significant relationship within each sex, though females had a stronger relationship (R^2 =0.436, p=0.059) than males (R^2 =0.212, p=0.069) (Figure S10). Finally, as our human sample is predominantly male, we explored potential allometric differences between populations. We found no significant relationship across all humans (R^2 =0.058, p=0.170) and neither in the sedentary population (R^2 =0.221, p=0.280) or the active population (R^2 =0.012, p=1.000) (Figure S11).

6 | DISCUSSION

This study investigated trabecular variation in the distal femur of great apes and *Homo*. We expected trabecular architecture to differ based on different types of locomotion and predicted differences in habitual knee joint postures in extant hominid taxa. Also, we expected to find differences in trabecular architecture between female and male *Gorilla*, due to higher female arboreality, and to find no sex differences within *Pan* and *Homo*. We found general support for all our predictions.

6.1 | Trabecular bone structure of the distal femur in human bipedal walking

We predicted that *Homo* would be significantly different from other great apes in having a trabecular structure of the distal femur that reflected habitual use of extended knee postures during bipedalism. This prediction was supported. High rBV/TV values in posteroinferior regions of both condyles (Figure 3) were consistent with the extended knee postures during all gait phases of human walking. High rBV/TV concentration in lateral condyle (Figure 3) was consistent with the resistance, provided by the quadriceps and gastrocnemius muscles and medial collateral ligament, of the knee adduction moment (when the tibia medially rotates on the knee joint in the frontal plane) and with valgus knee postures (Nordin & Frankel, 2001; Racic et al., 2009). High rBV/TV concentration in the lateral condyle is consistent with human bipedal heel strike and subsequently transferring weight from the lateral side of the foot to the medial side (Elftman & Manter, 1935; Napier, 1967). The distinct rBV/TV distribution in patellar surface in *Homo* compared to great apes (Figure 3) most likely reflected a more convex trochlea, such

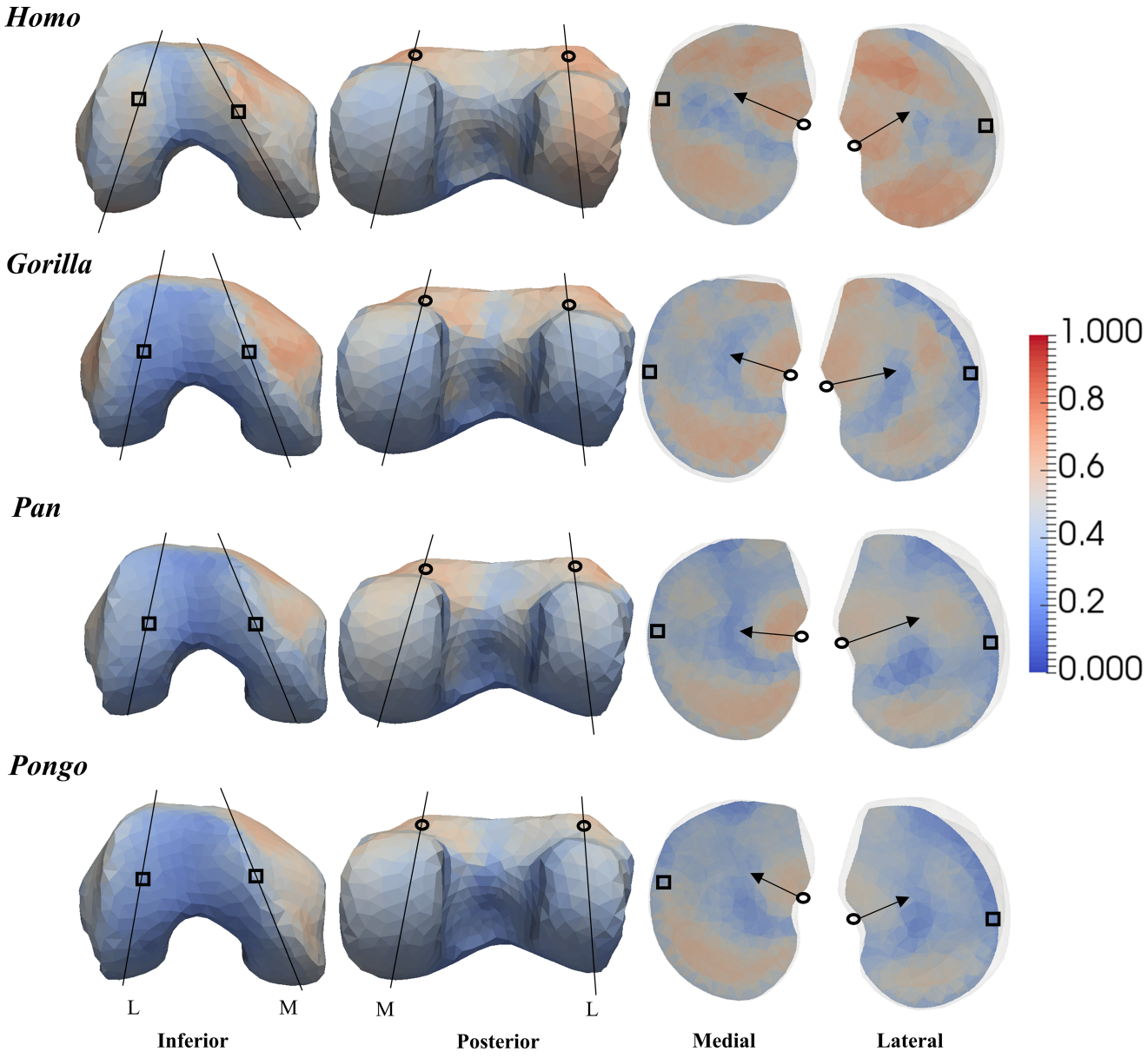

FIGURE 7 Species mean models of DA distribution in the patellar articular surface (marked with square) and in the presumed insertions of gastrocnemius muscle attachments (marked with circle) of the distal femur of *Homo*, *Gorilla*, *Pan* and *Pongo*. Vertical lines through the inferior view mean models show where the slices are positioned. Cross sections were positioned in the middle of lateral and medial condyle. L, lateral; M, medial.

loading is distributed, with flatter trochlea, more evenly across the patellar articular surface in great apes. We found high rBV/TV values on the patellar articular surface being extended more mediolaterally, reflecting the patella's more extensive articulation with the lateral part of the trochlea than with its medial part (Figure 3). Moreover, high rBV/TV was also found beneath the presumed insertions of gastrocnemius and those of the femoral ligaments (Figures 3–6) (see next). The human distal femur was more anisotropic posterosuperiorly/inferiorly in both condyles and under the patellar articular surface than in great apes (Figure 7). This DA pattern was also consistent with what we would expect from loading during human's stereotypical extended knee postures. Furthermore, high DA was also found beneath the presumed insertions of gastrocnemius and vastus lateralis and medialis muscles (Figures 7, 8; Figure S5) (see next). Overall, the trabecular distribution patterns found in our human sample are consistent with variation in trabecular structure found in previous studies of the proximal (Cazenave et al., 2019; Georgiou et al., 2019; Georgiou et al., 2020; Ruff et al., 2013; Ryan & Ketcham, 2002; Ryan & Walker, 2010; Volpato et al., 2008) and distal (Georgiou et al., 2018; Sylvester & Terhune, 2017) femur and with our current biomechanical understanding of human walking cycle (Alexander, 1991, 2004; Elftman & Manter, 1935; Javois et al., 2009; Landis & Karnick, 2006; Napier, 1967; Organ & Ward, 2006; Sylvester & Pfisterer, 2012; Tardieu, 1999).

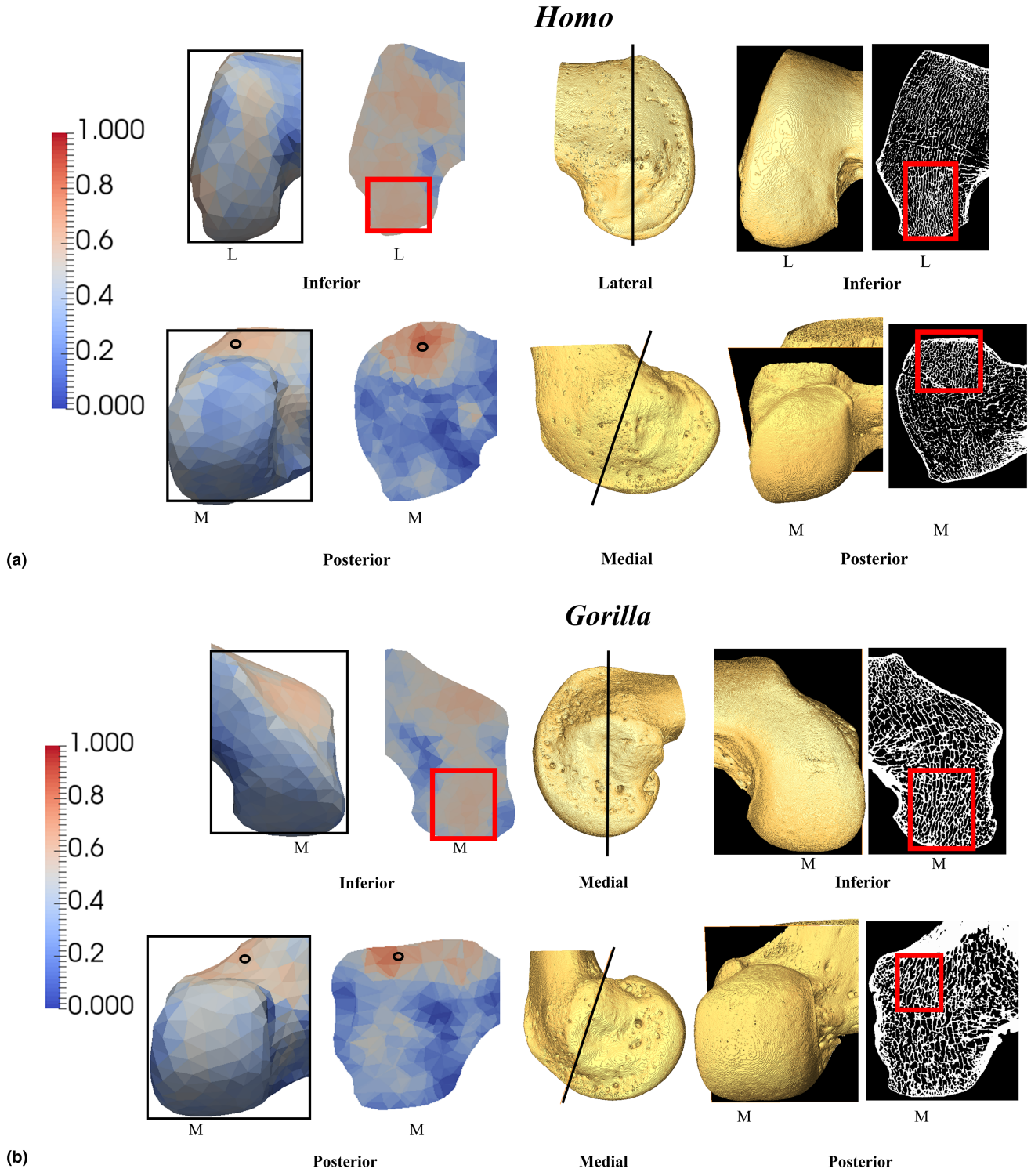

FIGURE 8 HMA and segmented models showing high DA concentration in the lateral/medial condyle and under the presumed insertions of gastrocnemius muscle attachments (marked with circle) of the distal femur of (a) *Homo* and (b) *Gorilla* individual. Vertical lines/squares show where the slices are positioned. L, lateral; M, medial.

6.2 | African ape trabecular bone structure and locomotor behaviour

We predicted that *Pan* and *Gorilla* would significantly differ from *Homo* and *Pongo*, but not from each other, in having a trabecular structure of the distal femur that reflected habitual use of a flexed knee posture during terrestrial and arboreal locomotion. This prediction was not fully supported. Compared to higher rBV/TV in the inferior patellar articulation in *Homo*, we found rBV/TV concentration posterosuperiorly in the condyles and mediolaterally

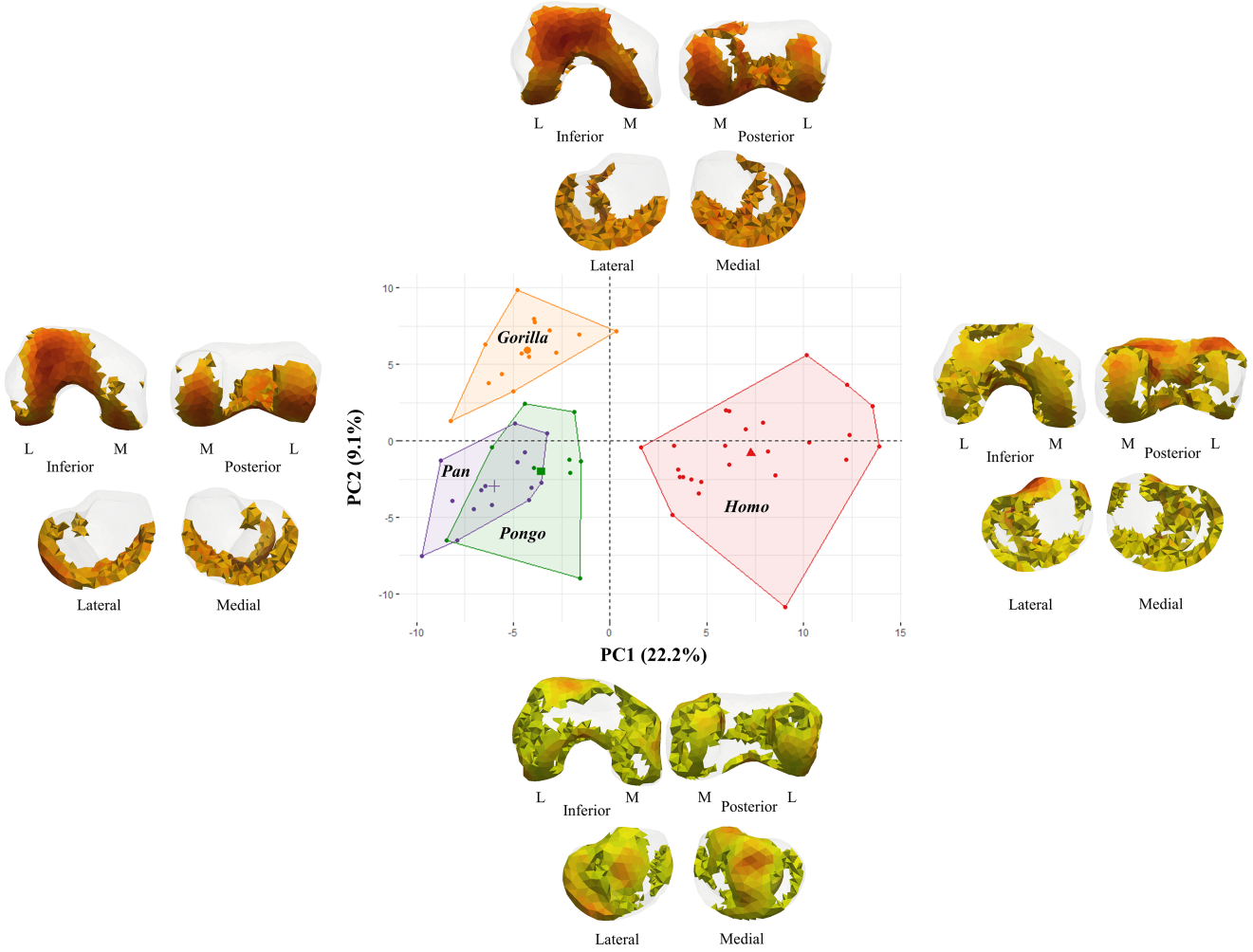

FIGURE 9 PCA of rBV/TV distribution in the distal femur of *Homo*, *Gorilla*, *Pan* and *Pongo* showing separation among studied taxa. Thresholding models represent high 30% of the range of rBV/TV values for negative and positive PCAs. Models demonstrate the highest loading causing the separation between humans (negative PC1 − 3SD) and great apes (positive PC1 + 3SD); between *Pongo*, *Pan* (negative PC2 − 3SD) and *Gorilla* (positive PC2 + 3SD). L, lateral; M, medial.

on the patellar articulation in African apes (Figure 3). This trabecular pattern is consistent with higher and more uniaxial loading of the distal femur in a flexed knee posture, which is used during quadrupedal knuckle-walking and vertical climbing in both taxa (D'Août et al., 2002, 2004; Georgiou et al., 2020; Isler, 2005). However, we also found some trabecular patterns that separate *Gorilla* from *Pan* (Figures 3, 9). The more homogenous rBV/TV distribution between and within both condyles of distal femur in *Pan* compared to *Gorilla* (Figure 3) may reflect the more variable knee loading that has been documented during climbing in captive *Pan* (Isler, 2005). However, the trabecular pattern under the patellar articular surface in *Pan* (Figure 9) suggested an opposite functional signal, with higher lateral loading of the patellar articular surface, which might be related to the quadriceps muscles that are active regardless of climbing posture and thus always pulling on the patella in the same way. Moreover, high rBV/TV was also found beneath the presumed insertions of gastrocnemius and under the presumed insertions of femoral ligaments (Figures 4–6) (see next). *Gorilla* and *Pan* both displayed the highest DA in the posteroinferior/superior regions of (especially) the medial condyle (Figure 7), which is again consistent with their stereotypically flexed knee postures and higher loading of medial knee compartment (Ankel-Simons, 2010; Crompton et al., 2008; D'Août et al., 2004; Georgiou et al., 2018; Isler, 2005; Kozma et al., 2018; Lee et al., 2012; Pontzer et al., 2009). High DA was also found at the presumed insertion sites of muscle tendons (Figures 7, 8; Figure S5) (see next).

6.3 | *Pongo* trabecular bone structure and locomotor behaviour

We predicted that *Pongo* would exhibit the most homogenous trabecular distribution across the distal femur compared to other apes due to their more variable knee joint postures during locomotion. This prediction was not fully supported. Even though *Pongo* trabecular structure was found to be quite homogenous, *Pan* also exhibited

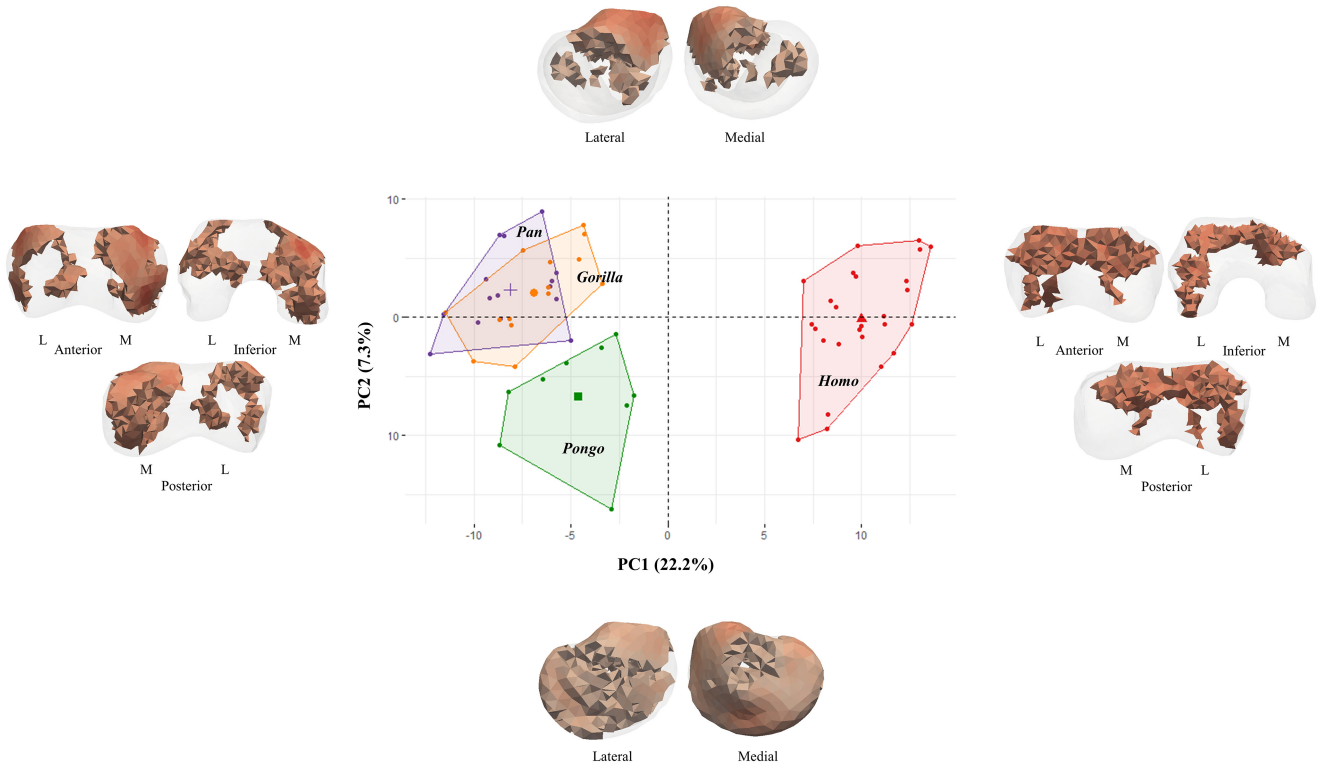

FIGURE 10 PCA of DA distribution in the distal femur of *Homo*, *Gorilla*, *Pan* and *Pongo* showing separation among studied taxa. Thresholding models represent high 30% of the range of DA values for negative and positive PCAs. Models demonstrate the highest loading causing the separation between humans (positive PC1 + 3SD) and great apes (negative PC1 − 3SD); between *Gorilla*, *Pan* (positive PC2 + 3SD) and *Pongo* (negative PC2 − 3SD). L, lateral; M, medial.

a similar pattern (Figure 3). Like African apes, *Pongo* did not show trabecular concentrations at the anterior regions of both condyles (Figure 3). *Pongo* shared with *Pan* low rBV/TV in the posteroinferior region of the medial condyle but had higher rBV/TV in the posteroinferior region of the lateral condyle (Figure 3). This pattern may suggest higher lateral loading during knee extension or higher degree of knee extension in *Pongo* compared with *Pan*. Posterior regions of both condyles were anisotropic as in African apes in *Pongo*. Moreover, we found rBV/TV concentration beneath the presumed insertions of gastrocnemius and under the presumed insertions of femoral ligaments (Figures 4–6) (see next). As in *Homo* and African apes, highly aligned trabeculae were also found at the presumed insertion sites of muscle tendons (Figures 7; Figure S5) (see next). *Pongo* is thought to have the most variable knee range of motion (Payne et al., 2006; Pina et al., 2014; Zihlman et al., 2011), together, these results are consistent with the highly mobile knee joint (Morbeck and Zihlman, 1989) that enables more variable loading during a diverse locomotor repertoire (Cant, 1987; Thorpe 2009; Thorpe & Crompton, 2006; Thorpe et al., 2007).

6.4 | Sex differences in *Gorilla*

We predicted that female and male *Gorilla* would significantly differ from each other due to higher arboreality and/or more extended knee posture when climbing in females (e.g. Hammond, 2014; Isler, 2005). This prediction was supported. We found distinct sex differences in our *Gorilla* sample, with females showing higher rBV/TV concentration in the posterior regions of lateral condyle, laterally on patellar surface and medially above intercondylar fossa (Figure 11a). In contrast, *Gorilla* males had higher rBV/TV concentrations in the medial epicondyle (Figure 11a). This sex pattern could suggest that in females there is higher lateral knee compartment loading and/or a more extended knee posture, as previously discussed in some studies (Crompton et al., 2008; Isler, 2005; Kozma et al., 2018) compared to more flexed knee position and/or greater lateral knee rotation during extension in males. Lateral knee rotation during extension has been previously discussed in *Pan* (Lovejoy, 2007), but it is currently unknown if this rotation is also found in *Gorilla*. Additionally, it is possible that low degree of extension (more common in males) is compensated for by the lateral rotation, but when the knee is highly extended, there may be more medial knee rotation (more common in females). Alternatively, when the knee flexes, posterior regions of the femoral condyles are expected to resist continuous compression, resulting in denser bone in these regions (Georgiou et al., 2018; Sylvester & Terhune, 2017). Thus, rBV/TV values potential higher increase in medial condyle compared to lateral condyle, as seen in our *Gorilla* male sample, could also suggest higher knee flexion in males compared to females. Moreover, we found females separating from males due to

FIGURE 11 PCA of rBV/TV and DA distribution in the distal femur of *Gorilla* and *Pan*. (a) PCA of rBV/TV distribution of *Gorilla* and *Pan* showing separation between sexes in *Gorilla* and no separation in *Pan*. (b) PCA of DA distribution of *Gorilla* and *Pan* showing separation between sexes in *Gorilla* and no separation in *Pan*. Thresholding models represent high 30% of the range of rBV/TV and DA values for negative and positive PCs. Models demonstrate the highest loading causing the separation between female and male gorillas. L, lateral; M, medial; *F*, female; *M*, male.

the higher anisotropy under both presumed insertions of gastrocnemius muscle (Figure 11b) (see next). However, the discussion of locomotor behaviour of lowland *Gorilla* is limited by lack of locomotor data in wild populations; with the exception of Remis (1994, 1995), all other locomotor studies derive from mountain gorillas (e.g. Doran, 1997; Thompson et al., 2018).

6.5 | Can trabecular structure underlying ligament/tendon attachments inform loading?

Our analysis also highlighted clear concentrations of rBV/TV at the presumed insertion sites of muscle tendons and knee joint ligaments (Figures 4–6) and high DA at the presumed insertion sites of muscle tendons in all taxa (Figures 7, 8; Figure S5). High rBV/TV values in the presumed insertions of cruciate ligaments illustrate that loading of these ligaments is resulting in modelling of underlying trabecular bone. Higher bone density at both cruciate ligaments insertion sites in all taxa (Figure 4) likely reflects the need to protect and stabilize the femur from dislocation throughout its range of motion. However, at both ligament insertion sites, *Pan* and *Pongo* showed higher trabecular density that extended deeper into the epiphysis compared with *Gorilla* (Figure 4), which may reflect more variable knee loading in the former. Potential support for this hypothesis would be more well-developed trabeculae under the cruciate ligament sites in female *Gorilla* compared to males, which we did find (Figure 11a). In addition, loading of the collateral ligaments also appears to stimulate increased rBV/TV under their insertion points in all taxa. Collateral ligaments, in theory, should be loose when the knee is flexed to allow more rotational movements, and tightened when the knee is extended. Here it seems they are equally loaded in African apes, which could suggest a certain degree of medial and lateral knee rotation when knee is not in full flexion (eventually when knee is extended). Lateral knee rotation during knee extension has been previously discussed in *Pan*. However, this would imply higher bone density under the insertion of medial collateral ligament compared to lateral collateral ligament. The separation of *Homo* from great apes was driven primarily by differences in trabecular structure at both collateral ligament insertion sites (Figure 9), suggesting different loading when knee is in extension and/or flexion.

In humans, gastrocnemius is a complex muscle that is involved in running, jumping and other fast movements of the leg, and to a lesser degree in walking and standing (e.g. Huijing, 1985; Ishikawa et al., 2007; Maganaris, 2003; Muramatsu et al., 2001). rBV/TV distribution beneath the insertions of gastrocnemius in *Homo* could result from forceful extension of knee and/or the hip joint in our sample (Anderson & Pandy, 2001; Baltzopoulos, 1995; Georgiou et al., 2020; Hardt, 1978; Simpson & Pettit, 1997; Taylor et al., 2004; Zheng et al., 1998). The specific activation of this muscle during different locomotor and postural activities in *Homo* is not known (Ishikawa et al., 2007), but the highly aligned trabeculae in the presumed insertions of gastrocnemius suggest that this region of the bone is loaded frequently and in a similar direction. Although Stern Jr and Susman (1981) have not measured the activity of the gastrocnemius muscle, they found activation of the gluteus medius and, to a lesser extent, the gluteus superficialis muscles to be similar in African ape climbing as in humans during bipedality. Since gastrocnemius is in action during most of the hindlimb activities in *Homo* (Georgiou et al., 2018; Ishikawa et al., 2007; Lichtwark et al., 2007; Neptune et al., 2001), it is presumably actively involved during arboreal locomotion in African apes as well. It has been previously found that gastrocnemius muscle becomes an extensor at highly flexed postures of the knee (Goh et al., 2017). Both *Pan* and *Gorilla* are characterized by flexed knee postures during quadrupedalism (Finestone et al., 2018) and particularly during climbing (Crompton et al., 2008; D'Août et al., 2002; Isler, 2005; Kozma et al., 2018) and thus, we would not expect they would separate from each other based on both presumed gastrocnemius insertions. We suggest that this could be the case of either more robust quadriceps muscle in *Gorilla* (e.g. Zihlman et al., 2011) or this muscle is somehow involved more during locomotion in *Gorilla* compared to *Pan*. The separation of female *Gorilla* from male *Gorilla* due to the higher anisotropy under both presumed insertions of gastrocnemius muscle suggests more stereotypical loading of gastrocnemius muscle in females compared to males and that perhaps this muscle is more active during climbing, which female *Gorilla* are thought to do more frequently than males (Isler, 2005; Kozma et al., 2018). The high rBV/TV and DA values in both presumed insertions of gastrocnemius muscle in *Pongo* could be the result of the involvement of this muscle during suspension by the lower limbs, which is common in *Pongo* (Thorpe & Crompton, 2006).

We also found that *Gorilla* and *Pan* are distinguished from *Pongo*, and likewise male *Gorilla* from female *Gorilla*, in their much more aligned trabecular structure at the presumed insertions of vastus lateralis and medialis. In quadrupedal primates, vastus lateralis and medialis are pulled towards the joint as the knee is flexed, causing the moment arm to decrease with increasing flexion (Krevolin et al., 2004; Spoor & Van Leeuwen, 1992; Visser et al., 1990). Thus, this might be a result of higher knee flexion in African apes compared to *Pongo* and of higher knee flexion in male *Gorilla* compared to female *Gorilla*. However, it is not clear if this anisotropy is caused by the contraction of vastus medialis and lateralis or/and joint reaction forces experienced by the femoral condyles towards the shaft.

6.6 | Trabecular bone and body mass

Although current research on allometry has not yielded consistent results (e.g. Barak et al., 2011; Cotter et al., 2009; Doube et al., 2011; Ryan & Shaw, 2013), one of the factors affecting trabecular bone structure is body mass. Thus, comparative research incorporating taxa of variable body mass should consider the effects of allometry when interpreting biomechanical and behavioural signals (Ruff et al., 2006). As body size increases, the gravitational forces also increase and thus the loads imposed upon the joints are higher (Doube et al., 2011). As bones get longer, they tend to become more

robust in overall external shape (Doube et al., 2011). Altering any of several properties of trabecular bone such as its volume, thickness or number can be an effective way to resist increasing joint loads caused by increasing body mass (Currey, 2003; Doube et al., 2011). Trabecular thickness, spacing, connectivity and number have been shown to significantly correlate with body mass such that trabeculae are thinner, more widely spaced and more numerous in smaller mammals compared to larger mammals (e.g. Barak et al., 2013; Cotter et al., 2009; Doube et al., 2011; Ryan & Shaw, 2013; Saers et al., 2019). In contrast, BV/TV and DA show no significant correlation with body mass and are considered to be relatively constant across species of various sizes (Barak et al., 2013; Cotter et al., 2009; Doube et al., 2011; Ryan & Shaw, 2013). However, Barak et al. (2013) also noted that BV/TV can increase through different mechanisms depending on body mass; in humans (70 kg), BV/TV increased via increases in trabecular thickness, while in rodents (e.g. 40 g and orders of magnitude smaller), BV/TV increased via increases in trabecular number (Barak et al., 2013).

In our study, average body mass varies from 36 kg (female *Pongo*) to 170 kg (male *Gorilla*; Smith & Jungers, 1997) and previous studies of extant hominid trabecular bone structure confirm no significant allometric effect on the variables (BV/TV and DA) that we analysed (e.g. Barak et al., 2013; Cotter et al., 2009; Ryan & Shaw, 2013). We found no significant allometric relationship on inter-specific level across our sample and only a weak significant negative relationship in *Pan* (sexes pooled) on the intra-specific level. Thus, we consider allometry to have little to no effect on our results of rBV/TV distribution and species separation. However, future investigation on intra-specific allometric effects on larger samples of females and males within each taxon, particularly for highly sexually dimorphic taxa, would be interesting to explore in more detail.

6.7 | Limitations

There are some limitations to this study that should be acknowledged. First, the colour maps of DA show regions with high/low anisotropy, but do not show the direction in which the trabeculae are oriented (Figures 7, 8; Figures S3–S5). The technical limitation of cHMA is that vectors and tensors cannot (yet) be transformed into the canonical space. Thus, we did not quantitatively explore the direction of loading in the highly anisotropic parts of distal femur (especially under the presumed insertions of vastus lateralis and medialis tendons). We suggest that future studies of trabecular structure should explore difference in the direction of trabecular orientation in extant primates; this may provide more informed functional interpretations of how the ligaments and muscles are involved in knee movements during specific types of locomotion. In addition, our functional interpretations are also limited by a lack of kinetic and kinematic data of the knee in non-human great apes, and most notably in wild populations.

Second, our study also found that *Pongo* has the most homogenous trabecular distribution, which not only is expected but also may be the result of the conflation of two *Pongo* species. The difficulty in obtaining high-resolution CT scans of complete adult *Pongo* distal femur also resulted in a lower sample size for this group and thus we were not able to explore sex differences. Future analysis of a larger *Pongo* sample could lead to a better understanding of knee postures/loading of this taxon.

Finally, analyses of sex differences of *Homo* were limited by the lack of sex information for most of the sample. Sex for only 11 (male) individuals was known. These individuals are from Mary Rose population only and thus sex differences could have been tested only by splitting *Homo* populations. However, even though we see partial separation between the populations, the relative PCA positions for rBV/TV and DA remained constant when PCA for studied species was split by *Homo* population (Figure S7).

7 | CONCLUSION

This study provided a holistic approach of trabecular bone architecture within the hominid distal femur. We showed that trabecular pattern distinguishes taxa based on their locomotor repertoires. Trabecular structure in *Homo* reflects habitual use of extended knee postures during bipedalism, habitual use of flexed knee posture during terrestrial and arboreal locomotion in African apes and the highly mobile knee joint in *Pongo*. Moreover, our results reflect differences in the level of knee extension/flexion between female and male *Gorilla*, which is consistent with our current understanding of greater arboreality in female *Gorilla*. Trabecular structure was not significantly different between sexes in *Pan* or *Homo*, which also reflects greater similarity in their locomotor behaviour between sexes. The emergence and form of bipedality in fossil hominins remains a central research focus in paleoanthropology (Barak et al., 2013; Carey & Crompton, 2005; Fajardo et al., 2007; Griffin et al., 2010; Raichlen et al., 2010; Ryan & Ketcham, 2002; Saparin et al., 2011; Shaw & Ryan, 2012; Skinner et al., 2015; Stern Jr & Susman, 1983; Susman, 1991; Susman et al., 1984) and extant great apes are often used to model aspects of fossil hominin locomotor repertoire, including the frequency of arboreality and types of bipedalism (e.g. facultative versus obligate). This study offers a comparative sample of trabecular structure in the hominoid distal femur and can contribute to future studies of locomotion in extinct taxa.

AUTHOR CONTRIBUTIONS

Andrea Lukova conceived and designed the experiments, acquired data, analysed and interpreted the data, prepared figures and tables, authored the first draft and revised subsequent drafts of the article and approved the final manuscript. Christopher J. Dunmore, Sebastian Bachmann, Alexander Synek and Dieter H. Pahr provided tools for data analysis, provided critical revision of the manuscript and approved of the final manuscript. Tracy L. Kivell and Matthew M. Skinner conceived and designed the experiments, contributed data, assisted with the interpretation of the data, provided critical revision of the manuscript and approved the final manuscript.

ACKNOWLEDGEMENTS

For access to specimens in their collections, we thank the following individuals/institutions: Max Planck Institute for Evolutionary Anthropology (C. Boesch, J-J. Hublin); Museum für Naturkunde – Leibniz Institute for Evolution and Biodiversity Science (F. Mayer, C. Funk); Powell-Cotton Museum (I. Livne); Royal Museum for Central Africa (E. Gilissen); University of Florence (J. Moggi-Cecchi, S. Bortoluzzi); Johann-Friedrich-Blumenback-Institute for Zoology and Anthropology, Georg-August University, Goettingen (B. Grosskopf); Frankfurt Senckenberg Museum (V. Volpato); University of the Witswatersand (L. Berger, B. Zipfel); Science Academy of the Czech Republic (J. Svoboda). We thank the Editor-in-Chief, J. Saers and one anonymous reviewer for these constructive comments that greatly improved our manuscript. This project has received funding from the European Research Council (ERC) under the European Union's Horizon 2020 research and innovation programme (grant agreement no. 819960).

DATA AVAILABILITY STATEMENT

Copies of all scans are curated by the relevant curatorial institutions that are responsible for the original specimens and access can be requested through each institution. The authors confirm that the data supporting the findings of this study are available from the corresponding author upon reasonable request.

ORCID

Andrea Lukova https://orcid.org/0009-0001-9843-336X
Christopher J. Dunmore https://orcid.org/0000-0002-8634-9777

REFERENCES

Ahrens, J., Geveci, B., Law, C., Hansen, C. & Johnson, C. (2005) 36-paraview: an end-user tool for large-data visualization. *The Visualization Handbook*, 717, 50038-1.

Alexander, R.M. (1991) Characteristics and advantages of human bipedalism. In: Rayner, J.M.V. & Wooton, R.J. (Eds.) *Biomechanics in evolution*. Cambridge: Cambridge University Press, pp. 225–266.

Alexander, R.M. (2004) Bipedal animals, and their differences from humans. *Journal of Anatomy*, 204(5), 321–330.

Anderson, F.C. & Pandy, M.G. (2001) Dynamic optimization of human walking. *Journal of Biomechanical Engineering*, 123(5), 381–390.

Ankel-Simons, F. (2010) *Primate anatomy: an introduction*. Burlington: Academic press.

Bachmann, S., Dunmore, C.J., Skinner, M.M., Pahr, D.H. & Synek, A. (2022) A computational framework for canonical holistic morphometric analysis of trabecular bone. *Scientific Reports*, 12(1), 5187.

Baltzopoulos, V. (1995) A videofluoroscopy method for optical distortion correction and measurement of knee-joint kinematics. *Clinical Bbiomechanics*, 10(2), 85–92.

Barak, M.M. (2019) Bone modeling or bone remodeling: that is the question. *American Journal of Physical Anthropology*, 172(2), 153–155.

Barak, M.M., Lieberman, D.E. & Hublin, J.J. (2011) A Wolff in sheep's clothing: trabecular bone adaptation in response to changes in joint loading orientation. *Bone*, 49(6), 1141–1151.

Barak, M.M., Lieberman, D.E., Raichlen, D., Pontzer, H., Warrener, A.G. & Hublin, J.J. (2013) Trabecular evidence for a human-like gait in *Australopithecus africanus*. *PLoS One*, 8(11), e77687.

Barak, M.M., Weiner, S. & Shahar, R. (2008) Importance of the integrity of trabecular bone to the relationship between load and deformation of rat femora: an optical metrology study. *Journal of Materials Chemistry*, 18(32), 3855–3864.

Barker, R. (1992) Shipshape for discoveries, and return. *The Mariner's Mirror*, 78(4), 433–447.

Berger, L.R. & Tobias, P.V. (1996) A chimpanzee-like tibia from Sterkfontein, South Africa and its implications for the interpretation of bipedalism in *Australopithecus africanus*. *Journal of Human Evolution*, 30(4), 343–348.

Biewener, A.A., Fazzalari, N.L., Konieczynski, D.D. & Baudinette, R.V. (1996) Adaptive changes in trabecular architecture in relation to functional strain patterns and disuse. *Bone*, 19(1), 1–8.

Cant, J.G. (1987) Positional behavior of female Bornean orangutans (*Pongo pygmaeus*). *American Journal of Primatology*, 12(1), 71–90.

Carey, T.S. & Crompton, R.H. (2005) The metabolic costs of 'bent-hip, bent-knee' walking in humans. *Journal of Human Evolution*, 48(1), 25–44.

Carlson, K.J. (2005) Investigating the form-function interface in African apes: relationships between principal moments of area and positional behaviors in femoral and humeral diaphyses. *American Journal of Physical Anthropology: The Official Publication of the American Association of Physical Anthropologists*, 127(3), 312–334.

Cazenave, M., Braga, J., Oettlé, A., Pickering, T.R., Heaton, J.L., Nakatsukasa, M. et al. (2019) Cortical bone distribution in the femoral neck of *Paranthropus robustus*. *Journal of Human Evolution*, 135, 102666.

Coelho, P.G., Fernandes, P.R., Rodrigues, H.C., Cardoso, J.B. & Guedes, J.M. (2009) Numerical modeling of bone tissue adaptation – a hierarchical approach for bone apparent density and trabecular structure. *Journal of Biomechanics*, 42(7), 830–837.

Cotter, M.M., Simpson, S.W., Latimer, B.M. & Hernandez, C.J. (2009) Trabecular microarchitecture of hominoid thoracic vertebrae. *The Anatomical Record: Advances in Integrative Anatomy and Evolutionary Biology*, 292(8), 1098–1106.

Crompton, R.H., Vereecke, E.E. & Thorpe, S.K. (2008) Locomotion and posture from the common hominoid ancestor to fully modern hominins, with special reference to the last common panin/hominin ancestor. *Journal of Anatomy*, 212(4), 501–543.

Currey, J.D. (2003) The many adaptations of bone. *Journal of Biomechanics*, 36(10), 1487–1495.

Currey, J.D. (2012) The structure and mechanics of bone. *Journal of Materials Science*, 47, 41–54.

Dalstra, M., Huiskes, R., Odgaard, A.V. & Van Erning, L. (1993) Mechanical and textural properties of pelvic trabecular bone. *Journal of Biomechanics*, 26(4–5), 523–535.

D'Août, K., Aerts, P., De Clercq, D., De Meester, K. & Van Elsacker, L. (2002) Segment and joint angles of hind limb during bipedal and quadrupedal walking of the bonobo (*Pan paniscus*). *American Journal of Physical Anthropology: The Official Publication of the American Association of Physical Anthropologists*, 119(1), 37–51.

D'Août, K., Vereecke, E., Schoonaert, K., De Clercq, D., Van Elsacker, L. & Aerts, P. (2004) Locomotion in bonobos (*Pan paniscus*): differences and similarities between bipedal and quadrupedal terrestrial walking, and a comparison with other locomotor modes. *Journal of Anatomy*, 204(5), 353–361.

DeMars, L.J., Kuo, S., Saers, J.P., Stock, J.T. & Ryan, T.M. (2022) Trabecular bone structural variation of the human distal tibia, talus, and calcaneus. *The FASEB Journal*, 36.

Demes, B. (2007) In vivo bone strain and bone functional adaptation. *American Journal of Physical Anthropology*, 133(1), 717–722.

Demes, B., Jungers, W.L. & Walker, C. (2000) Cortical bone distribution in the femoral neck of Strepsirrhine primates. *Journal of Human Evolution*, 39(4), 367–379.

DeSilva, J.M. (2009) Functional morphology of the ankle and the likelihood of climbing in early hominins. *Proceedings of the National Academy of Sciences*, 106(16), 6567–6572.

DeSilva, J.M., Churchill, S.E., Zipfel, B., Walker, C.S., Sylvester, A.D., McNutt, E.J. et al. (2018) *Australopithecus sediba* – the anatomy of the lower limb skeleton of *Australopithecus sediba*. *PaleoAnthropology*, 2018, 357–405.

DeSilva, J.M. & Devlin, M.J. (2012) A comparative study of the trabecular bony architecture of the talus in humans, non-human primates, and *Australopithecus*. *Journal of Human Evolution*, 63(3), 536–551.

Doran, D.M. (1993) Comparative locomotor behavior of chimpanzees and bonobos: The influence of morphology on locomotion. *American Journal of Physical Anthropology*, 91(1), 83–98.

Doran, D.M. (1996) Comparative positional behavior of the African apes. In: McGrew, W., Marchant, L. & Nishida, T. (Eds.) *Great ape societies*. Cambridge: Cambridge University Press, pp. 213–224.

Doran, D.M. (1997) Ontogeny of locomotion in mountain gorillas and chimpanzees. *Journal of Human Evolution*, 32(4), 323–344.

Doube, M., Kłosowski, M.M., Wiktorowicz-Conroy, A.M., Hutchinson, J.R. & Shefelbine, S.J. (2011) Trabecular bone scales allometrically in mammals and birds. *Proceedings of the Royal Society B: Biological Sciences*, 278(1721), 3067–3073.

Dunmore, C.J., Bachmann, S., Synek, A., Pahr, D.H., Skinner, M.M. & Kivell, T.L. (2023) The deep trabecular structure of first metacarpals in extant hominids. *American Journal of Biological* Anthropology.

Dunmore, C.J., Kivell, T.L., Bardo, A. & Skinner, M.M. (2019) Metacarpal trabecular bone varies with distinct hand-positions used in hominid locomotion. *Journal of Anatomy*, 235(1), 45–66.

Dunmore, C.J., Skinner, M.M., Bardo, A., Berger, L.R., Hublin, J.J., Pahr, D.H. et al. (2020) The position of *Australopithecus sediba* within fossil hominin hand use diversity. *Nature Ecology & Evolution*, 4(7), 911–918.

Dunmore, C.J., Wollny, G. & Skinner, M.M. (2018) MIA-clustering: a novel method for segmentation of paleontological material. *PeerJ*, 6, e4374.

Elftman, H. & Manter, J. (1935) The evolution of the human foot, with especial reference to the joints. *Journal of Anatomy*, 70(Pt 1), 56–67.

Eriksen, E.F., Melsen, F. & Mosekilde, L. (1984) Reconstruction of the resorptive site in iliac trabecular bone: A kinetic model for bone resorption in 20 normal individuals. *Metabolic Bone Disease & Related Research*, 5(5), 235–242.

Fajardo, R.J., Müller, R., Ketcham, R.A. & Colbert, M. (2007) Nonhuman anthropoid primate femoral neck trabecular architecture and its relationship to locomotor mode. *The Anatomical Record: Advances in Integrative Anatomy and Evolutionary Biology*, 290(4), 422–436.

Finestone, E.M., Brown, M.H., Ross, S.R. & Pontzer, H. (2018) Great ape walking kinematics: implications for hominoid evolution. *American Journal of Physical Anthropology*, 166(1), 43–55.

Frelat, M.A., Shaw, C.N., Sukhdeo, S., Hublin, J.J., Benazzi, S. & Ryan, T.M. (2017) Evolution of the hominin knee and ankle. *Journal of Human Evolution*, 108, 147–160.

Galdikas, B.M. (1988) Orangutan diet, range, and activity at Tanjung Puting, Central Borneo. *International Journal of Primatology*, 9, 1–35.

Georgiou, L., Dunmore, C.J., Bardo, A., Buck, L.T., Hublin, J.J., Pahr, D.H. et al. (2020) Evidence for habitual climbing in a Pleistocene hominin in South Africa. *Proceedings of the National Academy of Sciences*, 117(15), 8416–8423.

Georgiou, L., Kivell, T.L., Pahr, D.H., Buck, L.T. & Skinner, M.M. (2019) Trabecular architecture of the great ape and human femoral head. *Journal of Anatomy*, 234(5), 679–693.

Georgiou, L., Kivell, T.L., Pahr, D.H. & Skinner, M.M. (2018) Trabecular bone patterning in the hominoid distal femur. *PeerJ*, 6, e5156.

Girgis, F.G., Marshall, J.L. & Jem, A.A.M. (1975) The cruciate ligaments of the knee joint: anatomical. Functional and experimental analysis. *Clinical Orthopaedics and Related Research®*, 106, 216–231.

Glatt, V., Canalis, E., Stadmeyer, L. & Bouxsein, M.L. (2007) Age-related changes in trabecular architecture differ in female and male C57BL/6J mice. *Journal of Bone and Mineral Research*, 22(8), 1197–1207.

Goh, C., Blanchard, M.L., Crompton, R.H., Gunther, M.M., Macaulay, S. & Bates, K.T. (2017) A 3D musculoskeletal model of the western lowland gorilla hind limb: moment arms and torque of the hip, knee and ankle. *Journal of Anatomy*, 231(4), 568–584.

Griffin, N.L., D'Août, K., Ryan, T.M., Richmond, B.G., Ketcham, R.A. & Postnov, A. (2010) Comparative forefoot trabecular bone architecture in extant hominids. *Journal of Human Evolution*, 59(2), 202–213.

Gross, T., Kivell, T.L., Skinner, M.M., Nguyen, N.H. & Pahr, D.H. (2014) A CT-image-based method for the holistic analysis of cortical and trabecular bone. *Submitted to Pal Elec*, 17, 33A.

Haile-Selassie, Y., Saylor, B.Z., Deino, A., Levin, N.E., Alene, M. & Latimer, B.M. (2012) A new hominin foot from Ethiopia shows multiple Pliocene bipedal adaptations. *Nature*, 483(7391), 565–569.

Halloran, B.P., Ferguson, V.L., Simske, S.J., Burghardt, A., Venton, L.L. & Majumdar, S. (2002) Changes in bone structure and mass with advancing age in the male C57BL/6J mouse. *Journal of Bone and Mineral Research*, 17(6), 1044–1050.

Hammond, A.S. (2014) In vivo baseline measurements of hip joint range of motion in suspensory and nonsuspensory anthropoids. *American Journal of Physical Anthropology*, 153(3), 417–434.

Harcourt-Smith, W. (2016) Early hominin diversity and the emergence of the genus *Homo*. *Journal of Anthropological Sciences*, 94, 19–27.

Harcourt-Smith, W.E., Throckmorton, Z., Congdon, K.A., Zipfel, B., Deane, A.S., Drapeau, M.S. et al. (2015) The foot of *Homo naledi*. *Nature Communications*, 6(1), 8432.

Hardt, D.E. (1978) Determining muscle forces in the leg during normal human walking – an application and evaluation of optimization methods. *Journal of Biomechanical Engineering*, 100(2), 72–78.

Harrison, L.C., Nikander, R., Sikiö, M., Luukkaala, T., Helminen, M.T., Ryymin, P. et al. (2011) MRI texture analysis of femoral neck: detection of exercise load-associated differences in trabecular bone. *Journal of Magnetic Resonance Imaging*, 34(6), 1359–1366.

Hirschmann, M.T. & Müller, W. (2015) Complex function of the knee joint: the current understanding of the knee. *Knee Surgery, Sports Traumatology, Arthroscopy*, 23, 2780–2788.

Homminga, J., Mccreadie, B.R., Weinans, H. & Huiskes, R. (2003) The dependence of the elastic properties of osteoporotic cancellous bone on volume fraction and fabric. *Journal of Biomechanics*, 36(10), 1461–1467.

Huijing, P.A. (1985) Architecture of the human gastrocnemius muscle and some functional consequences. *Cells, Tissues, Organs*, 123(2), 101–107.

Ishikawa, M., Pakaslahti, J. & Komi, P.V. (2007) Medial gastrocnemius muscle behavior during human running and walking. *Gait & Posture*, 25(3), 380–384.

Isler, K. (2005) 3D-kinematics of vertical climbing in hominoids. *American Journal of Physical Anthropology: The Official Publication of the American Association of Physical Anthropologists*, 126(1), 66–81.

Javois, C., Tardieu, C., Lebel, B., Seil, R., Hulet, C. & Société française d'arthroscopie. (2009) Comparative anatomy of the knee joint: effects on the lateral meniscus. *Orthopaedics & Traumatology, Surgery & Research*, 95(8), 49–59.

Kamibayashi, L., Wyss, U.P., Cooke, T.D.V. & Zee, B. (1995) Trabecular microstructure in the medial condyle of the proximal tibia of patients with knee osteoarthritis. *Bone*, 17(1), 27–35.

Kozma, E.E., Webb, N.M., Harcourt-Smith, W.E., Raichlen, D.A., D'Août, K., Brown, M.H. et al. (2018) Hip extensor mechanics and the evolution of walking and climbing capabilities in humans, apes, and fossil hominins. *Proceedings of the National Academy of Sciences*, 115(16), 4134–4139.

Krevolin, J.L., Pandy, M.G. & Pearce, J.C. (2004) Moment arm of the patellar tendon in the human knee. *Journal of Biomechanics*, 37(5), 785–788.

Kuo, S., Saers, J.P., Scott, R.S. & Ryan, T.M. (2022) Trabecular and cortical bone morphology of the distal radius in humans, chimpanzees, cercopithecids, and anteaters. *The FASEB Journal*, 36.

Landis, E.K. & Karnick, P. (2006) A three-dimensional analysis of the geometry and curvature of the proximal tibial articular surface of hominoids. *In Three-Dimensional Image Capture and Applications VII*, 6056, 189–200.

Lee, L.F., O'Neill, M.C., Demes, B., LaBoda, M.D., Thompson, N.E., Larson, S.G. et al. (2012) Joint kinematics in chimpanzee and human bipedal walking. *The Hip*, 20(10), 32–42.

Lichtwark, G.A., Bougoulias, K. & Wilson, A.M. (2007) Muscle fascicle and series elastic element length changes along the length of the human gastrocnemius during walking and running. *Journal of Biomechanics*, 40(1), 157–164.

Loewen, N., Fautsch, M.P., Peretz, M., Bahler, C.K., Cameron, J.D., Johnson, D.H. et al. (2001) Genetic modification of human trabecular meshwork with lentiviral vectors. *Human Gene Therapy*, 12(17), 2109–2119.

Loudon, J.K. (2016) Biomechanics and pathomechanics of the patellofemoral joint. *International Journal of Sports Physical Therapy*, 11(6), 820–830.

Lovejoy, C.O. (1988) Evolution of human walking. *Scientific American*, 259(5), 118–125.

Lovejoy, C.O. (2007) The natural history of human gait and posture: part 3. *The Knee Gait & Posture*, 25(3), 325–341.

Lovejoy, C.O., Simpson, S.W., White, T.D., Asfaw, B. & Suwa, G. (2009) Careful climbing in the Miocene: the forelimbs of *Ardipithecus ramidus* and humans are primitive. *Sciences*, 326(5949), 70-70e8.

Maganaris, C.N. (2003) Force-length characteristics of the in vivo human gastrocnemius muscle. *Clinical Anatomy: The Official Journal of the American Association of Clinical Anatomists and the British Association of Clinical Anatomists*, 16(3), 215–223.

Mann, R.A. & Hagy, J. (1980) Biomechanics of walking, running, and sprinting. *The American Journal of Sports Medicine*, 8(5), 345–350.

Maquer, G., Musy, S.N., Wandel, J., Gross, T. & Zysset, P.K. (2015) Bone volume fraction and fabric anisotropy are better determinants of trabecular bone stiffness than other morphological variables. *Journal of Bone and Mineral Research*, 30(6), 1000–1008.

Masouros, S.D., Bull, A.M.J. & Amis, A.A. (2010) Biomechanics of the knee joint. *Orthopaedics and Traumatology*, 24(2), 84–91.

Mazurier, A., Nakatsukasa, M. & Macchiarelli, R. (2010) The inner structural variation of the primate tibial plateau characterized by high-resolution microtomography. Implications for the reconstruction of fossil locomotor behaviours. *Comptes Rendus Palevol*, 9(6–7), 349–359.

Mittra, E., Rubin, C. & Qin, Y.X. (2005) Interrelationship of trabecular mechanical and microstructural properties in sheep trabecular bone. *Journal of Biomechanics*, 38(6), 1229–1237.

Morbeck, M.E. & Zihlman, A.L. (1989) Body size and proportions in chimpanzees, with special reference to *Pan troglodytes schweinfurthii* from Gombe National Park, Tanzania. *Primates*, 30, 369–382.

Muramatsu, T., Muraoka, T., Takeshita, D., Kawakami, Y., Hirano, Y. & Fukunaga, T. (2001) Mechanical properties of tendon and aponeurosis of human gastrocnemius muscle in vivo. *Journal of Applied Physiology*, 90(5), 1671–1678.

Napier, J. (1967) The antiquity of human walking. *Scientific American*, 216(4), 56–67.

Neptune, R.R. & Kautz, S.A. (2001) Muscle activation and deactivation dynamics: the governing properties in fast cyclical human movement performance? *Exercise and Sport Sciences Reviews*, 29(2), 76–81.

Nilsson, J. & Thorstensson, A. (1987) Adaptability in frequency and amplitude of leg movements during human locomotion at different speeds. *Acta Physiologica Scandinavica*, 129(1), 107–114.

Nordin, M. & Frankel, V.H. (Eds.). (2001) *Basic biomechanics of the musculoskeletal system*. 3rd ed. Philadelphia, PA: Lippincott Williams & Wilkins.

Novitskaya, E., Zin, C., Chang, N., Cory, E., Chen, P., D'Lima, D. et al. (2014) Creep of trabecular bone from the human proximal tibia. *Materials Science and Engineering: C*, 40, 219–227.

Odgaard, A., Kabel, J., van Rietbergen, B., Dalstra, M. & Huiskes, R. (1997) Fabric and elastic principal directions of cancellous bone are closely related. *Journal of Biomechanics*, 30(5), 487–495.

Ohman, J.C., Krochta, T.J., Lovejoy, C.O., Mensforth, R.P. & Latimer, B. (1997) Cortical bone distribution in the femoral neck of hominoids: implications for the locomotion of *Australopithecus afarensis*. *American Journal of Physical Anthropology: The Official Publication of the American Association of Physical Anthropologists*, 104(1), 117–131.

Organ, J.M. & Ward, C.V. (2006) Contours of the hominoid lateral tibial condyle with implications for *Australopithecus*. *Journal of Human Evolution*, 51(2), 113–127.

Pahr, D.H. & Zysset, P.K. (2009) From high-resolution CT data to finite element models: development of an integrated modular framework. *Computer Methods in Biomechanics and Biomedical Engineering*, 12(1), 45–57.

Paternoster, L., Lorentzon, M., Lehtimäki, T., Eriksson, J., Kähönen, M., Raitakari, O. et al. (2013) Genetic determinants of trabecular and cortical volumetric bone mineral densities and bone microstructure. *PLoS Genetics*, 9(2), e1003247.

Payne, R.C., Crompton, R.H., Isler, K., Savage, R., Vereecke, E.E., Günther, M.M. et al. (2006) Morphological analysis of the hindlimb in apes and humans. I. Muscle architecture. *Journal of Anatomy*, 208(6), 709–724.

Pearson, O.M. & Lieberman, D.E. (2004) The aging of Wolff's "law": ontogeny and responses to mechanical loading in cortical bone. *American Journal of Physical Anthropology*, 125(S39), 63–99.

Pina, M., Almecija, S., Alba, D.M., O'Neill, M.C. & Moya-Sola, S. (2014) The middle Miocene ape *Pierolapithecus catalaunicus* exhibits extant great ape-like morphometric affinities on its patella: inferences on knee function and evolution. *PLoS One*, 9(3), e91944.

Pontzer, H., Lieberman, D.E., Momin, E., Devlin, M.J., Polk, J.D., Hallgrimsson, B. et al. (2006) Trabecular bone in the bird knee responds with high sensitivity to changes in load orientation. *Journal of Experimental Biology*, 209(1), 57–65.

Pontzer, H., Raichlen, D.A. & Sockol, M.D. (2009) The metabolic cost of walking in humans, chimpanzees, and early hominins. *Journal of Human Evolution*, 56(1), 43–54.

Preuschof, H. & Tardieu, C. (1996) Biomechanical reasons for the divergent morphology of the knee joint and the distal epiphyseal suture in hominoids. *Folia Primatologica*, 66(1–4), 82–92.

Racic, V., Pavic, A. & Brownjohn, J.M.W. (2009) Experimental identification and analytical modelling of human walking forces: literature review. *Journal of Sound and Vibration*, 326(1–2), 1–49.

Rafferty, K.L. (1998) Erratum structural design of the femoral neck in primates. *Journal of Human Evolution*, 35, 109–383.

Raichlen, D.A., Gordon, A.D., Harcourt-Smith, W.E., Foster, A.D. & Haas, W.R., Jr. (2010) Laetoli footprints preserve earliest direct evidence of human-like bipedal biomechanics. *PLoS One*, 5(3), e9769.

Remis, M. (1995) Effects of body size and social context on the arboreal activities of lowland gorillas in the Central African Republic. *American Journal of Physical Anthropology*, 97(4), 413–433.

Remis, M.J. (1994) *Feeding ecology and positional behavior of western lowland gorillas (Gorilla gorilla gorilla) in the Central African Republic*. Ph.D. dissertation. Yale University Press London.

Rodan, G.A. (1997) Bone mass homeostasis and bisphosphonate action. *Bone*, 20(1), 1–4.

Rubin, C., Turner, A.S., Mallinckrodt, C., Jerome, C., McLeod, K. & Bain, S. (2002) Mechanical strain, induced noninvasively in the high-frequency domain, is anabolic to cancellous bone, but not cortical bone. *Bone*, 30(3), 445–452.

Rueckert, D., Frangi, A.F. & Schnabel, J.A. (2003) Automatic construction of 3-D statistical deformation models of the brain using nonrigid registration. *IEEE Transactions on Medical Imaging*, 22(8), 1014–1025.

Ruff, C., Holt, B. & Trinkaus, E. (2006) Who's afraid of the big bad Wolff?:"Wolff's law" and bone functional adaptation. *American Journal of Physical Anthropology: The Official Publication of the American Association of Physical Anthropologists*, 129(4), 484–498.

Ruff, C.B. (2002) Long bone articular and diaphyseal structure in Old World monkeys and apes. I: locomotor effects. *American Journal of Physical Anthropology: The Official Publication of the American Association of Physical Anthropologists*, 119(4), 305–342.

Ruff, C.B., Burgess, M.L., Bromage, T.G., Mudakikwa, A. & McFarlin, S.C. (2013) Ontogenetic changes in limb bone structural proportions in mountain gorillas (*Gorilla beringei beringei*). *Journal of Human Evolution*, 65(6), 693–703.

Ryan, T.M. & Ketcham, R.A. (2002) The three-dimensional structure of trabecular bone in the femoral head of Strepsirrhine primates. *Journal of Human Evolution*, 43(1), 1–26.

Ryan, T.M. & Shaw, C.N. (2013) Trabecular bone microstructure scales allometrically in the primate humerus and femur. *Proceedings of the Royal Society B: Biological Sciences*, 280(1758), 20130172.

Ryan, T.M., Stephens, N., Doershuk, L.J., Saers, J.P., Jashashvili, T., Carlson, K.J. et al. (2019) Trabecular bone structural variation in the human postcranial skeleton. *The FASEB Journal*, 33(S1), 19.2.

Ryan, T.M. & Walker, A. (2010) Trabecular bone structure in the humeral and femoral heads of anthropoid primates. *The Anatomical Record: Advances in Integrative Anatomy and Evolutionary Biology*, 293(4), 719–729.

Saers, J.P., Cazorla-Bak, Y., Shaw, C.N., Stock, J.T. & Ryan, T.M. (2016) Trabecular bone structural variation throughout the human lower limb. *Journal of Human Evolution*, 97, 97–108.

Saers, J.P., Gordon, A.D., Ryan, T.M. & Stock, J.T. (2022) Trabecular bone ontogeny tracks neural development and life history among humans and non-human primates. *Proceedings of the National Academy of Sciences*, 119(49), e2208772119.

Saers, J.P., Ryan, T.M. & Stock, J.T. (2019) Trabecular bone functional adaptation and sexual dimorphism in the human foot. *American Journal of Physical Anthropology*, 168(1), 154–169.

Saers, J.P., Ryan, T.M. & Stock, J.T. (2020) Baby steps towards linking calcaneal trabecular bone ontogeny and the development of bipedal human gait. *Journal of Anatomy*, 236(3), 474–492.

Saparin, P., Scherf, H., Hublin, J.J., Fratzl, P. & Weinkamer, R. (2011) Structural adaptation of trabecular bone revealed by position resolved analysis of proximal femora of different primates. *The Anatomical Record: Advances in Integrative Anatomy and Evolutionary Biology*, 294(1), 55–67.

Scorrer, J., Faillace, K.E., Hildred, A., Nederbragt, A.J., Andersen, M.B., Millet, M.A. et al. (2021) Diversity aboard a Tudor warship: investigating the origins of the Mary Rose crew using multi-isotope analysis. *Royal Society Open Science*, 8(5), 202106.

Seeman, E. (2003) Invited review: pathogenesis of osteoporosis. *Journal of Applied Physiology*, 95(5), 2142–2151.

Shaw, C.N. & Ryan, T.M. (2012) Does skeletal anatomy reflect adaptation to locomotor patterns? Cortical and trabecular architecture in human and nonhuman anthropoids. *American Journal of Physical Anthropology*, 147(2), 187–200.

Simpson, K.J. & Pettit, M.I.C.H.A.E.L. (1997) Jump distance of dance landings influencing internal joint forces: II. Shear forces. *Medicine and Science in Sports and Exercise*, 29(7), 928–936.

Sinclair, K.D., Farnsworth, R.W., Pham, T.X., Knight, A.N., Bloebaum, R.D. & Skedros, J.G. (2013) The artiodactyl calcaneus as a potential 'control bone' cautions against simple interpretations of trabecular bone adaptation in the anthropoid femoral neck. *Journal of Human Evolution*, 64(5), 366–379.

Skinner, M., Tsegai, Z.J., Kivell, T.L., Gross, T., Nguyen, N.H., Pahr, D.H. et al. (2013) Trabecular bone structure correlates with hand posture and use in hominoids. *PLoS One*, 8(11), 1–14.

Skinner, M.M., Stephens, N.B., Tsegai, Z.J., Foote, A.C., Nguyen, N.H., Gross, T. et al. (2015) Human-like hand use in *Australopithecus africanus*. *Science*, 347(6220), 395–399.

Smith, R.J. & Jungers, W.L. (1997) Body mass in comparative primatology. *Journal of Human Evolution*, 32(6), 523–559.

Spoor, C.W. & Van Leeuwen, J.L. (1992) Knee muscle moment arms from MRI and from tendon travel. *Journal of Biomechanics*, 25(2), 201–206.

Steiner, L., Synek, A. & Pahr, D.H. (2021) Femoral strength can be predicted from 2D projections using a 3D statistical deformation and texture model with finite element analysis. *Medical Engineering & Physics*, 93, 72–82.

Stephens, N.B., Kivell, T.L., Gross, T., Pahr, D.H., Lazenby, R.A., Hublin, J.J. et al. (2016) Trabecular architecture in the thumb of *Pan* and *Homo*: implications for investigating hand use, loading, and hand preference in the fossil record. *American Journal of Physical Anthropology*, 161(4), 603–619.

Stern, J.T., Jr. & Susman, R.L. (1981) Electromyography of the gluteal muscles in *Hylobates*, *Pongo*, and *Pan*: implications for the evolution of hominid bipedality. *American Journal of Physical Anthropology*, 55(2), 153–166.

Stern, J.T., Jr. & Susman, R.L. (1983) The locomotor anatomy of *Australopithecus afarensis*. *American Journal of Physical Anthropology*, 60(3), 279–317.

Stirland, A.J. & Waldron, T. (1997) Evidence for activity related markers in the vertebrae of the crew of the Mary Rose. *Journal of Archaeological Science*, 24(4), 329–335.

Su, A., Wallace, I.J. & Nakatsukasa, M. (2013) Trabecular bone anisotropy and orientation in an Early Pleistocene hominin talus from East Turkana, Kenya. *Journal of Human Evolution*, 64(6), 667–677.

Sugiyama, T., Neuhaus, M., Cole, R., Giles-Corti, B. & Owen, N. (2012) Destination and route attributes associated with adults' walking: a review. *Medicine and Science in Sports and Exercise*, 44(7), 1275–1286.

Sukhdeo, S., Parsons, J., Niu, X.M. & Ryan, T.M. (2020) Trabecular bone structure in the distal femur of humans, apes, and baboons. *The Anatomical Record*, 303(1), 129–149.

Susman, R.L. (1991) Who made the Oldowan tools? Fossil evidence for tool behavior in Plio-Pleistocene hominids. *Journal of Anthropological Research*, 47(2), 129–151.

Susman, R.L., Stern, J.T. & Jungers, W.L. (1984) Arboreality and bipedality in the Hadar hominids. *Folia Primatologica*, 43(2–3), 113–156.

Sylvester, A.D. (2013) A geometric morphometric analysis of the medial tibial condyle of African hominids. *The Anatomical Record*, 296(10), 1518–1525.

Sylvester, A.D., Mahfouz, M.R. & Kramer, P.A. (2011) The effective mechanical advantage of AL 129-1a for knee extension. *The Anatomical Record: Advances in Integrative Anatomy and Evolutionary Biology*, 294(9), 1486–1499.

Sylvester, A.D. & Organ, J.M. (2010) Curvature scaling in the medial tibial condyle of large bodied hominoids. *The Anatomical Record: Advances in Integrative Anatomy and Evolutionary Biology*, 293(4), 671–679.

Sylvester, A.D. & Pfisterer, T. (2012) Quantifying lateral femoral condyle ellipticalness in chimpanzees, gorillas, and humans. *American Journal of Physical Anthropology*, 149(3), 458–467.

Sylvester, A.D. & Terhune, C.E. (2017) Trabecular mapping: leveraging geometric morphometrics for analyses of trabecular structure. *American Journal of Physical Anthropology*, 163(3), 553–569.

Tardieu, C. (1999) Ontogeny and phylogeny of femoro-tibial characters in humans and hominid fossils: functional influence and genetic determinism. *American Journal of Physical Anthropology: The Official Publication of the American Association of Physical Anthropologists*, 110(3), 365–377.

Taylor, W.R., Heller, M.O., Bergmann, G. & Duda, G.N. (2004) Tibiofemoral loading during human gait and stair climbing. *Journal of Orthopaedic Research*, 22(3), 625–632.

Thompson, N.E., Ostrofsky, K.R., McFarlin, S.C., Robbins, M.M., Stoinski, T.S. & Almecija, S. (2018) Unexpected terrestrial hand posture

diversity in wild mountain gorillas. *American Journal of Physical Anthropology*, 166(1), 84–94.

Thomsen, J.S., Laib, A., Koller, B., Prohaska, S., Mosekilde, L.I. & Gowin, W. (2005) Stereological measures of trabecular bone structure: comparison of 3D micro computed tomography with 2D histological sections in human proximal tibial bone biopsies. *Journal of Microscopy*, 218(2), 171–179.

Thorpe, S.K. & Crompton, R.H. (2005) Locomotor ecology of wild orangutans (*Pongo pygmaeus abelii*) in the Gunung Leuser Ecosystem, Sumatra, Indonesia: a multivariate analysis using log-linear modelling. *American Journal of Physical Anthropology: The Official Publication of the American Association of Physical Anthropologists*, 127(1), 58–78.

Thorpe, S.K. & Crompton, R.H. (2006) Orangutan positional behavior and the nature of arboreal locomotion in Hominoidea. *American Journal of Physical Anthropology: The Official Publication of the American Association of Physical Anthropologists*, 131(3), 384–401.

Thorpe, S.K., Holder, R. & Crompton, R.H. (2009) Orangutans employ unique strategies to control branch flexibility. *Proceedings of the National Academy of Sciences*, 106(31), 12646–12651.

Thorpe, S.K., Holder, R.L. & Crompton, R.H. (2007) Origin of human bipedalism as an adaptation for locomotion on flexible branches. *Science*, 316(5829), 1328–1331.

Tocheri, M.W., Solhan, C.R., Orr, C.M., Femiani, J., Frohlich, B., Groves, C.P. et al. (2011) Ecological divergence and medial cuneiform morphology in gorillas. *Journal of Human Evolution*, 60(2), 171–184.

Tsegai, Z.J., Skinner, M.M., Gee, A.H., Pahr, D.H., Treece, G.M., Hublin, J.J. et al. (2017) Trabecular and cortical bone structure of the talus and distal tibia in *Pan* and *Homo*. *American Journal of Physical Anthropology*, 163(4), 784–805.

Tsegai, Z.J., Skinner, M.M., Pahr, D.H., Hublin, J.J. & Kivell, T.L. (2018) Ontogeny and variability of trabecular bone in the chimpanzee humerus, femur and tibia. *American Journal of Physical Anthropology*, 167(4), 713–736.

Tsegai, Z.J., Stephens, N.B., Treece, G.M., Skinner, M.M., Kivell, T.L. & Gee, A.H. (2017) Cortical bone mapping: an application to hand and foot bones in hominoids. *Comptes Rendus Palevol*, 16(5–6), 690–701.

Turner, C.H., Hsieh, Y.F., Müller, R., Bouxsein, M.L., Baylink, D.J., Rosen, C.J. et al. (2000) Genetic regulation of cortical and trabecular bone strength and microstructure in inbred strains of mice. *Journal of Bone and Mineral Research*, 15(6), 1126–1131.

Van Rietbergen, B., Odgaard, A., Kabel, J. & Huiskes, R. (1998) Relationships between bone morphology and bone elastic properties can be accurately quantified using high-resolution computer reconstructions. *Journal of Orthopaedic Research*, 16(1), 23–28.

Visser, J.J., Hoogkamer, J.E., Bobbert, M.F. & Huijing, P.A. (1990) Length and moment arm of human leg muscles as a function of knee and hip-joint angles. *European Journal of Applied Physiology and Occupational Physiology*, 61, 453–460.

Volpato, V., Viola, T.B., Nakatsukasa, M., Bondioli, L. & Macchiarelli, R. (2008) Textural characteristics of the iliac-femoral trabecular pattern in a bipedally trained Japanese macaque. *Primates*, 49, 16–25.

Wallace, I.J., Kwaczala, A.T., Judex, S., Demes, B. & Carlson, K.J. (2013) Physical activity engendering loads from diverse directions augments the growing skeleton. *Journal of Musculoskeletal & Neuronal Interactions*, 13(3), 283–288.

Wanner, J.A. (1977) Variations in the anterior patellar groove of the human femur. *American Journal of Physical Anthropology*, 47(1), 99–102.

Whitehouse, W.J. (1977) Cancellous bone in the anterior part of the iliac crest. *Calcified Tissue Research*, 23, 67–76.

Zaharie, D.T. & Phillips, A.T. (2018) Pelvic construct prediction of trabecular and cortical bone structural architecture. *Journal of Biomechanical Engineering*, 140(9), 091001.

Zheng, N., Fleisig, G.S., Escamilla, R.F. & Barrentine, S.W. (1998) An analytical model of the knee for estimation of internal forces during exercise. *Journal of Biomechanics*, 31(10), 963–967.

Zihlman, A.L., Mcfarland, R.K. & Underwood, C.E. (2011) Functional anatomy and adaptation of male gorillas (*Gorilla gorilla gorilla*) with comparison to male orangutans (*Pongo pygmaeus*). *The Anatomical Record: Advances in Integrative Anatomy and Evolutionary Biology*, 294(11), 1842–1855.

Zysset, P.K. (2003) A review of morphology–elasticity relationships in human trabecular bone: theories and experiments. *Journal of Biomechanics*, 36(10), 1469–1485.

SUPPORTING INFORMATION

Additional supporting information can be found online in the Supporting Information section at the end of this article.

How to cite this article: Lukova, A., Dunmore, C.J., Bachmann, S., Synek, A., Pahr, D.H., Kivell, T.L. et al. (2024) Trabecular architecture of the distal femur in extant hominids. *Journal of Anatomy*, 00, 1–25. Available from: https://doi.org/10.1111/joa.14026